Evolution in the palm of the human hand: Functional inferences from internal bone architecture in great apes and fossil hominins

Christopher J. Dunmore

School of Anthropology and Conservation

University of Kent

A thesis submitted in fulfilment of the requirements for the degree of Doctor of Philosophy in Anthropology at the University of Kent, March 2019.

"On becoming terrestrial the hand was never then 'freed' from branch-holding, it brought the branch with it…"

-Richards, 1986, pp.146

Acknowledgements

First and foremost I would like to thank my PhD supervisors Matt Skinner and Tracy Kivell for always pushing and supporting me throughout this process, while keeping my verbosity in check. I could not have asked for better supervisors and I believe you have each made me a better scientist. I would also like to extend my thanks to Nick Stephens for teaching me the finer points of medtool and for, with Zewdi Tsegai, providing stimulating technical discussions. I am grateful to Leoni Georgiou for rich discussion of trabecular analysis, entertaining my 'crazy ideas' and enduring my abuse of computer equipment. I offer my thanks to Ameline Bardo, who has provided me both technical support and lively discourse on ape hand use. I would also like to extend my thanks to Alastair Key who encouraged me to apply for this PhD position in the first place. Of course, I am also grateful to my parents Tim and Jan Dunmore, who supported me through the 'corporate years' and encouraged me to do something that inspires me. Last, but emphatically not least, I would like to thank Caroline Westoby for her constant and caring support over the last few years.

Contents

Acknowledgements iii
Contents iv
List of Figures vi
List of Tables viii
List of Abbreviations ix
General Introduction x
The scientific problem x
Aims xi
Overview xii
Chapter 1 General Background 1
Great ape hand morphology and grips 1
Inferring hand function in fossil hominins 7
The locomotion of Australopithecus afarensis 13
Bone functional adaptation 16
Other influences on internal bone structure 20
Inferring bone functional adaptation 30
Inferring primate hand use from trabecular architecture 30
The current project 37
Chapter 2 Materials and Methods 40
Materials 40
Methodology 45
Chapter 3 MIA-Clustering: A novel method for segmentation of paleontological material . 69
Abstract 69
Introduction 70
Materials 73
Methods 73
Results 78
Discussion 83
Conclusion 90

Chapter 4 Metacarpal trabecular bone varies with distinct hand-positions used in hominid locomotion 91
Abstract 91
Introduction 92
Hand use and locomotion 94
Predictions 99
Materials 100
Methods 103
Results 112
Discussion 128
Conclusion 140
Chapter 5 Trabecular variation in the first metacarpal reflects distinctive human manipulation among hominids 141
Abstract 141
Introduction 142
Locomotion, manipulation and thumb morphology 145
Predictions 152
Materials 153
Methods 154
Results 162
Discussion 171
Conclusion 177
Chapter 6 Fossil hominin hand use: Evidence for arboreality and human-like manipulation in *Australopithecus* 178
Abstract 178
Introduction 179
Predictions 181
Methods 183
Results 193
Discussion 203
Conclusion 206
Chapter 7 General Discussion and Conclusion 207
Limitations of analysing internal bone structure 207
The current limits of functional inference 209
Functional units of the great ape hand 210

Gorilla *as a model for the hominin hand* 211
Pongo *and trabecular anisotropy* 215
Pan *and the biomechanical significance of the non-human great ape thumb* 216
The significance of dorsal ridges on the metacarpal head 220
Human grips and the role of the fifth digit 221
Implications for the evolution of the hominin hand use 223
Conclusion 228
Current limitations and future directions 229
References 230
Appendix A Scanning Protocol and Samples 263
Scanning protocol 264
Samples analysed 265
Fossil samples not analysed 268
Appendix B Published work 269

List of Figures

Figure 2.1. Example of *Gorilla* metacarpophalangeal joints articulated by wire. 42
Figure 2.2. Example of specimen identification in data collection protocol. 44
Figure 2.3. Elements of several *Pongo* individuals. 45
Figure 2.4. Elements of the scanning process. 46
Figure 2.5. Example of cropping and cleaning specimens. 47
Figure 2.6. Example of image orientation steps on a right third metacarpal from a *Pan paniscus* individual. 48
Figure 2.7. Example of RCA segmentation steps. 50
Figure 2.8. Example of image processing steps in medtool. 58
Figure 2.9. Illustration of geometric morphometric mapping procedure. 62
Figure 2.10. Example of metacarpal reorientation procedure for cross-sectional geometry. 68
Figure 3.1. Diagram of MIA-Clustering algorithm in a 2D-image. 75
Figure 3.2. A 2D cross-section image of an example dry bone. 76
Figure 3.3. A 3D-surface view of the machined wire phantom. 77
Figure 3.4. The mid-slice of the wire scan in superior view. 79
Figure 3.5. A magnified section of the mid-slice of the wire phantom scan (Fig. 3.4) in superior view. 80
Figure 3.6. The effect of MIA-Clustering algorithm parameters on average thickness of the wire. 81

Figure 3.7. The effect of grid-size input on average thickness estimates of the fossil, after MIA-Clustering segmentation. 81
Figure 3.8. Cross-section (XY plane) through the fossil at various stages of segmentation using RCA and MIA-Clustering. 89
Figure 4.1. Diagrammatic representations of the metacarpophalangeal postures 94
Figure 4.2. Repeatability tests of landmarks. 106
Figure 4.3. Landmark template projected onto Mc3s of individual specimens 107
Figure 4.4. Methodological stages of metacarpal trabecular analysis 109
Figure 4.5. Species average absolute BV/TV 110
Figure 4.6. Species average RBV/TV 113
Figure 4.7. Species average DA 114
Figure 4.8. Inter-ray significant differences in RBV/TV 116
Figure 4.9. Inter-ray significant differences in DA 116
Figure 4.10. Significant differences in RBV/TV between species 118
Figure 4.11. Significant differences in DA between species 119
Figure 4.12. RBV/TV PCA plots showing species differences within each metacarpal head 122
Figure 4.13. RBV/TV PCA plots showing ray differences within each species. 123
Figure 4.14. DA PCA plots showing species differences within each metacarpal head. 125
Figure 4.15. DA PCA plots showing ray differences within each species. 128
Figure 4.16. The right hand of a captive orangutan engaged in a diagonal 'double-locked' grip around a piece of string. 130
Figure 4.17. *Gorilla* average RBV/TV by sex 131
Figure 5.1. Repeatability tests of landmarks. 158
Figure 5.2. Stages of Mc1 trabecular analysis. 161
Figure 5.3. Species Average trabecular values 163
Figure 5.4. Significant univariate differences in RBV/TV between species 166
Figure 5.5. Significant univariate differences in DA between species 167
Figure 5.6. PCA plots showing species differences within the first metacarpal head trabecular structure 168
Figure 5.7. PCA plots showing species differences within the first metacarpal base trabecular structure 169
Figure 6.1. Trabecular analysis method 189
Figure 6.2. Cross-sectional analysis method 191
Figure 6.3. Average relative trabecular bone (RBV/TV) distribution in great ape metacarpals during habitual hand postures. 194
Figure 6.4. Relative trabecular bone volume fraction (RBV/TV) distribution in the metacarpal heads of the palm. 195
Figure 6.5. Relative trabecular bone volume fraction (RBV/TV) distribution in the first metacarpal. 196
Figure 6.6. Relative cortical rigidity of first metacarpals at 50% diaphyseal mid-slice. 199
Figure 6.7. Extant species average distributions of subchondral RBV/TV across the metacarpus 201
Figure 6.8. Distributions of RBV/TV across fossil hominin metacarpi 202

List of Tables

Table 3.1. Mean and standard deviation of thickness calculated for each segmentation method. 79
Table 3.2. Summary of subjective user decisions minimized by the MIA-Clustering Algorithm. 86
Table 4.1. Study sample 101
Table 4.2. Anatomical landmark definitions 105
Table 4.3. Descriptive statistics of absolute *Z*-scores from significant pairwise inter-species landmark comparisons 120
Table 4.4. Descriptive statistics of absolute *Z*-scores from significant pairwise inter-ray landmark comparisons. 121
Table 4.5. Permutational MANOVAs on the first three principle components between all groups. 127
Table 5.1. Study sample enumerated by sex and side. 154
Table 5.2. Mc1 head anatomical landmark definitions 156
Table 5.3. Mc1 base anatomical landmark definitions. 157
Table 5.4. Descriptive statistics of absolute *Z*-scores from Mc1 significant pairwise landmark comparisons 165
Table 5.5. Permutational MANOVAs on the first three principle components between all groups. 170
Table 6.1. Extant sample composition. 184
Table 6.2. Fossil sample composition. 185
Table 6.3. Extant species trabecular comparisons. 196
Table 6.4. Fossil comparisons to extant species. 197
Table 6.5. Extant group and individual fossil sample comparisons of cross-sectional geometry variables. 200

List of Abbreviations

µCT	Micro-Computed Tomography (Micro-CT)
BV/TV	Bone Volume /Total Volume (bone volume fraction)
BMD	Bone Mineral Density
CGAL	Computational Geometry Algorithms Library
CMc joint	Carpometacarpal joint
CSG	Cross-Sectional Geometry
DA	Degree of Anisotropy
FPL	Flexor Pollicis Longus
Ggg	*Gorilla gorilla gorilla*
GM	Geometric Morphometrics
GRF	Ground Reaction Force
Hs	*Homo sapiens*
Iavg	Average (mean) area moment of inertia
IAP	Area moment of inertia, in the Anterior-Posterior plane
IML	Area moment of inertia, in the Medio-Lateral plane
kya	Thousands of years ago
Mc1	First Metacarpal
Mc2	Second Metacarpal
Mc3	Third Metacarpal
Mc4	Forth Metacarpal
Mc5	Fifth Metacarpal
Mc2-5	Non-pollical metacarpus
McP joint	Metacarpophalangeal joint
MIA	Medical Image Analysis
mya	Millions of years ago
PC	Principle Component
PCA	Principle Component Analysis
PCSA	Physiological Cross-Sectional Area
Pp	*Pan paniscus*
Ppy	*Pongo* spp.
Pt	*Pan troglodytes*
PTO	Principle Trabecular Orientation
RBV/TV	Relative Bone Volume/Total Volume (relative bone volume fraction)
RCA	Ray Casting Algorithm
Tb.N	Trabecular Number
Tb.Sp	Trabecular Spacing
Tb.Th	Trabecular Thickness
TMc joint	Trapeziometacarpal joint
VOI	Volume of Interest

General Introduction

The scientific problem

When and how did arboreal environments become less important, and technology become more important, for hominin survival? This fundamental question of our own evolution has been a focus of palaeoanthropological and archaeological debate for over a century. Wood-Jones (1916) may be retro-actively credited with the most succinct summary of this debate in the title of his work "Arboreal Man". Perhaps the most widely cited and accepted defining characteristic of a hominin is bipedalism (Harcourt-Smith and Aiello, 2004; DeSilva, 2009). Traditionally, the transition from arboreal locomotion to terrestrial bipedalism was thought to free the hands of locomotor selection pressures and allow them to be used for forceful precision manipulation (Napier, 1962). In turn, this manipulative ability allowed for the advent of complex hominin technology, access to novel ecological niches and more human-like cognition, though which of these traits came first is also unresolved (Kimbel and Villmoare, 2016). The discovery of "Lucy" (AL-288-1), a relatively complete *Australopithecus afarensis* skeleton (Johanson et al., 1982), subsequently sparked debate about this genus, common to eastern and South Africa. While several *Australopithecus* species were clearly bipedal, the functional interpretation of their more ape-like traits was debated (Ricklan, 1987; Kimbel and Delezene, 2009; Berger et al., 2010). Some researchers view these traits as retentions from a more arboreal ancestor (Latimer, 1991), an example of phylogenetic inertia, while others view them as functional and indicative of some arboreality in a species not yet fully committed to terrestrial bipedalism (Stern and Susman, 1983). Hominins were certainly capable of precision grips at least 3.3 million years ago as evidenced by stone tool technology (Harmand et al., 2015). However, this need not preclude the use of the hand in arboreal locomotion as forceful precision grips, if not their habitual use, are also used by extant hominids* that have a significant arboreal component in their locomotor repertoire (Marzke et al., 2015).

* Throughout this work, the term hominid is used to refer to humans and other great apes, whereas hominin is reserved for species more closely related to modern humans than chimpanzees (Crompton, 2016). Similarly, the term great ape here includes: humans, chimpanzees, bonobos, gorillas and orangutans.

The hand of *Australopithecus* offers a microcosm of the broader scientific problem. If species of this genus did use their hands for both arboreal locomotion and habitual forceful precision grips, the transition to bipedalism in hominins could be interpreted as more gradual. However, if this hand was used solely for manipulation, it suggests that at least some members of *Australopithecus* had become fully committed to terrestrial bipedalism, as we are today. This thesis is therefore concerned with a facet of the broader problem; are the morphological features associated with arboreal locomotion in the hand of *Australopithecus* functional or not?

Aims

The present work aims to address this scientific problem via the analysis of the internal structure of osteological and fossil material. Specifically the trabecular, or cancellous, epiphyseal structure and the cortical diaphyseal structure of long bones, have been experimentally demonstrated to change in response to loads they experience during life. This process, known as 'bone functional adaptation' (Cowin et al., 1985; Ruff et al., 2006), holds that bone will functionally adapt to its mechanical environment and so its architecture may be used to infer the behaviours that are consistent with this environment. Therefore, this internal bone architecture can be used to infer loads experienced by fossil hominin hands and thus hand postures used in arboreal locomotion or manipulation, consistent with these loads. The following analyses focus on metacarpals because they are the long bones of the hand, amenable to diaphyseal and trabecular analysis. The metacarpophalangeal joints are bi-axial, while the trapeziometacarpal joint is further mobile, and together they provide a range of potentially loaded hand postures adopted in different grips. The internal bone architecture of fossil and osteological hand bones was analysed via micro-computed tomography. This analysis proceeded in three stages.

First, this thesis aims to link the trabecular structure of the second to fifth metacarpals of extant hominids to what is known about their hand loading during their diverse habitual locomotor repertoires. Secondly, the trabecular structure of the first metacarpal of extant hominids is assessed in light of observed manipulative

grips habitually used by hominids, including modern humans. Finally, both the cortical and trabecular structure of the whole hominid metacarpus are brought together, to infer the habitual postures in which fossil hominin hands were likely habitually loaded.

Overview

Chapter 1 - General Background

Chapter 1 contextualises the scientific problem within an in-depth discussion of the manual fossil record and bone functional adaptation. It describes in detail why functional inference based on external fossil morphology alone is open to interpretative debate.

Chapter 2 - Materials and Methods

Chapter 2 describes the methods employed, from a hand bone on the collection bench to an analysed, segmented virtual model. It also provides a rationale for each successive stage of analysis.

Chapter 3 - MIA-Clustering: A novel method for segmentation of paleontological material

While mentioned in Chapter 2, this chapter presents the detailed description and testing of a new method of image segmentation, developed for the present thesis, in order to accurately delineate trabecular morphology in fossils: MIA-Clustering.

Chapter 4 - Metacarpal trabecular bone varies with distinct hand-positions used in hominid locomotion

Chapter 4 validates the assumption that the trabecular structure of the second to fifth metacarpals of extant hominids is consistent with what is known about hand loading, during the diverse habitual locomotor repertoires, of hominids. It provides validation of the method developed to test for inter-specific differences in trabecular distribution and, unexpectedly, provides a method of informal falsification for the current mode of fossil hominin behavioural inference.

Chapter 5 - Trabecular variation in the first metacarpal reflects distinctive human manipulation among hominids

Chapter 5 validates the assumption that the trabecular structure of the first metacarpal of extant hominids is consistent with the observed manipulative grips habitually used by great apes, including modern humans.

Chapter 6 - Fossil hominin hand use: Evidence for arboreality and human-like manipulation in *Australopithecus*

This chapter infers the likely grips of fossil hominins from both their trabecular and cortical structure. Importantly, it brings together all of the rays in a holistic analysis of internal fossil morphology, in the context of internal bone structure consistent with arboreal and manipulative grips practised by extant hominids.

Chapter 7 - Discussion and Conclusion

This chapter discusses how far the present results resolve the initial scientific problem and what we can say about fossil hominin hand use. Further this chapter acknowledges the limitations of the current approach and what future data or methodologies may ameliorate them.

Chapter 1

General Background

In order to understand when arboreal environments became less important for extinct hominins, such as *Australopithecus,* this thesis infers their hand use via internal bone morphology. This chapter begins by describing features of extant great ape hands and how these features have been associated with hand use in these species. How these features have been used to infer fossil hominin behaviour and the limitations of these approaches are then discussed, with special reference to the debate surrounding the locomotion of *Australopithecus*. Previous studies that have employed internal bone morphology to infer primate and fossil hominin behaviour have had varying success. The limitations of these more recent methodologies are also considered, and the present approach, both methodological and theoretical, is discussed in light of these studies.

Great ape hand morphology and grips

The anatomically modern human hand is easily distinguished among extant hominoids by its relatively short fingers and long, robust, well-muscled thumb (Huxley, 1863; Napier, 1962; Susman and Creel, 1979; Marzke and Shackley, 1986; Napier, 1993; Susman, 1998; Marzke et al., 1999; Tocheri et al., 2008; Almécija et al., 2015). These features of the thumb combined with a broad, moderately-curved sellar facet at the trapeziometacarpal (TMc) joint, broad apical phalangeal tufts, differently oriented radial carpals and a mobile fifth digit, have all been associated with enhanced human manipulation (Marzke and Shackley, 1986; Marzke, 1997; Tocheri, 2007; Tocheri et al., 2008; Almécija et al., 2010; Marzke, 2013; Kivell, 2015). The unique aspects of human manipulation compared with other primates have traditionally included habitual forceful precision grips (Marzke and Wullstein, 1996; Marzke, 1997), power ‘squeeze’ grips (Marzke et al., 1992) and precision in-hand manipulation (Christel, 1993; Fragaszy and Crast, 2016). Forceful precision grips involve securing an object between the fingers with little to no aid from the palm and are considered critical to lithic tool production, an activity known to have

occurred from at least 3.3 million years ago (Harmand et al., 2015). For example, a '3-jaw-chuck' forceful precision grip, in which the object is held by the second and third fingers forcefully opposing the thumb (like when grasping a baseball; Marzke and Shackley, 1986), is often the focus of discussion as it is used to hold hammerstones during lithic production (Marzke and Shackley, 1986; Marzke et al., 1998; Williams et al., 2012; Key et al., 2018). Such a grip is facilitated by a relatively high thumb to finger length ratio in humans compared with other hominoids (Napier, 1993; Almécija et al., 2015).

The morphology of the radial side of the human hand has been interpreted as advantageous for forceful precision grips. A moderately flat trapezial facet for the first metacarpal (Rafferty, 1990; Marzke et al., 2010) combined with a relatively short palmar beak at the base of the human first metacarpal (Niewoehner, 2005; Marchi et al., 2017) is thought to permit the compound abduction, flexion and axial rotation of the first metacarpal required for thumb opposition (D'Agostino et al., 2017). This morphology has been interpreted as a compromise between joint mobility and stability, required for forceful precision grips, such as those employed during lithic production (Tocheri, 2007; Marzke et al., 2010; Marzke, 2013). The broad flat surface of this articulation is thought to better dissipate large loads from the thumb (Marzke et al., 2010). During tool-related manipulation, external load is greatest at the first distal phalanx (Key and Dunmore, 2015; Williams-Hatala et al., 2018), and translated into increasingly higher loads at successively more proximal manual joints (Cooney and Chao, 1977; Rolian et al., 2011). The broad apical tufts of the distal phalanges, as well as the ability to passively dorsiflex the distal interphalangeal joints (Christel, 1993), are thought to provide a greater area for pad-to-pad opposition in humans (Marzke, 2013) and may also assist in dissipating strong forces, at least in the thumb, though baboons also possess broad apical tufts (Shrewsbury, 2003). The greater forces apparently resisted by the thumb relative to other digits in humans, may also be related to a significantly stronger first metacarpal diaphyseal shaft (Wong et al., 2018). The forces present in a forceful precision grips are the result of large thenar muscles, with significantly longer moment arms in humans relative to other apes (Marzke et al., 1999).

Many elements of the hand and wrist are also thought to aid human manipulation. The second metacarpal head is asymmetric in humans as it is radio-palmarly expanded, causing the index finger to pronate during flexion allowing more opposition of the second distal phalanx with an object (Lewis, 1977; Marzke, 1997). Below the second metacarpal, the human trapezoid is more proximo-distally oriented and palmarly expanded than in other great apes, creating its 'boot' shape (Marzke, 1997; 2013; Tocheri et al., 2005). This reorientation has also been argued to more efficiently dissipate radio-ulnar forces incurred in precision grips, such as those transmitted through the thumb during lithic production and use (Lewis, 1989; Tocheri, 2007; Rolian et al., 2011; Marzke, 2013). Unique to humans, the styloid process at the base of the third metacarpal has also been related to stabilising the wrist against large radial forces and thus preventing subluxation (Marzke and Marzke, 1987). Hypothenar muscles of the fifth metacarpal were found to play a critical role in object manipulation during lithic production (Marzke et al., 1998; 2013).The sellar-shaped fifth carpometacarpal (CMc) joint in humans allows the hand to be 'cupped' and when combined with a palmo-ulnarly expanded fifth metacarpal head (Lewis, 1977; Marzke, 1997), allows effective opposition the fifth digit to the thumb or held objects (Domalain, et al., 2017). The fifth ray is also argued to be important for power 'squeeze' grips (Marzke, 1992; 1997). These grips are unique to humans and, unlike forceful precision grips, involve 'cupping' a cylindrical object between thenar and hypothenar eminences of the palm, while the thumb is adducted with considerable force and controls the direction in which force is applied to the object (Marzke et al., 1992). Power 'squeeze' grips have been identified in lithic manipulation (Key et al., 2018) and make use of the unique morphology of the fifth ray and its musculature.

Power grips, in which the palm is recruited, are more frequently practised by non-human great apes than humans, and are generally used for gripping arboreal substrates in locomotion. There is a paucity of evidence for non-human great ape hand use compared to humans. However, gorillas, chimpanzees and bonobos have all been observed, either in captive or wild settings, using diagonal power grips in which the branch lies diagonally across the palm and the fingers, with more flexion

in more ulnar rays (Marzke and Wullstein, 1996; Neufuss et al., 2017; Samuel et al., 2018). While differences exist, such as a less adducted (ulnarly deviated) wrist in a chimpanzee diagonal power grip compared to that of a mountain gorilla, these grips tend to be performed by African apes on substrates of smaller diameters, such as branches (Neufuss et al., 2017). Larger diameter substrates, such as tree a trunk, tend to be gripped by African apes with an orthogonal power grip using all five digits and the palm (Sarmiento, 1994; Neufuss et al., 2017). Smaller diameter substrates, such as terminal branches, are gripped by orangutans in 'double-locked' grips whereby all joints of the non-pollical, second to fifth, rays are flexed and the distal phalanx contacts its proximal phalanx (Sarmiento, 1988; Rose, 1988). Orangutans, as well as chimpanzees, also use 'hook' grips on medium-sized branches in which the fingers hook over the top of a branch, possibly with some support from the palm, and the individual is suspended below it (Rose, 1988; Hunt, 1991; Alexander, 1994).

In all of these grips, the long curved digits of non-human great apes are thought to be useful for gripping arboreal substrates as they can conform to their curved surfaces providing more surface area from friction and thus grip (Sarmiento, 1988; Hunt, 1991). Curvature in ape phalanges has also been related to suspension, suggesting that this curvature might act to resist strong anterior-posterior loads (Richmond, 2007; Nguyen et al., 2014). In either case, the strong flexor sheath ridges on non-human great ape phalanges (Susman, 1979) have likely developed in response to the strong flexor muscles required for habitual arboreal power grips. The long metacarpals of non-human apes are also thought to be a derived feature and evolved in parallel, perhaps in response to a similar orthograde arboreal locomotor repertoire (Almécija et al., 2015). In the wrist, extant African apes have a more radio-ulnar alignment of the second metacarpal articulations with the capitate and the trapezium, as well as a narrower 'waisted' capitate than humans and no styloid process in the base of the third metacarpal (Tocheri et al., 2008). This morphology has been argued to better withstand proximo-distal forces generated in arboreal locomotion and knuckle-walking, as well as strong compression of the wrist in the latter behaviour (Tocheri, 2007). This emphasis on proximo-distal forces

from the non-pollical rays during arboreal grasping is also mirrored in the diaphyseal robusticity of non-human great apes non-pollical metacarpals (Mc2-5; Susman, 1979; Marchi, 2005) and relatively similar non-pollical digit lengths in orangutans (Rose, 1988). However, the robusticity of the African ape metacarpals has often been directly linked to knuckle-walking (Susman, 1979; Marchi, 2005).

While not a prehensile hand posture, knuckle-walking, in which the metacarpophalangeal (McP) joints are hyperextended and weight is borne on the intermediate phalanges (Tuttle, 1967; 1969; Wunderlich and Jungers, 2009), is the dominate form of locomotion for African apes (Doran, 1996). Much as the long, strong non-pollical metacarpals of African apes are likely derived (Marchi, 2005; Almécija et al., 2015), differences in digit use between chimpanzees and gorillas (Inouye, 1992; 1994; Matarazzo, 2013), development (Inouye, 1994; Dainton and Macho, 1999) as well as potential differences in wrist posture (Kivell and Schmitt, 2009), suggest this behaviour may have evolved in parallel rather than from a common ancestor.

In non-human great apes, the first metacarpal is small and gracile relative to the non-pollical metacarpals (Susman, 1979). While the first ray is never recruited during knuckle-walking (Tuttle, 1969; Wunderlich and Jungers, 2009; Matarazzo, 2013; 2013b), there is some evidence for its use in arboreal grasping in both orangutans (McClure, 2012) and chimpanzees, but especially in mountain gorillas as they descend lianas (Neufuss et al., 2017). However, the thumb is recruited in the majority of precision grips practised by non-human great apes (Christel, 1993; Marzke et al., 2015; Bardo et al., 2016; 2017; Neufuss et al., 2018).

During manipulation all non-human great apes engage in power grips, especially when handing larger objects (Pouydebat et al., 2009; Neufuss et al., 2016; 2018). However, non-human great apes are also capable of many precision grips that involve the thumb, and most frequently practise ‘pad-to-side’ grips in which the thumb is opposed to the radial side of the second ray (Christel, 1993; Marzke and Wullstein, 1996; Neufuss et al., 2016; Bardo et al., 2016; 2017). Similarly the ‘V-pocket’ grip (Lesnik et al., 2015), in which the object is held in the webbing between

the full thumb and index finger is also practised by all non-human great apes (Marzke et al., 2015; Bardo et al., 2016; 2017; Neufuss et al., 2017; 2018). Though both of these grips appear to vary in frequency ,depending on species and whether individuals were captive or wild (Marzke et al., 2015), the common element is that the pad of the thumb is usually opposed to the side of the second ray rather than its pad. When necessary, such as when very small objects are gripped, non-human great apes are capable of 'tip-to-tip' grips in which the apex of the thumb and another finger meet, though this does not include opposition of their ungual pads (Christel, 1993). Recent studies have demonstrated that apes are capable of more manipulative grips than previously thought (Neufuss et al., 2018) and rare 'pad-to-pad' precision grips have been observed in chimpanzees during feeding (Marzke et al., 2015). Nevertheless, the preponderance of 'pad-to-side' or 'V-pocket' grips in non-human great apes is related to their relatively long fingers, long metacarpals and short thumb (Napier, 1993; Almécija et al., 2015). The adduction of the thumb during these frequent grips (Bardo et al., 2017) has been linked to the myological anatomy of non-human great apes. Flexor pollicis brevis and opponens pollicis muscles tend to secondarily adduct the TMc joint in chimpanzees and, despite their overall slightly smaller thenar musculature, the transverse head of the adductor pollicis muscle can generate significantly more torque than in humans (Marzke et al., 1999, van Leeuwen et al., 2018).

The distinctive features of modern human and non-human great ape hands are often linked to manipulative and arboreal power grips, respectively, following a more refined version of Napier's (1993) grip schema. However, as demonstrated by, for example, rare 'pad-to-pad' precision grips observed in wild chimpanzees (Marzke et al., 2015), as well as in semi-free ranging macaques (Macfarlane and Graziano, 2009), manual morphology does not necessarily preclude different kinds of grips or hand use. The functional explanations that link comparative anatomy and observed manual behaviours in different species are not always explicit or tested, a problem that is only exacerbated when they are applied to fossil hand morphology.

Inferring hand function in fossil hominins

To infer hand function in fossil hominins, observed manual behaviours are often related to aspects of extant morphology via a functional explanation. Where this morphology exists in fossil hands the observed manual function in extant taxa is inferred. However, these functional explanations are rarely directly tested since measuring joint reaction forces or muscle recruitment *in vivo* can be difficult. Non-human great apes may choose to not perform a behaviour under investigation when being observed or measured, and *ex vivo* non-human great ape samples that allow this direct testing of functional explanations are rare (e.g. Marzke et al., 1999; van Leeuwen et al., 2018). Further, the behaviour or manual morphology of an extinct hominin need not necessarily have a modern analogue. The inference of fossil behaviour, in particular, is limited to less direct evidence that may be multifaceted, hierarchical, contingent and inductive rather than deductive (Smith, 2016). This is not to say that this inference is impossible, but that care must be taken to ensure functional explanations of extant morphology are as explicit as possible and to ensure that the inferred fossil behaviour is the most supported explanation based on currently available evidence. In this section, some examples of inferred hand use in fossil hominins, that propose somewhat implicit functional explanations that may not be supported by further evidence, are discussed to highlight some of the limitations of this inferential approach.

All African ape species possess a ridge at the dorsal limit of the non-pollical metacarpal heads, which has been thought to provide a 'bony stop' to help prevent luxation, and dissipate stresses, at the McP joints in hyperextension during knuckle-walking (Tuttle, 1969; Richmond et al., 2001). While dorsal ridges are also present in digitigrade primates, it has been argued that given these features are present in closely related African ape taxa that all knuckle-walk, the last common ancestor of hominins and great apes would also have had dorsal ridges, indicative of knuckle-walking (Gebo, 1996; Richmond et al., 2001). However, these dorsal ridges are not present in all individuals (Susman, 1979) and can also appear on metatarsals (Inouye and Shea, 2004). More recent work has found that this phylogenetic

argument for fossil hominin dorsal ridges and knuckle-walking can be strongly criticised. Not only do *Pan* and *Gorilla* knuckle-walk in different ways (Inouye, 1992; 1994; Dainton and Macho, 1999; Kivell and Schmitt, 2009; Matarazzo, 2013) but both of their hand proportions may be derived, especially in *Pan*, and likely acquired in parallel rather than from a common ancestor (Drapeau and Ward, 2007; Almécija et al., 2015). The functional explanation given for metacarpal dorsal ridges has also been questioned. Dorsal ridges in non-human great apes are small compared to the rest of the McP joint and so the forces that would be required for them to act as 'bony stops' would be so high they would cause injury to the joint (Lovejoy et al., 2009; Simpson et al., 2018). Instead, it has been argued that this feature may reflect only knuckle-walking stresses early in development when cartilage at the McP joint has yet to ossify (Simpson et al., 2018). In any case, the inference of knuckle-walking based on inferred metacarpal dorsal ridges in basal hominins is problematic. The original functional explanation for the dorsal ridge (Richmond et al., 2001) may not hold (Lovejoy et al., 2009; Simpson et al., 2018) and the phylogenetically inferred fossil morphology has yet to be found in the hominin fossil record. However, even when fossil manual morphology is measured, rather than inferred, there are also limitations to the inference of fossil manual behaviour on its basis.

Compared to other manual elements, fossil hominin first metacarpals are relatively well-represented in the Plio-Pleistocene fossil record and they are contemporaneous with lithic technology (Susman, 1994; Harmand et al., 2015). The human thumb is long and robust compared to the fingers, which has been related to manipulative grips used in lithic tool production and thus much research has been devoted to this morphology (Napier, 1960; 1993; Susman, 1994; Shrewsbury et al., 2003; Tocheri et al., 2008). Susman (1994) found that the breadth of the first metacarpal head, relative to the first metacarpal length, was significantly higher in modern *Homo sapiens* than in both species of *Pan.* Susman (1994) associated this wider distal first metacarpal with precision grips in humans, not found in *Pan* species, and proceeded to infer these grips in a Neanderthal (Shanidar 4) and two specimens that may be *Paranthropus robustus* or early *Homo* (SKX 5020 and SK 84)

which were similarly wide. Conversely, an *Australopithecus afarensis* first metacarpal (AL333w-39) had a width similar to apes and so was argued to not possess these grips. The functional explanation proposed for this derived morphology was that the robust thumb of these later hominins likely had well developed muscles to resist the high forces involved in tool manufacture and use, while this broader head would aid in the dissipation of these increased forces (Susman, 1994). This explanation has been supported by more recent experimental evidence for first McP forces that are indeed high in simulated stone tool use (Rolian et al., 2011), and a similar argument has been made regarding the large flat trapezial facet for the first metacarpal base (Marzke et al., 2010; 2013). However, researchers have pointed out that mountain gorillas also have a similarly wide first metacarpal head and do not engage in stone tool production or use (Hamrick and Inouye, 1995; Smith, 2000). Susman (1998) countered that mountain gorillas are known to be dexterous (see also Byrne et al., 2001; Neufuss et al., 2018) but did concede that this point weakened his functional inference. In this case, the functional explanation for a wide first metacarpal head (Susman, 1994) has been somewhat experimentally supported (Rolian et al., 2011). Yet, the association of this trait with two distinct modes of hand use in humans and gorillas, means that some level of dexterity, but not specifically lithic production or use, may be associated with its presence in fossil hominins. The functional explanation for a wide first metacarpal head is more biomechanically, rather than phylogenetically, based but it still does not allow for the inference of a specific kind of hand use.

Hand musculature may provide more direct functional explanations since it is, in part, responsible for hand movements. It has been experimentally shown that if muscles are habitually used to perform movements their mass is maintained and if they are not habitually used they atrophy (Fitts et al., 2001). However, since soft-tissue does not preserve in the fossil record, researchers have used the level of rugosity, shape and dimensions of entheses to infer fossil musculature, which can be challenging. For example, the extrinsic flexor pollicis longus muscle (FPL) inserts on the distal thumb phalanx and accounts for around 22% of the total human thumb muscle physiological cross-sectional area (PSCA; Marzke et al., 1999) and is

frequently not present as a distinct functioning muscle in non-human great apes (Strauss, 1942; Marzke, 1971). Though a well-developed tendon of the flexor digitorum profundus does insert on the distal phalanx in bonobos, its muscle belly is not differentiated from that of the tendon that inserts on the second phalanx, as in humans (van Leeuwen et al., 2018). This shared muscle belly is thought to limit the amount of independent movement of the first or second finger in bonobos and thus also limits their dexterity relative to humans (van Leeuwen et al., 2018). A distinct FPL does exist in gibbons, though it has been suggested that this muscle is normally used to recruit the thumb in branch grasping during their distinct locomotion (Susman, 1998, Diogo et al., 2012), where the human FPL is thought to facilitate complex manipulation (Tocheri et al., 2008). While the relative recruitment of the FPL by modern humans in stone tool production is still a matter of debate (Marzke et al., 1998; Hamrick et al., 1998), its insertion has often been used to infer a strong thumb in fossil hominins. Napier (1962b) implicitly used the size of the volar ungual fossa, where the FPL was thought to insert, to infer the size of the FPL, and thus the ability to forcefully oppose the thumb to use or produce of stone tools in *Homo habilis,* specimen OH7-A. Susman (1988) has described similar morphology on SKX 5016, attributed to *P. robustus*, and Trinkaus (1983) has done the same for a *Homo neanderthalensis* distal pollical phalanx from Shanidar. Ricklan (1987) even suggested that width to length ratio of the distal phalanx combined with this volar insertion in STW 294, attributed to *Australopithecus africanus,* offered a 14-17% greater mechanical advantage for FPL relative to modern humans. Shrewsbury et al. (2003), however, showed that this muscle tendon actually inserts proximal to the volar ungual fossa on a gabled ridge, in agreement with Wilkinson (1953) and that the size of this ridge shows no correlation with the size of the FPL. Therefore, the inferred powerful FPL and associated behaviours of some fossil hominins (Ricklan, 1987; Susman 1988) were based on incorrect morphology and, in the case of OH 7-A (Susman and Creel, 1979), particularly “odd” morphology (Almécija et al., 2010, pp. 3.). However, even when the correct insertion site is described (Lovejoy et al., 2009; Almécija et al., 2010; Kivell et al., 2011), the inference of a strong FPL from entheseal morphology has been questioned (Shrewsbury et al., 2003).

Rather than focus on one enthesis, Karakostis and colleagues (2017) found that the pattern of entheseal sizes across the hand broadly matched historically recorded professions of medieval individuals. Specifically, individuals with high grip force professions had relatively larger entheses on the second and fifth rays suggestive of power grips, whereas those with low grip force professions had relatively larger entheses on the first and second rays suggestive of precision grips. Karakostis et al. (2018a) also found that the pattern of enthesis sizes in *H. neanderthalensis* was consistent with precision grips. Although relationships between occupational activity categories and entheseal morphology appear promising, experimental studies have failed to find a relationship between entheseal morphology and activity. For example, neither magnitude nor frequency of muscle use was found to experimentally alter six different limb muscle attachment sites in a sheep model, despite an increase in muscle physiological cross-sectional area (PCSA) due to exercise (Zumwalt, 2006). It could be argued that sheep are inappropriate analogues for fossil hominins but Rabey (2014) found a similar pattern in captive *Pongo* and Williams-Hatala et al. (2016) found no relationship between muscle size and hand entheses in a cadaveric human sample. Karakostis et al. (2018b) have argued that Williams-Hatala et al. (2016) failed to find a relationship because of their elderly human sample, on average they were 78 years old. PSCA would likely be reduced in these individuals due to senescence, but the entheses developed during their lifetime would remain large due to a slower mechanical response rate in entheseal tissue than that of muscular PSCA (Karakostis et al., 2018b). However, Rabey et al. (2015) conducted an experiment in subadult mice and found again that while PSCA area increased with exercise, neither the shape nor size of entheses were affected. Further entheseal robusticity and frequencies are correlated with sexual dimorphism and age in great apes (Alves-Cardoso and Henderson, 2010; Milella, 2014), which complicates functional inferences from them. Kivell (2015) has noted this while interpreting the manual entheses of *A. sediba*. Therefore while the size of muscles certainly reflects movements of the hand for which they are recruited, providing an explicit functional explanation, the assocaition of this feature with entheseal form is debated, making inferences of fossil hand function challenging.

These examples demonstrate that correlating extant behaviour with a morphological trait, and then inferring this behaviour where the morphology exists in the fossil record, represents two inferential steps, which may contain less well-supported suppositions. These steps include inferring a behaviour is linked to certain morphological traits, and inferring fossil behaviour as a result. A morphological trait may occur with a behaviour, such as tool-making, but also with others, such as manipulation in *Gorilla.* Therefore, a clear functional relationship between extant morphology and behaviour may not be unequivocal. Further, it may be that the inference of a certain morphological trait in the record cannot be well supported, as is the case for the metacarpal dorsal ridge. Even when functional explanation provides clear links between extant morphology and behaviour, this morphology may not be faithfully recorded by the fossil record, as in fossil entheses.

Moving beyond one behaviourally diagnostic trait (Susman, 1994; 1998) to a functionally coherent pattern of them (Karakostis et al., 2017) can strengthen inferences of fossil manual behaviour. For example, the intrinsic hand proportions and broad distal phalanges of *Papio* are similar to that of *Homo* (Shrewsbury, 2003; Marzke, 2013; Alemcija et al., 2015), but when the wrist morphology is described it is clear that inferred and observed hand function are not the same in these species. However, a pattern of behaviourally diagnostic, fossil morphological traits may be not be found in a single extant species. Perhaps the best example of this in the hominin fossil record is the mosaic postcrania of *Australopithecus afarensis*, the best known of all australopith species (Kimbel and Delezene, 2009). Several behaviourally diagnostic morphological traits in this species are found in extant humans while another set are found in non-human great apes (Ward, 2002; Kimbel and Delezene, 2009). Since these traits do not exist as a coherent pattern in a single living species and they each imply quite a different form of locomotion and hand use, there has been considerable debate surrounding the functional interpretation of the same fossil evidence.

The locomotion of Australopithecus afarensis

The *Australopithecus afarensis* hypodigm demonstrates morphology compatible with facultative, habitual bipedalism (Ward, 2002). The lumbar vertebral column of A.L. 288-1 shows a marked lordosis that would have centred mass over bipedal legs (Latimer and Ward, 1993; Whitcome et al., 2007), which in turn, possess relatively large femoral heads, argued to better dissipate the load of the trunk on the lower limbs during bipedalism (Jungers, 1988). In addition to these phylogenetically stable traits, the high bicondylar angle at the articulation of A.L. 129a+b (Johanson et al., 1976) evidences a valgus angle of the knee in this species, a trait that does not occur in modern humans that cannot walk (Tardieu, 2010). Further behavioural evidence of bipedalism was found in the 3.6-3.75 million year old preserved footprints at Laetoli G made in easily-dated volcanic ash (Leakey and Hay, 1979). It is thus generally accepted that not only was *A. afarensis* capable of bipedalism, but that archaeological and morphological evidence supports that it did frequently engage in some form of this locomotion.

While *A. afarensis* was clearly bipedal, its upper limb morphology has been interpreted in different ways. In the hand, the thumb to finger ratio of this species has been argued to be advantageous for forceful precision grips (Alba et al., 2003), known to be used in the production and use of stone tools (Rolian, 2011; Marzke, 2013). Though this ratio would be advantageous for all manipulative grips in which the thumb is opposed to the other digits (Feix et al., 2016). In the wrist, this species has a disto-radially oriented second metacarpal-capitate articulation and a proximo-distal second metacarpal-trapezium articulation (Tocheri et al., 2008). This orientation of CMc joints is distinct from non-human great ape morphology, and in humans is thought to allow pronation of the second metacarpal in precision grips while providing more surface area at its base to dissipate loads from forceful precision grips (Marzke et al., 1997). Asymmetry of the second and fifth metacarpal heads in *A. afarensis* (Bush et al., 1982) has also been argued to facilitate pronation and supination of these digits, respectively (Marzke et al., 1997). Yet, the hands of this species also exhibit features associated with arboreal locomotion.

The curved phalanges of *A. afarensis* found at Afar locality 333 (Susman and Creel, 1979; Bush et al., 1982) have been argued to be indicative of arboreality, since this trait is only found in arboreal primates (Susman, 1979; Stern and Susman, 1983). Further, during ontogeny hominoid species that practise more terrestrial locomotion with age also tend to decrease in phalangeal curvature (Richmond, 2007). This curvature allows the finger to better conform to rounded substrates (Preuschoft and Demes, 1985), such as medium sized branches, known to be habitually used in arboreal locomotion by chimpanzees and gorillas (Neufuss et al., 2017). Phalangeal curvature may also dissipate large bending stresses at the expense of higher compressive strains in below-branch suspensory locomotion (Preuschoft, 1970). A 2D finite element model, validated by measuring the strains incurred *in vitro* in a highly suspensory *Hylobates* cadaver, found that curved phalanges experience lower bending moments than straight phalanges, as the longitudinal axis of the bone was more aligned with the joint reaction forces (Richmond, 2007). While this type of locomotion is primarily associated with hylobatids rather than great apes (Thorpe and Crompton, 2006), 3D micro-finite element models, that accounted for cortical thickness, found that the peak tensile strain in suspensory proximal phalanges was usually located at the flexor sheath ridges (Nguyen et al., 2014). Pronounced flexor sheath ridges and curved fingers are common to both non-human great apes (Susman, 1979) and *A. afarensis* (Bush et al., 1982; Stern and Susman, 1983). Indeed, Nguyen et al. (2014) posited that the increased curvature of one *Symphalangus syndactylus* proximal phalanx may have compensated its lack of pronounced flexor sheath ridges to some extent. Flexor sheath ridges are also thought to provide strong attachment points for the flexor sheaths to help resist tendon bowstringing of strong extrinsic digital flexors (Susman, 1979). The presence of these features in the hand of *A. afarensis*, as well as other elements of the upper limb such as a superiorly-facing glenoid fossa, are argued to be adaptations for arboreal grasping and locomotion, subject to stabilising selection (Stern and Susman, 1983; Stern, 2000; Green and Alemseged, 2012). How to reconcile these manipulative and arboreal features to infer hand use, and therefore locomotion, in *A. afarensis* has been a matter of interpretative debate (Ward, 2002).

Some researchers have argued that these functional interpretations are incompatible and, since we know that *A. afarensis* practised some form of bipedality, they argue that the hand of this species was primarily manipulative (Latimer, 1991; Gebo, 1996; Alba et al., 2003). Manual traits that would be advantageous for arboreality, in this view, are less biomechanically functional and more primitive retentions from a predominantly arboreal ancestor, not maintained by stabilising selection unlike those traits advantageous for bipedality and manipulation (Latimer, 1991; Gebo, 1996; Alba et al., 2003). Indeed, some authors have argued the relatively shorter fingers in *A. afarensis* compared to *Pan* would be actively detrimental to arboreal grasping and demonstrate a directional selective pressure for manipulation at the cost of arboreal abilities in the hand (Latimer, 1991; Alba et al., 2003). However, it has since been demonstrated that *Pan* hand proportions are likely derived and so it is unlikely that hominin fingers became shorter (Drapeau and Ward, 2007; Almécija et al., 2015). Conversely, some researchers have argued that these manipulative and arboreal functional interpretations, respectively based on the extant analogues of humans and extant apes, are compatible. These researchers hold that *A. afarensis* likely practised arboreal locomotion and terrestrial bipedalism (Stern and Susman, 1983; Stern, 2000). The gracile first metacarpal in *A. afarensis* (Bush et al., 1982; Susman, 1994) provides a good example of a manual trait detrimental for forceful manipulation with limited arboreal advantage and therefore suggests a selective regime on the hand, and upper limb, not totally dominated by manipulative selective pressures in this species (*contra* Alba et al., 2003).

This functional debate cannot be resolved with this external morphology alone, precisely because it is a question of functional interpretation rather than fossil evidence (Ward, 2002). Manipulative and arboreal features of the *A. afarensis* hand have extant non-human great ape and human analogues, respectively, forming a mosaic rather than coherent functional pattern shared by a single extant species. As a result, the mosaic pattern itself may be linked to either an arboreally functional hand or one which is primarily used for manipulation in this species. Recent advances in technology have allowed for the efficient analysis of internal bone

structure, and the processes governing the form of this structure are relatively well known. This internal evidence provides another, and perhaps a more explicit, line of 'hard' evidence for reconstructing fossil hominin behaviour (Kivell, 2016).

Bone functional adaptation

Internal bone architecture is analysed here at the mesoscale, or tissue level, which is divided into cortical (or compact) bone and trabecular (or cancellous) bone (Currey, 2012). Cortical bone encases the rest of the bone, provides majority of the structural support of the skeleton and is relatively stiff containing most of the inorganic hydroxyapatite (Currey, 2002). Trabecular bone is located throughout the inside of flat and short bones, but in the epiphyses of long bones (Currey, 2002). Trabecular tissue consists of trabecular struts surrounded by cavities that have led some researchers to describe this tissue as 'spongy bone' (e.g. Lindahl, 1976). Both types of bone change their form in response to their mechanical environment over time, via a process known as 'bone functional adaptation' (Cowin et al., 1985; Cowin, 2001; Ruff et al., 2006; Currey, 2012). Though this term is widely used in the literature, and throughout this thesis, its constituent element 'adaptation' does not conform to the traditional biological sense of the word. Where adaptation generally refers to a heritable trait on which selection may act, this term within 'bone functional adaptation' refers to the bone functionally adapting to the demands of its mechanical environment, a process that is not directly heritable and better described as an example of phenotypic plasticity. This process, which has been known since the 19th century (Roux, 1881), was traditionally labelled 'Wolff's law' and was proposed as a strict mathematical relation between loading and bone form (Wolff, 1892). However, Wolff did not recognise bone's ability to remodel throughout life (Cowin, 2001; Martin et al., 1998) and a more general conceptualisation of Wolff's law, that includes this remodeling throughout life, has now been more appropriately termed 'bone functional adaptation' (Cowin et al., 1985; Lanyon and Rubin, 1985; Cowin, 2001; Currey, 2002; 2012; Ruff et al., 2006; Kivell et al., 2016). While it is recognised that modeling refers to the formation of bone and remodeling refers to the maintenance of bone, researchers use these terms differently when referring to bone functional adaptation, since both

processes are involved (Martin et al., 1998; Allen and Burr, 2014). Here, the term modeling is used to refer to growth since the majority of bone shape is determined during this time. Remodeling is here used to refer to the functional adaptation of bone to mechanical stimuli, because it implies modification of the pre-existing shape of bone. The process of bone functional adaptation can still be divided into elements relating to bone formation and 'trajectoral theory', as described broadly by Wolff's law (Hammer, 2015).

Trabecular bone

The bone formation element of Wolff's law (1892) holds that bone apposition occurs in response to mechanical loading, and is lost in response to unloading, over time (Cowin, 2001; Currey, 2002; Ruff et al., 2006). Frost's (1987) 'mechanostat' model significantly refined the process of bone formation and loss. Many of the cellular processes resulting in bone deposition or resorption due to mechanical stimulus, or a lack thereof, are well known (Chen et al., 2010). In trabecular bone, deposition can be measured by either bone volume as a fraction of the total trabecular volume (BV/TV) or bone mineral density (BMD) that is the attenuation of X-rays over an area or per voxel on a radiograph (Currey, 2012). Bone functional adaptation predicts increased mechanical load should result in more or thicker trabeculae, or both, increasing the mineral content of a section of trabecular bone. BV/TV explains ~89% of the variance in the Young's modulus, a measure of mechanical stiffness, of human vertebral trabecular bone (Stauber et al., 2006) and, as this ratio measures elastic deformation in a particular direction, this measure has often been used as good indicator bone strength (Currey, 2012). Many experimental studies have found that exercised animal models have more BV/TV relative to controls (Barak et al., 2011) and even artificially induced loading appears to increase vertebral BV/TV, bone formation rate and trabecular stiffness relative to controls, in just 10 weeks (Lambers et al., 2013). Similarly Biewener et al. (1996) found that removing the Achilles tendon from potoroos resulted in a 35% reduction of BV/TV after eight weeks. A similar degree of trabecular bone loss has been reported in human astronauts (Lang et al., 2004). Therefore, experimental and

comparative evidence supports the idea that trabecular bone mass increases in response to load.

The trajectoral theory element of Wolff's law (1892) relates to the realignment of trabeculae, and secondarily external bone, to functionally adapt to mechanical loads (Bertram and Swartz, 1991). The level of uniform orientation of the trabeculae is measured by their degree of anisotropy (DA; Martin et al., 1998). Greater DA indicates relatively more trabeculae aligned to a given axis to better resist loads in that direction. DA is responsible for ~10% of the variance in Young's modulus, since this fourth rank fabric tensor incorporates direction and magnitude of a load (Cowin, 1985; Maquer et al., 2014). The trabecular bone of guinea fowl made to run on an incline has been shown to reorient by 13.7°, in line with a 13.6° more acutely flexed knee at the point of peak ground reaction force (GRF) relative to a control group (Pontzer et al., 2006). A similar experiment in a sheep model found that animals exercised on an incline extended their tarsal joints 3.6° further at peak GRF than the level group, and possessed 2.7°- 4.3° more obtuse trabeculae in a parasagittal plane (Barak et al., 2011). Unlike BV/TV, reorientation of trabeculae cannot be achieved be thickening existing bone but instead by the formation of *de novo* rods or plates in the tissue. However, several experiments find this response elicited from quite subtle mechanical stimuli (Pontzer et al., 2006; Barak et al., 2011). Reorientation may also occur with the loss of trabecular struts. Systematic resorption of bone that occurs with age weakens the trabecular bone of human vertebra, which transfers over 75% of the load through the bone (Eswaran et al., 2006). To compensate for this loss of bone it appears that osteoporotic vertebrae can have a 24% greater DA, with trabeculae aligned superior-inferiorly, than healthy vertebrae with more BV/TV (Homminga et al., 2004). That is, osteoporotic vertebrae appear to preferentially resorb the trabeculae not in the axial orientation, the direction of primary loading in this bone (Homminga et al., 2004). The same argument has been used to interpret the trabecular morphology in the femur of howler monkeys, *Alouatta seniculus* (Saparin et al., 2011). Again, this comparative and precise experimental evidence is consistent with the remodeling of trabecular architecture in response to experienced loads.

Cortical bone

Cortical bone formation is often measured via the cross-sectional geometry of mid-diaphyseal bone. Directional strains in a diaphysis promote deposition in that plane, to better counter them and this changes the cross-sectional geometry in the diaphyseal shaft in axial cross-section (Ruff et al., 2006). This change in bone geometry is usually measured as a ratio of area moments of inertia in different planes. Carlson and Judex (2007), for example, found that mice forced to turn during locomotion had a significantly higher area moment of inertia in the medio-lateral plane than free-ranging mice or those that were forced to locomote in a straight line. In a more controlled experiment, Robling et al. (2002) found that after applying force to the distal end of a fixed mouse ulna over time, medio-lateral bending was resisted by the formation of additional cortical bone in this plane. Analysis of human athlete long bones has demonstrated that specific demands of different sports causes an increase in cortical bone at different sites. The dominant humerus of tennis players demonstrates significantly thicker cortical bone than that of the non-dominant arm (Jones et al., 1977). Further, the mid-shaft of the second metatarsal of football players and the tibia of endurance runners, respectively, showed significantly more cortical area compared to controls (Macinstosh and Stock, 2019). These diaphyseal robusticity patterns also translate to recent human populations. Andaman Islanders that were known to swim or use watercraft had significantly more robust humeri and clavicles than Late Stone Age South Africans known be more terrestrially mobile, which themselves had significantly more robust femora and tibiae than the former group (Stock and Pfeiffer, 2001). In the hand, using a slightly different measure, Wong and colleagues (2018) demonstrated that the first metacarpal of humans was significantly more robust than the other metacarpals. While Sarringhaus (2005) did not find a significant laterality in the cortical area of second metacarpals in chimpanzees, Marchi (2005) found that knuckle-walking African apes had stronger diaphyses in the third and fourth metacarpals than both orangutans and humans. These studies are representative of a larger body of evidence for the functional adaptation of diaphyseal cortical bone to incurred loads.

Other influences on internal bone structure

While experimental testing provides a basis for clear functional interpretation of internal bone morphology, it also elucidates the limits of what we know about bone functional adaptation, and thus the limits of the functional interpretations made on its basis. In this section, the effects of allometry, phylogeny, genetics, systemic factors, and ontogeny on internal bone structure are discussed, along with the frequency and magnitude of load necessary to cause this bone functional adaptation.

Allometry

The range of species that show bone functional adaptation emphasizes its role as a robust tool for functional inference, but it also demonstrates that trabeculae do not scale with body size isometrically. Larger skeletons are more heavily loaded and thus must scale allometrically to maintain function (Biewener, 1990). Larger animals have absolutely thicker trabeculae but it appears ~460 μm is the maximum limit as, beyond it, the surface area to volume ratio prevents effective remodeling via osteocytes (Lozupone and Favia, 1990; Ryan and Shaw, 2013). Similarly, as part of the remodeling process, osteoclasts resorb bone in amounts ~40μm in diameter, and so this is the minimum thickness of trabeculae, as any struts thinner than this would be destroyed (Eriksen et al., 1985; Cowin, 2001; Barak et al., 2013). Therefore, in particularly large animals trabecular thickness scales with negative allometry since the isometric thickness required would be larger than biologically possible (Cotter et al., 2009; Barak et al., 2013; Ryan and Shaw, 2013). Conversely, Fajardo et al. (2013) found trabecular thickness scales isometrically within strepsirrhines, while Doube et al. (2011) found it scales with positive allometry across birds and mammals. As corollaries of this, trabecular spacing and number have also been found to scale with negative allometry, leaving researchers to question how trabecular strength is maintained in larger animals (Barak et al., 2013; Ryan and Shaw, 2013). Of course, the difference in phylogenetic distances across two closely related species (Fajardo et al., 2013), the order primates (Ryan and Shaw, 2013) or mammals and birds (Doube et al., 2011), are likely to result in different scaling factors for these trabecular parameters. However, the general

trend of allometry is a non-functional phenomenon that must be controlled for in trabecular analyses over large phylogenetic ranges. Nevertheless, the effect of this allometry does not confound studies of bone functional adaptation since the two most mechanically relevant trabecular parameters, trabecular bone volume fraction (BV/TV) and degree of anisotropy (DA; Maquer et al., 2014), appear to be independent of body mass (Barak et al., 2013; Tsegai et al., 2017b), scale with isometry, or at least scale with very weak positive allometry (Doube et al., 2011, Ryan and Shaw, 2013). The range of hominid body masses that are considered presently is therefore unlikely to affect trabecular signals of function. In cortical bone, it has been demonstrated that cross-sectional geometry of the mid-diaphysis of long bones also scales with isometry in *Homo sapiens* femora and tibiae (Ruff, 1984) and studies of anthropoid primates, and mammals more broadly, have revealed isometry, or at most very weak positive allometry, in these cortical bone measures (Alexander, 1979; Biewener, 1982; Ruff and Runestad, 1992; Ruff, 2002). Indeed, allometry in indriid cross-sectional geometry measures (Demes et al., 1991; 1993) also appears isometric in the context of a wider sample of mammal body sizes (Ruff and Runestad, 1992). Therefore, the measures of internal bone structure analysed here are not subject to strong allometric effects that may confound analysis, especially given that the current sample does not have a large diversity of body sizes relative to the primate order.

Phylogeny

It could be argued that linking internal bone architecture to the behaviour of extant non-human great apes is somewhat confounded since extant crown hominids are quite genetically close, especially bonobos and chimpanzees (Won and Hey, 2004). Trabecular bone functional adaptation, however, has been demonstrated to be mechanistically similar across phylogenetically disparate taxa (Biewener, et al., 1996; Pontzer et al., 2006; Barak et al., 2011; Christen and Müller, 2017). Indeed, when a substantial phylogenetic signal was explicitly tested for in primate trabecular studies, it has not been found (Ryan and Shaw, 2012; Tsegai et al., 2013). Further, closely related *Gorilla* species, often used as a model for speciation (Albrecht et al., 2003; Leigh et al., 2003), demonstrate significantly different cross-

sectional geometry in several limb bones related to their locomotor differences (Ruff et al., 2018). As a result it seems that internal bone morphology is not greatly constrained by phylogenetic factors.

Genetics

Though internal bone morphology may not be directly constrained by phylogeny, the process of its formation and maintenance, that is modeling and remodeling (Allen and Burr, 2014), must be genetically controlled to some extent. Cartilaginous precursors of bone are present at birth before significant biomechanical loading can occur (Carter et al., 1991). Young et al. (2018) have found inter-specific cross-sectional geometry differences in perinatal strepsirrhine femora, explicable by different types of locomotion that these individuals have yet to engage in. Indeed, though bone functional adaptation has been demonstrated in controlled experiments (Ruff et al., 2006; Pontzer et al., 2006; Barak et al., 2011; Macintosh and Stock, 2019), the mechanism by which bone can respond to load is somewhat genetically controlled (Almécija et al., 2015b; Wallace et al., 2017). Up to ~50% of the variation of bone mineral content, density and area could be explained by genetic factors in a large human sample over several skeletal sites (Havill et al., 2007). Further, Havill et al. (2010) found a heritability estimate of 55% for BV/TV in a known lineage population of *Papio hamadryas*. Controlled experiments have also found that the same loads applied to genetically different model organisms do not engender the same response. Robling and Turner (2002) found that the same load applied to the ulnae of different strains of mice did not produce the same bone functional adaptation in mid-diaphyseal cross-sectional geometry. One strain required greater mechanical load to produce an osteogenic response in cortical bone, that was itself less pronounced than in the other strain of mice. Similar results have also been found in the trabecular bone of mouse models (Judex et al., 2002; Wallace, 2013). However, the amount of genetic influence may not be the same in trabecular and cortical bone.

As trabecular bone does not bind osteocytes to the same extent as dense cortical bone (Chen et al., 2010; Erikssen, 2010), the surface area provided by trabeculae allows the relatively unimpeded cells to be more biologically active, turning over

trabecular bone at around ten times the speed of cortical bone (Eriksen, 1986; Huiskes et al., 2000). Since the remodeling rate of trabecular bone is faster than in cortical bone, it has been argued to be sensitive to smaller mechanical stimuli (Frost, 1987) and thus under less genetic control, though this has been debated (Skinner et al., 2015; 2015b; Almécija et al., 2015b). It should be stressed, however, that these studies do not invalidate the functional signal of internal bone, as implied by Lovejoy et al. (2003), but instead reveal that the process of bone functional adaptation is canalised by genetic factors in a biological organism (Wallace et al., 2017).

Systemic factors

Focussing on the process of bone functional adaptation highlights its similarity across taxa, but this process does not happen in isolation *in vivo* and is not entirely governed by a genetic 'blueprint' (Carter et al., 1991). Rather, bone functional adaptation is the result of several levels of biological organisation receiving signals and responding to them, a process termed mechanotransduction (Martin et al., 1998; Chen et al., 2010). Briefly, physical loading is converted into a tissue level response, that is then converted into a cellular response of, though not limited to, osteoclasts and osteoblasts, that themselves are then regulated by variously expressed portions of the genome (Rubin et al., 1990; Wallace et al., 2017). As the complex processes that occur at these levels can be simultaneous and interactive (Pearson and Lieberman, 2004) they are necessarily influenced by other factors. Therefore systemic factors, that is those that affect a whole organism, influence bone functional adaptation and resulting internal bone structure. Hormones, for example, are known to affect trabecular and cortical bone formation rates in model animals (Prakasam et al., 1999; Kim et al., 2003). Similarly, the composition of an animal's gut-biome has been thought to affect bone structure (Charles et al., 2015; McCabe et al., 2015). Further, other roles of the skeleton, such as the maintenance of mineral homeostasis, likely influence internal bone morphology (Clarke, 2008). Lieberman (1996) demonstrated that cranial vault cortical thickness in exercised pigs and armadillos increased more rapidly than in controls. He argued that bone functional adaptation had occurred, but part of this adaptation was systemic and

thus affected parts of the skeleton that were not, themselves, under any increased or different load. Studies of multiple anatomical sites have found a systemically lower amount of BV/TV in modern humans compared to non-human great apes (Griffin et al., 2010; Tsegai et al., 2013; 2018) and fossil humans, which has also been related to lower overall activity levels (Ryan and Shaw, 2015; Chirchir et al., 2015). More broadly, higher BV/TV has been found in the primate femoral head compared to the humeral head (Fajardo and Müller, 2001; Ryan and Walker, 2010; Tsegai et al., 2018). As this pattern appears to be consistent across primates with very different locomotor styles it is difficult to explain in terms of positional behaviour, though Tsegai et al. (2018) do point out that primate locomotion is generally 'hind-limb driven' (Kimura, 1979). It is therefore likely that systemic factors are responsible for these patterns of primate trabecular bone. Indeed, bonobos and chimpanzees are known to have heterochronic thyroid hormone levels that may affect bone formation (Behringer et al., 2014). Even within the same limb, trabecular structure appears to be somewhat dependent on anatomical site. Saers et al. (2016) found that BV/TV systemically decreased with smaller cortical shafts, at more distal elements of the lower limb, across several human populations. These studies highlight that bone functional adaptation does not occur in isolation and thus that an element of internal bone structure can be attributed to systemic rather than biomechanically functional factors. While these systemic factors are likely multi-facetted and poorly understood, this does not prevent functional inference from internal bone architecture. Rather, functional signals should be understood as one signal among many recorded by the palimpsest of internal bone architecture (Saers et al., 2016).

Ontogeny

While it is important to contextualise trabecular and cortical bone within the biological hierarchy of an organism, it is also important to remember that the organism is not static and that many factors influencing internal bone structure change during ontogeny. Much of the experimental evidence for functional adaptation in trabecular bone comes from studies of juvenile animals (Pontzer et al., 2006; Barak et al., 2011), which is perhaps unsurprising as the bone is most

biologically active and least ossified during growth (Scheuer and Black, 2000). Ryan and Krovitz (2006) have shown that changes in the architecture of femoral trabeculae occur with the adoption of bipedalism, and Raichlen et al. (2015) have shown this pattern becomes less variable with age suggesting a common functional response. Cunningham and Black (2009) found that trabecular architecture of the human ilium is essentially fixed in the juvenile skeleton with only slight modifications throughout adulthood. Further, increased humeral cortical thickness in the preferred arm of tennis players (Jones et al., 1977) has been argued to be the result of increased activity before adulthood (Lovejoy et al., 2003). A controlled experiment demonstrated that the polar moment of inertia in the diaphyseal shaft of exercised sheep tibiae increased less in subadult, and even less in adult sheep, relative to juveniles (Lieberman et al., 2001; 2003). Taken together these results may suggest that any functional signal found in trabeculae and diaphyseal cortical bone may only reflect the juvenile positional behaviour of an animal (Bertram and Swartz, 1991; Pearson and Liebermann, 2004; Wallace et al., 2017), which can be different in adult primates (Inoyue, 1994; Plavcan and van Schaik, 1997). In humans, Warden et al. (2014) demonstrated that changes to bone geometry in professional athletes were maintained to a large extent subsequent to retirement.

While bone functional adaptation may be reduced in adult life (Willie et al., 2013), trabecular and cortical bone continues to remodel throughout ontogeny (Martin et al., 1998). Kerr et al. (1996) demonstrated that small, but significant, gains in bone mineral density were found in exercised radii compared to the other, non-exercised, arms of post-menopausal women. Ruff et al. (2006) cite this as an example of an effect that would not be seen in shorter term studies and argue that a lack of strong bone functional adaptation evidence in older bone may be due to the time it takes for older bone to adapt. Small absolute gains in bone volume due to exercise in older individuals have been interpreted as ontogenetic degradation in bone adaptability (Wallace et al., 2017). However, just as bone can functionally adapt during growth and adulthood, it can also functionally adapt during senescence, without an increase in bone volume. For example, the lack of external stimulus in adult bone has been experimentally demonstrated to cause a loss of

trabecular bone (Biewener et al., 1996). Further, the greater alignment of trabeculae in the superior-inferior axis of osteoporotic human vertebrae demonstrates that bone functional adaptation to positional loads can occur even in a bone that is degrading as a result of senescence (Homminga et al., 2004). Indeed, ontogenetic responses in trabecular bone appear to be site specific, indicating heterogenic responses to different functional requirements (Amling et al., 1996). Based on this understanding, it is perhaps better to think of internal bone architecture as a result of cumulative functional signals over ontogeny, successively superimposed (Ruff et al., 2006; Saers et al., 2016). The internal bone structure analysed in adult bone or fossils is therefore reflective of both the mechanical demands placed on a highly responsive juvenile skeleton, as well as the cumulative demands experienced by the skeleton throughout adulthood.

Pathology

During senescence the human skeleton often develops osteoporosis and trabecular structure has been shown to alter as a result (e.g. Homminga, et al., 2004). This pathological signal has the potential to alter the functional signal sought here. To the author's knowledge, no similar investigation of osteoporotic effects on trabecular structure has been conducted in non-human great apes. However, a study of baboons, *Papio hamadryas*, did find evidence of osteopenia, if not osteoporosis (Havill et al., 2008). Osteoporosis was diagnosed in less than 12.4% of a rhesus macaque, *Macaca mulatta,* population (Cerroni et al., 2000). However, the BMD in osteoporotic individuals was similar to that of healthy individuals, leaving researchers to infer osteoporosis via fractures, that were the result of the loss of key trabeculae oriented in the main loading axis of the bone (Cerroni et al., 2000). Given the absence of such fractures in the extant sample (see Chapter 2), or any other signs of pathology in the examined elements, it unlikely that a strong pathological signal is present in the following analyses. Therefore, while a pathological influence on trabecular and cortical structure is still possible, it is unlikely to overwhelm the functional signal under investigation in subsequent chapters (4, 5 & 6).

The complexity of mechanical loading

As many biological processes are responsible for internal bone morphology, it is remarkable that a biomechanical loading signal is so often found. Yet, simply because a biomechanical effect on the cortical or trabecular bone is clear, that does not mean it is not complex. The relative roles of the frequency and strength of mechanical stimulus required to produce osteogenic changes necessary for bone functional adaptation have been debated (Turner, 1998; Ruff et al., 2006). The mechanostat hypothesis holds that the strength of the loading stimulus should be larger than the bone can currently cope with, and that there is a minimum threshold beyond which mechanical stimulus does not result in bone formation (Frost, 1987). Of course it is equally true that a single large load will not produce bone functional adaptation since it will not produce a mechanical signal larger than those transduced from habitual loading.

When a strong change to the magnitude of mechanical loading occurs, trabecular bone can functionally adapt relatively quickly. For example, sheep exercised for just 15 minutes a day over 34 days were found to have significantly higher BV/TV than a sedentary control group (Barak et al., 2011). The subset of these sheep that were made to walk on an incline that extended their tarsal joints by 3.6° also displayed 2.7°- 4.3° more obtuse trabeculae in a parasagittal plane than controls (Barak et al., 2011). Interestingly, however, a sedentary group of sheep were shod on their forelimbs to create a similar extension of the tarsal joint, but this did not result in significantly re-oriented trabeculae compared to the level exercised group, which Barak et al. (2011) interpret as a lack of mechanical stimulus for trabecular remodeling in the animals. Trabecular reorientation may take longer to occur than changes in BV/TV (Tanck et al., 2001). Once bone functional adaptation to a mechanical regime has been achieved the trabecular bone does not appear to modify any further. Lambers et al. (2013) demonstrated that a cyclical load in mice significantly increased BV/TV, bone formation rate and trabecular stiffness in a vertebra, relative to control mice, in just 10 weeks. The authors also found that bone formation rate, stiffness and BV/TV only minimally increased beyond 10 weeks suggesting that once bone functional adaptation occurred no further process

was elicited. Skerry and Lanyon (1995) also found that immobilised sheep, and sheep that were immobilised for a 12 week shorter period, had the same level of BV/TV reduction at the end of their experiment.

Mechanical stimulus or loading must be frequent and strong enough to elicit bone response but there has been much debate over whether it is primarily the result of static or dynamic loading. Indeed, muscular, as in the exercised animal studies discussed above, or gravitational loading are often used as respective proxies for static or dynamic forces (Judex and Carlson, 2009; Robling, 2009). Jee et al. (1983) found that rats taken into orbit for 18.5 days had significantly less humeral BV/TV than another group kept in similar mobility limiting cages on earth. Rats that returned from orbit regained BV/TV demonstrating the gravitational stimulus for bone formation and loss. Judex and Carlson (2009) highlight similar bone loss in human astronauts, though it was more pronounced at more gravitationally loaded skeletal sites (Vico et al., 2000). Rubin et al. (2002) have similarly found that postural, high frequency and low impact loads imposed by body weight in sheep in an oscillation machine for just 20 minutes per day were also enough to increase BV/TV by 32% in the absence of increased exercise. Therefore, a mechanical stimulus, gravitational or muscular, of sufficient frequency and magnitude, may cause functional adaptation of trabecular bone

As cortical bone remodels at a slower rate, it may take longer to functionally adapt to novel loads than trabecular bone (Eriksen, 1986; Huiskes et al., 2000). Carlson et al. (2008) divided mice into three locomotor groups, ‘linear’, ‘turning’ and ‘free-ranging’ and studied the trabecular architecture of their distal femora. Contrary to their predictions the authors found that the ‘linear’ mice did not have significantly greater DA than their ‘turning’ counterparts and the ‘free-ranging’ group had significantly higher BV/TV than either exercised group. Carlson et al. (2008) state their ‘free-ranging’ animals may have engaged in more activity whilst the experimental groups did not receive enough mechanical stimulus to adapt, but diaphyseal cortical bone did functionally adapt to the mechanical stimuli of ‘linear’ and ‘turning’ conditions in these mice (Carlson and Judex, 2007). In fact it may be the case that, since the mice were constantly subjected to locomotor controls over

57 days (Carlson et al., 2008), their slower remodeling cortical bone (Eriksen, 1986; Huiskes et al., 2000) functionally adapted to these relatively extreme conditions and their initial trabecular bone functional adaptations reversed as they were no longer necessary. In any case, repetitive low-impact, rare-high impact and high-magnitude sports have all been shown to significantly affect the cross-sectional geometry of the lower limb cortical bone in humans, though in different elements and locations (Macintosh and Stock, 2019). Thus, while cortical bone is responsive to sufficiently frequent and strong mechanical loads, its response may not always be simply interpreted.

Demes et al. (1998; 2001) measured the strains on two macaque ulnae and tibiae during walking and galloping, and found that the direction of the greatest strain did not approximate the axis of greatest diaphyseal cortical bone rigidity, as assessed by cross-sectional geometry. As a result, the authors argue that cross-sectional geometry did not reflect patterns of functional loading in these individuals. However, Ruff et al. (2006) highlight that the tibial bending stresses did move to within 19° of the plane of maximal bending rigidity in cross-section when the macaque galloped. The higher, if less frequent, strains imposed by this faster locomotion are thought to produce a stronger mechanical signal than walking, and so the bone is more functionally adapted to stresses engendered by galloping rather than those incurred in walking (Ruff et al., 2006). Though the ulna cross-section of these animals did not approximate the axis of greatest bending stresses (Demes et al., 1998), Ruff et al. (2006) argue that this was actually the result of the multifactorial use of the macaque forelimb relative to the locomotor dominated hindlimb (Kimura, 1979). That is, as the ulnae were recruited for many different functional roles, locomotion may not cause the most frequent or the highest magnitude strains on this bone, and so its cross-sectional geometry may not reflect the axes of these locomotor peak stresses well. These studies highlight that while bone does functionally adapt to biomechanical loads this process may not always be simple or straight-forward.

Inferring bone functional adaptation

In spite of the multifaceted influences on internal bone architecture, the concept of bone functional adaptation has a growing body of experimental evidence, as well as a reasonably well known set of biological processes that govern this process (Frost, 1987; Chen et al., 2010). Given the similar trabecular and cortical responses to mechanical loading in phylogenetically distant species (Jee et al., 1983; Homminga et al., 2004; Pontzer et al., 2006; Barak et al., 2011), it seems that internal bone architecture does respond to sufficiently strong or frequent mechanical loads in a broadly predictable manner. Therefore, this experimentally tested mechanism offers a direct functional explanation for fossil internal bone architecture and allows researchers to infer *in vivo* mechanical environments in fossil taxa. Of course, it could be argued that fossil trabecular structure may also contain pathological, rather than functional, signals even when the rest of the bone does not (Colombo et al., 2018). However, this reasoning requires other evidence to initially suggest pathology, which is absent for the fossils studied here. Thus the fossil trabecular bone analysed in this thesis is argued to primarily reflect function. This line of evidence, internal bone morphology, can therefore discriminate between biomechanically functional and non-functional morphology. The mechanical environments inferred for internal bone structure can then be associated with fossil hand use and locomotion. The link between cortical bone diaphyseal shape and mechanical loading in primates has been possible to demonstrate for some time (Jones et al., 1977; Ruff and Hayes, 1982; Stock and Pfeiffer, 2001; Ruff, 2002; Ruff et al., 2006; Carlson and Judex, 2007; Ruff et al., 2018; Macintosh and Stock, 2019; but see Demes et al., 1998; 2001; Young et al., 2018). Yet, the technology required to efficiently image and analyse trabecular structure is relatively recent and linking extant primate trabecular structure to locomotion and hand use is not necessarily simple.

Inferring primate hand use from trabecular architecture

Since Wolff's (1892) 'trajectoral theory' was originally proposed in the light of trabecular orientation in the human femoral neck, it is no surprise that most of the research regarding trabecular indication of locomotion has been focussed on

human bipedality and risks of hip fracture (e.g. Smith et al., 1989). Nevertheless, Rafferty and Ruff (1994) were the first to compare trabecular bone in extant haplorrhines by digitising 2D X-rays of the humeri and femora of *Hylobates syndactylus, Colobus guereza* and *Papio cyanocephalus.* The authors measured the optical luminescence across a transect drawn through the humeral and femoral heads at half the depth of the articular surface to measure trabecular bone density. They found that the humeral density of all three species was similar but that the femoral head of the gibbon was less dense than expected and related this to its forelimb dominated method of locomotion, brachiation. Rafferty and Ruff (1994) chose a scaled, but relatively arbitrary 2D, measure from which to draw their inferences, since any increase in articular area studied would not be biologically homologous. Similarly, variation in trabecular architecture may go uncaptured in different parts of the humeral or femoral head with this technique (Whitehouse and Dyson, 1974) and the third dimension not analysed (Rafferty and Ruff, 1994).

Fajardo and Müller (2001) expanded on this early work by using micro-CT scans to analyse several trabecular variables in a spherical volume of interest (VOI) placed in the humeral and femoral heads of primates. Their results did not support BMD as a discriminator of locomotor mode but instead found that suspensory genera *Ateles* and *Hylobates* had lower DA in both proximal limbs than did terrestrial genera *Papio* and *Macaca,* consistent with variable loading due to more variable, arboreal substrates. MacLatchy and Müller (2002) also argued for a locomotor signal in the femoral head and neck of strepsirrhines when they found that leaping bush babies, *Galago senegalensis,* had more antero-posteriorly aligned trabeculae and greater DA than the slow moving arboreal quadruped *Perodicticus potto.* Using three central cubic VOIs of the femoral head and a slightly different method of calculating trabecular orientation, Ryan and Ketcham (2002) independently confirmed an association of greater DA in leaping strepsirrhines. However, the authors did note that intra-specific variation was high, with two individuals of one species demonstrating greatest DA in the superior and inferior VOIs of the femoral head, respectively. Ryan and Ketcham (2005) also found that in 11 species of strepsirrhines, the leaping genera had not only more supero-anteriorly oriented

trabeculae, but that these showed less variation than in the arboreally quadrupedal species. Conversely, micro-finite element models demonstrated that pattern and magnitude of strain at the hip of a *Loris tardigradus* and a *Galago senegalensis* specimen were not differentiated (Ryan and van Rietbergen, 2005). This study, however, only had a small sample size (n=1) and substantial intra-specific variation in trabecular bone has been reported in these species (Ryan and Ketchum, 2002) suggesting that a broader sample might show inter-specific differences. There seems, therefore, to be comparative evidence in prosimians for a link between trabecular architecture of the femoral head and locomotion, though this link may not be simple.

In haplorrhines, initially promising results linking locomotor mode and trabecular architecture in the proximal limbs (Fajardo and Müller, 2001) became increasingly complex with further study. Fajardo et al. (2007) placed two VOIs in the femoral neck of a wide variety of anthropoids, representing many locomotor modes, but found that BV/TV and DA values in these species were not statistically distinct (*contra* Fajardo and Müller, 2001). Similarly, Ryan and Walker (2010) found that there were no inter-specific differences in the humeral and femoral heads across five phylogenetically disparate anthropoids. Rather than a locomotor signal, these authors found that BV/TV and DA in the femora of each species sample were significantly greater than in the humeri. This apparent order-level difference in the trabecular bone of primate humeral and femoral heads was also found by Shaw and Ryan (2012), while a locomotor signal could be elicited from the diaphyseal cortical bone of the same sample. These studies show a distinct lack of a clear locomotor signal in the trabecular bone of haplorrhines, in the contrast to many controlled experiments that have found this signal in diverse animals (Biewener et al., 1996; Pontzer et al., 2006; Barak et al., 2011). A key difference may be that the experiments all considered relatively simple joints that primarily flex and extend in one axis. Carlson et al. (2008) argued that their lack of locomotor signal in the distal femur of 'turning' mice might be because this behaviour stresses the antero-posterior 'hinge' joint in the medio-lateral plane. The humeral and femoral heads of primates are complex ball-and-socket joints, used in many separate planes, and

whilst it is intuitively easy to connect lower BV/TV and DA in primate arms (Ryan and Walker, 2010; Shaw and Ryan, 2012) to their order-level 'hind-limb drive' pattern (Kimura et al., 1979), some biomechanical assumptions of the mobile primate shoulder continue to be challenged (Larson, 1995; Chan, 2008; Green et al., 2015; Püschel and Sellers, 2015). Thus, while it is unsurprising that the proximal femur has received much study given its initial role in the 'trajectoral theory' (Wolff, 1892) and apomorphic nature in hominin bipeds (Ward, 2002), its complex loading regime is unlikely to produce the same clear re-alignment of trabeculae as in more simple joints, such as those of the calcaneus (Skredros and Baucom, 2007). Furthermore, proximal limb elements may be well-insulated from peak GRF by distal elements and so may not receive the magnitude of stimulus necessary for remodeling (Kivell, 2015). Therefore, the lack of locomotor differentiation in haplorrhine proximal femora and humeri (Ryan and Walker, 2010; Shaw and Ryan, 2012) may reflect the biomechanical complexities of these joints.

Trabecular studies of primate distal limbs have also yielded equivocal results. Maga et al. (2006) compared the trabecular architecture of the calcaneus in hominoids and humans and found that, despite stark differences in locomotor mode, all trabeculae were oriented antero-posteriorly, though the habitual bipeds did have the highest DA. DeSilva and Devlin (2012) analysed quadrants in the trabecular compartment of tali in anthropoids but did not find any differences relating to locomotor mode, with similar trabecular architecture found in humans and orangutans. Conversely, Su et al. (2013) divided the talus into nine areas and specifically analysed subarticular trabecular bone. The authors found that, relative to other hominoids, the human trabeculae were more anisotropic, particularly in the lateral portion of the talus, which was argued to be a result of the relatively stereotypical movements of the human foot relative to other hominoids. In the wrist, three human carpals have been shown to have significantly lower BV/TV than in hominoids that habitually use their forelimb for locomotion but no other locomotor signal was found in these bones (Schilling et al., 2014). Using three volumes of interest in the third metacarpal head, Chirchir et al. (2017) found that BV/TV was significantly higher in distal and palmar portions of the third metacarpal

head in orangutans and, to a lesser extent, in humans, consistent with flexed-finger grips used during arboreal locomotion and manipulation, respectively. Barak et al. (2017), conversely, found the dorsal VOI in both chimpanzees and humans had significantly lower BV/TV and DA than the distal or palmar VOIs using a similar method. Though these results conflict, both studies found that humans possessed significantly less BV/TV throughout the third metacarpal head relative to other primate species (Barak et al., 2017; Chirchir et al., 2017). Matarazzo (2015) analysed many trabecular parameters in the several VOIs taken from the distal and proximal portions of third proximal and middle phalanges, as well as the third metacarpal head of hominoids and macaques. Using these five locations, the orientation of the trabeculae, as well as their shape, were able to clearly differentiate species into 'suspensory', 'quadrupedal' and 'knuckle-walking' groups while traditional measures of BV/TV and DA alone could not. Nevertheless, considering this suite of trabecular measures together did improve species locomotor classifications, and a similar suite of measures has found locomotor signal in the primate humeral and femoral heads (Ryan and Shaw, 2012; Matarazzo, 2015).

Although a suite of trabecular measures may differentiate between locomotor modes, they are a conflation of different biomechanical responses. This conflation then makes it difficult to relate trabecular patterns to a specific bone functional adaptation, obscuring the link between trabecular architecture and habitual locomotion (Ryan and Shaw, 2012; Scherf et al., 2013). Therefore, the fact that trabecular shape and orientation, alone, can predict locomotor mode is very intriguing, especially as the principle orientation of trabeculae reported by Matarazzo (2015) appears to reflect assumed principle directions of strain; quadrupedal macaques had palmo-dorsal alignment in their proximal phalanges whereas suspensory orangutans and gibbons had proximo-distal orientation in the same location. It should be noted, however, that fabric orientation and shape were coded into three categorical states in this study, based, in the former case, on "stronger directionality" (Matarazzo, 2015, pp.5). Thus, while this study certainly does demonstrate a bony locomotor signal, its clarity may be in part an artefact of the loss of biological variability in a continuous variable, and none of the continuous

variables could classify species alone. Distal elements of the limbs therefore appear to provide a better, but still equivocal, trabecular signal of primate locomotion and some of these varying results may be attributed to methodological issues arising from the VOIs chosen for analysis.

A two dimensional analysis of trabecular bone proceeds by analysing either a transect drawn through (Rafferty and Ruff, 1994), or an area demarcated on (Zeininger et al., 2011), an X-ray image. This approach necessarily ignores variation in bone structure in the third dimension (Whitehouse and Dyson, 1974). Advances in micro-computed tomography that allowed researchers to begin analysing in 3D required the definition of a VOI. From the inception of this 3D trabecular research, Fajardo and Müller (2001) noted that a standardised size of VOI would over-sample the trabeculae of smaller primates, relative to larger taxa because the absolute size (thickness) of trabeculae does not scale isometrically. Lazenby et al. (2011) have shown that the size of VOI in the same bone can dramatically affect many trabecular parameters and support the use of scaled VOIs, though Kivell et al. (2011b) have found that the choice of scaling factor also influences some trabecular values. Similarly, the location of the VOI can confound a biologically homologous comparison of trabecular bone, since it may be placed in a position thought to be relevant to a functional hypothesis *a priori*. If this assumption is incorrect, the researcher may not be measuring relevant trabecular structure for their research question (Whitehouse and Dyson, 1974; Kivell et al., 2011b). Similarly, even hypothesis-neutral locations, such as the centre of the humeral head (Ryan and Walker, 2010; Shaw and Ryan, 2012; Scherf et al., 2013) are problematic, since their relatively arbitrary definition may not yield biologically homologous VOIs between species, possessing differently shaped bones (Kivell et al., 2011b). Thus, the conflicting results found in some trabecular architecture studies (Fajardo and Müller, 2001; Fajardo et al., 2007; DeSilva and Devlin, 2012; Su et al., 2013) may be in part due to methodology.

Recognising the limitation of VOI methods, more recent studies (Tsegai et al., 2013; Skinner et al., 2015; Hoechel et al., 2015; Stephens et al., 2016) have employed a 'whole-epiphysis' approach (Gross et al., 2014) that essentially samples many VOIs

over a whole epiphysis, creating a biologically homologous unit of trabecular architecture for comparison. This method allowed Tsegai et al. (2013) to find a locomotor signal in the third metacarpal head of extant hominoids. Specifically, the authors found that knuckle-walking taxa had higher BV/TV and DA than suspensory hominoids and especially in the dorsal region of the third metacarpal head, which is thought to incur a high load during knuckle-walking. Suspensory hominoids were found to have more isotropic trabeculae, lower BV/TV and more palmar disposition of trabecular bone consistent with hook grips. *Homo sapiens* demonstrated an even lower BV/TV and isotopic structure, that Tsegai et al. (2013) argued was consistent with lower and more varied joint loading during manipulation. Similarly, Skinner et al. (2015) found that, like the committed tool-making species *H. sapiens* and *H. neanderthalensis, A. africanus* had a palmar concentration of trabecular bone in the base of first metacarpal (Mc1) and an asymmetrical disto-palmarly ulnar concentration in the head of the third metacarpal. Since these trabecular patterns were not found in other hominoids and correspond well with the position of the hand in precision grips (Marzke and Shackley, 1986), it was argued that all of these hominins likely also used forceful precision grips and potentially frequent tool-related behaviours (Skinner et al., 2015). Whilst these two studies represent a significant step forward in inferring bone functional adaptation from trabecular architecture, Tsegai et al. (2013) report high-intra specific variation in *Pongo,* with one individual indistinguishable from African apes, and Skinner et al. (2015) confirm the human-like asymmetric pattern in the third metacarpal of another *Pongo* specimen. These individual specimens do not invalidate the connection between bone functional adaptation and behaviours, but they do highlight that species comparisons of trabecular bone over a whole epiphysis are often qualitative or statistically compare trabecular values over a larger biological region that may not be appropriate for some research questions.

When the distribution of trabecular bone within an epiphysis appears to hold an inter-specifically different functional signal (Tsegai et al., 2013; Skinner et al., 2015), comparing whole-epiphysis trabecular values does not necessarily capture this signal. Similarly, qualitative comparisons cannot provide species averages with

which to infer a stable trabecular and functional pattern. Nor can these comparisons assess the extent of outliers from this species average pattern. Very recent studies have dealt with this issue by dividing the whole-epiphysis values into geometrically regular sections and statistically assessing differences between them intra- and inter-specifically (Georgiou et al., 2018; Stephens et al., 2018; Sukhdeo et al., 2018). While these sections represent an analytical step forward, this approach, like VOIs, risks missing biologically meaningful differences in trabecular value distribution where they lie across these biologically arbitrary, regular sections.

Many comparative studies have provided evidence for a connection between trabecular variables and locomotor mode (MacLatchy and Müller, 2002; Tsegai et al., 2013; Su et al., 2013; Matarazzo, 2015), yet studies of the functionally complex proximal primate limbs (Ryan and Walker, 2010; Shaw and Ryan, 2012) failed to clearly demonstrate this connection, in contradiction to earlier results (Fajardo and Müller, 2001; Fajardo et al., 2007). Similarly, VOI-based approaches (e.g. DeSilva and Devlin, 2012; Schilling et al., 2014) may inherently bias results (Lazenby et al., 2011; Kivell et al., 2011b). Recent methodological advances, however, such as the 'whole-epiphysis' method (Gross et al., 2014) obviate many of these issues and have been used to connect behaviour and functional adaptation of bone (Tsegai et al., 2013; Skinner et al., 2015; Hoechel et al, 2015). Further statistical methods are now being developed for this 'whole-epiphysis' approach that allow for the identification of average species trabecular patterns that may be associated with bone function (Georgiou et al., 2018; Stephens et al., 2018; Sukhdeo et al., 2018).

The current project

The current project endeavours to build on these studies, and connect the differences in the trabecular architecture in primate hands with distinct locomotor modes, as well as different types of manipulation, in order to infer fossil hominin hand use from preserved internal bone structure. The association of extant morphology with observed behaviours, via functional explanation, is key to inferring these behaviours in similar fossil morphology. Internal bone offers additional fossil morphology, formed by relatively well-known biological processes common to vertebrates, that records the *in vivo* mechanical environment, and thus

biomechanical function of fossil hominin bones. While this functional signal is just one of many, including systemic and ontogenetic signals among others discussed above, it not only reflects what a species is *capable* of but also has the potential to reflect what an individual *actually* did (Ruff and Runestad, 1992). Therefore, when internal bone structure is combined with external morphology, it can distinguish between functional and non-functional anatomy. Whilst comparative studies have yielded mixed results, new methodological advances in trabecular analysis (Tsegai et al., 2013; Gross et al., 2014; Skinner et al., 2015; Georgiou et al., 2018; Stephens et al., 2018; Sukhdeo et al., 2018) and the creation of micro-finite element models (Richmond, 2007; Nguyen et al., 2014) present a growing body of evidence that fossil hominin bone function can be reliably inferred.

The present thesis brings together geometric morphometric methods and the 'whole-epiphysis' method of trabecular analysis to test for statistical differences in trabecular architecture distribution across the metacarpal heads, and the first metacarpal base, of great apes. These elements were chosen as the subject of trabecular analysis as they are positioned at relatively simple bi-axial joints. Different prehensile hand postures generally require the use of different finger postures that, in turn, load these bi-axial joints from different directions and thus should produce a different distribution of trabecular architecture in the metacarpal heads, as well as the first metacarpal base. Of course, prehensile hand postures often also incorporate the palm, the position of which is determined by the carpal joints. Therefore study of the trabecular structure of the carpals may also yield interesting results and is consistent with the forces thought to act during the 'dart-throwers arc' motion of the human wrist (Stephens et al., 2018). However early work in this regard has not elicited a clear interspecific functional signal likely due to the complexity of the carpal joints (Schilling et al., 2014). Similarly the trabecular structure non-pollical metacarpal bases maybe useful for certain research questions, such as the biomechanical role of the styloid process of the third metacarpal in humans. However, the CMc joints are largely static in great apes and so the trabeculae of non-pollical metacarpal bases are unlikely to reflect different hand postures, with the possible exception of the fifth metacarpal base in humans

which is sellar and capable of some movement (Lewis, 1977). Nevertheless, trabecular analysis of the metacarpal heads necessitated the acquisition of scans of whole bones and therefore allowed for this thesis to present a holistic approach, by assessing the relative cross-sectional geometry of cortical diaphyseal bone across the long bones of the hand; the great ape metacarpus.

Where great ape metacarpal internal structure is associated with observed grips, similar fossil internal architecture is used to infer hand use and function in fossil hominin species, including the complete metacarpus of *A. sediba.* This thesis proceeds by testing if observed habitual hand postures, used in non-human great ape locomotion (Chapter 4) and in great ape manipulation (Chapter 5), can be associated with metacarpal trabecular architecture. This extant context is then used to infer hand use in fossil hominins, in order to ascertain their habitual mode of locomotion and manipulative capabilities (Chapter 6). The methods employed in these analyses are described in Chapters 2 and 3.

Chapter 2

Materials and Methods

While the analysis of trabecular and cortical bone has been approached in a variety of ways, this thesis provides: a novel method of the segmentation of bone or fossil material (Dunmore et al., 2018 ; Chapter 3), extends the recently developed 'whole-epiphysis' method (Gross et al., 2014) of trabecular analysis via geometric morphometric techniques and describes a novel automated orientation technique used for cortical analysis. These methods are used to separate and analyse trabecular bone in the non-pollical metacarpals of extant species (Chapter 4) and their pollical metacarpals (Chapter 5). These methods, as well as the cross-sectional geometry methods, are then applied to the whole metacarpus of extant, and fossil hominin, taxa (Chapter 6).The MIA-Clustering segmentation technique is discussed in further detail in Chapter 3.

Materials

Material selection

This thesis is concerned with the internal bone morphology of metacarpals, rather than other manual elements, as the distribution of trabecular structure in their distal heads is hypothesized to reflect the habitually loaded positions of the fingers, and therefore grips, of primate hands. The complex joints of the carpus mean that analysis of their trabecular structure is challenging to interpret (Schilling et al., 2014). Conversely, the interphalangeal joints are simple hinges and their trabecular structure is only likely to reflect the degree of digit flexion habitually employed by primate hands, unlike the bi-axial degrees of freedom permitted by the metacarpophalangeal joints. The bases of the non-pollical metacarpus are also not the focus of this thesis, as the carpometacarpal joint have fewer degrees of freedom than the interphalangeal joints. However, since metacarpals are rarely sectioned the whole bone, including the base, was scanned for analysis (see Methodology). The selection of whole metacarpals also permitted the cross-sectional analysis of their diaphyseal bone.

The aim of this thesis was initially to test if trabecular and cortical bone morphology of the metacarpus reflected hand use in different primates. It would therefore be ideal to sample primates with a broad range of different habitual hand postures. In practise, however, most non-hominid primates are much smaller than great apes. As discussed in the previous chapter, trabecular struts have a minimum thickness, due to the cellular process of bone remodeling (Barak et al., 2013). As a result smaller primates tend to have thicker trabeculae, relative to body mass (Ryan and Shaw, 2013), and therefore, based on first principles, fewer trabeculae in a smaller epiphysis (but see Ryan and Shaw, 2013, for further discussion). The methods used for analysis in this thesis were developed to analyse hominid trabecular bone, to ultimately infer fossil hominin hand use, where trabeculae are numerous and may be treated as a tissue. The lower trabecular number in non-hominid metacarpal heads means that the definition of this structure as a tissue is debatable. Therefore, while this type of analysis in other primates may yield interesting results, those results may not be directly comparable to those of fossil hominins. Large haplorrhine species such as *Mandrillus* spp. may be comparable in such analyses but their hand bones are relatively rare in collections. Similarly the most closely group related to hominids, hylobatids, are small by comparison and have highly specialised hand morphology, with no close analogue in the fossil record. Therefore the current sample is exclusively composed of great apes, to create a comparable extant sample with which to infer hand use in fossil hominins.

Data collection

The initial aim was to CT-scan as many complete disarticulated, dry and adult hominid metacarpi as possible to increase power of subsequent statistical tests. However, care was also taken to ensure sample sizes across extant species were similar, as well as of a similar sex composition and ratio of left-to-right hands. The exception to this was the recent human sample that was entirely composed of right hands. Humans are the only extant species studied that are cross-populationally, predominantly right-handed (Faurie et al., 2005) and the recent humans sampled were of unknown hand preference. Therefore, the use of right hands was more likely to capture the osteogenic signal of manipulative behaviours, on average, in

human populations. However, handedness is unlikely to greatly affect the strength or significance of differences at the inter-specific level in the trabecular and cortical bone of primate hands (Sarringhaus, 2005; Skinner et al., 2015; Stephens et al., 2016).

While some of the of the scans analysed were available from the database created by Dr. Matthew Skinner and Prof. Tracy Kivell, several research trips were required to produce the current sample. Over several months, agreements to visit, organise and loan material were made with several institutions in Germany and the UK. The majority of the *Pongo* sample was sourced via the kind permissions of Mr. Michael Hiermeier and Dr. Anneke van Heteren from the Bavarian State Collection in Munich, Germany. *Pan paniscus* scans from the Royal Museum for Central Africa, Tervuren, were analysed at the permission of Emmanuel Gilissen and Wim Wendelen. *Pan troglodytes verus* samples were accessed at the permission of Uta Schwarz and Prof. Christophe Boesch at the Department of Human Evolution the Max Planck Institute for Evolutionary Anthropology (MPI-EVA), Leipzig, Germany. All *Pan* specimens were all scanned in the Department of Human Evolution, MPI-EVA by David Plotski. Specimens were also sought in the Phyletisches Museum in Jena, Germany, however, most had been articulated with metal wire or springs and so could not be scanned (Fig. 2.1). In CT-scanning, metal attenuates X-rays far more than rock or bone and as a result this creates many artefacts obscuring the rest of the image. In this case, the wire was also often secured via drilled holes in the metacarpal heads and such drilling would destroy trabecular structure.

Figure 2.1. Example of *Gorilla* metacarpophalangeal joints articulated by wire.

Gorilla specimens were primarily sourced from the Powell-Cotton Museum, Birchington, U.K., accessed at the permission of Dr. Inbal Livine. After the negotiation of two formal loan agreements specimens were transported by the researcher to and from the Cambridge Biotomography Centre, Department of Zoology, University of Cambridge, UK where they were scanned by Keturah Smithson. A single *Pongo* specimen from the Smithsonian National Museum of Natural History, USA was also kindly scanned at the American Museum of Natural History, USA by Dr. Anna Ragni.

Fossil hominin micro-CT scans were made available through existing collaborations and permissions organised by Dr. Skinner and Prof. Kivell. Fossil metacarpi from Sterkfontein and Swartkrans housed at the Evolutionary Studies Institute, University of the Witwatersrand, S.A. (with Prof. Berhnard Zipfel and Prof. Francis Thackeray) and Ditsong National Museum of Natural History (with Stephanie Potze) were micro-CT scanned in a collaborative agreement with the Department of Human Evolution, MPI-EVA. *Australopithecus sediba* fossils were scanned at the Evolutionary Studies Institute, University of the Witwatersrand with permission from the Fossil Access Committee. Kebara 2 and Ohalo II were scanned in Department of Human Evolution, MPI-EVA, by permission of Prof. Israel Hershkovitz and Prof. B. Arensburg. Scans of *Australopithecus afarensis* material were scanned by David Plotzki and Prof. Fred Spoor. These scans were shared with permission from Prof. William Kimbel and Prof. Zeray Alemseged. *Homo neanderthalensis* material from El Sidrón was scanned by Prof. Antonio Rosas and provided by Dr. Nick Stephens.

Protocol

On arrival at each institution, catalogues were sought to aid in efficient identification of suitable specimens. Where specimens were not organised by postcranial element these were organised into separate bags for left and right hands as well as feet. A combination of White et al. (2011), Susman (1979) and Rose (1988) was used as a reference for identifying and siding bones, as well as previous instruction in hand anatomy from Prof. Kivell. Additionally several disarticulated reproductions of great ape hands were used to aid in this process (Fig. 2.2). Where

bones were not organised, all elements were first counted, in order to estimate the number of individuals present. Next tarsals and carpals as well as metapodials and phalanges were separated. Manual elements were then aligned with their antimeres, where possible, to help side them. In some cases it was necessary to sample articulated hands to increase sample size (Fig. 2.3). Photographic records were taken of each potentially viable specimen along with large associated postcranial elements and crania. Together these were used to check that specimens were adult, via the fusion of external epiphyseal lines and cranial sutures as well as the eruption of a third molar (Fig. 2.3a-c). Of the 365 hands put through this protocol only wild-caught, adult, complete metacarpi with no obvious pathology were analysed.

Samples

Samples used in each analysis are listed in each relevant chapter. See Appendix A for full enumeration.

Figure 2.2. Example of specimen identification in data collection protocol. Elements of a dry disarticulated *Gorilla* hand are positioned next to their antimeres where available. White reproduction *Gorilla* carpals are pictured next to bone material (top left). Scale bar is 7 cm.

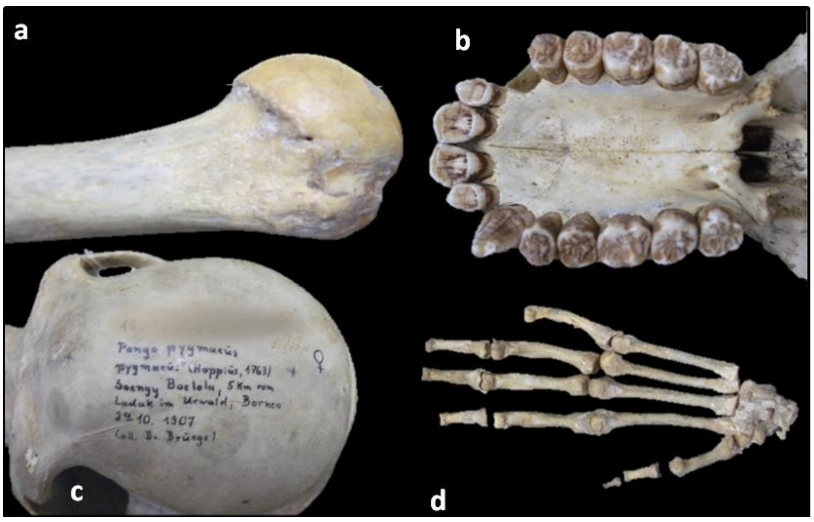

Figure 2.3. Elements of several *Pongo* individuals. a) Example of a humerus with no visible epiphyseal line, b) a maxilla with erupted third molars and c) a skull with complete fusion of cranial sutures. d) An example of an articulated hand that was scanned.

Methodology

High-resolution scanning

To image the inner architecture of hand bones in three dimensions, samples were placed in several micro-computed tomographic (µCT) scanners. These scanners included BIR ACTIS 225/300 and Diondo D3 static scanners as well as a Skyscan 1172 desktop µCT scanner, all housed in the Department of Human Evolution, MPI-EVA, and a Nikon XTH225 ST at the Cambridge Biotomography Centre. X-ray emitters within these scanners pass rays through a filter (Fig. 2.4a) and subsequently through a sample (Fig. 2.4b) where they are to some extent absorbed. The remainder of the X-ray energy then strikes a detector panel opposite creating an image. The sample is placed at the minimum distance from the emitter that still allows the X-rays to pass through the entire sample being scanned. This minimum distance ensures that samples were scanned at a resolution that allowed for accurate visualisation of thin trabecular bone. Resolutions varied proportional to the continuum of biological variation in the size of the manual elements both within and between species. Similarly time and financial considerations meant that multiple elements were scanned together creating a larger volume and a slightly lower resolution. The scanning protocol is detailed in Appendix A.

All scans analysed achieved an isometric voxel size of <57 µm, at 100-160kV and 100-140µA, using a brass or copper filter of 0.25-0.5mm and clearly resolved individual trabeculae. As X-rays are emitted the sample is turned about an axis of rotation orthogonal to the floor. This allows 1080 projections to be generated in 360° around this centre of rotation at ~0.333° increments (Fig. 2.4c). After corrections for beam hardening and ring artefacts, that may still be present, projections were averaged using various proprietary reconstruction software packages and a volumetric image of the bone was produced as 16-bit TIFF stack (Fig. 2.4d).

Figure 2.4. Elements of the scanning process. a) A static µCT-scanner (top) and its X-ray gun with a copper filter (bottom). b) An articulated *Pan* hand close to the maximum size of µCT-scanner aperture, c) projection image of disarticulated metacarpals and d) parasagittal cross-section of a reconstructed scan of an articulated hand, with adequate resolution for visualisation of individual trabeculae.

Reorientation

The reconstructed TIFF stack was loaded into Avizo 6.3 (Visualization Sciences Group, Berlin, Germany) using the resolution of the scan. In some cases the reconstruction algorithm unfortunately mirrored the image in the y-axis, as checked against photographs and, where possible, re-evaluation of material in person. In these cases the whole reconstructed image was flipped in the y-axis using the crop editor in Avizo. Subsequently, each bone was cropped from the scan, virtually

cleaned using label fields and limit lines in Avizo 6.3 (Fig. 2.5). All present elements of hands were scanned and separated for future work, with the exception of distal phalanges, as these rarely preserve trabeculae. Separated TIFF stacks of metacarpals were reoriented, so that their proximo-distal axis was aligned with the z-axis with their base approximating the xy-plane. The palmar surface of the metacarpals was reoriented parallel to the y-axis and faced away from the origin (Fig. 2.6a). These images were then further cropped and saved. The exact transformation matrix used, and the number of pixels cropped, were recorded to ensure repeatability (Fig. 2.6b-d). Where necessary, particularly large metacarpals were stack-scanned, resulting in two TIFF stacks that were merged with an overlap of ~10 voxels to ensure no stitching mark artefacts were present in the scan. Depending on the segmentation method used (see below), the bone image was then saved as a .RAW file or a .Nii (Nifti) format file.

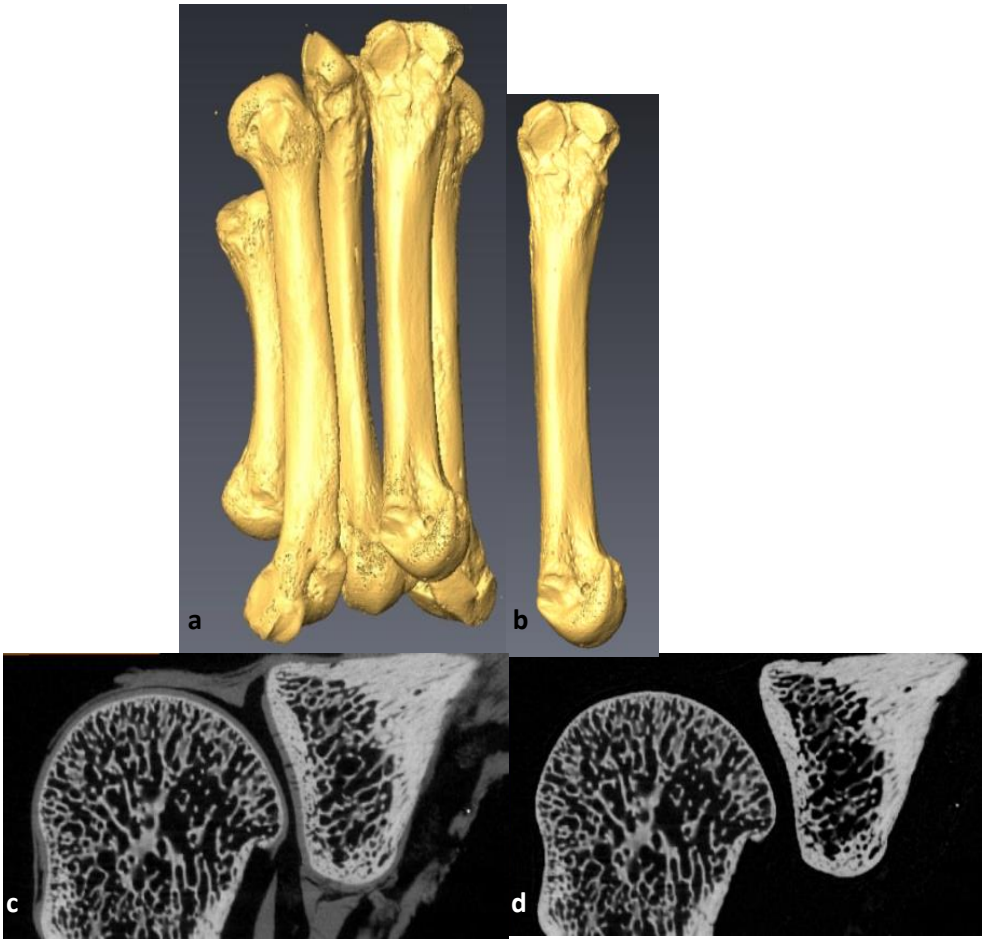

Figure 2.5. Example of cropping and cleaning specimens. a) An isosurface of disarticulated metacarpals scanned together that was then b) cropped to create images of single bones. c) Cross-section of an articulated metacarpophalangeal joint with desiccated soft-tissue and d) the cleaned joint with separated bones.

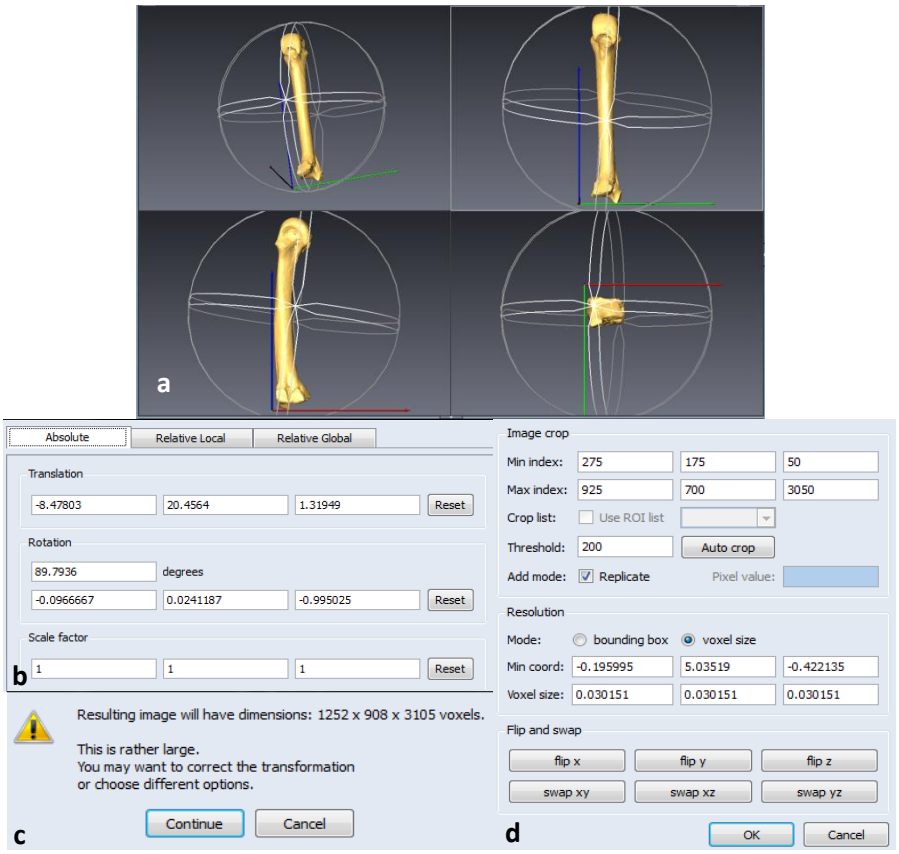

Figure 2.6. Example of image orientation steps on a right third metacarpal from a *Pan paniscus* individual. a) Anatomical orientation of the bone from various views b) the transformation matrix used to achieve this orientation, c) the size of the image on transforming it and d) the size of the final volume image after it is cropped for faster processing.

Segmentation

Images were segmented to produce binary, black and white, 3D images of bone that excluded any noise or non-bone, or non-fossil, material from analysis. This segmentation was achieved in bone material, using the Ray-Casting Algorithm (RCA) outlined in Scherf and Tilgner (2009). This algorithm first applies a 3D Sobel operator in the X, Y and Z dimensions, respectively, at each voxel (Fig. 2.7a-b). These operators use 3 x 3 x 3 kernel matrices, orthogonally opposed, to convolve with original gray values around each voxel and approximate the first derivative of the grayscale gradient in one direction. These three grayscale gradients at the voxel are combined to create the steepest grayscale gradient $M = \sqrt{G_x^2 + G_y^2 + G_z^2}$. This gradient is then steeper where there is a stark difference in neighbouring grayscale values, such as at the edge of bone, but much lower within materials such as air or bone. A non-maximum suppression filter is subsequently applied to remove all but

the zenith of local M which is then represented as a 1 voxel thick contour that traces the edge of the bone (Fig. 2.7c). Since an image may include some very low background gray values or 'noise', it is possible steep local gradients in this section of the image will also be counted as edges. This is obviated by the selection of a minimum M or 'edge-strength' threshold below which a gradient is not counted as an edge. Further, the algorithm allows the selection of lower and upper limits of gray-values within the image that are to be considered for the segmentation, thereby thresholding out some of these 'noise' edges at low or background gray values. These thresholds were defined by the researcher using test runs of the segmentation algorithm in Avizo via a plug-in. In rarer cases where 'noise' was close to the edge of the bone and it was possible that maximal local M or calculated edge would be adjacent to, rather than at, the edge of the bone. Therefore, as a matter of procedure, a 3D median filter with kernel size of 3 was applied to all images before test segmentation, and actual segmentations, to remove any high level noise that may cause this effect.

Scherf and Tilgner (2009) test RCA against threshold-based segmentations that simply employ a minimum gray-scale value, below which voxels are not considered bone. They find that RCA performs much more accurate segmentations since it does not only use one global threshold for the whole image, but rather a local maximum cline as described above. In this way, regional changes in grayscale values caused by underlying artefacts such as beam-hardening are mitigated rather than included above a single static threshold. Indeed other similar, though more computationally intensive, methods such as the algorithm proposed by Burghardt et al. (2007) incorporate local grayscale gradients. Of course, the disadvantage of this method is that it allows for very small gaps in contours where the value of M selected may adequately exclude non-edges but not include the entirety of the contour. This issue is resolved by the next step of RCA that casts mathematical rays at 11.25° steps around ±45° of the normal of each contour voxel. Rays terminate where they hit a contour voxel at or above M and so very few rays originate at the correct position with the correct angle to pass through the gap in the contour, instead hitting neighbouring contour voxels. Voxels for which most rays are

terminated are then marked as contour voxels filling any gaps and creating an unbroken edge of the segmentation (Fig. 2.7d). The voxels that define these contours are then used as seed points for a 3 x 3 x 3 neighbourhood joining filter that connects voxels that are <10% of the maximum gray value in the ray casting data set.

This process produces an 8-bit binary image, segmented with bone as white and non-bone as black, and is run on at least two 50 XY slice sections at the proximal and distal ends of the bone via an Avizo 6.3 plug-in (Fig. 2.7e). This allows the researcher to test if parameters performed equally well, via comparison to the original image, when segmenting different parts of the bone. Subsequently, segmentation of the entire bone was achieved via separate executable program that takes a batch file defining the input, output and segmentation parameters, as previously determined.

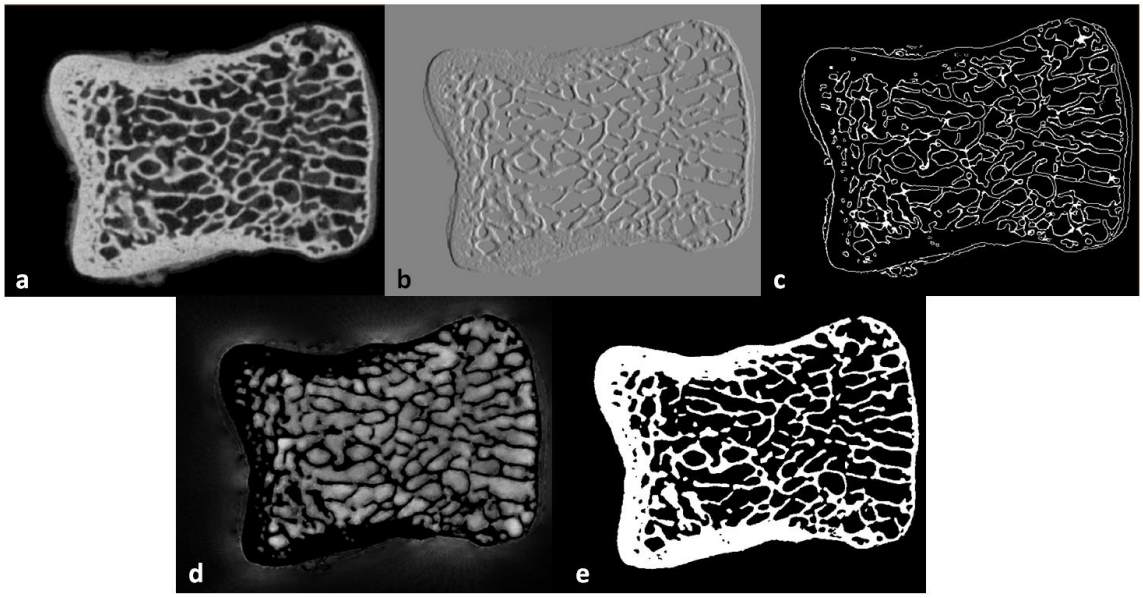

Figure 2.7. Example of RCA segmentation steps. a) A µCT- scan, b) the image after a Sobel filter in the x-axis, c) the edges defined by the maximum-suppression filter, d) the rays cast at the image and e) the segmented image.

MIA-Clustering segmentation

As outlined in Chapter 3, I developed a new method for the segmentation of fossil material that can be particularly problematic to segment (Dunmore et al., 2018). Difficulties with segmentation can be due to introgression of adherent substances of varying densities that can make it challenging to separate bone from non-bone

and to create an accurate binary segmentation. Sometimes, these intrusive substances can be manually segmented but this can be extremely time consuming and is often not repeatable or, at times, objective. Briefly, MIA- (Medical Image Analysis) clustering segmentation uses K-means clustering to assign voxels in an image to one of a number of specified classes. Typically, there are three classes in a fossil image; fossilised bone, introgressed adherent, and the background air. In each case, the centre of a cluster is found by finding an average grayscale value for each class and then iterating this value until it becomes as equidistant as possible from all other values. The three clusters are found simultaneously and voxels closest to each cluster centre are assigned to that class, resulting in a trinary image. More classes are specified if required. Subsequently the K-means clustering values are used to perform c-means clustering in which the assignment of class is done over a probability function rather than a binary decision; that is, a voxel is not simply gray and not black, it is 70% likely to be gray and 30% likely to be black. This process results in a global segmentation of the image.

To capture fine detail in the image, in this case trabecular structure, this process is then repeated in overlapping regular cubes. The edge-length of these cubes is determined by the grid size parameter that was found by selecting three random two-dimensional slices and measuring the thinnest trabecular strut. The grid-size selected is 2 pixels larger than this thinnest strut to ensure the algorithm does not look for features at a scale below that of these trabecular analyses. The classes clustered in each cube do not include those that had a probability of <2% in the global segmentation, this ensures the algorithm does not waste time looking for black voxels in the middle of a fossil or bone. Finally the probabilities of each overlapping cube are fused and the highest probability class is assigned to that voxel. This results in segmented images that contain more than one class, are not dependent on high contrast gradients in an image, and are more objective, since not only is one parameter selected instead of three, but this parameter is based on the image rather than a sequence of user-selected thresholds. Since these thresholds are user selected, they are to some extent subjective and may take many iterations to find acceptable parameter values, as there is no objective

starting point for a researcher, only a stepwise iteration of progressively 'better' segmentations, analogous to an adaptive peak model (*sensu* Wright, 1932). This approach also avoids the issue of equifinality present in RCA where two sets of values may produce a very similar if not identical segmentation.

Fossils were segmented with MIA 2.4.6 (Wollny et al., 2012) as part of the MIAtools Docker Image. Docker is a cross-operating system (OS) platform that uses virtualisation technology to provide the bare minimum version of a different operating system. Here, MIA uses the Unix shell language Bash, to parse commands in a Linux environment that does not exist in the Windows OS. As such, Docker was used to run these Linux commands but read and wrote files through the Windows OS. Once segmented, binary Nifti images were saved as .RAW images in Avizo for further processing.

Fossil caveats and procedures

Every fossil has a different state of preservation owing to different taphonomic processes. So while an effort was made to standardise all fossil segmentations, some extra steps were taken when needed. Fossils were initially median filtered using a kernel size of three in Avizo 6.3. If necessary, global grayscale clines were ameliorated by median filtering the image using a kernel of 25, inverting this image using an arithmetic operation and then adding a fraction of this to the initial image. In this way, contrast of the fossil trabeculae was improved using only the data within the image. 16-bit images were then segmented with MIA clustering (Dunmore et al., 2018) and then binarised using Avizo 6.3. Any cracks or edges of invasive material were removed by performing several median filters on the segmented image. While this did distort trabeculae, the filters eroded these very thin lines, caused by cracks or edges of invasive material, until they were non-existent. This image could then be taken from the original binarised segmentation using an arithmetic operation and the resulting skeleton of cracks and edges could be extracted with a label field in Avizo 6.3. Finally, this cleaned skeleton image of cracks and edges could be subtracted from the original binarised segmentation using an arithmetic operation, leaving undistorted trabeculae.

Medtool

The binary image of the segmented bone (Fig. 2.8a) was then processed in medtool 4.2 (Dr. Pahr Ingenieurs E.U.), a script manager that allows the automatic execution of a series of image filters and analyses, in native and third party programs, written in a variety of computational languages. This program employs C++ and a native Python 2.7.9 distribution that is used for the majority of computation, though this itself interfaces with Fortran77 during computation via F2Py functions. Several variables for each bone image were recorded in a parameter file, including image dimensions and the resolution, in order to perform batch processes on a number of bone and fossil specimens with custom parameters. A customised shell script executed these processes including, several of the morphological filters outlined in Gross et al. (2014) and Pahr and Zysset (2009). Broadly, these processing steps allow the segmentation of cortical and trabecular bone within the image, as well as the production of a 3D model required for the analyses of these structures. As this process requires several parallel steps, filtered volumetric images are below formatted in ***bold and italics*** to aid the reader.

The RCA or MIA segmented data was subjected to a ***Clean*** filter which identifies white 'bone' voxels that do not connect to the bone. The main structure in the image was identified as the structure with the most contiguous voxels with a grayscale value of one, i.e. white voxels, then any 'floating' voxels not contiguous with the bone are set to zero or black. Next, a ***Close*** filter used a spherical kernel to mark any black voxels as 'bone' if they would otherwise join two bone voxels across a gap defined by the radius of the kernel. This morphological 'closing' operation was computed by Fortran and removed fine shape detail, in this case cortical pores, by sequentially dilating and then eroding contours while assessing if there is a gap to be closed based on the size of kernel radius. This kernel size or $kc is a key value read from the parameter file and was initially set to three voxels, though this value was later evaluated and changed as necessary (see below). In this way, the fine porosity of cortical bone was lost and moderate gaps that represent real differences in shape or separation of trabeculae were maintained. The closing of cortical holes was necessary for the logic of the subsequent steps which generate

several 3D masks of the image each representing different types of bone present in the image, as outlined in Pahr and Zysset (2009).

The first of these masks was an ***Outer Mask*** which defined the limit of the bone from the 'air' surrounding it (Fig. 2.8b). This morphological fill operation used the same kernel size ($Kc Out) as the ***Close*** along with some of the same logic as the RCA as it cast mathematical rays at the bone from seven directions, the three orthogonal axes (X,Y,Z) as well as the four diagonal axes of a unit cube. Where the rays hit the first bone voxel, that direction it was marked as 'fill'. Where a voxel is marked as 'fill' in over five of the seven directions it was treated as bone. Where the rays have marked 'fill' voxels on opposite sides of the bone the distance between them is also marked as bone and a region growing function as well as 'opening' and 'closing' operations ensured internal structures were lost, leaving a solid outline of the bone. The image grayscale values were then scaled from 0:1 to 0:255 for further processing.

In certain cases the bone may have a particularly deep concavity, such that not all of the 5 required rays hit the nadir of the 'C' shaped feature as their angle is blocked by the rim of the concavity. This can lead to artefacts in the masking process and often occurs in metacarpal heads beneath projecting palmar epicondyles. To remedy this issue, a subsequent bounding box was found by the researcher in Avizo 6.3, and its coordinates were used to create a second instance of mathematical ray casting. Since these rays begin from inside the 'C-shape' they were not blocked by the rim of the concavity and the artefact was removed. Where used, this masking correction was iterated 15 times and checked by the researcher before proceeding.

The second mask is an ***Inner Mask*** which delimited the 'trabecular' space inside the cortical shell (Fig. 2.8c). This was achieved using much the same process, excepting that rays began at the edge of the ***Outer Mask*** and were marked 'fill' voxels where they met 'air' voxels. If the ***Close*** operation did not precede this, rays would likely have contacted pores in the cortical bone and incorrectly assigned sections of cortical bone to the ***Inner Mask*** and ultimately trabeculae. Again 'opening' and 'closing' morphological operations were used to create a solid mask of the inner

structure but the kernel size ($Kc In) used here was twice that of the other filters, beginning at six voxels. The $Kc and $Kc Out operations were designed to close small holes in the cortical bone but not artificially join trabeculae. Thus, the average trabecular thickness (see below) is halved and rounded down to the nearest integer to generate $Kc and $Kc Out, to close holes that were half the average width of trabeculae. However for the ***Inner Mask*** rays may have travelled from the outer contour of the cortical bone along trabeculae attached to it and not immediately hit 'air' creating channels in the solid inner mask. As these channels were the inverse of trabeculae, they were the same width and so in this case a closing operation that joined the edges of these channels was assigned the same kernel size as that of average trabecular thickness. Therefore where $Kc Out was half a trabecular strut at three voxels, $Kc In was a full strut width at six voxels. On completion of the 'fill' operation another cleaning filter was used to remove any unconnected elements leaving only the ***Inner Mask*** which was then also scaled from 0:1 to 0:255. Another optional bounding box correction could have been applied if necessary.

The ***Thickness Mask*** of the solid cortical bone was then created, by subtracting the ***Inner Mask*** from the ***Outer Mask***, and subjected to a cleaning filter and scaled to 0:255. This ***Thickness Mask*** is in turn subtracted from the image created by the ***Clean*** filter leaving the detail of the inner architecture and air as the ***Trabecular Mask***.

Having segmented the bone into a cortical shell and inner architecture, an evaluation step was carried out to ensure the kernel sizes used are unlikely to erroneously assign voxels to the wrong element of the bone. At this point a Windows command line execution called headerless ImageJ (Schneider et al., 2012) to run the BoneJ plugin, as described in Doube et al. (2010), on the ***Trabecular Mask***. The plugin calculated trabecular thickness, in pixels, as the diameter of the greatest sphere that fit within the bone structure. The centres of these spheres were sampled within the bone structure in a non-redundant manner and the maximum diameter was averaged to generate one thickness value per bone (Hildebrand and Rüegsegger, 1997; Dougherty and Kunzelmann, 2007). This mean value was then rounded down to provide the $Kc In value for this specific bone and

divided by two, again rounding down, to generate the $Kc and $Kc Out values. If these differ from the initial values of six and three the morphological operations from the ***Close*** to the ***Trabecular Mask*** were repeated with the new kernel size. Medtool allows for each Kernel size to be visualised as different colour overlays of the original CT-scan allowing for both quantitative and qualitative identification of the optimal kernel size; in practice this ranged from $Kc3–$Kc5.

These different masks were brought together into a single segmented mask with four values denoting 'outer air', 'inner air', trabecular bone and cortical bone. The trabecular model was combined with 'inner air' in order to create a ***MaskSegIn***, a continuous 3D model for analysis, since the ***Trabecular Mask*** is not continuous within the diaphyseal shaft where trabeculae are often absent. Specifically, the ***MaskSegIn*** was created by adding a scaled version of the ***Clean*** image to the ***Inner Mask*** creating a trinary image of the 'inner air' and 'trabeculae' on a black background. A ***MaskSegOut*** was then made by applying the same process to the **Clean** image except the ***Inner Mask*** is replaced by the ***Thickness Mask*** resulting in the definition of 'cortical bone', 'inside' and 'outside air'. These two images were then combined into a quaternary image, the ***MaskSeg*** (Fig. 2.8d), by converting the cortical shell into a gray value of three and adding this to the other image.

Having segmented the three different materials in the 3D image it is possible to mesh these into a 3D finite element model. Slight modifications of the masks were required before formatting the models for a third party meshing program. Both the inner and outer masks were reduced in resolution by a factor of four, and each was subjected to a 'closing' filter with kernel size of three. The effect of this was to slightly increase the limits of each mesh and re-resolve its edges, such that finite elements at the edge of the bone could be created within the mesh. The ***Outer Mask*** was additionally dilated with a kernel size of three, since some of the cortical bone was very thin. Without the slight inflation of this area it was likely that an element would not fit in the mesh, resulting in a hole in the model. Finally the ***Inner Mask*** was taken from the modified ***Outer Mask*** to produce the modified cortical shell mask and both were converted into Inira files for the mesher.

The CGAL (Computational Geometry Algorithms Library) 4.9 mesher discretised a 3D domain into an isotropic simplicial mesh using a restricted 3D Delaunay triangulation. The elements made were tetrahedra with 30° angles at vertices, to guarantee termination of the meshing process at smooth boundary surfaces. The size of the elements was equal to the distance between them, as well as the size of each facet of the element, to ensure contiguous tessellation of the mesh. This size was determined by the $inmesh and $outmesh variables defined by the user in the parameter file but the $outmesh was usually calculated as half the $inmesh to ensure at least two elements were created in the thinnest sections of the cortical mesh. This initial mesh may have contained slivers, i.e. degenerate tetrahedra with overlapping vertices, which were removed with several optimisers applied to the mesh. The Lloyd and Optimal Delaunay Triangulation (ODT) global optimisers minimised mesh energy resulting from the interpolation of linear piecewise functions to better approximate curved surfaces. Local optimisers either moved vertices of a degenerate tetrahedron, the perturber, or optimally reweighted the vertices, the exuder, to make these slivers disappear. This process results in three optimised meshes: the cortical bone, the inner domain and an analysis version of the inner domain set at a mesh with a cell size of 1mm. Further analysis was carried out on the analysis mesh as this ensures parity between models. These meshes were written as Abaqus (2007) files which were then converted into Ensight files for visualisation in the Paraview (Ayachit, 2015).

Trabecular analysis of the bone proceeds in medtool 4.2 by creating a rectangular background grid of 2.5mm cells in which the ***MaskSegIn*** Image is placed (Fig. 2.8e). Volumes of interest (VOI) spheres with a diameter of 5 mm, in order to ensure overlap between spheres, were centred on each vertex in the grid and trabecular parameters were measured. In practise, this led to the minimum number of VOIs per whole bone to range from 756 to 7,728 in non-pollical metacarpals, and from 481 to 2,161 in first metacarpals (Mc1). Spheres were used to avoid cornering effects, which can poorly sample features close to orthogonal axes, found in cubic VOIs (Ryan and Ketcham, 2004). Trabecular bone volume fraction (BV/TV) and degree of anisotropy (DA) were measured by the mia-multi module in medtool 4.2.

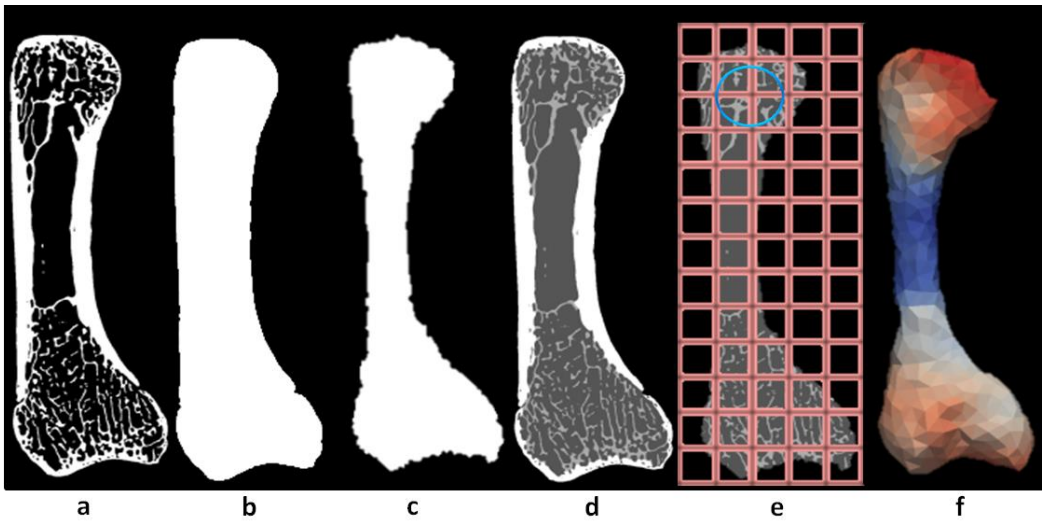

Figure 2.8. Example of image processing steps in medtool. Sagittal cross-section of a) A segmented metacarpal, b) the outer mask, c) the inner mask, d) the trinary MaskSeg, e) the overlaid background grid (red) and a representation of a VOI centred on a vertex (blue). f) Trabecular values from overlapping VOIs interpolated onto the inner analysis 3D mesh.

Trabecular variables

Previous studies have shown that BV/TV and DA are good predictors of trabecular bone strength and functional bone adaptation (Odgaard, 1997; Uchiyama et al., 1999; Pontzer et al., 2006; Barak et al., 2011; Lambers et al., 2013b) and that they are not subject to strong allometric effects (Doube et al., 2011; Barak et al., 2013; Ryan and Shaw, 2013). Analyses have used other trabecular variables such as trabecular spacing (Tb.Sp), number (Tb.N) and thickness (Tb.Th; e.g. Ryan and Walker, 2010; Saers et al., 2016, Reina et al., 2017). Together these values constitute BV/TV and are dependent on each other to some extent. Tb.Th and Tb.Sp are the inverse of each other and sum to the total trabecular space. Similarly, for a given BV/TV, Tb.N is proportional to Tb.Th, as only so many trabecular struts of a given thickness will be accommodated by a given trabecular space. Given the dependence of these variables, analysing them all is somewhat redundant (but see Ryan and Shaw, 2013), but they do reveal information about the relative contributions of these variables to BV/TV. However, these three variables have all been shown to scale with strong allometry that may mask a functional signal in trabeculae where BV/TV would not (Ryan and Shaw, 2013), and so were not retained for analysis in subsequent chapters.

DA measures to what extent trabeculae are uniformly aligned in a direction, whereas principle trabecular orientation (PTO) provides their actual direction (Pontzer et al., 2006; Barak et al., 2011; Matarazzo, 2015; Barak et al., 2017). However, PTO is a meaningless measure when trabecular structure is close to isotropic, as there is no 'principle' orientation (Barak et al., 2017). Indeed researchers have manually coded the 'main' orientation of trabeculae when trabeculae are almost equally oriented in two different directions (Matarazzo, 2015). Unfortunately scaling PTO by DA does not obviate this issue as, in the case two similarly represented orientations, the second strongest orientation is not included in DA (see below). That is, we do not know to what degree the principle orientation of trabeculae is differentiated from their second most prominent orientation. Therefore while this measure has yielded promising results in early 3D applications (Matarazzo, 2015; Barak et al., 2017) it is challenging both to interpret, and to compare with older literature which only employs DA. Consequently PTO was not retained for analysis in favour of DA.

DA is calculated using the mean intercept length algorithm (MIL) following Odgaard (1997). This algorithm casts equal length vectors, originating from random points within the image, through the sample in different directions, until they hit a white or bone voxel. A mean intercept length is generated by dividing the length of the vectors at these terminations by how many terminations occurred. A second rank tensor is then fitted to the directions and lengths of these mean intercept vectors, and they are decomposed into three primary eigenvectors. DA for this spheroid is then calculated by subtracting the largest of the three eigenvalues, divided by the smallest of the three eigenvalues, from one. BV/TV was calculated by dividing the amount of segmented bone voxels by the total number of voxels in each VOI sphere. The centroid of each finite element in the mesh is then assigned a value for each trabecular parameter. These values are a linear interpolation of the spheres in the background grid and saved as an .Esca1 file (Fig. 2.8f; Pahr and Zysset, 2009).

Geometric morphometric mapping

One of the key issues with the whole-epiphysis approach is that while it provides models for qualitative analysis, quantitative trabecular analysis has largely been restricted to the comparisons of whole-epiphyses (Tsegai et al., 2013; Skinner et al., 2015), or sections of them (Georgiou et al., 2018; Stephens et al., 2018; Sukhdeo et al., 2018). As these sections are geometric divisions that may not be biologically meaningful, a new approach was developed to statistically analyse trabecular variables using geometric morphometric techniques (Gunz and Mitteroecker, 2013). Accordingly, analysis was limited to the surface of the trabecular models created by medtool 4.2, although there is also good biological reason to focus on subarticular (otherwise known as subchondral) trabecular bone. This region of bone must transmit loads from adjacent joints to deeper trabecular structure, and eventually the diaphysis, by virtue of its position (Zhou et al., 2014; Sylvester and Terhune, 2017). Therefore, subchondral trabecular bone disposition is likely to reflect habitual joint loading via the mechanism of bone functional adaptation (Ruff et al., 2006).

The surface of the trabecular mesh (Fig. 2.9a) was extracted using Paraview (Fig. 2.9b; Ayachit, 2015) and was smoothed (Fig. 2.9c), to permit landmark sliding (see below), in Meshlab (Cignoni et al., 2008) via a screened Poisson surface reconstruction filter (Kazhdan and Hoppe, 2013). For left hand bones this surface mesh was mirrored in Meshlab so that it was oriented in the same manner as those from the right hand. The smoothed surface of trabecular model was then landmarked in Checkpoint (Stratovan, Fig. 2.9d) using external anatomical landmarks (see Chapters 4 and 5 for location and type of landmarks following Bookstein, 1991). These landmarks were easily translated to the inner trabecular surface of metacarpals as the overlying cortical bone is very thin in hominids (Tsegai et al., 2017). A separate set of anatomical landmarks was used for the first metacarpal base, the first metacarpal head, and the non-pollical metacarpal heads, as these three sets of epiphyses have different developmental and evolutionary histories in primates (Pazzaglia et al., 2018). In each case, a repeatability test was performed to ensure landmarks were stable and reproducible by the researcher.

Three landmark templates were created on two randomly chosen specimens, a non-pollical metacarpal and a first metacarpal, in Checkpoint. These templates consisted of the anatomical landmarks and sliding semi-landmarks constrained to curves or distributed over the subchondral surface (Fig. 2.9d). These curves were located between anatomical landmarks and at the edge of the subarticular surface to constrain semi-sliding landmarks to this surface, as recommended by Gunz et al. (2005). These templates were then projected onto each of the appropriate trabecular models via the Morpho package in R (Schlager, 2017), using the manually placed anatomical landmarks on each metacarpal specimen for reference. The semi-sliding landmarks were then relaxed onto the surface of each model by minimising bending energy and were then slid along their respective curves and over the subarticular surface, by minimising Procrustes distances. Bending energy was used as the algorithmic criterion for relaxation as it prioritises smooth global deformation and takes into account all landmarks together, producing a more stable criterion over a large range of shape variation that is likely present at the inter-specific level. Conversely, landmarks were slid using Procrustes distance as this is computationally faster. Since the curves terminated in anatomical landmarks and themselves surrounded surface sliding semi-landmarks, there was no way landmarks could slide beyond their proscribed limits with this method (Gunz and Mitteroecker, 2013). BV/TV and DA values, as calculated in medtool, were mapped to these homologous landmarks for statistical comparisons, unconstrained by geometric divisions of continuous trabecular structure. A custom Python script plugin for Paraview (Ayachit, 2015) was used to assign trabecular values of each tetrahedron of the trabecular model (Fig. 2.9e) to the centre of their surface triangle facet(s). These surface values could then be interpolated to their nearest landmark via the Python module SciPy (Jones et al., 2001; Fig. 2.9f). This interpolation was carried out in medtool 4.2 for BV/TV and DA separately. It should be noted that this data is interpolated from VOIs that cover the articular surfaces analysed. These overlapping VOIs number from 72 to 336 in non-pollical metacarpals, and from 60 to 180 in first metacarpals. After values were associated with landmarks, a generalised Procrustes procedure was performed using the Geomorph package (Adams et al., 2017) in R to create three sets of homologous

landmarks across the hominid metacarpals, each associated with two trabecular values.

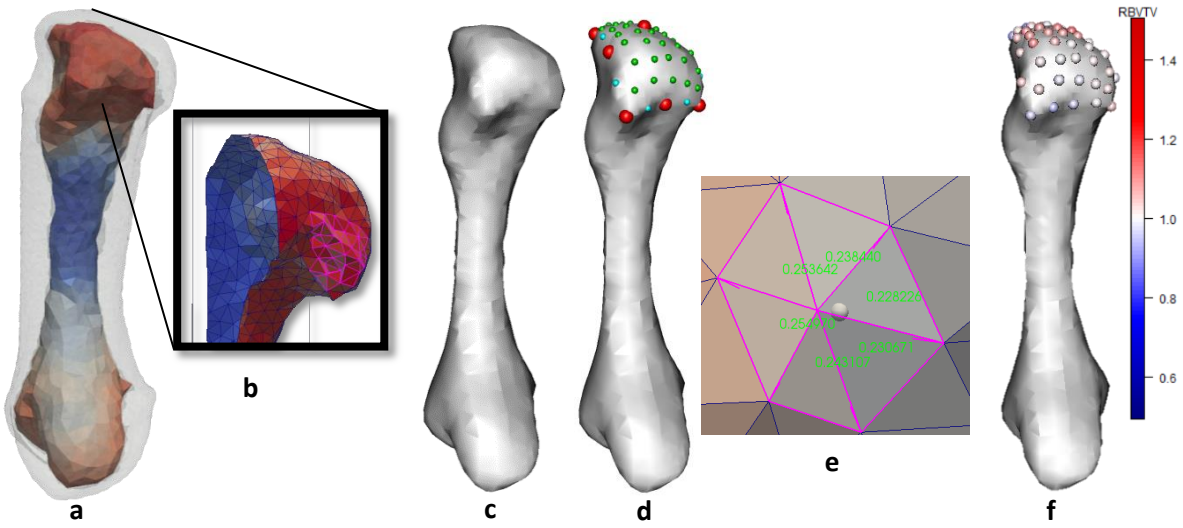

Figure 2.9. Illustration of geometric morphometric mapping procedure. a) The trabecular mesh of a *Pan troglodytes* Mc1, inside its cortical shell (translucent) with interpolated trabecular values (red = high BV/TV and blue = lower BV/TV). b) The extracted surface of the trabecular mesh cut in the sagittal plane to show its inner (blue) and outer surface (red) with some surface facet triangles selected (pink outline). c) The smoothed trabecular mesh, d) with anatomical landmarks (red) and sliding semi-landmarks on curves (cyan) as well as on the subarticular surface (green). e) A close up of selected surface facets, as in b), with their interpolated trabecular values and an example landmark. In this case the landmark would be associated with the 0.228226 value as this is the closest surface triangle centre. f) The entire landmark configuration with RBV/TV values as per scale bar. Note that as much of the original surface (a) had similar values, most of the landmark values are close to one, or the average BV/TV of this subchondral epiphysis.

Visualisation

To visualise the results of the subarticular trabecular analysis in a manner unbiased by a species metacarpal morphology, a canonical mesh was created using WxRegSurf (Gee et al., 2015; Tsegai et al., 2017). Specifically, a statistical shape model was constructed by registering the surfaces of each smoothed trabecular model to a single randomly chosen specimen using local affine deformation over 200 iterations. This was performed separately for each metacarpal position to create five canonical meshes on which the relevant landmark template could be projected, relaxed and slid to homologous positions as done for the real metacarpals using the R package Morpho (Schlager, 2017). Average values per species, and individual fossil values, could then be visualised on the appropriate

canonical metacarpal mesh using a continuous scale, created in R using the colorRamps package (Keitt, 2008). This approach was also used to depict the relative contributions of landmarks to a principle component (see below). Furthermore, each landmark was coloured individually to visualise significant differences where appropriate.

Statistical Analysis

Previous approaches to trabecular analysis (see Chapter 1), including a smaller number of large VOIs or sections of a whole epiphysis, artificially section the continuous structure of trabecular bone but they do provide units amenable to statistical analysis. The approach taken here was designed to capture differences in subarticular trabecular architecture without these artificial sections but presents less clear-cut units of analysis. Analysis proceeded with two complimentary statistical approaches, multivariate and mass-univariate, for relative trabecular volume (RBV/TV; see below) and DA, respectively.

The multivariate approach tests for differences in the distribution of trabecular values across landmark configurations, between species and rays. Sylvester and Terhune (2017) detailed a method in which geometric morphometric techniques have been used to analyse trabecular bone. In this study, overlapping spherical VOIs were placed just beneath surface sliding semi-landmarks on a trabecular mask. As there were a greater number of VOIs than specimens, and the VOIs also overlapped, their data were multi-collinear and therefore the authors opted to perform non-parametric MANOVAs, designed to deal with high-dimensional data to test for group differences in trabecular distribution (Sylvester and Terhune, 2017). Further interpretation was aided by principle components analyses (PCA) of trabecular values, to visualise the separation of groups and individuals at the extremes of principal components (PCs). The present approach employs much of the same logic as Sylvester and Terhune (2017) but builds on it in several significant ways. First the present approach effectively subsamples values interpolated from overlapping VOIs, at fewer landmarks than Sylvester and Terhune (2017), somewhat obviating the issue of multi-colinearity. Second, the present approach first conducts a PCA using the trabecular values at each landmark as a separate

variable. This variable reduction technique preserves most of the variation in trabecular values but reduces higher-dimensional data to a number of variables, PCs, far less than the number of specimens studied. As higher-dimensional data is not an issue for this approach, a less specialised permutational MANOVA was run on a response variable composed of the number of PCs that explained a substantial portion of the variability in trabecular dataset. A permutational MANOVA was used to test for differences between groups as the assumptions of multivariate normality were not always met by the distribution of PC scores. This omnibus test was conducted using the Adonis function in the Vegan package (Oksanen et al., 2018) in R. Although it is non-parametric, this test is still based on group variance and so a test of multivariate homogeneity of variances was performed on the Euclidean distance matrix that describes the PC scores, using the dist and betadisper functions in the Vegan package. In no case did groups have a significantly different variance of their PC scores. If this omnibus test was significant, pairwise permutational MANOVAs were conducted using the RVAideMemoire Package (Hervé, 2017) to determine which groups differed in their trabecular value distribution. For all permutational MANOVAs pseudo-*F* statistics describe the effect size of differences (Anderson, 2017).

Significance was set at $p<0.05$ subsequent to a Bonferroni correction for pairwise comparisons. While the current approach plots individual PC scores to visualise intra-group variation, it departs from previous work in that it uses the signed contributions of each landmark to each PC axis, to visualise the trabecular configuration at each end of each axis, rather that visualising one specimen that lies close to this extreme. This approach, therefore, does not rely on one individual falling near the extremes of a particular PC axis. To compare fossils to extant groups, a permutational one-sample Hotelling's T^2 test was run on the multivariate response variable made of PC scores. This was run using the Compositional package in R (Tsgaris and Athineou, 2018). Importantly this multivariate approach can identify significant differences in trabecular distribution between species or rays. However, this multivariate method does not directly test for significant regional differences in subchondral trabecular structure. That is, the method tells us that a

significant difference exists but not where that difference lies in the subchondral epiphysis.

To determine which regions of the trabecular architecture differed between groups, this analysis also employed a 'mass-univariate' approach as advocated by Friston et al. (1995). This type of statistical approach has also been used to analyse cortical bone in ape metacarpals (Tsegai et al., 2017), although in this case the authors performed statistical tests directly on the vertices of a mesh, resulting in many more statistical tests that could be refined using *p*-value clustering. The present thesis employs a lower resolution version of this approach utilising landmark data, as registering surfaces to achieve homologous vertices for analysis is difficult at the inter-species level. Registration of hominoid third metacarpal surfaces, for example, has been shown to be affected by both the relatively featureless smooth diaphyseal shaft and inter-specific differences in morphology, such as the presence of a styloid process in humans to the exclusion of other hominoids (Tsegai et al., 2017). Therefore, the trabecular values at each landmark are independently analysed, to ensure biological homology, using univariate statistics. Shapiro-Wilk tests found non-normal data at a minority of landmarks in every group comparison. To maintain consistent comparisons, a non-parametric Kruskal-Wallis test was applied at each landmark and a Dunn's test was used to test for pairwise differences if the omnibus test was significant. Dunn's test was chosen as it uses the pooled variance of the Kruskal-Wallis tests and is thus conservative. The level of significance was set at $p<0.05$ subsequent to a Bonferroni correction in each case. This univariate approach consists of homologous landmark value comparisons across groups rather than with spatially auto-correlated neighbouring landmarks. *Z*-scores were used to determine the polarity, as well as the effect size, of significant differences between groups. Mapping significant differences at landmarks allows for the identification of regions within a subchondral metacarpal epiphysis that are significantly different between species or rays.

Relative trabecular volume

Since bone volume fraction has been shown to be influenced by systemic factors in great apes (Tsegai et al., 2018), each landmark's raw BV/TV value was divided by the mean of every landmark BV/TV value on that metacarpal subchondral surface, to generate a relative measure of bone volume (RBV/TV, Fig. 2.9f). This measure allows for the comparison of the distribution of trabecular values rather than their magnitude, analogous to the *Z*-scores used by Sylvester and Terhune (2017) or the standardised BV/TV used by Sukhdeo et al. (2018). The magnitude of BV/TV, not measured by this scaled factor, has yielded interesting results, such as the overall lower BV/TV in recent humans relative to other hominids and fossil hominins (Chirchir et al., 2015; Ryan and Shaw, 2015; Tsegai et al., 2018). However, there is debate whether these group differences are systemic or related to functional bone adaptation. Low BV/TV in recent humans may primarily reflect either selection for a systemic reduction in bone mass, or anatomical site-specific bone functional adaptation due to sedentism and dependence on technology (Ryan and Shaw, 2015; Chirchir et al., 2015). Differentiating between these causes of decreased BV/TV magnitude is further complicated by the fact that this putatively systemic pattern appears to be expressed differently at different anatomical sites (Chirchir et al., 2015; Saers et al., 2016; Tsegai et al., 2018). This differential expression of the BV/TV pattern is usually associated with a functional aetiology but does not match observed behaviour. For example, within chimpanzee anatomical sites BV/TV is highest in the femur, but this is not the case in bipedal humans (Tsegai et al., 2018). A normalised BV/TV variable does not allow for this thesis to directly address interspecific differences in the magnitude of BV/TV and thus inferred differences in the frequency or extent of loading at the analysed joints. However, it preserves a bone functional adaptation signal in the distribution of BV/TV across a subchondral joint surface, when other factors, such as skeletal element, may obscure this in raw BV/TV values (Saers et al., 2016; see Chapter 4). RBV/TV controls for systemic differences and is also analogous to the process of bone remodeling itself, where a finite amount of energy is spent depositing bone to bear habitual load (RBV/TV >1) at the cost of depositing bone where there is less habitual load (RBV/TV <1).

Cross-sectional geometry of cortical bone

Cross-sectional geometry offers a complementary approach to the analysis of trabecular bone functional adaptation in diaphyseal cortical bone. Differences in the mid-diaphyseal shape and rigidity of long bones are often analysed to infer their function during life (Biewener and Bertram, 1994; Ruff, 2002; Marchi, 2005; Carlson and Judex, 2007; Young et al., 2018; Ruff et al., 2018; Macintosh and Stock, 2019). For appropriate comparisons of the cross-sectional geometry, each axial cross-section of a diaphysis must be placed in a homologous location. Protocols exist, particularly those of Ruff (2002), to orient and accurately assess the length of long bones to then define a 50% mid-shaft point. However, several metacarpals studied, particularly those of *Pongo*, were curved (Fig. 2.10). Such curvature adds extra variation to linear measures of length and, more importantly, means that axial cross-sections orthogonal to the long axis of anatomically oriented bones are not homologous to those of straighter metacarpals. This curvature can therefore distort the shape of a cross-section in the same manner as a non-orthogonal axial cross-section through a straight metacarpal would.

To somewhat control for the effect of diaphyseal curvature in metacarpals, a 2D sagittal cross-section of each segmented 3D metacarpal image was created using medtool 4.2 (Dr. Pahr Ingenieurs e.U.). A PCA was then run in the Numpy Python module, treating the bone pixels as 2D coordinates. The eigenvector that best described the variation in bone pixel distribution was then used as the new long axis of the bone, as it is the best way to mathematically describe the length of both curved and relatively straight metacarpals in linear manner (Fig. 2.10a). The 3D metacarpal image was then rotated through the sagittal axis by the angle between the original, anatomical, y-axis and the eigenvector in medtool 4.2 (Fig. 2.10b-c). The most proximal and distal bone voxels in a sagittal cross-section of the rotated metacarpal were then used to find the 50% mid-diaphyseal point in ImageJ (Schneider et al., 2012). Homologous axial cross-sections were created from the 3D image at this point using medtool. These axial cross-sections were then analysed using a Macro, developed by the researcher, to run mass Slice Geometry commands from BoneJ (Doube et al., 2010). The average, minimum and maximum area area

moments of inertia, and the maximum area moment of inertia in antero-posterior and medio-lateral, here radio-ulnar, planes, were calculated in mm^4 for each mid-diaphysis.

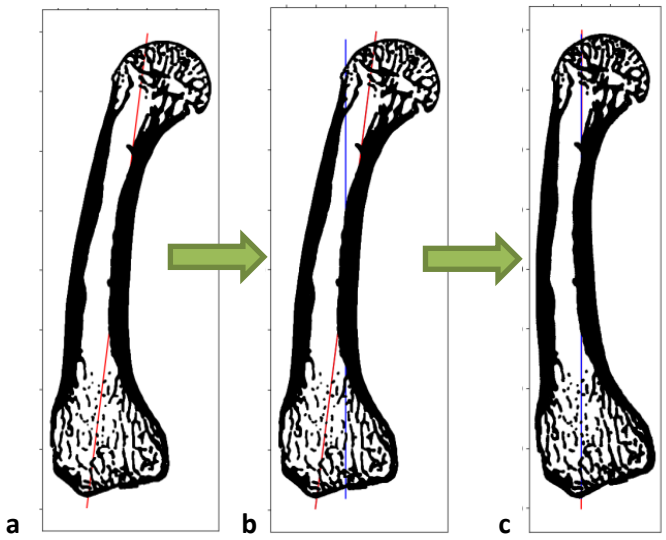

Figure 2.10. Example of metacarpal reorientation procedure for cross-sectional geometry. a) 2D sagittal cross-section of a metacarpal a principle eigenvector describing its long axis marked in red and b) with its anatomical long axis marked in blue. c) The cross-section after rotation of the 3D image; the angle between the two axes is now 0°.

Chapter 3
MIA-Clustering: A novel method for segmentation of paleontological material

Abstract

Paleontological research increasingly uses high-resolution micro-computed tomography (µCT) to study the inner architecture of modern and fossil bone material to answer important questions regarding vertebrate evolution. This non-destructive method allows for the measurement of otherwise inaccessible morphology. Digital measurement is predicated on the accurate segmentation of modern or fossilized bone from other structures imaged in µCT scans, as errors in segmentation can result in inaccurate calculations of structural parameters. Several approaches to image segmentation have been proposed with varying degrees of automation, ranging from completely manual segmentation, to the selection of input parameters required for computational algorithms. Many of these segmentation algorithms provide speed and reproducibility at the cost of flexibility that manual segmentation provides. In particular, the segmentation of modern and fossil bone in the presence of materials such as desiccated soft tissue, soil matrix or precipitated crystalline material can be difficult. Here we present a free open-source segmentation algorithm application capable of segmenting modern and fossil bone, which also reduces subjective user decisions to a minimum. We compare the effectiveness of this algorithm with another leading method by using both to measure the parameters of a known dimension reference object, as well as to segment an example problematic fossil scan. The results demonstrate that the MIA-clustering method produces accurate segmentations and offers more flexibility than those of equivalent precision. Its free availability, flexibility to deal with non-bone inclusions, and limited need for user input give it broad applicability in anthropological, anatomical, and paleontological contexts.

Published Article: Dunmore C.J., Wollny G., Skinner M.M. (2018) MIA-Clustering: a novel method for segmentation of paleontological material. *PeerJ* 6:e4374 (see Appendix B)

Introduction

Over the last decade, there has been an abundance of high-resolution micro-computed tomography (μCT) studies within the paleontological and anthropological communities, likely due to the ability of this method to non-destructively image extant and fossil specimens. This has been used to investigate the inner osseous architecture of a diverse range of orders including, but not limited to : primates (Ryan et al., 2010), galliformes (Pontzer et al., 2006), xenarthrans (Amson et al., 2017) and diprotodontians (Biewener et al., 1996). The technique allows the visualization of internal structures, such as trabeculae (Fajardo et al., 2007), the enamel-dentine junction of teeth (Skinner et al., 2009) or the inner ear (Spoor et al., 2007). This is of particular importance for fossils, whose inner architecture could only be destructively analyzed otherwise (Witmer et al., 2008; Kivell, 2016). To visualize very small biological structures, it is necessary to ensure adequate X-ray penetration of the bone or fossil material being CT-scanned, as well as to control for common artefacts such as beam hardening (Herman, 1979). To digitally measure these structures and their properties, it is necessary to define them in the scan image and so the image must be accurately segmented (Hara et al., 2002).

Various segmentation protocols have been developed for anthropological applications. Simple thresholding involves the visual selection of a grayscale value, any part of the image composed of voxels above this value is considered the phase of interest. Iterative adaptive thresholding (Ridler and Calvard, 1978; Trussell, 1979; Ryan and Ketcham, 2002) improves on this simple thresholding by optimizing the threshold value between the present phases. Conversely, Half-Maximum-Height thresholding (HMH, Spoor et al., 1993; Coleman and Colbert, 2007) re-calculates the threshold over a row of pixels, which cross a phase boundary, periodically in the z-axis of a three-dimensional (3D) image. These three methods are all sensitive to intensity inhomogeneity and background noise in a scan (Scherf and Tilgner, 2009). In all cases, a grayscale value threshold calculated from a different or larger section of an image may not accurately segment all parts of the structure.

Instead of using grayscale values alone, region-based segmentation approaches incorporate the spatial information in a scan. Region growing methods use seed

points, manually selected by the researcher, known to be in the phase of interest. A segmented region is then grown from the seed by connecting neighboring voxels that meet specific, pre-defined criteria (Pham et al., 2000). Region splitting, conversely, does not use seed points but divides the image into distinct regions and re-fuses the image based on selected criteria. Both region-based approaches, however, often require *a priori* knowledge of image features to select seed points or criteria, and can be sensitive to intensity inhomogeneity (Pham et al., 2000; Dhanachandra and Chanu, 2017).

Edge-detection-based segmentation offers an alternative method that discerns the transition between two phases and delineates these voxels as an edge. The Ray Casting Algorithm (RCA, Scherf and Tilgner, 2009) is an example of this method used in anthropology (e.g. Tsegai et al., 2013). This algorithm uses a 3D-Sobel filter to mark voxels at the peak of rapid changes in grayscale values and subsequently removes the rest of the image with a non-maximum suppression filter. To be considered part of the remaining edge of the phase of interest, the gradient of the grayscale transition must be above a user-defined 'minimum edge strength' parameter. This one-voxel-thick edge may have infrequent gaps due to local, more gradual, transitions not quite satisfying the 'minimum edge strength' threshold. In order to ameliorate this, a series of rays are subsequently cast at 11.25° steps around the normal of each edge voxel in an arc of ±45°. The rays are set to terminate on meeting a voxel with the specified 'minimum edge strength', so edge voxels that neighbor these gaps terminate the rays at most angles, and the gap is closed. The RCA segmentation produces a structure with the continuous edge described (Scherf and Tilgner, 2009).

Edge-based segmentation techniques provide an advantage over other techniques in that they are resistant to the effects of both background noise and intensity inhomogeneity. Tests of segmentation methods have found RCA is more accurate than thresholding methods (Scherf and Tilgner, 2009). Similarly, algorithms such as RCA require less prior knowledge of the image, as they need no seed points or initial manual segmentation. Still, the RCA requires the selection of the 'minimum edge strength' value and may also incorporate minimum or maximum threshold

values. These input values are found during trial segmentation of a subset of the data (Scherf and Tilgner, 2009). The selection of these three parameters is partially subjective, as is the case with all segmentation algorithms. This input parameter selection represents another source of error, that an algorithm must be robust to, in addition to background noise and intensity inhomogeneity. An algorithm run with extreme parameters is unlikely to produce an accurate segmentation. With RCA, the same segmentation can be produced with different sets of input values. This equifinality is not a problem of the method *per se*, but allows for additional potential difficulty in reproducing the same segmentation. A researcher cannot be sure that a visually similar segmentation was produced using the RCA parameters. Here we present a segmentation method, Medical Image Analysis (MIA)-Clustering, implemented as free and open-source software (Wollny et al., 2013), that reduces subjective user decisions to a minimum. Broadly, clustering approaches sort the voxels or pixels of an image into a number of clusters defined by the user. This sorting is accomplished by iteratively calculating the center of a cluster and its distance to the other voxels in that cluster. This iteration then converges on stable clusters by minimizing this distance and the voxels in each cluster are segmented as distinct phases. The MIA-Clustering algorithm performs this sorting both globally and locally to segment an image based on its properties.

We test the efficacy of the MIA-Clustering algorithm by segmenting a reference model of known thickness. Results of this segmentation and a RCA segmentation of the same material following Scherf and Tilgner (2009) are compared. To assess the robusticity of the MIA-Clustering algorithm to variation in parameter selection, segmentations of this synthetic material, produced by a range of inputs, are analyzed. Similarly, a fossil sample is segmented with different parameters to assess their effect on the segmentation of a highly variable, embedded, natural structure. This fossil also presents a challenging segmentation, due to multiple phases of invasive matrix as well as bright inclusions, and so permits an assessment of the MIA-Clustering algorithm's robusticity to background noise and intensity inhomogeneity. The fossil is also segmented using the RCA to compare the simplicity and accuracy of both methods.

Materials

A coiled stainless steel wire, which is rectangular in cross-section, was used as a reference object of known thickness (40 µm). This materially homogeneous phantom was scanned in air, with the SkyScan 1173 µCT scanner at the Max Planck Institute for Evolutionary Anthropology, Leipzig, Germany, at 80 kV and 62 µA. This shape of object has previously been shown to both approximate trabecular bone and be susceptible to beam hardening due to its structure (Scherf and Tilnger, 2009). The 4224 x 4224 x 2240 voxel reconstructed image had an isometric voxel size of 7.86 µm. This was cropped to an image size of 3240 x 3240 x 150 voxels to reduce processing time. The example fossil was scanned at 90 kV and 200 µA using a Nikon Metrology XTH 225/320 at the University of the Witwatersrand. This fossil is U.W.88-119, a first metacarpal of Malapa hominin 2, *Australopithecus sediba,* dated to 1.98 million years ago and found in peloidal sandstone (Berger et al. 2010; Pickering et al., 2011). Permission to use this material was granted by Fossil Access Committee of the Evolutionary Studies Institute at this institution. The reconstructed image was 726 x 551 x 1826 voxels and had an isometric voxel size of 22.6 µm.

Methods

MIA-Clustering Algorithm

The MIA-Clustering algorithm is a machine-learning approach, based on fuzzy c-means clustering (Pham and Prince, 1999) and initialized by the K-means algorithm (Forgy, 1965; Lloyd, 1982). First, the K-means algorithm clusters the input data, based on voxel intensity, into the number of classes specified by the user (Fig. 3.1a-b). A subsequent fuzzy c-means algorithm iteratively estimates all class membership probabilities for each voxel, expressed as a vector (Fig. 3.1c). Based on their highest membership probability, voxels are globally clustered into distinct classes representing structures in the whole image. However, this global segmentation does not always capture fine detail because the input images may suffer from intensity inhomogeneities, which result from scanning artifacts or different levels of

fossil mineralization. Therefore, subsequent local fuzzy c-means segmentation is applied.

Based on a user-defined grid-size parameter, the volume is subdivided into overlapping cubes. For each cube, the class membership probability vector is initialized by using the globally obtained probabilities (Fig. 3.1d). If the sum of membership probabilities of all voxels in a sub-volume falls below a threshold, then this class is not taken into account for the local, refined c-means clustering. This threshold can be specified by the user if desired, but the default value of 2% appears to generate acceptable segmentations and was used in all cases here. Therefore in this case, if there was no more than 2% of a cube that was globally clustered as a certain class, this class was not considered for that cube's local c-means segmentation. Subsequently, class probabilities for each voxel in overlapping cubes are merged, and voxels are assigned to the class for which they have the highest membership probability, producing the whole segmented image (Fig. 3.1e). This local segmentation allows the algorithm to compensate for local intensity variations. It follows that a grid-size value smaller than the structure of interest will cause the algorithm to attempt to find clusters within these structures, such as small inhomogeneities in cortical bone, that are generally not of interest. Therefore, to balance between compensating for inhomogeneities resulting from imaging artifacts and ignoring small inhomogeneities within the structures of interest, the grid-size parameter selected should be slightly larger than the largest dimension of the phase of interest for the segmentation. For a variable and continuous structure, such as trabecular bone, we recommend looking at 2D cross-sections in each plane and measuring thicker trabeculae to ascertain their width in pixels. The grid-size value should then be set a few voxels larger than these measurements to ensure the local segmentation is not looking for features within the phase of interest (e.g. Fig. 3.2). The global and local segmentations can be generated at the same time for comparison of each segmentation step.

Finally, an optional threshold can then also be applied to the calculated class membership probabilities of each voxel. A voxel is excluded from a class if its highest membership coefficient does not meet or exceed the threshold given.

Voxels that do not meet the threshold for their highest class are assigned to a grayscale value of zero and all other classes are elevated by one gray value. Since the vector of membership probabilities sums to one, in practice, this allows the user 50 threshold values (51-100%) to fine tune the segmentation based on the initial, data-led, analysis. The black or zero-class voxels that did not meet the threshold can be considered a margin of error for the segmentation (Fig. 3.1f).

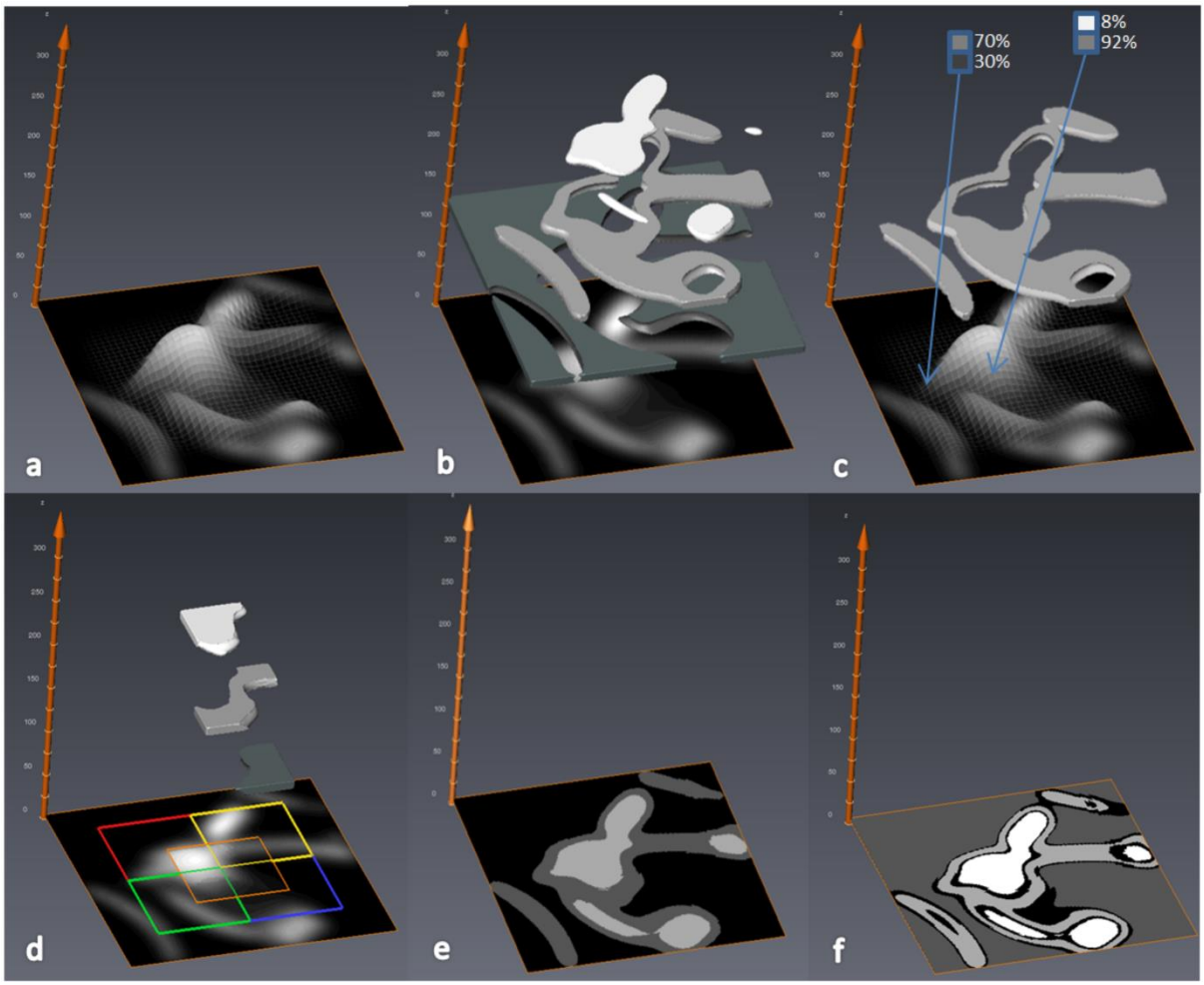

Figure 3.1. Diagram of MIA-Clustering algorithm in a 2D-image. a) Gray values are mapped to the z-axis. b) Gray values are initially clustered into three classes by the K-means algorithm; the black-class is represented as dark-gray in the 3D overlay for clarity. c) The fuzzy c-means algorithm iteratively estimates a class membership probability vector for each voxel (two example voxels are shown in blue boxes) and globally clusters each voxel based on its highest class probability. d) Local fuzzy c-means clustering is performed in overlapping sub-volumes, here represented by the colored squares. e) Overlapping class probabilities are merged and voxels are clustered based on their highest membership probability. f) An optional probability threshold is then applied at an arbitrary 75%, for illustrative purposes. All voxels with their highest membership probabilities below 75% are labeled as zero, or black, and voxels above this threshold are clustered into three classes labeled by gray values elevated by one; here one to three.

Wire Segmentation

In order to test its efficacy, the MIA-Clustering algorithm was used to segment a scan of a machined wire phantom, previously measured at 40 µm thickness, following Scherf and Tilgner (2009; Fig. 3.3). The RCA was also used to segment the same image for comparison. 3D-thickness was measured at every point, in each segmentation of the same 3240 x 3240 x 150 voxel volume in the center of the wire, using the BoneJ plugin for ImageJ (Hildebrand and Rüegsegger, 1997; Doube et al., 2010). Average 3D-thicknesses within one voxel, or ~8 µm, of the measured thickness were considered effective segmentations. In the case of RCA, 3240 x 3240 x 10 voxel trial segmentations were run to find the three input parameters that produced acceptable segmentations. In the case of the MIA-Clustering algorithm, the wire thickness of 40 µm divided by the resolution yielded a voxel size of approximately five, thus the grid-size was set just above this at seven. The probability threshold used was found after two trial segmentations.

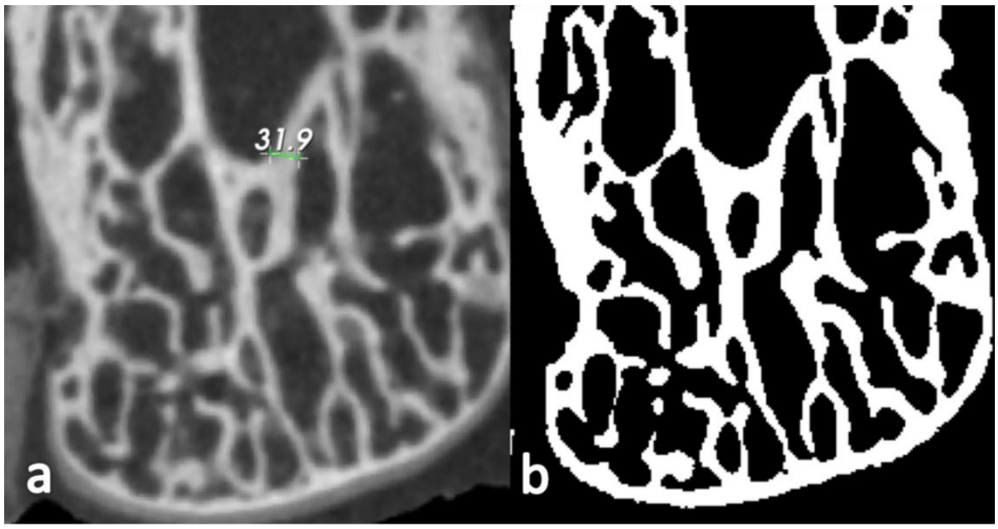

Figure 3.2. A 2D cross-section image of an example dry bone. a) One of its thickest trabecular struts in the image measured in Paraview, at ~32 pixels. b) A binarized image of the same cross-section after 3D segmentation of the bone, using the MIA-Clustering algorithm. The grid-size input parameter selected for the segmentation was 35 voxels as this was just larger than the measurement in a).

Parameter robusticity

In order to test the robusticity of MIA-Clustering algorithm, the full range of both input parameters was independently varied and average thickness of the wire in the resulting segmentations was measured. The probability threshold was varied in 5% increments from 50% to 95%. Grid-size was varied from the smallest maximum dimension of the data-set, here 150 voxels, to the minimum value of three. The fossil specimen was segmented at grid-sizes from 10 to 100 voxels, since these more extreme values did not produce a visually satisfactory segmentation. This allowed comparison between segmentations produced by a range of possible values and the grid-size value attained from a cursory visual inspection (e.g. Fig. 3.2), in a variable structure of largely unknown thickness.

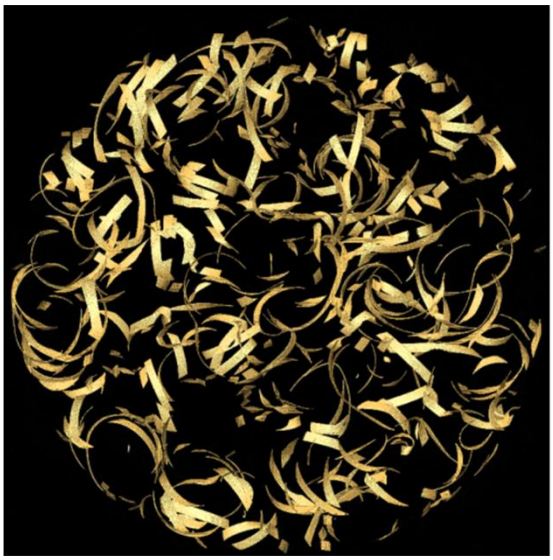

Figure 3.3. A 3D-surface view of the machined wire phantom.

Fossil application

In order to assess the performance of the presented method on paleontological material, the fossil is segmented using the RCA as well as the MIA-Clustering algorithm; pre- and post- processing steps are described. Every fossil scan is likely to present different issues, owing to disparate diagenetic processes over varying timescales. In some fossils, invasive matrix may be relatively uniform, but overlap in attenuation intensity with the fossil bone phase preventing its removal by a global threshold. Similarly small bright mineral inclusions may provide grayscale value

outliers, thus decreasing contrast in the majority of the material, markedly affecting segmentation approaches based on thresholding of a grayscale value range such as the iterative, adaptive threshold method (Ryan and Ketcham, 2002; Fajardo et al., 2007). Also, cracks and multiple phases of invasive matrix may create edges within the fossil that are distinct from the fossil bone. The present fossil scan contains all of these issues to some extent, as well as a global-gradient that becomes brighter towards the center of the fossil. This centrally higher attenuation artefact is the result of photons with less energy than is required to uniformly penetrate this dense fossil and is essentially the inverse of beam hardening.

Implementation

The RCA segmentations were run as a stand-alone executable on the Windows command line. The MIA-Clustering algorithm was run as command line tool using Medical Image Analysis (MIA, Wollny et al., 2013). MIA was run from a Docker image as a Docker container in order to run a lightweight virtual Linux machine in Windows (Boettiger, 2015). This approach allows MIA to be run on most widely available operating systems. Instructions for downloading and use of MIA are available at http://mia.sourceforge.net/.

Results

Wire segmentation

Two acceptable sets of parameters were found for RCA segmentations, after at least 10 trial segmentations for each. The probability threshold value for the MIA-clustering algorithm was found after two trial segmentations at 80% and 90%. MIA-clustering algorithm segmentations of the 3 gigabyte wire phantom scan ran in ~10 minutes using four cores whereas RCA ran this object in ~8 minutes using 16 cores.

Table 3.1. Mean and standard deviation of thickness calculated for each segmentation method.

Segmentation Method	Thickness Mean (Pixels)	σ (Pixels)	Thickness Mean (µm)	σ (µm)
RCA.1	5.054	1.340	39.728	10.533
RCA.2	5.026	1.386	39.508	10.895
MIA-Clustering Algorithm	5.111	0.952	40.176	7.484

RCA.1 used parameters lower threshold: 7,000, upper threshold: 20,000 and minimum edge strength: 5,000; RCA.2 used lower threshold: 18,000, upper threshold: 26,000 and minimum edge strength: 20,000. Note the near identical measurements using two different sets of values. Parameters for the MIA-Clustering algorithm were grid-size: 7 and probability threshold 85%.

As can be seen in Table 3.1 and Figure 3.4, both algorithms can produce accurate segmentations, segmenting the wire at thicknesses within 1 micron of the known width of the wire. Figure 3.5, however, demonstrates that at least for some local areas the MIA-Clustering algorithm segments the closely packed, fine structures more accurately than either of the equifinal RCA segmentations. The average thickness values are within 1% and 0.5% of the known thickness, respectively. This is considered acceptable given an isometric voxel size of eight microns (Table 3.1). The standard deviation of the thickness measured in the RCA segmentation is slightly higher than the voxel size whereas the MIA-Clustering algorithm segmentation standard deviation is below this level of variability and therefore is the result of partial volume effects.

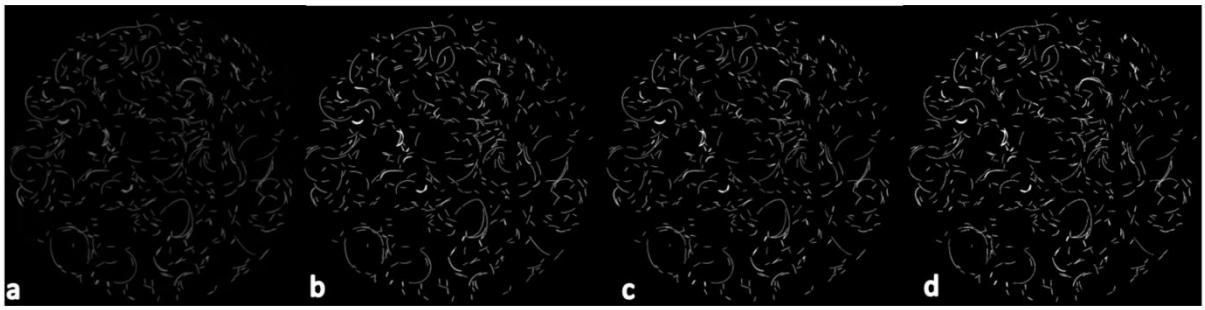

Figure 3.4. The mid-slice of the wire scan in superior view. a) The reconstructed image. b) The segmented image produced by the MIA-Clustering algorithm. c) The segmented image produced by the RCA.1 and d) the equifinal RCA.2 segmentation. Note the similarity of the segmentations of a) in each method (b, c, d).

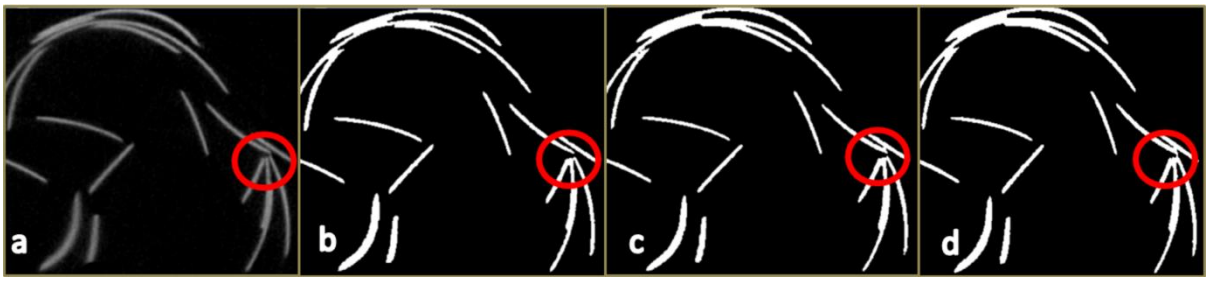

Figure 3.5. A magnified section of the mid-slice of the wire phantom scan (Fig. 3.4) in superior view. a) The reconstructed image. b) The segmented image produced by the MIA-Clustering algorithm. c) The segmentation produced by the RCA.1 and d) the equifinal RCA.2 segmentation. Note the separation of closely packed wire in the red circles in a) and b) but not in c) and d).

Parameter robusticity

In order to evaluate the potential effect of input error in the MIA-Clustering algorithm, the wire was segmented over the full range of each input variable, and average 3D-thickness of each segmentation was measured. Figure 3.6a demonstrates the linear relationship between probability threshold and thickness for this image. The range of grid-size values result in a thickness range of 12 µm. Figure 3.6b demonstrates an exponential relationship from the maximum possible (150) to the minimum possible grid-size (3) and a thickness range of 9 µm. This parameter quickly converges on values within 10% of the known thickness of the wire when grid-size becomes small enough to segment the finer structures of the image at ~25 voxels. From this point lower grid-sizes produce a larger variation in thickness values as fine structures are more consistently segmented, only underestimating thickness when a grid-size smaller than the width of the fine structures is used. As expected, different grid-sizes produced a wider range of mean thickness measures (~100 µm) for the structurally variable fossil, than the machined wire (Figs. 3.6 and 3.7). It should be noted that these values include cortical bone and reflect variation in segmentation of the whole image rather than a trabecular analysis. Despite this larger range, thickness values display an exponential relationship with grid-size quickly converging on the value obtained from visual inspection. Much as in the grid-size comparison for the machined wire (Fig. 3.6b), when grid-size becomes small enough to segment the finer structures of the image at ~35 voxels variation in thickness increases (Fig. 3.7). This trend continues until a grid-size smaller than the width of the fine structures is used and the method begins to detect inhomogeneities within the osseous structure.

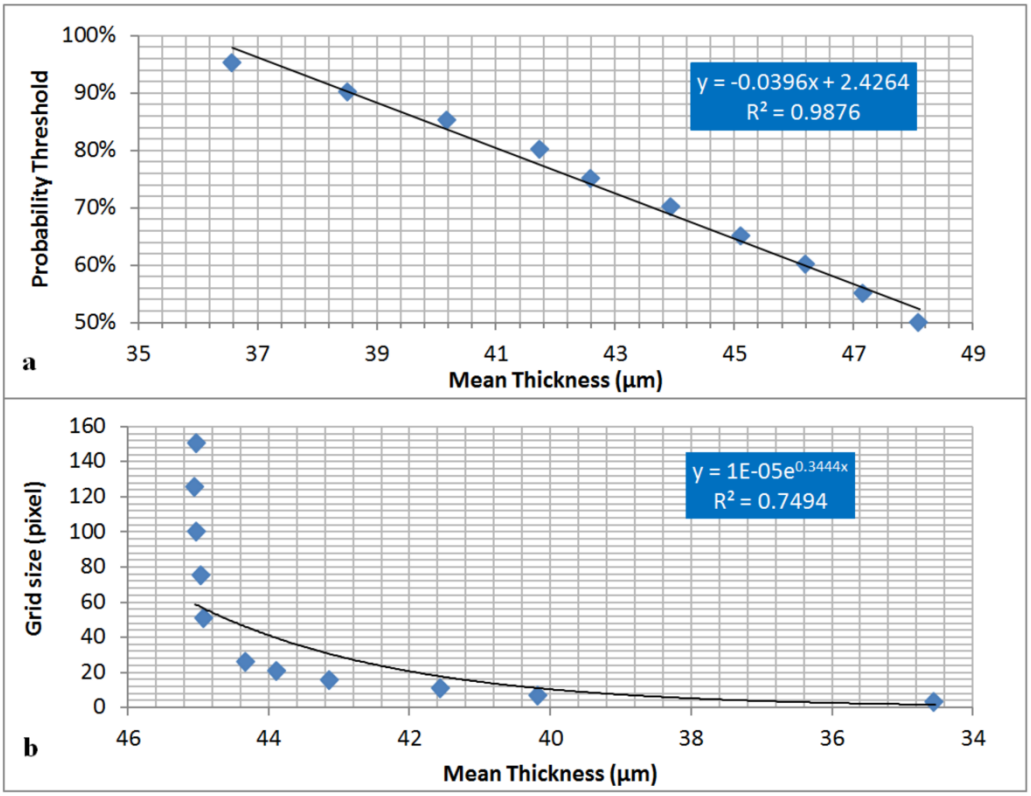

Figure 3.6. The effect of MIA-Clustering algorithm parameters on average thickness of the wire. a) Full range of possible probability thresholds and with grid-size of 7 held constant. b) Full range of possible grid-sizes with probability threshold held constant at 85%.

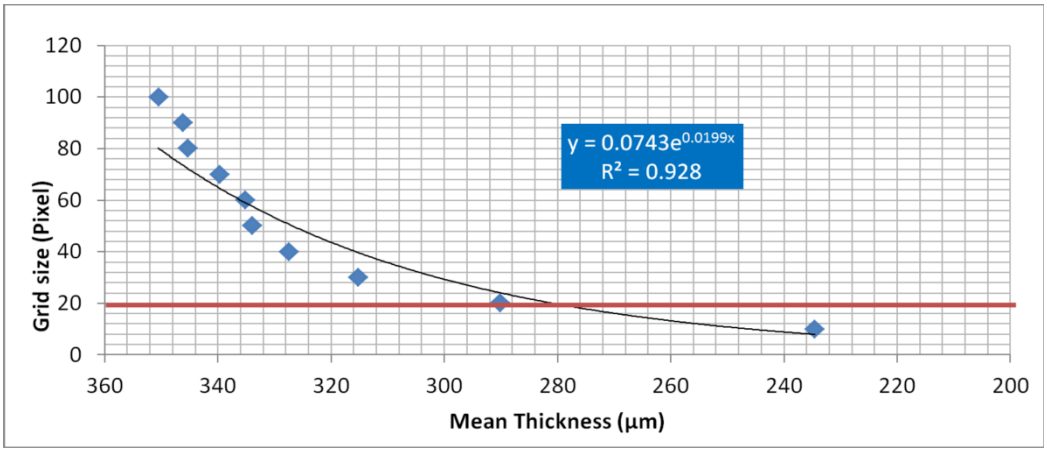

Figure 3.7. The effect of grid-size input on average thickness estimates of the fossil, after MIA-Clustering segmentation. Grid-size ranged from 10 to 100 voxels. The red line represents the grid-size of 20, ascertained from manual measurement of the fossil as per the technique in Fig. 3.2.

RCA fossil segmentation

RCA is only able to segment the highest attenuation phase in an image, because it will only exclude voxels on the other side of a gradient-defined edge if they have a lower gray value than the phase of interest. Since the structure of interest was not the brightest part of the image (Fig. 3.8a), it was necessary to invert the image in Avizo 6.3 (Visualization Sciences Group, Fig. 3.8b). A median filter of kernel size three was run as part of the RCA program using a lower threshold of 19,000, an upper threshold of 29,000 and minimum edge strength of 2,500 (Fig. 3.8c). This was not a satisfactory segmentation of the image, as much of the trabeculae near the center of the bone were lost. Therefore, in order to somewhat reduce the artifactual global-gradient, the original image was subjected to a median filter of kernel size 25, obliterating structures but preserving the global-gradient (Fig. 3.8d). The resultant image could then be added to the inverted image to 'cancel-out' the global grayscale gradient without affecting the edge gradients of the trabeculae to a large extent (Fig. 3.8e). RCA segmentation could then produce an improved segmentation with same parameters as initially used (Fig. 3.8f).

MIA-Clustering algorithm fossil segmentation

As a pre-processing step, a noise reducing median filter of kernel size three was applied, and the image was thresholded at 10,000 to remove noise in the background of the image (Fig. 3.8a). The MIA-Clustering algorithm was run to look for three classes with a grid-size of 20, since the thickest elements of the trabecular bone were ~15 voxels in dimension from a cursory inspection in Avizo 6.3 (Fig. 3.8g). No probability threshold was needed in this case for refinement, though running the command with a threshold of 50% achieves the same result. Subsequently the image was binarized on the second brightest class in the image, leaving only the fossil bone phase (Fig. 3.8h). This post-processing step allows for direct comparison with the RCA segmentation but is not necessary (Fig. 3.8f, c, i).

Discussion

Wire segmentation

The current study presents a novel open-source method for segmenting bone or fossil bone phases from high-resolution µCT images. Tests using a wire phantom indicate that both this technique and RCA are capable of producing accurate segmentations that are within 1% of the wire phantom's thickness (Table 3.1; Figs. 3.5 and 3.6). Therefore, in scans with high material contrast, including those of the present synthetic sample and many examples of dry bone, it appears both segmentation techniques would produce accurate results. However, in practice, the MIA-Clustering algorithm offers several advantages over other segmentation techniques by keeping subjective user decisions to a minimum to increase the reproducibility of results.

Parameter robusticity

Many segmentation approaches can require manual interaction with the image to provide appropriate input parameters, such as the placement of seed points for a region-based segmentation or the visual inspection of trial RCA segmentations. In this case, the user must iteratively determine whether one set of trial RCA parameters produced a better segmentation of the wire phantom than the last and when these parameters could no longer be improved. It can often take many attempts to find acceptable parameters, since there is no objective starting point other than the range of grayscale values in the image for the lower and upper thresholds. Since 'minimum edge strength' is not easily visualized, it can be initially difficult to find an acceptable value for this parameter. Conversely, the MIA-Clustering algorithm input parameters are data-led, as grid-size selection is based on the dimensions of the structure to be segmented, either through prior knowledge or an initial, manual, inspection of the material (Fig. 3.2). In the case of the wire, a grid-size of seven is just larger than its (known) five voxel thickness, and six voxels may be too small due to potential partial volume averaging effects. In the case of the fossil, cursory measurements in three orthogonal 2D-slices of the image were sufficient to determine an appropriate grid-size of 20. Average thickness measures of segmentations produced by different grid-sizes demonstrate that a

grid-size of 20 is within the range of values that greatly affect the segmentation result (Fig. 3.7) but is not so small that algorithm detects inhomogeneities within the phase of interest and begins to break-up and thin trabeculae (Fig. 3.8g, h, i). In both cases, as the grid-size parameter selection was data-led, there was an objective justification for the value used. Though this value may not necessarily produce the optimal MIA-Clustering segmentation, especially in the fossil, it does provide a starting point within a narrow range of values that allow the segmentation of finer structures to varying degrees. Further, as the grid-size parameter defines a local reapplication of a machine-learning algorithm, it could be argued it is more objective than a user-defined threshold of either absolute grayscale values or their gradients. Therefore, this data-led parameter selection requires minimal manual interaction with an image and provides an objective justification for the value used, even when segmenting a structure of largely unknown and variable dimensions, such as osseous or fossil material.

The optional probability threshold parameter, however, is more subjective as it is only found by trialing values. Yet, this final step of the algorithm may only fine tune the segmentation from the data-led clustering results. Indeed, over the full range of 50 possible values not only did the segmented wire phantom show just a 30% variation in measured average thickness, it did so in a predictable way with strong a linear relationship (Fig. 3.6a).This is due to the fact that voxels at the boundary of each segmented phase will have lower membership coefficients than those in the middle on the phase (Fig. 3.1c). As the threshold is raised, more of these boundary voxels are no longer considered part of this phase and the thickness of the structure will reduce in-kind (Fig. 3.1f). This relationship allows the user to potentially derive an acceptable value after just two trials. The probability threshold is particularly useful for the accurate segmentation of abrupt phase transitions, such as the edge of the machined wire. In structures with more gradual or complex edge transitions, such as fossilized or extant bone, this parameter is less useful as the effects of different values will be less predictable; the probability threshold was not used in the fossil segmentation. Therefore the MIA-Clustering algorithm keeps subjective user decisions to a minimum by basing input parameters on the

properties of the image, rather than iterative manual interaction and more subjective refinement of the result is done in a predictable way, over a small range of input values.

Another way the MIA-Clustering algorithm reduces subjective user decisions is by limiting input parameters to a minimum. The algorithm only takes two input parameters, each with a smaller range of values than the three of RCA, since minimum edge strength ranges from 0-32,000 and the thresholding limits are based on the potential gray value range of 16-bit data, 0-65,535. Initially, the relatively small range of inputs for the MIA-Clustering algorithm could be seen as detrimental, affording the researcher less freedom to find values to segment the data accurately. However, this constraint allows for less error in parameter selection and is sufficient to quickly converge on a single pair of parameters that produce an acceptable segmentation (Figs. 3.6 and 3.7). An additional benefit to having a small range of input values is that it does not allow for multiple combinations that yield similar results. Here, there are at least two sets of input parameters for the RCA that can produce near identical segmentations and thickness value measurements (Table 3.1; Figs. 3.4 and 3.5). The MIA-Clustering algorithm is not subject to the same equifinality and so results are more reproducible since they can only be achieved via the same input.

The MIA-Clustering algorithm appears to be as accurate as another leading segmentation technique, RCA, in segmenting the wire phantom. Yet, the method presented here reduces subjective user decisions to a minimum by grounding input parameters in the properties of the image as well as limiting the range of these input parameters and in doing so, obviating the issue of equifinality. This increased objectivity allows for faster more reproducible segmentations (Table 3.2). Indeed, since these parameters are not based on grayscale values but rather the structures at hand, they may be applied uniformly across a sample of different scans of similar synthetic, or dry osseous, material removing another potential source of error in segmentation and measurement across a sample. However, perhaps the most useful property of the MIA-Clustering algorithm is its ability to segment more complex, embedded structures, with less clear contrast, such as fossil material.

Table 3.2. Summary of subjective user decisions minimized by the MIA-Clustering Algorithm.

Subjective user-decision	Minimized by the MIA-Clustering Algorithm?	Minimized by RCA?
Initial input parameter selection	Yes, grid-size should be slightly larger than cursory measurement of the structure of interest.	No, while maximum upper and lower thresholds may be found from the data range in the image, appropriate minimum edge strength values are not clear initially.
The number of decisions required.	Yes, only the single parameter, grid-size, must be chosen. The additional probability threshold is optional and simply a refinement of the segmentation.	No, three parameters must be chosen, each of which could have a great effect on the segmentation.
The input parameter values selected from the possible range.	Yes, grid-size should be slightly larger than the maximum 2D dimension of desired structure and only values close to the initial grid-size value will have a great effect on the segmentation.	No, the full range of 16-bit data grayscale values (0-65,535) and minimum edge strength values from 0-32,000 are available. Further different combinations may produce the same result.
How to invert or otherwise, pre-process an image where the desired structure is not the brightest in the image.	Yes, multiple classes can be segmented at once; the desired class can be thresholded out if required. Similarly, other types of data such as 8-bit may be segmented.	No, pre-processing steps required for the algorithm are not standardized and maybe unique to particular images.
How to ensure parameters used in segmentation of different scans do not introduce additional variation into the structures analyzed.	Yes, similar structures (such as trabeculae in two fingers of the same hand) should have similar grid-sizes applied.	No, scans of two very similar materials may have different gray values and so require different sets of input parameters.

Fossil Segmentation

One of the clearest challenges uniquely presented by segmentation of the fossil material is the high-attenuation invasive matrix. As the highest attenuation phase is selected by default in RCA, it was necessary to invert the foreground image, where matrix has a higher attenuation than the fossil bone (Fig. 3.8b), adding another pre-processing step and a potential source of error. Conversely, the MIA-Clustering method can segment multiple classes at once. Matrix, background and bone may each be a distinct initial cluster set, used to segment the image into separate gray value classes. Any of these classes can be extracted from the image via a simple threshold if subsequent analysis requires a binarized image (Fig. 3.8h). MIA (Wollny et al., 2013) offers a number of single-task command line tools, including a binarize filter that was used to produce the present result. The highest attenuation structure need not be the one of interest, and so the extra step of inverting the image is not required. Since matrix is also segmented, it is also easier to compare the segmentation to the original image by eye, as the white of binarized image may appear larger than the original simply because it is brighter (e.g. Fig. 3.8a, g, h).

A further challenge of this particular fossil image is the global-gradient which makes the center of the object appear brighter than the edges. The ray casting step of the RCA was invented to close gaps in Sobel filter defined edges that are caused by local grayscale transitions, not steep enough to meet the globally set 'minimum edge strength' parameter. The first derivative of grayscale value transitions, rather than absolute values, is still based on a global, if locally applied, threshold. Therefore, although RCA mitigates the effects of a global-gradient, it is not immune to them (*contra* Scherf and Tilgner, 2009). The global intensity gradient may affect one side of an edge more than the other if one edge is more central and, in doing so, may change the grayscale gradient over the transition. Therefore, RCA may not find edges where they exist in the cases of these artefacts. The present fossil scan appears to be darker in the center of the inverted image (Fig. 3.8b). RCA accurately segments the trabeculae closer to the edge of the fossil but fails to segment the central trabeculae as their grayscale gradients relative to the matrix phase are not steeper than the 'minimum edge strength' threshold applied (Fig. 3.8c).

Ameliorating this global-gradient as per the extra pre-processing steps allows the RCA with the same parameters to segment these central trabeculae (Fig. 3.8f). However, these extra un-prescribed steps make the segmentation process less efficient and potentially less reproducible. The MIA-Clustering algorithm, however, does not use grayscale based thresholds but considers only the local sub-volumes at the edge or the center of the fossil when segmenting them and can therefore segment the trabeculae in both areas of the bone concurrently (Fig. 3.8g, h, i).

Both fossil segmentations contain thin rings at the boundary of invasive matrix and air as these features are present in the initial image and have similar characteristics as trabecular bone (Fig. 3.8c, f, i). While both algorithms fully segment the image, researchers may wish to remove these features, before analysis, as they are not of biological origin. While this is beyond the scope of the current method, we would suggest applying a connected component algorithm, as available in software such as Avizo, to remove many of these features that are unconnected to the segmented bone. Unfortunately, to the authors' knowledge, remaining connected features must be removed manually at the researcher's discretion.

Unlike RCA and single threshold methods, the MIA-Clustering algorithm has the flexibility to concurrently segment multiple classes across a fossil specimen affected by a global-gradient scanning artefact, segmenting a phase of interest that is not necessarily the brightest in the image. The preservation of multiple classes in the segmentation provides a higher fidelity comparison between the segmentation and the original image. Also, the lack of additional pre-processing steps required for this segmentation allows for fewer potential sources of error and greater reproducibility of results. Therefore, this method is particularly suitable for the segmentation of complex images containing several embedded structures. These images may include fossils with invasive matrix or possibly even images of several tissues produced by magnetic image resonance (MRI) techniques. The presented algorithm can also be used on 8-bit data though the efficacy of the segmentation will depend on the clarity of the original image.

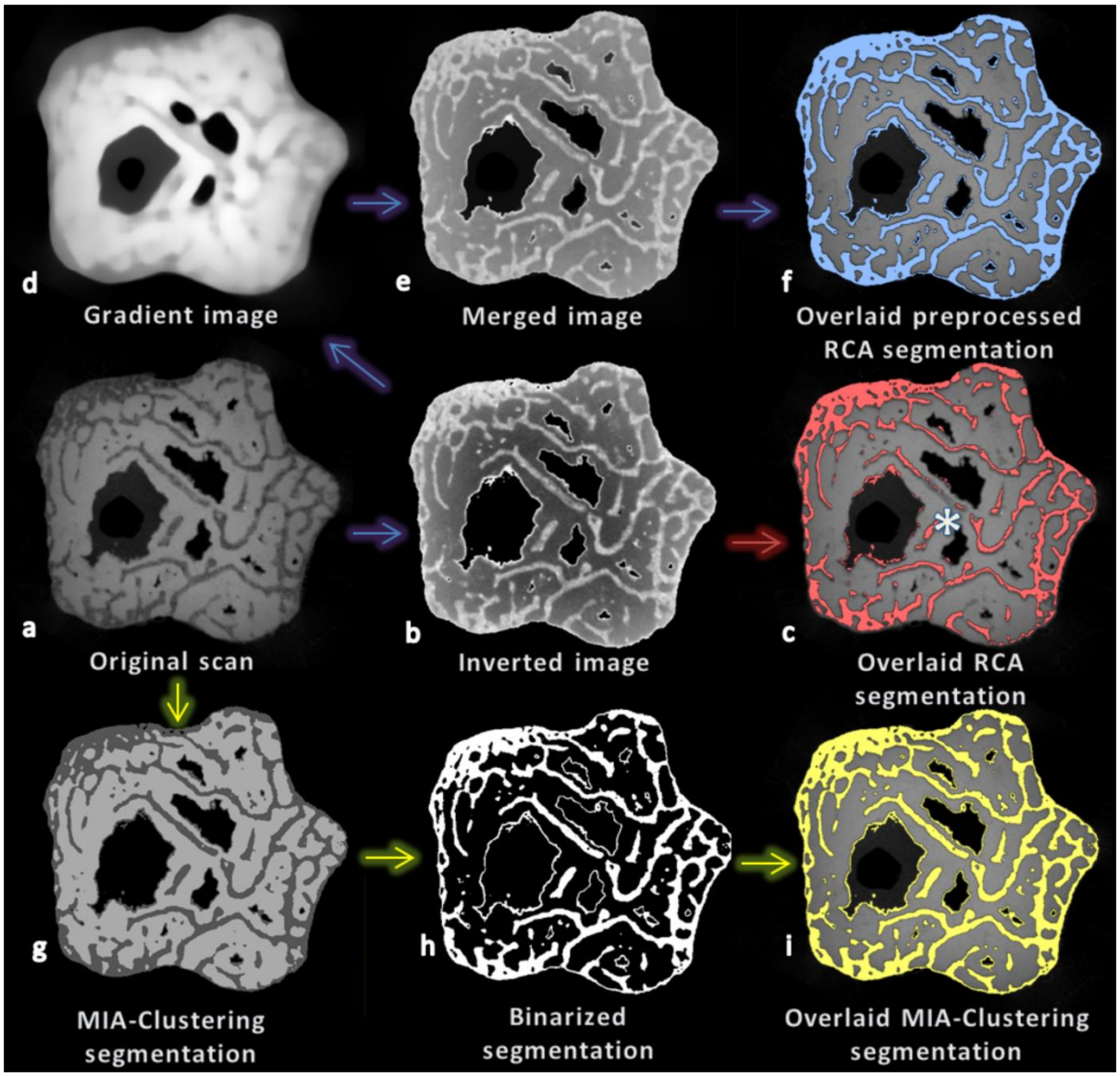

Figure 3.8. Cross-section (XY plane) through the fossil at various stages of segmentation using RCA and MIA-Clustering. a) The fossil scan. b) The image after foreground inversion. c) The RCA segmentation of the inverted image overlaid on the original image (red), note the lack of segmentation of central trabeculae (e.g. above the white asterisk). d) An image preserving the global gradient of the fossil scan but little of its spatial structure, after a strong median filter. e) The result of merging the global gradient and the inverted image. f) The RCA segmentation of the merged result overlaid on the original image (blue). g) The MIA-Clustering segmentation of the three classes in the image. h) The MIA-Clustering segmentation binarized on the second brightest class, the fossilized bone phase. i) This binarized segmentation overlaid on the original image (yellow).

Conclusion

Here, we present a segmentation algorithm implemented in free open-source software, which can be run on most operating systems and is as effective as other leading algorithms, in terms of segmentation accuracy. The move from a gray value based approach to a data-led, machine-learning approach allows the MIA-Clustering algorithm to lessen the amount of subjective user choices required for segmentation. Therefore, MIA-Clustering segmentations of µCT data offer increased reproducibility. Further, the flexibility of this MIA-Clustering algorithm allows for segmentation of problematic modern or fossil material, which often contains more than two structures and may be affected by common scanning artifacts. The robusticity of the algorithm is demonstrated by the lack of need for additional image processing steps and by how quickly the range of possible input parameters converge on those acceptable for segmentation. The MIA-Clustering algorithm is a flexible, robust method that produces highly reproducible results, ideal for segmenting fossil bone. As RCA provides an equivalent level of accurate segmentation in extant bone, it is used to segment these samples for subsequent thesis chapters. MIA-clustering could also have been used for this purpose but was still under development when work began on these chapters. However, due to its objectivity and ability to deal with complex fossil scans, the MIA-clustering approach had to be used to segment all fossil scans analysed in the present thesis.

Chapter 4
Metacarpal trabecular bone varies with distinct hand-positions used in hominid locomotion

Abstract

Trabecular bone remodels during life in response to loading and thus should, at least in part, reflect potential variation in the magnitude, frequency and direction of joint loading across different hominid species. Here we analyse the trabecular structure across all non-pollical metacarpal distal heads (Mc2-5) in extant non-human great apes, expanding on previous volume of interest and whole-epiphysis analyses that have largely focussed on only the first or third metacarpal. Specifically, we employ both a univariate statistical mapping and a multivariate approach to test for both inter-ray and interspecific differences in relative trabecular bone volume fraction (RBV/TV) and degree of anisotropy (DA) in Mc2-5 subchondral trabecular bone. Results demonstrate that while DA values only separate orangutans (*Pongo*) from African apes (*Pan troglodytes, Pan paniscus, Gorilla gorilla*), RBV/TV distribution varies with the predicted loading of the metacarpophalangeal (McP) joints during locomotor behaviours in each species. Gorillas exhibit a relatively dorsal distribution of RBV/TV consistent with habitual hyperextension of the McP joints during knuckle-walking, whereas orangutans have a palmar distribution consistent with flexed McP joints used to grasp arboreal substrates. Both chimpanzees and bonobos possess a disto-dorsal distribution of RBV/TV, compatible with multiple hand postures associated with a more varied locomotor regime. Further, inter-ray comparisons reveal RBV/TV patterns consistent with varied knuckle-walking postures in chimpanzees and bonobos, in contrast to higher RBV/TV values toward the midline of the hand in Mc2 and Mc5 of gorillas, consistent with habitual palm-back knuckle-walking. These patterns of trabecular bone distribution and structure reflect different behavioural signals that could be useful for determining the behaviours of fossil hominins.

Published Article: Dunmore, C.J., Kivell, T.L., Bardo, A., and Skinner, M.M. (2019) Metacarpal trabecular bone varies with distinct hand-positions used in hominid locomotion. *Journal of Anatomy*, 235 (1), 45-66 (see Appendix B)

Introduction

Trabecular, or cancellous, bone has been experimentally shown to remodel (Cowin, 1986; Frost, 1987) in response to loading across a range of phylogenetically disparate taxa (Biewener et al., 1996; Pontzer et al., 2006; Barak et al., 2011). Therefore, trabecular architecture can provide additional information about how a bone was loaded during life, compared to external morphology alone (Ruff and Runestad, 1992; Tsegai et al., 2013). The term 'remodeling' is used here, rather than 'modeling', as it occurs throughout life and is therefore key to a bone's "ability to function in a changing mechanical environment" (Martin et al., 1998 pp. 96; see Allen and Burr, 2014). When trabeculae are preserved in fossil hominins they have been used to infer habitual loading and reconstruct both locomotor (DeSilva and Devlin, 2012; Barak et al., 2013; Su et al., 2013; Zeininger et al., 2016; Ryan et al., 2018) as well as manipulative (Skinner et al., 2015; Stephens et al., 2018) behaviours during human evolution. These functional inferences rely on comparative analyses that associate known behaviours of extant primates with variation in trabecular architecture at particular joints (Orr, 2016).

The hand makes direct contact with the substrate during non-human primate locomotion, and therefore its trabecular structure may provide a clearer functional signal than skeletal elements that are further removed from substrate reaction forces, such as the humerus (Ryan and Walker, 2010; Scherf et al., 2016). Indeed, previous studies of the internal bone structure of hand bones have found substantial differences between primate species with distinct habitual locomotor modes (Zeininger et al., 2011; Lazenby et al., 2011b; Tsegai et al., 2013; Skinner et al., 2015; Matarazzo, 2015; Stephens et al., 2016; Chirchir et al., 2017; Barak et al., 2017). The majority of these studies have investigated trabecular bone structure in the third metacarpal (Mc3) head because the central ray is buffered from radio-ulnar forces, is consistently involved in weight bearing during locomotion, and often experiences peak reaction forces in ape locomotion (Zeininger et al., 2011; Tsegai et al., 2013; Matarazzo, 2015; Chirchir et al., 2017; Barak et al., 2017).

Different methodological approaches to the analysis of trabecular structure in the primate Mc3 head have yielded varied results. Tsegai et al. (2013) applied a whole-epiphysis approach and found that African apes had higher trabecular bone volume fraction (BV/TV) and degree of anisotropy (DA) than suspensory hominoids, especially in the dorsal region of the Mc3 head, consistent with an extended metacarpophalangeal (McP) joint during knuckle-walking. Suspensory orangutans and hylobatids were found to have more isotropic trabeculae and lower overall BV/TV that was highest in the palmar aspect of the Mc3, consistent with flexed-finger arboreal grips. Using fewer volumes of interest (VOI), Chirchir et al. (2017) found that there were no significant differences in DA across a sample of chimpanzees, orangutans, baboons and humans, but that BV/TV was significantly higher in distal and palmar portions of the Mc3 head in orangutans and, to a lesser extent in humans, consistent with flexed-finger grips used during arboreal locomotion and manipulation, respectively. In contrast, Barak et al. (2017), using a similar method, found the dorsal VOI in both chimpanzees and humans had significantly lower BV/TV and DA than the distal or palmar VOIs. Despite these conflicting results, these studies uniformly found that humans possessed significantly less BV/TV throughout the Mc3 head relative to other primate species (Tsegai et al., 2013; Barak et al., 2017; Chirchir et al., 2017). This finding is consistent with other skeletal elements (Chirchir et al., 2015; Ryan and Shaw, 2015) and may reflect, at least in part, lower loading of the hand during manipulation compared with that of locomotion (Tsegai et al., 2013), or sedentism in recent human populations, or both (Ryan and Shaw, 2015). Although the whole-epiphysis approach has found a relationship between variation in metacarpal trabecular structure and hand use (Tsegai et al., 2013), this approach has been limited to comparisons of average trabecular parameters (Tsegai et al., 2013; Skinner et al., 2015; Stephens et al., 2016) or sections thereof (Georgiou et al., 2018). Recently some researchers have called for (Chirchir et al., 2017), or developed (Sylvester and Terhune, 2017), new methods that can better quantify and statistically compare trabecular structure across different individuals and species. Here, we build on this previous work by analysing trabecular structure across all of the non-pollical metacarpal heads (Mc2-5) and applying a geometric morphometric, statistical

mapping method to trabecular bone data produced by the whole-epiphysis approach. We compare relative trabecular bone volume fraction (RBV/TV) and degree of anisotropy (DA) between Mc2-5 both within and across the following species: bonobos (*Pan paniscus*), chimpanzees (*Pan troglodytes*), gorillas (*Gorilla gorilla gorilla*) and orangutans (*Pongo abelii* and *Pongo pygmaeus*). RBV/TV values are BV/TV values divided by the average BV/TV of each metacarpal head (see methods). This approach allows for the quantification of trabecular architecture in a heuristic sample, less affected by issues of subsampling of a continuous structure, to infer differences in habitual hand loading and posture associated with hominid locomotor modes.

Hand use and locomotion

Hand postures vary greatly during different types of arboreal and terrestrial locomotion in apes (Hunt et al., 1996; Schmitt et al., 2016). However, detailed studies of hominid hand postures in the wild (Hunt, 1991; Neufuss et al., 2017; Thompson et al., 2018) and captive settings (Wunderlich and Jungers, 2009; Matarazzo, 2013; Samuel et al., 2018) can inform predictions of frequent McP joint positions and loading across the hand in different species. While frequent McP joint postures may only reflect part of a large and varied locomotor repertoire, previous research suggests that subchondral trabecular patterns of the metacarpal head can be statistically discerned among species with different locomotor modes (Tsegai et al., 2013; Chirchir et al., 2017; Barak et al., 2017).

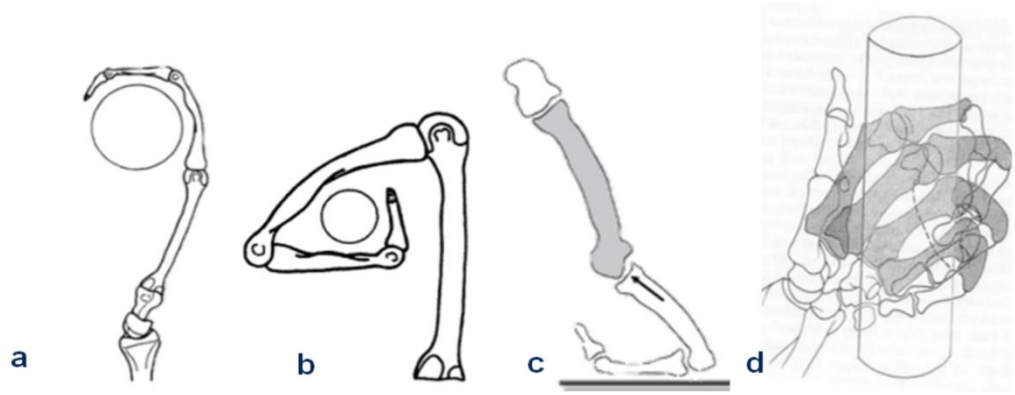

Figure 4.1. Diagrammatic representations of the metacarpophalangeal postures during a) a hook grip, b) a 'double-locked' grip and c) knuckle-walking and d) a diagonal power-grip. Images are adapted from Lewis (1977), Rose (1988), and Tsegai et al. (2013).

Pongo

Orangutans (here including *P. pygmaeus* and *P. abelii*) are primarily arboreal, engaging in suspensory locomotion to move through the canopy via tree branches and lianas (Cant, 1987; Sugardjito and Cant, 1994; Thorpe and Crompton, 2005). Specifically, researchers have emphasized the use of multiple supports and quadrumanous orthograde locomotion in orangutans (Thorpe and Crompton, 2006; Manduell et al., 2011), though specific hand grips have not been reported in detail (Thorpe and Crompton, 2005). However, during suspension orangutans are thought to employ a hook-grip, in which the proximal phalanges align with the proximo-distal axis of the metacarpal, such that the distal McP joint is thought to be loaded in tension (Sarmiento, 1988; Rose, 1988; Schmitt et al., 2016; Fig. 4.1a.). Similarly a double-locked grip, in which all joints of the ray, including the McP, are greatly flexed around a small substrate, is also adopted in orangutan locomotion (Napier, 1960; Rose, 1988; Fig. 4.1b.).

The McP joints in orangutans possess a limited degree of possible hyperextension at 19 degrees (Susman, 1979; Rose, 1988). Mc2-4 are also dorso-palmarly thicker at the diaphysis, and all the non-pollical metacarpal heads possess palmarly wide articular heads suggestive of habitual McP flexion (Susman, 1979). As the fourth intermediate and proximal phalanges may often equal or exceed the length of those comprising the third phalanx in orangutans (68% and 42% respectively; Susman, 1979), Rose (1988) has argued that the fourth ray is more in line with the second and third rays, which would be advantageous for both hook and double-locked grips in which rays 2-5 are typically all engaged. While body size in orangutans is sexually dimorphic (Rodman, 1984) and there is some evidence for differential locomotion between the sexes (Sugardjito and van Hooff, 1986), further work has found these differences to be relatively slight (Thorpe and Crompton, 2005). Therefore, we do not expect habitual prehensile postures to greatly differ between male and female orangutans.

Gorilla

The most frequent locomotor mode of gorillas terrestrial knuckle-walking (Inouye, 1994; Doran, 1996; Remis, 1998). However, this genus can vary substantially in their degree of arboreality based on the species, sex and local ecology (Doran, 1996; Remis, 1998; Neufuss et al., 2017). The western lowland gorilla (*Gorilla gorilla gorilla*) is reported to probably spend at least 20% of its time in trees (Tuttle and Watts, 1985; Remis, 1998). During knuckle-walking, the McP joint is hyperextended to place the arm above the weight-bearing intermediate phalanges (Tuttle, 1969; Matarazzo, 2013; Fig. 4.1c). Gorillas usually uses a 'palm-back' hand posture during knuckle-walking, which places the McP orthogonal to the direction of travel while consistently loading rays 2-5. This differs from the more variable hand postures, as well as digit loading, found in chimpanzees and probably reflects the relatively longer fifth digit of gorillas (Tuttle, 1969b; Susman, 1979; Inouye, 1992; 1994; Wunderlich and Jungers, 2009; Matarazzo, 2013; but see Thompson et al., 2018). In a study of digit pressures during knuckle-walking captive gorillas, Matarazzo (2013) found that the fifth digit always touches down first with weight moving radially until the second (61%) or third (39%) digit lifts off. Peak pressures were significantly lower on the fifth digit and highest on the third, but overall gorillas maintained a more even distribution of pressure across rays 2-5 than that of captive chimpanzees.

Compared to terrestrial knuckle-walking, far less is known about hand postures used by gorillas during arboreal locomotion. In captivity, gorillas are described as using a power grip with little McP flexion when vertically climbing large-diameter substrates (Sarmiento, 1994). Neufuss et al. (2017) also described a similar type of power grip using all five digits and the palm in wild mountain gorillas (*Gorilla beringei beringei*) when climbing larger substrates. However, when climbing medium-sized substrates (6-10 cm diameter), mountain gorillas used a diagonal power grip, in which the substrate lies diagonally across the fingers and palm, with an extremely ulnarly-deviated wrist posture (Neufuss et al., 2017; Fig. 4.1d). In this diagonal power grip, weight appeared to be frequently borne by digits 2-4 while the fifth McP joint was unable to flex to the same extent due to the irregular shape of

some substrates. Although similar data on arboreal hand postures is not available, we assume that during arboreal locomotion the McP joints of lowland gorillas are moderately flexed, and that this flexion increases as the substrate diameter decreases, with potentially less flexion at the fifth McP joint. However, this arboreal McP posture is likely less frequent than that associated with knuckle-walking in gorillas. Indeed, while female gorillas are more arboreal than larger males (Remis, 1995), the primary locomotor mode for both sexes is knuckle-walking (Tuttle and Watts, 1985; Remis, 1995; Crompton et al., 2010).

Pan troglodytes

Generally, chimpanzees (*P. troglodytes*) are thought to be more arboreal than gorillas (Remis, 1995; Doran, 1996; Thorpe and Crompton, 2006) though this may be the result of comparisons to mountain gorillas that are better habituated to humans than their more arboreal lowland counterparts (Doran, 1997; Hunt, 2016; Neufuss et al., 2017). There is a large degree of variation in the chimpanzee locomotor repertoire depending on the local ecology (Doran and Hunt, 1994; Carlson et al., 2006). *Pan troglodytes verus* engages in knuckle-walking, both arboreal and terrestrial, in ~85% of their locomotion and spend more time in the trees than *P. troglodytes schweinfurthii* (Doran and Hunt, 1994; Carlson et al., 2006). Compared with gorillas, chimpanzees use more varied hand postures during knuckle-walking (Tuttle, 1969; Inouye, 1994; Matarazzo, 2013). Chimpanzees have been thought to primarily load digits 3 and 4 during knuckle-walking (Tuttle, 1969; Tuttle and Basmajian, 1978). Inouye (1994) found that during captive terrestrial knuckle-walking, larger chimpanzees used their second digit significantly less often than gorillas of equivalent size and both chimpanzees and bonobos generally used their fifth digit significantly less often than gorillas. Pressure studies also found that the fifth digit of chimpanzees did not touch-down in 20% of knuckle-walking steps and that this digit experienced significantly less load than the other digits when it was used (Wunderlich and Jungers, 2009; Matarazzo, 2013). Further, chimpanzees use both 'palm-back' (~40%) and 'palm-in' (~60%) postures, compared with a more consistent use of mainly 'palm-back' (~86%) knuckle-walking postures in gorillas (Wunderlich and Jungers, 2009; Matarazzo, 2013). During 'palm-in' knuckle-walking

the intermediate phalanges roll radially in the direction of travel and the second or third digit usually experiences the highest pressures (Wunderlich and Jungers, 2009; Matarazzo, 2013). In 'palm-back' knuckle-walking, the third digit is typically placed in front the others, and usually is the last to touch off, which may be related to the fact that the third ray may be relatively longer in chimpanzees than in gorillas (Matarazzo, 2013; 2013b). Compared to gorillas, the peak pressures experienced by digits 2-4 are more variable in chimpanzees (Wunderlich and Jungers, 2009; Matarazzo, 2013).

P. troglodytes verus most often uses climbing and scrambling locomotion in trees (60-77%, Doran, 1992; 1993). Chimpanzees are described as using power grips, diagonal power grips and hook grips during arboreal locomotion, all of which typically involve some degree of flexion at the McP joint (Alexander, 1994; Hunt, 1991; Marzke et al., 1992; Marzke and Wullstein, 1996; Napier, 1960). Climbing often encompasses vertical climbing and clambering in naturalistic studies. Hunt (1991) has emphasized the role of vertical climbing in wild chimpanzees and while the grips employed tend to be ulnarly deviated at the wrist, they are dependent on substrate diameter. Neufuss et al. (2017) also found that chimpanzees used both power grips and diagonal power grips, but with a less ulnarly deviated wrist than in gorillas. A diagonal power grip involves greater flexion of the more ulnar rays and in some cases flexion at the fifth carpometacarpal joint, which may likely be associated with ulnar deviation at the wrist (Marzke and Wullstein, 1996; Fig. 4.1d). Therefore the locomotor hand postures of chimpanzees may be characterised as primarily those of knuckle-walking but with a more frequent arboreal grasping component than in gorillas. Given the lower sexual dimorphism in chimpanzees relative to gorillas and orangutans (Doran, 1996), there may be less variation in grasping postures in this species.

Pan paniscus

While bonobos (*P. paniscus*) have a relatively similar locomotor repertoire to chimpanzees, they are thought to be more arboreal (Alison and Badrian, 1977; Susman et al., 1980; Susman, 1984) and have been shown to use significantly more palmigrady in the trees (Doran, 1993; Doran and Hunt, 1994; Crompton et al.,

2010). The former claim, however, may be an artefact of incomplete habituation of the individuals in these studies and more data is needed (Hunt, 2016), the relatively longer and heavier lower limbs of this species make for more generalised anatomy than that of chimpanzees (Zihlman, 1984; D'Août et al., 2004). During terrestrial knuckle-walking bonobos use the fifth digit even less than chimpanzees and Mc5 is shorter than the rest of the metacarpals in bonobos (Inouye, 1994). In a pressure study of arboreal locomotion, Samuel et al. (2018) found that captive bonobos used 'palm-back' (64%) or 'palm-in' (36%) knuckle-walking hand postures, and that peak pressure was experienced by or around the third digit. However, unlike chimpanzees (Wunderlich and Jungers, 2009), they did not roll radially across their digits and the fifth digit always made contact with the substrate (Samuel et al., 2018). During vertical climbing and suspensory postures, bonobos used flexed-finger power grips similar to those described in other non-human great apes and again peak pressure was experienced by or around the third digit (Samuel et al., 2018). In summary, the hand postures used during locomotion in bonobos can be characterised as similar to those of chimpanzees, including a relatively low level of sexual dimorphism compared to other non-human great apes (Doran, 1996), although more frequent palmigrady and arboreal grasping differentiate this species from chimpanzees.

Predictions

Based on the summary above, we predict RBV/TV and DA in *Pongo* will be significantly higher in the disto-palmar region of the metacarpal heads compared to other hominids and no significant inter-ray differences in both measures due to the more consistent recruitment of rays 2-5 during hook and double-locked grasping. In *Gorilla* we predict a significantly higher dorsal distribution of RBV/TV and DA in each metacarpal head compared with all other hominids, reflecting McP joints frequently loaded in a hyperextended posture during knuckle-walking. As *P. troglodytes* may be more arboreal and uses more variable knuckle-walking postures, we predict this species will have significantly lower dorsal RBV/TV and DA, with more significant differences across rays, than that of *Gorilla*. We also predict this mixture of arboreality and terrestrially in *P. troglodytes* will elicit higher dorsal

RBV/TV and DA than *Pongo* but with a more homogeneous distribution within each metacarpal head. We predict *P. paniscus* trabecular patterning will be similar to that of *P. troglodytes*, and thus possess significantly higher palmar distribution of RBV/TV and DA compared to *Gorilla* and a more dorsal distribution of these measures than in *Pongo.* However, we also expect *P. paniscus* to have lower DA and further homogenised distribution of RBV/TV than *P. troglodytes* due to more frequent use of palmigrady and arboreal grips.

Materials

Subchondral trabecular bone was analysed in the metacarpus of *Pan paniscus* (*n*=10), *Pan troglodytes* (*n*=13), *Gorilla gorilla gorilla* (*n*=12), *Pongo* sp. indet. (*n*=1), *Pongo pygmaeus* (*n*=7) and *Pongo abelii* (*n*=3). Metacarpi were sampled from: the Royal Museum for Central Africa, Tervuren, Belgium, the Max Planck Institute for Evolutionary Anthropology, Leipzig, Germany, the Powell-Cotton Museum, Birchington-on-sea, U.K., Bavarian State Collection of Zoology, Munich, Germany, the Natural History Museum, Berlin, Germany, the Senckenberg Natural History Museum, Frankfurt Germany, and the Smithsonian National Museum of Natural History, Washington D.C., U.S.A (Table 4.1). All specimens were adult, wild shot and free from external signs of pathology. Within each taxon efforts were made to ensure the samples were sex balanced with even numbers of right and left metacarpi, neither ratio was more imbalanced than 5:7 for any sample. While non-human great ape locomotion is sexually biased (Doran, 1996) and there has been some evidence for lateralized asymmetry in both the trabecular (Stephens et al., 2016) and cortical bone of hominid metacarpals (Sarringhaus et al., 2005), neither of these signals seems likely to be greater than species locomotion differences under investigation here. Further, the use of evenly mixed samples should ameliorate these effects (see discussion).

Table 4.1. Study sample

Taxonomy	Accession ID	Sex	Side	Institution
Gorilla gorilla gorilla	PC_MER_300	Female	Left	Powell-Cotton Museum
Gorilla gorilla gorilla	PC_MER_264	Male	Right	Powell-Cotton Museum
Gorilla gorilla gorilla	PC_MER_372	Male	Left	Powell-Cotton Museum
Gorilla gorilla gorilla	PC_MER_95	Female	Right	Powell-Cotton Museum
Gorilla gorilla gorilla	PC_MER_962	Male	Left	Powell-Cotton Museum
Gorilla gorilla gorilla	PC_CAMI_230	Male	Left	Powell-Cotton Museum
Gorilla gorilla gorilla	PC_MER_138	Female	Left	Powell-Cotton Museum
Gorilla gorilla gorilla	PC_MER_174	Male	Right	Powell-Cotton Museum
Gorilla gorilla gorilla	PC_MER_696	Female	Right	Powell-Cotton Museum
Gorilla gorilla gorilla	PC_MER_856	Female	Left	Powell-Cotton Museum
Gorilla gorilla gorilla	PC_MER_879	Male	Left	Powell-Cotton Museum
Gorilla gorilla gorilla	PC_ZVI_32	Male	Right	Powell-Cotton Museum
Pan troglodytes verus	MPITC_11789	Male	Right	Max Planck Institute for Evolutionary Anthropology
Pan troglodytes verus	MPITC_11778	Female	Right	Max Planck Institute for Evolutionary Anthropology
Pan troglodytes verus	MPITC_13439	Female	Right	Max Planck Institute for Evolutionary Anthropology
Pan troglodytes verus	MPITC_15002	Female	Left	Max Planck Institute for Evolutionary Anthropology
Pan troglodytes verus	MPITC_11800	Female	Right	Max Planck Institute for Evolutionary Anthropology
Pan troglodytes verus	MPITC_11903	Male	Left	Max Planck Institute for Evolutionary Anthropology
Pan troglodytes verus	MPITC_11781	Male	Left	Max Planck Institute for Evolutionary Anthropology
Pan troglodytes verus	MPITC_14996	Female	Left	Max Planck Institute for Evolutionary Anthropology
Pan troglodytes verus	MPITC_15012	Male	Right	Max Planck Institute for Evolutionary Anthropology
Pan troglodytes verus	MPITC_15013	Female	Right	Max Planck Institute for Evolutionary Anthropology
Pan troglodytes verus	MPITC_15014	Male	Right	Max Planck Institute for Evolutionary Anthropology
Pan troglodytes verus	MPITC_15032	Male	Left	Max Planck Institute for Evolutionary Anthropology
Pan troglodytes*	ZSM_AP_122	Male	Right	Bavarian State Collection of

				Zoology
Pongo abelii	SMF_6785	Male	Right	Senckenberg Natural History Museum, Frankfurt
Taxonomy	**Accession ID**	**Sex**	**Side**	**Institution**
Pongo abelii	SMF_6779	Female	Left	Senckenberg Natural History Museum, Frankfurt
Pongo pygmaeus	ZSM_1907_0633b	Female	Right	Bavarian State Collection of Zoology
Pongo pygmaeus pygmaeus	ZSM_1907_0660	Female	Right	Bavarian State Collection of Zoology
***Pongo* sp. indet.**	ZSM_AP-120	Male	Left	Bavarian State Collection of Zoology
Pongo pygmaeus pygmaeus	ZSM_1907_0483	Female	Right	Bavarian State Collection of Zoology
Pongo pygmaeus pygmaeus	ZSM_1909_0801	Male	Right	Bavarian State Collection of Zoology
Pongo abelii	NMNH_267325	Male	Left	Smithsonian Institution National Museum of Natural History
Pongo pygmaeus	ZMB_6948	Female	Left	Natural History Museum, Berlin
Pongo pygmaeus	ZMB_6947	Male	Left	Natural History Museum, Berlin
Pongo pygmaeus	ZMB_87092	Female	Right	Natural History Museum, Berlin
Pan paniscus	MRAC_15293	Female	Left	Royal Museum for Central Africa, Tervuren
Pan paniscus	MRAC_15294	Male	Left	Royal Museum for Central Africa, Tervuren
Pan paniscus	MRAC_20881	Male	Left	Royal Museum for Central Africa, Tervuren
Pan paniscus	MRAC_27696	Male	Right	Royal Museum for Central Africa, Tervuren
Pan paniscus	MRAC_27698	Female	Left	Royal Museum for Central Africa, Tervuren
Pan paniscus	MRAC_29042	Female	Right	Royal Museum for Central Africa, Tervuren
Pan paniscus	MRAC_29044	Male	Right	Royal Museum for Central Africa, Tervuren
Pan paniscus	MRAC_29045	Female	Left	Royal Museum for Central Africa, Tervuren
Pan paniscus	MRAC_29052	Male	Right	Royal Museum for Central Africa, Tervuren
Pan paniscus	MRAC_29060	Female	Right	Royal Museum for Central Africa, Tervuren

***** Though this specimen was marked as *Pongo* in the collection, CT-scans demonstrate it has a fused scaphoid and os centrale, and so this specimen is treated as *Pan troglodytes*.

Methods

Micro-CT Scanning

Specimens were scanned with BIR ACTIS 225/300 and Diondo D3 high resolution micro-CT scanners at the Department of Human Evolution, Max Planck Institute for Evolutionary Anthropology, Germany, as well as with the Nikon 225/XTH scanner at the Cambridge Biotomography Centre, University of Cambridge, U.K. Scan parameters were 100-160 kV and 100-140 µA, using a brass or copper filter of 0.25-0.5 mm, resulting in reconstructed images with an isometric voxel size of 24-45 µm.

Image processing

Micro-CT scans of each metacarpal were isolated in Avizo 6.3 (Visualization Sciences Group; Fig. 4.4a) and segmented using the Ray Casting Algorithm (Scherf and Tilgner, 2009). The segmented volume images were then processed as per the whole-epiphysis method, outlined in Gross et al. (2014). Briefly, a series of filters run in medtool 4.2 (Dr. Pahr Ingenieurs e.U.) isolated the inner trabecular structure (Fig. 4.4b) by casting rays at different angles from the outer cortical shell and terminating them on contact with background, non-bone, voxels. A spherical kernel, with a diameter equal to the measured average trabecular thickness in that bone, was then used to close this inner structure (Pahr and Zysset, 2009). The 3D edge of this solid inner structure defined the boundary between subchondral trabecular and cortical bone. Subsequently, a regular 3D background grid, spaced at 2.5mm intervals, was overlaid and a spherical VOI 5 mm in diameter was centred at each vertex of the grid in which BV/TV and DA was measured (Fig. 4.4c). Previous studies have shown that these two variables are correlated with the mechanical properties of trabecular bone, reflect bone functional adaptation (Odgaard et al., 1997; Uchiyama et al., 1999; Pontzer et al., 2006; Barak et al., 2011; Lambers et al., 2013; 2013b) and that they are not strongly allometric (Doube et al., 2011; Barak et al., 2013; Ryan and Shaw, 2013). DA was measured via the mean intercept length (MIL) method and was bounded between 0, total isotropy, and 1, total anisotropy, using the calculation: 1 – (lowest eigenvalue of the fabric tensor / greatest eigenvalue fabric tensor). Both trabecular values were then separately interpolated on a regular 3D tetrahedral mesh of the trabecular model (Fig. 4.4d), created using

CGAL (www.cgal.org; Computational Geometry Algorithms Library). The surface of the trabecular mesh was extracted using Paraview (Ayachit, 2015) and it was smoothed, to permit landmark sliding (see below), in Meshlab (Cignoni et al., 2008) via a screened Poisson surface reconstruction filter (Kazhdan and Hoppe, 2013; Fig. 4.4e). For left hand bones this surface mesh was mirrored in Meshlab, so that it was oriented in the same manner as those from right hands to permit homologous functional comparisons.

Geometric morphometric mapping

While the whole-epiphysis method maps the entire volumetric trabecular model, we focus our analysis on the trabecular bone beneath the articular surface of the metacarpal heads because external loads necessarily pass through these subchondral trabeculae before they can be transmitted to any other part of the trabecular structure (Zhou et al., 2014; Sylvester and Terhune, 2017). We employ a 3D geometric morphometric (GM) approach (Gunz and Mitteroecker, 2013) to trabecular analysis similar to that of Sylvester and Terhune (2017) and test for significant differences between groups using homologous landmarks on the subchondral trabecular surface.

Anatomical landmark definitions

Many landmarks have been identified on the non-pollical metacarpals for morphometric studies (Susman, 1979; Inouye, 1992; Drapeau, 2015) but there have been relatively few studies that have applied GM methods to the primate metacarpus and these have focussed on the first metacarpal (Mc1) base (Niewoehner, 2005; Marchi et al., 2017). Metatarsals are developmental serial homologues of metacarpals (Rolian et al., 2010) and a relatively recent study captured their shape variation using a patch of 3D landmarks (Fernández et al., 2015). A recent study of Mc3 head shape used most of the same landmarks that bordered this metatarsal patch, at the analogous metacarpal locations (Rein, 2018). Based on these studies, the location and type (Bookstein, 1991) of anatomical landmarks used here are given in Table 4.2. Although the internal trabecular subchondral surface is landmarked, cortical bone is very thin at the metacarpal

head in hominids (Tsegai et al., 2017) and so the correspondence between these surfaces is generally high. Though the articular surface may not reach the same extent in all species studied, the same landmarks are used for comparison as they are present on all metacarpal heads studied.

Table 4.2. Anatomical landmark definitions.

Number	Type	Description	Provenance
1	II	Most proximal point under the ulnar palmar epicondyle (anterior eminence)	(Yeh and Wolf, 1977; Fernández, 2015; Rein, 2018)
2	III	The point of maximum curvature on the inter-epicondylar ridge between points 1 and 3	(Drapeau, 2015; Fernández, 2015; Rein, 2018)
3	II	Most proximal point under the radial palmar epicondyle (anterior eminence)	(Yeh and Wolf, 1977; Fernández, 2015; Rein, 2018)
4	III	Point of maximum curvature on the radial ridge separating the articular surface from the radial lateral sulcus	(Yeh and Wolf, 1977; Fernández, 2015; Rein, 2018)
5	II	Most radially projecting point under the radial dorsal tubercle	(Yeh and Wolf, 1977; Susman, 1979; Inouye, 1992; Fernández, 2015; Rein, 2018)
6	III	Mid-point between the posterior tubercles on the intertubercular ridge, underlying the dorsal ridge if present.	(Yeh and Wolf, 1977; Fernández, 2015)
7	II	Most ulnarly projecting point under the ulnar posterior tubercle	(Yeh and Wolf, 1977; Susman, 1979; Inouye, 1992; Fernández, 2015; Rein, 2018)
8	III	Point of maximum curvature on the ulnar ridge separating the articular surface from the ulnar lateral sulcus	(Yeh and Wolf, 1977; Fernández, 2015; Rein, 2018)
9	II	Most distally projecting point on the subchondral surface	(Fernández, 2015; Susman, 1979; Inouye, 1992; Rein, 2018)

Types of landmark (Bookstein, 1991) and their provenance. Each article describes the landmark, uses it as the terminus of a linear measure or directly uses it for GM analysis.

Repeatability

Landmarks were manually placed in Checkpoint (Stratovan Corporation, Davis, CA) and repeated ten times on three randomly selected specimens from each species over several days. A different ray was used from each species to ensure landmarks were repeatable across elements following Fernández et al. (2015). The landmarks were then aligned using Procrustes superimposition in the Morpho package in R (Schlager, 2017; R Development Core team, 2016). Landmark configurations were then plotted in the first two principal components (PCs) of shape space. Landmarks were considered stable if repeated measures were more clustered than those of different individuals. Significant pairwise permutational MANOVAs conducted on PC1 and PC2 combined scores, demonstrated that group means (the three individuals and their repeats) are significantly different in each case and that variance in landmark placement is significantly less than that between specimens (p<0.001; Fig. 4.2).

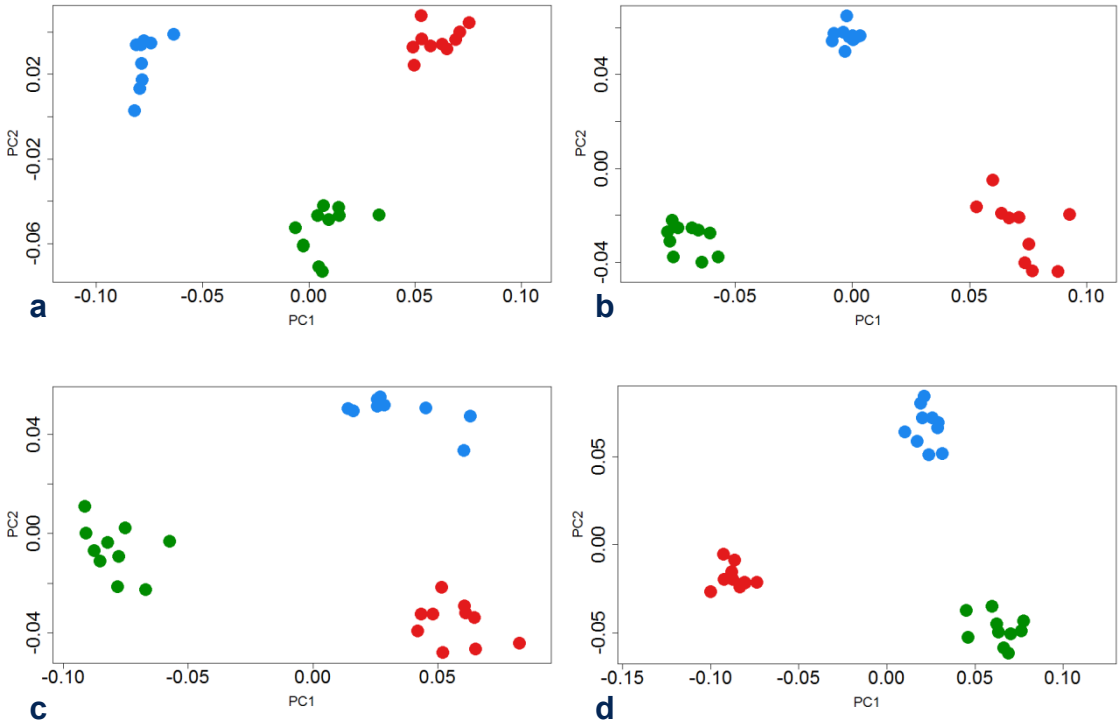

Figure 4.2. Repeatability tests of landmarks. Each individual metacarpal (marked in a different colour) was landmarked 10 times on different days. The same rays from three individuals of the same species were then subjected to Procrustes transformation in each case. Subsequent permutational omnibus and pairwise MANOVAs were run on the combined PC1 and PC2 scores, as these cumulatively explained >80% of the variation: a) *Gorilla* Mc2s (Cumulative Variance 83%); b) *Pongo* Mc3s (Culm. Var. 80%); c) *Pan paniscus* Mc4s (Culm. Var. 85%); d) *Pan troglodytes* Mc5s (Culm. Var. 87%). All individual specimen repeats were significantly different from each other subsequent to a Bonferroni correction (p≤0.0006).

Geometric morphometric procedure

To create the landmark template a random specimen was selected and eight curves were defined at the margins of the subarticular surface, in Checkpoint (Stratovan Corporation, Davis, CA), each bordered by anatomical landmarks as recommended by Gunz et al. (2005). Three sliding semi-landmarks were placed on each of these curves and an additional 140 were equally distributed over the subarticular surface in Avizo 6.3 (Visualization Sciences Group, Germany) to create a 173 landmark template. The anatomical landmarks were subsequently placed on every specimen, then the landmark template (Fig. 4.4f) was projected onto each of the 183 other metacarpal heads and relaxed onto the surface of each metacarpal using the Morpho package in R (Schlager, 2017) by minimising bending energy. This package was then used to slide the semi-landmarks along their respective curves and over the surface by minimising Procrustes distances. This slid template is plotted on an individual Mc3 from each species to provide a sense of the shape variation present (Fig. 4.3).

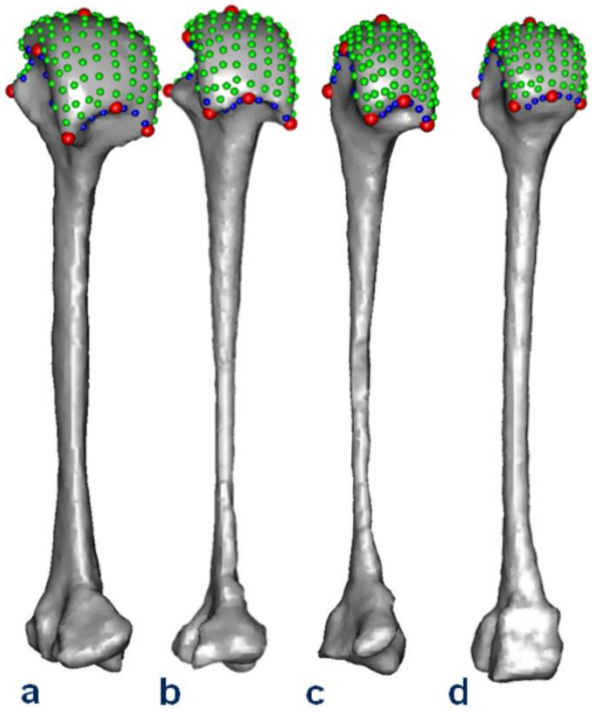

Figure 4.3. Landmark template projected onto Mc3s of individual specimens of a) *Gorilla gorilla*, b) *Pan troglodytes ,* c) *Pan paniscus* and d) *Pongo pygmaeus*. Note the homology of these landmarks across shape variation in species.

Data mapping

Using a custom Python script plugin for Paraview (www.paraview.org) the non-smoothed surface mesh triangles inherited trabecular values from their originating tetrahedra. The Python module SciPy (Jones et al., 2001) was then used in medtool 4.2 (Dr. Pahr Ingenieurs e.U.) to interpolate the trabecular values to the nearest landmark; this was done separately for BV/TV and DA. Interpolating these trabecular values from the outer tetrahedra of the trabecular model is analogous to using spherical VOIs, 1 mm in diameter, centred 0.5 mm beneath an inner trabecular surface landmark. Finally, the geomorph package (Adams et al., 2017) was used to perform a generalised Procrustes procedure in R, resulting in 184 sets of 173 homologous landmarks each with two associated trabecular values (Fig. 4.4g).

Relative trabecular volume

We employ a relative measure of bone volume fraction (RBV/TV), in which the raw BV/TV value of each landmark is divided by the mean of all landmark BV/TV values on that metacarpal head. Thus RBV/TV values ~1 indicate landmarks close to the average BV/TV of that metacarpal head, while values above or below 1 indicate a deviation from this average at these landmarks. This relative measure was preferred because, while BV/TV can vary systemically across extant hominid species (Tsegai et al., 2018) and may show considerable intraspecific variation, the relative patterns of trabecular architecture appear to preserve a functional signal superimposed on this variation (Saers et al., 2016). RBV/TV measures the position of the greatest subchondral trabecular bone of a given metacarpal head rather the absolute volume of bone and therefore is argued to reflect the habitually loaded joint positions of extant hominids while controlling, at least in part, for intra-species and systemic inter-species differences. Species average absolute BV/TV landmark values are depicted (Fig. 4.5) for comparison with RBV/TV values (Fig. 4.6).

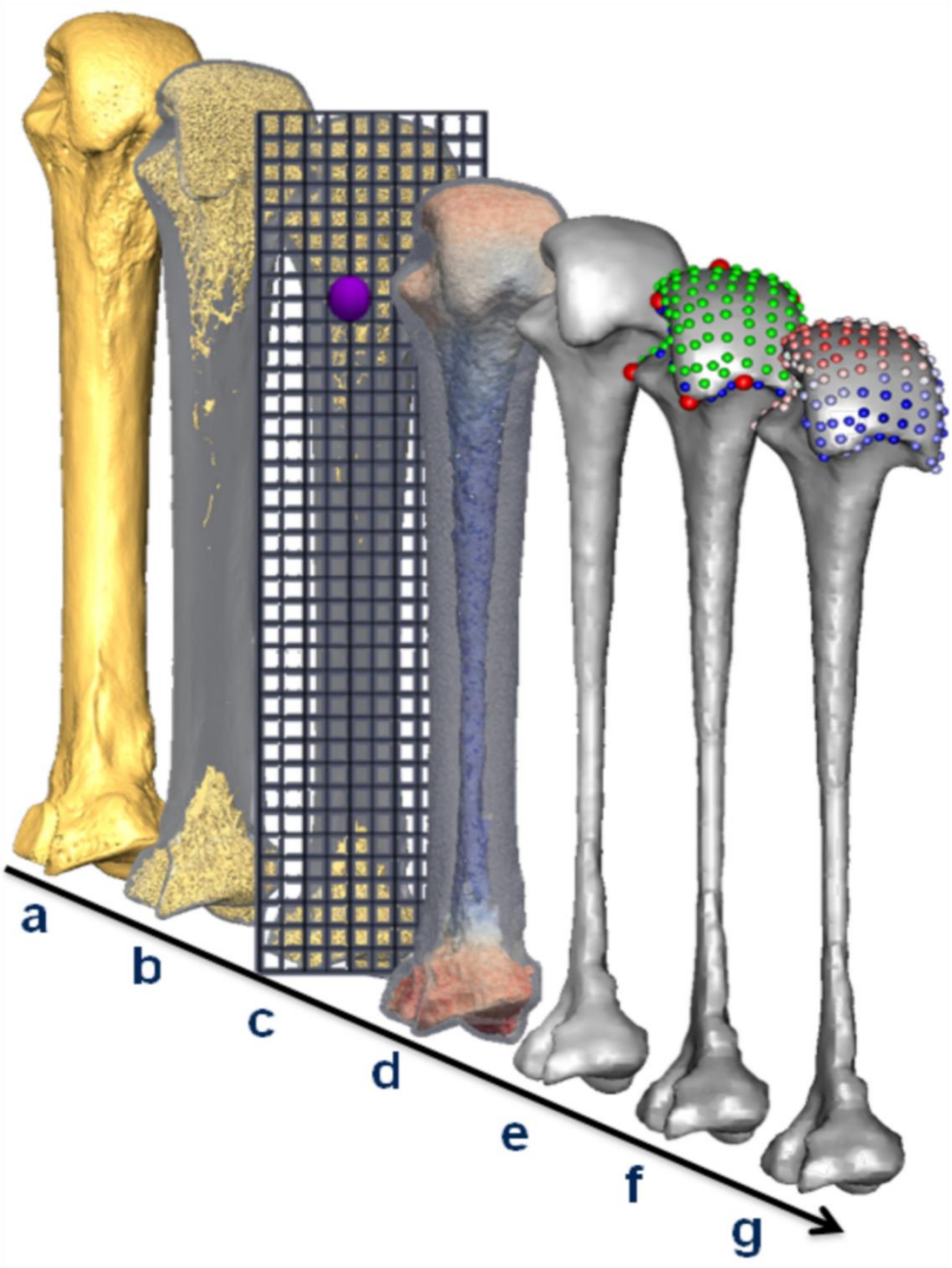

Figure 4.4. Methodological stages of metacarpal trabecular analysis, shown in a third metacarpal as an example: a) isosurface model, b) segmented trabecular structure inside cortical shell, c) diagram of the background grid and one of the VOI's at a vertex (purple), d) volume mesh coloured by BV/TV (0-45%), e) smoothed trabecular surface mesh, f) surface landmarks (anatomical = red, semi-sliding landmarks on curves = blue and on surfaces = green), g) RBV/TV interpolated to each surface landmark.

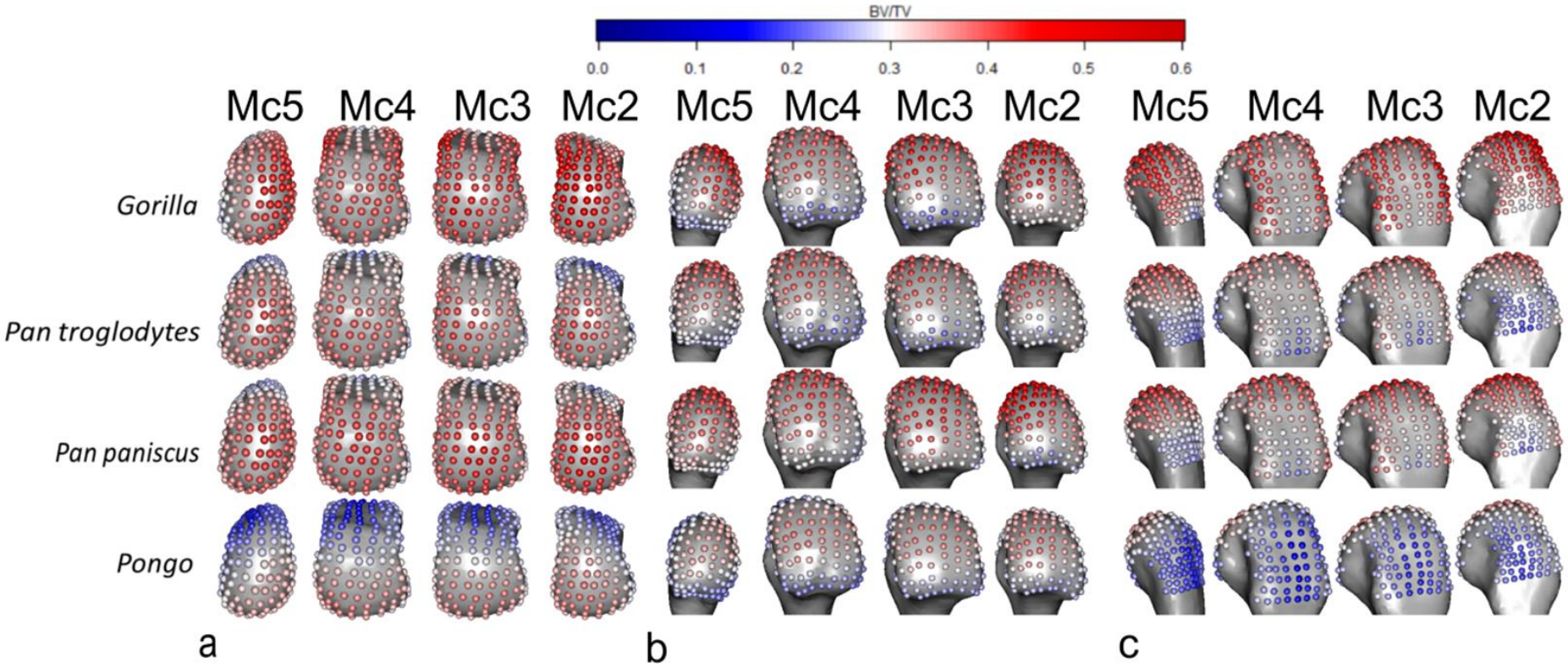

Figure 4.5. Species average absolute BV/TV, mapped to average models of each Mc head in a) distal, b) palmar and c) dorsal views. Note that absolute BV/TV interspecies or inter-ray comparisons are more likely to reveal overall differences in subchondral BV/TV than differences in the regional distribution of BV/TV, which are consistent with certain McP postures, as is the case for the scaled RBV/TV.

Statistical analysis

We employ a 'mass-univariate' approach as advocated by Friston et al. (1995) similar to that used to statistically analyse cortical bone in ape metacarpals (Tsegai et al., 2017). Specifically, the trabecular values between species and rays at each landmark are independently analysed using univariate statistics. Inter-ray comparisons do not include comparisons between rays two and four, or between rays three and five, as they are not biologically contiguous and thus are less informative when prehensile hand postures are considered. However, comparisons of rays two and five are included to test for significant differences between the most ulnar and radial aspects of the metacarpus. Shapiro-Wilk tests found a non-normal distribution of data at one or more landmarks in one or both groups in every pairwise, inter-ray and interspecific, comparison. To maintain consistent comparisons a non-parametric Kruskal-Wallis test was applied at each landmark, and a post-hoc test was used to test for pairwise differences if the omnibus test was significant. Dunn's test was chosen as it uses the pooled variance of the Kruskal-Wallis tests and so is conservative. Significance was set at $p<0.05$ subsequent to a Bonferroni correction in each case. This univariate approach means that homologous landmark values are compared across groups rather than with spatially auto-correlated neighbouring landmarks. *Z*-scores were used to determine the polarity, as well as the effect size, of significant differences between groups. These *Z*-scores were transformed into absolute, rather than signed, values and summarised for significant landmark differences, in both interspecific and inter-ray pairwise comparisons (Tables 4.3 and 4.4). Resulting plots of significant univariate differences map regional differences between species and rays, but were only considered meaningful if they were found at nine contiguous landmarks, as this represents just over 5% of the subarticular surface, in order to further ameliorate any Type I error. Despite the fact this univariate method can identify where regions of significant difference lie, it can be susceptible to Type I error. Therefore, to provide a multivariate corollary to this approach, a principle components analysis (PCA) of trabecular values, using landmarks as individual variables, was also run for all comparisons. Subsequent omnibus and pairwise one-way permutational

MANOVAs were run with a Bonferroni correction, using the Vegan package (Oksanen et al., 2018) package in R (R Core Development team, 2016), on the principal component scores of these PCAs to test for significant overall, rather than regional, differences in trabecular patterns.

Results

Univariate landmark comparisons

Pongo

Average RBV/TV was higher in the palmar aspect of all *Pongo* metacarpal heads than in their dorsal aspect (Fig. 4.6). The significant differences among the rays included those between Mc2 and Mc5, in which each had a small patch of significantly higher RBV/TV at the ulnar and radial aspects of the metacarpal head, respectively (Fig. 4.8). Mc3 also had a patch of significantly higher RBV/TV at radio-palmar landmarks relative to Mc2. Interspecifically, *Pongo* RBV/TV was significantly higher at landmarks in the palmar region of the metacarpal heads than in *P. troglodytes* and especially *Gorilla* (Fig. 4.10). Compared with *P. paniscus, Pongo* was again significantly higher at more palmar landmarks in Mc4 and Mc5 but there were fewer significantly higher landmarks in Mc3 and almost none in the Mc2 comparison.

Pongo had high DA values throughout the subarticular metacarpal heads with few significant differences between rays (Figs. 4.7, 4.9, 4.15). Interspecifically, *Pongo* DA was significantly greater than that of *Gorilla* in all metacarpal heads except for the central disto-palmar aspects of Mc3-4 and radio-palmar aspects of Mc5. *Pongo* had significantly higher DA on the disto-dorsal aspects of Mc2 and Mc5 relative to both *P. troglodytes* and *P. paniscus*. *Pongo* also had higher DA at landmarks situated on the dorsal aspects of Mc3 and 4 relative to *P. paniscus* (Fig. 4.11).

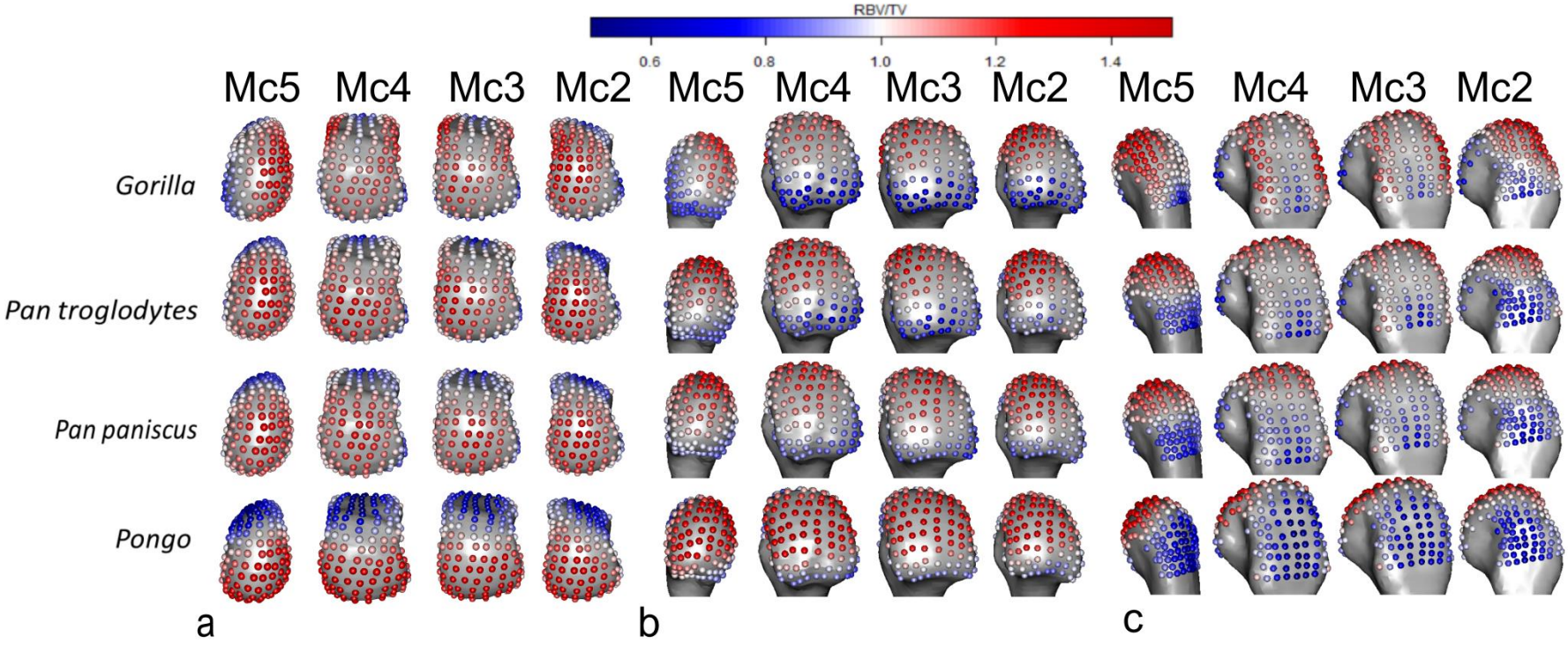

Figure 4.6. Species average RBV/TV, mapped to average models of each Mc head in a) distal, b) palmar and c) dorsal views. RBV/TV values around one (white) indicate landmarks close to the average BV/TV of that Mc head, while values above (red) or below one (blue) indicate a deviation from this average at these landmarks.

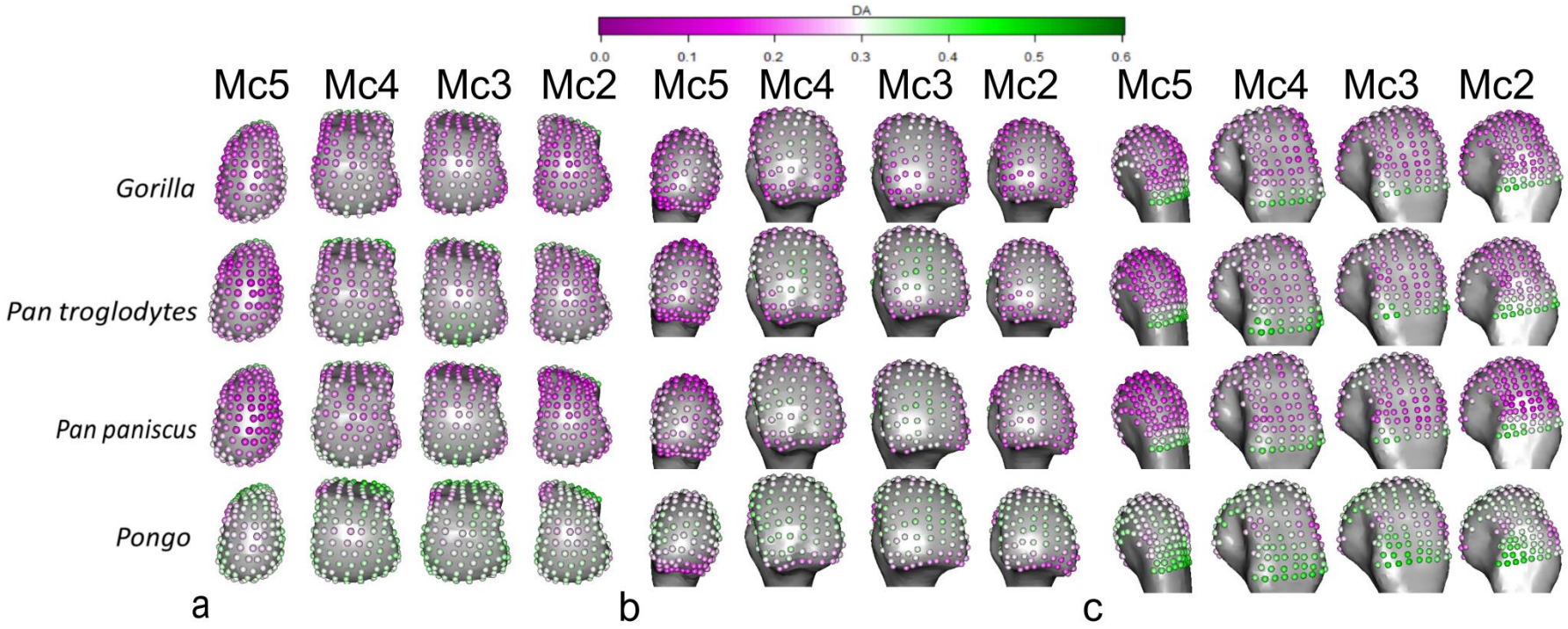

Figure 4.7. Species average DA, mapped to average models of each Mc head in a) distal, b) palmar and c) dorsal views.

Gorilla

The highest RBV/TV values in *Gorilla* were concentrated in the disto-dorsal portion of each metacarpal head extending dorsally on the medio-lateral edges of Mc3 and 4 but toward the mid-line of the hand in the Mc2 and Mc5 heads (Fig. 4.6). This latter pattern was clear in the inter-ray comparison, with significantly greater RBV/TV found at the radial aspect of Mc5 relative to Mc2 and Mc4 as well as on the ulnar aspect of these rays relative to Mc5 (Fig. 4.8). Interspecifically, *Gorilla* was significantly higher in RBV/TV dorsally compared to *Pongo*, though the radio-palmar aspect of Mc5 was not significantly different between these groups. Compared with *Pan*, *Gorilla* generally had significantly higher RBV/TV dorsally but this was restricted to the medio-lateral edges of each metacarpal head in the regional comparison (Fig. 4.10). Specifically, *Gorilla* had significantly higher RBV/TV than *Pan* species on the radio-dorsal aspect of Mc5 and both medio-lateral edges of Mc4, as well as the ulno-dorsal aspect of Mc2, though this is extended across the dorsal aspect in the *P. troglodytes* comparison. The Mc3 of *Gorilla* was also had significantly higher RBV/TV than *P. paniscus* at landmarks on its dorso-ulnar aspect but was not significantly different from *P. troglodytes* in any region. *Gorilla* had less significant regional differences with *P. troglodytes* than with *P. paniscus* in RBV/TV.

Gorilla had low DA throughout the subchondral metacarpal head trabeculae with slightly higher values distally on Mc3 and Mc4, though only the ulno-distal aspect of Mc3 had values that were significantly larger than Mc2 (Figs. 4.7 and 4.9). Mc5 had significantly higher DA on its radial side relative to Mc2 (Fig. 4.9). *Gorilla* was not significantly higher in DA than other taxa, apart from the radial border of the distal Mc5 head compared with *Pan paniscus* (Fig. 4.11).

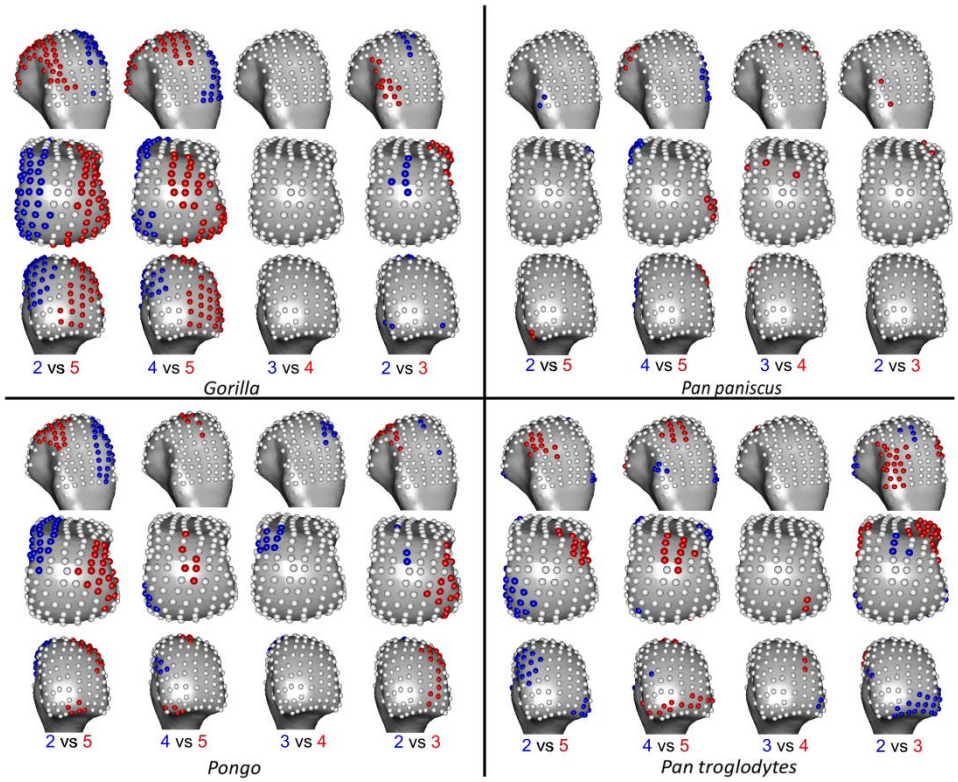

Figure 4.8. Inter-ray significant differences in RBV/TV, mapped to an average right Mc3 head in each case in dorsal (top), distal (middle) and palmar (bottom) views. Where RBV/TV values at landmarks are significantly higher in one ray than the other, they are coloured as per the ray numbers in each comparison.

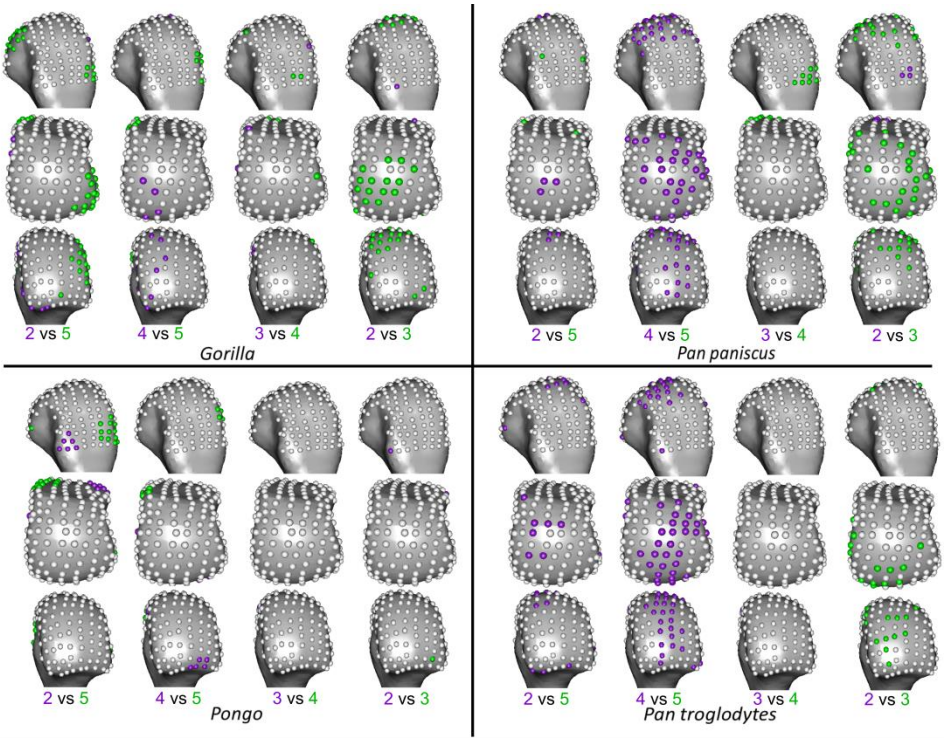

Figure 4.9. Inter-ray significant differences in DA, mapped to an average right Mc3 head in each case in dorsal (top), distal (middle) and palmar (bottom) views. Where DA values at landmarks are significantly higher in one ray than the other, they are coloured as per the ray numbers in each comparison

Pan troglodytes

P. troglodytes had disto-dorsally higher average RBV/TV values in the subchondral trabeculae of all the metacarpal heads, though this pattern was more dorsally-positioned in Mc3 and Mc4 (Fig. 4.6). Mc2 and Mc5 showed significantly higher RBV/TV at their most palmar extent relative to Mc3 and Mc4, respectively (Fig. 4.8). Interspecifically, *P. troglodytes* showed almost no significant differentiation from *P. paniscus* in RBV/TV in any ray (Fig. 4.10). *P. troglodytes* had significantly higher RBV/TV across the palmar extent of Mc2, and disto-palmarly on the ulnar aspect of Mc5 compared to that of *Gorilla*, and significantly higher RBV/TV dorsally than *Pongo* in each ray. *P. troglodytes* generally had low DA through all of the metacarpal heads, although DA values were slighter higher in the palmar regions of Mc3 and Mc4 (Fig. 4.7). DA values were significantly higher in Mc4 relative to Mc5 and higher in Mc3 relative to Mc2 (Fig. 4.9). *P. troglodytes* showed the fewest significant differences in DA with *P. paniscus*, significantly higher DA in the palmar aspects of Mc2 and Mc3 compared with *Gorilla*, and significantly lower DA than *Pongo* throughout all the rays (Fig. 4.11).

Pan paniscus

Like *P. troglodytes, P. paniscus* had the highest RBV/TV values at the disto-dorsal aspect of metacarpal heads but subchondral trabecular structure was more homogenous within and between the rays (Figs. 4.6 and 4.8). Interspecifically, *P. paniscus* showed the fewest significant differences with *P. troglodytes* apart from a small concentration of higher RBV/TV landmarks in the most palmar extent of Mc3 (Fig. 4.10). *P. paniscus* possessed significantly higher RBV/TV dorsally than *Pongo* across the rays and significantly higher palmar RBV/TV than *Gorilla* in all of the rays. This latter pattern extended distally on Mc2 and Mc5 (Figs. 4.6 and 4.10). *P. paniscus* had a similar DA pattern to *P. troglodytes*, with similar inter-ray significant differences and almost no significant differences between these species (Figs. 4.7, 4.9 and 4.11). *P. paniscus* showed significantly higher DA than *Gorilla* in landmarks across the Mc2 and Mc3 heads, in the palmar regions (Fig. 4.11). As with all other African apes, *P. paniscus* had significantly lower DA than *Pongo* across the metacarpal heads, particularly in the dorsal regions.

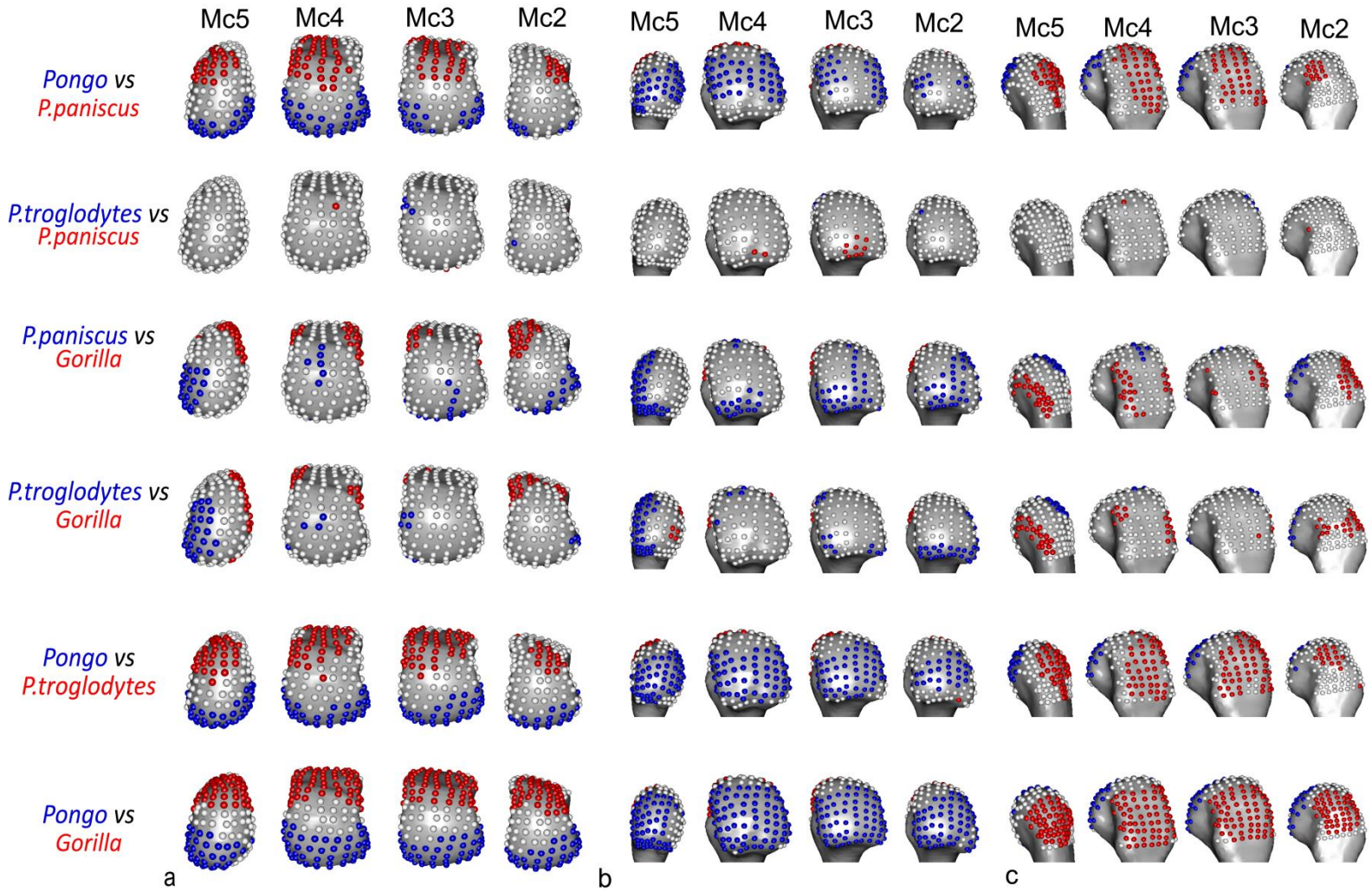

Figure 4.10. Significant differences in RBV/TV between species, mapped to average models of each Mc head in a) distal b) palmar and c) dorsal views. Where RBV/TV values at landmarks are significantly higher in one species than the other, they are coloured as per the species name in each comparison.

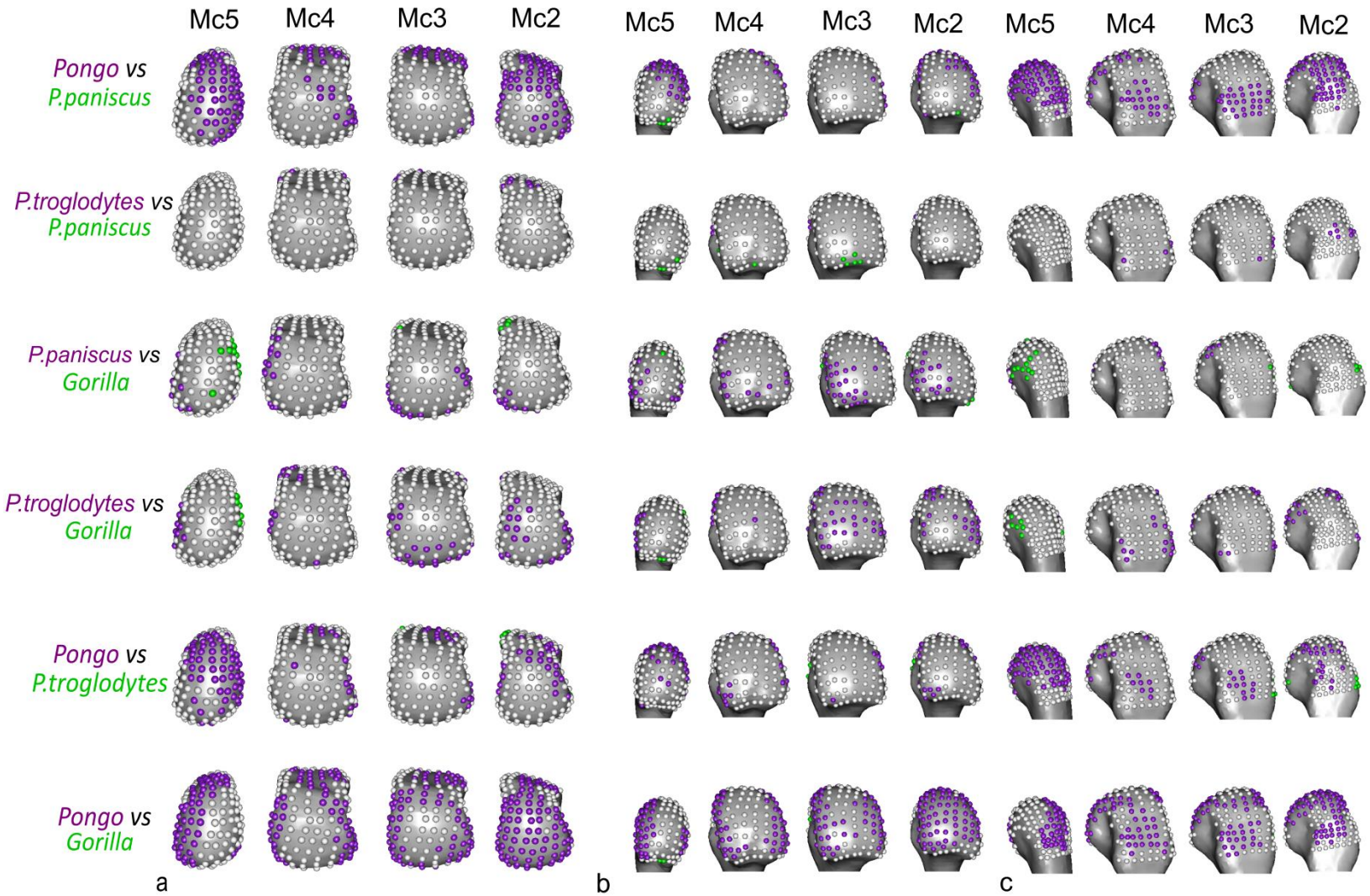

Figure 4.11. Significant differences in DA between species, mapped to average models of each Mc head in a) distal b) palmar and c) dorsal views. Where DA values at landmarks are significantly higher in one species than the other, they are coloured as per the species name in each comparison.

Table 4.3. Descriptive statistics of absolute *Z*-scores from significant pairwise inter-species landmark comparisons.

	Mc2						Mc3						Mc4						Mc5					
RBV/TV	**Ggg - Pp**	**Ggg - Ppy**	**Ggg - Pt**	**Pp - Ppy**	**Pp - Pt**	**Ppy - Pt**	**Ggg - Pp**	**Ggg - Ppy**	**Ggg - Ptv**	**Pp - Ppy**	**Pp - Pt**	**Ppy - Pt**	**Ggg - Pp**	**Ggg - Ppy**	**Ggg - Ptv**	**Pp - Ppy**	**Pp - Pt**	**Ppy - Pt**	**Ggg - Pp**	**Ggg - Ppy**	**Ggg - Pt**	**Pp - Ppy**	**Pp - Pt**	**Ppy - Pt**
Min	2.41	2.44	2.40	2.42	2.42	2.41	2.42	2.48	2.40	2.40	2.40	2.45	2.44	2.41	2.45	2.40	2.63	2.42	2.41	2.41	2.40	2.40	n/s	2.43
Max	4.33	5.59	4.79	3.54	3.21	4.15	4.32	5.63	3.27	4.19	3.22	4.73	3.87	5.92	3.59	4.94	2.78	4.88	3.89	5.76	3.95	3.79	n/s	5.18
SD	0.48	0.82	0.67	0.34	0.39	0.47	0.55	0.79	0.27	0.41	0.24	0.57	0.36	0.77	0.32	0.71	0.07	0.58	0.44	0.98	0.34	0.35	n/s	0.73
Mean	3.14	3.90	3.31	2.92	2.81	3.11	3.25	4.25	2.65	2.96	2.71	3.44	3.03	4.18	2.98	3.41	2.72	3.45	3.12	4.13	3.01	2.95	n/s	3.54
DA	**Ggg - Pp**	**Ggg - Ppy**	**Ggg - Pt**	**Pp - Ppy**	**Pp - Pt**	**Ppy - Pt**	**Ggg - Pp**	**Ggg - Ppy**	**Ggg - Pt**	**Pp - Ppy**	**Pp - Pt**	**Ppy - Pt**	**Ggg - Pp**	**Ggg - Ppy**	**Ggg - Pt**	**Pp - Ppy**	**Pp - Pt**	**Ppy - Pt**	**Ggg - Pp**	**Ggg - Ppy**	**Ggg - Pt**	**Pp - Ppy**	**Pp - Pt**	**Ppy - Pt**
Min	2.40	2.40	2.45	2.41	2.41	2.40	2.40	2.41	2.42	2.42	2.41	2.40	2.41	2.41	2.42	2.40	2.42	2.40	2.40	2.40	2.40	2.41	2.56	2.40
Max	3.48	4.77	3.89	4.84	3.34	3.41	4.58	4.84	4.00	4.40	3.11	3.14	3.40	4.42	4.13	4.14	2.69	3.45	4.03	4.44	3.87	4.72	3.25	4.27
SD	0.36	0.59	0.38	0.59	0.30	0.27	0.50	0.56	0.41	0.58	0.26	0.19	0.27	0.55	0.49	0.46	0.12	0.31	0.40	0.47	0.44	0.57	0.28	0.49
Mean	2.83	3.43	2.94	3.21	2.82	2.76	2.94	3.21	2.84	3.25	2.74	2.82	2.88	3.23	2.99	2.97	2.52	2.84	3.01	3.15	2.94	3.29	2.92	3.16

Species abbreviations are: Ggg = *Gorilla*, Pt = *Pan troglodytes*, Pp = *Pan paniscus*, Ppy = *Pongo* spp. The minimum differences between species at a given landmark are over 2.4 normalized standard deviations from each other.

Table 4.4. Descriptive statistics of absolute *Z*-scores from significant pairwise inter-ray landmark comparisons.

	Gorilla gorilla				*Pan paniscus*				*Pongo* spp.				*Pan troglodytes*			
RBV/TV	**2 - 3**	**3 - 4**	**4 - 5**	**2 - 5**	**2 - 3**	**3 - 4**	**4 - 5**	**2 - 5**	**2 - 3**	**3 - 4**	**4 - 5**	**2 - 5**	**2 - 3**	**3 - 4**	**4 - 5**	**2 - 5**
Min	2.41	n/s	2.42	2.49	2.51	2.60	2.41	2.43	2.41	2.47	2.47	2.42	2.45	2.41	2.42	2.39
Max	3.59	n/s	4.51	5.39	3.02	2.60	3.60	3.52	3.30	2.79	3.19	4.73	4.10	2.89	3.86	4.00
SD	0.40	n/s	0.45	0.71	0.26	0.00	0.37	0.38	0.24	0.09	0.21	0.64	0.46	0.18	0.39	0.45
Mean	2.95	n/s	3.19	3.69	2.76	2.60	2.75	2.85	2.66	2.62	2.79	3.40	3.10	2.64	3.03	3.03
DA	**2 - 3**	**3 - 4**	**4 - 5**	**2 - 5**	**2 - 3**	**3 - 4**	**4 - 5**	**2 - 5**	**2 - 3**	**3 - 4**	**4 - 5**	**2 - 5**	**2 - 3**	**3 - 4**	**4 - 5**	**2 - 5**
Min	2.42	2.48	2.45	2.42	2.41	2.47	2.41	2.43	2.67	n/s	2.64	2.41	2.46	n/s	2.39	2.41
Max	3.97	3.02	3.65	4.33	3.71	3.44	3.42	3.35	3.00	n/s	3.25	4.12	3.09	n/s	3.82	3.51
SD	0.50	0.22	0.35	0.59	0.37	0.41	0.30	0.28	0.17	n/s	0.19	0.41	0.21	n/s	0.29	0.29
Mean	2.86	2.63	2.79	3.11	2.86	2.96	2.85	2.69	2.84	n/s	2.84	2.84	2.69	n/s	2.81	2.67

The minimum differences between rays at a given landmark are over 2.4 normalized standard deviations from each other.

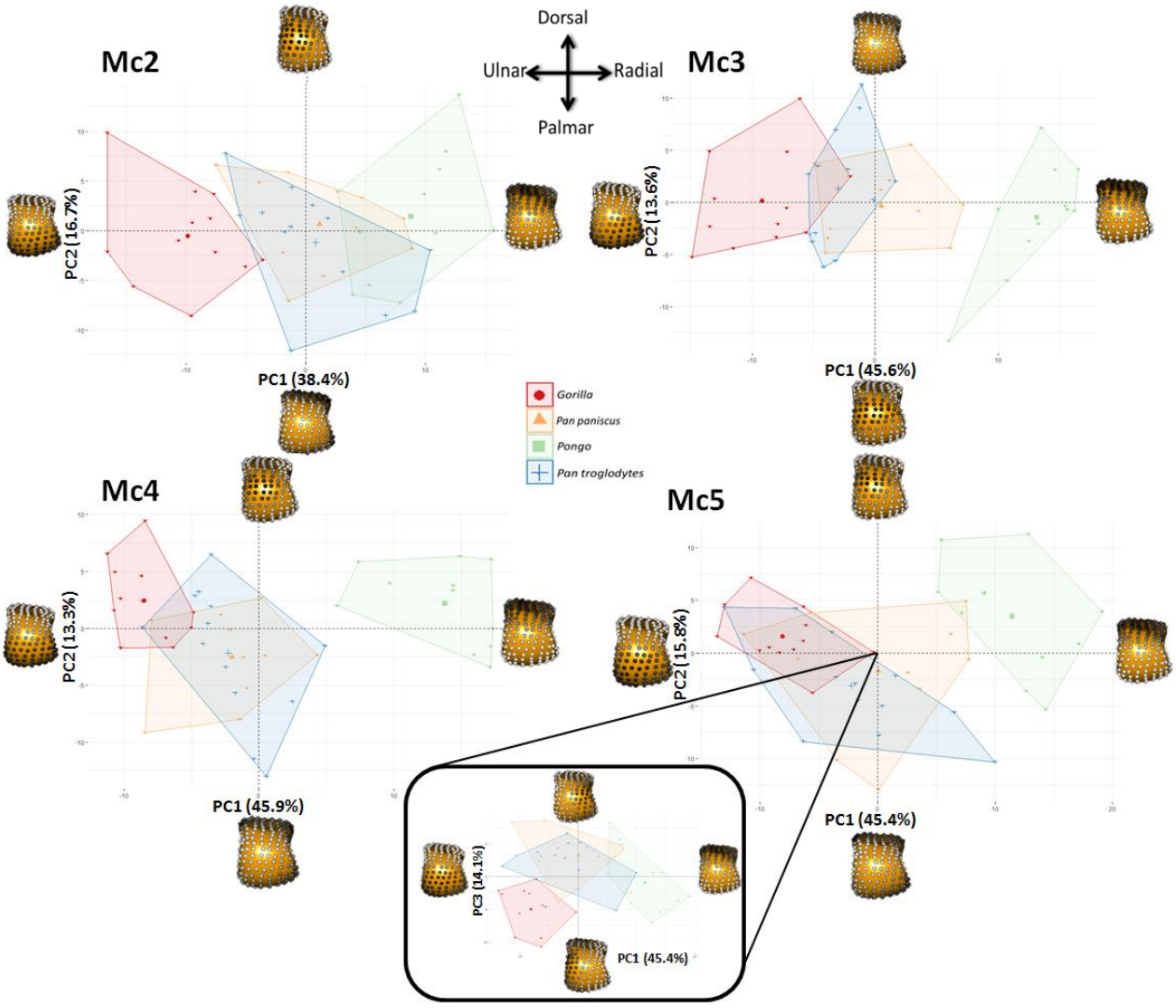

Figure 4.12. RBV/TV PCA plots showing species differences within each metacarpal head Each plot shows the first two principle components (PC) in each ray. For Mc5, PC3 is depicted with PC1, inset, as PC2 and PC3 explain a similar amount of the variance (16% and 14% respectively) in this case. Landmarks at each extreme of a PC are coloured in grayscale, according to their signed contribution to that PC and plotted on a Mc3 in distal view. White landmarks indicate the highest signed contribution to the PC and black the least.

Multivariate whole-surface comparisons

Interspecific results

Figure 4.12 depicts the results of the PCA on RBV/TV values, showing species differences within each metacarpal head. Within the Mc2-5 of all the taxa, the first principal component (PC1) explains 38-46% variation in RBV/TV and was driven by dorsal and palmar landmarks. PC2 in Mc2-Mc5 described 13-17% of the variation and reflected variation of values at landmarks that were distally and non-distally situated, respectively. In Mc5, PC3 described 14% of RBV/TV variation in values at radio-ulnar landmarks. Permutational MANOVA omnibus tests were run using PC1-

3 in each case, as for some comparisons the PC2 and PC3 explained a similar amount of variance whereas further PCs each explained less than 10% of the variance. These omnibus tests were significant in every ray. As with the individual landmark comparisons described above, *Pongo* had significantly higher palmar RBV/TV compared to all other species, especially *Gorilla.* The overall configuration of *Gorilla* RBV/TV was significantly higher dorsally compared to all other species in Mc2-4, and radio-dorsally in Mc5 (Fig. 4.12, Table 4.5). *P. troglodytes* and *P. paniscus* were not significantly different from each other in any of the species comparisons (Table 4.5).

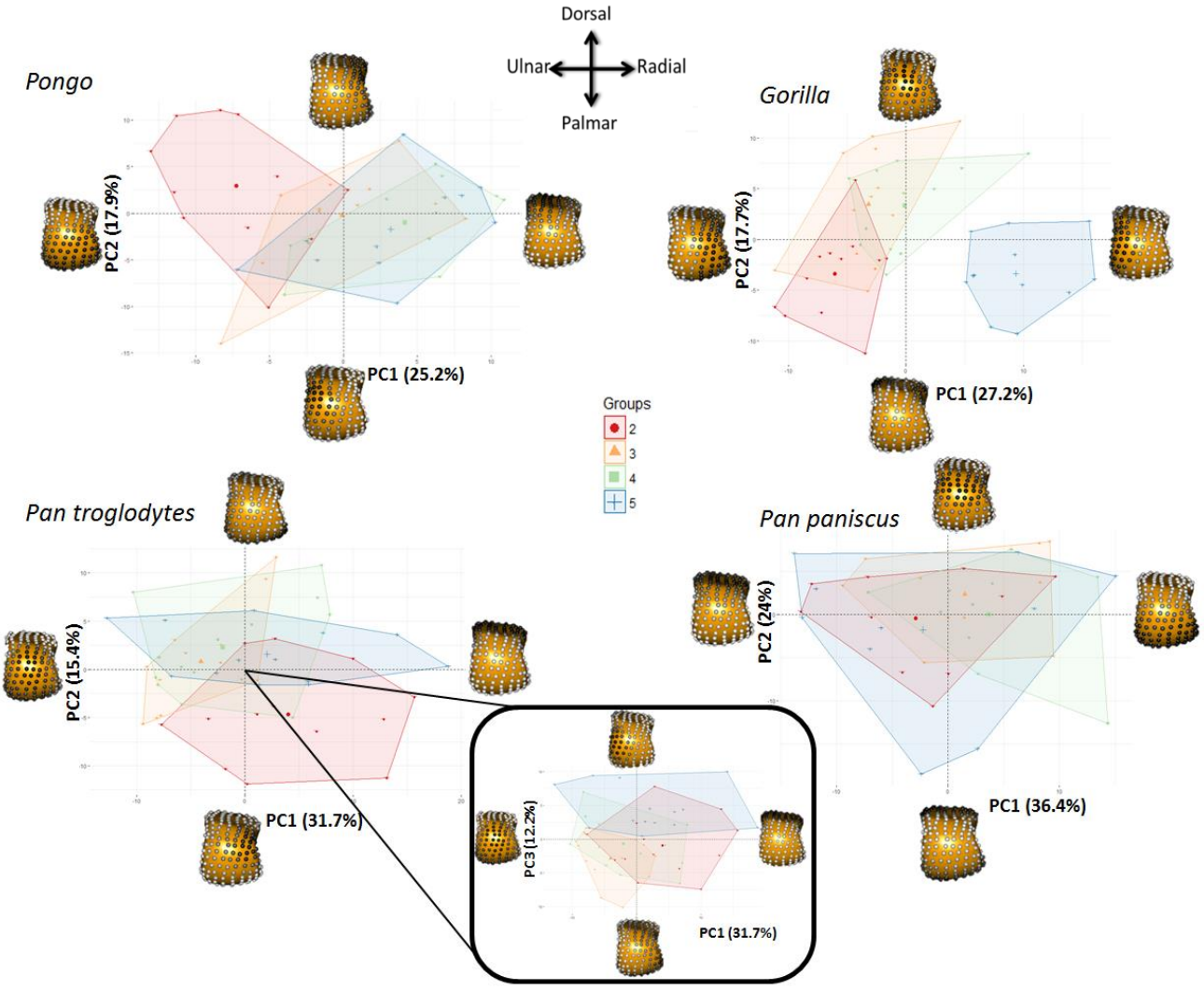

Figure 4.13. RBV/TV PCA plots showing ray differences within each species. Each plot shows the first two principle components (PC) in each ray, except for *Pan troglodytes* where PC3 is depicted with PC1, inset, as PC2 and PC3 explain a similar amount of the variance (15% and 12% respectively) in this case. Landmarks at each extreme of a PC are coloured in grayscale, according to their signed contribution to that PC and plotted on a Mc3 in distal view. White landmarks indicate the highest signed contribution to the PC and black the least

Following the limited interspecific differences in DA described above, a PCA of DA values yielded poor separation among the sampled taxa. PC1 in DA for each ray, across species, described 34-36% of the variation and was driven by higher values at most landmarks. PC2 described 10-14% of the variation and was driven by landmarks situated dorsally and disto-palmarly, respectively (Fig. 4.14). While *Pongo* tended to occupy the positive end of PC1, reflecting higher DA, permutational MANOVAs on PC1-3 revealed they were only significantly different in every ray from *Gorilla*. This result may be partially driven by the larger intra-species variation in *Pongo* DA relative to other species studied (Fig. 4.14; see discussion). *Pongo* was significantly different from *P. paniscus* in Mc2, Mc3 and Mc5 as well as from *P. troglodytes* in Mc2 and Mc5 by having generally higher DA (Table 4.5). Again, *P. paniscus* and *P. troglodytes* were not significantly different from each other at any ray, though both species were slightly, but significantly, higher in DA than *Gorilla* in most rays, *P. troglodytes* was not significantly different from *Gorilla* in DA across Mc4. Both *Pan* species had significantly lower DA than *Gorilla* in the radio-distal aspect of Mc5.

Inter-ray results

Figure 4.13 depicts the results of PCA of RBV/TV values, showing inter-ray differences within each species. Overall metacarpal head variation in RBV/TV across rays was different for each species, but generally consistent with individual landmark comparisons described above. In *Pongo,* PC1 explained 25% of the variation and was driven by dorso-palmar landmark values, while PC2 explained 18% of the variation and reflected radio-ulnar landmark RBV/TV. The significant omnibus result was driven solely by a Mc2 configuration that had significantly higher disto-ulnar RBV/TV than the other rays. In *Gorilla,* PC1 reflected 27% of the variation as a result of radio-ulnar landmark values, while PC2 reflected 18% of the variation in RBV/TV due to distal and more dorso-palmarly located landmarks (Fig. 4.13). Permutational MANOVAs on PC1-3 demonstrated the *Gorilla* Mc5 had significantly higher RBV/TV disto-radially relative to all other rays. *Gorilla* Mc2 had significantly higher disto-ulnar RBV/TV than the other rays, whereas Mc3 and Mc4 had significantly higher RBVTV dorsally than Mc2 and Mc5, and were not

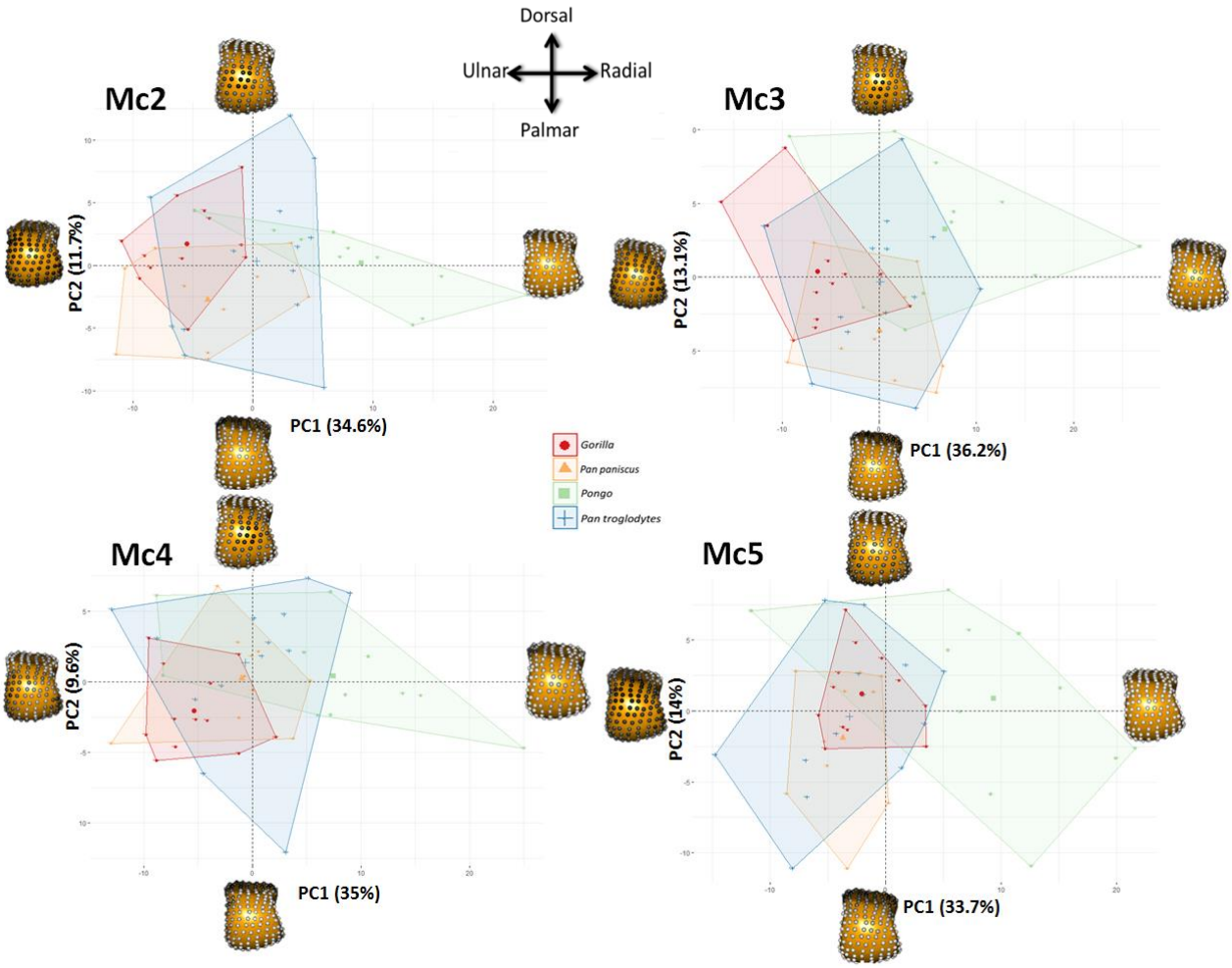

Figure 4.14. DA PCA plots showing species differences within each metacarpal head. Each plot shows the first two principle components (PC) in each ray. Landmarks at each extreme of a PC are coloured in grayscale, according to their signed contribution to that PC and plotted on a Mc3 in distal view. White landmarks indicate the highest signed contribution to the PC and black the least.

not significantly different from each other (Table 4.5). For *P. troglodytes* variation in overall RBV/TV was chiefly driven by dorso-palmar landmarks on PC1, which explained 32% of the variation, while PC2 explained 15% of the variation and reflected differences in the disto-ulnar landmarks. PC3 in *P. troglodytes* RBV/TV describes 12% of the variation and is driven by radio-ulnar landmarks (Fig. 4.13). *P. troglodytes* Mc2 had significantly higher RBTV/TV disto-palmarly on its ulnar aspect relative to all other rays, whereas Mc5 had significantly higher RBV/TV disto-palmarly on its ulnar aspect compared to Mc2 and Mc3. While Mc3 and Mc4 were not significantly different from each other as both had higher dorsal RBV/TV, Mc4 was not significantly different from Mc5. In *Pan paniscus* PC1 explained 36% of the variance in RBV/TV and was driven by dorso-palmar landmarks while PC2 explained

24% of the variance and reflected distal and non-distal landmarks. However, no significant differences in RBV/TV were found between *P. paniscus* rays (Table 4.5).

Variation in DA values did not show many significant differences across the metacarpal heads but was broadly consistent with the individual landmark comparisons. For all species sampled, PC1 was driven by higher values at most landmarks in PC1 and explained 19-45% of the variation. PC2 described 10-16% of the variation in DA and reflected distal as opposed to non-distal landmarks in all species (Fig. 4.15). In *Pongo* no ray was significantly different from any other in overall configuration of DA values (Table 4.5). In *Gorilla* PC3 explained 9% of the variance and was driven by radio-ulnar landmarks. Mc5 in *Gorilla* had significantly higher DA at radial landmarks than Mc2 and Mc3. The *Gorilla* Mc4 had slightly, but significantly, higher DA over most landmarks relative to Mc2. Both *P. troglodytes* and *P. paniscus* had significantly lower DA at landmarks on the distal aspect of Mc5 compared to Mc3 and Mc4. *P. paniscus* alone, also had significantly lower DA over most landmarks on Mc2 compared to Mc3.

Table 4.5. Permutational MANOVAs on the first three principle components between all groups.

	RBV/TV MC2	***RBV/TV MC3***	***RBV/TV MC4***	***RBV/TV MC5***		***RBV/TV Ggg***	***RBV/TV Pp***	***RBV/TV Ppy***	***RBV/TV Pt***
All (n=46)	10.764*	21.595*	26.081*	16.008*	***All***	14.983* (n=48)	1.667 (n=40)	6.472* (n=44)	5.336* (n=52)
Ppy-Pp (n=21)	6.893*	18.627*	35.572*	11.279*	***2-3***	6.088* (n=24)	n/s	4.998*(n=22)	8.399* (n=26)
Pt-Pp (n=23)	0.538	2.142	0.512	0.519	***3-4***	1.553 (n=24)	n/s	1.780 (n=22)	1.026 (n=26)
Pp-Ggg (n=22)	14.230*	11.165*	14.534*	13.257*	***4-5***	19.235* (n=24)	n/s	4.006 (n=22)	3.289 (n=26)
Pt-Ggg (n=25)	9.956*	5.925*	9.209*	13.999*	***2-5***	32.396* (n=24)	n/s	11.963* (n=22)	5.015* (n=26)
Pt-Ppy (n=24)	5.598*	33.532*	31.306*	20.794*	***3-5***	23.657* (n=24)	n/s	3.384 (n=22)	7.813* (n=26)
Ppy-Ggg (n=23)	33.495*	50.945*	75.214*	45.695*	***2-4***	11.776* (n=24)	n/s	12.434* (n=22)	6.333* (n=26)
	DA MC2	***DA MC3***	***DA MC4***	***DA MC5***		***DA Ggg***	***DA Pp***	***DA Ppy***	***DA Pt***
All (n=46)	9.449*	6.308*	5.921*	8.574*	***All***	4.160* (n=48)	6.496* (n=40)	0.274 (n=44)	3.531* (n=52)
Ppy-Pp (n=21)	15.689*	5.899*	5.720	11.344*	***2-3***	2.645 (n=24)	7.215*(n=20)	n/s	2.466 (n=26)
Pt-Pp (n=23)	2.219	1.148	1.409	0.637	***3-4***	1.504 (n=24)	2.462 (n=20)	n/s	0.880 (n=26)
Pp-Ggg (n=22)	4.599*	8.049*	5.423*	11.599*	***4-5***	3.888 (n=24)	7.019* (n=20)	n/s	5.615* (n=26)
Pt-Ggg (n=25)	5.293*	5.100*	4.179	4.341*	***2-5***	6.020* (n=24)	2.874 (n=20)	n/s	2.602 (n=26)
Pt-Ppy (n=24)	6.917*	3.772	4.344	9.896*	***3-5***	6.066* (n=24)	15.040* (n=20)	n/s	9.133* (n=26)
Ppy-Ggg (n=23)	24.985*	13.466*	14.051*	12.116*	***2-4***	5.945* (n=24)	4.987 (n=20)	n/s	0.695 (n=26)

Species abbreviations are: Ggg = *Gorilla*, Pt = *Pan troglodytes*, Pp = *Pan paniscus*, Ppy = *Pongo* spp. Subsequent pairwise Permutational MANOVAs were carried out if the omnibus test was significant; otherwise pairwise tests are marked as non-significant (n/s). All Pseudo-*F* values that represented a significant difference, subsequent to a Bonferroni correction, are marked with asterisks(*).

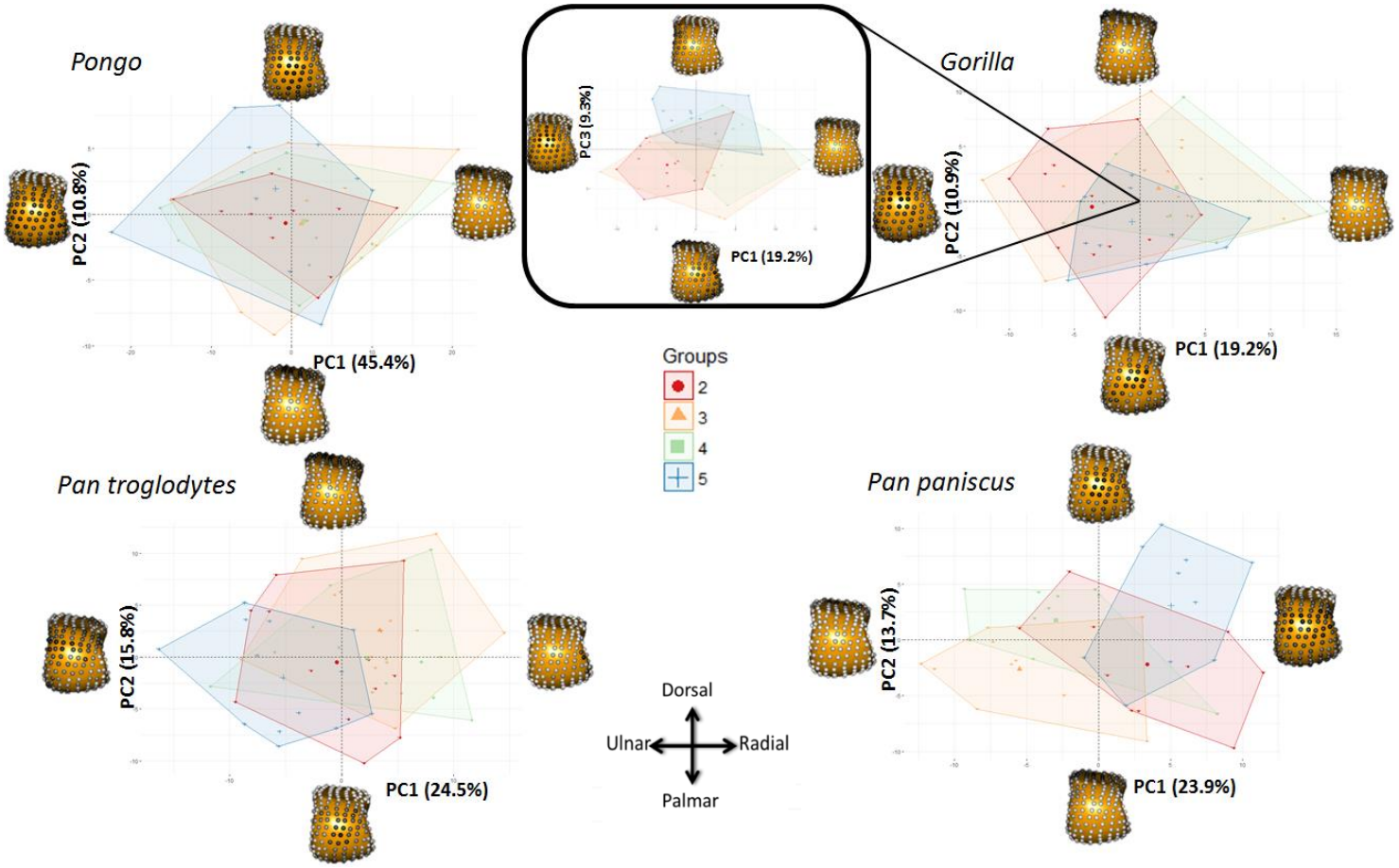

Figure 4.15. DA PCA plots showing ray differences within each species. Each plot shows the first two principle components (PC) in each ray. For *Gorilla*, PC3 is depicted with PC1, inset, as PC2 and PC3 explain a similar amount of the variance (11% and 9% respectively) in this case. Landmarks at each extreme of a PC are coloured in grayscale, according to their signed contribution to that PC and plotted on a Mc3 in distal view. White landmarks indicate the highest signed contribution to the PC and black the least.

Discussion

The aim of this study was to associate inferred loading during particular hand postures in non-human great apes during locomotion with subchondral trabecular architecture across the non-pollical metacarpal heads. The results confirm and build upon previous studies of trabecular bone (most often focussed on only the Mc3 head; Tsegai et al., 2013; Barak et al., 2017; Chichir et al., 2017), demonstrating that not only is this association possible, but that regional trabecular patterns within metacarpal heads, both within and across species, can be statistically discerned. Further, locomotor signals within trabecular structure are not limited to the Mc3 and analysis of all non-pollical metacarpals can provide greater insight into inter-ray and interspecific differences in digit loading.

Relative trabecular bone volume fraction

Pongo

We predicted the orangutans would show significantly higher RBV/TV in the disto-palmar region of the metacarpal heads compared to other hominids and that there would be no significant differences between rays, reflecting the flexed or neutral McP joint posture of all the fingers that characterises flexed-finger power, hook and double-locked grips typically used during arboreal locomotion (Rose, 1988; Sarmiento, 1988). We found general support for these predictions. Orangutans demonstrated significantly higher RBV/TV in the disto-palmar aspect of the subchondral trabeculae in all non-pollical metacarpal heads compared to that of all other taxa. We also found few inter-ray differences, with orangutans generally showing fewer significantly different landmarks in RBV/TV compared with gorillas and chimpanzees (Fig. 4.8) and no significant difference in overall RBV/TV between adjacent rays (Table 4.5). The only exception to this was Mc2 of orangutans, which had significantly higher RBV/TV in the disto-dorsal region of its ulnar aspect, relative to the other rays (Figs. 4.8 and 4.13). Overall, our results are consistent with previous studies using differing methodologies that also found a higher BV/TV in the disto-palmar region of the orangutan Mc3 head (Zeininger et al., 2011; Tsegai et al., 2013; Skinner et al., 2015; Chirchir et al., 2017) and Mc5 head (Skinner et al., 2015). It should be noted, however, that the present study sample includes five of the same Mc3 specimens and three of the Mc5 specimens used by Tsegai et al. (2013) and Skinner et al. (2015), respectively. The generally similar pattern of RBV/TV distribution across the Mc2-5 heads is consistent with using all of the fingers during power, hook and double-lock grips to grasp arboreal substrates (Rose, 1988). The diverging pattern found in the orangutan Mc2 could reflect the relatively more extended second digit posture during a diagonal double-locked grip of very thin substrates, as pictured by Napier (1960) in captivity (Fig. 4.16). However, although challenging data to collect, more behavioural studies of types and frequency of hand grips used by orangutans during arboreal locomotion are needed to substantiate this.

Figure 4.16. The right hand of a captive orangutan engaged in a diagonal 'double-locked' grip around a piece of string. Note the extension of the second metacarpophalangeal joint. Image adapted from Napier (1960).

Gorilla

We predicted gorillas would show a significantly higher dorsal distribution of RBV/TV in each metacarpal head compared with all other hominids, reflecting McP joints loaded in a hyperextended posture during frequent knuckle-walking and this prediction was supported. RBV/TV in the gorilla subchondral trabeculae was significantly higher dorsally than in all other species (Figs. 4.10 and 4.12). This RBV/TV pattern was also found in previous studies of the Mc3 in gorillas (Tsegai et al., 2013; Skinner et al., 2015). The present results, however, also revealed high RBV/TV along the disto-ulnar region of the Mc2 head and disto-radial region of the Mc5 head, which was not predicted, although a similar pattern was also found in the Mc5 by Skinner et al. (2015). This pattern is present in both the average male and female RBV/TV distribution (Fig. 4.17). The gorilla fifth digit is more frequently used in knuckle-walking (Inouye, 1994) and is more similar in length to the other rays than that of chimpanzees (Susman, 1979; Inouye, 1992), which may explain the more even distribution of knuckle-walking pressure across the digits in captive

gorillas (Matarazzo, 2013). As the fifth digit is often not involved in grips of thinner arboreal substrates (Neufuss et al., 2017) and this RBV/TV pattern is mirrored in the Mc2, it seems parsimonious to argue it reflects more frequent and less variable knuckle-walking hand postures in gorillas relative to chimpanzees and bonobos (Tuttle and Basmajian, 1978; Matarazzo, 2013; Samuel et al., 2018; Thompson et al., 2018). The Mc3 and Mc4 of gorillas also showed high RBV/TV dorsally, especially at the radio-ulnar margins (Figs. 4.6 and 4.8), which is consistent with the idea that the fingers work in concert to buffer medio-lateral forces during locomotion (Chirchir et al., 2017). The medio-lateral forces generated during 'palm-back' knuckle-walking, which places the McP joints orthogonal to the direction of travel, may be considerable.

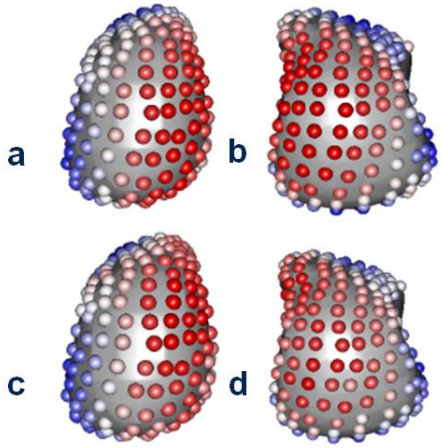

Figure 4.17. *Gorilla* average RBV/TV by sex, mapped to average models of right Mc heads in distal view for a) Male Mc5, b) Male Mc2, c) Female Mc5 and d) Female Mc2, specimens. Note that the radio-ulnar bias is present in both sexes.

Pan troglodytes

We predicted that chimpanzees would have significantly higher dorsal RBV/TV than orangutans but lower than in gorillas, with a more homogeneous distribution of RBV/TV within each metacarpal head and more inter-ray differences, reflecting their more varied locomotor regime. These predictions were generally supported. The disto-dorsal pattern of higher RBV/TV across the subchondral metacarpus of chimpanzees (Fig. 4.6) was more dorsally concentrated than that of orangutans and more distally-extended than in gorillas (Figs. 4.10 and 4.12). This RBV/TV pattern is consistent with previous studies of chimpanzee subchondral trabecular bone

(Zeininger et al., 2011) and whole–epiphyseal analyses that found a similar signal in the subchondral trabeculae of Mc3 and Mc5 (Tsegai et al., 2013; Skinner et al., 2015). It should be noted, however, that the present study sample includes five of the same Mc3 specimens and four of the Mc5 specimens used by Tsegai et al. (2013) and Skinner et al. (2015), respectively. In contrast to these analyses, studies using larger volume of interest (VOI) methods have found higher BV/TV in centrally-placed VOIs relative to palmar or dorsally placed VOI's in the chimpanzee Mc3 head (Barak et al., 2017; Chirchir et al., 2017). However, the use of fewer large VOIs in these studies, as opposed to the many smaller VOIs produced by the whole-epiphysis approach employed here, may exacerbate issues of VOI placement and size that have been shown to dramatically affect trabecular measures in the primate Mc3 (Kivell et al., 2011b).

In partial support of our prediction, we found that chimpanzees showed several significant differences in RBV/TV between the metacarpal heads, although there were not more differences than those found in gorilla metacarpals. Specifically, RBV/TV was significantly higher palmarly in Mc2 and Mc5 but higher distally in Mc3 and Mc4 in chimpanzees (Figs. 4.8 and 4.13). This pattern may reflect relatively more weight bearing by digits 3 and 4 during knuckle-walking than in the second or fifth digit (Tuttle and Basmajian, 1978). Some captive chimpanzees with injuries to digits 2 and 5 appeared to be unimpaired when knuckle-walking, and some healthy individuals were observed flexing these digits so that they did not bear weight during this mode of locomotion (Tuttle, 1967). Larger captive chimpanzees have been observed using their second digit significantly less often than gorillas of equivalent size during knuckle-walking, and chimpanzees of all sizes used their fifth digit significantly less often and loaded it less than gorillas did (Inouye, 1994; Wunderlich and Jungers, 2009; Matatrazzo, 2013). Matarazzo (2013) found the third digit regularly lifted-off last during 'palm-back' knuckle-walking in captive chimpanzees and that peak pressure was often experienced by the third digit. Wunderlich and Jungers (2009) also found that peak pressures were higher on digits 3 and 4 than on digits 2 and 5 when young chimpanzees practised arboreal knuckle-walking and when they used a 'palm-back' posture during terrestrial knuckle-

walking. Therefore it could be argued that the more palmar RBV/TV distribution in Mc2 and Mc5, relative to Mc3 and Mc4, might reflect less loading in McP hyperextension during knuckle-walking and a need to flex digits 2 and 5 during arboreal grasping. Marzke and Wullstein (1996) have argued that the fifth digit should be the most flexed in diagonal power grips, known to be used by wild chimpanzees while vertically climbing (Hunt, 1991; Neufuss et al., 2017).

That being said, in previous hand pressure studies, all mature chimpanzees experienced peak pressures on digits 2-4 when terrestrially knuckle-walking and the second digit usually lifts-off during 'palm-in' knuckle-walking (Wunderlich and Jungers, 2009; Matatrazzo, 2013). Further, the second digit should be the most extended during diagonal power grips (Marzke and Wullstein, 1996) which opposes the relative flexion thought to be indicated here by the relatively palmar RBV/TV pattern found in the chimpanzee Mc2 head. Therefore, in the absence of kinematic and kinetic studies of locomotor hand postures in wild chimpanzees, we suggest that this pattern may reflect a more varied hand postures and distribution of pressure across the digits during knuckle-walking (Wunderlich and Jungers, 2009; Matarazzo, 2013) or more frequent arboreal grasping compared with gorillas, or a combination of both (Remis, 1995; Doran, 1996; Thorpe and Crompton, 2006).

Pan paniscus

Given the general similarities in locomotion and hand use between chimpanzees and bonobos, we predicted that bonobos would have a RBV/TV pattern that was very similar to that of chimpanzees, but with a more homogenised distribution of RBV/TV within each metacarpal head. Our results supported these predictions; bonobos showed higher RBV/TV disto-dorsally on their metacarpal heads, that was more distally-extended than in gorillas and more dorsally concentrated than that of orangutans (Figs. 4.6, 4.10 and 4.12). Bonobos differed from chimpanzees in that they possessed almost no significant inter-ray differences and they showed the most landmarks closest to the mean of BV/TV throughout each head's trabecular surface (i.e., RBV/TV being ~1; Figs. 4.6, 4.8 and 4.13). This RBV/TV distribution is consistent with the expectation raised by Tsegai et al. (2013), that bonobos would have an intermediate Mc3 trabecular structure between that of African and Asian

non-human great apes (Fig.4.12), and consistent with the intermediate thickness of Mc3 cortical bone in this species (Susman, 1979). If the relatively higher dorsal RBV/TV in chimpanzee Mc3 and Mc4 is a knuckle-walking signal, then the lack of it in bonobos, as well as the significantly higher palmar RBV/TV of Mc3, may either reflect more loading of a flexed McP joint consistent with the presumed greater arboreality in this species (Alison and Badrian, 1977; Susman et al., 1980; Susman, 1984; Crompton et al., 2010) or direct palmar loading of the metacarpal head as a result of a significant amount of arboreal palmigrady (Doran, 1993; Doran and Hunt, 1994).

Trabecular anisotropy

In contrast to the RBV/TV results, the degree of anisotropy (DA) in the subchondral trabecular bone was less variable, both in inter-species and inter-ray comparisons. Interestingly, every species studied possesses higher average DA values across the most dorsal aspect of each metacarpal (Fig.4.7). As this pattern also appears in orangutans, it is likely not reflective of hyperextension of the McP during knuckle-walking but may instead reflect fewer trabeculae at the limit of the subarticular surface. Fewer subchondral trabecular struts would reduce the variability of alignment and thus increase DA. The main significant differences in DA were found in orangutans, which were generally more anisotropic than any other taxon, especially gorillas (Figs. 4.7, 4.9, 4.14, 4.15 and Table 4.5). This did not support our prediction that orangutan DA would be significantly higher in the disto-palmar region, nor that gorilla DA would be significantly higher in the dorsal region of the metacarpal heads compared to other hominids. Given this lack of specific regional differences it is difficult to attribute the general lack of inter-ray differences in orangutans and gorillas to functional grips as per our predictions (Figs. 4.9; 4.15). Conversely, the analyses of chimpanzees and bonobos did partially support our predictions, as they showed the least significantly different landmarks in DA between them (Fig.4.11) and the most inter-ray differences within each species (Fig.4.9), though again it is difficult to link this to specific hand postures.

High DA in orangutans did not support our predictions and appears contradictory to previous results showing significantly lower DA in orangutans and other suspensory

taxa (Tsegai et al., 2013). However, Tsegai et al. (2013) quantified and averaged trabecular DA throughout the entire Mc3 head, as opposed to just the subchondral trabeculae, which can mask the signal of higher DA in particular regions of the head. In particular, subchondral trabeculae are responsible for the initial dissipation of load from the articular, compact cortical bone through to the more internal trabecular structure in long bones such as metacarpals (Currey, 2002). Thus, it may be possible that trabeculae in this region are more constrained in their orientation, as they must link the cortical shell of the metacarpal head and the deeper trabecular structure, explaining the lack of variability in DA in our sample. If this is true, the variation in DA we did find, significantly higher DA in orangutans than in other species, might be due to a general lower number of trabeculae in orangutans. However, Chirchir et al. (2017) also found that DA was consistently, if not significantly, higher in orangutans compared with chimpanzees in all three of their VOIs which sampled most of the Mc3 head. Further, higher DA has been found in other regions of in the orangutan skeleton, such as at superior-central region of humerus (Kivell et al., 2018b). Therefore, it is unlikely that the significantly higher DA in orangutans is solely an artefact of sampling subchondral trabeculae.

High subchondral DA in orangutans may reflect a lower extension range of motion (19°) compared to that of African apes (50°) (Napier, 1960; Rose, 1988). Although orangutans have been assumed to load their hands in a greater range of postures, to accommodate their diverse arboreal locomotor repertoire, relative to the frequent and consistent knuckle-walking postures of African apes (Tsegai et al., 2013), the orangutan McP joint will, presumably, always be in a neutral-to-flexed posture when grasping arboreal substrates. Indeed, while variability in DA values for orangutans appears to be higher than in other taxa studied, higher average DA values are not solely driven by outlying individuals (Fig. 4.14) nor, on further interrogation, those of a particular species or sex. An analysis of trabeculae in the whole Mc3 head has reported similar intra-species variability in orangutans (Tsegai et al., 2013). Yet, one constant across orangutan species and sexes is their high frequency of arboreal locomotion requiring flexed McP grasping and perhaps a more stereotypically-aligned trabecular structure, reflected in the high average DA

found here. In contrast, African apes load their McP joints in both hyperextension during knuckle-walking, and a range of neutral-to-flexed postures during arboreal locomotion. The greater isotropy found within African apes subchondral trabeculae may reflect loading of the McP joint from multiple directions during arboreal, as well as terrestrial, behaviours.

Inferring bone functional adaptation

Many explorative comparative anatomy analyses, including the present study, can be thought of as adaptationist (Gould and Lewontin, 1979), presenting functionally adaptive explanations for the observed data that are not easily falsified (Smith, 2016). Note that the term adaptation, within the adaptationist framework, is typically used to refer to heritable traits on which selection may act (Smith, 2016). The bone functional adaptation inferred here is considerably simpler, unconcerned with the fitness of a trait but merely its causal link with loading and a behaviour. Yet, the co-occurrence of behaviour and trabecular structure need not be linked causally and so this inference could still be termed, functionally, adaptationist. Here, however, we submit that as the clearest differences in subchondral RBV/TV and DA patterns in the metacarpal heads are between the two species with the most disparate locomotor modes (orangutans and gorillas) and the least differences are between the two species with the most similar locomotor modes (chimpanzees and bonobos). If the chimpanzees and bonobos were the most disparate in trabecular pattern this would provide an informal falsification of the broad underlying logic of our predictions. Conversely, with respect to our more specific predictions that were not met, for example those regarding regional DA in orangutans and gorillas, alternative data must be sought to explain these results (as detailed above). For example, future work that scales DA by trabecular number, analyses of the differences between subchondral and deeper trabecular structure, or detailed studies of locomotor hand postures in wild orangutans, could all potentially falsify some of these explanations. Nevertheless, it must be noted that the broader logic underlying more predictions holds for DA, as chimpanzees and bonobos did not display the most significant differences.

In the same vein, it could be argued that the lack of differences between chimpanzees and bonobos is due to their close phylogenetic distance rather than their similar locomotor regimes. Trabecular bone structure is controlled, at least to some extent, by genetic factors (Lovejoy et al., 2003; Havill et al., 2010; Judex et al., 2013; Almécija et al., 2015) and role of trabecular remodeling is not solely functional (Skinner et al., 2015; 2015b); for example, trabecular bone is also important for mineral homeostasis (Clarke, 2008). There were clear differences in absolute BV/TV, however, such that bonobos demonstrated much greater subchondral BV/TV in all elements of the hand studied compared to chimpanzees (Fig. 4.5). This difference has been previously reported within the Mc3 of the same individuals in this study, for which the phylogenetic influence was assessed (Tsegai et al., 2013). The relative measure used here appears to have effectively controlled for this difference in subchondral metacarpal head BV/TV. This suggests that the absolute difference in BV/TV is not functional in origin, as it is unlikely bonobos practise a form of locomotion very similar to chimpanzees but with remarkably greater force. The only comparable kinematic data available demonstrates both captive chimpanzees and captive bonobos experience similar peak pressures on their fingers during arboreal knuckle-walking (Wunderlich and Jungers, 2009; Samuel et al., 2018). If not functional in origin, the absolute difference in BV/TV between chimpanzees and bonobos may be systemic. Though a study of metatarsal trabeculae failed to find a large difference in absolute BV/TV between chimpanzees and bonobos, that later did have higher values (Griffin et al., 2010), Tsegai et al. (2018) have noted that systemic differences in BV/TV between species may be variably pronounced at different anatomical sites. While the reasons for systemic differences in trabeculae might be varied, including hormones, diet and disparate intestinal biomes (Tsegai et al., 2018), this difference in absolute BV/TV is marked between these phylogenetically close species. As a corollary it would seem that there is little reason to suspect non-functional systematic forces are driving the similarities between RBV/TV in *Pan* species. Although the relative measure appears to have effectively controlled for possible systemic differences in subchondral trabeculae of the non-pollical metacarpal heads, there are still small differences

between the species which, by process of elimination, appear to be functional origin.

Work on intra-species variation in a large sample of a single species also supports this idea of both a systemic and functional signal in trabecular architecture (Chirchir et al., 2015; Saers et al., 2016). While current studies have focused on humans, likely due to the availability of specimens, data from several anatomical joints have demonstrated lower BV/TV in sedentary humans relative to great apes (Chirchir et al., 2015; Ryan and Shaw, 2015; Tsegai et al., 2018). Lower limb BV/TV in recent sedentary humans is also lower than early modern humans and recent mobile forager populations, suggesting that this lower BV/TV reflects lower mechanical demands of a sedentary human lifestyle (Chirchir et al., 2015; Ryan and Shaw, 2015). However, BV/TV in the upper limb of recent sedentary humans is also lower than great apes and early modern humans, even though this limb is not necessarily loaded less in sedentary populations. As a result it remains possible that the reduction in the BV/TV in sedentary modern human populations is partly systemic (Chirchir et al., 2015). That is, reduction in upper limb BV/TV in sedentary modern human populations may be an indirect consequence of less lower limb loading, rather than less mechanical load on the upper limb (Chirchir et al., 2015). Within the lower limb, this lower BV/TV in sedentary human populations relative to mobile foragers, appears to be superimposed on a pattern of increasing trabecular gracility with increasingly distal elements of the limb in both types of population (Saers et al., 2016). The transition to sedentism in human populations provides a natural experiment that allows the identification of a trabecular functional signal superimposed onto a structural limb tapering signal, which is also found in cortical bone (Saers et al., 2016). The difference in upper limb and lower limb BV/TV between mobile and sedentary populations, allows us to begin explaining the variance structure in BV/TV values via both indirect (systemic) and direct (functional) factors (Chirchir et al., 2015). Similarly, this known difference in BV/TV can highlight other non-functional factors determining BV/TV such as a systemic limb tapering signal (Saers et al., 2016). We argue that the phylogenetic proximity and similar locomotion of both *Pan* species also provide a natural experiment,

holding some influences on BV/TV constant, that begins to separate functional and systemic differences between these species, as seen in the present RBV/TV and BV/TV results. Future work should consider the possibility of clarifying functional and systemic signals in trabecular bone.

It would be interesting to apply these methods to the pollicial metacarpal of hominids, and perhaps a larger sample of primates, in order to test for manipulative behaviour signals that may lie in the subchondral trabecular bone. Even this relatively small comparative sample may be used to contextualise fossil hominin trabeculae to shed light on their habitually loaded hand postures. Fossil hominins with a distribution of trabeculae similar to that found in extant hominids here, likely loaded their hand in similar manner and practised similar grips to these species. Therefore this comparative context has the potential to distinguish between habitual knuckle-walking and aboreality in fossil hominins. Though relatively complete fossil hominin hands are rare in the paleontological record, this comparative sample demonstrates that isolated Mc2 or Mc5 elements are more important than previously thought for identifying habitual hand use in our ancestors.

Conclusion

Using a geometric morphometric approach, we demonstrated significant differences in the distribution of subchondral trabecular RBV/TV across non-human great apes that were consistent with our predicted differences in McP joint loading during locomotion. Results of this study generally confirm previous analyses of metacarpal head trabecular structure that have largely focused only on the Mc3, but provide, for the first time, a statistically robust comparison using the whole-epiphysis approach. Building upon previous work, to analyse trabecular structure across all of the non-pollical metacarpals, we revealed novel RBV/TV patterns in the inter-ray comparisons within gorillas, chimpanzees and bonobos, that are consistent with differences in hand posture during knuckle-walking as well as the frequency of arboreal locomotion in these species. However, these inferences require testing with more detailed kinematic and kinetic analyses of the hand, ideally in wild non-human great apes. Contrary to our predictions, we found few significant differences in DA across taxa, with orangutans demonstrating significantly higher DA than African ape taxa. We conclude that the interspecific variation in subchondral trabecular RBV/TV revealed here is consistent with what is currently known about non-human great ape hand use and McP joint loading. Therefore, subchondral trabecular structure provides a valuable comparative context in which to interpret the trabecular structure of fossil hominoid or hominin metacarpal heads (see Chapter 6).

Chapter 5
Trabecular variation in the first metacarpal reflects distinctive human manipulation among hominids

Abstract

The dexterity of fossil hominins is often inferred by assessing the comparative manual anatomy and behaviors of extant hominids, with a focus on the thumb. The aim of this study is to test whether trabecular structure is consistent with what is currently known about habitually loaded thumb postures across extant hominids. We analyse first metacarpal (Mc1) subarticular trabecular architecture in humans (*Homo sapiens*, n=10), bonobos (*Pan paniscus*, n=10), chimpanzees (*Pan troglodytes,* n=11), as well as, for the first time, gorillas (*Gorilla gorilla gorilla,* n=10) and orangutans (*Pongo* sp. indet., n=1, *Pongo abelii,* n= 3 and *Pongo pygmaeus,* n=5). Using a combination of subarticular and whole-epiphysis approaches, we test for significant differences in relative trabecular bone volume (RBV/TV) and degree of anisotropy (DA) between species. Humans have significantly greater RBV/TV on the radio-palmar aspects of both the proximal and distal Mc1 subarticular surfaces and greater DA throughout the Mc1 head than other hominids. Non-human great apes have greatest RBV/TV on the ulnar aspect of the Mc1 head and the palmar aspect of the Mc1 base. Gorillas possessed significantly lower DA in the Mc1 head than any other taxon in our sample. These results are consistent with abduction of the thumb during forceful pad-to-pad precision grips in humans and, in non-human great apes, a habitually adducted thumb that is typically used in precision and power grips. This comparative context will help infer habitual manipulative and locomotor grips in fossil hominins.

Submitted Article: Dunmore C.J., Bardo A., Skinner M.M. & Kivell T.L. (*in review*) Trabecular variation in the first metacarpal and manipulation in hominids. *American Journal of Physical Anthropology*

Introduction

The unique dexterity of the human hand is often linked to two major events in hominin evolution, the development of obligate bipedalism and complex technology (Wood-Jones, 1916; Napier, 1993; Marzke, 2013; Lemelin and Schimtt, 2016; Richmond et al., 2016). The discovery in the late 1950s of stone tools in association with the OH 7 *Homo habilis* fossil hand, dated to approximately 1.75 million years ago (mya), was interpreted as potential anatomical and behavioural evidence of human-like dexterity (Napier, 1962b; Leakey, et al., 1964; de la Torre, 2011). Archaeological evidence of hominin tool behaviours has since been found in earlier contexts, dating back to at least 3.3 mya (Harmand et al., 2015), and is likely a preserved facet of a larger hominin manipulative repertoire that may have older origins (Panger, et al., 2002; Haslam et al., 2009; Alba et al., 2003; Kivell, 2015). When and how the manipulative capability required for stone tool behaviours evolved, however, is still a key question in human evolution (Panger et al., 2002; Richmond et al., 2016).

As hominids are our closest living relatives, their manipulative abilities of have been used to functionally interpret fossil hand bones (e.g. Susman, 1994; 1998; Marzke, 1997). Napier's (1956; 1993) broad schema of power grips, usually practised by apes in locomotion, and precision grips, generally practised by humans during manipulation, provides an intuitive dichotomy of phylogenetic polarity that has been the basis for this functional inference. Ape-like aspects of fossil hominin hand morphology are often interpreted as useful for arboreal locomotion whereas human-like morphological features are interpreted as advantageous for manipulation (e.g., Susman, 1994; Tocheri et al., 2008; Marzke, 2013; Kivell et al., 2015). In particular, compared to other apes, humans possess a relatively long thumb with a robust first metacarpal (Mc1) and broad phalanges that have been interpreted as key to enabling forceful pad-to-pad precision grips. Forceful precision grips have been traditionally considered unique to humans (Marzke and Wullstein, 1996) and facilitate stone tool production (Marzke and Shackley, 1986; Marzke et al., 1998; Key and Dunmore, 2015) as well as use (Williams-Hatala et al., 2018; Key et al., 2018). Here, rather than external shape or size, we analyse another

aspect of the Mc1 morphology across hominids, the internal trabecular architecture.

Despite having comparatively short and gracile thumbs and long fingers compared with that of humans, captive non-human great apes are capable of several human-like precision grips (Christel, 1993; Christel and Fragaszy, 2000; Pouydebat et al., 2009; Bardo et al., 2017) and are more adept at tool-use than previously thought (Wright, 1972; Toth, et al., 1993; Pouydebat et al., 2005; Bardo et al., 2017). While the manipulative repertoires of captive non-human great apes can differ from their wild counter-parts (Tuttle, 1969; Marzke et al., 2015; Neufuss et al., 2016), all wild non-human great apes show high levels of dexterity during food processing (Byrne et al., 2001; Marzke et al., 2015; Neufuss, et al., 2018) and, in some species, tool-use (Boesch and Boesch, 1990; Matsuzawa, 1996; Nishida and Hiraiwa, 1982; Sugiyama, 1994; Fox and Bin'Muhammad, 2002). Further, the use of stone tools naturally occurs in some non-hominid primate communities including capuchins (*Cebus libidinosus,* Fragaszy et al., 2004; *Sapajus libidinosus*, Proffitt et al., 2016) and macaques (*Macaca fascicularis*, Malaivijitnond et al., 2007; Proffitt et al., 2018). Thus, behavioural inferences concerning fossil hominin manipulation have become more nuanced (Marzke et al., 2015; Kivell, 2015), as non-human great ape hand morphology has been shown to be more dexterous than previously thought (e.g. Susman, 1998).

Fossil hominin manipulative capabilities have also been inferred from a biomechanical perspective. For example, compared to non-human great apes, humans have a larger and less curved sellar trapezium-first metacarpal facet, a palmarly-expanded trapezium, and a reorientation of the radial carpal bones that is thought to help facilitate the transfer of large forces, that occur during forceful manipulation from the thumb, across the wrist and palm (Tocheri et al., 2005; Tocheri, 2007; Marzke et al., 2010). The presence of these morphological features in Neanderthals (Trinkaus, 1983; Niewoehner, 2005; Tocheri, 2007) or many of these features in *Homo naledi* (Kivell et al., 2015), has been interpreted as morphological evidence of committed tool behaviours in these fossil hominins. The hand bones of australopiths show a variety of external morphological features that

are shared with either humans or apes, from which inferences about their manipulative abilities have been made (e.g. Marzke, 1983; Clarke, 1999; Green and Gordon, 2008; Kivell et al., 2011; Rolian and Gordon, 2013; Alba et al., 2003). However, these functional interpretations can suggest the grips a particular fossil hominin may have been biomechanically capable of performing, but less so which grips were frequently used.

Internal trabecular structure can provide additional evidence of how a bone was loaded during life (Ruff and Runestad, 1992; Currey, 2002) and thus potentially provide novel insight into fossil hominin hand use. Biomechanical loading causes trabeculae to remodel (Cowin, 1986; Frost, 1987), as experimentally demonstrated in a variety of non-primate taxa (Biewener et al., 1996; Pontzer et al., 2006; Barak et al., 2011; Christen and Müller, 2017). Trabecular studies of primate hands have also found that the distribution of trabecular bone is consistent with hand positions thought to be used by different species during locomotion (Zeininger et al., 2011; Tsegai et al., 2013; Chirchir et al., 2017; Barak et al., 2017; Dunmore et al., 2019). Preserved trabeculae in fossil hominins have been used to infer habitual loading and reconstruct locomotor (e.g. DeSilva and Devlin, 2012; Barak et al., 2013b; Su et al., 2013; Zeininger et al., 2016; Ryan et al., 2018) and manipulative (e.g. Skinner et al., 2015; Stephens et al., 2018) behaviours during human evolution. These functional inferences are based on the comparative context of extant great apes and an association between variation in their trabecular architecture and assumptions about the joint postures they most commonly use (Orr, 2016).

Studies of trabeculae in the thumb have mainly focussed on humans. Right human Mc1s have a significantly greater trabecular bone volume fraction (BV/TV) than those from left hands (Stephens et al., 2016) consistent with cross-populational right-hand bias in our species (Faurie et al., 2005; Reina et al., 2017) though the trabecular difference was small in absolute terms (Skinner et al., 2015; Stephens et al., 2016; Reina et al., 2017). While BV/TV is significantly greater in the Mc1 head of both humans and chimpanzees relative to the base (Lazenby et al., 2011b; Stephens et al., 2016) the species differ in the Mc1 base. Specifically, the human Mc1 base has a greater concentration of trabecular bone in its palmar aspect relative to

human non-pollical metacarpals (Wong et al., 2018) and the Mc1 of *Pan* species (Skinner et al., 2015). Where Skinner et al. (2015) inferred function by qualitatively analysing 3D trabecular models, Stephens et al. (2018) quantitatively analysed an expanded sample of pre- and post-Neolithic humans and found that BV/TV was greatest in the radio-palmar segments of the Mc1 head and base, consistent with a flexed, abducted thumb in precision grips.

We build on this work by analysing Mc1 trabeculae across extant hominids including modern humans (*Homo* sapiens), bonobos (*Pan paniscus*), chimpanzees (*Pan troglodytes*), and for the first time, gorillas (*Gorilla gorilla gorilla*) and orangutans (*Pongo abelii, Pongo pygmaeus* and *Pongo* sp. indet.). A geometric morphometric, statistical mapping method (Dunmore et al., 2019) is applied to subarticular regions of trabecular models produced by the whole-epiphysis approach. Specifically, we measure and statistically analyse variation in relative trabecular bone volume (RBV/TV; see below) and degree of anisotropy (DA) in the proximal and distal Mc1 to assess whether it is consistent with habitual thumb loading postures in these species.

Locomotion, manipulation and thumb morphology

While trapeziometacarpal (TMc) and metacarpophalangeal (McP) joint movement and loading is a product of both bony and soft tissue morphology (van Leeuwen, et al., 2018), combining what is known of this morphology with observed habitual thumb use allows us to characterise habitual thumb loading postures in the species studied.

Homo sapiens

Humans are obligate bipeds and so rarely employ grips in locomotion but power grips are used to habitually climb in some populations (Kraft et al., 2014). The uniquely human power-squeeze grip is also used in manipulation (Marzke et al., 1992; Key et al., 2018). This grip flexes fingers around a cylindrical object, which diagonally lies across the palm, while the thumb is adducted with considerable force and controls the direction in which force is applied to the object (Cooney and Chao, 1977; Marzke et al., 1992).

Human precision grips can also be uniquely forceful as demonstrated by the relatively high levels of pressure on the distal thumb of both hands during stone tool production and use (Key and Dunmore, 2015; Williams-Hatala et al., 2018). During stone tool production, a 'three-jaw-chuck' grip is commonly used to wield hammerstones, in which the thumb is abducted and rotated to oppose the second and third digits (Marzke, 1997). When using small flake stone tools, humans tend to use 'pad-to-side' grips whereas for larger flakes or handaxes they often employ a 'cradle' or 'five-jaw buttressed pad-to-pad' power grip, which both oppose the thumb to the other fingers with support from the palm (Rolian et al., 2011; Key et al., 2018). Biomechanical analysis has also shown large pollical flexion forces are required to stabilise a simulated tool during use (Rolian et al., 2011). While the role of the flexor pollicis longus muscle is debated (Hammrick et al., 1998; Marzke et al., 1998), electromyography data has highlighted that flexor pollicis brevis and opponens pollicis are strongly recruited to oppose the thumb to the rest of the fingers in these strong precision grips (Marzke et al., 1998).

Humans possess the longest thumb relative to the fingers among hominids (Almécija et al., 2015), which facilitates opposition of thumb to the fingers (Napier, 1956; Marzke, 1997; Feix et al., 2015; Bardo et al., 2018). Human distal phalanges are capable of passive hyperextension as our deep flexor tendons are long compared to those of other great apes (Preuschoft, 1965; Tuttle, 1967). This movement permits full pad-to-pad precision grips (Napier, 1960) frequently used by humans to forcefully manipulate small objects, especially within the hand (Christel, 1993; Marzke and Wullstein, 1996; Bardo et al., 2017; Key et al., 2018). Humans are unique among hominids in possessing a distinct extensor pollicis brevis muscle, which is well-developed and stabilises the extended McP joint while the first interphalangeal joint is forcefully flexed (Marzke et al., 1999; Diogo, Richmond and Wood, 2012). This force is achieved through high potential torques of human musculature compared to non-human great apes (Marzke et al., 1999). Further, during finger opposition, large human thenar muscles allow a forceful compound movement of axial rotation, flexion and abduction of the human thumb (Napier, 1961; Halilaj et al., 2014; Feix et al., 2016; D'Agostino et al., 2017). The larger and

flatter sellar-facet (Tocheri et al., 2005; Marzke et al., 2010), as well as a less curved proximal Mc1 and a shorter palmar beak (Niewoehner, 2005; Marchi et al., 2017), are associated with greater TMc mobility in humans compared to other great apes (Cooney et al., 1981; Rose, 1992). Although the high radio-ulnar congruence at the TMc joint may limit abduction, it facilitates resistance to large axial forces generated in human manipulation (Marzke et al., 2010; 2013).

Pongo

Orangutans are primarily arboreal and engage in quadrumanous torso-orthograde locomotion (Thorpe and Crompton, 2006; Manduell et al., 2011). Hand use during arboreal locomotion is not well studied (Thorpe and Crompton, 2005), but orangutans are thought to habitually use hook-grips or 'double-locked' grips that only recruit their fingers (Sarimento, 1988; Rose, 1988). However, orangutans may oppose the thumb to the fingers when climbing small-diameter substrates (Sarmiento, 1988), and preliminary behavioural evidence shows more frequent recruitment of the thumb than traditionally thought (McClure et al., 2012).

In captivity, orangutans do recruit the thumb in pad-to-side precision grips during manipulative tasks (Christel, 1993; Bardo et al., 2017). However, they far more frequently use a power-grip, especially for larger objects (Pouydebat et al., 2009), or a 'V-pocket' grip (Marzke, et al., 2015), in which the object is held in the webbing between the full thumb and index finger (Bardo et al., 2017). In both grips, the thumb may provide support but is not strongly recruited and orangutans frequently reposition tools with their mouths rather than with their hand (Christel, 1993; Bardo et al., 2017). In the wild, orangutans have not yet been observed using precision grips, even during tool production and use of tools (e.g. van Schaik et al., 1996; Fox et al., 1999).

The lack of thumb recruitment in orangutan grips is likely because the orangutan thumb is the shortest, relative to the fingers, of any great ape (Tuttle, 1969b; Almécija et al., 2015; Bardo et al., 2018). As such, the theoretical 'work space' for manipulating small objects between the tip of the thumb and the tip of the index finger, a 'tip-to-tip' grip, has been shown to be the smallest of all great apes (Feix,

et al., 2015). The manipulative capability of orangutans is also constrained by a lack of a distinct flexor pollicis longus that inserts on the distal phalanx, as well as the well-developed thenar musculature, found in humans (Strauss, 1942; Tuttle, 1969b; Zihlman et al., 2011). Orangutans, however, have the largest range of hyperextension (25°) and radio-ulnar movement at the first McP (36°) of all non-human great apes, especially ulnarly (Tuttle, 1969b). This range of movement may relate to the fact that unlike other non-human great apes, the palmar aspect of the orangutan Mc1 head is rotated ulnarly relative to its base, which is argued to be a consequence of the short thumb opposing the rigid palm rather than mobile fingers in this species (Drapeau, 2015). This McP joint mobility may partially offset a TMc joint that has been described as generally more congruent in orangutans than in other great apes which presumably limits its range of motion somewhat (Rafferty, 1990). However, the range of movement at this joint has also been described as highly variable (Rafferty, 1990) and a quantitative study found few significant differences in surface congruity at this joint between orangutans and other great apes (Marzke et al., 2010).

Pan troglodytes

Chimpanzees predominantly knuckle-walk, a mode of locomotion that does not recruit the thumb (Doran, 1996; Wunderlich and Jungers, 2009). However, chimpanzees are also arboreal and those of the Taï Forest, Ivory Coast, frequently vertically climb or scramble in trees (Doran, 1993), and this species has been described as more arboreal than gorillas (Remis, 1995; Doran, 1996; Thorpe and Crompton, 2006). Depending on branch diameter, chimpanzees use their thumbs in adducted, abducted, and opposed positions during power or hook grips (Hunt, 1991; Marzke and Wullstein, 1996; Neufuss et al., 2017). Unlike gorillas, chimpanzees only oppose the thumb in-line with, rather than wrapping it around, arboreal substrates during diagonal power grasping (Marzke et al., 1992; Alexander, 1994; Neufuss et al., 2017).

The chimpanzee thumb is frequently involved in tip-to-tip and pad-to-side precision grips during manipulative activities in captivity (Christel, 1993; Marzke and Wullstein, 1996; Jones-Engels and Bard, 1996; Pouydebat et al., 2011). In the wild,

rare pad-to-pad precision grips have been observed in chimpanzees during feeding but pad-to-side grips are the most frequent, employing an adducted thumb (Marzke et al, 2015).

These observed grips may be a result of the chimpanzee thumb to finger ratio that is intermediate between that of gorillas and orangutans (Drapeau and Ward, 2007; Almécija et al., 2015). Chimpanzees generally have smaller thenar muscles than those of humans (Ogihara et al., 2005) that can generate lower potential torques, due to shorter moment arms (Marzke et al., 1999). Conversely, the transverse head of the adductor pollicis muscle is equivalent to, or larger than, that of humans in chimpanzees and can create larger potential torques (Tuttle, 1969b; Marzke et al., 1999; Jacofsky, 2009). As the flexor pollicis brevis and opponens pollicis muscles tend to secondarily adduct the TMc joint in chimpanzees, while they abduct the joint in humans, Marzke et al. (1999) have linked this myological morphology to adduction of the thumb in pad-to-side grips in this species. The chimpanzee TMc joint itself is relatively incongruent, especially dorso-palmarly, which may allow for mobility at this joint at the cost of stability (Rafferty, 1990; Marzke et al., 2010).

Pan paniscus

Like chimpanzees, bonobos also primarily knuckle-walk, both arboreally and terrestrially, which does not recruit the thumb. However, they are argued to be more arboreal than chimpanzees (Alison and Badrian, 1977; Susman and Badrian, 1980; Crompton, Sellers and Thorpe, 2010) and engage in arboreal palmigrady more frequently (Doran, 1993). While the bonobo thumb is frequently observed in use during vertical climbing and suspension, it may not be meaningfully loaded (Samuel et al., 2018). Similarly, while the thumb may be recruited in palmigrady, data on this are lacking, and so it is possible the thumb is most frequently loaded during manipulative behaviour in this species.

Captive bonobos use precision grips and, uniquely among non-human great apes, they frequently independently flex their first distal phalanx while picking up small objects (Christel, 1993; Christel et al., 1998). The most frequent grips used by bonobos during manipulative tasks that employ the thumb are the V-pocket and

pad-to-side grips, in which the thumb is adducted (Bardo et al., 2016). In naturalistic environments, bonobos use, albeit rarely, tools in social and feeding behaviours, as well as to shelter from rain (Ingmanson, 1996; Hohmann and Fruth, 2003; Furuichi et al., 2015). Sanctuary-living bonobos have also been reported to employ a variety of different grips during nut-cracking, including many that involve an adducted thumb that may be flexed or extended (Neufuss et al., 2016).

Bonobos have a similar relative thumb length (Almécija et al., 2015) and a comparable kinematic workspace to chimpanzees (Feix et al., 2015). This species has well-developed thenar musculature that can exert high pressures at the TMc joint and includes a tendon of the flexor digitorum profundus that flexes the distal phalanx (van Leeuwen et al., 2018; 2018b), a trait that is weakly expressed or absent in chimpanzees (Tuttle, 1969b; Susman, 1998). However, the bonobo thumb is not capable of the same level of force as is the human thumb (van Leeuwen et al., 2018). Further, this species demonstrates a fusion of thumb and index finger musculature that may limit complex precision grips that require independent movement of these digits (van Leeuwen et al., 2018). The shape of the bonobo TMc joint is similar to that of humans, but unlike humans strong volar ligaments at this joint in bonobos restrict the extension at the TMc to just 30° (van Leeuwen et al., 2018b). The rounded Mc1 base palmar beak is also thought to limit axial rotation and medio-lateral movements of the Mc1 on the trapezium and therefore the compound movement involved in pad-to-pad opposition grips (van Leeuwen et al., 2018b)

Gorilla

The most frequent locomotor mode in gorillas is terrestrial knuckle-walking, which does not recruit the thumb (Inouye, 1994; Remis, 1998; Matarazzo, 2013). Gorillas are also arboreal, and when captive lowland gorillas climb large diameter supports they recruit, but do not oppose, the thumb keeping it in line with the rest of the digits (Sarmiento, 1994). Unfortunately, relatively little is known about wild western lowland gorilla hand use compared to that of mountain gorillas (Byrne et al., 2001; Neufuss et al., 2017). Wild mountain gorillas also adduct their thumbs in grips of >50cm diameter substrates but they oppose the thumb in-line with, or around, 6-

10cm diameter substrates, and the thumb is particularly important in counter-stabilising descent grips on lianas (Neufuss et al., 2017). While arboreal behaviours may have been traditionally underestimated in gorillas (Crompton et al., 2010; Neufuss et al., 2017), this genus most frequently terrestrially knuckle-walks, which does not recruit the thumb, and therefore the thumb may be most often used during manipulation.

Captive gorillas can perform tip-to-tip precision grips (Christel, 1993; Pouydebat et al., 2008), although they also often use power grips and 'interdigital brace' grips during manipulative tasks (Bardo et al., 2017). The latter grip threads an object between the adducted thumb and index finger, as well as the palmar or dorsal aspects of the ulnar digits (Lesnik et al., 2015; Bardo et al., 2017). Wild mountain gorillas most frequently employ precision grips including interdigital brace, 'thumb wrap', and pad-to-side grips during food processing, which all adduct the thumb (Neufuss et al., 2018). However, Neufuss et al. (2018) have emphasized the great variety of grips and thumb positions used by mountain gorillas in food processing and while they did not observe precise in-hand manipulation (*sensu* Landsmeer, 1962) in this community, it has been reported in others (Byrne et al., 2001; Bardo et al., 2017). Gorillas have also been observed engaging in tool-use behaviours (Breuer et al., 2005; Kinani and Zimmerman, 2015).

The use of the gorilla thumb in a variety of grips may be linked to its long thumb, relative to the fingers, which is relatively longer than that of all non-human great apes (Susman, 1979; Almécija et al., 2015). These hand proportions provide for the largest theoretical kinematic workspace, between the thumb and index finger, compared with all other non-human great apes (Feix et al., 2015). The Mc1 head is of comparable breadth to that of humans, which may facilitate a similar degree of movement at the McP joint in gorillas (Hamrick and Inouye, 1995; Susman, 1998). The distal fibres of abductor pollicis longus muscle do not separate into a distinct muscle belly in gorillas (*contra* Sarmiento, 1994), which is the extensor pollicis brevis muscle in humans. However, the abductor pollicis longus muscle does insert on the gorilla proximal phalanx more frequently than in other non-human great apes (Diogo et al., 2012), which may facilitate increased thumb dexterity. Similarly,

gorillas have a less congruent TMc than orangutans (Rafferty, 1990) allowing for a greater range of motion at this joint, although this difference is small quantitatively (Marzke et al., 2010) and different approaches used to quantify TMc surface congruence are often difficult to compare (Halilaj et al., 2014b).

Predictions

We predict that **(P1)** the subarticular trabecular architecture in the Mc1 head humans will be distinct from non-human great apes, with gorillas possibly displaying a distinct pattern within the latter group. All non-human great apes appear to habitually use pad-to-side or V-pocket grips in which the thumb is adducted (Jacofsky, 2009; Marzke et al., 2015; Bardo et al., 2016; 2017; Neufuss et al., 2018). Therefore, we predict (**P1a**) that both subarticular relative trabecular volume (RBV/TV; see methods) and degree of anisotropy (DA) will be greatest ulnarly in the Mc1 head of these species. Gorillas may be an exception to this pattern because while they frequently adduct the thumb in some interdigital brace'grips (Bardo et al., 2017), they also have a wide Mc1 head (Hamrick and Inouye, 1995; Susman, 1998) and frequently recruit the thumb in abducted positions (Neufuss et al., 2018). As a result we expect that (**P1b**) gorillas may have lower DA across the Mc1 head than other non-human great apes. Conversely, due to frequent use of forceful precision grips in which the thumb is flexed and abducted (Napier, 1956; Feix et al., 2016; Marzke, 2013), we predict that (**P1c**) humans will have greater subarticular DA and RBV/TV in the radio-palmar aspect of the Mc1 head.

In the Mc1 base we predict **(P2)** that the trabecular structure of humans will again be distinct from non-human great apes. However, given the lower range of motion in the joint compared to the McP in non-human great apes (Napier, 1960), we do not predict differences within this group. Given the frequent, forceful use of the relatively mobile human TMc joint, we predict (**P2a**) that subarticular DA will be lower throughout the Mc1 base in humans than in non-human great apes. Similarly we predict (**P2b**) RBV/TV will be greater in the palmar aspect of the Mc1 base in non-human great apes as the TMc is primarily flexed in these species during arboreal power grasping (Neufuss et al., 2017) and precision grasping (Marzke,

1997; Marzke et al., 2015; Bardo et al., 2016; 2017; Neufuss et al., 2018). Conversely, in humans we predict (**P2c**), RBV/TV will be greater in the radio-palmar aspect of the Mc1 base due to habitual abduction and flexion during precision grasping (Napier, 1956; Feix et al., 2016; D'Agostino et al., 2017) as has been demonstrated previously (Stephens et al., 2018).

Materials

Subarticular trabecular bone was analysed in the Mc1 of *Homo sapiens* (n=10), *Pan paniscus* (*n*=10), *Pan troglodytes* (*n*=11), *Gorilla gorilla gorilla* (*n*=10), *Pongo* sp. indet. (*n*=1), *Pongo pygmaeus* (*n*=5) and *Pongo abelii* (*n*=3, Table 5.1). All specimens were considered adult based on complete epiphyseal fusion of the Mc1 as well as other postcranial elements, and free from external signs of pathology. All non-human specimens were wild-caught. Human specimens were drawn from four populations: Nubians of ~5th century AD Sayala, Egypt (Strouhal and Jungwirth, 1979; Paoli et al., 1993), Yámanas individuals from 19th century Tiera del Fuego (Marangoni et al., 2011), 20th century individuals from Syracuse and 20th century individuals from a cemetery in Inden, Germany (Großkopf, 2015). The samples were sex balanced for each species, although one *Pongo pygmaeus* and two *H. sapiens* specimens were of unknown sex. For the non-human apes, an effort was made to analyse even numbers of antimeres as there are some signs of lateral asymmetry in metacarpal trabecular (Stephens et al., 2016) and cortical bone (Sarringhaus et al., 2005), though these differences are slight in absolute terms (Sarringhaus et al., 2005; Skinner et al., 2015). Conversely, humans are cross-culturally right-handed (Faurie et al., 2005) and this is reflected in Mc1 trabecular bone (Stephens et al., 2016; Reina et al., 2017). Therefore, the human sample was drawn from right hands to avoid potential bias related to handedness.

Table 5.1. Study sample enumerated by sex and side.

		Side	
Species	**Sex**	**Left**	**Right**
Gorilla gorilla gorilla	Female	3	2
	Male	2	3
Homo sapiens	Female	-	4
	Male	-	4
	Unknown	-	2
Pan paniscus	Female	3	2
	Male	2	3
Pan troglodytes	Female	2	3
	Male	3	3
Pongo abelii	Female	1	1
	Male	-	1
Pongo pygmaeus	Female	1	2
	Male	-	1
	Unknown	1	-
***Pongo* sp. indet.**	Male	1	-

Methods

Micro-CT Scanning

Specimens were scanned with a BIR ACTIS 225/300, Diondo D3, or a Skyscan 1172 high resolution micro-CT scanner at the Department of Human Evolution, Max Planck Institute for Evolutionary Anthropology, Germany, or with the Nikon 225/XTH scanner at the Cambridge Biotomography Centre, University of Cambridge, UK. Scans were performed at 100-160 kV and 100-140 µA, using a brass or copper filter of 0.25-0.5 mm. The scans were reconstructed to create images with an isometric voxel size of 28-41 µm depending on the size of the specimen.

Image processing

Avizo 6.3 (Visualization Sciences Group) was used to isolate and rotate micro-CT scans of each Mc1 into a standardised anatomical position (Fig. 5.2a) and the Ray Casting Algorithm (Scherf and Tilgner, 2009) was used to segment bone tissue. Trabecular structure was analysed with the whole-epiphysis method, which has been described and tested in detail (Gross et al., 2014). Briefly, medtool 4.2 (Dr. Pahr Ingenieurs e.U.) was used to run the image through a series of image filters that separated the inner trabecular structure from the cortical shell (Fig. 5.2b).

Specifically, an algorithm casts mathematical rays from the edge of the cortical bone inward in seven directions, the three orthogonal axes as well as at the four diagonals of the unit cube. Where at least five of these seven rays met the first 'inner-air' voxel, that is part of the image that is not bone and inside the cortical shell, they were marked as part of the inner structure. A smooth kernel, with a diameter equal to the measured average trabecular thickness in that bone, was then used to close the gaps in this inner structure, the trabeculae, to delimit the volume of the inner trabecular structure (Pahr and Zysset, 2009). A three-dimensional (3D) grid was then superimposed on the inner structure and overlapping spherical volumes of interest (VOI) with a 5mm diameter were positioned at each vertex within the 2.5mm-spaced grid. Trabecular bone volume (BV/TV) and degree of anisotropy (DA) were then measured for each VOI (Fig. 5.2c), as several studies have demonstrated these properties correlate with bone biomechanics (Odgaard, 1997; Uchiyama et al., 1999; Pontzer et al., 2006; Barak et al., 2011; Lambers et al., 2013), and are not strongly affected by allometry (Doube et al., 2011; Barak et al., 2013; Ryan and Shaw, 2013). The mean intercept length (MIL) method was used to calculate the second order fabric tensor and DA as 1 – (lowest eigenvalue / greatest eigenvalue). Thus, DA values of 0 represent total isotropy and values of 1 represent total anisotropy. Each trabecular variable was then separately interpolated on 3D tetrahedral mesh created using CGAL (Computational Geometry Algorithms Library; www.cgal.org; Fig. 5.2d). The outer surface of this trabecular mesh was then isolated using Paraview (Ayachit, 2015), and smoothed to permit landmark sliding (see below) in Meshlab (Cignoni et al., 2008) via a screened Poisson surface reconstruction filter (Kazhdan and Hoppe, 2013; Fig. 5.2e). For left Mc1s, this smoothed mesh was oriented in the same way as right Mc1s by a reflection filter in Meshlab to allow for homologous comparisons.

Geometric morphometric mapping

Only the subarticular trabecular bone of the Mc1 head and base was analysed rather than the entire volumetric trabecular model created by the whole-epiphysis approach. This subarticular trabecular bone is the first point of transmission for

external loads from the cortical shell to the deeper trabecular structure and should contain a bone functional adaptation signal (Marzke et al., 2010; Zhou et al., 2014; Sylvester and Terhune, 2017). We apply 3D geometric morphometric (GM) techniques (Gunz and Mitteroecker, 2013) to the analysis of trabecular bone (Dunmore et al., 2019) in a similar manner to the method described by Sylvester and Terhune (2017).

Table 5.2. Mc1 head anatomical landmark definitions.

Number	Type	Description	Reference
1	II	Most proximal point under the ulnar palmar epicondyle (anterior eminence)	(Yeh and Wolf, 1977; Fernández , 2015; Rein, 2018)
2	III	The point of maximum curvature on the inter-epicondylar ridge between points 1 and 3	(Drapeau, 2005; Rein, 2018)
3	II	Most proximal point under the radial palmar epicondyle (anterior eminence)	(Yeh and Wolf, 1977; Fernández , 2015)
4	III	Point of maximum curvature on the radial ridge separating the articular surface from the radial lateral sulcus	(Yeh and Wolf, 1977; Fernández , 2015; Rein, 2018)
5	II	Most radially projecting point on the dorsal aspect of the distal articular surface	(Fernández , 2015; Rein, 2018)
6	III	The midpoint point on the dorsal limit of the distal articular surface, between points 5 and 7	(Fernández , 2015; Rein, 2018)
7	II	Most ulnarly projecting point on the dorsal aspect of the distal articular surface	(Fernández , 2015; Rein, 2018)
8	III	Point of maximum curvature on the ulnar ridge separating the articular surface from the ulnar lateral sulcus	(Yeh and Wolf, 1977; Fernández , 2015; Rein, 2018)
9	II	Most distally projecting point on the subarticular surface	(Fernández , 2015; Rein, 2018)

Types of landmarks (Bookstein, 1991) and their provenance. Each article describes the landmark, uses it as the terminus of a linear measure or directly uses it for geometric morphometric analysis.

Anatomical landmark definitions

Many landmark sets have been used to analyse the primate Mc1 proximal base (Niewoehner, 2005; Marchi et al., 2017), although few have been employed to analyse the Mc1 distal head (Drapeau, 2015). Recently, however, Rein (2018) has used landmarks to quantify shape in the distal articular surface of the third metacarpal and a patch of 3D landmarks have been used to quantify metatarsal shape (Fernández et al., 2015), which is the serial homologue of a metacarpal (Rolian et al., 2010). The location and type (Bookstein, 1991) of anatomical

landmarks used here for the head and base of Mc1 are given in Tables 5.2 and 5.3, respectively. Previously identified cortical landmarks were accurately transposed to the inner trabecular surface, as thin cortical bone at the metacarpal head and base in hominids (Tsegai et al., 2017) allows for high correspondence between these surfaces.

Table 5.3. Mc1 base anatomical landmark definitions.

Number	Type	Description	Reference
1	Type II	Most palmar aspect of the proximal articular surface, the 'tip' of the palmar beak.	(Marchi et al., 2017)
2	Type II	The most dorsal aspect of the articular surface on the metacarpal base.	(Marchi et al., 2017)
3	Type II	The most ulnar aspect of the articular surface on the metacarpal base.	(Marchi et al., 2017)
4	Type II	The most radial aspect of the articular surface on the metacarpal base.	(Marchi et al., 2017)
5	Type III	The deepest point of the articular surface, that lies on the intersection of the orthogonal chords formed between points 1 & 2 and 3 & 4, respectively.	-

Types of landmark (Bookstein, 1991) and their provenance. Each article describes the landmark, uses it as the terminus of a linear measure or directly uses it for geometric morphometric analysis.

Repeatability

Three random Mc1 specimens from each species were landmarked on their head and base, five times respectively, over several days (by one observer supervised by a second observer), with Checkpoint (Stratovan Corporation, Davis, CA), following Fernández et al. (2015). The Morpho package in R (Schlager, 2017; R Development Core team, 2016) was then used to generate Procrustes coordinates for the five repeats of three individuals per species and articular surface. These coordinates were then plotted on the first two principle components (PCs) of each of the 10 repeatability comparisons (Fig. 5.1). Pairwise permutational MANOVAs, with Bonferroni correction, conducted on combined PC1 and PC2 scores demonstrated that repeats of individual configurations were significantly different from the other two specimens in each case ($p< 0.05$), so landmarks were considered repeatable (Fig. 5.1).

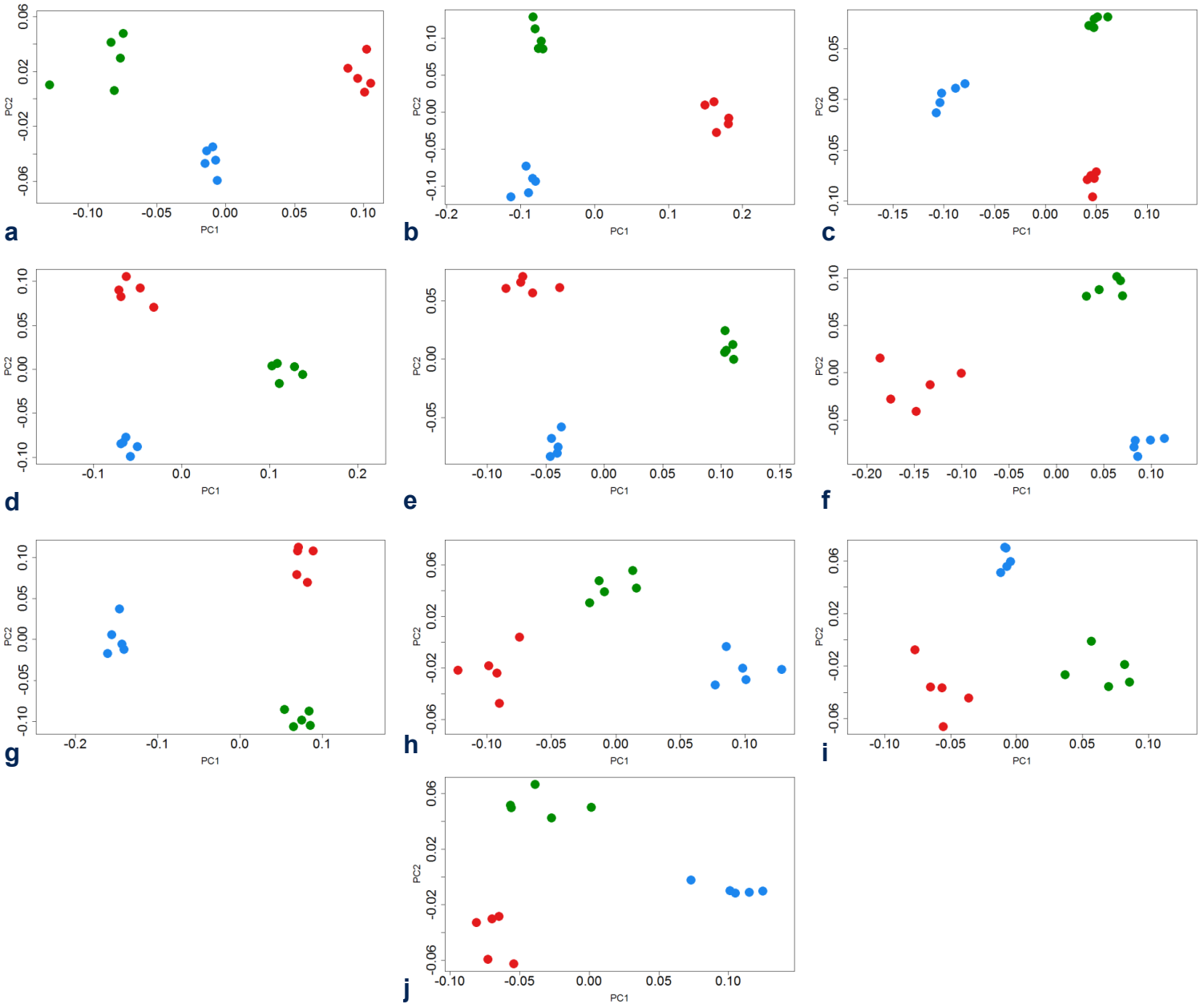

Figure 5.1. Repeatability tests of landmarks. Each individual first metacarpal head and base was landmarked 5 times on different days. Three individuals (each marked in a different colour) of the same species were then subjected to Procrustes transformation in each case. Subsequent permutational omnibus and pairwise MANOVAs were run on the combined PC1 and PC2 scores, as these cumulatively explained >85% of the variation: a) *Pan troglodytes* heads, b) *Pongo* heads, c) *Pan paniscus* heads, d) *Gorilla* heads, e) *Homo sapiens* heads, f) *Pan troglodytes* bases, g) *Pongo* bases, h) *Pan paniscus* bases, i) *Gorilla* bases and j) *Homo sapiens* bases. All individual specimen repeats were significantly different from each other subsequent to a Bonferroni correction ($p \leq 0.028$).

Geometric morphometric procedure

Both landmark templates (Fig. 5.2f) were created by defining sliding semi-landmarks on curves at the subarticular surface margins of a random specimen in Checkpoint. These curves were each bordered by anatomical landmarks following Gunz et al. (2005). For the Mc1 head template, single sliding semi-landmarks were defined on each of the eight curves. For the Mc1 base template, three sliding semi-landmarks were defined for each of the four curves between anatomical landmarks. Where subarticular margins were smoothed, a translucent model of the cortical surface was overlaid in Paraview to ensure correct placement of the template landmarks. Additional sliding semi-landmarks were then distributed over each subarticular surface in Avizo 6.3 (Visualization Sciences Group, Germany) to produce a 49 landmark template for the Mc1 head, comprising nine anatomical landmarks, eight sliding semi-landmarks on curves and 32 surface sliding semi-landmarks. The 40 landmark template for the base contained five anatomical landmarks, 12 sliding semi-landmarks on curves and 23 surface sliding semi-landmarks (Fig. 5.2f). Subsequently, anatomical landmarks were placed on every specimen and then each landmark template was projected onto each of the other 49 Mc1 heads and 48 bases, respectively, using the Morpho package in R (Schlager, 2017). A single *Pongo pygmaeus* specimen did not have a fully-preserved base and was excluded from the base analyses. Each template was relaxed onto the surface of each Mc1 by minimising bending energy and then semi-landmarks were slid along their respective curves or surfaces by minimising Procrustes distances, using the Morpho package in R (Schlager, 2017) .

Data mapping

A custom Python script was run using Paraview to allow the non-smoothed surface mesh triangles to inherit trabecular values (BV/TV and DA) from their originating tetrahedra. The Python module SciPy (Jones et al., 2001) was then used in medtool 4.2 (Dr. Pahr Ingenieurs e.U.) to interpolate the trabecular values to the closest landmark (Fig. 5.2g). This procedure is analogous to measuring trabecular structure with 1 mm diameter spherical VOIs, centred 0.5 mm deep to the normal of the inner trabecular surface, at the location of a landmark. A Procrustes procedure was

then performed using the geomorph package (Adams et al., 2017) in R to produce two sets of homologous landmarks each with the trabecular parameters mapped to them (Fig. 5.2g).

Relative trabecular volume (RBV/TV)

A relative measure of bone volume fraction (RBV/TV) was calculated for interspecific comparisons, in which the raw BV/TV values were divided by the mean of all landmark BV/TV values on that subarticular surface. If a landmark value is close to the average of that Mc1 surface it will have a value of ~1, whereas a landmark with a lower than the average BV/TV will have an RBV/TV <1, and with a higher value it will have RBV/TV >1. This normalisation of BV/TV values was performed for several reasons. BV/TV can vary systemically across species (Tsegai et al., 2018) and thus may diminish the potential functional signal under investigation here. Further, while BV/TV yields functional information relating to the response of trabecular bone to both magnitude and direction of load, it conflates these signals. The present study is focussed on the latter response, as it is more directly related to thumb joint postures in extant hominids. Finally, intraspecific variation in BV/TV has been shown to be considerable in a large sample of humans, yet the relative differences in BV/TV at several VOIs appear to show a consistent functional signal across populations (Saers et al., 2016). Therefore, we here opt to use a relative measure to somewhat control for non-functional trabecular signals and analyse which areas of the subarticular trabecular bone have most functionally adapted to habitual loads.

Statistical analysis

Species differences in trabecular parameters were independently tested for each landmark using 'mass-univariate' statistics, following Friston et al. (1995). Shapiro-Wilk tests identified significantly non-normal data (p<0.05) for both trabecular parameters at some landmarks. Therefore non-parametric Kruskal-Wallis tests were run at each homologous landmark for consistency. Post-hoc Dunn's tests identified significant pairwise species differences at p<0.05 after a Bonferroni correction. Trabecular values were compared at homologous landmarks between species

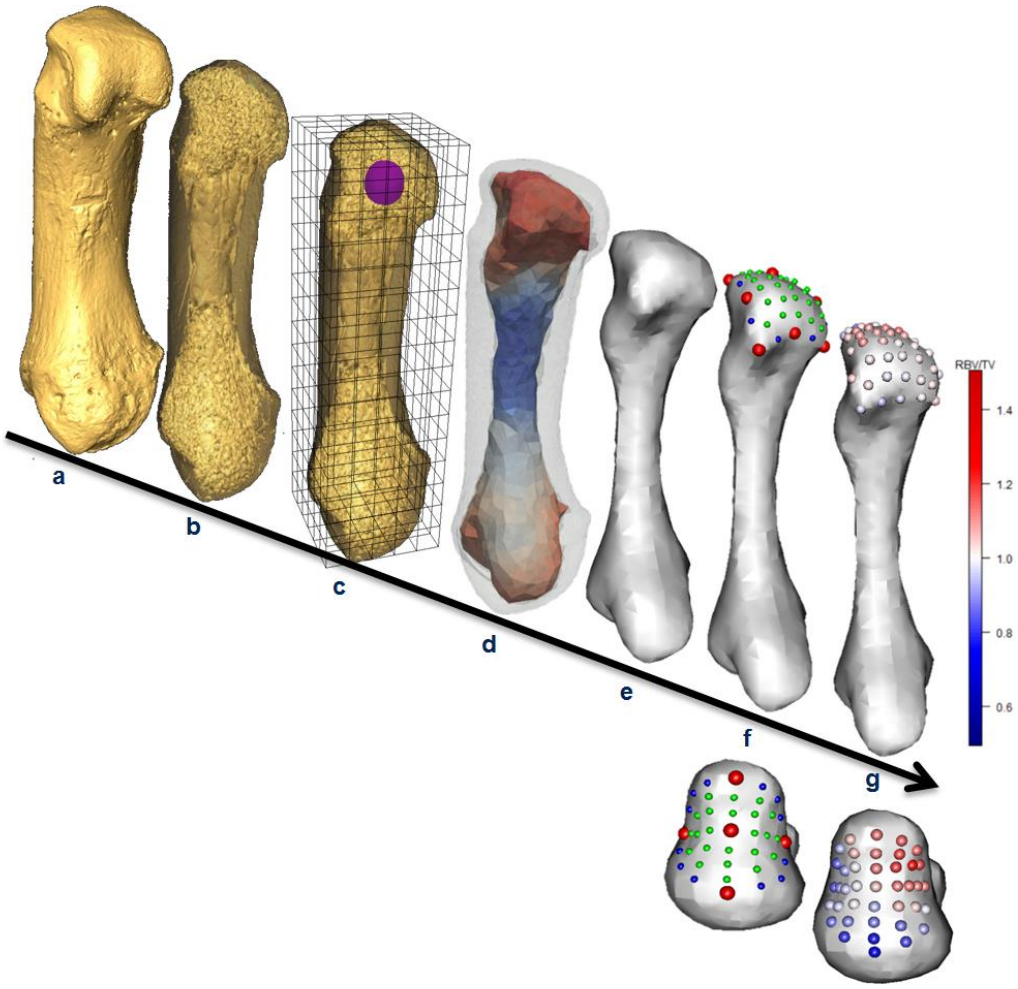

Figure 5.2. Stages of Mc1 trabecular analysis. a) Isosurface model of a *Pan troglodytes* right first metacarpal, b) Segmented trabecular structure inside cortical shell, c) Diagram of the background grid and one of the spherical VOIs at a vertex (purple), d) Volume mesh coloured by BV/TV, shown as a range of 0% (blue) to 45% (red), e) Smoothed trabecular surface mesh, f) Surface landmarks on the subarticular head (top) and base (bottom; anatomical = red, semi-sliding on curves=blue and on surfaces =green), g) RBV/TV interpolated to each surface landmark on the Mc1 head (top) and base (bottom).

rather than with spatially auto-correlated neighbouring landmarks. Polarity and the effect size of pairwise comparisons were determined via *Z*-scores. Significant univariate species differences at each landmark could then be mapped to an average Mc1 model, to show regional differences for functional interpretation. Significant trabecular value differences were only considered functionally meaningful if they occurred at a minimum of four spatially contiguous landmarks (as this was 8-10% of each template) to further ameliorate any Type I error.

To investigate whether distribution of RBV/TV and DA were different between species over the whole subarticular surface of the head and base, a principle components analysis (PCA) was performed using each landmark as a variable.

Significant overall differences between species were tested for using omnibus and pairwise, one-way permutational MANOVAs on the first three principle component scores generated from each PCA. These tests were run using the Vegan package (Oksanen et al., 2018) in R (R Core Development team, 2016), with a Bonferroni correction.

Results

Average species values and univariate landmark comparisons

Average values at each landmark, per species are depicted in for RBV/TV (Fig. 5.3a) and DA (Fig. 5.3b), respectively. Significantly different values at each landmark, in each pairwise species comparison are depicted for RBV/TV (Fig. 5.4) and DA (Fig. 5.5) for both subarticular surfaces of the Mc1. As post-hoc Dunn's test pairwise comparisons were too numerous to be easily interpreted in table format, the effects size of each significant test, the *Z*-test statistics, are summarized as descriptive statistics in Table 5.4. These *Z*-scores were transformed into unsigned, absolute values to demonstrate the size of differences between species.

Homo sapiens

H. sapiens had the largest range of average RBV/TV values among the sample, with higher values at disto-palmar landmarks on the radial aspect of the Mc1 head (Fig. 5.3a). This region had significantly higher RBV/TV values compared with all other great apes (Fig. 5.4). In the Mc1 base, average RBV/TV values were highest radio-palmarly, although not at the most palmar landmarks (Fig. 5.3a). *H. sapiens* had significantly higher RBV/TV in the central and radial aspects of the Mc1 base compared to all other apes, though these differences were most pronounced with *Gorilla* and *P. troglodytes* (Fig. 5.4). *H. sapiens* displayed the highest average DA values throughout the head compared to all other species (Fig. 5.3b), which resulted in significantly higher values than *Gorilla* at almost every landmark (Fig. 5.5). Further, *H. sapiens* had significantly higher DA than *P. troglodytes* at disto-ulnar landmarks and *P. paniscus* at palmar landmarks. The average *H. sapiens* DA values were highest in the radio-palmar and ulnar aspects of the Mc1 base. Radio-palmar Mc1 base landmarks had significantly higher DA values than *P. paniscus.*

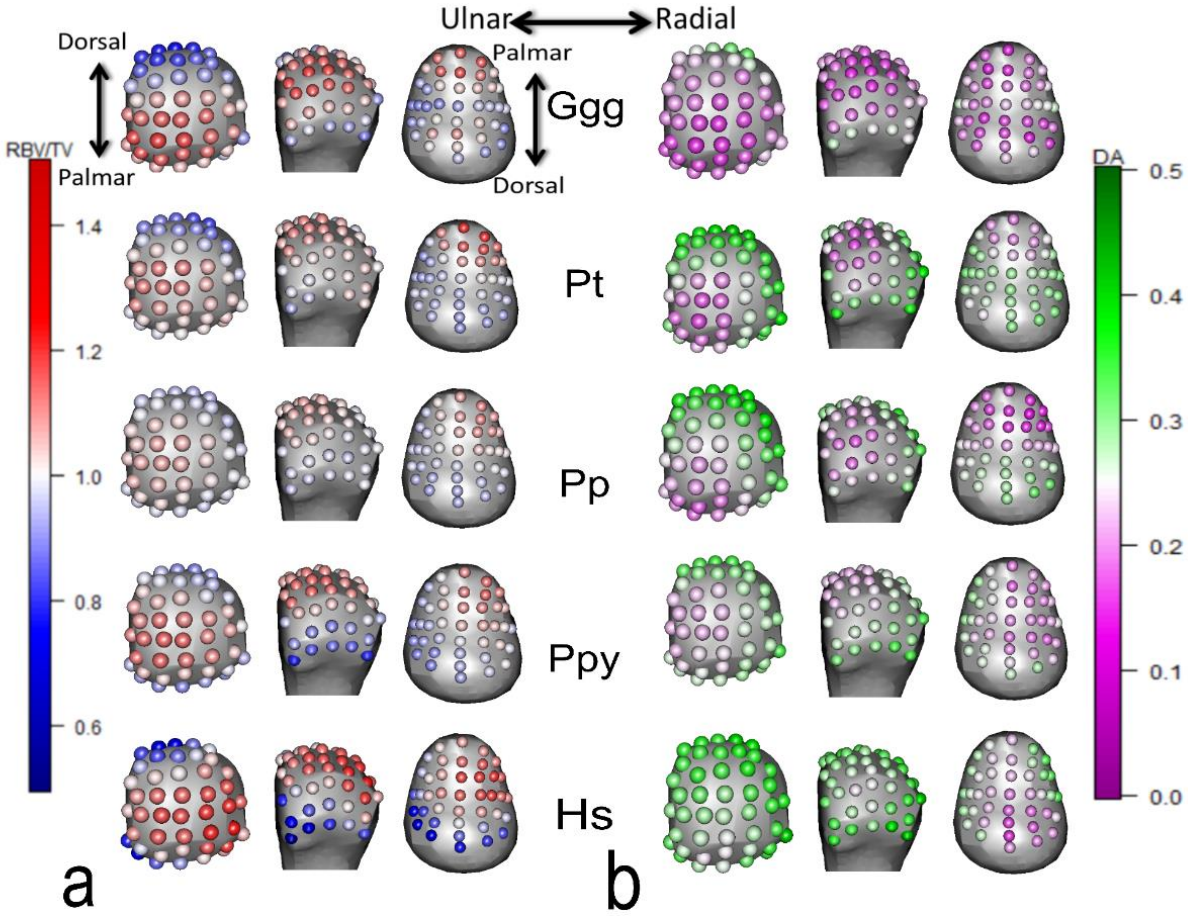

Figure 5.3. Species Average trabecular values, mapped to average models of a right Mc1 in distal and palmar views of the head as well as a proximal view of the base (left to right) for a) RBV/TV and b) DA. (Ggg = *Gorilla* (*n*=10), Pt = *Pan troglodytes* (*n*=11), Pp = *Pan paniscus* (*n*=10), Ppy = *Pongo* spp. (*n*=9), Hs = *Homo sapiens*).

Pongo

In the Mc1 head, the average RBV/TV in *Pongo* was highest in the ulno-distal region (Fig.5.3a). *Pongo* had significantly greater RBV/TV at landmarks situated ulno-dorsally than *Gorilla* and *H. sapiens* (Fig. 5.4). In the average Mc1 base, *Pongo* displayed a slightly higher RBV/TV in the central palmar region, though the range of values throughout the base was small (Fig. 5.3a). *Pongo* only had significantly higher RBV/TV relative to *H. sapiens,* at landmarks situated on the radio-dorsal extreme of the Mc1 base. DA in the *Pongo* average Mc1 head was lowest ulno-distally (Fig. 5.3b) and significantly higher than *Gorilla* in the palmar region (Fig. 5.5). In the base, *Pongo* had a slightly higher average DA ulnarly, but did not show a contiguous patch of landmarks significantly different from any other species, expect *P. troglodytes* where *Pongo* had significantly higher DA at dorso-central landmarks.

Pan troglodytes

P. troglodytes had the highest RBV/TV values at ulnar landmarks on the disto-palmar aspect of the Mc1 head (Fig. 5.3a). RBV/TV in this species was significantly higher at radio-palmar landmarks compared to *Pongo* and at ulnar landmarks relative to *H. sapiens* (Fig. 5.4). The Mc1 base in *P. troglodytes* had the highest range of average RBV/TV values among non-human great apes (Fig. 5.3a). Average RBV/TV was highest in the central palmar base but values were only significantly greater than *H. sapiens* at dorso-ulnar landmarks. The Mc1 head of *P. troglodytes* had lower DA at disto-palmar landmarks on its ulnar side (Fig. 5.3b). *P. troglodytes* DA was only significantly greater than *Gorilla*, across radial and dorsal landmarks (Fig. 5.5). The highest average DA values were in the dorsal Mc1 base of *P. troglodytes* and these DA values were significantly higher than *Gorilla*, *H. sapiens* and, to a lesser extent, *Pongo* at radio-dorsal landmarks.

Pan paniscus

P. paniscus possessed the lowest range of average RBV/TV values in the Mc1 head across the sample. The homogenous distribution of RBV/TV values in this species resulted in significantly higher RBV/TV than in *Gorilla* at dorso-ulnar landmarks and *H. sapiens* at both dorso-ulnar and palmo-ulnar landmarks (Fig. 5.4). In the Mc1 base, *P. paniscus* had slightly higher average RBV/TV at its central palmar landmarks, although like *Pongo* the range of values was low throughout the base. This species had significantly higher RBV/TV relative to *H. sapiens* at the most extreme dorsally-positioned landmarks in the Mc1 base. For DA, the *P. paniscus* Mc1 head had a similar average pattern to *P. troglodytes*, although lower DA values were found at more palmar landmarks (Fig. 5.3b). DA values of the Mc1 head were significantly higher than in *Gorilla* at dorsal and radial landmarks (Fig. 5.5). In the average Mc1 base, *P. paniscus* showed higher DA values at dorsal landmarks (Fig. 5.3b) that were significantly greater, especially radially, than in *H. sapiens* and *Gorilla* (Fig. 5.5).

Gorilla

Gorilla had the highest range of average RBV/TV values across Mc1 head landmarks in non-human great apes. The highest RBV/TV values were located ulnarly on the disto-palmar aspect of the Mc1 head (Fig. 5.3a). *Gorilla* was significantly higher in RBV/TV than *H. sapiens* ulno-palmarly, and significantly higher than all other great apes disto-palmarly (Fig. 5.4). The average *Gorilla* Mc1 base had higher RBV/TV values centred at its most palmar extent. RBV/TV was only significantly higher than that of *H. sapiens*, at dorso-ulnar landmarks (Fig. 5.4). *Gorilla* had the lowest average DA of all species throughout both the Mc1 head and base subarticular surfaces (Fig. 5.3b). This species showed significantly lower DA than any other species at most landmarks on the Mc1 head and at radio-dorsal landmarks in comparison with both *Pan* species (Fig. 5.5).

Table 5.4. Descriptive statistics of absolute *Z*-scores from Mc1 significant pairwise landmark comparisons.

	RBV/TV Base	***DA Base***	***RBV/TV Head***	***DA Head***
Min	2.582	2.598	2.588	2.577
Max	4.416	5.133	5.093	5.093
Std.Dev	0.557	0.551	0.625	0.549
Mean	3.359	3.229	3.413	3.293

The minimum differences between species at a given landmark are over 2.5 normalized standard deviation

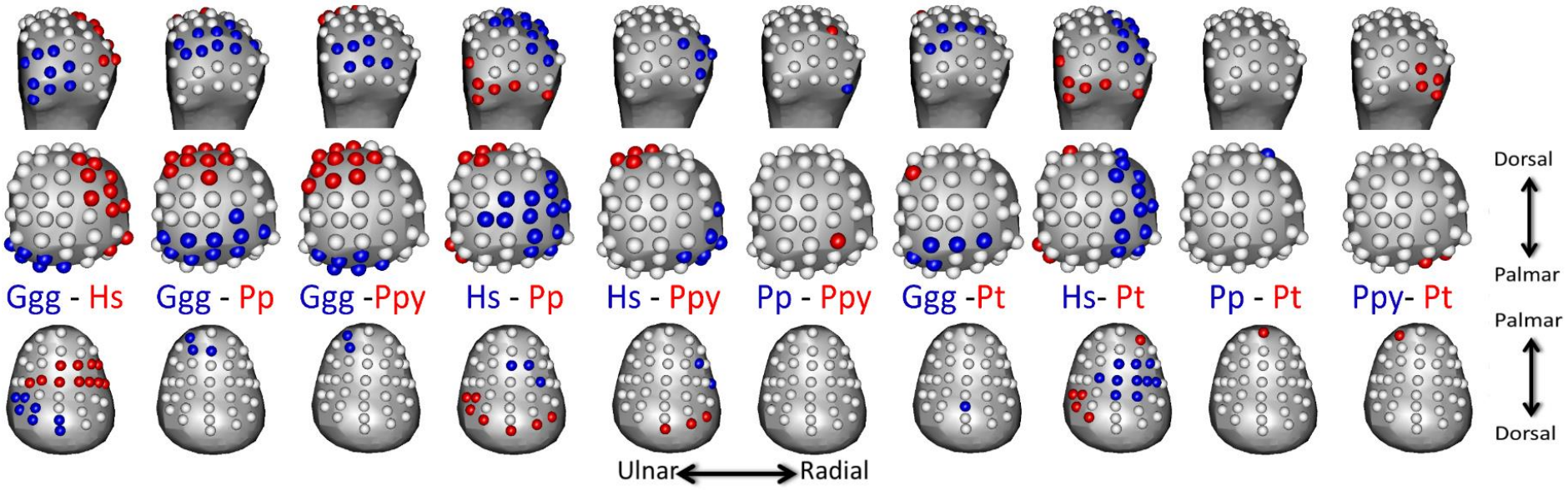

Figure 5.4. Significant univariate differences in RBV/TV between species, mapped to average right Mc1 models in palmar (top) and distal (middle) views of the head, as well as a proximal view of the base (bottom). In all views left is ulnar and right is radial. The significantly higher RBV/TV at each landmark is coloured as per species names of that column (Ggg = *Gorilla,* Pt = *Pan troglodytes,* Pp = *Pan paniscus,* Ppy = *Pongo* spp. Hs = *Homo sapiens*).

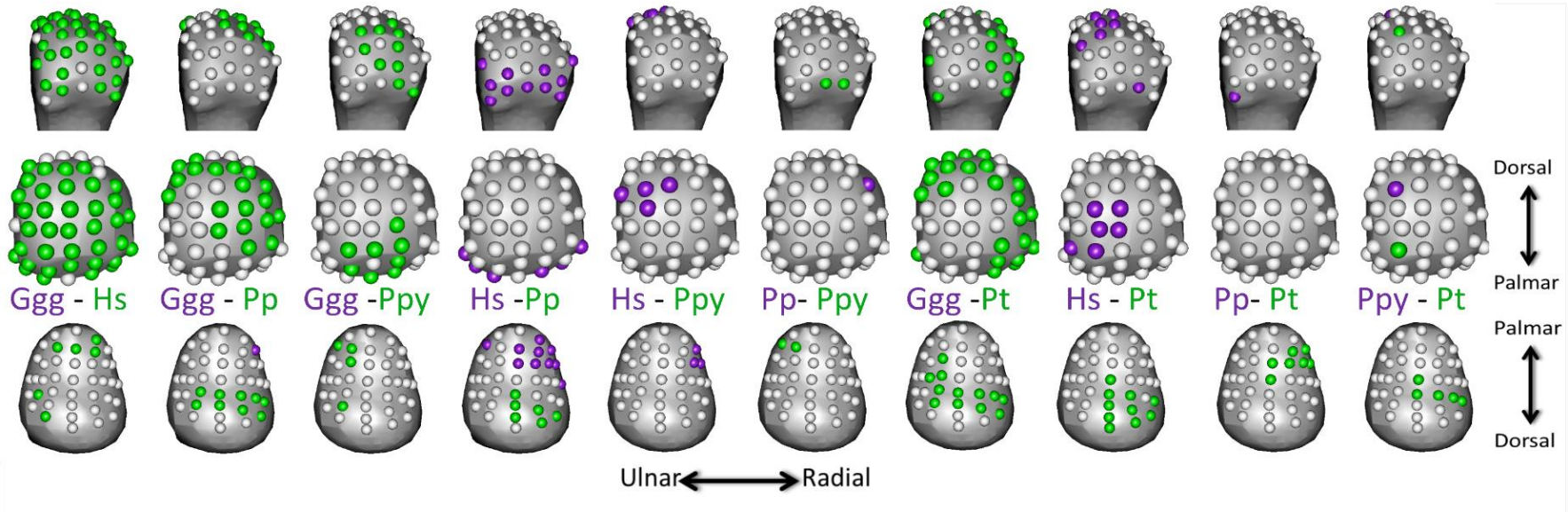

Figure 5.5. Significant univariate differences in DA between species, mapped to average right Mc1 models in palmar (top) and distal (middle) views of the head, as well as a proximal view of the base (bottom). In all views left is ulnar and right is radial. The significantly higher DA at each landmark is coloured as per species names of that column (Ggg = *Gorilla,* Pt =*Pan troglodytes,* Pp = *Pan paniscus,* Ppy = *Pongo* spp. Hs = *Homo sapiens*).

Multivariate whole-surface comparisons

PCA results for RBV/TV and DA values in the Mc1 head and base are depicted in Figures 5.6 and 5.7 respectively. Permutational MANOVAs were run using the first three PCs of each subarticular surface, as further PCs each explained less than 10% of the variance in each PCA. These omnibus tests were significant for both RBV/TV and DA for in the head and base (Table 5.5) indicating there were significant differences between species in overall subarticular trabecular structure.

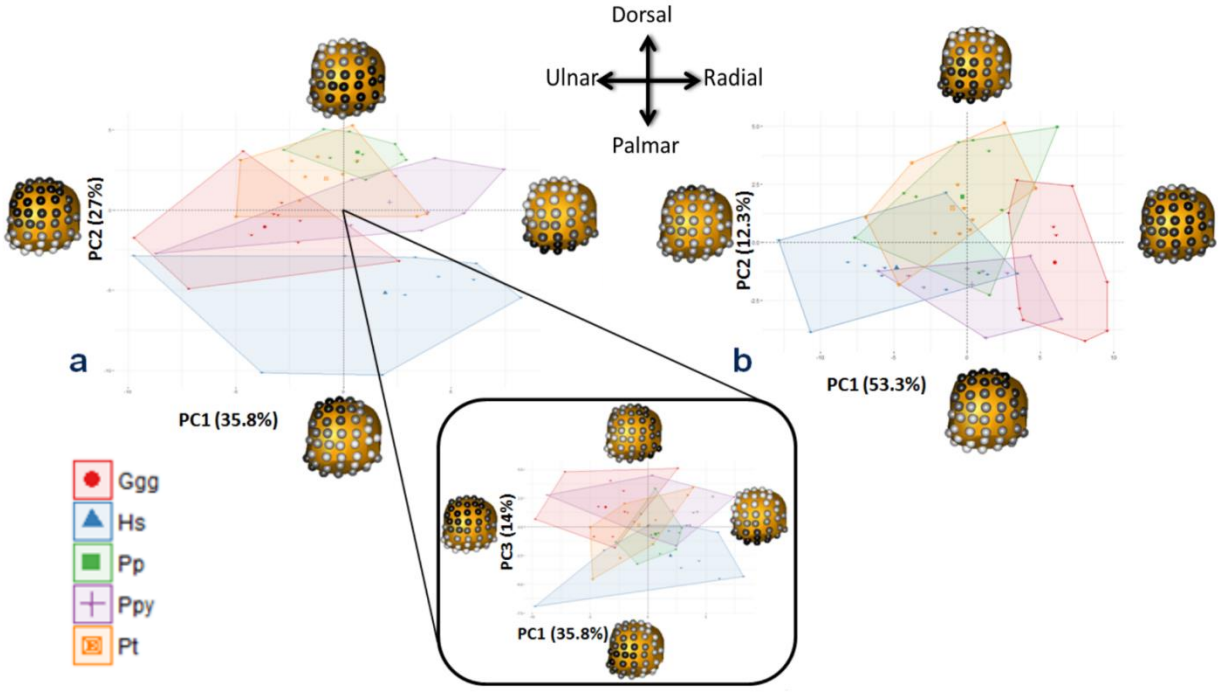

Figure 5.6. PCA plots showing species differences within the first metacarpal head trabecular structure in a) RBV/TV and b) DA values. Each plot shows the first two principle components (PC) in each ray. For RBV/TV PC3 is depicted with PC1, inset, as PC3 explains a non-trivial amount of the variance (14%) in this case. Landmarks at each extreme of a PC are coloured in grayscale, according to their signed contribution to that PC and plotted on a PC in distal view. White landmarks indicate the highest signed contribution to the PC extreme and black the least. Species abbreviations as in Fig. 5.3.

Mc1 heads

The first principal component (PC1) of the RBV/TV data explained 36% of the variation and reflected variation in RBV/TV values at dorsal and palmar Mc1 head landmarks. PC2 represented 27% of the variation in RBV/TV values at radio-palmar and disto-ulnar landmarks, whereas PC3 explained 14% of the variation and reflected radio-ulnar landmark variation (Fig. 5.6a). Pairwise permutational MANOVAS demonstrated that *H. sapiens* was significantly different in RBV/TV

distribution compared with all other hominids, distinguished primarily by radio-palmarly higher RBV/TV in the Mc1 head, on PC2 and PC3 (Fig. 5.6a, Table 5.5). *Gorilla* was also significantly different from *P. paniscus* and *P. troglodytes* with higher RBV/TV values ulno-palmarly.

For DA, PC1 described 53% of the variation and reflected lower or higher values at most landmarks across the Mc1 head (Fig. 5.6b). PC2 explained 12% of the variation and reflected variation in DA values at disto-palmar and dorsal landmarks. Pairwise tests revealed that *Gorilla* was significantly different from all other species in its overall lower DA (Table 5.5). Conversely, *H. sapiens* was not significantly different in its overall configuration relative to any other species, save for *Gorilla*, despite being distinguished by higher DA values at most landmarks on PC1 (Fig. 5.6b). Neither PC2 nor PC3 differentiated the studied taxa to a notable extent.

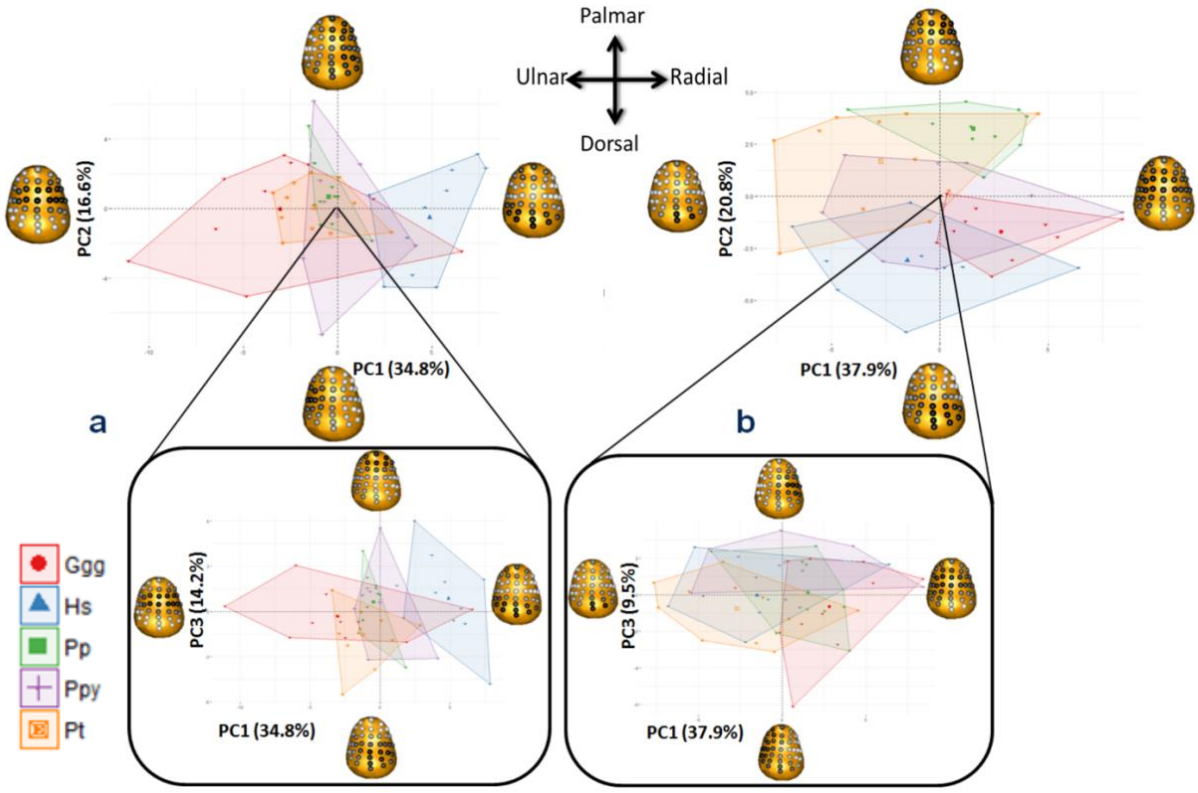

Figure 5.7. PCA plots showing species differences within the first metacarpal base trabecular structure in a) RBV/TV, b) DA values. Each plot shows the first two principle components (PC) in each ray and PC3 is depicted with PC1, inset, as PC3 explains a non-trivial amount of the variance (14% and 10%, respectively) in each case. Landmarks at each extreme of a PC are coloured in grayscale, according to their signed contribution to that PC and plotted on a PC in proximal view. White landmarks indicate the highest signed contribution to the PC extreme and black the least. Species abbreviations as in Fig. 5.3.

Table 5.5. Permutational MANOVAs on the first three principle components between all groups.

	RBV/TV Head	*RBV/TV Base*		*DA Head*	*DA Base*
All	8.446* (n=50)	5.110*(n=49)	***All***	8.141*(n=50)	6.905*(n=49)
Ggg - Hs	10.308* (n=20)	11.880* (n=20)	***Ggg - Hs***	23.588* (n=20)	6.083 (n=20)
Ggg - Pp	15.539* (n=20)	1.915 (n=20)	***Ggg - Pp***	12.001* (n=20)	10.097* (n=20)
Hs - Pp	16.563* (n=20)	9.904* (n=20)	***Hs - Pp***	5.069 (n=20)	16.584* (n=20)
Ggg - Ppy	6.677 (n=19)	1.1461 (n=18)	***Ggg - Ppy***	9.190* (n=19)	3.207 (n=18)
Hs - Ppy	6.187* (n=19)	4.473* (n=18)	***Hs - Ppy***	4.665 (n=19)	2.663 (n=18)
Pp - Ppy	4.211 (n=19)	0.276 (n=18)	***Pp - Ppy***	3.255 (n=19)	4.461 (n=18)
Ggg - Pt	5.302* (n=21)	1.220 (n=21)	***Ggg - Pt***	17.438* (n=21)	11.694* (n=21)
Hs - Pt	11.860*(n=21)	15.197* (n=21)	***Hs - Pt***	4.514 (n=21)	6.479* (n=21)
Pp - Pt	2.244 (n=21)	3.156 (n=21)	***Pp - Pt***	0.626 (n=21)	6.910* (n=21)
Ppy - Pt	2.686 (n=20)	1.681(n=19)	***Ppy - Pt***	3.288 (n=20)	3.745 (n=19)

Species abbreviations as in Figure 5.3. Subsequent pairwise tests were carried as all omnibus tests were significant. All Pseudo-*F* values that were significant, subsequent to a Bonferroni correction, are marked with asterisks(*).

Mc1 bases

In the Mc1 base RBV/TV values, 35% of the variation was explained by values at radio-palmar and a combination of extremely palmar and dorsal landmarks in PC1 (Fig. 5.7a). PC2 explained 17% of the variation in RBV/TV values and was driven by radio-ulnar landmark RBV/TV values, while PC3 explained 14% of the variation and was driven by dorso-palmar landmark values.

H. sapiens was significantly different to all other species and was distinguished by higher RBV/TV in the palmar and radial aspects of the Mc1 base on PC1 (Table 5.5). *Gorilla* was separated from the other taxa by higher RBV/TV at extremely palmar and dorsal landmarks at the opposite end of PC1, while all other taxa were intermediate between the two. However, there were no significant differences in RBV/TV of the Mc1 base across non-human great apes. While PC2 and PC3 were driven by contiguous patches of landmark values they did not distinguish any taxa.

In subarticular DA of the Mc1 base, PC1 explained 38% of the variation and mainly differences in central and dorsal landmark DA (Fig. 5.7b). PC2 explained 21% of the variation reflecting radio-palmar and dorsal landmark DA values. PC3 explained 10% of the variation and was driven by DA values at radio-ulnar landmarks. *P. troglodytes* and *P. paniscus* were both separated from *H. sapiens* and *Gorilla* on PC2, as both *Pan* species had highest DA at dorsal landmarks, while the latter two

species had highest DA at radio-palmar landmarks (Fig. 5.7b). These two groups were significantly different from each other whereas *Pongo* plotted between them on PC2 and was not significantly different from any other species (Table 5.5). *Pan* species were also significantly different from each other in overall DA configuration, though this appears to be due to a larger range of variation in *Pan troglodytes* DA values. PC1 and PC3 did not discriminate between taxa.

Discussion

We investigated variation in the subarticular trabecular bone structure of the Mc1 across extant hominids to test whether it is consistent with what is known about their habitual thumb postures. In the Mc1 head, our prediction that subarticular RBV/TV and DA would be greatest at ulnar landmarks in non-human hominids (**P1a**) was partially supported. The prediction that gorillas would have lower DA throughout the head was supported (**P1b**). Conversely in humans we predicted DA and RBV/TV would be highest at radio-palmar landmarks on the Mc1 head (**P1c**), which was only partially supported as DA was high throughout the human Mc1 head. We also predicted that humans would have lower DA throughout the Mc1 base than other hominids but this was not well supported by the data (**P2a**). Non-human hominids were predicted to have the highest RBV/TV values in the central palmar aspect of the Mc1 base (**P2b**) while humans would have highest RBV/TV values radio-palmarly (**P2c**). These last two predictions were fully supported by the results.

Mc1 heads

The data support our predictions concerning subarticular RBV/TV across hominid Mc1 heads (**P1a** and **c**) but only partially support those relating to DA (**P1 b** and **c**). Average RBV/TV was higher at ulno-distal landmarks in the Mc1 head across all non-human great apes, consistent with a habitually adducted thumb used in pad-to-side or V-pocket grips (Marzke et al., 2015; Bardo et al., 2016; 2017; Neufuss et al., 2016; 2018) and some power grasps used in African ape locomotion (**P1a**; Neufuss et al., 2017; Samuel et al., 2018). Contrary to our hypothesis, however, DA was lowest at the ulno-distal landmarks, where RBV/TV was highest, in

chimpanzees, bonobos and orangutans (**P1a**). This prediction was based on the concept that stereotypical loading of the first McP would cause the realignment of trabeculae, via remodeling, in the direction of this load, resulting in higher DA. Interpreting the results in this way would imply orangutans do not load their Mc1 head in a flexed McP posture, the disto-palmar Mc1 articular surface, which does not agree with overwhelming behavioural and anatomical evidence, nor the present RBV/TV results. This coincidence of highest RBV/TV and lowest DA values at ulno-distal landmarks instead reflects more trabecular bone with less alignment in this subarticular region that may be better able to withstand load from multiple directions. Indeed, while RBV/TV may be the result of thicker or more trabeculae, or some combination of both, it is notable that this average lower ulno-distal DA pattern was present in the three species with the smallest Mc1s (i.e., chimpanzees, bonobos and orangutans; Fig. 5.3b) and smaller bones tend to have thicker and fewer trabeculae (Barak et al., 2013). This DA pattern, therefore, is likely the result of the number of trabeculae and is consistent with high ulnar loading of the McP joint in the chimpanzee, bonobo and orangutan Mc1 head, despite displaying the opposite trend to that predicted. However, further work that accounts for variation in trabecular number is needed to substantiate this interpretation of the present DA results.

For both DA and RBV/TV, the predominantly Taï chimpanzee sample, a population known to use tools (Boesch and Boesch, 1993), displayed almost no significant differences from bonobos or orangutans. This may be surprising, as though bonobos have been observed using very few tools in the wild (Kano, 1982; Koops et al., 2015), and neither wild bonobos nor orangutans are known to engage in percussive tool use (van Schaik et al., 1996; Meulman and van Schaik, 2013). It may be that nut-cracking (Boesch and Boesch, 1993) and the use of precision forceful grips during food processing (Marzke et al., 2015) are simply not frequent or forceful enough to stimulate subarticular trabecular remodeling in the Mc1 head. A similar sample of Taï chimpanzee Mc1s have previously been shown to have less robust trabecular architecture than another group of chimpanzees that do not habitually nut-crack (Lazenby et al., 2011b). Therefore, either a strong osteogenic

signal does not exist for this behaviour, or it is constrained by more habitual or greater loading of the Mc1 during Taï chimpanzee locomotion (Lazenby et al., 2011b; Neufuss et al., 2017).

The Mc1 heads of gorillas also had the highest RBV/TV at ulno-distal landmarks consistent with pad-to-side, interdigital brace and thumb wrap grips frequently used in wild manipulation (Neufuss et al., 2018). This subarticular pattern, however, is statistically distinguished from bonobos, orangutans and, to a lesser extent, chimpanzees by the greater range of RBV/TV values across the gorilla Mc1 head, suggestive of more habitual or greater loading of the pollical McP joint in adduction in this species. DA values in the gorilla Mc1 were significantly lower than all other species studied and displayed a low range throughout the head (**P1b**). Combined, this trabecular pattern is consistent with the habitual use of varied thumb positions in gorillas but also more frequent or forceful loading in thumb adduction, relative to the other non-human great apes (Neufuss et al., 2018). However, it must be noted that this prediction was based on the greater volume of behavioural evidence from mountain gorillas (*Gorilla gorilla beringei*) rather than the western lowland (*Gorilla gorilla gorilla*) species studied here. Furthermore, there are limited detailed studies of grip and hand use in other non-human hominids in the wild (Marzke et al., 2015), and this interpretation must thus be treated with some caution.

Humans displayed both significantly higher RBV/TV at radial landmarks and higher DA throughout the subarticular Mc1 head than in other great apes (**P1c**). This RBV/TV distribution is consistent with a habitually and forcefully opposed thumb, a movement which entails flexion, and importantly, abduction at the McP joint (Napier, 1956). An opposed thumb is used in forceful precision grips during the production (Marzke, 1997; 1998) and use of stone tools (Rolian et al, 2011; Key et al., 2018) among other manipulative activities (Napier, 1993; Bardo et al., 2017). A radio-palmar concentration has also been found, in a similar sample of humans, using a method that analysed absolute BV/TV in the whole distal epiphysis of the Mc1 rather than just the subarticular region (Stephens et al., 2018).

In contrast to these RBV/TV results, high DA throughout the human Mc1 head, while not overall significantly different from any species except gorillas, does not match our prediction of the highest DA at radio-palmar landmarks (**P1c**). Stephens et al. (2018) found slightly lower average DA values in a similar human Mc1 sample, likely due to their sampling of the whole distal epiphysis, but also found little regional differentiation across the Mc1 head in agreement with the results here. The present result may reflect the higher frequency of forceful prehensile thumb use in humans than in other extant hominids. Though the highest or most habitual forces may be resisted by the radio-palmar McP joint during thumb abduction, the frequently-used, powerful and mobile human thumb likely engenders a stronger osteogenic signal throughout the head than in other apes and therefore more aligned trabeculae (i.e. higher DA). For example, humans are unique among extant hominids in their ability to forcefully extend and stabilise the first proximal phalanx on the Mc1 while flexing the distal phalanx via distinct flexor pollicis longus and extensor pollicis brevis muscles (Marzke et al., 1998; Hammrick et al., 1998; Diogo et al., 2012). The thumb held in this position probably induces considerable loads on the distal McP, even if these are not as large as those loads resisted in forceful abduction (Cooney and Chao, 1977; Toft and Berme, 1980).

Mc1 bases

The subarticular trabeculae of the Mc1 base did support our predictions for RBV/TV but not for DA. Contrary to our predictions, DA values throughout the human subarticular Mc1 base were not significantly lower than in other great apes (**P2a**). Rather, our results indicate a regional pattern, in which chimpanzees and bonobos had the highest DA values in the dorsal Mc1 palmar base and were both significantly different from gorillas and humans, which had higher palmar DA values on the radio-ulnar edges of the Mc1 base. The functional significance of this pattern is not immediately apparent though it may relate to more varied habitual thumb positions in humans and gorillas relative to the other species studied.

All non-human hominids displayed the highest RBV/TV at extremely palmar and central landmarks consistent with habitual flexion at the TMc joint (**P2b**), though the range of values throughout the base was lower than in humans. This more

homogenous distribution of subarticular RBV/TV is consistent with previous studies of absolute BV/TV throughout a similar sample of *Pan* species Mc1 proximal epiphyses (Skinner et al., 2015; Stephens et al., 2016). Humans displayed a significantly different pattern with the highest RBV/TV values at the radial and less extreme palmar region of Mc1 base landmarks, consistent with a habitually and forcefully abducted thumb, flexed in opposition (**P2c**; Napier, 1956; Halilaj et al., 2014; Feix et al., 2016; D'Agostino et al., 2017; Marchi et al., 2017). These results agree with other studies that have found a palmar concentration of Mc1 base BV/TV in comparison to other apes (Skinner et al., 2015) and other metacarpals (Wong et al., 2018). The subchondral radio-palmar RBV/TV concentration found here was also found using the whole-epiphysis method, on a similar sample (Stephens et al., 2016; 2018), and is the same region of the Mc1 base in which osteoarthritis first develops (Koff et al., 2003). The present results further refine this radio-palmar RBV/TV distribution to a less markedly palmar subarticular area than that found in other great apes. This pattern is consistent with habitual loading of the human TMc joint in a less flexed position than in other extant hominids, as occurs during McP flexion in cadaveric humans (Moulton et al., 2001). The distinct extensor pollicis brevis muscle of humans is thought to counteract thenar flexors to stabilise the thumb during manipulation (Marzke et al., 1998; Diogo et al., 2012). This morphology combined with a greater range of flexion, and especially extension, of the TMc joint in humans (Cooney et al., 1981; Rose, 1992, van Leeuwen et al., 2018b) and the possible limitation of TMc flexion imposed by a large thenar eminence (Tuttle et al., 1969b) is also suggestive of a TMc loaded in less markedly flexed position than in other extant hominids.

Functional interpretation

Taken together the current results are consistent with habitual loading of the TMc joint in flexion, and the McP joint in adduction, during frequently used precision and power grips in all non-human great apes studied. The results also suggest that gorillas use more varied thumb postures than chimpanzees, bonobos or orangutans, as they have lower DA at both joints. Chimpanzees, bonobos and orangutans all demonstrate a similar trabecular distribution at both articular

surfaces which, at first, may appear inconsistent with observed differences habitual thumb use in these species. Orangutans are thought to employ the thumb less frequently during power-grasping than in chimpanzees or bonobos (Sarimento, 1988; Rose, 1988; but see McClure et al., 2012) and also use their feet, as well as their mouth, more frequently in manipulation (Bardo et al., 2017). However, all three of these species use a habitually adducted thumb in pad-to-side grips during manipulation (Marzke et al., 2015; Bardo et al., 2016; 2017; Neufuss et al., 2018). Therefore the similar distribution of trabecular bone volume is consistent with a habitually adducted thumb, more often and perhaps more forcefully employed by chimpanzees and bonobos than by orangutans. While RBV/TV does not reflect the inferred magnitude of loading, visual inspection of species average absolute BV/TV values beneath both articular surfaces demonstrates they are higher in both *Pan* species relative to orangutans, consistent with this interpretation. Humans, unlike the other great apes, exhibit a trabecular morphology that suggests a habitually less flexed more abducted TMc joint and a more strongly, or frequently, recruited flexed abducted McP joint. This pattern is consistent with habitual forceful precision grips uniquely practised by humans.

While these results appear consistent with hominid behaviour and anatomy, the function of trabecular bone is not only biomechanical but also physiological, as it is important for mineral homeostasis (Clarke, 2008). Furthermore, trabecular structure may be affected by systemic factors (Tsegai et al., 2018) and is determined genetically to some extent (Lovejoy et al., 2003; Havill, 2010; Judex, et al., 2013; Almécija et al., 2015b). The Mc1 also has a different developmental, and thus possibly evolutionary, history from the other metacarpals (Pazzaglia et al., 2018) in that its head develops from a pseudo-epiphysis whereas the base arises from a true secondary ossification centre (Haines, 1974). This developmental difference may also potentially affect trabecular architecture (Lazenby et al., 2011b). The functional signal found here, however, appears to be relatively strong, given these potentially confounding variables.

The interpretation of this functional trabecular signal must also consider the shape of the cortical bone which surrounds it, as well as soft tissue morphology. It could

be argued that the radio-palmar concentration of RBV/TV in humans is due to ulnar deviation of the Mc1 head relative to the base (Drapeau, 2015) in this species, rather than an interspecific difference in manipulation. That is, the trabecular pattern is caused by the same vector of manipulative load in all species, but in humans the McP joint load angle differs due to the shape of the Mc1. However, an ulnar trabecular signal is found in the orangutan Mc1 head, that is also ulnarly deviated relative to the Mc1 base (Drapeau, 2015) and therefore this signal is likely due to species differences in manipulation. Similarly the size of subarticular Mc1 surfaces (Tocheri et al., 2005) may also affect the current results, since a constant number of landmarks will necessarily sample less subarticular trabeculae of a larger surface or redundantly over-sample a smaller subarticular surface. The use of interpolated trabecular values, however, should ameliorate this sampling effect and it appears to not have affected the relatively large regional patterns found here. Nevertheless, as discussed for the Mc1 head, it would be advantageous to scale DA by trabecular number in future studies to ensure more direct and intuitive comparison of species with differently sized bones.

Conclusion

In conclusion, interspecific variation found in the subarticular trabecular architecture of the hominid Mc1 head and base reveals a distinct pattern in humans, that is consistent with a habitually abducted thumb used during forceful precision grips, which are employed in many manipulative behaviours, including stone tool production. This manipulative signal is significantly different from other great apes and so may be used as a basis to infer the habitual manipulation in fossil hominin hands, where trabeculae are preserved. The similar trabecular volume distribution in the chimpanzee, bonobo and orangutan Mc1 also highlights their similar use of an adducted thumb, although this use may be in different grips employed in different frequencies. Further, the prehensile signal found in gorilla Mc1 trabeculae is consistent with more frequent and varied habitual manipulation than has yet been observed in other wild non-human great apes. This signal is distinct from that of humans, and is especially interesting as gorillas are the most terrestrial non-human great ape.

Chapter 6
Fossil hominin hand use: Evidence for arboreality and human-like manipulation in *Australopithecus*

Abstract

The human lineage is defined by a transition to bipedalism and an associated shift in the use of the hands from locomotion towards increasingly dextrous manipulation. The habitual forceful precision grips used by modern humans likely evolved in the context of stone tool manufacture and use, but when and how hominin hands became principally manipulative remains a matter of debate. Here, we analyse the internal structure of the metacarpi of fossil hominins including: *Homo sapiens, Homo neanderthalensis, Australopithecus afarensis, Australopithecus africanus, Australopithecus sediba* and material attributed to either early *Homo* or *Paranthropus.* Results indicate that fossil *H. sapiens* display an internal morphology similar to recent humans, while *H. neanderthalensis* is argued to display an intraspecifically varied pattern, more consistent with habitual power squeeze grips. *A. afarensis* and *A. africanus* display intermediate internal morphology between recent humans and non-human great apes. We demonstrate that the Malapa hominin (MH2) hand (*Australopithecus sediba*) has a distinct pattern of both trabecular and cortical bone structure across its metacarpus. The metacarpals of the palm have an internal morphology most similar to orangutans and consistent with arboreal power grasping with the fingers, while cortical and trabecular morphology of the thumb is consistent with human-like manipulation. These results support the evolution of human-like manipulation within a hand still partially used for arboreal locomotion in at least one *Australopithecus* species, contemporaneous with *Homo* and *Paranthropus.*

Introduction

The dexterity of the modern human hand is often contrasted with the less dexterous hands of other apes, primarily employed for locomotion (Susman, 1994; Tocheri et al., 2008; Kivell et al., 2011). The long thumb relative to the fingers (Almécija et al., 2015), strong thenar musculature (Marzke et al., 1999), reoriented radial carpals and broad phalangeal apical tufts in humans (Marzke, 1997; Tocheri et al., 2008) are thought to facilitate habitual forceful precision grips (Marzke et al., 2013), power 'squeeze' grips (Marzke et al., 1992) and precision in-hand manipulation in our species (Christel et al., 1993). The evolution of this enhanced dexterity is challenging to infer in Plio-Pleistocene hominins, since some of its associated morphological features often occur together with ape-like features associated with arboreal locomotion, such as curved fingers with well-developed flexor sheath ridges (Bush et al., 1982; Ricklan, 1987). This mosaic of ape-like and human-like manual traits is replicated in other postcranial elements of *Australopithecus afarensis* and *Australopithecus africanus* (Green et al., 2007; Kimbel and Delezene, 2009). There is consensus that human-like features of the lower limb indicate at least facultative bipedality in *Australopithecus* (Kimbel and Delezene, 2009). However, the significance of ape-like upper limb features has been debated for decades, with some interpreting them as non-functional retentions from an arboreal ancestor (Latimer, 1991) while others consider these features as clear evidence of sustained selection for arboreal locomotion (Stern and Susman, 1983). These differing interpretations imply that either our manipulative abilities began to evolve in hands freed of the demands of locomotion, or in an arboreal hominin(s) that was not yet an obligate biped.

The *A. sediba* partial skeleton, Malapa Hominin 2 (MH2), offers a unique Pleistocene perspective on the debate concerning locomotion in *Australopithecus,* as it is characterised by a mosaic of ape-like and human-like features. At 1.98 million years old (Berger et al., 2010; Pickering et al., 2011), MH2 lived just after the oldest known lithic technology found in South Africa (Granger et al., 2015; 2.18mya; mya = millions of years ago) and well after the earliest evidence of this technology known elsewhere (Harmand et al., 2015; 3.3mya). Several morphological features

of the lower limb and pelvis indicate straight-legged bipedalism in this species, perhaps with a uniquely hyperpronated foot (Zipfel et al., 2011; DeSilva et al., 2013; Kibii et al., 2011). In contrast, MH2 has a relatively long upper limb and superiorly-oriented glenoid fossa of the scapula, which it shares with other australopiths, that could be interpreted as either primitive retentions or functionally-significant arboreal adaptations, under stabilising selection (Churchill et al., 2013). Similarly, a human-like thumb-to-finger length ratio would be advantageous for a manipulative hand in *A. sediba* but this is concomitant with moderately curved phalanges with well-developed flexor ridges considered useful for arboreal locomotion (Kivell et al., 2011). Stable-carbon isotope, as well as dental calculus and micro-wear analyses, indicate this species was distinct from other South African hominins in having a predominantly C_3 diet, similar to savannah chimpanzees that predominantly consume arboreal foods, such as gallery-forest fruits (Henry et al., 2012). Therefore, as with other *Australopithecus* species, the ape-like morphological features in the MH2 hand may be interpreted as biomechanically non-functional in the context of contemporaneous lithic evidence for habitual forceful precision grips, or indicative of a significant arboreal component in this species' locomotor repertoire and diet. As behaviour can change faster than external morphology, current fossil evidence cannot discriminate between these interpretations. To resolve this debate, we analyse morphological information that directly reflects behaviour of fossil individuals during their lifetime.

Internal bone structure, cortical bone distribution and trabecular architecture, can provide additional insight into behaviour inferred from external shape. Trabecular structure has been experimentally shown to remodel in response to load, via bone functional adaptation (Ruff et al., 2006), across a range of phylogenetically distant taxa (Biewener et al., 1996; Pontzer et al., 2006; Barak et al., 2011). Several comparative studies have shown a correlation between trabecular structure and inferred habitual hand posture in apes (Tsegai et al., 2013; Skinner et al., 2015; Chirchir et al., 2017; Stephens et al., 2018). The cross-sectional geometry of cortical bone diaphyses has also been shown to remodel in various mammals and birds (Ruff et al., 2006; Wallace et al., 2017), and to reflect different locomotor modes in

primate hands (Marchi, 2005). Habitual locomotor modes are thought to produce strains on a long-bone diaphysis, stimulating the formation of new bone to resist these strains, producing a change in cross-sectional shape and robusticity (Ruff et al., 2006; Carlson and Judex, 2007). Combined, the evidence of functional adaptation in cortical and trabecular bone during the life of an individual can provide critical information for reconstructing behaviour in the past.

Here we analyse the relative cortical structure and quantify, for the first time, the subchondral trabecular bone volume fraction (BV/TV) across the metacarpal heads, as well as the mobile first metacarpal base, in extant non-human great apes, humans and fossil hominins. As there was strong variation in the magnitude of BV/TV across species, and the distribution of these values is more informative for habitually loaded hand postures, we standardised BV/TV values for each subchondral surface to calculate relative BV/TV (RBV/TV) values. Initially, we assess whether variation in these internal bone structures reflect the presumed habitual hand postures employed by great apes during locomotion and manipulation. Next, we use this comparative context to infer habitual hand postures and grips in fossil *Homo sapiens* and *Homo neanderthalensis* from their internal fossil architecture. Finally, we infer hand use in Plio-Pleistocene hominins, including a putative *Paranthropus* specimen and several species of *Australopithecus*. In particular, we test if ape-like traits in the external morphology of the *A. sediba* hand were functionally significant or primitive retentions that were not yet lost.

Predictions

In order to objectively assess which interpretations of external manual morphology the analysed internal architecture of the metacarpus supports, no predictions were made for fossil hominins. Given the subchondral trabecular analyses of individual non-pollical metacarpal heads (Chapter 4, Dunmore et al., 2019) their combined analysis is predicted to yield similar results. *Gorilla* is predicted to have a trabecular bone volume distribution that is higher across the dorsal metacarpus, and higher on the ulnar aspect of the second metacarpal (Mc2) as well as the radial aspect of the fifth metacarpal (Mc5), compared to other aspects of the metacarpal heads. This distribution is consistent with a predominantly terrestrial palm-back style of

knuckle-walking in *Gorilla* (Inouye, 1994; Remis, 1998; Matarazzo, 2013; Thompson et al., 2018). Conversely, the *Pan* locomotor repertoire includes more varied knuckle-walking style (Wunderlich and Jungers, 2009; Matarazzo, 2013) and a greater arboreal component relative to *Gorilla* (Remis, 1995; Doran, 1996; Thorpe and Crompton, 2006). This habitual locomotion is predicted to produce a more dorso-distal distribution of higher trabecular bone volume in *Pan paniscus* and *Pan troglodytes*, that is not significantly different between them. As *Pongo* does not habitually knuckle-walk but is thought to grasp branches in double-locked or hook grips (Rose, 1988; Sarmiento, 1988) and so trabecular bone volume is predicted to be higher in the disto-palmar aspect, relative to other aspects, of the non-pollical metacarpus in this genus. While the non-pollical metacarpus of recent *Homo sapiens* were not previously analysed, they also use their hands primarily for manipulation and so habitually flex their metacarpophalangeal joints. Unlike *Pongo*, however, *H. sapiens* have asymmetrical Mc2 and Mc5 heads which cause the second finger to pronate and move radially, but the fifth finger to supinate and move ulnarly, during flexion (Lewis, 1977; Marzke, 1997). However the human fifth finger has a larger freedom of movement than the second in the radio-ulnar plane (Coupier et al., 2016). This is likely due to the greater overall freedom of ulnar, rather than radial, deviation of the fingers allowed by the positions of the collateral ligaments (Landsmeer, 1955; Lewis, 1977). As a result *H. sapiens* are predicted to have higher trabecular bone volume on the palmar aspect of the non-pollical metacarpus, as well as on increasingly palmo-ulnar aspects of more ulnar metacarpals, especially the fifth metacarpal (Mc5), compared to other aspects of the metacarpal heads.

The separate trabecular analyses of the proximal and distal subarticular surfaces of first metacarpals (Mc1s; Chapter 5) are also predicted to be consistent with the current combined first metacarpal analysis. Non-human great apes are predicted to demonstrate higher trabecular bone volume at the palmar aspect of the Mc1 base and the ulnar aspect of the Mc1 head due to their use of adducted thumb in frequent pad-to-side grips (Marzke et al., 2015; Bardo et al, 2017;2017; Neufuss et al., 2018). Conversely, a concentration of higher trabecular bone volumes in the

palmo-radial Mc1 base and the radial aspect of the Mc1 head is predicted humans due to the use of a abducted thumb in habitual pad-to-pad precision grips (Napier, 1956; 1961; D'Agostino et al., 2017; Stephens et al., 2018).

Methods

Sample

Table 6.1 enumerates the sex and side of extant hominid metacarpals analysed in this study. All extant non-human hominid samples were from wild populations and are curated at the following institutions: the Royal Museum for Central Africa (Tervuren, Belgium), the Max Planck Institute for Evolutionary Anthropology (Leipzig, Germany), the Powell-Cotton Museum (Birchington, UK), Bavarian State Collection of Zoology (Munich, Germany), the Natural History Museum (Berlin, Germany), the Senckenberg Natural History Museum (Frankfurt, Germany) and the Smithsonian National Museum of Natural History (Washington D.C, USA). Recent human specimens were drawn from four populations: Nubians of ~5th century AD Sayala, Egypt (Strouhal and Jungwirth, 1979; Paoli et al., 1993) curated at Natural History Museum Vienna, Yámanas individuals from 19th century Tiera del Fuego (Marangoni et al., 2011), 20th century individuals from Syracuse, both curated at the University of Florence, and 20th century individuals from a cemetery in Inden, Germany (Großkopf, 2015) curated at the University of Göttingen.

All extant specimens were considered adult based on complete epiphyseal fusion of postcranial elements and had no external signs of pathology. An effort was made to balance left and right hands as well as sex for each non-human species, although one *Pongo pygmaeus* was of unknown sex and the *Gorilla* sample contains five females and seven males. Two humans were also of unknown sex. As humans cross-populationally right-handed (Faurie et al., 2005), and this is reflected in Mc1 trabecular bone (Stephens et al., 2016; Reina et al., 2017), the human sample was drawn from right hands in an attempt to avoid potential bias related to handedness. The hand preference of the human sample was unavailable, it is therefore possible that some left handed individuals are included in the sample, but given the preponderance of right-handed humans (Faurie et al., 2005), right hands

were analysed in order to be conservative. Table 6.2 lists the fossil hominin hand bones analysed in this study. All fossils included in the trabecular analysis have no major elements of subchondral trabecular bone missing from the metacarpal heads or first metacarpal base. Similarly, metacarpals without a diaphyseal shaft were excluded from the cortical cross-sectional geometry analysis.

Table 6.1. Extant sample composition.

		Mc1			Mc2-5		
Species	**Sex**	**Left**	**Right**	**Total**	**Left**	**Right**	**Total**
Gorilla gorilla gorilla	Female	3	2	5	3	2	5
	Male	2	3	5	4	3	7
	Total	5	5	**10**	7	5	**12**
Homo sapiens	Female	-	4	4	-	4	4
	Male	-	4	4	-	6	6
	Unknown	-	2	2	-	2	2
	Total	-	10	**10**	-	12	**12**
Pan paniscus	Female	3	2	5	3	2	5
	Male	2	3	5	2	3	5
	Total	5	5	**10**	5	5	**10**
Pan troglodytes	Female	2	3	5	2	4	6
	Male	3	3	6	3	4	7
	Total	5	6	**11**	5	8	**13**
Pongo abelii	Female	1	1	2	1	-	1
	Male	-	1	1	1	1	2
Pongo pygmaeus	Female	1	2	3	1	4	5
	Male	-	1	1	1	1	2
	Unknown	1	-	1	-	-	-
Pongo sp. indet.	Male	1	-	1	1	-	1
	Total	4	5	**9**	5	6	**11**

Note: Only metacarpals drawn from the same hands were used for the cross-sectional geometry analysis.

Table 6.2. Fossil sample composition.

Fossil	Taxonomy	Side	Sex	Element	Unassociated metacarpals	Date	Reference
STW 418	*A. africanus*	left	unknown	Mc1		1.95-2.95 mya	Pickering et al., 2011
SK84	*Homo/ Paranthropus*	left	unknown	Mc1		~1.6-1.8 mya	Susman et al., 2001
Neanderthal 1, Feldhofer 1	*H. neanderthalensis*	left	unknown	Mc1		40 kya	Schmitz et al., 2002
Barma Grande 2	*H. sapiens*	left	male	Mc1		19 kya	Bisson et al., 1996
Malapa Hominin 2	*A. sediba*	right	female	Mc1-5		1.98 mya	Kivell et al., 2011
Kebara 2	*H. neanderthalensis*	left	male	Mc1-5		60 kya	Valladas et al., 1987
El Sidrón	*H. neanderthalensis*	left	unknown	Mc1-5	SD-661 SDR-73 SDR-74 SDR-70 SDR-77	49kya	Wood et al., 2013
Ohalo 2 H2	*H. sapiens*	left	male	Mc1-5		23 kya	Hershkovitz et al., 1995
Arene Candide 2	*H. sapiens*	left	male	Mc1-5		12kya	Formicola et al., 1990
Hadar, Afar localities 438 and 333	*A. afarenisis*	LLR	male*	Mc2, 3 and 5	AL438-1d AL438-1e AL333-141	~3-3.2 mya	Kimbel et al., 2004
Sterkfontein Member 4	*A. africanus*	LLR	unknown	Mc2, 3 and 4	STW394 STW382 STW552	1.95-2.95 mya	Pickering et al., 2011
Tabun C1	*H. neanderthalensis*	left	female	Mc1, 3 and 5		~122 kya	Bar-Yosef and Callander, 1999

Where fossil metacarpals are not associated, the fossils that comprise the composite metacarpi are given. LLR refers to side of the metacarpals used for composite, in this case a left Mc2 and 3 with a right Mc 4 or 5.*This sex designation only applies to AL438-1; AL333-141 is of unknown sex. (kya = thousands of years ago)

Scanning and Image segmentation

Extant specimens were micro-CT scanned with a BIR ACTIS 225/300, Diondo D3, or Skyscan 1172 high resolution micro-CT scanners at the Department of Human Evolution, Max Planck Institute for Evolutionary Anthropology, Germany, or with the Nikon 225/XTH scanner at the Cambridge Biotomography Centre, University of Cambridge, UK. Fossils were scanned at these or their host institutions. Scans were performed at 100-160 kV and 100-140 µA, using a brass or copper filter of 0.25-0.5 mm. The scans were reconstructed to create volumetric images with an isometric voxel size of 13-57 µm, depending on the size of the specimen.

If the quality of micro-CT reconstructed volume, as well as the trabecular and cortical preservation, were appropriate for at least one of the analyses, the metacarpal image was cropped and reoriented into standard anatomical positions (Fig.6.1a, inset), and unwanted dense inclusions that would be erroneously classified as bone were removed in Avizo 6.3 (Visualization Sciences Group, SAS). The Ray Casting Algorithm (Scherf and Tilgner, 2009) was used to segment bone from other materials in bone metacarpals whereas fossils, often with several types of introgressive material and degrees of fossilisation, were segmented with the MIA-Clustering method (Dunmore et al., 2018; Chapter 3; Fig. 6.1b, c).

Trabecular analysis

Segmented metacarpal images were processed with the whole-epiphysis method, outlined in Gross et al. (2014) and subsequent geometric morphometric landmark analysis was performed in a similar manner to that described by Dunmore et al. (2019). In brief, a number of image filters, run via medtool 4.2 (Dr. Pahr Ingenieurs e.U.), automatically isolated the inner trabecular structure from the cortical bone by casting rays from the outer cortical shell at multiple angles and terminating them at non-bone voxels. The volume delimited by these rays was then effectively dilated by a number of voxels equal to the average trabecular thickness in that bone, to create a solid volume within the cortical shell of the metacarpal (Pahr and Zysset, 2009). A grid of 2.5 mm cubes was superimposed on the isolated trabecular volume and overlapping spherical volumes of interest (VOI), 5 mm in diameter, were centred at each of its vertices (Fig. 6.1c). Trabecular bone volume fraction (BV/TV)

was then measured in each VOI and the values were interpolated on a regular 3D tetrahedral mesh of the trabecular volume, created with CGAL (Computational Geometry Algorithms Library; www.cgal.org, Fig. 6.1d). BV/TV is strongly correlated with the mechanical properties of trabecular bone (Odgaard et al., 1997; Uchiyama et al., 1999; Pontzer et al., 2006; Barak et al., 2011; Lambers et al., 2013) and is not markedly allometric (Doube et al., 2011; Barak et al., 2013; Ryan and Shaw, 2013).

The present study focuses on subchondral or subarticular BV/TV, since forces at a joint must pass through part of the subchondral trabecular structure before reaching the deep trabecular structure or diaphyseal cortical bone. Therefore, if bone functional adaptation to habitually loaded joint positions exists, it should be found in this subchondral trabeculae (Marzke et al., 2010; Zhou et al., 2014; Sylvester and Terhune, 2017; Dunmore et al., 2019). To achieve this subchondral trabecular analysis, the outer surface of the 3D trabecular mesh was isolated in Paraview (Ayachit, 2015) and a Poisson surface reconstruction filter (Kazhdan and Hoppe, 2013) was used to smooth the surface in in Meshlab (Cignoni et al., 2008). Metacarpal surfaces from left hands were then mirrored so that they were oriented in the same manner as those from right hands, for homologous functional comparison. Surfaces of all metacarpal heads and first metacarpal bases were manually landmarked in Checkpoint (Stratovan Corporation, Davis, CA). Anatomical landmarks used here, have been previously shown to be repeatable and are listed in Chapters 4 and 5 (Tables 4.2, 5.2 and 5.3). A template of landmarks was manually created on a randomly chosen specimen for non-pollical metacarpal heads, first metacarpal heads and first metacarpal bases, respectively in Avizo 6.3 (Visualization Sciences Group, Germany), following Dunmore et al. (2019). The sliding semi-landmarks that bordered, and those that were equally distributed over, the subarticular surface of each template were then projected onto the appropriate surface of each metacarpal in the sample via the Morpho package (Schlager, 2017) in R (R Core Development team, 2016). This package was also used to relax projected landmarks onto each metacarpal surface by minimising bending energy and to slide the semi-landmarks along their respective curves and over the surface by minimising Procrustes distances (Fig. 6.1e). In order to interpolate BV/TV to these landmarks, a custom python script was used to assign BV/TV values of each

tetrahedra in the unsmoothed trabecular mesh created in medtool 4.2 (Dr. Pahr Ingenieurs e.U.) to the centre of their surface triangles. The Python module SciPy (Jones et al., 2001) was used to interpolate these centre BV/TV values to the closest landmark on the smooth surface (Fig. 6.1f). This approach is analogous to measuring BV/TV in spherical VOIs, 1 mm in diameter, centred 0.5 mm beneath an inner trabecular surface and projecting the values onto the surface. In R (R Core Development team, 2016), a generalised Procrustes procedure was run on these landmarks using the Geomorph package (Adams et al., 2017) to create 204 sets of 173 homologous 3D non-pollical metacarpal head landmarks, and 58 sets of both 49 first metacarpal head, and 40 first metacarpal base, 3D homologous landmarks, all with an associated BV/TV value. Several studies that have standardised measures of BV/TV in order to analyse distribution rather than raw magnitude of trabecular volume as raw values may incorporate both biomechanically functional and systemic differences in BV/TV between species or individuals (Saers et al., 2016; Tsegai et al., 2018; Sukhdeo et al., 2018; Dunmore et al., 2019). Following this logic, the BV/TV value at each landmark was divided by the arithmetic mean of all landmark BV/TV values on that subarticular surface to derive a relative measure of bone volume fraction (RBV/TV). RBV/TV values close to one indicate BV/TV values close to the average BV/TV of that subarticular surface.

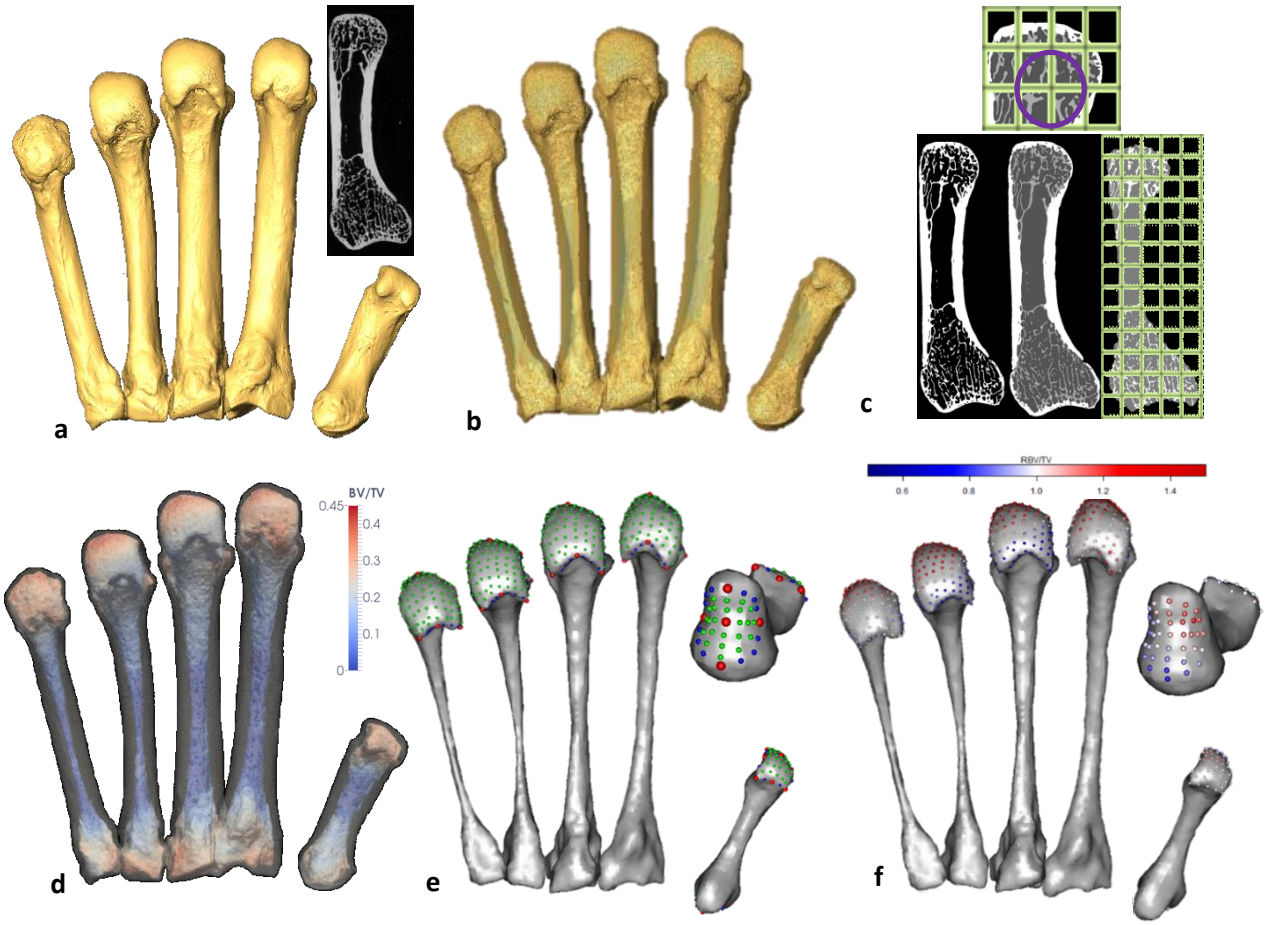

Figure 6.1. Trabecular analysis method, example on *Pan troglodytes* metacarpus. a) An isosurface model of the metacarpus with inset parasagittal cross-section of the first metacarpal. b) 3D isosurface showing inner trabecular structure of the metacarpus. c) Segmented 2D cross-section of the first metacarpal (left), cortical and trabecular segmentation (centre), regular background grid overlaid on the isolated trabecular structure (right) and a close-up of this grid with a representation of the overlapping volumes of interest (VOIs) centred at each vertex of the background grid in purple (top). d) Interpolation of BV/TV values, measured in overlapping VOIs, onto 3D trabecular meshes. e) Anatomical landmarks (red), sliding semi-landmarks on curves (blue) and across the subarticular surfaces (green), on the smoothed surface of the trabecular models. f) BV/TV values interpolated to each landmark and then divided by the mean value of each articular surface to produce RBV/TV values on each landmark.

Cross-sectional geometry

Several palaeoanthropological and bio-archaeological studies have employed cross-sectional geometry (CSG) at the mid-diaphysis of long bones to investigate cortical bone functional adaptation (Ruff, 2003; Marchi et al., 2005; Young et al., 2018; Ruff et al., 2018; Macintosh and Stock, 2019). Though recent findings have cautioned against a simple interpretation of comparative results (Wallace, et al., 2017; Young et al., 2018), several experimental studies have shown that loading regime does affect the cross-sectional properties of cortical bone (Biewener and Bertram, 1994; Robling et al., 2002; Lieberman et al., 2004; Carlson and Judex, 2007).

In order to generate a 50% mid-diaphysis axial cross-section, a 2D sagittal cross-section of each segmented metacarpal image was created using medtool 4.2 (Dr. Pahr Ingenieurs e.U.). A homologous axial cross-section requires a mid-slice orthogonal to the long axis of the metacarpal; however, several specimens studied, particularly those of *Pongo*, were curved resulting in an oblique axial cross-section in anatomical position, that is not homologous to those of straighter metacarpals. In order to ameliorate the effect of metacarpal curvature on axial cross-section homology, the Numpy Python module was used to find the largest eigenvector of the bone pixels in the 2D sagittal cross-section image (Fig. 6.2a). As this vector mathematically best describes the long axis of a metacarpal, it incorporates the relative amount of curvature in each bone. The angle between the eigenvector and the y-axis was found and the segmented 3D volume was then rotated by this angle in the sagittal plane using medtool 4.2 (Fig. 6.2b). ImageJ (Schneider et al., 2012) was then used to find the most proximal and distal bone pixel in the rotated sagittal image and the midpoint between them in the y-axis (Fig. 6.2c). Medtool 4.2 was used to extract a homologous axial mid-slice from the rotated 3D segmented volume at this 50% diaphysis point (Fig. 6.2d). The Slice Geometry function of BoneJ (Doube et al., 2010) was used to calculate the maximum (*Imax*) and minimum (*Imin*) area moments of inertia as well as the area moment of inertia in the anteroposterior (*IAP*) and medio-lateral, or radio-ulnar, (*IML*) planes (Fig. 6.2e,f). The average area moment of inertia (*Iavg*) for each mid-slice, calculated as the mean of *Imax* and *Imin,* was used as a measure of overall diaphyseal stiffness as it is directly proportional to the average bending rigidity of a bone (Ruff, 2002). The ratio of *IAP/IML* measures how far the bone can resist bending forces in each anatomical plane, with ratios above one indicating a more anteroposterior bending rigidity, ratios below one indicating more medio-lateral bending rigidity and ratios around one indicating similar resistance in both planes. These measures were calculated in mm^4, as they are calculated by taking the second integral of the distance to a reference axis, multiplied by the differential element of area (a measurement to the second power). Both *Iavg* and *IAP/IML* of the first metacarpal were divided by the arithmetic mean *Iavg* and *IAP/IML* of the non-pollical metacarpals. The resulting ratios indicate the biomechanical bending rigidity at

mid-diaphysis of the first metacarpal relative to the rest of the metacarpus, and how far the direction of this resistance to bending departs from the non-pollical metacarpus.

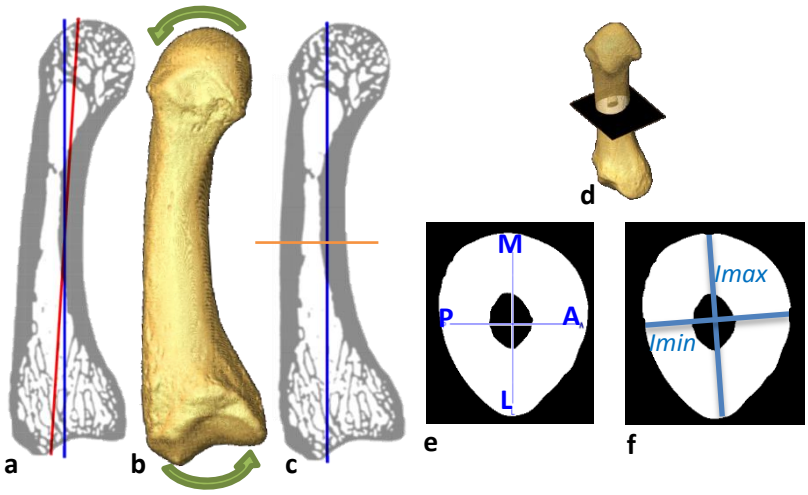

Figure 6.2. Cross-sectional analysis method, example on a *Pongo* first metacarpal. a) A parasagittal cross-section image with its manual proximo-distal axis marked in blue and the computed eigenvector that best describes this axis marked in red. b) The 3D image is rotated by the angle between the two axes (green arrows). c) The cross-section of the rotated image shows the eigenvector now equals the proximo-distal axis of the bone and a 50% coronal cross-section, marked in orange, is orthogonal to the new axis. d) The position of this 50% diaphyseal mid-slice shown in 3D and e) the anatomical axes used to calculate directional area moments of inertia are medio-lateral (ML), anteroposterior (AP). f) The minimum (*Imin*) and maximum (*Imax*) area moments of inertia calculated for this bone are depicted and were averaged to generate the average area moment of inertia (*Iavg,* mm^4).

Statistical analysis

In order to analyse the distribution of subchondral RBV/TV, the mean values of each landmark per species were visualised on canonical metacarpal surfaces created using a statistical shape model in wxRegSurf (http://mi.eng.cam.ac.uk/~ahg/wxRegSurf/). For non-pollical metacarpals, each of the 692 landmark values were treated as variables in a principle components analysis (PCA). The first three principle components (PCs) comprised 54% of the variation and further PCs each described less than 10% additional variation. Therefore in order to test if overall RBV/TV distribution was different between extant species, omnibus and subsequent pairwise one-way permutational MANOVAs were run on the first three PC scores of each non-pollical metacarpus, using the Vegan (Oksanen et al., 2018) and RVAideMemoire (Hervé, 2017) packages

in R (R Core Development team, 2016). Before these tests were performed, a test of multivariate homogeneity of variance was performed on the Euclidean distance matrix that describes the PC scores and a Bonferroni correction was applied to all pairwise results, to ensure valid comparisons. A permutation approach was taken as not all data met the assumption of multivariate normality (Anderson, 2017). This approach was separately applied to the subchondral RBV/TV of the non-pollical metacarpus (Mc2-5) and the first metacarpal, as this bone has two mobile epiphyses with a different developmental, and evolutionary, history than the rest of the metacarpus (Pazzaglia et al., 2018). For this analysis both epiphyses were combined, in the same manner as the four non-pollical metacarpal heads. In order to determine if individual fossils were significantly different from extant groups, a permutational Hotelling's one-sample T^2 test was employed from the R Package Compositional (Tsagris and Athineous, 2018) for the first and non-pollical metacarpals separately. While one-sample test results must be interpreted with caution, as their statistical power is limited, these tests provide some statistical interpretation of the results visualised in the PCAs until further fossils are discovered. To test for significant differences in the relative cortical rigidity and shape of metacarpal diaphyses between extant species, a Kruskal-Wallis with post-hoc Dunn's tests were run on *Iavg* and *IAP/ IML* ratios respectively, with a Bonferroni correction. This test was chosen as neither variable was normally distributed, as demonstrated by significant Shapiro-Wilk test results. A one-sample Wilcoxon signed rank test was used to determine if individual fossils were significantly different from extant species for each variable separately, though again these are interpreted with caution. All statistical tests were performed in R (R Core Development team, 2016), and a *p*-value less than 0.05 was considered significant.

Results

Metacarpals in extant great apes

We tested the hypothesis that distribution of RBV/TV would be consistent with metacarpophalangeal (McP) and trapeziometacarpal (TMc) joint positions, thought to be habitually loaded together in great ape locomotion and manipulation. As depicted in Figure 6.3, red landmarks with higher average RBV/TV in each species correspond with predicted McP and TMc joint positions. Higher dorsal RBV/TV in *Gorilla* (Fig. 6.3a) and *Pan* is consistent with the hyperextended McP joints adopted during knuckle-walking (Tuttle, 1967; Fig. 6.7). A principle components analysis (PCA) of subchondral RBV/TV distribution in second to fifth metacarpal heads (Mc2-Mc5; Fig. 6.4a) demonstrates that *P. trgolodytes* and *P. paniscus*, sharing a similar locomotor repertoire (Doran, 1993) and assumed habitual hand use, were statistically similar to each other. This PCA also statistically distinguishes knuckle-walking African apes from *Pongo* and *Homo* at these joints (Fig. 6.4a; Table 6.3). Higher palmar RBV/TV in *Pongo* (Fig. 6.3b) is consistent with habitually-flexed McP joints employed in arboreal power grasps, such as a 'double-locked' grip (Rose, 1988). Recent humans also show high palmar RBV/TV, but this distribution is asymmetrical, showing increasingly palmar high RBV/TV from Mc2 to Mc5, which is consistent with simultaneous flexion and ulnar deviation of the McP joints during opposition of the fingers to the thumb in manipulation (Skinner et al., 2015; Stephens et al., 2018; Fig. 6.3c). Recent *H. sapiens* displayed a statistically distinct pattern of higher RBV/TV values in first metacarpal compared to other extant great apes (Figs. 6.3c, 6.5; Fig. 6.8). This distribution of higher RBV/TV at radial Mc1 head landmarks and radio-palmar Mc1 base landmarks is compatible with thumb abduction, flexion and opposition during forceful precision grips and in-hand manipulation (D'Agostino et al., 2017; Stephens et al., 2018). Conversely, the non-human great ape pattern of higher average RBV/TV values at disto-ulnar Mc1 head landmarks and palmar Mc1 base landmarks is consistent with thumb flexion and adduction (Fig. 6.3b) during pad-to-side grips frequently practised by wild and captive apes (Marzke et al., 2015; Bardo et al., 2017; Neufuss et al., 2018). *Gorilla* showed a more pronounced pattern of the non-human great ape RBV/TV value distribution though this was only significantly different from *Pan* species (Table 6.3).

Combining the whole metacarpus allowed us to assess the biomechanical importance of the thumb in each species, by analysing the rigidity and shape of metacarpal diaphyses at a 50% mid-slice along their length. We hypothesized that due to higher radio-ulnar loading of the muscular thumb of recent humans during manipulation (Tocheri, 2008; Marzke et al., 1999), the Mc1 diaphysis would be medio-laterally wider and stiffer, relative to Mc2-5, than in extant apes. The human first metacarpals have a significantly higher average area moment of inertia than extant non-human great apes (Table 6.5). However, though human Mc1 midshafts are medio-laterally wider relative to Mc2-5, this is not significantly different from most non-human great apes, as this trait appears to be variable for these species (Fig. 6.6).

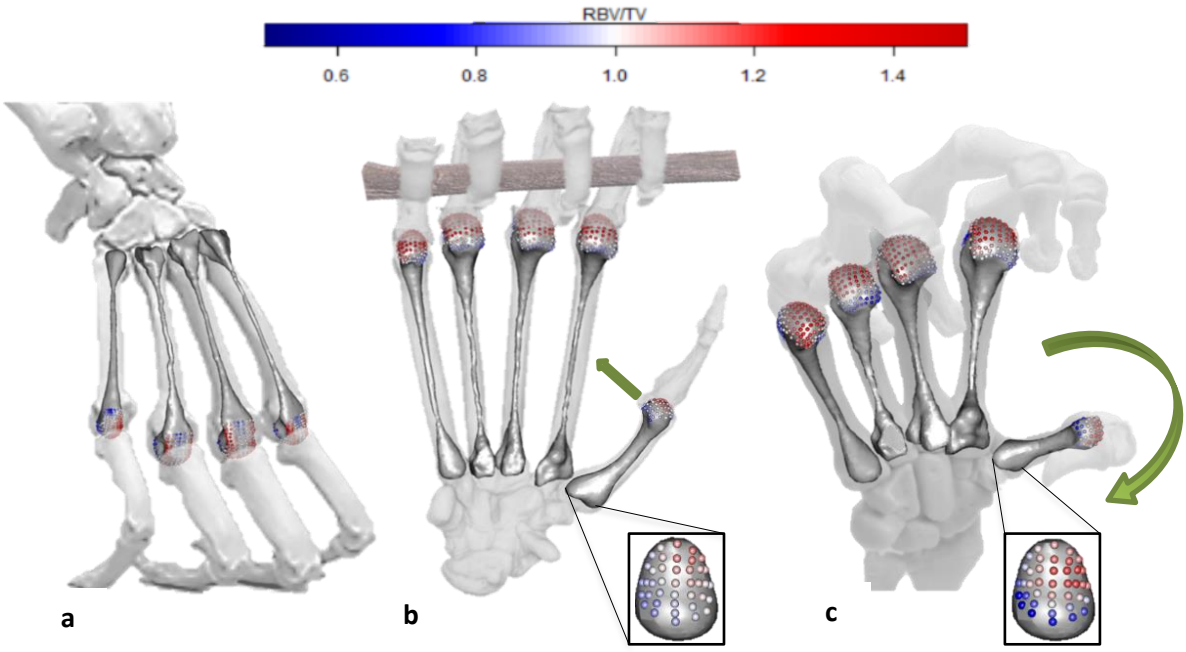

Figure 6.3. Average relative trabecular bone (RBV/TV) distribution in great ape metacarpals during habitual hand postures. RBV/TV is the ratio of subchondral trabecular bone to space at each landmark divided by the average values for all landmarks on that subchondral surface. Higher RBV/TV indicates relatively more bone in this part of the metacarpal (red landmarks) while lower RBV/TV indicate relatively less bone (blue landmarks). RBV/TV values ~1 indicate trabecular bone is near the average of the surface in this area (white landmarks)**.** Hand postures are shown for a) knuckle-walking in *Gorilla*, b) arboreal locomotion in *Pongo* and c) manipulation in humans. The arrow in b) illustrates adduction of the thumb during 'pad-to-side' grips habitually used by non-human apes and in c) abduction of the 'pad-to-pad' opposed thumb in humans during precision grips. Species average RBV/TV distribution in the Mc1 base is depicted inset for b) and c).

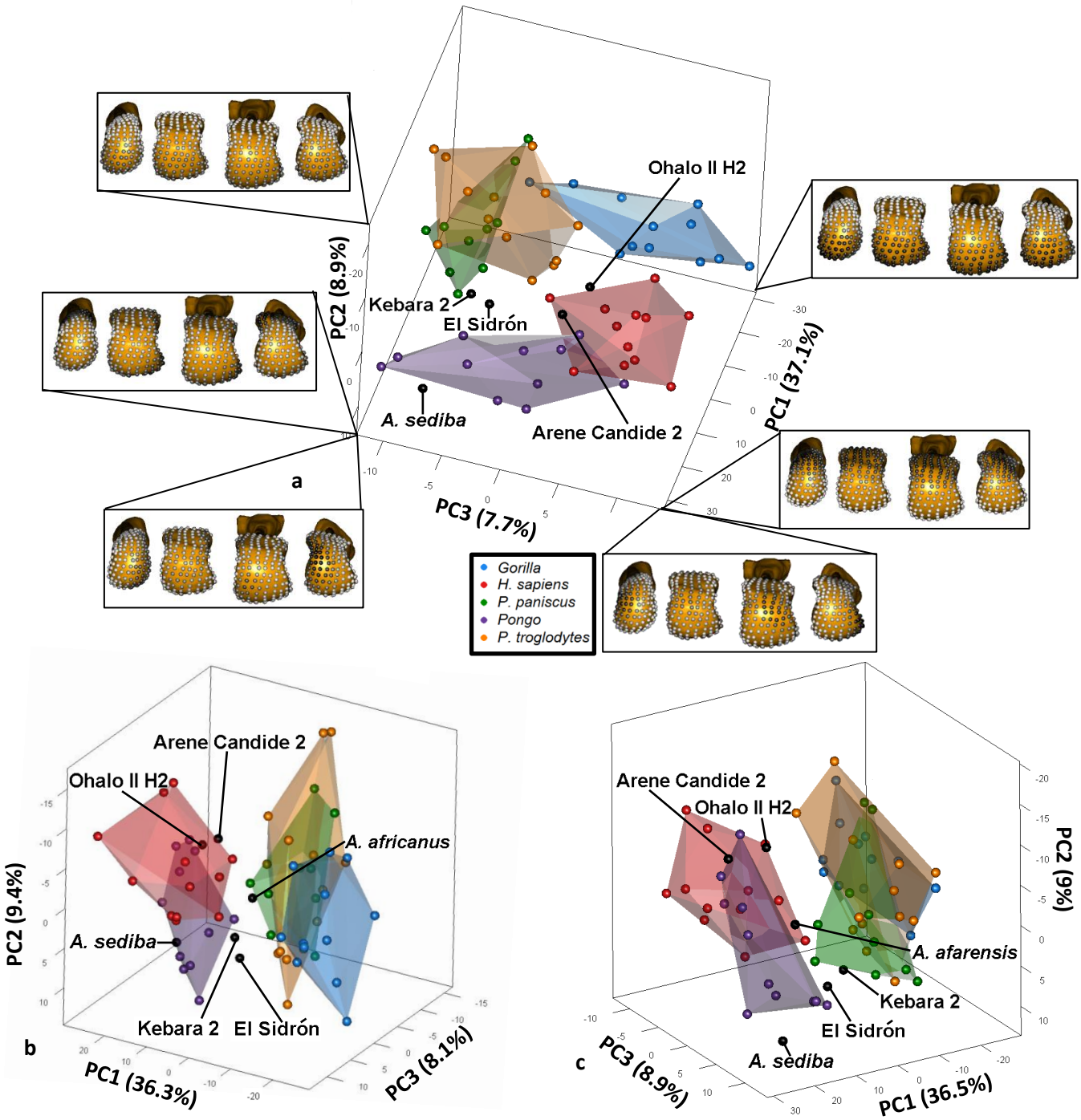

Figure 6.4. Relative trabecular bone volume fraction (RBV/TV) distribution in the metacarpal heads of the palm. a) A 3D PCA depicting subchondral RBV/TV variation across the non-pollical metacarpus (Mc2-5). Landmarks at each extreme of a PC are coloured in grayscale, according to their signed contribution to that PC, and plotted on distal view of a right non-pollical metacarpus. Each point represents the pattern of RBV/TV across an associated metacarpus in one individual. Fossils are plotted in black and labelled. RBV/TV distribution clearly distinguishes among the extant taxa, apart from both *Pan* species that have similar locomotor repertoires. Both fossil *H. sapiens* (Ohalo II and Arene Candide 2) fall within the proximity of recent humans, while *H. neanderthalensis* specimens (Kebara 2 and El Sidrón) are separated from humans on PC3. *A. sediba* is distinct, situated closest to *Pongo* and far from humans and other great apes. b) The same PCA but based on just Mc2-4 for comparison with *A. africanus* composite sample, and c) based on just Mc2, 3 and 5, for comparison with *A. afarensis* composite sample. Though interpretation of incomplete and composite metacarpi must be undertaken with caution, note that in neither case do *A. afarensis* or *A. africanus* have a similar RBV/TV distribution to that of *A. sediba*.

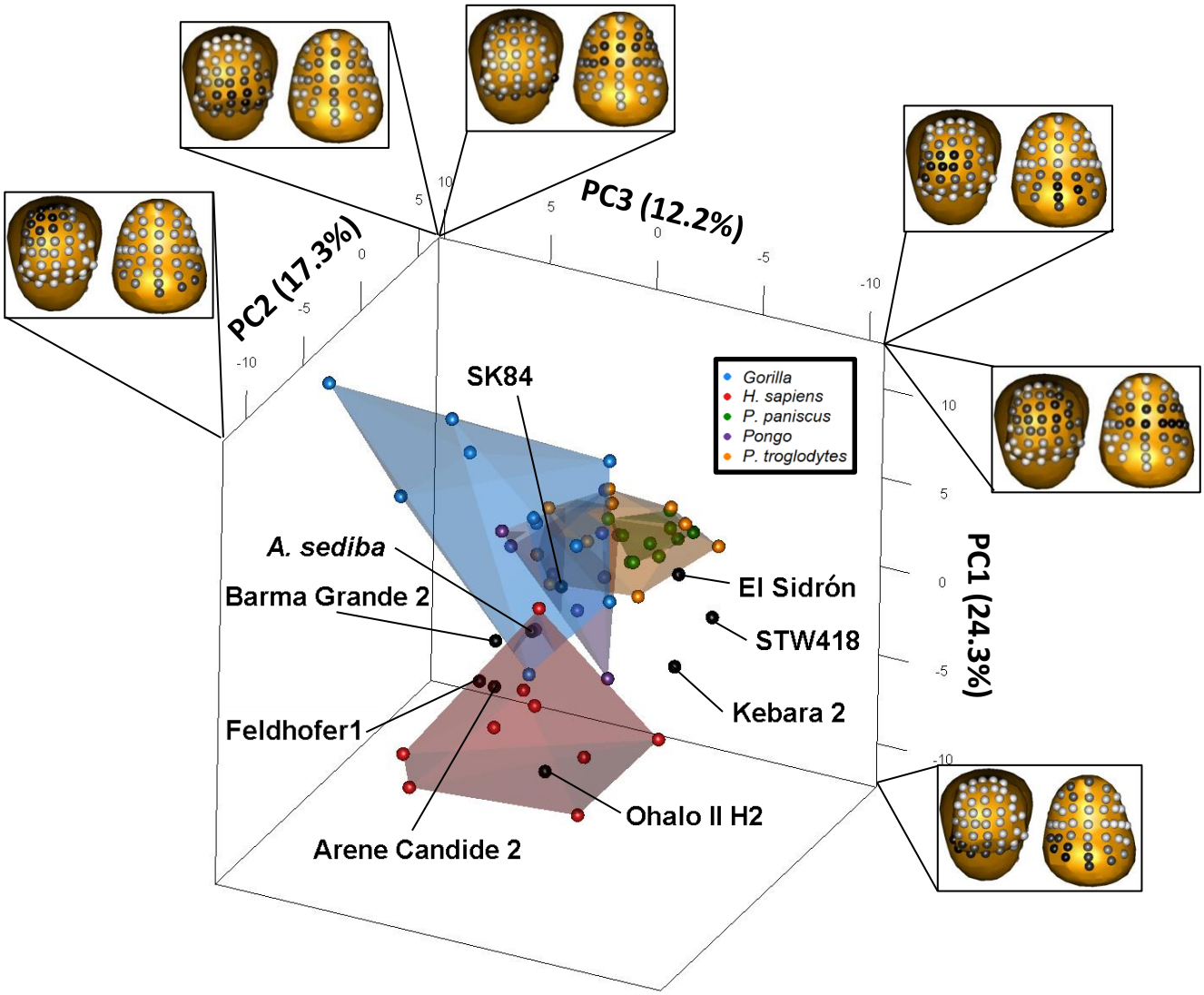

Figure 6.5. Relative trabecular bone volume fraction (RBV/TV) distribution in the first metacarpal. A 3D PCA depicting subchondral RBV/TV variation across the first metacarpal head and base. Landmarks at each extreme of a PC are coloured in grayscale, according to their signed contribution to that PC. These landmarks are plotted on a right Mc1 in distal (left) and proximal (right) views. Each point represents the pattern of RBV/TV across both epiphyseal surfaces in one individual. Fossils are plotted in black and labelled. RBV/TV clearly distinguishes modern humans from non-human great apes and *Gorilla* somewhat departs from the non-human great ape pattern. SK84 is situated within the non-human great apes. All fossil *H. sapiens* (Arene Candide 2, Barma Grande 2 and Ohalo II H2) and Feldhofer 1 (*H. neanderthalensis*) fall close to the recent human sample. Kebara 2, El Sidrón (*H. neanderthalensis*) and STW418 (*A. africanus*) are separated from all extant species. *A. sediba* plots within the range of recent humans.

Table 6.3. Extant species trabecular comparisons.

	Gorilla	***Homo sapiens***	***Pan paniscus***	***Pan troglodytes***	***Pongo***
Gorilla		10.912*	12.516*	5.167*	5.473*
Homo sapiens	63.428*		14.940*	12.519*	5.272*
Pan paniscus	24.149*	20.851*		2.735	3.426
Pan troglodytes	16.465*	22.905*	0.672		2.766
Pongo	92.890*	8.823*	26.350*	32.485*	

Permutational MANOVAs conducted on the first 3 PCs of subchondral RBVTV landmark values**,** for non-pollical metacarpi are highlighted in blue (n=58) and first metacarpal comparisons in green (n=49). Multivariate homogeneity of variances were not significantly different and an omnibus permutational MANOVA was significant for both samples. All Pseudo-*F* values that were significant, subsequent to a Bonferroni correction, are marked with asterisks(*).

Table 6.4. Fossil comparisons to extant species.

Mc2-5	Arene Candide 2	Ohalo II H2	Kebara 2	El Sidrón	*A. sediba*
Gorilla	241.430*	131.554*	167.503*	162.052*	545.462*
Homo sapiens	18.674*	12.578*	57.942*	48.488*	105.626*
Pan paniscus	90.560*	98.043*	8.017	18.819*	40.654*
Pan troglodytes	95.942*	45.991*	39.179*	35.206*	236.387*
Pongo	16.168*	45.550*	51.805*	49.828*	7.264*

Mc1	Arene Candide 2	Ohalo II H2	Kebara 2	El Sidrón	*A. sediba*	Feldhofer 1	SK84	STW418	Barma Grande 2
Gorilla	18.293*	36.960*	11.844	11.857	6.608	21.331*	8.407	21.078*	12.583
Homo sapiens	1.325	2.053	11.406	20.452	4.939	2.826	12.004	20.184*	5.222
Pan paniscus	322.242*	715.610*	211.717*	25.393*	192.874*	293.713*	55.515*	79.318*	293.295*
Pan troglodytes	71.141*	180.898*	54.234*	7.602*	40.538*	63.550*	8.758*	25.981*	65.560*
Pongo	22.719	39.256	31.242	24.384	6.106	29.375	0.576	30.470	13.410

Permutational one-sample Hotelling's T^2 tests conducted between the first 3 PCs of subchondral RBV/TV landmark values of each fossil and each extant sample. Significant *F*-values (note this is not pseudo-*F* but a transformation of T^2) , at $p < 0.05$ are marked in with an asterisk(*). Note the due to the lower sample size in *Pongo,* in particular, some Mc1 results were close to (p = 0.05-0.07), but did not reach, significance.

Hand use in fossil Homo

The trabecular distribution within fossil *H. sapiens* and *H. neanderthalensis* is consistent with manipulation and forceful opposition of the thumb, but also suggests that these species employed slightly different habitual loaded hand postures than recent humans. The fossil *H. sapiens* RBV/TV distribution places them close to, or within the range of, recent humans across the metacarpals (Figs. 6.4; 6.5). Fossil *H. sapiens* exhibit the same shape ratio, but a Mc1 diaphysis more resitant to bending, compared to recent *H. sapiens* (Table 6.5). Conversely, *H. neanderthalensis* specimens maintain a similar relative diaphyseal rigidity of the Mc1 to that of recent humans, but a less radio-ulnarly wide Mc1. The RBV/TV distribution of the majority of *H. neanderthalensis* Mc1 specimens also departs from that of *H. sapiens,* with higher values in the ulnar aspect of the Mc1 head. However, one *H. neanderthalsensis* Mc1 (Neanderthal 1, Feldhofer 1) did cluster with *H. sapiens* to the exclusion of its conspecifics.

Hand use in Plio-Pleistocene hominins

The internal bone structure of Plio-Pleistocene hominin metacarpi demonstrates significant diversity. SK84 is an Mc1 that may be attributed to *Paranthropus* or *Homo* (Trinkhaus and Long, 1990) with trabecular structure that suggests it was loaded in a similar manner to those of extant non-human great apes. The *A. africanus* Mc1 (STW418) clustered near those of *H. neanderthalensis* (Fig. 6.5) but displayed a distinct pattern of RBV/TV values unlike any *Homo* specimens studied. The relative biomechanical bending rigidity of this Mc1 is also significantly lower than that of recent humans, falling within the range of extant apes (Fig. 6.6). The trabecular disposition of *A. africanus* Mc2-4 is relatively intermediate between all extant taxa (Fig.6.4b), as is the distribution of Mc2,3, and 5 (Fig. 6.4c). However, these two results are not directly comparable as a different metacarpal is omitted from each PCA, Mc5 (Fig.6.4b), and Mc4 (Fig.6.4c), respectively. Further, it must also be borne in mind that these analyses are based on chimeric and incomplete metacarpi. The associated Mc2-5 of *A. sediba* (MH2), however, maintains a different RBV/TV distribution than either of the other *Australopithecus* species and consistently falls at the edge of the *Pongo* range (Fig.6.4). This is in stark contrast to

the associated Mc1 of MH2, which has a trabecular structure within the range of recent humans (Fig. 6.5). This unique 'dual' trabecular bone pattern has a corollary in the uniquely intermediate rigidity of the Mc1 diaphysis of *A. sediba* which, while relatively radio-ulnarly wide, lies between that of extant non-human great apes and recent humans (Fig. 6.6).

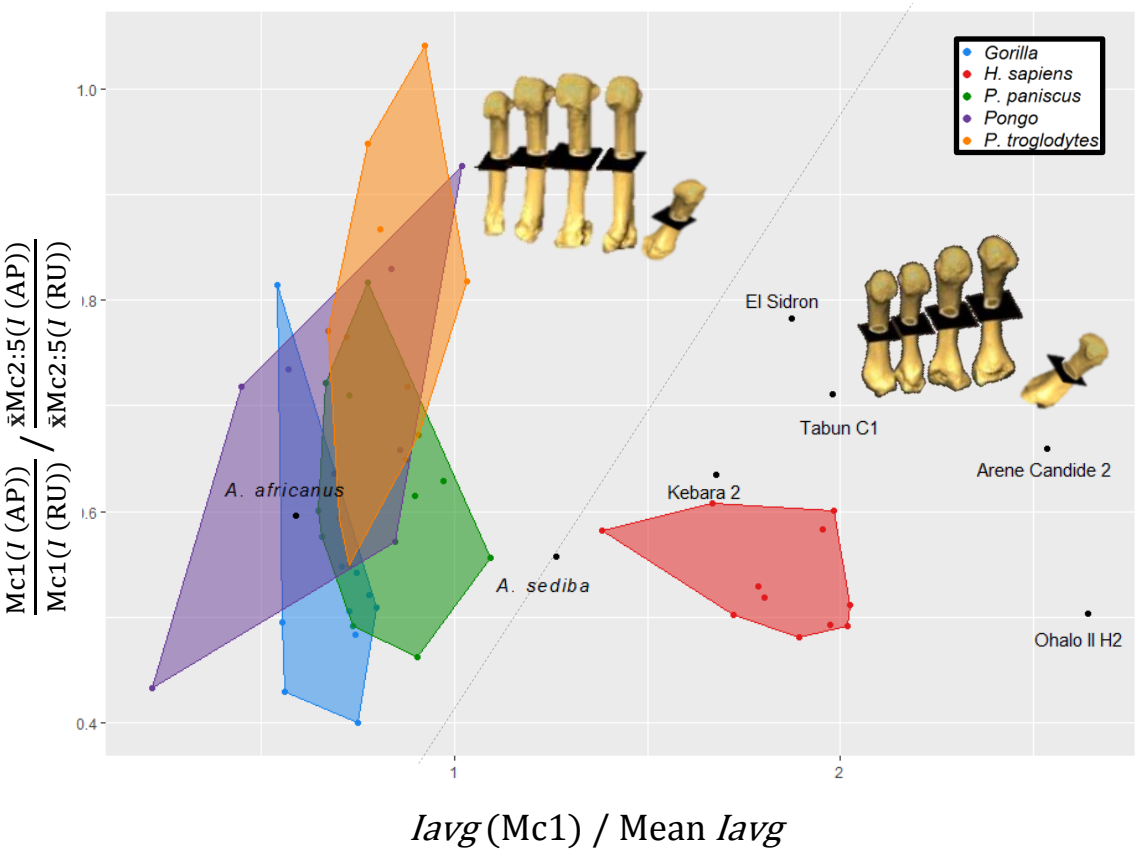

Figure 6.6. Relative cortical rigidity of first metacarpals at 50% diaphyseal mid-slice. A bivariate plot of cross-sectional geometry variables. For each hand a ratio of the first metacarpal and the average non-pollical metacarpal average area moments of inertia (*Iavg,* mm^4) is plotted on the X-axis. The ratio of area moments of inertia (mm^4) in the anterior-posterior (AP) and medio-lateral (ML) planes is a shape index for a metacarpal diaphysis. A ratio of these shape indices between the first metacarpal and average non-pollical metacarpals is plotted on the y-axis. Representative metacarpi of *P. troglodytes* and *H. sapiens* are depicted adjacent to their respective values. Note the separation of recent and fossil *H. sapiens* (Ohalo II H2, Arene Candide 2) as well as *H. neanderthalensis* (Kebara 2, El Sidrón and Tabun C1) from other great apes and *A. africanus*. *A. sediba* is situated between recent humans and non-human great apes.

Table 6.5. Extant group and individual fossil sample comparisons of cross-sectional geometry variables.

	***Iavg* ratio**					***IAP/IML* ratio**				
	Gorilla	*Homo sapiens*	*Pan paniscus*	*Pan troglodytes*	*Pongo*	*Gorilla*	*Homo sapiens*	*Pan paniscus*	*Pan troglodytes*	*Pongo*
Gorilla (n=10)										
Homo sapiens (n=10)	4.723*					0.442				
Pan paniscus (n=10)	1.120	3.580*				1.871	1.473			
Pan troglodytes (n=11)	1.486	3.320*	0.340			3.868*	3.510*	1.953		
Pongo (n=7)	0.394	4.041*	0.662	0.995		2.730*	2.371	0.965	0.850	
Arene Candide 2	3.097*	3.097*	2.886*	3.097*	2.418*	1.970*	3.097*	0.597	1.610	0.650
Ohalo II H2	3.097*	3.097*	2.886*	3.097*	2.418*	0.049	1.273	2.335*	3.097*	1.987*
Kebara 2	2.886*	1.970*	2.886*	3.097*	2.418*	1.728*	3.097*	0.319	1.970*	0.489
El Sidrón	2.886*	1.273	2.886*	3.097*	2.418*	2.886*	3.097*	2.660*	0.352	1.230
Tabun C1	2.517*	1.728*	2.886*	3.097*	2.418*	2.407*	3.097*	1.785*	0.220	0.650
A. sediba	1.728*	3.097*	2.886*	3.097*	2.418*	0.588	1.160	0.994	2.886*	1.601
A. africanus	2.207*	3.097*	2.886*	3.097*	0.298	2.206	2.584*	0.511	2.584*	1.043

Extant species were compared with Kruskal-Wallis tests and pairwise post-hoc Dunn's tests with a Bonferroni correction. Fossils were compared with extant species via one-sample Wilcoxon signed rank tests. Absolute *Z*-values are reported for each variable and significant *p*-values below 0.05 are marked with an asterisk(*).

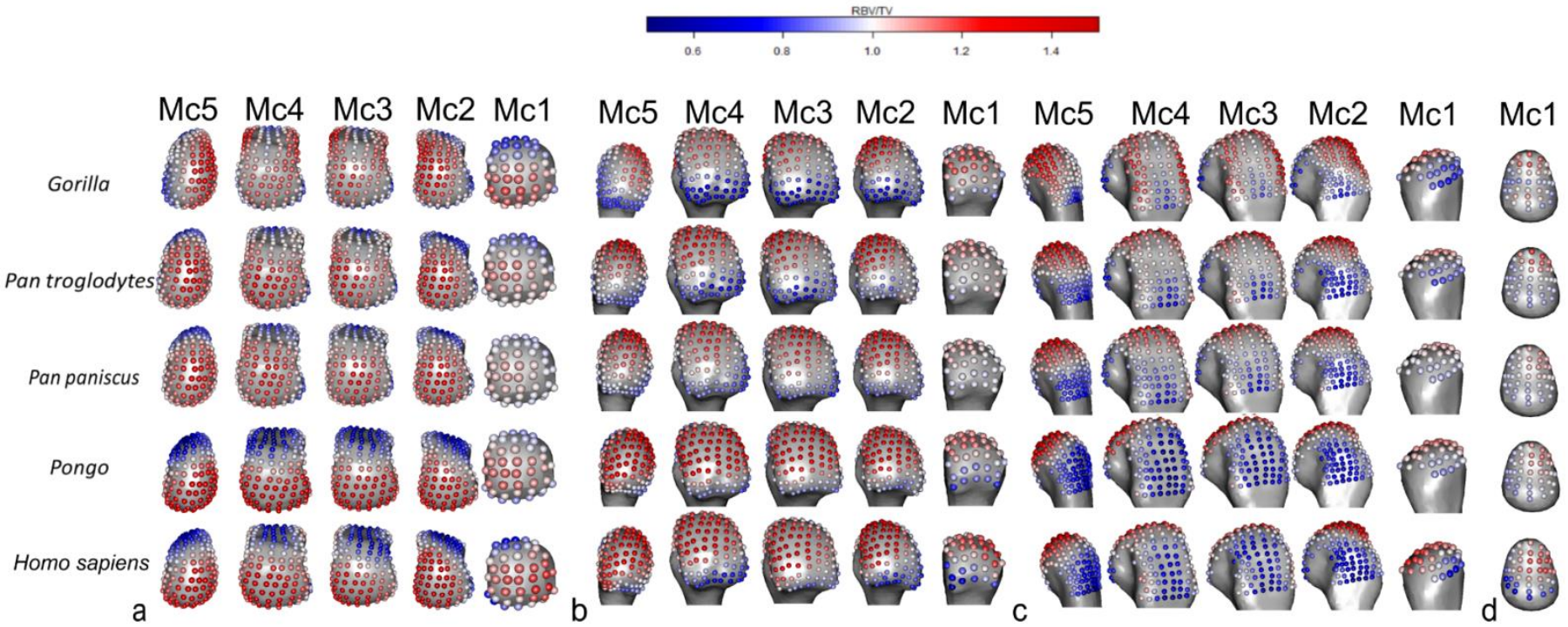

Figure 6.7. Extant species average distributions of subchondral RBV/TV across the metacarpus in a) distal, b) palmar and c) dorsal views, in addition d) depicts the average distributions of RBV/TV across the first metacarpal base.

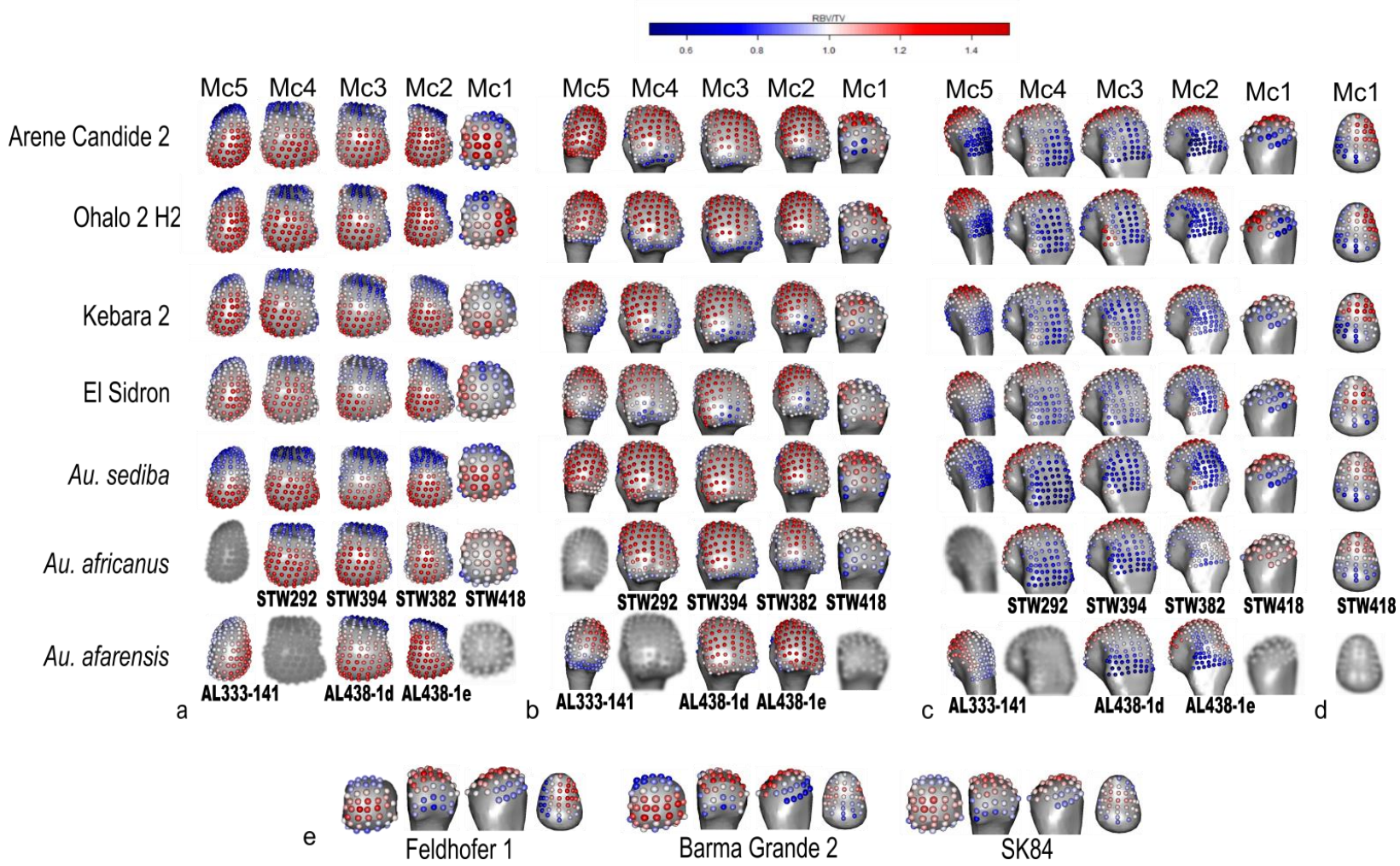

Figure 6.8. Distributions of RBV/TV across fossil hominin metacarpi, in a) distal, b) palmar and c) dorsal views. Also d) depicts the average distributions of RBV/TV across the first metacarpal base and e) displays distal, palmar, dorsal and proximal views of individual fossil first metacarpals

Discussion

The combined cortical and trabecular structure analysed here is argued to be primarily the result of behaviour performed in that individual's life (Ruff et al., 2006). Yet, the relative importance of the magnitude or frequency of biomechanical loading in generating these plastic osteogenic responses is not yet well known (Wallace et al., 2017). Indeed, the interaction of trabecular and cortical bone also requires more analysis, as does the role of systemic factors such as hormones, intestinal-biomes and genetic factors in shaping internal bony architecture (Ruff et al., 2006; Wallace et al., 2017; Tsegai et al., 2018). In spite of all of these potential sources of variation, both comparative and experimental studies have produced a growing body of evidence for *in vivo* loading as a primary determinate of mid-diaphyseal and trabecular bone structure (Biewener et al., 1996; Pontzer et al., 2006; Ruff et al., 2006; Barak et al., 2011; Wallace et al., 2017). The RBV/TV distribution and cortical bone cross-sectional geometry analysed here reflect presumed, and observed, habitually loaded hand-postures in extant great apes and so also appear to hold a functional signal.

As expected, fossil *H. sapiens* demonstrated a pattern of internal bone architecture very similar to that of recent *H. sapiens,* except for the higher relative diaphyseal rigidity of their fossil Mc1s. This disparity may reflect a mosaic element in the systemic reduction of robusticity thought to have occurred by the Neolithic in Europe (Chirchir et al., 2015), though further research is required to substantiate this. The internal bone structure of *H. neanderthalensis* evinced a more distally loaded Mc2-5 than in recent humans. The lower radio-ulnar asymmetry in the second (Mc2) and fifth metacarpal (Mc5) heads, a flatter Mc5 base and a more laterally oriented Mc2-capitate articulation, may have restricted the pronation of the ulnar rays to the thumb during precision grips in *H. neanderthalensis* relative to *H. sapiens* (Niewoehner, 2006). This interpretation is consistent with a more distally loaded metacarpus, as inferred from the current results. Internal bone evidence for ulnar Mc1 head loading in this species is consistent with the adduction of the first McP during both human power 'squeeze' grips (Marzke et al., 1992) and pad-to-side grips, which may have been frequently employed to grip hafted tools or secure

scrapers, respectively, by *H. neanderthalensis* (Niewoehner, 2006). The fact that one *H. neanderthalensis* Mc1 (Neanderthal 1, Feldhofer 1), deviates from this pattern is not surprising, as the diversity of lithic tools thought to have been produced by this species likely required different habitual grips (Hardy et al., 2013). External morphological evidence also supports a distinction between northern and southern European *H. neanderthalensis* (Rosas et al., 2006), that may also be reflected in manual behaviours.

The diversity of Plio-Pleistocene Mc1 loading regimes indicated by the internal bone structure in *A. africanus* and the species represented by SK84, is further underlined by the Mc2-5 of several *Australopithecus* species, as might be expected for a sample that potentially comprises several fossil hominin genera. Together the present trabecular results suggest *A. africanus* loaded is metacarpus in a unique manner not found in non-human great apes or recent humans. However the relative bending stiffness of the Mc1 diaphysis in this species suggests its thumb was not significantly loaded in manipulation, as in recent humans. The *A. afarensis* Mc2, 3 and 5 is similar in trabecular structure to that of *A. africanus* Mc2-4, but is consistent with metacarpal loading in a slightly more flexed position, aligning *A. afarensis* more closely with orangutans and recent humans. However, no associated metacarpus of either *A. afarensis* or *A. africanus* has yet been found, and comparisons between different sets of metacarpals are difficult. Yet, it seems that *A. sediba* loaded its hand distinctly differently to these species. Perhaps the diverse habitual hand use of *Australopithecus* (4.2-1.98 mya) is not surprising because just as we do not know which of these hominin species made stone tools, we are equally unaware of how far each species adopted obligate bipedalism or if they did so in similar manner.

The distinct internal bone structure of *A. sediba* suggests this species habitually used its fingers in a flexed power grip posture that recruited all the fingers in a similar manner, like orangutans, without the same degree of opposition of fingers towards the thumb as in humans. *A. sediba* appears to have loaded its non-pollical McP joints in a manner similar to orangutans but need not have practised the exact same grips as orangutans. Just as the *H. neanderthalensis* and bonobo specimens

appear to load their non-pollical metacarpophalangeal (McP) joints in a similar distal manner, but likely did so in quite different grips. The present trabecular evidence in the Mc1 of *A. sediba* is consistent with an abducted opposed thumb, as in recent human forceful precision grips, and so does not support the idea that this species used manipulative power grips like the power 'squeeze' grip in this species, in which the thumb is adducted. This apparently contradictory trabecular evidence for a human-like manipulation in the Mc1 and non-human great ape-like arboreal power grasping in Mc2-5 of *A. sediba* can be understood in the context of the biomechanics of its cortical bone. The unique relative robusticity of the Mc1 in *A. sediba* was intermediate between than that of apes and humans, indicating these trabecular signals are present within a distinct mosaic morphology.

External morphological evidence supports this interpretation of mosaic manual morphology as the MH2 Mc1 is longer, relative to its non-pollical metacarpals, than recent humans and all other known fossil hominins, but it is gracile with poorly developed entheses (Kivell et al., 2011; 2018). These features are associated with an increased ability to oppose the fingers to the thumb but simultaneously a limited degree of force production relative to that seen in modern human precision grips. Similarly, the asymmetrical second metacarpal head in *A. sediba* is thought to aid thumb to index opposition (Kivell et al., 2018) yet the Mc2-capitate articulation is lateral, as in *H. neanderthalensis*, limiting Mc2 pronation in precision grips (Niewoehner, 2006; Kivell et al., 2018). The non-pollical metacarpals appear gracile possessing a medio-lateral width within the range of modern humans with uniquely large proximal bases and distal heads (Kivell et al., 2018). Unlike humans, however, fourth (Mc4) and fifth (Mc5) metacarpals are more robust than the second and third metacarpals in *A. sediba* (Wong et al., 2018; Kivell et al., 2018), a pattern more like orangutans, thought to reflect more uniform use of digits in arboreal grasping (Marchi, 2005; Rose, 1988). The Mc5 is particularly robust with well-developed entheses and a medio-distal hamate articulation suggesting a flexed abducted fifth digit in *A. sediba* that could have been forcefully opposed to the thumb. Conversely, the lack of a sellar Mc5-hamate articulation would limit lateral rotation, and thus pronation, of the fifth digit limiting opposition of the fifth digit and thumb, though

the Mc5 head is medially asymmetric in *A. sediba* (Kivell et al., 2018). Other external morphology of the MH2 hand, such as moderate curvature of the proximal phalanges, as well as flexor sheath ridges on the proximal and, uniquely, intermediate phalanges (Kivell et al., 2018), is consistent with a mosaic manual morphology in *A. sediba.*

Conclusion

The integrated cortical and trabecular structure of the great ape metacarpus analysed here is consistent with both manipulative and locomotor hand positions used by extant great apes, as well as the relative prominence of thumb use in humans. Within this context, the cortical and trabecular morphology of fossil *H. sapiens* is similar to their extant counterparts, and that of *H. neanderthalensis* appears intra-specifically variable while evincing power squeeze grips when it departs form the recent human pattern. *A. sediba* is consistent with the rest of its relatively complete mosaic postcrania. Specifically, the internal morphology of the MH2 metacarpus is consistent with non-pollical arboreal power grasping in Mc2-5 and human-like manipulation in the Mc1, which has a relative robusticity intermediate between that of non-human great apes and humans. Since trabecular and cortical bone remodel in response to their ontogenetic loading history during life, these results provide the first evidence for the use of ape-like aspects of the mosaic manual morphology in *A. sediba,* and do not support the hypothesis that these features were non-functional primitive retentions from a more arboreal ancestor. Together, this record of *in vivo* manual behaviour reveals that while the hand of *A. sediba* was used for manipulation, possibly including stone tools, it was also used for arboreal power grasping, possibly to access arboreal food sources. We do not mean to imply that this model necessarily holds for other *Australopithecus* species. Current partial evidence suggests that *A. afarensis* and *A. africanus* were using their hands in a different manner to *A. sediba* and this species may reflect but one of many transitions to obligate bipedalism in Plio-Pleistocene hominins. Nevertheless, here we present the first behavioural evidence consistent with an australopith that used its hand both for manipulation and arboreal locomotion in a distinct manner

Chapter 7
General Discussion and Conclusion

The aim of this thesis was to link observed manual behaviours to loads experienced during habitual hand postures across the great ape metacarpus, via internal bone structure, in order to then infer fossil hominin hand use. This chapter begins by addressing the methodological and inferential limitations of the current analysis, and subsequently discusses how far the methods created to produce (Chapters 3-4) internal bone structure results, and the results themselves (Chapters 4-6), achieve the thesis aim. Subsequently, the main results of the preceding chapters are discussed as a whole and in the context of other studies. Finally, the implications of the present evidence for the evolution of hominin hand use are considered.

Limitations of analysing internal bone structure

Despite recent advances in the efficiency and availability of micro-computed tomography scanning and analytical techniques, there are current limitations to the analysis of internal bone anatomy (Scherf and Tilgner, 2009; Gross et al., 2014; Sylvester and Terhune, 2017; Georgiou et al., 2018; Suhdeko et al., 2018; Stephens et al., 2018; Georgiou et al., 2019). Analysis of internal bone morphology is predicated on the accurate segmentation of the structure of interest from other material in a scanned image. In the present thesis, I developed a new technique in order to perform this segmentation in a more objective manner in a number of complex situations that arise on scanning fossil material (Chapter 3; Dunmore et al., 2018). However, there is still no 'gold standard' for the segmentation of biological material. Biological tissues, and particularly trabeculae, are non-uniform in structure and variation in scanned images can be introduced by the scanning process itself. Therefore, there is as yet, no quantitative way of assessing the quality of segmentation, as any comparison of structure necessitates an 'accurate' segmentation *a priori*. Here a phantom image of known dimensions was used to test the accuracy of segmentation carried out using the novel MIA-clustering technique (Chapter 3; Dunmore et al., 2018) but removing the scanning step completely, by creating 3D digital models with known geometric properties, may

also allow for the testing of segmentation protocols at a fraction of the cost. For example, a network of cylinders of a known thickness range, akin to the that measured in trabeculae, could be procedurally generated providing a 'gold standard' with which to test a segmentation. Other variables, such as the angles between cylinders, may also be held constant, allowing the researcher to assess what property of the structure is altering the accuracy of their segmentation. In any case, this would be a useful area of further methodological development and would provide a standard model closer to biological reality.

Another method developed in the present thesis was the morphometric mapping of the 'whole-epiphysis' data (Gross et al., 2014) to landmarks for analysis, using geometric morphometric techniques (Dunmore et al., 2019; Chapters 4-6). This technique builds on recent 'proof-of-concept' work (Sylvester and Terhune, 2017) and adds statistical rigor to trabecular analysis, while not sectioning data into subsets that may not be biologically meaningful. The major limitation of this method, however, is that it is restricted to the surface of the trabecular space. While there are good reasons to look for functional signals at the trabecular surface (Zhou et al., 2014), the 'whole-epiphysis' method has demonstrated that functional signals may lie in deeper trabecular architecture (Schilling, et al., 2014; Georgiou et al., 2018; Stephens et al., 2018). In particular, epiphyseal trabeculae are thought to direct multidirectional loads from a joint to the diaphyseal cortical bone, which lies in the main axis of a long bone (Currey , 2002). This biomechanical transfer path (Zhou et al., 2014) should, therefore, be reflected in deeper trabecular architecture, and provide a further record of how bone responds to loading. For example, since African apes knuckle-walk (Inoyue, 1994) and arboreally grasp, we might expect their trabecular structure deep to the metacarpal head, to consolidate more loading directions than in orangutans which arboreally grasp but no not knuckle-walk (Rose, 1988). However, identifying homologous units of deeper internal bone architecture for statistical analysis remains the largest challenge of these analytical techniques. Analysis of deeper trabecular structure would be a profitable area for future research.

The current limits of functional inference

While bone functional adaptation records the mechanical environment, and thus loading of great ape hand bones, relating this loading signal to a specific grip is not always straightforward. Several prehensile movements may cause similar loading at the metacarpophalangeal (McP) joints; for example, both a pad-to-side grip and a power grip with an adducted thumb, such as those frequently used on tree trunks in chimpanzees and gorillas, may both cause ulnar loading at the first McP joint (Bardo et al., 2017; Neufuss et al., 2017). The addition of evidence from multiple joints, as presented here, allows the inference of certain kinds of grips, as there is more opportunity for data to depart from the hypothesized grips' loading pattern. However, this problem is further compounded by the lack of detailed ape hand use data compared to that of humans (Marzke, 2013). Although this thesis would not have been possible without recent studies that have enhanced what we know about non-human great ape hand use (Marzke et al., 2015; Bardo et al., 2016; 2017; Neufuss et al., 2016; 2017; 2018; Samuel et al., 2018; Thompson et al., 2018), many of these studies have necessarily been undertaken with captive animals (Bardo et al., 2016; 2017; Samuel et al., 2018) and so may not reflect the diversity of wild non-human great ape hand use (Marzke et al., 2015). This problem is further compounded by the fact that wild, and especially arboreal, non-human great ape hand use is difficult to observe (Thorpe and Crompton, 2005) and even when it is, researchers must estimate the amount of force applied. Studies of knuckle-walking pressures (Wunderlich and Jungers, 2009; Matarazzo, 2013) have broadly aligned with observations of this behaviour (Tuttle, 1967; Inoyue, 1992; 1994; Samuel et al., 2018; Thompson et al., 2018), but Samuel et al. (2018) found that observed hand use during arboreal locomotion did not always match the part of the hand being loaded. Specifically, the bonobo thumb was frequently used during locomotion, but recorded little to no pressure on a force mat attached to the simulated arboreal substrate. Therefore, when manual behaviours are infrequently observed, such as the use of the first digit in orangutan locomotion (McClure et al., 2012), this certainly provides data on their kinematics but it may not provide data on their kinetics (those forces transduced in bone functional adaptation). Thus, while the

broad locomotor and manipulative grips inferred in the present work are supported by much primatological experimentation and observation, more detailed data on hand use, and actual loading, are needed before more specific grips can be inferred in the fossil hominin record.

Functional units of the great ape hand

The structure and the aims of this thesis are, necessarily, to some degree opposed. One of the key ways in which the present thesis builds upon previous work, is that it analyses the internal bone structure of all five rays of the hand. While some early work analysed several rays (Lazenby et al., 2011b), most previous studies have focused their analysis on the trabecular architecture of the third metacarpal head (Zeininger et al., 2011; Tsegai et al., 2013; Zeininger et al., 2016; Barak et al., 2017; Chirchir et al., 2017). The third metacarpal is often chosen due to its central position within the hand and regular use during most locomotor and, less so, manipulative grips (Zeininger et al., 2011; Tsegai et al., 2013). However, the third ray is thought to be somewhat insulated from radio-ulnar forces (Chirchir et al., 2017) and it is argued here, that radio-ulnar forces incurred by the hand during locomotion or manipulation are just as important in shaping internal bone structure as those in any other plane. The analysis of all five digits is necessary because habitual great ape hand postures and grips are rarely limited to a single digit (Marzke and Shackley, 1986; Marzke et al., 1992; Christel, 1993; Bardo et al., 2016; 2017; Neufuss et al., 2016; 2017; 2018). To infer hand postures, all of the rays recruited by them should therefore be analysed, and analysis should not be confined to selected rays since, relative to humans, wild non-human great ape hand use is poorly documented (Thorpe and Crompton, 2005; Neufuss et al., 2017). Conversely, there are hand postures habitually employed by apes in locomotion that do not recruit the first ray, such as knuckle-walking or hook grips (Tuttle, 1967; 1969; Wunderlich and Jungers, 2009; Rose, 1988; Sarmiento, 1988). Further, as the relatively short proportions of digits 2-5 in humans have been argued to be plesiomorphic, and shared with other primates (Drapeau and Ward, 2007; Almécija, et al., 2015), the relative size and robusticity of the first ray has become increasingly important as a morphological indicator of uniquely human grips and manipulation

(Napier, 1993; Susman, 1994; Marzke, 1998; Shrewsbury, 2003; Marchi et al., 2017). Indeed, this ray has been the sole focus of some research into internal bone architecture (Stephens et al., 2016).

The structure of this thesis reflects this paradigmatic dichotomy by analysing the non-pollical metacarpals (Mc2-5) in non-human great apes (Chapter 4) before separately analysing the first metacarpals (Mc1) of great apes and humans (Chapter 5). Indeed, when both of these regions of the hand are analysed together their interaction is reduced to a ratio (Fig. 6.6). Thus, while this thesis does consider all the rays involved in great apes postures, it does so in stages, directed by previous work and behavioural observation. That is, the structure and the aims of this work are opposed figuratively, because the first ray and second to fifth rays, are frequently opposed literally. These major functional units of the great ape hand are further broken down for analysis of each of the metacarpal heads and, since it is mobile the Mc1 base, in preceding chapters (4,5) before being considered together statistically (Chapter 6). However, as these chapters were focussed on a functional unit of the hand or the inference of fossil hominin manual behaviour, they did not consider the present results together, as a record of habitual postures adopted by the whole hand of great apes. Below the present results are discussed in this holistic context for each species, as well as unexpected emergent results that occurred during analysis.

Gorilla *as a model for the hominin hand*

As the species that knuckle-walks the most frequently in the analysed sample (Remis, 1998; Crompton et al., 2010), it is intuitive to think of gorillas as the most removed from humans in terms of habitually loaded hand postures. It is important to note that gorilla locomotion, and manipulation, has been primarily studied in mountain gorillas (Remis, 1995; Byrne et al., 2001; Neufuss et al., 2017; 2018), whereas the current sample is of western lowland gorillas, which are thought to be more arboreal (Remis, 1995; Neufuss et al., 2017). Nevertheless, the limited information available demonstrates that these two species of *Gorilla* practise similar hand postures (Sarmiento, 1994; Matarazzo, 2013; Neufuss et al., 2017; Thompson et al., 2018). Further, the level of analysis presented here is unlikely to

be confounded by these subtle differences. That is, while lowland gorillas may move differently to mountain gorillas, this difference is thought to far smaller than that between chimpanzees and gorillas (Doran, 1996; Crompton, 2010; Neufuss et al., 2017). Indeed, the general lack of internal morphology differences between *Pan* species found here, supports this idea (Chapters 4, 5 and 6).

Certainly, the hyperextended McP joint position frequently adopted by gorillas (Tuttle, 1967; 1969; Matarazzo, 2013) is very unlike that of humans, and consistent with their dorsal distribution of relative trabecular bone volume fraction (RBV/TV; Figs. 4.5 and 4.6). Yet, this distribution of higher RBV/TV is restricted to the radio-ulnar edges of the dorsal metacarpal in the third (Mc3) and fourth metacarpals (Mc4) and, unexpectedly, is concomitant with a generally ulnar trabecular concentration in the second metacarpal (Mc2), as well as a radial concentration in the fifth metacarpal (Mc5). This concentration of dorsal trabecular bone toward the mid-line of the hand is consistent with the columnar, palm-back style of knuckle-walking that usually recruits the fifth digit, frequently practised by gorillas (Inoyue, 1994; Kivell and Schmitt, 2009; Matarazzo, 2013; Thompson et al., 2018). As the palm is held consistently orthogonal to the direction of travel in this style of knuckle-walking, it likely incurs many radio-ulnar forces on contact with uneven substrates. This result not only highlights the importance of studying all of the rays recruited in different hand postures, but also the functional signal apparently engendered by radio-ulnar forces in gorillas (*contra* Chirchir et al., 2017). However, the fact this dorsal signal is restricted to the radio-ulnar edges of the metacarpal head highlights that the gorilla hand is, like all other primates (Patel, 2016), still primarily functions to flex at McP joints. While gorillas are the most terrestrial of the species studied, especially mountain gorillas (Remis, 1998), they are also arboreal, using power grips that extend the McP on larger arboreal substrates but diagonal power grips on medium size substrates, in which the McP joints are flexed and the thumb may be opposed to the rest of the rays (Neufuss et al., 2017). This dual role of McP flexion and hyperextension is reflected in the distal concentration of the RBV/TV values as well as the low degree of anisotropy (DA) across Mc2-5 heads of gorillas (Figs. 4.6 and 4.7). The latter feature is consistent with a pattern of

habitual loads primarily experienced dorsally but with an important disto-palmar component, that does not allow trabeculae to preferentially align in either direction. The importance of prehensile postures for gorilla is further underscored by a thumb that is longer relative to the other digits than in other non-human great apes (Susman, 1979; Almécija, et al., 2015). Mountain gorillas often oppose the thumb when using a diagonal power grip on medium-sized substrates, such as lianas, either keeping it in-line with the vertical axis of a substrate or wrapped around it (Neufuss, 2017). The relatively long, absolutely robust, Mc1 of mountain gorillas has a broad Mc1 head comparable to that of humans, and is shared with lowland gorillas (Hamrick and Inoyue, 1995; Galletta et al., 2018). This morphology is capable of resisting large forces during plant food processing in both species (Neufuss et al., 2018). Further, although the mountain gorilla thumb is frequently used in pad-to-side grips during precision grasping of food items, it is also used in a wide variety of manipulative postures (Neufuss et al., 2018). This is consistent with the strongest concentration of RBV/TV on the ulnar side of the gorilla Mc1 head and the lowest DA, across the subchondral Mc1 base and head, of any species studied here (Fig.5.3).

Given this evidence for a relatively long robust Mc1 (Susman, 1979; Hamrick and Inoyue, 1995; Almécija, et al., 2015) for arboreal and manipulative thumb use (Neufuss et al., 2017; 2018), it may seem surprising that the comparison of cross-sectional geometry of the gorilla hand did not differentiate it from other non-human apes. Neufuss et al. (2018) highlight that while the thumb of gorillas is relatively larger than other non-human great apes, it is likely still not capable of the forces of a human hand. However, the fact that gorillas are not significantly different from other non-human apes in the ratio of average area moment of inertia is interesting (Fig. 6.6). Marchi (2005) investigated the cross-sectional geometry of Mc2-5 in gorillas, and found that they had lower polar moment of area relative to chimpanzees, once this variable was size corrected. Almécija et al. (2015) demonstrated that the intrinsic and extrinsic hand proportions of gorillas were more similar to humans than chimpanzees, and interpreted this as a more plesiomorphic condition. However, when scaled by ulnar length, gorilla metacarpals

are significantly longer than in humans (Drapeau and Ward, 2007) and could be interpreted as more derived than in humans but less so than in chimpanzees. The disparity between these two results is likely a result of a significantly longer thumb in gorillas relative to chimpanzees or orangutans (Almécija et al., 2015), which also has a broader Mc1 head (Hamrick and Inouye, 1995). If this is the case, then the ratio of Mc1 to Mc2-5 diaphyseal average area moments of inertia found here (Fig. 6.6), may be the result of absolutely stiffer metacarpals in both of these functional units (Mc1 and Mc2-5) of the gorilla hand, relative to those of chimpanzees (Marchi et al., 2005; Hamrick and Inouye, 1995). That is, the ratio of gorillas is similar to other non-human great apes as both Mc1 and Mc2-5 are more robust than in these species. However, this absolutely robust Mc1 does not imply gorillas have the same manipulative abilities, nor manual proportions, as humans and present evidence cannot distinguish between the relative roles of locomotion and manipulation in the putative aetiology of internal metacarpal architecture. Rather, this confluence of Mc1 and Mc2-5 morphology and observed behaviours suggest that locomotor and manipulative traits may have both influence the mophrology the gorilla hand. This is important in the context of human evolution since fossil hominins often preserve a mosaic of locomotor and manipulative traits not seen in modern humans (Chapters 1 and 6; Tocheri, 2008; Kimbel and Delezene, 2009; Kivell, 2011; 2015). Indeed, the co-occurrence of knuckle-walking and manipulative abilities within the hand, may make the gorilla a useful extant model for some questions relating to the evolution of human manipulation and terrestrial bipedalism. Complex manipulation and tool-use have been linked to terrestrial behaviour in general (Meulman et al., 2012; Heldstab et al., 2016). In any case, the internal structure of gorilla metacarpals analysed here is consistent with, and builds on, previous morphological and primatological studies of their manual behaviour, highlighting that they are not simply knuckle-walkers or the most functionally removed from modern humans in terms of great ape hand use.

Pongo *and trabecular anisotropy*

As the least terrestrial of the non-human great apes analysed, orangutans present a very distinct pattern of internal bone architecture consistent with its primarily arboreal locomotion characterised by quadrumanous orthograde positional behaviour (Cant, 1987; Sugardjito and Cant, 1994; Thorpe and Crompton, 2006; Manduell et al., 2011). The hook and double-locked grips thought to be practised by orangutans (Rose,1988; Sarmiento, 1988) have not yet been systematically observed in the wild due to the difficulties of observing these grips in the arboreal milieu (Thorpe and Crompton, 2005), though hook grips have been observed in captivity (Alexander, 1994). In both grips, the McP joints in rays 2-5 are all either strongly flexed or extended (Rose, 1988; Sarmiento, 1988) which is consistent with the uniformly disto-palmar distribution of RBV/TV across the subchondral surfaces of the Mc2-5 heads (Fig. 4.6). Although it should be noted the second metacarpal (Mc2) maintains a significantly more ulno-distal concentration of RBV/TV in orangutans than in Mc3-5 (Fig. 4.13). The uniformly high DA across the metacarpal heads of orangutans is consistent with a lower range of habitual McP joint motion than is found in other non-human great apes, that all knuckle-walk and thus hyperextend these joints (Napier, 1960; Tuttle, 1969; 1969b; Rose, 1988; Doran, 1996). Certainly the complexity of arboreal substrates has led authors to assume a variety McP positions are required to effectively grasp them, engendering a variety of loads and thus low DA (Tsegai et al., 2013; Chapter 4). Yet, in each case the branch is gripped with a flexed or extended McP in accordance with the present results. It could be argued that as DA is dependent on trabecular number and a lower number of trabeculae can necessarily be aligned in fewer directions, these results may reflect systemic, or otherwise non-functional, lower trabecular number in this genus rather than a functional signal. However, orangutan DA values and indeed RBV/TV values, in the Mc1 head and base are very similar to chimpanzees and bonobos (Fig. 5.3) as well as lower than those seen in Mc2-5 in the same species. This suggests that either this putative systemic signal is either restricted to Mc2-5 or that high DA in these digits is indeed a functional signal. As higher RBV/TV values appear to have a similar spatial distribution as that of lower DA values in the

orangutan Mc1 (Fig. 5.3), it is likely that they are the result of a low number of trabeculae that can be aligned in fewer directions. Conversely high DA values in Mc2-5 heads (Fig. 4.7) are not distributed in the same manner as either absolute or relative trabecular bone volume fraction value distributions (Fig. 4.5 and 4.6). Since there is no reason, *a priori*, why trabecular thickness should be strongly inversely proportional to trabecular number in a linear relationship, RBV/TV is a reasonable proxy for trabecular number. Therefore, high DA in orangutan Mc2-5 heads is likely a functional signal when the whole hand, including the Mc1, is considered.

Pan *and the biomechanical significance of the non-human great ape thumb*

Chimpanzees and bonobos possess a broadly similar locomotor repertoire characterised by arboreal and terrestrial knuckle-walking (Doran and Hunt, 1994; Carlson et al., 2006) as well as vertical climbing, arboreal scrambling and suspensory behaviour (Hunt, 1991; Marzke and Wullstein, 1996; Neufuss et al., 2017). Both chimpanzees and bonobos are thought to be more arboreal than gorillas (Remis, 1995; Doran, 1996; Thorpe and Crompton, 2006). Chimpanzees use a less radially deviated wrist compared to gorillas during diagonal power grips (Neufuss et al., 2017), while captive bonobos use similar arboreal grips (Samuel et al., 2018). The internal structure found here is consistent with the very similar locomotor modes employed by these two species. Not only is the concentration of high RBV/TV values in Mc2-5 in a less palmar position than in orangutans, but it extends less dorsally than in gorillas, consistent with a more varied locomotor regime, including arboreal grasping and knuckle-walking, in both chimpanzees and bonobos relative to other non-human great apes (Figs. 4.6 and 4.10).

Chimpanzees tend to use both palm-in and palm-back knuckle-walking postures that differ from those of gorillas (Tuttle, 1969; Inouye, 1994; Matarazzo, 2013). During palm-back knuckle-walking, chimpanzees tend to extend their third digit in front of the others and often do not recruit the fifth digit (Inoyue, 1994; Wunderlich and Jungers, 2009; Matarazzo, 2013). During palm-in knuckle-walking, chimpanzees roll their digits in ulno-radial succession, though the fifth digit is again frequently

not recruited (Inoyue, 1994; Wunderlich and Jungers, 2009; Matarazzo, 2013). The varied digit use in chimpanzee knuckle-walking appears to be reflected in the significantly more dorsal, though still primarily distal, concentration of RBV/TV in Mc3-4 and a more palmar concentration in Mc2 and 5. The extension of Mc3 past the other joints in palm-back knuckle-walking and the lack of use of the fifth digit in this hyperextended posture match these patterns and Mc4 is also thought to be heavily loaded in this type of locomotion (Tuttle, 1969; Tuttle and Basmajian, 1978). However, as the peak substrate reaction forces in chimpanzee knuckle-walking are borne on Mc2 (Wunderlich and Jungers, 2009; Matarazzo, 2013), it may be expected that this digit has a more dorsal concentration of the RBV/TV. Conversely, larger captive chimpanzees used their second digit significantly less often than gorillas of equivalent size during captive terrestrial knuckle-walking (Inouye, 1994).

Although still relatively poorly studied, bonobos do not roll their hand during arboreal knuckle-walking and more frequently recruit the fifth digit than in chimpanzees (Samuel et al., 2018). In Mc2-5, the uniformly disto-dorsal pattern of RBV/TV distribution appears to reflect this lack of differential digit use. Bonobos are also thought to be more arboreal than chimpanzees (Alison and Badrian, 1977; Susman et al., 1980; Susman, 1984), although this may be an artefact of the fact that no bonobo community has yet been fully habituated to humans, and so flee into the trees when observers are present (Hunt, 2016). While absence of evidence is not evidence of absence, the current internal bone morphology results do not strongly support bonobos using their hands for arboreal grasping more frequently than chimpanzees. In either case, bonobos have been shown to be more palmigrade in the trees than chimpanzees (Doran, 1993; Doran and Hunt, 1994; Crompton et al., 2010) and this seems to be reflected in significantly higher RBV/TV values in the palmar aspect for the subchondral Mc3 (Fig. 4.10). This localised concentration is consistent with either a more habitually flexed third digit in bonobos, which seems unlikely given its central position in the hand, or direct loading of this surface form the substrate during palmigrady.

In general, the present results demonstrate that the trabecular structure of the subchondral metacarpus of both chimpanzees and bonobos is remarkably similar

and not statistically distinguishable, overall, across any epiphyseal surface for DA or RBV/TV, except for the DA of the Mc1 base (Figs. 4.6, 4.7, 4.10, 4.11, 5.3, 5.4 and 5.5). Neither of these species are significantly different in RBV/TV values when Mc2-5, or both ends of the Mc1, are taken as a whole (Figs. 6.4, 6.5). This is consistent with their similar locomotion but is somewhat at odds with what is known about their manipulative abilities. The manipulative abilities of chimpanzees are well-studied (Christel, 1993; Marzke and Wullstein, 1996; Jones-Engels and Bard, 1996; Pouydebat et al., 2011; Marzke et al., 2015) compared to bonobos, however, both species are known to use frequent pad-to-side grips, in which the thumb is adducted (Marzke and Wullstein, 1996; Christel et al., 1998; Bardo et al., 2016; Neufuss et al., 2016) and diagonal power grips in which the thumb may or may not be loaded (Marzke and Wullstein, 1996; Neufuss et al., 2017; Samuel et al., 2018). The slightly higher RBV/TV, and lower DA, values in the ulnar Mc1 head of these species are consistent with these grips (Fig. 5.3). However, orangutans also share this distribution of internal bone architecture with chimpanzees and bonobos, yet have not been thought to frequently use diagonal power grips (Sarmiento, 1988; Rose, 1988) and the importance of their thumb during arboreal grips is debatable (Rose, 1988; McClure et al., 2012).

Orangutans frequently manipulate objects with their mouth (Bardo et al., 2017) and, with the longest finger-to-thumb ratio among hominids, are at the greatest disadvantage when opposing the fingers to the thumb (Almécija et al., 2015; Feix et al., 2016). Drapeau (2015) theorised that the ulnar torsion of the orangutan Mc1 shaft allowed it to more effectively oppose the relatively immobile palm, due to a lack of effective opposition with the fingers. Given that the orangutan Mc1 trabecular signal is not statistically different from either bonobos or chimpanzees when the head and base are considered separately (Figs. 5.3, 5.4 and 5.5), or together (Fig. 6.5), it initially appears to be inconsistent with differences observed in habitual thumb use in these species (Bardo et al., 2017). However, chimpanzees, bonobos and orangutans all employ pad-to-side grips, associated with high ulnar RBV/TV in the Mc1 head, when they use the thumb to manipulate objects (Marzke et al., 2015; Bardo et al., 2017). Therefore, it may be that observed intergeneric

differences in thumb use may be primarily of frequency. That is, while chimpanzees and bonobos possess a more dexterous thumb and manipulate objects with it more often, orangutans perform similar movements of the Mc1 when they use it in manipulation. The distribution of trabeculae measured by RBV/TV here thus accurately records these similar joint positions, but does not reflect the difference in magnitude or frequency of loading presumably engendered by observed differences in thumb use between chimpanzees, bonobos, and orangutans (Bardo et al., 2017). Preliminary analysis of species average absolute subarticular trabecular volume fractions (BV/TV) in the Mc1 supports this interpretation, as orangutans appear to show lower values than either chimpanzees or bonobos. Gorillas, conversely, have both significantly more regionalised RBV/TV distribution and the highest BV/TV of all the non-human great apes, consistent with their observed manipulative behaviour and larger Mc1 relative to all other non-human great apes (Hammrick and Inoyue, 1995; Neufuss et al., 2018). Thus this interpretation of chimpanzee, bonobo and orangutan internal Mc1 morphology is consistent with external morphology, observed hand use and the current trabecular results. This suggests that the thumb of chimpanzees, bonobos and orangutans is likely used in a similar position, if to differing extents, relative to the significantly different Mc1 architecture of gorillas and recent humans. Combined with the lack of trabecular bone in the Mc1 head implied by the coincidence of lower DA and higher RBV/TV values, this trabecular distribution suggests a relative lack of use, or at least a biomechanically less important role, of the first digit in chimpanzees, bonobos, and especially orangutans, relative to gorillas. The subtle differences in trabecular architecture between chimpanzees or bonobos and orangutans, not clearly resolved by measuring their distribution with RBV/TV, further underlines that this measure will not clearly distinguish between differences in the magnitude or frequency of joint loading in fossil hominins. This example therefore emphasizes the need to consider external morphology, observed extant behaviour and all available skeletal elements when inferring fossil hominin hand use.

The significance of dorsal ridges on the metacarpal head

Considering all the trabecular structure of the non-human apes together provides unexpected insights into the dorsal ridge on metacarpal heads. Perhaps the simplest explanation for higher DA in the dorsal extreme of Mc2-5 in African great apes (Fig. 4.7) would be that it occurs directly beneath the dorsal ridge and therefore reflects alignment of local trabeculae that have remodelled to better transmit a dorsal load incurred by a hyperextended McP during knuckle-walking. However, as discussed in Chapter 1, these dorsal ridges are too small to act as 'bony stops' during McP hyperextension, which was the functional hypothesis traditionally invoked to explain their existence (Tuttle, 1969; Richmond et al., 2001). The forces at the McP joint during locomotion would be so great as to be injurious to the joint (Lovejoy et al., 2009; Simpson et al., 2018). Instead it has been proposed that the epiphyseal mass of the metacarpal head is displaced palmarly, prior to or during ossification, due to the loads incurred at the McP joint during knuckle-walking (Simpson et al., 2018). This palmar movement of the epiphyseal mass would explain more uniformly oriented trabeculae at the growth plate, beneath the dorsal ridge. This higher DA signal would then be the result of one end of the trabeculae near, or at, the growth plate between the metaphysis and epiphysis, moving palmarly with the whole epiphyseal mass. Therefore, as argued for the dorsal ridge, this internal structure can then be seen as partly a functional and partly developmental signal. However, mountain gorillas and chimpanzees are more arboreal in their infancy and employ palmigrade quadrupedalism terrestrially, rather than knuckle-walking, until 2.5-4 or 6 years of age, respectively (Doran, 1997). Therefore, while there may be a period where the metacarpal head is not fully fused and knuckle-walking is acquired, it seems counter-intuitive that the adult form of the metacarpal is shaped early in ontogeny by a behaviour that is more frequently practised later in ontogeny.

Indeed, the presence of this high DA in the dorsal metacarpal head of orangutans, given that they do not knuckle-walk, suggests that either this internal bone signal is divorced from the overlying cortical bone's shape, or that the palmar displacement of the cartilaginous epiphyseal mass is not the result of knuckle-walking behaviour.

As it is unlikely that internal bone structure is independent of its over-lying joint, the high dorsal DA at the fused remnant of the growth plate found in all great apes is indeed likely the result of palmar displacement of the cartilaginous epiphyseal mass (Simpson et al., 2018). However, since the less pronounced "bipartite extensions of the articular surface" in orangutans (Susman, 1979, p.220) and dorsal ridges of African apes both overlie a locally, highly organised trabecular architecture, that these morphologies are unlikely the result of knuckle-walking in young non-human great apes. Instead, it is here argued that this putative palmar displacement, common to all great apes, may be purely developmental and mostly genetically controlled, or the result of strong flexion at the McP joint, such as that employed in arboreal grasping, a behaviour common to all immature non-human great apes (Doran, 1997; Thorpe and Crompton, 2006). Strong digital flexion may 'pull' the epiphyseal mass forward rather than knuckle-walking behaviour 'pushing' it forward, in immature non-human great apes. Whatever the reason, the presence of a dorsally high DA in orangutans likely offers more of a developmental signal than a functional one, and provides further evidence that the dorsal ridge of African ape metacarpals is unlikely to be the result of adult knuckle-walking.

Human grips and the role of the fifth digit

The recent human hands analysed here present the most distinct internal bone architecture of all species sampled, almost assuredly due to their primarily manipulative mode of use. The diaphysis of human Mc1 is consistently better at resisting loads in the radio-ulnar plane and has a higher overall bending rigidity relative to Mc2-5 (Fig. 6.6). This has been previously reported in humans via a different measure (Wong et al., 2018) but the present results demonstrate that this inter-ray difference in average area moment of inertia is significantly larger than in other great apes (Fig. 6.6). This biomechanically robust thumb, along with features of the human wrist (Marzke, 1997; Tocheri, 2007), likely resists strong pollical forces incurred by the human thumb during precision grips and manipulation (Cooney and Chao, 1977; Marzke and Shackley, 1986; Rolian et al., 2011; Key and Dunmore, 2015; Williams-Hatala et al., 2018). The trabecular architecture of the thumb supports this functional interpretation of the cortical evidence, with a

concentration of high RBV/TV values radially in the Mc1 head and radio-palmarly in the Mc1 base, as well as high DA in the Mc1 head. Analysed separately (Figs. 5.3-5.7) or combined (Fig. 6.5), the trabeculae of these subchondral surfaces are significantly different from those of other great apes. The human pattern is consistent with a Mc1 that is habitually, and likely forcefully, abducted at both the McP and trapeziometacarpal (TMc) joints. This trabecular distribution is consistent with the abduction, ulnar rotation in the axial plane, and flexion of the TMc, a complex motion that is necessary for full pad-to-pad opposition of the fingers, collectively termed the 'screw-home' mechanism (Halilaj et al., 2014; D'Agostino et al., 2017). This radial pattern of RBV/TV at both joints has also been found in a more expansive sample of recent humans (Stephens et al., 2018). The first McP joint is less well-investigated than the TMc in the literature but early work described this joint as abducted in human precision grips (Napier, 1956). A recent functional interpretation of a similar trabecular pattern includes the wide-abduction of the thumb (Stephens et al., 2018), which would be facilitated by abduction at the McP and TMc joints. The significantly higher DA in the human Mc1 head relative to other great apes may seem counter-intuitive given the highly mobile human thumb and the broad Mc1 head (Susman, 1994). However, humans can extend the first McP while flexing the distal phalanx due to distinct flexor pollicis longus and extensor pollicis brevis muscles (Marzke et al., 1998; Hammrick et al., 1998; Diogo et al., 2012). The high DA may reflect a combination of a relatively small number of forceful movements in the human thumb during multiple prehensile grasps over a relatively small range of motion at the McP. Indeed, where flexion at the first McP joint is limited to 90° in gorillas, orangutans and most chimpanzees by the thenar eminence (Tuttle, 1969b), clinical data suggest modern humans are limited to just 70° (Barakat, et al., 2013), likely also as a result of the relatively large human thenar eminence.

Moving beyond the thumb, the asymmetric inclination of the Mc2 and Mc5 heads towards the midline of the palm has been suggested to aid the opposition of the fingers to the thumb, and grasped objects, in humans (Marzke, 1997; Kivell, 2015). Further, the hypothenar eminence of the human hand and associated powerful

flexion of the fifth digit are thought to be crucial for effective power 'squeeze' grips (Marzke et al., 1992). The present trabecular evidence supports these functional interpretations of external metacarpal anatomy. Like orangutans, high RBV/TV is concentrated palmarly in the Mc2-5 heads of recent humans but maintains a significantly different overall subchondral trabecular pattern (Fig. 6.4). This difference lies in the ulnar skew of higher RBV/TV values of Mc2-4, particularly Mc2, and the palmarly extended RBV/TV distribution in the human Mc5. This pattern is consistent with pronation of the second digit, as well as supination and pronounced ulnar deviation of the fifth digit, during manipulation (Landsmeer,1955; 1962; Lewis 1977; Marzke, 1997). It is also consistent with strong flexion of the fifth digit in power 'squeeze' grips (Marzke et al., 1992). This result highlights the role of non-pollical digits in human manipulation and warrants further investigation.

Implications for the evolution of the hominin hand use

The evolution of hominin hand use has traditionally been simplified to the development of a dexterous modern human hand, capable of precision grips and tool-production or use, from a more ape-like hand that was adept at locomotor power grips (Napier, 1993). More recent work and fossil discoveries have argued that the modern human, and indeed basal hominin hand, is far more plesiomorphic than previously thought, and that the few living non-human great apes possess more apomorphic hand morphology (Drapeau and Ward, 2007; Lovejoy et al., 2009; Almécija et al., 2015). This view of a primitive human hand was actually articulated much earlier (Wood-Jones, 1916) but a focus on the human thumb, manipulation and stone tools is predominant in the hominin hand literature (Napier, 1962; Marzke and Shackley, 1986; Susman, 1994; Marzke et al., 1998; Shrewsbury, 2003; Tocheri, 2005; Rolian et al., 2011; Williams et al., 2012; Key and Dunmore, 2015; Harmand, 2015; Skinner et al., 2015; Key et al., 2018). This long-standing focus is perhaps unsurprising, since stone tools offer the only surviving direct evidence of early hominin manual behaviour and were linked closely associated with the first Plio-Pleistocene member of our genus discovered, *Homo habilis* (Napier, 1962b). Further, the robust nature of the human thumb is unique among great apes (Tocheri, 2008; Marzke, 2013), as is the use of the human hand primarily for

manipulation rather than locomotion. Therefore, the derived human hand has been historically linked to tool use (Darwin, 1871) and consequently was intimately linked with the defining trait of hominini, bipedalism. However, the current results argue for a more nuanced, mosaic and piecemeal view of hominin hand evolution, comprising a diversity of hand use that included arboreal locomotion.

The present results agree with the interpretation of several more recently discovered fossils, including *Homo floresiensis* (Tocheri et al., 2007b), *Australopithecus sediba* (Kivell et al., 2011) and *Homo naledi* (Kivell et al., 2015), that evidence mosaic hand morphology. That is, the internal bone structure of the fossil *Homo sapiens, Homo neanderthalensis, Australopithecus africanus, Australopithecus afarensis* and *Australopithecus sediba* do not evince a linear progression of increasingly more manipulative hand, or more modern human-like thumb use, with time in the hominin lineage. Rather, this evidence is more consistent with an adaptive radiation (Foley, 2005) of hominin hand use that was not always completely removed from the requirements of locomotion, or solely subject to selection pressures of modern human-like manipulation. For example, *H. neanderthalensis* was the last hominin species, well-represented in the current archaeological record to become extinct (some 30 thousand years ago; Stringer and Davies, 2001). The two individuals of this species for which the complete, associated trabecular architecture could be analysed (El Sidrón and Kebara 2) do not show a distribution of trabecular bone consistent with either fossil or recent *Homo sapiens* (Figs. 6.4 and 6.5). Instead, these specimens demonstrate a trabecular architecture consistent with disto-palmar loading of Mc2-5 and unique combination of radio-palmar loading of Mc1 base and ulno-central loading of the Mc1 head (Fig. 6.8). While it is difficult to equate this loading with specific grips, as this pattern does not appear in any extant species studied, it is consistent with power 'squeeze' grips (Marzke et al., 1992), thought to be used by this species when using hafted tools or scrapers (Anderson-Gerfaud, 1990; Niewoehner, 2006). Of course, this does not mean *H. neanderthalensis* individuals were incapable of modern human precision grips, but rather indicates that they appeared to habitually load their hand in different ways. Certainly, the independent evidence

that at least some *H. neanderthalensis* individuals used their teeth in manipulation (Fox and Frayer, 1997) and that their lithic tool-kit was somewhat distinct from that of *H. sapiens,* supports this interpretation (Hardy and Moncel, 2011). Indeed, the Mc1 of Feldhofer (Neanderthal) 1 has a modern human-like pattern, indicating that this individual did in engage in modern human-like loading of their thumb. This does not invalidate the previous interpretation as trabecular architecture is a plastic trait and substantial variation in *H. neanderthalensis* tool kits implies variation in their hand use (Hardy and Moncel, 2011). Further, some researchers have pointed to a distinction between Northern and Southern European *H. neanderthalensis* (Rosas et al., 2006), which may be reflected in different tool kits and thus habitual hand use. Therefore, the present evidence from the whole metacarpus indicates that the advent of modern human manipulation appears to be rather recent, as the fossil *H. sapiens* studied here are 12-23 thousand years old (Formicola et al., 1990; Hershkovitz et al., 1995; Bisson et al., 1996) and have a similar trabecular structure as that of recent *H. sapiens* (Figs. 6.4 and 6.5). Even though the hands of fossil *H. neanderthalensis* and *H. sapiens* are ostensibly similar (Niewoehner, 2006), the present trabecular results demonstrate a diversity of Upper Palaeolithic hominin hand use. This inter- and intra-species variability in internal bone structure in late surviving fossil hominins underscores the fact that the evolution of modern human manipulation was not a linear progression with time.

The present evidence for hand use in *Australopithecus* species also supports the idea of several adaptive radiations of hominin hand use. Though it must, again, be stressed that the present samples of *A. africanus* and *A. afarensis* are chimeric and incomplete, the internal structure that is available from these bones evinces very different habitual hand loading to that of the geologically younger *A. sediba* (Kimbel et al., 2006; Pickering et al, 2011; Granger et al., 2015). Only in *A. sediba* does the trabecular pattern evince orangutan-like arboreal grasping in Mc2-5 and human-like manipulation in the Mc1, which itself is more robust than in apes but less so than in recent humans (Figs. 6.4, 6.5, 6.6). This diversity in habitual hand loading is made even more intriguing by the fact that SK 84, attributed to either early *Homo* or *Paranthropus robustus,* and geographically as well as temporally proximate to *A.*

sediba (Trinkhaus and Long, 1990), demonstrates trabecular structure consistent with thumb use in non-human great apes (Fig. 6.5). Therefore not only does the present evidence argue for diversity of habitually loaded hand postures and grips in *Australopithecus*, which do not necessarily become more human-like in younger fossils, but also that this diversity extends to other contemporaneous hominin genera.

The internal bone structure of the MH2 hand is perhaps the most exciting finding of the present thesis. Not only do the trabecular and cortical signals of this associated metacarpus present a similar functional signal of mosaic hand use, this mosaic signal is replicated thoughout MH2 skeleton and *A. sediba* hypodigm (Berger et al., 2010; Berger, 2013). As internal bone architecture is plastic and these results are, at least in part, a record of loads experienced *in vivo*, this evidence reveals what MH2 actually did with its hands rather than their capabilities. These results, therefore, represent the first evidence for the use of ape-like arboreal features in *Australopithecus* postcrania, and do not support the hypothesis that these were non-mechanically functional retentions from a more arboreal ancestor (*contra* Latimer, 1991). As discussed in Chapter 6, this does not necessarily mean that arboreal features in other australopith species were also functionally significant, but it raises the probability that they were to some extent. While caution must be exercised when drawing inferences from the internal bone structure of incomplete, chimeric metacarpi, the present results do allow for some discussion of hand use in *Australopithecus afarensis* and *Australopithecus africanus.* The *A. afarensis* Mc2-3 and Mc5 have a combined trabecular distribution most similar to orangutans but fall on the opposite side of the orangutan range and much closer to recent humans relative to *A. sediba* (Fig. 6.4c). This combination tentatively suggests that the Mc2-5 of *A. afarensis* were more adapted for manipulation, as has been argued based on their hand proportions (Alba et al., 2003), than in *A. sediba.* Unlike *A. afarensis* and *A. sediba*, the *A. africanus* Mc2-4 analysed here displays a distribution of RBV/TV closer to that of bonobos, as well as an Mc1 distribution that clusters near *H. neanderthalensis* (Figs. 6.4b and 6.5). It may be tempting to ascribe this *A. africanus* pattern to manipulative power grips such as those practised by *H. neanderthalensis*,

as discussed above. However, the cortical cross-sectional geometry of this chimeric specimen is similar to that of all non-human great apes studied and suggests that the thumb was less biomechanically important in *A. africanus* hand use, a finding that is supported by relative narrow Mc1 in this species (Green and Gordon, 2008). Conversely, as STW418 has the most distinctive Mc1 trabecular pattern in the whole sample suggesting *A. africanus* used its first digit in a manner unlike that of any of the extant species studied. It seems parsimonious to then ascribe the Mc2-4 trabecular pattern found here to arboreal power grips in *A. africanus* rather than to manipulation (*contra* Skinner et al., 2015), an inference supported by its more ape-like limb proportions compared with *A. afarensis* (Green et al., 2007). Though again, it must be stressed that these inferences are tentative, the internal bone architecture of *A. sediba* found here is distinct from that known of *A. afarensis* and *A. africanus*. This *A. sediba* pattern has implications for the evolution of hominin manipulation and bipedalism, as it can now be demonstrated that at least one hominin used its hands for both manipulation and locomotion. Therefore, the advent of enhanced hominin manipulation need not have succeeded the development of obligate bipedalism in our lineage but could have been concomitant with it.

Conclusion

The initial goal of this thesis was to establish a link between observed habitual manual behaviours and internal bone structure across the great ape metacarpus. To achieve this goal, I developed two novel methodologies, MIA-clustering segmentation (Dunmore et al., 2018; Chapter 3) and geometric morphometric mapping of 'whole-epiphysis' trabecular data (Dunmore et al., 2019; Chapters 4-6). These methods allowed for the statistical analysis of subchondral trabecular patterns in great apes (Chapters 4-5). The distribution of relative trabecular volume and degree of anisotropy in these species were largely statistically distinct and reflected hand postures known, or thought, to be habitually employed during great ape manipulation and locomotion. Further, the examination of all five metacarpals offered the first holistic analysis of hominid hand internal bone structure and yielded novel, and at times unexpected, results that were also explicable in terms extant great ape hand use. This extant context then allowed for the inference of habitually employed hand postures and grips in fossil hominins (Chapter 6). These results indicated that the evolution of modern human-like hand use was not a linear progression but rather an adaptive radiation, or possibly several, within the hominin clade. Despite intra-specific variation, results indicated that *Homo neanderthalensis* likely used different habitual grips to those of fossil and recent *Homo sapiens.* Further evidence for hand use diversity was found in species of *Australopithecus*. Finally, the present results indicate, for the first time, that the ape-like arboreally-advantageous aspects of manual morphology in *Australopithecus sediba*, were indeed functional rather than simply a retention from a more arboreal ancestor. These results have implications for the evolution of hominin manipulation, the development of hominin tool use and the adoption of obligate bipedalism in our lineage.

Current limitations and future directions

The limitations discussed at the start of this chapter, pertaining to the analysis of internal bone structure and the inference of specific grips, are limitations of kind, that will require novel techniques to overcome. However, there are aspects of the present work that are subject to limitations of degree, which simply require more resources to surmount. Perhaps the most obvious of the latter type of limitations is sample size. The sample of associated great ape metacarpi analysed here is the largest known to myself, but still represents a small fraction of those potentially available in collections. While it is difficult to find non-pathological adult associated metacarpi, that have not been artificially articulated, an expansion of the current sample size will likely reveal more patterns of intra- and inter-species variability. The addition of relatively rare mountain gorilla (*Gorilla gorilla beringei*) metacarpi to the sample would be of particular value, as functional inference of grips for this genus is based on behavioural accounts of this subspecies. Smaller metacarpi such as those of platyrrhines, especially those of *Ateles,* would be interesting to add to the current sample but as they preserve few trabeculae, due to allometry, comparisons of them with great ape metacarpals using the present methods must be attempted with caution. Larger monkeys, belonging to genera such as *Mandrillus* and *Theropithecus*, would be more comparable and may yield additional insights into internal bone architectural response to the demands of digitigrady and manipulation. Further, outgroups that practise similar locomotion to non-human great apes, such as knuckle-walking *Myrmecophaga*, would be good case studies with which to interpret the internal bone architecture of non-human great ape metacarpals. Even within great apes the quantification of internal bone structure between adjacent elements, such as the proximal phalanges and carpus with respect to the metacarpus, may help us interpret force distributions through the hand during manual behaviours. This data would be of great use in finite element studies that seek to reverse engineer some of these forces *in silico*. Indeed, the analysis of internal bone morphological integration between adjacent elements, may allow functional inferences to be made with further clarity and elucidate the extent of mechanical interplay between external shape, cortical bone and

trabecular structure. The opportunity to further understand the biomechanics of bone, primate hand use and fossil hominin ecomorphology, makes further research in the present vein an exciting prospect.

References

Adams, D. C., L., C. M., Kaliontzopoulou, A., & Sherratt, E. (2017). Geomorph: Software for geometric morphometric analyses. *R package version 3.0.5.*

Alba, D. M., Moyà-Solà, S., & Köhler, M. (2003). Morphological affinities of the Australopithecus afarensis hand on the basis of manual proportions and relative thumb length. *Journal of Human Evolution, 44*(2), 225-254.

Albrecht, G. H., Gelvin, B. R., & Miller, J. M. (2003). The hierarchy of intraspecific craniometric variation in gorillas: A population-thinking approach with implications for fossil species recognition studies. In A. B. Taylor & M. Goldsmith (Eds.), *Gorilla Biology: A Multidisciplinary Perspective* (pp. 62-103). Cambridge: Cambridge University Press.

Alexander, C. (1994). Utilisation of joint movement range in arboreal primates compared with human subjects: an evolutionary frame for primary osteoarthritis. *Annals of the Rheumatic Diseases, 53*, 720-725.

Alexander, R. M., Jayes, A. S., Maloiy, G. M., & Wathuta, E. M. (1979). Allometry of the limb bones of mammals from shrews (Sorex) to elephant (Loxodonta). *Journal of Zoology, 189*(3), 305-314.

Alison, F., & Badrian, N. (1977). Pygmy chimpanzees. *Oryx, 13*, 463-468.

Allen, M. R., & Burr, D. B. (2014). Bone modeling and remodeling. In D. B. Burr& M. R. Allen (Eds)., *Basic and Applied Bone Biology* (pp. 75-90). London: Academic Press.

Almécija, S., & Alba, D. M. (2014). On manual proportions and pad-to-pad precision grasping in Australopithecus afarensis. *Journal of Human Evolution, 73*, 88-92.

Almécija, S., Moyà-Solà, S., & Alba, D. M. (2010). Early origin for human-like precision grasping: a comparative study of pollical distal phalanges in fossil hominins. *PLoS One, 5*(7), e11727.

Almécija, S., Smaers, J. B., & Jungers, W. L. (2015). The evolution of human and ape hand proportions. *Nature Communications, 6*.

Almécija, S., Wallace, I. J., Judex, S., Alba, D. M., & Moyà-Solà, S. (2015b). Comment on "Human-like hand use in Australopithecus africanus". *Science, 348*(6239), 1101-1102.

Alves Cardoso, F., & Henderson, C. Y. (2010). Enthesopathy formation in the humerus: Data from known age-at-death and known occupation skeletal collections. *American Journal of Physical Anthropology, 141*(4), 550-560.

Amling, M., Herden, S., Pösl, M., Hahn, M., Ritzel, H., & Delling, G. (1996). Heterogeneity of the skeleton: comparison of the trabecular microarchitecture of the spine, the iliac crest, the femur, and the calcaneus. *Journal of Bone and Mineral Research, 11*(1), 36-45.

Amson, E., Arnold, P., van Heteren, A. H., Canoville, A., & Nyakatura, J. A. (2017). Trabecular architecture in the forelimb epiphyses of extant xenarthrans (Mammalia). *Frontiers in Zoology, 14*(52), 1-17.

Anderson, M. J. (2017). Permutational multivariate analysis of variance (PERMANOVA). *Wiley StatsRef: Statistics Reference Online*, 1-15. doi:10.1002/9781118445112.stat07841

Anderson-Gerfaud, P. (1990). Aspects of behavior in the Middle Paleolithic: Functional analysis of stone tools from Southwest France. In P. Mellars (Ed.), *The Emergence of Modern Humans: An Archaeological Perspective* (pp. 389-418). Edinburgh: Edinburgh University Press.

Ayachit, U. (2015). *The paraview guide: a parallel visualization application.* New York: Kitware, Inc.

Barak, M. M., Lieberman, D. E., & Hublin, J. J. (2011). A Wolff in sheep's clothing: trabecular bone adaptation in response to changes in joint loading orientation. *Bone, 49*(6), 1141-1151.

Barak, M. M., Lieberman, D. E., & Hublin, J. J. (2013). Of mice, rats and men: Trabecular bone architecture in mammals scales to body mass with negative allometry. *Journal of Structural Biology, 183*(2), 123-131.

Barak, M. M., Lieberman, D. E., Raichlen, D., Pontzer, H., Warrener, A. G., & Hublin, J. J. (2013b). Trabecular evidence for a human-like gait in Australopithecus africanus. *PloS One, 8*(11), e77687.

Barak, M. M., Sherratt, E., & Lieberman, D. E. (2017). Using principal trabecular orientation to differentiate joint loading orientation in the 3rd metacarpal heads of humans and chimpanzees. *Journal of Human Evolution, 113*, 173-182.

Barakat, M. J., Field, J., & Taylor, J. (2013). The range of movement of the thumb. *Hand, 8*(2), 179-182.

Bardo, A., Borel, A., Meunier, H., Guéry, J. P., & Pouydebat, E. (2016). Behavioral and functional strategies during tool use tasks in bonobos. *American Journal of Physical Anthropology, 161*(1), 125-140.

Bardo, A., Cornette, R., Borel, A., & Pouydebat, E. (2017). Manual function and performance in humans, gorillas, and orangutans during the same tool use task. *American Journal of Physical Anthropology, 164*(4), 821-836.

Bardo, A., Vigouroux, L., Kivell, T., & Pouydebat, E. (2018). The impact of hand proportions on tool grip abilities in humans, great apes and fossil hominins: a biomechanical analysis using musculoskeletal simulation. *Journal of Human Evolution*.

Bar-Yosef, O., & Callander, J. (1999). The woman from Tabun: Garrod's doubts in historical perspective. *Journal of Human Evolution, 6*(37), 879-885.

Behringer, V., Deschner, T., Murtagh, R., Stevens, J. M., & Hohmann, G. (2014). Age-related changes in thyroid hormone levels of bonobos and chimpanzees indicate heterochrony in development. *Journal of Human Evolution, 66*, 83-88.

Berger, L. R. (2013). The mosaic nature of Australopithecus sediba. *Science, 340*, 163-165.

Berger, L. R., de Ruiter, D. J., Churchill, S. E., Schmid, P., Carlson, K. J., Dirks, P. H., et al. (2010). Australopithecus sediba: A new species of Homo-like australopith from South Africa. *Science, 328*(5975), 195-204.

Bertram, J. E., & Swartz, S. M. (1991). The 'law of bone transformation': a case of crying Wolff? *Biological Reviews, 66*(3), 245-273.

Biewener, A. A. (1982). Bone strength in small mammals and bipedal birds: do safety factors change with body size? *Journal of Experimental Biology, 98*(1), 289-301.

Biewener, A. A. (1990). Biomechanics of mammalian terrestrial locomotion. *Science, 250*(4984), 1097-1103.

Biewener, A. A., & Bertram, J. E. (1994). Structural response of growing bone to exercise and disuse. *Journal of Applied Physiology, 76*(2), 946-955.

Biewener, A. A., Fazzalari, N. L., Konieczynski, D. D., & Baudinette, R. V. (1996). Adaptive changes in trabecular architecture in relation to functional strain patterns and disuse. *Bone, 19*(1), 1-8.

Bisson, M. S., Tisnerat, N., & White, R. (1996). Radiocarbon dates from the Upper Paleolithic of the Barma Grande. *Current anthropology, 37*(1), 156-162.

Boesch, C., & Boesch, H. (1990). Tool use and tool making in wild chimpanzees. *Folia Primatologica, 54*(1-2), 86-99.

Boesch, C., & Boesch, H. (1993). Different hand postures for pounding nuts with natural hammers by wild chimpanzees. In H. Preuschoft, & D. Chivers (Eds.), *Hands of Primates* (pp. 31-43). Vienna: Springer-Verlag.

Boettiger, C. (2015). An introduction to Docker for reproducible research. *ACM SIGOPS Operating Systems Review, 49*(1), 71-79.

Bookstein, F. L. (1991). *Morphometric tools for landmark data: geometry and biology.* Cambridge, UK: Cambridge University Press.

Breuer, T., Ndoundou-Hockemba, M., & Fishlock, V. (2005). First observation of tool use in wild gorillas. *PLoS Biology, 3*(11), e380.

Burghardt, A. J., Kazakia, G. J., & Majumdar, S. (2007). A local adaptive threshold strategy for high resolution peripheral quantitative computed tomography of trabecular bone. *Annals of Biomedical Engineering, 35*(10), 1678-1686.

Bush, M. E., Lovejoy, C. O., Johanson, D. C., & Coppens, Y. (1982). Hominid carpal, metacarpal, and phalangeal bones recovered from the Hadar Formation: 1974–1977 collections. . *American Journal of Physical Anthropology, 57*(4), 651-677.

Byrne, R. W., Corp, N., & Byrne, J. M. (2001). Manual dexterity in the gorilla: bimanual and digit role differentiation in a natural task. *Animal Cognition, 4*(3-4), 347-361.

Cant, J. G. (1987). Effects of sexual dimorphism in body size on feeding postural behavior of Sumatran orangutans. *American Journal of Physical Anthropology, 74*(2), 143-148.

Cant, J. G. (1987). Positional behavior of female Bornean orangutans (Pongo pygmaeus). *American Journal of Primatology, 12*(1), 71-90.

Carlson, K. J., & Judex, S. (2007). Increased non-linear locomotion alters diaphyseal bone shape. *Journal of Experimental Biology, 210*(17), 3117-3125.

Carlson, K. J., Doran-Sheehy, D. M., Hunt, K. D., Nishida, T., Yamanaka, A., & Boesch, C. (2006). Locomotor behavior and long bone morphology in individual free-ranging chimpanzees. *Journal of Human Evolution, 50*(4), 394-404.

Carlson, K. J., Lublinsky, S., & Judex, S. (2008). Do different locomotor modes during growth modulate trabecular architecture in the murine hind limb? *Integrative and Comparative Biology, 48*(3), 385-393.

Carter, D. R. (1991). Musculoskeletal ontogeny, phylogeny, and functional adaptation. *Journal of Biomechanics, 24*, 3-16.

Cerroni, A. M., Tomlinson, G. A., Turnquist, J. E., & Grynpas, M. D. (2000). Bone mineral density, osteopenia, and osteoporosis in the rhesus macaques of Cayo Santiago. *American Journal of Physical Anthropology*, 113(3), 389-410.

Chan, L. K. (2008). The range of passive arm circumduction in primates: Do hominoids really have more mobile shoulders? *American Journal of Physical Anthropology, 136*(3), 265-277.

Charles, J. F., Ermann, J., & Aliprantis, A. O. (2015). The intestinal microbiome and skeletal fitness: Connecting bugs and bones. *Clinical Immunology, 159*(2), 163-169.

Chen, J. H., Liu, C., You, L., & Simmons, C. A. (2010). Boning up on Wolff's Law: mechanical regulation of the cells that make and maintain bone. *Journal of Biomechanics, 43*(1), 108-118.

Chirchir, H., Kivell, T. L., Ruff, C. B., Hublin, J. J., Carlson, K. J., Zipfel, B., et al. (2015). Recent origin of low trabecular bone density in modern humans. *Proceedings of the National Academy of Sciences, 112*(2), 366-371.

Chirchir, H., Kivell, T. L., Ruff, C. B., Hublin, J. J., Carlson, K. J., Zipfel, B., et al. (2015). Recent origin of low trabecular bone density in modern humans. *Proceedings of the National Academy of Sciences, 112*(2), 336-371.

Chirchir, H., Zeininger, A., Nakatsukasa, M., Ketcham, R. A., & Richmond, B. G. (2017). Does trabecular bone structure within the metacarpal heads of primates vary with hand posture? *Comptes Rendus Palevol, 16*(5-6), 533-544.

Christel, M. (1993). Grasping techniques and hand preferences in Hominoidea. In H. Preuschof t& D. Chivers(Eds.), *Hands of Primates* (pp. 91-108). Vienna: Springer.

Christel, M. I., & Fragaszy, D. (2000). Manual function in Cebus apella. Digital mobility, preshaping, and endurance in repetitive grasping. *International Journal of Primatology, 21*(4), 697-719.

Christel, M. I., Kitzel, S., & Niemitz, C. (1998). How precisely do bonobos (Pan paniscus) grasp small objects? *International Journal of Primatology, 19*(1), 165-194.

Christen, P., & Müller, R. (2017). In vivo visualisation and quantification of bone resorption and bone formation from time-lapse imaging. *Current Osteoporosis Reports, 15*(4), 311-317.

Churchill, S. E., Holliday, T. W., Carlson, K. J., Jashashvili, T., Macias, M. E., Mathews, S., et al. (2013). The upper limb of Australopithecus sediba. *Science, 340*(6129), 1233477.

Cignoni, P., Callieri, M., Corsini, M., Dellepiane, M., Ganovelli, F., & Ranzuglia, G. (2008). Meshlab: an open-source mesh processing tool. In V. Scarano, R. De Chiara, & U. Erra (Eds.), *Eurographics Italian Chapter Conference (2008)* (pp. 129-136).

Clarke, B. (2008). Normal bone anatomy and physiology. *Clinical journal of the American Society of Nephrology, 3*(Supplement 3), S131-S139.

Coleman, M. N., & Colbert, M. W. (2007). CT thresholding protocols for taking measurements on three-dimensional models. *American Journal of Physical Anthropology, 133*(1), 723-725.

Colombo, A., Hoogland, M., Coqueugniot, H., Dutour, O., & Waters-Rist, A. (2018). Trabecular bone microarchitecture analysis, a way for an early detection of genetic dwarfism? Case study of a dwarf mother's offspring. *International Journal of Paleopathology*, *20*, 65-71.

Cooney, W. P., Lucca, M. J., Chao, E. Y., & Linscheid, R. L. (1981). The kinesiology of the thumb trapeziometacarpal joint. *The Journal of Bone and Joint Surgery, 63*(9), 1371-1381.

Cooney, W., & Chao, E. (1977). Biomechanical analysis of static forces in the thumb during hand function. *The Journal of Bone & Joint Surgery, 59*(1), 27-36.

Coupier, J., Hamoudi, S., Telese-Izzi, S., Feipel, V., Rooze, M., & Jan, S. V. S. (2016). A novel method for in-vivo evaluation of finger kinematics including definition of healthy motion patterns. *Clinical Biomechanics*, 31, 47-58.

Cotter, M. M., Simpson, S. W., Latimer, B. M., & Hernandez, C. J. (2009). Trabecular microarchitecture of hominoid thoracic vertebrae. *The Anatomical Record, 292*(8), 1098-1106.

Cowin, S. (2001). *Bone Mechanics Handbook.* New York: CRC Press.

Cowin, S. C. (1985). The relationship between the elasticity tensor and the fabric tensor. *Mechanics of Materials, 4*(2), 137-147.

Cowin, S. C. (1986). Wolff's law of trabecular architecture at remodeling equilibrium. *Journal of Biomechanical Engineering, 108*(1), 83-88.

Cowin, S. C., Hart, R. T., Balser, J. R., & Kohn, D. H. (1985). Functional adaptation in long bones: establishing in vivo values for surface remodeling rate coefficients. *Journal of Biomechanics, 18*(9), 665-684.

Crompton, R. H. (2016). The hominins: a very conservative tribe? Last common ancestors, plasticity and ecomorphology in Hominidae. Or, What's in a name? *Journal of Anatomy, 228*(4), 686-699.

Crompton, R. H., Sellers, W. I., & Thorpe, S. K. (2010). Arboreality, terrestriality and bipedalism. *Philosophical Transactions of the Royal Society B: Biological Sciences, 365*(1556), 3301-3314.

Cullen, D. M. (2000). Time course for bone formation with long-term external mechanical loading. *Journal of Applied Physiology, 88*(6), 1943-1948.

Cunningham, C. A., & Black, S. M. (2009). Anticipating bipedalism: trabecular organization in the newborn ilium. *Journal of Anatomy, 214*(6), 817-829.

Currey, J. D. (2002). *Bones: Structure and Mechanics.* Princeton: Princeton University Press.

Currey, J. D. (2012). The structure and mechanics of bone. *Journal of Materials Science, 47*(1), 41-54.

D'Août, K., Vereecke, E., Schoonaert, K., De Clercq, D., Van Elsacker, L., & Aerts, P. (2004). Locomotion in bonobos (Pan paniscus): differences and similarities between bipedal and quadrupedal terrestrial walking, and a comparison with other locomotor modes. *Journal of Anatomy, 204*(5), 353-361.

D'Agostino, P., Dourthe, B., Kerkhof, F., Stockmans, F., & Vereecke, E. E. (2017). In vivo kinematics of the thumb during flexion and adduction motion: Evidence for a screw-home mechanism. *Journal of Orthopaedic Research, 35*(7), 1556-1564.

Dainton, M., & Macho, G. A. (1999). Did knuckle walking evolve twice? *Journal of Human Evolution, 36*(2), 171-194.

Darwin, C. (1871). *The descent of man and selection in relation to sex (Vol. 1).* 2nd Ed. London: John Murray.

de la Torre, I. (2011). The early Stone age lithic assemblages of Gadeb (Ethiopia) and the Developed Oldowan/early Acheulean in east Africa. *Journal of Human Evolution, 60*(6), 768-812.

Demes, B. J. (1991). Body size, locomotion, and long bone cross-sectional geometry in indriid primates. *American Journal of Physical Anthropology, 86*(4), 537-547.

Demes, B., & Jungers, W. L. (1993). Long bone cross-sectional dimensions, locomotor adaptations and body size in prosimian primates. *Journal of Human Evolution*, 57-74.

Demes, B., Qin, Y. X., Stern, J. T., Larson, S. G., & Rubin, C. T. (2001). Patterns of strain in the macaque tibia during functional activity. *American Journal of Physical Anthropology, 116*(4), 257-265.

Demes, B., Stern, J. T., Hausman, M. R., Larson, S. G., McLeod, K. J., & Rubin, C. T. (1998). Patterns of strain in the macaque ulna during functional activity. *American Journal of Physical Anthropology, 106*(1), 87-100.

DeSilva, J. M. (2009). Functional morphology of the ankle and the likelihood of climbing in early hominins. *Proceedings of the National Academy of Sciences, 106*(16), 6567-6572.

DeSilva, J. M., & Devlin, M. J. (2012). A comparative study of the trabecular bony architecture of the talus in humans, non-human primates, and Australopithecus. *Journal of Human Evolution, 63*(3), 536-551.

DeSilva, J. M., Holt, K. G., Churchill, S. E., Carlson, K. J., Walker, C. S., Zipfel, B., et al. (2013). The lower limb and mechanics of walking in Australopithecus sediba.*Science, 340*(6129), 1232999.

Dhanachandra, N., & Chanu, Y. J. (2017). A Survey on Image Segmentation Methods using Clustering Techniques. *European Journal of Engineering Research and Science, 2*(1), 15-20.

Diogo, R., Richmond, B. G., & Wood, B. (2012). Evolution and homologies of primate and modern human hand and forearm muscles, with notes on thumb movements and tool use. *Journal of Human Evolution, 63*(1), 64-78.

Domalain, M., Bertin, A., & Daver, G. (2017). Was Australopithecus afarensis able to make the Lomekwian stone tools? Towards a realistic biomechanical simulation of hand force capability in fossil hominins and new insights on the role of the fifth digit. *Comptes Rendus Palevol, 16*(5-6), 572-584.

Doran, D. M. (1992). The ontogeny of chimpanzee and pygmy chimpanzee locomotor behavior: a case study of paedomorphism and its behavioral correlates. *Journal of Human Evolution, 23*(2), 139-157.

Doran, D. M. (1993). Comparative locomotor behavior of chimpanzees and bonobos: the influence of morphology on locomotion. *American Journal of Physical Anthropology, 91*(1), 83-98.

Doran, D. M. (1996). Comparative positional behavior of the African apes. In W. C. McGrew, L. F. Marchant, & T. Nishida (Eds.), *Great Ape Societies* (pp. 213-224). Cambridge, UK: Cambridge University Press.Doran, D. M. (1997). Ontogeny of locomotion in mountain gorillas and chimpanzees. *Journal of Human Evolution, 32*(4), 323-344.

Doran, D. M., & Hunt, K. D. (1994). Comparative locomotor behavior of chimpanzees and bonobos. In R. W. Wrangham, W. C. McGrew, F. B. deWaal, & P. G. Heltne (Eds.), *Chimpanzee Cultures* (pp. 93-108). Cambridge, MA: Havard University Press.

Doube, M., Kłosowski, M. M., Wiktorowicz-Conroy, A. M., Hutchinson, J. R., & Shefelbine, S. J. (2011). Trabecular bone scales allometrically in mammals and birds. *Proceedings of the Royal Society of London B: Biological Sciences, 278*(1721), 3067-3073.

Doube, M., Kłosowski, M., Arganda-Carreras, I., Cordelières, F., Dougherty, R., J.S., J., et al. (2010). BoneJ: free and extensible bone image analysis in ImageJ. *Bone, 47*(6), 1076-1079.

Dougherty, R., & Kunzelmann, K. H. (2007). Computing local thickness of 3D structures with ImageJ. *Microscopy and Microanalysis, 13*(S02), 1678-1679.

Drapeau, M. S. (2015). Metacarpal torsion in apes, humans, and early Australopithecus: implications for manipulatory abilities. *PeerJ, 3*, e1311.

Drapeau, M. S., & Ward, C. V. (2007). Forelimb segment length proportions in extant hominoids and Australopithecus afarensis. *American Journal of Physical Anthropology, 132*(3), 327-343.

Drapeau, M. S., Ward, V., C., Kimbel, W. H., Johanson, D. C., & Rak, Y. (2005). Associated cranial and forelimb remains attributed to Australopithecus afarensis from Hadar, Ethiopia. *Journal of Human Evolution, 48*(6), 593-642.

Dunmore, C. J., Wollny, G., & Skinner, M. M. (2018). MIA-Clustering: a novel method for segmentation of paleontological material. *PeerJ, 6*, e4374.

Dunmore, C., Bardo, A., Skinner, M., & Kivell, T. (2019). Metacarpal trabecular bone varies with distinct hand-positions used in hominid locomotion. *Journal of Anatomy*, 235(1):45-66.

Eriksen, E. F. (1986). Normal and Pathological Remodeling of Human Trabecular Bone: Three Dimensional Reconstruction of the Remodeling Sequence in Normals and in Metabolic Bone Disease. *Endocrine Reviews, 7*(4), 379-408.

Eriksen, E. F. (2010). Cellular mechanisms of bone remodeling. *Reviews in Endocrine and Metabolic Disorders, 11*(4), 219-227.

Eriksen, E. F., Mosekilde, L., & Melsen, F. (1985). Trabecular bone resorption depth decreases with age: differences between normal males and females. *Bone, 6*(3), 141-146.

Eswaran, S. K., Gupta, A., Adams, M. F., & Keaveny, T. M. (2006). Cortical and trabecular load sharing in the human vertebral body. *Journal of Bone and Mineral Research, 21*(2), 307-314.

Fajardo, R. J., & Müller, R. (2001). Three-dimensional analysis of nonhuman primate trabecular architecture using micro-computed tomography. *American Journal of Physical Anthropology, 115*(4), 327-336.

Fajardo, R. J., DeSilva, J. M., Manoharan, R. K., Schmitz, J. E., Maclatchy, L. M., & Bouxsein, M. L. (2013). Lumbar Vertebral Body Bone Microstructural Scaling in Small to Medium-Sized Strepsirhines. *The Anatomical Record, 296*(2), 210-226.

Fajardo, R. J., Müller, R., Ketcham, R. A., & Colbert, M. (2007). Nonhuman anthropoid primate femoral neck trabecular architecture and its relationship to locomotor mode. *The Anatomical Record, 290*(4), 422-436.

Fragaszy, D., Izar, P., Visalberghi, E., Ottoni, E. B., & de Oliveira, M. G. (2004). Wild capuchin monkeys (Cebus libidinosus) use anvils and stone pounding tools. *American Journal of Primatology,* 64(4), 359-366.

Faurie, C., Schiefenhvel, W., leBomin, S., Billiard, S., & Raymond, M. (2005). Variation in the frequency of left-handedness in traditional societies. *Current Anthropology, 46*(1), 142-147.

Feix, T., Kivell, T. L., Pouydebat, E., & Dollar, A. M. (2015). Estimating thumb–index finger precision grip and manipulation potential in extant and fossil primates. *Journal of the Royal Society Interface, 12*(106), e20150176.

Feix, T., Romero, J., Schmiedmayer, H. B., Dollar, A. M., & Kragic, D. (2016). The grasp taxonomy of human grasp types. *IEEE Transactions on Human-Machine Systems, 46*(1), 66-77.

Fernández, P. J., Almécija, S., Patel, B. A., Orr, C. M., Tocheri, M. W., & Jungers, W. L. (2015). Functional aspects of metatarsal head shape in humans, apes, and Old World monkeys. *Journal of Human Evolution, 86*, 136-146.

Fitts, R. H., Riley, D. R., & Widrick, J. J. (2001). Functional and structural adaptations of skeletal muscle to microgravity. *Journal of Experimental Biology, 204*(18), 3201-3208.

Foley, R. (2005). Species diversity in human evolution: challenges and opportunities. *Transactions of the Royal Society of South Africa, 60*(2), 67-72.

Forgy, E. (1965). Cluster analysis of multivariate data: efficiency versus interpretability of classifications. *Biometrics, 21*, 768-769.

Formicola, V., & Holt, B. M. (2015). Tall guys and fat ladies: Grimaldi's Upper Paleolithic burials and figurines in an historical perspective. *Journal of Anthropological Sciences, 93*, 71-88.

Formicola, V., Frayer, D. W., & Heller, J. A. (1990). Bilateral absence of the lesser trochanter in a Late Epigravettian skeleton from Arene Candide (Italy). *American Journal of Physical Anthropology, 83*(4), 425-437.

Fox, C. L., & Frayer, D. W. (1997). Non-dietary marks in the anterior dentition of the Krapina Neanderthals. *International Journal of Osteoarchaeology, 7*(2), 133-149.

Fox, E. A., & Bin'Muhammad, I. (2002). New tool use by wild Sumatran orangutans (Pongo pygmaeus abelii). *American Journal of Physical Anthropology, 119*(2), 186-188.

Fox, E. A., Sitompul, A. F., & Van Schaik, C. P. (1999). Intelligent tool use in wild Sumatran orangutans. In S. Parker, R. Mitchel & H. Miles (Eds.), *The Mentality of Gorillas and Orangutans* (pp. 99-116). Cambridge: Cambridge University Press.

Fragaszy, D. M., & Crast, J. (2016). Functions of the hand in primates. In T. Kivell, P. Lemelin, B. Richmond, D. Schmitt, & Eds., *The Evolution of the Primate Hand* (pp. 313-344). New York: Springer.

Friston, K. J., Holmes, A. P., Worsley, K. J., Poline, J. P., Frith, C. D., & Frackowiak, R. S. (1995). Statistical parametric maps in functional imaging: a general linear approach. *Human Brain Mapping, 2*(4), 189-210.

Frost, H. M. (1987). Bone "mass" and the "mechanostat": a proposal. *The Anatomical Record, 219*(1), 1-9.

Furuichi, T., Sanzb, C., Koops, K., Sakamakia, T., Ryua, H., Tokuyamaa, N., et al. (2015). Why do wild bonobos not use tools like chimpanzees do? *Behaviour, 152*, 425-460.

Galletta, L., Stephens, N. B., Bardo, A., Kivell, T. L., & Marchi, D. (2019). Three-dimensional geometric morphometric analysis of the first metacarpal distal articular surface in humans, great apes and fossil hominins. *Journal of Human Evolution*, 132, 119-136.

Gebo, D. (1996). Climbing, brachiation, and terrestrial quadrupedalism: historical precursors of hominid bipedalism. *American Journal of Physical Anthropology, 101*(1), 55-92.

Gee, A. H., Treece, G. M., Tonkin, C. J., Black, D. M., & Poole, K. E. (2015). Association between femur size and a focal defect of the superior femoral neck. *Bone, 81*, 60-66.

Georgiou, L., Kivell, T. L., Pahr, D. H., & Skinner, M. M. (2018). Trabecular bone patterning in the hominoid distal femur. *PeerJ, 6*, e5156.

Georgiou, L., Kivell, T. L., Pahr, D. H., Buck, L. T., & Skinner, M. M. (2019). Trabecular architecture of the great ape and human fermoral head. *Journal of Anatomy 234*(5) 679-693.

Gould, S. J., & Lewontin, R. C. (1979). The spandrels of San Marco and the Panglossian paradigm: a critique of the adaptationist programme. *Proceedings of the Royal. Society of London Series B, Biological Sciences., 205*(1161), 581-598.

Granger, D. E., Gibbon, R. J., Kuman, K., Clarke, R. J., Bruxelles, L., & Caffee, M. W. (2015). New cosmogenic burial ages for Sterkfontein Member 2 Australopithecus and Member 5 Oldowan. *Nature, 522*(7554), 85-88.

Green, D. J., & Alemseged, Z. (2012). Australopithecus afarensis scapular ontogeny, function, and the role of climbing in human evolution. *Science, 338*(6106), 517-517.

Green, D. J., & Gordon, A. D. (2008). Metacarpal proportions in Australopithecus africanus. *Journal of Human Evolution, 54*(5), 705-719.

Green, D. J., Gordon, A. D., & Richmond, B. G. (2007). Limb-size proportions in Australopithecus afarensis and Australopithecus africanus. *Journal of Human Evolution, 52*(2), 187-200.

Green, D. J., Serrins, J. D., Seitelman, B., Martiny, A. R., & Gunz, P. (2015). Geometric morphometrics of hominoid infraspinous fossa shape. *The Anatomical Record, 298*(1), 180-194.

Griffin, N., D'Août, K., Ryan, T., Richmond, B., Ketcham, R., & Postnov, A. (2010). Comparative forefoot trabecular bone architecture in extant hominids. *Journal of Human Evolution, 59*(2), 202-213.

Gross, T., Kivell, T. L., Skinner, M. M., Nguyen, H., & Pahr, D. (2014). A CT-image-based framework for the holistic analysis of cortical and trabecular bone morphology. *Palaeontologia Electronica, 17*(3), 1-13.

Großkopf, B. (2015). *Kulturgeschichtliche und naturwissenschaftliche Ergebnisse zur Ausgrabung des neuzeitlichen katholischen Friedhofes in Götttingen.* Göttingen: Göttingen University Press.

Gunz, P., & Mitteroecker, P. (2013). Semilandmarks: a method for quantifying curves and surfaces. *Hystrix, The Italian Journal of Mammalogy, 24*(1), 103-109.

Gunz, P., Mitteroecker, P., & Bookstein, F. L. (2005). Semilandmarks in three dimensions. In D. E. Slice (Ed.), *Modern Morphometrics in Physical Anthropology* (pp. 73-98). Boston, MA: Springer.

Haines, R. W. (1974). The pseudoepiphysis of the first metacarpal of man. *Journal of Anatomy, 117*, 145-158.

Halilaj, E., Rainbow, M. J., Got, C., Schwartz, J. B., Moore, D. C., Weiss, A. P., et al. (2014). In vivo kinematics of the thumb carpometacarpal joint during three isometric functional tasks. *Clinical Orthopaedics and Related Research, 472*(4), 1114-1122.

Halilaj, E., Moore, D. C., Patel, T. K., Laidlaw, D. H., Ladd, A. L., Weiss, A. P., et al. (2014b). Thumb carpometacarpal joint congruence during functional tasks and thumb range-of-motion activities. *Engineering in Medicine and Biology Society, 36th Annual International Conference of the IEEE* , 4354-4357.

Hammer, A. (2015). The paradox of Wolff's theories. *Irish Journal of Medical Science, 184*(1), 13-22.

Hamrick, M. W., & Inouye, S. E. (1995). Thumbs, tools, and early humans. *Science, 268*(5210), 586-587.

Hamrick, M. W., Churchill, S. E., Schmitt, D., & Hylander, W. L. (1998). EMG of the human flexor pollicis longus muscle: implications for the evolution of hominid tool use. *Journal of Human Evolution, 34*(2), 123-136.

Hara, T., Tanck, E., Homminga, J., & Huiskes, R. (2002). The influence of microcomputed tomography threshold variations on the assessment of structural and mechanical trabecular bone properties. *Bone, 31*(1), 107-109.

Harcourt-Smith, W. E., & Aiello, L. C. (2004). Fossils, feet and the evolution of human bipedal locomotion. *Journal of Anatomy, 204*(5), 403-416.

Hardy, B. L., & Moncel, M. H. (2011). Neanderthal use of fish, mammals, birds, starchy plants and wood 125-250,000 years ago. *PloS One, 6*(8), e23768.

Harmand, S., Lewis, J., Feibel, C., Lepre, C., Prat, S., Lenoble, A., et al. (2015). 3.3-million-year-old stone tools from Lomekwi 3, West Turkana, Kenya. *Nature* (521), 310-315.

Haslam, M., Hernandez-Aguilar, A., Ling, V., Carvalho, S., de La Torre, I., DeStefano, A., et al. (2009). Primate archaeology. *Nautre, 460*(7253), 339-344.

Havill, L. M., Mahaney, M. C., Binkley, L. & Specker, L. B. (2007). Effects of genes, sex, age, and activity on BMC, bone size, and areal and volumetric BMD. *Journal of Bone and Mineral Research, 22*(5), 737-74.

Havill, L. M., Levine, S. M., Newman, D. E., & Mahaney, M. C. (2008). Osteopenia and osteoporosis in adult baboons (*Papio hamadryas*). Journal of medical primatology, 37(3), 146-153.

Havill, L., Allen, M., Bredbenner, T., Burr, D., Nicolella, D., Turner, C., et al. (2010). Heritability of lumbar trabecular bone mechanical properties in baboons. *Bone, 46*(3), 835-840.

Heldstab, S. A., Kosonen, Z. K., Koski, S. E., Burkart, J. M., Van Schaik, C. P., & Isler, K. (2016). Manipulation complexity in primates coevolved with brain size and terrestriality.*Scientific Reports*,(6), e24528 .

Henry, A., Ungar, P., Passey, B., Sponheimer, M., Rossouw, L., Bamford, M., et al. (2012). The diet of Australopithecus sediba. *Nature, 487*(7405), 90-93.

Herman, G. (1979). Correction for beam hardening in computed tomography. *Physics in Medicine and Biology, 24*(1), 81-106.

Hershkovitz, I., Speirs, M. S., Frayer, D., Nadel, D., Wish-Baratz, S., & Arensburg, B. (1995). Ohalo II H2: A 19,000-year-old skeleton from a water-logged site at the Sea of Galilee, Israel. *American Journal of Physical Anthropology, 96*(3), 215-234.

Hervé, M. (2017). RVAideMemoire: testing and plotting procedures for biostatistics. *R package version* 0.9–68.

Hildebrand, T., & Rüegsegger, P. (1997). A new method for the model-independent assessment of thickness in three-dimensional images. *Journal of Microscopy, 185*(1), 67-75.

Hoechel, S., Schulz, G., & Müller-Gerbl, M. (2015). Insight into the 3D-trabecular architecture of the human patella. *Annals of Anatomy-Anatomischer Anzeiger, 200*, 98-104.

Hohmann, G., & Fruth, B. (2003). Culture in bonobos? Between-species and within-species variation in behavior. *Current Anthropology, 44*(4), 563-571.

Homminga, J., van Rietbergen, B., Lochmüller, E. M., Weinans, H., Eckstein, F., & Huiskes, R. (2004). The osteoporotic vertebral structure is well adapted to the loads of daily life, but not to infrequent “error” loads. *Bone, 34*(3), 510-516.

Huiskes, R., Ruimerman, R., Van Lenthe, G. H., & Janssen, J. D. (2000). Effects of mechanical forces on maintenance and adaptation of form in trabecular bone. *Nature, 405*(6787), 704-706.

Hunt, K. (1991). Mechanical implications of chimpanzee positional behavior. *American Journal of Physical Anthropology, 86*(4), 521-536.

Hunt, K. D. (2016). Why are there apes? Evidence for the co-evolution of ape and monkey ecomorpholog. *Journal of Anatomy, 228*(4), 630-685.

Hunt, K. D., Cant, J. G., Gebo, D. L., Rose, M. D., Walker, S. E., & Youlatos, D. (1996). Standardized descriptions of primate locomotor and postural modes. *Primates, 37*(4), 363-387.

Huxley, T. (1863). *Evidence as to Man's Place in Nature.* NewYork: D.Appleton and Company.

Ingmanson, E. J. (1996). Tool-using behavior in wild Pan paniscus: Social and ecological considerations. In A. Russon, K. Bard, & S. Parkers (Eds.), *Reaching Into Thought: The Minds of the Great Apes* (pp. 190-210). Cambridge: Cambridge University Press.

Inouye, S. (1994). Ontogeny of knuckle-walking hand postures in African apes. *Journal of Human Evolution, 26*(5), 459-485.

Inouye, S. E. (1992). Ontogeny and allometry of African ape manual rays. *Journal of Human Evolution, 23*(2), 107-138.

Inouye, S. E., & Shea, B. T. (2004). The implications of variation in knuckle-walking features for models of African hominoid locomotor evolution. *Journal of Anthropological Sciences, 82*, 67-88.

Jacofsky, M. (2009). *Comparative muscle moment arms of the primate thumb: Homo, Pan, Pongo, and Papio.* (Doctoral Dissertation): Arizona State University.

Jee, W. S., Wronski, T. J., Morey, E. R., & Kimmel, D. B. (1983). Effects of spaceflight on trabecular bone in rats. *American Journal of Physiology-Regulatory, Integrative and Comparative Physiology, 244*(3), R310-R314.

Johanson, D. C. (1976). Plio-pleistocene hominid discoveries in Hadar, Ethiopia. *Nature, 260*(5549), 293-297.

Johanson, D. C., Taieb, M., & Coppens, Y. (1982). Pliocene hominids from the Hadar Formation, Ethiopia (1973–1977): stratigraphic, chronologic, and paleoenvironmental contexts, with notes on hominid morphology and systematics. *American Journal of Physical Anthropology, 57*(4), 373-402.

Jones, E., Oliphant, T., & Peterson, P. (2001). SciPy: open source scientific tools for Python. *http://www.scipy.org/*.

Jones, H. H., Priest, J. D., Hayes, W. C., Tichenor, C. C., & Nagel, D. A. (1977). Humeral hypertrophy in response to exercise. *Journal of Bone and Joint Surgery, 59*(2), 204-208.

Jones-Engels, L., & Bard, K. A. (1996). Precision grips in young chimpanzees. *American Journal of Primatology, 39*(1), 1-15.

Judex, S., & Carlson, K. J. (2009). Is bone's response to mechanical signals dominated by gravitational loading. *Medicine & Science in Sports & Exercise, 41*(11), 2037-2043.

Judex, S., Donahue, L. R., & Rubin, C. (2002). Genetic predisposition to low bone mass is paralleled by an enhanced sensitivity to signals anabolic to the skeleton. *The FASEB Journal, 16*(10), 1280-1282.

Judex, S., Zhang, W., Donahue, L. R., & Ozcivici, E. (2013). Genetic loci that control the loss and regain of trabecular bone during unloading and reambulation. *Journal of Bone and Mineral Research, 28*(7), 1537-1549.

Jungers, W. L. (1988). Relative joint size and hominoid locomotor adaptations with implications for the evolution of hominid bipedalism. *Journal of Human Evolution, 17*(1), 247-265.

Kano, T. (1982). The use of leafy twigs for rain cover by the pygmy chimpanzees of Wamba. *Primates, 19*, 187-193.

Karakostis, F. A., Hotz, G., Scherf, H., Wahl, J., & Harvati, K. (2017). Occupational manual activity is reflected on the patterns among hand entheses. *American Journal of Pphysical Anthropology, 164*(1), 30-40.

Karakostis, F. A., Hotz, G., Tourloukis, V., & Harvati, K. (2018a). Evidence for precision grasping in Neandertal daily activities. *Science Advances, 4*(9), eaat2369.

Karakostis, F. A., Vlachodimitropoulos, D., Piagkou, M., Scherf, H., Harvati, K., & Moraitis, K. (2018b). Is bone elevation in hand muscle attachments associated with biomechanical stress? A histological approach to an anthropological question. *The Anatomical Record 302(7)* 1093-1103.

Kazhdan, M., & Hoppe, H. (2013). Screened poisson surface reconstruction. *ACM Transactions on Graphics (ToG), 32*(3), 29.

Keitt, T. H. (454). Coherent ecological dynamics induced by large scale disturbance. *Nature, 7202*, 331-334.

Kerr, D., Morton, A., Dick, I., & Prince, R. (1996). Exercise effects on bone mass in postmenopausal women are site-specific and load-dependent. *Journal of Bone and Mineral Research, 11*(2), 218-225.

Ketcham, R. A., & Ryan, T. M. (2004). Quantification and visualization of anisotropy in trabecular bone. *Journal of Microscopy, 213*(2), 158-171.

Key, A. J., & Dunmore, C. J. (2015). The evolution of the hominin thumb and the influence exerted by the non-dominant hand during stone tool production. *Journal of Human Evolution, 78*(1), 60-69.

Key, A., Merritt, S., & Kivell, T. (2018). Hand grip diversity and frequency during the use of Lower Palaeolithic stone cutting-tools. *Journal of Human Evolution*.

Kibii, J. M., Churchill, S. E., Schmid, P., Carlson, K. J., Reed, N. D., De Ruiter, D. J., et al. (2011). A partial pelvis of Australopithecus sediba. *Science, 333*(6048), 1407-1411.

Kim, C. H., Takai, E., Zhou, H., Von Stechow, D., Müller, R., Dempster, D. W., et al. (2003). Trabecular bone response to mechanical and parathyroid hormone stimulation: the role of mechanical microenvironment. *Journal of Bone and Mineral Research, 18*(12), 2116-2125.

Kimbel, W. H., & Delezene, L. K. (2009). “Lucy” redux: A review of research on Australopithecus afarensis. *American Journal of Physical Anthropology, 140*(S49), 2-48.

Kimbel, W. H., & Villmoare, B. (2016). From Australopithecus to Homo: the transition that wasn't. *Philosophical Transactions of the Royal Society B: Biological Sciences, 371*(1698), 20150248.

Kimbel, W. H., Lockwood, C. A., Ward, C. V., Leakey, M. G., Rak, Y., & Johanson, D. C. (2006). Was Australopithecus anamensis ancestral to A. afarensis? A case of

anagenesis in the hominin fossil record. *Journal of Human Evolution, 51*(2), 134-152.

Kimura, T. (1979). Kinesiological characteristics of primate walking: its significance in human walking. In M. Morbeck, H. Preuschoft, & N. Gomberg (Eds.), *Environment, Behaviour and Morphology: Dynamic Interactions in Primates* (pp. 297-311). New York: G.Fischer.

Kinani, J. F., & Zimmerman, D. (2015). Tool use for food acquisition in a wild mountain gorilla (Gorilla beringei beringei). *American Journal of Primatology, 77*(3), 353-357.

Kivell, T. (2016). A review of trabecular bone functional adaptation: what have we learned from trabecular analyses in extant hominoids and what can we apply to fossils? *Journal of Anatomy*,*228(4),* 569-594.

Kivell, T. L. (2015). Evidence in hand: recent discoveries and the early evolution of human manual manipulation. *Philosophical Transactions of the Royal Society B: Biological Sciences, 370*(1682), 20150105.

Kivell, T. L., & Schmitt, D. (2009). Independent evolution of knuckle-walking in African apes shows that humans did not evolve from a knuckle-walking ancestor. *Proceedings of the National Academy of Sciences, 106*(34), 14241-14246.

Kivell, T. L., Davenport, R., Hublin, J. J., Thackeray, J. F., & Skinner, M. M. (2018b). Trabecular architecture and joint loading of the proximal humerus in extant hominoids, Ateles, and Australopithecus africanus. *American Journal of Physical Anthropology, 167*(2), 348-365.

Kivell, T. L., Kibii, J. M., Churchill, S. E., Schmid, P., & Berger, L. R. (2011). Australopithecus sediba hand demonstrates mosaic evolution of locomotor and manipulative abilities. *Science, 333*(6048), 1411-1417.

Kivell, T. L., Skinner, M. M., Lazenby, R., & Hublin, J. J. (2011b). Methodological considerations for analyzing trabecular architecture: an example from the primate hand. *Journal of Anatomy, 218*(2), 209-225.

Kivell, T., Churchill, S., Kibii, J., Schmid, P., & L.R., B. (2018). The Hand of Australopithecus sediba. *PaleoAnthropology*, 282-333.

Kivell, T., Deane, A., Tocheri, M., Orr, C., Schmid, P., Hawks, J., et al. (2015). The hand of Homo naledi. *Nature Communications, 6*.

Koff, M. F., Ugwonali, O. F., Strauch, R. J., Rosenwasser, M. P., Ateshian, G. A., & Mow, V. C. (2003). Sequential wear patterns of the articular cartilage of the thumb carpometacarpal joint in osteoarthritis. *The Journal of Hand Surgery, 28*(4), 597-604.

Koops, K. F. (2015). Chimpanzees and bonobos differ in intrinsic motivation for tool use. *Scientific Reports, 5*, 11356.

Kraft, T. S., Venkataraman, V. V., & Dominy, N. J. (2014). A natural history of human tree climbing. *Journal of Human Evolution, 71*, 105-118.

Kuman, K., & Clarke, R. J. (2000). Stratigraphy, artefact industries and hominid associations for Sterkfontein, Member 5. *Journal of Human Evolution, 38*(6), 827-847.

Lambers, F. M., Bouman, A. R., Rimnac, C. M., & Hernandez, C. J. (2013b). Microdamage caused by fatigue loading in human cancellous bone: relationship to reductions in bone biomechanical performance. *PLoS One, 8*(12), e83662.

Lambers, F. M., Koch, K., Kuhn, G., Ruffoni, D., Weigt, C., Schulte, F. A., et al. (2013). Trabecular bone adapts to long-term cyclic loading by increasing stiffness and normalization of dynamic morphometric rates. *Bone, 55*(2), 325-334.

Landsmeer, J. M. (1955) Anatomical and functional investigations on the articulation of the human fingers. *Acta Anatomica Supplementum*, *25*(24), 1-69

Landsmeer, J. M. (1962). Power grip and precision handling. *Annals of the Rheumatic Diseases, 21*(2), 164-170.

Lang, T., LeBlanc, A., Evans, H., Lu, Y., Genant, H., & Yu, A. (2004). Cortical and trabecular bone mineral loss from the spine and hip in long-duration spaceflight. *Journal of Bone and Mineral Research, 19*(6), 1006-1012.

Lanyon, L., & Rubin, C. (1985). Functional adaptation in skeletal strucutures. In M. Hildebrand, D. Bramble, K. Liem, & B. Wake (Eds.), *Functional Vertebrate Morphology* (pp. 1-25). Cambridge, Massachusetts: Belknap Press.

Larson, S. G. (1995). New characters for the functional interpretation of primate scapulae and proximal humeri. *American Journal of Physical Anthropology, 98*(1), 13-35.

Latimer, B. (1991). Locomotor behaviour in Australopithecus afarensis: The issue of arboerality. In Y. Coppens, & B. Senut (Eds.), *Origine(s) de la Bipédie chez les Hominidés* (pp. 169-176). Paris: CNRS Cahiers de Paleoanthropologie.

Latimer, B., & Ward, C. V. (1993). The thoracic and lumbar vertebrae. In A. Walker, & R. Leakey (Eds.), *The Nariokotome Homo erectus Skeleton* (pp. 266-293). Cambridge, MA: Harvard University Press.

Lazenby, R. A., Skinner, M. M., Kivell, T. L., & Hublin, J. J. (2011). Scaling VOI size in 3D µCT studies of trabecular bone: A test of the over-sampling hypothesis. *American Journal of Physical Anthropology, 144*(2), 196-203.

Lazenby, R., Skinner, M., Hublin, J., & Boesch, C. (2011b). Metacarpal trabecular architecture in the chimpanzee (Pan troglodytes): evidence for locomotion and tool use. *American Journal of Physical Anthropology, 144*, 215-225.

Leakey, L. S., Tobias, P. V., & Napier, J. R. (1964). A new species of the genus Homo from Olduvai Gorge. *Nature, 202*(4927), 7-9.

Leakey, M. D., & Hay, R. L. (1979). Pliocene footprints in the Laetolil Beds at Laetoli, northern Tanzania. *Nature, 278*(5702), 317-323.

Leigh, S. R., Relethford, J. H., Park, P. B., & Konigsberg, L. W. (2003). Morphological differentiation of Gorilla subspecies. In A. Taylor, & M. Goldsmith (Eds.), *Gorilla Biology: A Multidisciplinary Perspective* (pp. 104-131). Cambridge: Cambridge University Press.

Lemelin, P., & Schmitt, D. (2016). On primitiveness, prehensility, and opposability of the primate hand: the contributions of Frederic Wood Jones and John Russell Napier. In T. Kivell, P. Lemelin, B. Richmond & D. Schmitt (Eds.), *The Evolution of the Primate Hand* (pp. 5-13). New York: Springer.

Lesnik, J. J., Sanz, C. M., & Morgan, D. B. (2015). The interdigital brace and other grips for termite nest perforation by chimpanzees of the Goualougo Triangle, Republic of Congo. *American Journal of Physical Anthropology, 157*(2), 252-259.

Lewis, O. J. (1977). Joint remodeling and the evolution of the human hand. *Journal of Anatomy, 123*(1), 157-201.

Lewis, O. J. (1989). *Functional morphology of the evolving hand and foot.* Oxford University Press, USA.

Lieberman, D. E. (1996). How and why humans grow thin skulls: experimental evidence for systemic cortical robusticity. *American Journal of Physical Anthropology, 101*(2), 217-236.

Lieberman, D. E., Devlin, M. J., & Pearson, O. M. (2001). Articular area responses to mechanical loading: effects of exercise, age, and skeletal location. *American Journal of Physical Anthropology, 116*(4), 266-277.

Lieberman, D. E., Polk, J. D., & Demes, B. (2004). Predicting long bone loading from cross-sectional geometry. *American Journal of Physical Anthropology, 123*(2), 156-171.

Lieberman, D. E., Pontzer, H., Momin, E., Devlin, M., Polk, J., Hallgrimsson, B., et al. (2004). An experimental test of Wolffs law in the knee. *Intergrative and Comparative Biology, 44*(6), 592.

Lindahl, O. (1976). Mechanical properties of dried defatted spongy bone. *Acta Orthopaedica, 47*(1), 11-19.

Lloyd, S. (1982). Least squares quantization in PCM. *IEEE Transactions on Information Theory, 28*(2), 129-137.

Lovejoy, C. O., McCollum, M. A., Reno, P. L., & Rosenman, B. A. (2003). Developmental biology and human evolution. *Annual Review of Anthropology*, 85-109.

Lovejoy, C. O., Simpson, S. W., White, T. D., Asfaw, B., & Suwa, G. (2009). Careful climbing in the Miocene: the forelimbs of Ardipithecus ramidus and humans are primitive. *Science, 326*(5949), 70-70e8.

Lozupone, E., & Favia, A. (1990). The structure of the trabeculae of cancellous bone. *Calcified Tissue International, 46*(6), 367-372.

Macfarlane, N. B., & Graziano, M. S. (2009). Diversity of grip in Macaca mulatta. *Experimental Brain Research, 197*(3), 255-268.

Macintosh, A. A., & Stock, J. T. (2019). Intensive terrestrial or marine locomotor strategies are associated with inter-and intra-limb bone functional adaptation in living female athletes. *American Journal of Physical Anthropology*.

MacLatchy, L., & Müller, R. (2002). A comparison of the femoral head and neck trabecular architecture of Galago and Perodicticus using micro-computed tomography. *Journal of Human Evolution, 43*(1), 89-105.

Maga, M., Kappelman, J., Ryan, T. M., & Ketcham, R. A. (2006). Preliminary observations on the calcaneal trabecular microarchitecture of extant large-bodied hominoids. *American Journal of Physical Anthropology, 129*(3), 410-417.

Malaivijitnond, S., Lekprayoon, C., Tandavanittj, N., Panha, S., Cheewatham, C., & Hamada, Y. (2007). Stone-tool usage by Thai long-tailed macaques (Macaca fascicularis). *American Journal of Primatology, 69*(2), 227-233.

Manduell, K. L., Morrogh-Bernard, H. C., & Thorpe, S. K. (2011). Locomotor behavior of wild orangutans (Pongo pygmaeus wurmbii) in disturbed peat swamp forest, Sabangau, Central Kalimantan, Indonesia. *American Journal of Physical Anthropology, 145*(3), 348-359.

Maquer, G., Musy, S. N., Wandel, J., Gross, T., & Zysset, P. K. (2014). Bone Volume Fraction and Fabric Anisotropy Are Better Determinants of Trabecular Bone Stiffness Than Other Morphological Variables. *Journal of Bone and Mineral Research, 30*(6), 1000-1008.

Marangoni, A., Belli, M. L., Caramelli, D., Moggi Cecchi, J., Zavattaro, M., & Manzi, G. (2011). Tierra del Fuego, its ancient inhabitants, and the collections of skeletal remains in the Museum of Anthropology of Florence and Rome. *Museologia Scientifica, 5*(1-2), 88-96.

Marchi, D. (2005). The cross-sectional geometry of the hand and foot bones of the Hominoidea and its relationship to locomotor behavior. *Journal of Human Evolution, 49*(6), 743-761.

Marchi, D., Proctor, D. J., Huston, E., Nicholas, C. L., & Fischer, F. (2017). Morphological correlates of the first metacarpal proximal articular surface with manipulative capabilities in apes, humans and South African early hominins. *Comptes Rendus Palevol, 16*(5-6), 645-654.

Martin, R. B., Burr, D. B., & Sharkey, N. A. (1998). *Skeletal tissue mechanics.* New York: Springer.

Marzke, M. (1997). Precision grips, hand morphology, and tools. *American Journal of Physical Anthropology, 102*(1), 91-110.

Marzke, M. W. (1971). Origin of the human hand. *American Journal of Physical Anthropology, 34*(1), 61-84.

Marzke, M. W. (2013). Tool making, hand morphology and fossil hominins. *Philosophical Transactions of the Royal Society B: Biological Sciences, 368*(1630), 20120414.

Marzke, M. W., & Marzke, R. F. (1987). The third metacarpal styloid process in humans: origin and functions. *American Journal of Physical Anthropology, 73*(4), 415-431.

Marzke, M. W., & Shackley, M. S. (1986). Hominid hand use in the Pliocene and Pleistocene: evidence from experimental archaeology and comparative morphology. *Journal of Human Evolution, 15*(6), 439-460.

Marzke, M. W., & Wullstein, K. L. (1996). Chimpanzee and human grips: a new classification with a focus on evolutionary morphology. *International Journal of Primatology, 17*(1), 117-139.

Marzke, M. W., Marchant, L. F., McGrew, W. C., & Reece, S. P. (2015). Grips and hand movements of chimpanzees during feeding in Mahale Mountains National Park, Tanzania. *American Journal of Physical Anthropology, 156*(3), 317-326.

Marzke, M. W., Marzke, R. F., Linscheid, R. L., Smutz, P., Steinberg, B., Reece, S., et al. (1999). Chimpanzee thumb muscle cross sections, moment arms and potential torques, and comparisons with humans. *American Journal of Physical Anthropology, 110*(2), 163-178.

Marzke, M. W., Wullstein, K. L., & Viegas, S. F. (1992). Evolution of the power ("squeeze") grip and its morphological correlates in hominids. *American Journal of Physical Anthropology, 89*(3), 283-298.

Marzke, M., Tocheri, M., Steinberg, B., Femiani, J., Reece, S., Linscheid, R., et al. (2010). Comparative 3D quantitative analyses of trapeziometacarpal joint surface curvatures among living catarrhines and fossil hominins. *American Journal of Physical Anthropology, 141*(1), 38-51.

Marzke, M., Toth, N., Schick, K., Reece, S., Steinberg, B., Hunt, K., et al. (1998). EMG study of hand muscle recruitment during hard hammer percussion manufacture of Oldowan tools. *American Journal of Physical Anthropology, 105*(3), 315-332.

Matarazzo, S. A. (2013). Manual pressure distribution patterns of knuckle-walking apes. *American Journal of Physical Anthropology, 152*(1), 44-50.

Matarazzo, S. A. (2013b). *Knuckle-Walking Signal in the Manual Phalanges and Metacarpals of the Great Apes (Pan and Gorilla)* (Vol. Paper 755). UMass Amherst: PhD thesis.

Matarazzo, S. A. (2015). Trabecular Architecture of the Manual Elements Reflects Locomotor Patterns in Primates. *PloS One, 10*(3), e0120436.

Matsuzawa, T. (1996). Field experiments on use of stone tools by chimpanzees in the wild. In R. W. Wrangham(Ed.), *Chimpanzee cultures* (pp. 351-370). Cambridge: Harvard University Press.

McCabe, L., Britton, R. A., & Parameswaran, N. (2015). Prebiotic and probiotic regulation of bone health: role of the intestine and its microbiome. *Current Osteoporosis Reports, 13*(6), 363-371.

McClure, N. K., Phillips, A. C., Vogel, E. R., & Tocheri, M. W. (2012). Unexpected pollex and hallux use in wild Pongo pygmaeus wurmbii. *American Journal of Physical Anthropology, 147*(Supp.54), 203.

Meulman, E. J., & van Schaik, C. P. (2013). Orangutan tool use and the evolution of technology. In C. Sanz, J. Call, B. C., & (Eds.), *Tool Use in Animals: Cognition and Ecology* (pp. 176-202). Cambridge: Cambridge University Press.

Meulman, E. J., Sanz, C. M., Visalberghi, E., & van Schaik, C. P. (2012). The role of terrestriality in promoting primate technology. *Evolutionary Anthropology: Issues, News, and Reviews, 21*(2), 58-68.

Milella, M. (2014). The Influence of Life History and Sexual Dimorphism on Entheseal Changes in Modern Humans and African Great Apes. *PLoS One*, e107963.

Moulton, M. J., Parentis, M. A., Kelly, M. J., Jacobs, C., Naidu, S. H., & Pellegrini Jr, V. D. (2001). Influence of metacarpophalangeal joint position on basal joint-loading in the thumb. *The Journal of Bone and Joint Surgery, 83*(5), 709-716.

Napier, J. (1961). Prehensility and opposability in the hands of primates. *Symposia of the Zoological Society of London, 5*, 115-132.

Napier, J. R. (1956). The prehensile movements of the human hand. *The Journal of Bone and Joint surgery. British volume, 38*(4), 902-913.Napier, J. R. (1960). Studies of the hands of living primates. In *Proceedings of the Zoological Society of London* (pp. 647-657). Oxford: Blackwell Publishing.

Napier, J. R.(1962). The evolution of the hand. *Scientific American, 207*(6), 56-65.

Napier, J. R. (1962b). Fossil hand bones from Olduvai Gorge. *Nature, 196*, 409-411.

Napier, J. R. (1993). *Hands.* Princeton: Princeton University Press.

Neufuss, J., Humle, T., Cremaschi, A., & Kivell, T. L. (2016). Nut-cracking behaviour in wild-born, rehabilitated bonobos (Pan paniscus): a comprehensive study of hand-preference, hand grips and efficiency. *American Journal of Primatology, 79*(2), 1-16.

Neufuss, J., Robbins, M. M., Baeumer, J., Humle, T., & Kivell, T. L. (2017). Comparison of hand use and forelimb posture during vertical climbing in mountain gorillas (Gorilla beringei beringei) and chimpanzees (Pan troglodytes). *American Journal of Physical Anthropology, 164*(4), 651-664.

Neufuss, J., Robbins, M., Baeumer, J., Hulme, T., & Kivell, T. (2018). Manual skills for food processing by mountain gorillas in Bwindi Impenetrable National Park, Uganda. *Biological Journal of the Linnean Society*, 1-20.

Nguyen, N. H., Pahr, D. H., Gross, T., Skinner, M. M., & Kivell, T. L. (2014). Micro-finite element (μFE) modeling of the siamang (Symphalangus syndactylus) third proximal phalanx: The functional role of curvature and the flexor sheath ridge. *Journal of Human Evolution, 67*(1), 60-75.

Niewoehner, W. A. (2005). A geometric morphometric analysis of Late Pleistocene human metacarpal 1 base shape. In D. E. Slice (Ed.), *Modern Morphometrics in Physical Anthropology* (pp. 285-298). Boston, MA: Springer.

Niewoehner, W. A. (2006). Neanderthal hands in their proper perspective. In K. Harvati, & T. Harrison (Eds.), *Neanderthals revisited: New Approaches and Perspectives* (pp. 157-190). Netherlands: Springer Netherlands.

Nishida, T., & Hiraiwa, M. (1982). Natural history of a tool-using behavior by wild chimpanzees in feeding upon wood-boring ants. *Journal of Human Evolution, 11*(1), 73-99.

Odgaard, A. (1997). Three-dimensional methods for quantification of cancellous bone architectur. *Bone, 20*(4), 315-328.

Odgaard, A., Kabel, J., van Rietbergen, B., Dalstra, M., & Huiskes, R. (1997). Fabric and elastic principal directions of cancellous bone are closely related. *Journal of Biomechanics, 30*(5), 487-495.

Ogihara, N., Kunai, T., & Nakatsukasa, M. (2005). Muscle dimensions in the chimpanzee hand. *Primates, 46*(4), 275-280.

Oksanen, J., Blanchet, F., Friendly, M., Kindt, R., Legendre, P., McGlinn, D., et al. (2018). vegan: Community Ecology, *R Package*.

Orr, C. M. (2016). Functional morphology of the primate hand: Recent approaches using biomedical imaging, computer modeling, and engineering methods. In T. Kivell, P. Lemelin, B. Richmond, D. Schmitt, & Eds., *The Evolution of the Primate Hand.* (pp. 227-257). New York: Springer.

Pahr, D. H., & Zysset, P. K. (2009). From high-resolution CT data to finite element models: development of an integrated modular framework. *Computer methods in Biomechanics and biomedical engineering, 12*(1), 45-57.

Panger, M. A., Brooks, A. S., Richmond, B. G., & Wood, B. (2002). Older than the Oldowan? Rethinking the emergence of hominin tool use. *Evolutionary Anthropology: Issues, News, and Reviews: Issues, News, and Reviews, 11*(6), 235-245.

Paoli, G., Tarli, S. M., Klír, P., Strouhal, E., Tofanelli, S., Del Santo Valli, M. T., et al. (1993). Paleoserology of the Christian population at Sayala (Lower Nubia): an evaluation of the reliability of the results. *American Journal of Physical Anthropology, 92*(3), 263-272.

Patel, B. A., & Maiolino, S. A. (2016). Morphological diversity in the digital rays of primate hands. In T. L. Kivell, P. Lemelin, B. G. Richmond, & D. Schmitt (Eds.), *The Evolution of the Primate Hand* (pp. 55-100). New York: Springer.

Pazzaglia, U. E., Sibilia, V., Casati, L., Salvi, A. G., Minini, A., & Reguzzoni, M. (2018). The missing segment of the autopod 1st ray: new insights from a morphometric study of the human hand. *Journal of Anatomy*.

Pearson, O. M., & Lieberman, D. E. (2004). The aging of Wolff's “law”: ontogeny and responses to mechanical loading in cortical bone. *American Journal of Physical Anthropology, 125*(S39), 63-99.

Pham, D. L., Xu, C., & Prince, J. L. (2000). Current methods in medical image segmentation. *Annual Review of Biomedical Engineering, 2*(1), 315-337.

Pham, D., & J.L.Prince. (1999). An adaptive fuzzy C-means algorithm for image segmentation in the presence of intensity inhomogeneities. *Pattern Recognition Letters, 20*(1), 57-68.

Pickering, R., & Kramers, J. D. (2010). Re-appraisal of the stratigraphy and determination of new U-Pb dates for the Sterkfontein hominin site, South Africa. *Journal of Human Evolution, 59*(1), 70-86.

Pickering, R., Dirks, P. H., Jinnah, Z., De Ruiter, D. J., Churchill, S. E., Herries, A. I., et al. (2011). Australopithecus sediba at 1.977 Ma and implications for the origins of the genus Homo. *Science, 333*(6048), 1421-1423.

Plavcan, J. M., & Van Schaik, C. P. (1997). Intrasexual competition and body weight dimorphism in anthropoid primates. *American Journal of Physical Anthropology, 103*(1), 37-68.

Pontzer, H., Lieberman, D. E., Momin, E., Devlin, M. J., Polk, J. D., Hallgrimsson, B., et al. (2006). Trabecular bone in the bird knee responds with high sensitivity to changes in load orientation. *Journal of Experimental Biology, 209*(1), 57-65.

Pouydebat, E., Berge, C., Gorce, P., & Coppens, Y. (2005). Use and manufacture of tools to extract food by captive Gorilla gorilla gorilla: experimental approach. *Folia Primatologica, 76*(3), 180-183.

Pouydebat, E., Gorce, P., Coppens, Y., & Bels, V. (2009). Biomechanical study of grasping according to the volume of the object: human versus non-human primates. *Journal of Biomechanics, 42*(3), 266-272.

Pouydebat, E., Laurin, M., Gorce, P., & Bels, V. (2008). Evolution of grasping among anthropoids. *Journal of Evolutionary Biology, 21*(6), 1732-1743.

Pouydebat, E., Reghem, E., Borel, A., & Gorce, P. (2011). Diversity of grip in adults and young humans and chimpanzees (Pan troglodytes). *Behavioural Brain Research, 218*(1), 21-28.

Prakasam, G., Yeh, J. K., Chen, M. M., Castro-Magana, M., Liang, C. T., & Aloia, J. F. (1999). Effects of growth hormone and testosterone on cortical bone formation and bone density in aged orchiectomized rats. *Bone, 24*(5), 491-497.

Preuschoft, H. (1965). Muskeln und gelenk der vorderextremitat des gorillas. *Gegenbaurs Morphologisches Jahrbuch, 107*, 99-183.

Preuschoft, H. (1970). Functional anatomy of the lower extremity. In G. Bourne (Ed.), *The Chimpanzee, vol. 3.* (pp. 221-294). Basel: Karger.

Preuschoft, H., & Demes, B. (1985). Influence of size and proportions on the biomechanics of brachiation. In W. Jungers(Ed.), *Size and Scaling in Primate Biology* (pp. 383-399). Boston: Springer.

Preutz, J. D., & Bertolani, P. (2007). Savanna chimpanzees, Pan troglodytes verus, hunt. *Current Biology, 17*, 412-417.

Proffitt, T., Luncz, L. V., Falótico, T., Ottoni, E. B., de la Torre, I., & Haslam, M. (2016). Wild monkeys flake stone tools. *Nature, 539*(7627), 85-88.

Proffitt, T., Luncz, V. L., Malaivijitnond, S., Gumert, M., Svensson, M. S., & Haslam, M. (2018). Analysis of wild macaque stone tools used to crack oil palm nuts. *Royal Society Open Science, 5*(3), 171904.

Püschel, T. A., & Sellers, W. I. (2015). Standing on the shoulders of apes: Analyzing the form and function of the hominoid scapula using geometric morphometrics and finite element analysis. *American Journal of Physical Anthropology*, DOI: 10.1002/ajpa.22882.

R Core Development Team. (2016). *R: a language and environment for statistical computing.* Vienna.

Rabey, K. (2014). *Forelimb muscle and muscle attachment morphology.* PhD thesis: University of Toronto.

Rabey, K. N., Green, D. J., Taylor, A. B., Begun, D. R., Richmond, B. G., & McFarlin, S. C. (2015). Locomotor activity influences muscle architecture and bone growth but not muscle attachment site morphology. *Journal of Human Evolution, 78*, 91-102.

Rafferty, K. (1990). The functional and phylogenetic significance of the carpometacarpal joint of the thumb in anthropoid primates. *M.A. Dissertation*, New York University.

Rafferty, K. L., & Ruff, C. B. (1994). Articular structure and function in Hylobates, Colobus, and Papio. *American Journal of Physical Anthropology, 94*(3), 395-408.

Raichlen, D., Gordon, A., Foster, A., Webber, J., Sukhdeo, S., Scott, R., et al. (2015). An ontogenetic framework linking locomotion and trabecular bone architecture with applications for reconstructing hominin life history. *Journal of Human Evolution, 81*(1), 1-12.

Rein, T. R. (2018). A geometric morphometric examination of hominoid third metacarpal shape and its implications for inferring the precursor to terrestrial bipedalism. *The Anatomical Record 302*(6), 983-998.

Reina, N., Cavaignac, E., Trousdale, W. H., Laffosse, J. M., & Braga, J. (2017). Laterality and grip strength influence hand bone micro-architecture in modern humans, an HR p QCT stud. *Journal of Anatomy, 230*(6), 796-804.

Remis, M. (1995). Effects of body size and social context on the arboreal activities of lowland gorillas in the Central African Republic. *American Journal of Physical Anthropology, 97*(4), 413-433.

Remis, M. (1998). The gorilla paradox: The effects of body size and habitat on the positional behavior of lowland and mountain gorillas. In E. Stasser, J. Fleagle, A. Rosenberger, & H. McHenry (Eds.), *Primate Locomotion* (pp. 95-106). Boston, MA: Springer.

Richards, G. (1986). Freed hands or enslaved feet? A note on the behavioural implications of ground-dwelling bipedalism. *Journal of Human Evolution, 15*(3), 413-150.

Richmond, B. G. (2007). Biomechanics of phalangeal curvature. *Journal of Human Evolution, 53*(6), 678-690.

Richmond, B. G., Begun, D. R., & Strait, D. S. (2001). Origin of human bipedalism: the knuckle-walking hypothesis revisited. *American Journal of Physical Anthropology, 116*(s33), 70-105.

Richmond, B. G., Roach, N. T., & Ostrofsky, K. R. (2016). Evolution of the early hominin hand. In T. Kivell, P. Lemelin, B. Richmond, & D. Schmitt (Eds.), *The Evolution of the Primate Hand* (pp. 515-543). New York: Springer.

Ricklan, D. E. (1987). Functional anatomy of the hand of Australopithecus africanus. *Journal of Human Evolution, 16*(7-8), 643-664.

Ridler, T., & Calvard, S. (1978). Picture thresholding using an iterative selection method. *IEEE Transactions on Systems, Man, and Cybernetics, SMC-8*, 630-632.

Robling, A. G. (2009). Is bone's response to mechanical signals dominated by muscle forces? *Medicine & Science in Sports & Exercise, 41*(11), 2044-2049.

Robling, A. G., & Turner, C. H. (2002). Mechanotransduction in bone: genetic effects on mechanosensitivity in mice. *Bone, 31*(5), 562-569.

Robling, A. G., Hinant, F. M., Burr, D. B., & Turner, C. H. (2002). Improved bone structure and strength after long-term mechanical loading is greatest if loading is separated into short bouts. *Journal of Bone and Mineral Research, 17*(8), 1545-1554.

Rodman, P. (1984). Foraging and social systems of orangutans and chimpanzees. In P. Rodman, & J. Cant (Eds.), *Adaptations for Foraging in Non-Human Primates* (pp. 134 –160). New York: Columbia University.

Rolian, C., & Gordon, A. D. (2013). Reassessing manual proportions in Australopithecus afarensis. *American Journal of Physical Anthropology, 152*(3), 393-406.

Rolian, C., Lieberman, D. E., & Hallgrímsson, B. (2010). The coevolution of human hands and feet. *Evolution, 64*(6), 1558-1568.

Rolian, C., Lieberman, D. E., & Zermeno, J. P. (2011). Hand biomechanics during simulated stone tool use. *Journal of Human Evolution, 61*(1), 26-41.

Rosas, A., Martínez-Maza, C., Bastir, M., García-Tabernero, A., Lalueza-Fox, C., Huguet, R., et al. (2006). Paleobiology and comparative morphology of a late Neandertal sample from El Sidrón, Asturias, Spain. *Proceedings of the National Academy of Sciences, 103*(51), 19266-19271.

Rose, M. (1988). Functional anatomy of the cheiridia. In J. Schwartz (Ed.), *Orangutan Biology* (pp. 299-310). Oxford, UK: Oxford University Press.

Rose, M. D. (1992). Kinematics of the trapezium-1st metacarpal joint in extant anthropoids and Miocene hominoids. *Journal of Human Evolution, 22*(4-5), 255-266.

Roux, W. (1881). *Der kampf der theile im organismus.* Leipzig: W. Engelmann.

Rubin, C. T., McLeod, K. J., & Bain, S. D. (1990). Functional strains and cortical bone adaptation: epigenetic assurance of skeletal integrity. *Journal of Biomechanics, 23*, 43-54.

Rubin, C., Turner, A. S., Mallinckrodt, C., Jerome, C., McLeod, K., & Bain, S. (2002). Mechanical strain, induced noninvasively in the high-frequency domain, is anabolic to cancellous bone, but not cortical bone. *Bone, 30*(3), 445-452.

Ruff, C. B. (1984). Allometry between length and cross-sectional dimensions of the femur and tibia in Homo sapiens sapiens. *American Journal of Physical Anthropology, 65*(4), 347-358.

Ruff, C. B. (2002). Long bone articular and diaphyseal structure in Old World monkeys and apes. I: locomotor effects. *American Journal of Physical Anthropology, 119*(4), 305-342.

Ruff, C. B., & Hayes, W. C. (1982). Subperiosteal expansion and cortical remodeling of the human femur and tibia with aging. *Science, 217*(4563), 945-948.

Ruff, C. B., & Runestad, J. A. (1992). Primate limb bone structural adaptations. *Annual Review of Anthropology*, 407-433.

Ruff, C. B., Burgess, M. L., Junno, J. A., Mudakikwa, A., Zollikofer, C. P., Ponce de León, M. S., et al. (2018). Phylogenetic and environmental effects on limb bone structure in gorillas. *American Journal of Physical Anthropology, 166*(2), 353-372.

Ruff, C. B., Trinkaus, E., Walker, A., & Larsen, C. S. (1993). Postcranial robusticity in Homo. I: Temporal trends and mechanical interpretation. *American Journal of Physical Anthropology, 91*(1), 21-53.

Ruff, C., Holt, B., & Trinkaus, E. (2006). Who's afraid of the big bad Wolff?:"Wolff's law" and bone functional adaptation. *American Journal of Physical Anthropology, 129*(4), 484-498.

Ryan, T. M., & Ketcham, R. A. (2002). The three-dimensional structure of trabecular bone in the femoral head of strepsirrhine primates. *Journal of Human Evolution, 43*(1), 1-26.

Ryan, T. M., & Ketcham, R. A. (2005). Angular orientation of trabecular bone in the femoral head and its relationship to hip joint loads in leaping primates. *Journal of Morphology, 265*(3), 249-263.

Ryan, T. M., & Krovitz, G. E. (2006). Trabecular bone ontogeny in the human proximal femur. *Journal of Human Evolution, 51*(6), 591-602.

Ryan, T. M., & Shaw, C. N. (2012). Unique suites of trabecular bone features characterize locomotor behavior in human and non-human anthropoid primates. *PloS one, 7*(7), e41037.

Ryan, T. M., & Shaw, C. N. (2013). Trabecular bone microstructure scales allometrically in the primate humerus and femur. *Proceedings of the Royal Society of London B: Biological Sciences, 280*(1758), 20130172.

Ryan, T. M., & Shaw, C. N. (2015). Gracility of the modern Homo sapiens skeleton is the result of decreased biomechanical loading. *Proceedings of the National Academy of Sciences, 112*(2), 372-377.

Ryan, T. M., & van Rietbergen, B. (2005). Mechanical significance of femoral head trabecular bone structure in Loris and Galago evaluated using micromechanical finite element models. *American Journal of Physical Anthropology, 126*(1), 82-96.

Ryan, T. M., & Walker, A. (2010). Trabecular bone structure in the humeral and femoral heads of anthropoid primates. *The Anatomical Record, 293*(4), 719-729.

Ryan, T. M., Carlson, K. J., Gordon, A. D., Jablonski, N., Shaw, C. N., & Stock, J. T. (2018). Human-like hip joint loading in Australopithecus africanus and Paranthropus robustus. *Journal of Human Evolution., 121*(1), 12-24.

Ryan, T. M., Colbert, M., Ketcham, R. A., & Vinyard, C. J. (2010). Trabecular bone structure in the mandibular condyles of gouging and nongouging platyrrhine primates. *American Journal of Physical Anthropology, 141*(4), 583-593.

Saers, J. P., Cazorla-Bak, Y., Shaw, C. N., Stock, J. T., & Ryan, T. M. (2016). Trabecular bone structural variation throughout the human lower limb. *Journal of Human Evolution, 97*, 97-108.

Samuel, D. S., Nauwelaerts, S., Stevens, J. M., & Kivell, T. L. (2018). Hand pressures during arboreal locomotion in captive bonobos (Pan paniscus). *Journal of Experimental Biology*, e170910.

Saparin, P., Scherf, H., Hublin, J. J., Fratzl, P., & Weinkamer, R. (2011). Structural adaptation of trabecular bone revealed by position resolved analysis of proximal femora of different primates. *The Anatomical Record, 294*(1), 55-67.

Sarmiento, E. E. (1988). Anatomy of the hominoid wrist joint: its evolutionary and functional implications. *International Journal of Primatology, 9*(4), 281-345.

Sarmiento, E. E. (1994). Terrestrial traits in the hands and feet of gorillas. *American Musuem Novitates*(3091), 1-56.

Sarringhaus, L. A., Stock, J. T., Marchant, L. F., & McGrew, W. C. (2005). Bilateral asymmetry in the limb bones of the chimpanzee (Pan troglodytes). *American Journal of Physical Anthropology, 128*(4), 840-845.

Scherf, H., & Tilgner, R. (2009). A new high-resolution computed tomography (CT) segmentation method for trabecular bone architectural analysis. *American Journal of Physical Anthropology, 140*(1), 39-51.

Scherf, H., Harvati, K., & Hublin, J. J. (2013). A comparison of proximal humeral cancellous bone of great apes and humans. *Journal of Human Evolution, 65*(1), 29-38.

Scherf, H., Wahl, J., Hublin, J. J., & Harvati, K. (2016). Patterns of activity adaptation in humeral trabecular bone in Neolithic humans and present-day people. *American Journal of Physical Anthropology, 159*(1), 106-115.

Scheuer, L., & Black, S. (2000). *Developmental juvenile osteology.* Oxford: Elsevier Academic Press.

Schilling, A. M., Tofanelli, S., Hublin, J. J., & Kivell, T. L. (2014). Trabecular bone structure in the primate wrist. *Journal of Morphology, 275*(5), 572-585.

Schlager, S. (2017). Morpho and Rvcg–Shape Analysis in R: R-Packages for Geometric Morphometrics, Shape Analysis and Surface Manipulations. In G. Zheng, S. Li, & G. Székely (Eds.), *Statistical Shape and Deformation analysis: Methods, Implementation and Applications* (pp. 217-256). Cambridge, MA: Academic Press.

Schmitt, D., Zeininger, A., & Granatosky, M. C. (2016). Patterns, variability, and flexibility of hand posture during locomotion in primates. In T. Kivell, P. Lemelin, B. Richmond, & D. Schmitt (Eds.), *The Evolution of the Primate Hand* (pp. 345-369). New York, NY: Springer.

Schmitz, R., Serre, D., Bonani, G., Feine, S., Hillgruber, F., Krainitzki, H., et al. (2002). The Neandertal type site revisited: interdisciplinary investigations of skeletal remains from the Neander Valley, Germany. *Proceedings of the National Academy of Sciences, 99*(20), 13342-13347.

Schneider, C. A., Rasband, W. S., & Eliceiri, K. W. (2012). NIH Image to ImageJ: 25 years of image analysis". *Nature Methods, 9*(97), 671-675.

Shaw, C. N., & Ryan, T. M. (2012). Does skeletal anatomy reflect adaptation to locomotor patterns? Cortical and trabecular architecture in human and nonhuman anthropoids. *American Journal of Physical Anthropology, 147*(2), 187-200.

Shrewsbury, M. M., Marzke, M. W., Linscheid, R. L., & Reece, S. P. (2003). Comparative morphology of the pollical distal phalanx. *American Journal of Physical Anthropology, 121*(1), 30-47.

Simpson, S. W., Latimer, B., & Lovejoy, C. O. (2018). Why Do Knuckle-Walking African Apes Knuckle-Walk? *The Anatomical Record, 301*(3), 496-514.

Skedros, J. G., & Baucom, S. L. (2007). Mathematical analysis of trabecular 'trajectories' in apparent trajectorial structures: the unfortunate historical emphasis on the human proximal femur. *Journal of Theoretical Biology, 244*(1), 15-45.

Skerry, T. M., & Lanyon, L. E. (1995). Interruption of disuse by short duration walking exercise does not prevent bone loss in the sheep calcaneus. *Bone, 16*(2), 269-274.

Skinner, M. M., Gunz, P., Wood, B. A., Boesch, C., & Hublin, J. J. (2009). Discrimination of extant Pan species and subspecies using the enamel–dentine junction morphology of lower molars. *American Journal of Physical Anthropology, 140*(2), 234-243.

Skinner, M. M., Stephens, N. B., Tsegai, Z. J., Foote, A. C., Nguyen, N. H., Gross, T., et al. (2015). Human-like hand use in Australopithecus africanus. *Science, 347*(6220), 395-399.

Skinner, M. M., Stephens, N. B., Tsegai, Z. J., Foote, A. C., Nguyen, N. H., Gross, T., et al. (2015b). Response to comment on "Human-like hand use in Australopithecus africanus". *Science, 348*(6239), 1101.

Smith, E. L., Gilligan, C., McAdam, M., Ensign, C. P., & Smith, P. E. (1989). Deterring bone loss by exercise intervention in premenopausal and postmenopausal women. *Calcified Tissue International, 44*(5), 312-321.

Smith, R. J. (2016). Explanations for adaptations, just-so stories, and limitations on evidence in evolutionary biology. *Evolutionary Anthropology: Issues, News, and Reviews, 25*(6), 276-287.

Smith, S. L. (2000). Shape variation of the human pollical distal phalanx and metacarpal. *American Journal of Physical Anthropology, 113*(3), 329-348.

Spoor, C., Zonneveld, F., & Macho, G. (1993). Linear measurements of cortical bone and dental enamel by computed tomography: applications and problems. *American Journal of Physical Anthropology, 91*, 469-484.

Spoor, F., Garland, T., Krovitz, G., Ryan, T. M., Silcox, M. T., & Walker, A. (2007). The primate semicircular canal system and locomotion. *Proceedings of the National Academy of Sciences, 104*(26), 10808-10812.

Stauber, M., Rapillard, L., van Lenthe, G. H., Zysset, P., & Müller, R. (2006). Importance of individual rods and plates in the assessment of bone quality and their contribution to bone stiffness. *Journal of Bone and Mineral Research, 21*(4), 586-595.

Stephens, N., Kivell, T., Gross, T., Pahr, D., Lazenby, R., Hublin, J., et al. (2016). Trabecular architecture in the thumb of Pan and Homo: implications for investigating hand use, loading, and hand preference in the fossil record. *American Journal of Physical Anthropology, 161*(4), 603-619.

Stephens, N., Kivell, T., Pahr, D., Hublin, J., & Skinner, M. (2018). Trabecular bone patterning across the human hand. *Journal of Human Evolution, 123*, 1-23.

Stern Jr, J. T. (2000). Climbing to the top: a personal memoir of Australopithecus afarensis. *Evolutionary Anthropology: Issues, News, and Reviews: Issues, News, and Reviews, 9*(3), 113-133.

Stern Jr, J. T., & Susman, R. L. (1983). The locomotor anatomy of Australopithecus afarensis. *American Journal of Physical Anthropology, 60*(3), 279-317.

Stock, J., & Pfeiffer, S. (201). Linking structural variability in long bone diaphyses to habitual behaviors: foragers from the southern African Later Stone Age and the Andaman Islands. *American Journal of Physical Anthropology, 115*(4), 337-348.

Straus, W. L. (1942). Rudimentary digits in primates. *The Quarterly Review of Biology, 17*(3), 228-243.

Stringer, C. &. (2001). Archaeology: those elusive Neanderthals. *Nature, 413*(6858), 791-792.

Strouhal, E., & Jungwirth, J. (1979). Paleogenetics of the late Roman-early Byzantine cemeteries at Sayala, Egyptian Nubia. *Journal of Human Evolution, 8*(7), 699-703.

Su, A., Wallace, I. J., & Nakatsukasa, M. (2013). Trabecular bone anisotropy and orientation in an Early Pleistocene hominin talus from East Turkana, Kenya. *Journal of Human Evolution, 64*(6), 667-677.

Sugardjito, J., & Cant, J. G. (1994). Geographic and sex differences in posltional behavior of orang-utans. *Treubia, 31*(1), 31-41.

Sugardjito, J., & van Hooff, J. (1986). Age-sex class differencesin the positional behavior of the Sumatran orangutan (Pongopygmaeus abelii) in the Gunung Leuser National Park, Indonesia. *Folia Primatologica, 47*, 14 –25.

Sugiyama, Y. (1994). Tool use by wild chimpanzees. *Nature, 367*(6461), 327.

Sukhdeo, S., Parsons, J., Niu, X., & Ryan, T. (2018). Trabecular bone structure in the distal femur of humans, apes, and baboons. *The Anatomical Record,* doi:10.1002/ar.24050

Susman, R. L. (1979). Comparative and functional morphology of hominoid fingers. *American Journal of Physical Anthropology, 50*(2), 215-236.

Susman, R. L. (1984). The Locomotor Behavior of Pan paniscus in the Lomako Forest. In R. L. Susman (Ed.), *The Pygmy Chimpanzee* (pp. 369-393). Boston, MA: Springer.

Susman, R. L. (1988). Hand of Paranthropus robustus from Member 1, Swartkrans: fossil evidence for tool behavior. *Science, 240*(4853), 781-784.

Susman, R. L. (1994). Fossil evidence for early hominid tool use. *Science, 265*(5178), 1570-1573.

Susman, R. L. (1998). Hand function and tool behavior in early hominids. *Journal of Human Evolution, 35*(1), 23-46.

Susman, R. L., & Badrian, A. J. (1980). Locomotor behaviour of Pan paniscusin Zaire. *American journal of Physical Anthropology, 53*, 69-80.

Susman, R. L., & Creel, N. (1979). Functional and morphological affinities of the subadult hand (OH 7) from Olduvai Gorge. *American Journal of Physical Anthropology, 51*(3), 311-331.

Susman, R. L., Badrian, N. L., & Badrian, A. J. (1980). Locomotor behaviour of Pan paniscus in Zaire. *American Journal of Physical Anthropology, 53*, 69-80.

Susman, R. L., de Ruiter, D., & Brain, C. K. (2001). Recently identified postcranial remains of Paranthropus and early Homo from Swartkrans Cave, South Africa. *Journal of Human Evolution, 46*(1), 607-629.

Sylvester, A. D., & Terhune, C. E. (2017). Trabecular mapping: Leveraging geometric morphometrics for analyses of trabecular structure. *American Journal of Physical Anthropology, 163*(3), 553-569.

Tanck, E., Homminga, J., Van Lenthe, G. H., & Huiskes, R. (2001). Increase in bone volume fraction precedes architectural adaptation in growing bone. *Bone, 28*(6), 650-654.

Tardieu, C. (2010). Development of the human hind limb and its importance for the evolution of bipedalism. *Evolutionary Anthropology: Issues, News, and Reviews, 19*(5), 174-186.

Thompson, N. E., Ostrofsky, K. R., McFarlin, S. C., Robbins, M. M., Stoinski, T. S., & Almécija, S. (2018). Unexpected terrestrial hand posture diversity in wild mountain gorillas. *American Journal of Physical Anthropology, 166*(1), 84-94.

Thorpe, S. K., & Crompton, R. H. (2005). Locomotor ecology of wild orangutans (Pongo pygmaeus abelii) in the Gunung Leuser Ecosystem, Sumatra, Indonesia: A multivariate analysis using log-linear modeling. *American Journal of Physical Anthropology, 127*(1), 58-78.

Thorpe, S. K., & Crompton, R. H. (2006). Orangutan positional behavior and the nature of arboreal locomotion in Hominoidea. *American Journal of Physical Anthropology, 131*(3), 384-401.

Tocheri, M. (2007). *Three-dimensional riddles of the radial wrist: derived carpal and carpometacarpal joint morphology in the genus Homo and the implications for understanding the evolution of stone tool-related behaviors in hominins.* PhD Dissertation Tempe, Arizona USA: Arizona State University.

Tocheri, M. W., Orr, C. M., Jacofsky, M. C., & Marzke, M. W. (2008). The evolutionary history of the hominin hand since the last common ancestor of Pan and Homo. *Journal of Anatomy, 212*(4), 544-562.

Tocheri, M. W., Orr, C. M., Larson, S. G., Sutikna, T., Saptomo, E. W., Due, R. A., et al. (2007b). The primitive wrist of Homo floresiensis and its implications for hominin evolution. *Science, 317*(5845), 1743-1745.

Tocheri, M. W., Razdan, A., Williams, R. C., & Marzke, M. W. (2005). A 3D quantitative comparison of trapezium and trapezoid relative articular and nonarticular surface areas in modern humans and great apes. *Journal of Human Evolution, 49*(5), 570-586.

Toft, R., & Berme, N. (1980). A biomechanical analysis of the joints of the thumb. *Journal of Biomechanics, 13*(4), 353-360.

Toth, N., Schick, K. D., Savage-Rumbaugh, E. S., Sevcik, R. A., & Rumbaugh, D. M. (1993). Pan the tool-maker: investigations into the stone tool-making and tool-using capabilities of a bonobo (Pan paniscus). *Journal of Archaeological Science, 20*(1), 81-91.

Trinkaus, E. (1983). *The Shanidar Neandertals.* New York: Academic Press.

Trinkaus, E., & Long, J. C. (1990). Species attribution of the Swartkrans Member 1 first metacarpals: SK 84 and SKX 5020. *American Journal of Physical Anthropology, 83*(4), 419-424.

Trussell, H. (1979). Comments on "Picture thresholding using an iterative selection method". *IEEE Transactions on Systems, Man, and Cybernetics, SMC-9*, 311-311.

Tsagris, M., & Athineou, G. (2018). *Compositional: Compositional Data Analysis. R package version 3.1*

Tsegai, Z. J., Kivell, T. L., Gross, T., Nguyen, N. H., Pahr, D. H., Smaers, J. B., et al. (2013). Trabecular bone structure correlates with hand posture and use in hominoids. *PLoS One, 8*(11), e78781.

Tsegai, Z. J., Skinner, M. M., Gee, A. H., Pahr, D. H., Treece, G. M., Hublin, J. J., et al. (2017b). Trabecular and cortical bone structure of the talus and distal tibia in Pan and Homo. *American Journal of Physical Anthropology, 163*(4), 784-805.

Tsegai, Z. J., Skinner, M. M., Pahr, D. H., Hublin, J. J., & Kivell, T. L. (2018). Systemic patterns of trabecular bone across the human and chimpanzee skeleton. *Journal of Anatomy*, 1-16.

Tsegai, Z. J., Stephens, N. B., Treece, G. M., Skinner, M. M., Kivell, T. L., & Gee, A. H. (2017). Cortical bone mapping: An application to hand and foot bones in hominoids. *Comptes Rendus Palevol, 16*(5-6), 690-701.

Turner, C. (1998). Three rules for bone adaptation to mechanical stimuli. *Bone, 23*(5), 399-407.

Tuttle, R. H. (1967). Knuckle-walking and the evolution of hominoid hands. *American Journal of Physical Anthropology, 26*(2), 171-206.

Tuttle, R. H. (1969). Knuckle-walking and the problem of human origins. *Science, 166*(3908), 953-961.

Tuttle, R. H. (1969b). Quantitative and functional studies on the hands of the Anthropoidea. I. The Hominoidea. *Journal of Morphology, 128*(3), 309-363.

Tuttle, R. H., & Basmajian, J. V. (1978). Electromyography of pongid shoulder muscles. III. Quadrupedal positional behavior. *American Journal of Physical Anthropology, 49*(1), 57-69.

Tuttle, R. H., & Watts, D. P. (1985). The positional behavior and adaptive complexes of Pan (Gorilla). In S. Kondo (Ed.), *Primate Morphophysiology, Locomotor Analyses and Human Bipedalism* (pp. 261-288). Tokyo: University of Tokyo Press.

Uchiyama, T., Tanizawa, T., Muramatsu, H., Endo, N., Takahashi, H. E., & Hara, T. (1999). Three-dimensional microstructural analysis of human trabecular bone in relation to its mechanical properties. *Bone, 25*(4), 487-491.

Valladas, H., Joron, J., Valladas, G., Arensburg, B., Bar-Yosef, O., Belfer-Cohen, A., et al. (1987). Thermoluminescence dates for the Neanderthal burial site at Kebara in Israel. *Nature, 330*(6144), 159-160.

van Leeuwen, T., Vanhoof, M. J., Kerkhof, F. D., Stevens, J. M., & Vereecke, E. E. (2018). Insights into the musculature of the bonobo hand. *Journal of Anatomy 233*(3), 382-340.

van Leeuwen, T., Vanneste, M., Kerkof, F., D'Agostino, P., Vanhoof, M., Stevens, J., et al. (2018b). Mobility and structural constraints of the bonobo trapeziometacarpal joint. *Biological Journal of the Linnean Society*,*127*(3) 681-693.

van Schaik, C. P., Fox, E. A., & Sitompul, A. F. (1996). Manufacture and use of tools in wild Sumatran orangutans. *Naturwissenschaften, 83*(4), 186-188.

Vico, L., Collet, P., Guignandon, A., Lafage-Proust, M. H., Thomas, T., Rehailia, M., et al. (2000). Effects of long-term microgravity exposure on cancellous and cortical weight-bearing bones of cosmonauts. *The Lancet, 355*(9215), 1607-1611.

Wallace, I. J., Kwaczala, A. T., Judex, S., Demes, B., & Carlson, K. J. (2013). Physical activity engendering loads from diverse directions augments the growing skeleton. *Journal of Musculoskeletal and Neuronal Interactions, 13*(3), 283-288.

Wallace, I., Demes, B., & Judex, S. (2017). Ontogenetic and Genetic Influences on Bone's Responsiveness to Mechanical Signals. In C. Percival & J. Richtsmeier (Eds.), *Building Bones: Bone Formation and Development in Anthropology* (pp. 233-253). Cambridge: Cambridge University Press.

Ward, C. V. (2002). Interpreting the posture and locomotion of Australopithecus afarensis: where do we stand? *American Journal of Physical Anthropology, 119*(s35), 185-215.

Warden, S. J., Kersh, M. E., Hurd, A. L., Fleisig, G. S., Pandy, M. G., & Fuchs, R. K. (2014). Physical activity when young provides lifelong benefits to cortical bone size and strength in men. *Proceedings of the National Academy of Sciences, 111*(14), 5337-5342.

Whitcome, K., Shapiro, L. J., & Lieberman, D. E. (2007). Fetal load and the evolution of lumbar lordosis in bipedal hominins. *Nature, 450*(7172), 1075-1078.

White, T. D., Black, M. T., & Folkens, P. A. (2011). *Human Osteology.* London: Academic Press.

Whitehouse, W. J., & Dyson, E. D. (1974). Scanning electron microscope studies of trabecular bone in the proximal end of the human femur. *Journal of Anatomy, 118*(3), 417-444.

Wilkinson, J. (1953). The insertion of the flexores pollicis longus et digitorium profundus. *Journal of Anatomy, 87*, 75-91.

Williams, E. M., Gordon, A. D., & Richmond, B. G. (2012). Hand pressure distribution during Oldowan stone tool production. *Journal of Human Evolution, 62*(4), 520-532.

Williams-Hatala, E. M., Hatala, K. G., Gordon, M., Key, A., Kasper, M., & Kivell, T. L. (2018). The manual pressures of stone tool behaviors and their implications for the evolution of the human hand. *Journal of Human Evolution, 119*(1), 14-26.

Williams-Hatala, E., Hatala, K., Hiles, S., & Rabey, K. (2016). Morphology of muscle attachment sites in the modern human hand does not reflect muscle architecture. *Scientific Reports(6)*, 28353.

Willie, B., Birkhold, A., Razi, H., Thiele, T., Aido, M., Kruck, B., et al. (2013). Diminished response to in vivo mechanical loading in trabecular and not cortical bone in adulthood of female C57Bl/6 mice coincides with a reduction in deformation to load. *Bone, 55*(2), 335-346.

Witmer, L. M., Ridgely, R. C., Dufeau, D. L., & Semones, M. C. (2008). Using CT to peer into the past: 3D visualization of the brain and ear regions of birds, crocodiles, and nonavian dinosaurs. In H. Endo, & R. Frey (Eds.), *Anatomical imaging* (pp. 67-87). Tokyo: Springer.

Wolff, J. (1892). *The Law of Bone Remodeling (Das Gesetz der Transformation der Knochen, Hirschwald).* (P. Maquet, & R. Furlong, Trans.) Berlin: Springer.

Wollny, G., Kellman, P., Ledesma-Carbayo, M. J., Skinner, M. M., Hublin, J. J., & Hierl, T. (2013). MIA-A free and open source software for gray scale medical image analysis. *Source code for Biology and Medicine, 8*(1), 8-20.

Won, Y. J., & Hey, J. (2004). Divergence population genetics of chimpanzees. *Molecular Biology and Evolution, 22*(2), 297-307.

Wong, A. L., Meals, C. G., & Ruff, C. B. (2018). Computed tomographic analysis of the internal structure of the metacarpals and its implications for hand use, pathology, and surgical intervention. *Anatomical Science International, 93*(2), 231-237.

Wood, R., Higham, T., De Torres, T., Tisnérat-Laborde, N., Valladas, H., Ortiz, J., et al. (2013). A new date for the Neanderthals from El Sidrón Cave (Asturias, northern Spain). *Archaeometry, 55*(1), 148-158.

Wood-Jones, F. (1916). *Arboreal Man.* London: Edward Arnold.

Wright, R. V. (1972). Imitative learning of a flaked stone technology—the case of an orangutan. *Mankind, 8*(4), 296-306.

Wright, S. (1932). The roles of mutation, inbreeding, crossbreeding and selection in evolution. In D. Jones (Ed.), *Proceedings of the Sixth International Congress of Genetics* (pp. 356–366). New York.

Wunderlich, R. E., & Jungers, W. L. (2009). Manual digital pressures during knuckle-walking in chimpanzees (Pan troglodytes). *American Journal of Physical Anthropology, 139*(3), 394-403.

Yeh, H. C., & Wolf, B. S. (1977). Radiographic Anatomical Landmarks of the Metacarpo-Phalangeal Joints. *Radiology, 122*(2), 353-355.

Young, J. W., Jankord, K., Saunders, M. M., & Smith, T. D. (2018). Getting into shape: Limb bone strength in perinatal Lemur catta and Propithecus coquereli. *The Anatomical Record.*, 1-15 doi:10.1002/ar.24045.

Zeininger, A., Patel, B. A., Zipfel, B., & Carlson, K. J. (2016). Trabecular architecture in the StW 352 fossil hominin calcaneus. *Journal of Human Evolution, 97*(1), 145-158.

Zeininger, A., Richmond, B. G., & Hartman, G. (2011). Metacarpal head biomechanics: A comparative backscattered electron image analysis of trabecular bone mineral density in Pan troglodytes, Pongo pygmaeus, and Homo sapiens. *Journal of Human Evolution, 60*(6), 703-710.

Zhou, G.-Q., Pang, Z.-H., Chen, Q.-Q., He, W., Chen, Z.-Q., Chen, L.-L., et al. (2014). Reconstruction of the biomechanical transfer path of femoral head necrosis: A subject-specific finite element investigation. *Computers in Biology and Medicine, 52*, 96-101.

Zihlman, A. L. (1984). Body build and tissue composition in Pan paniscus and Pan troglodytes, with comparisons to other hominoids. In R. L. Susman (Ed.), *The Pygmy Chimpanzee* (pp. 179-200). Boston, MA: Springer.

Zihlman, A. L., Mcfarland, R. K., & Underwood, C. E. (2011). Functional anatomy and adaptation of male gorillas (Gorilla gorilla gorilla) with comparison to male orangutans (Pongo pygmaeus). *The Anatomical Record, 294*(11), 1842-1855.

Zipfel, B., DeSilva, J. M., Kidd, R. S., Carlson, K. J., Churchill, S. E., & Berger, L. R. (2011). The foot and ankle of Australopithecus sediba. *Science, 333*(6048), 1417-1420.

Zumwalt, A. (2006). The effect of endurance exercise on the morphology of muscle attachment sites. *Journal of Experimental Biology, 209*(3), 444-454.

Appendix A
Scanning Protocol and Samples

Scanning protocol

Metacarpals

- Use the small Perspex tube for each set of five metacarpals.
- Wrap open cell foam around the metacarpals lengthways.
- Secure with scotch tape the entire way around at both ends .
- Place the large second to fifth metacarpals in the tube, if there is space gently wedge the first metacarpal in the space.

Carpals

- Use the four black foam inserts I cut to fit each general carpal shape and fit the two or three carpals in each piece.
- Arrange them so the line between each bone is orthogonal to the one above (this ensures bones fall to the edge rather than touch in the middle).
    - For close packing insert an open cell foam disc in the top hand and gently push down flat with a smaller tube or pen.

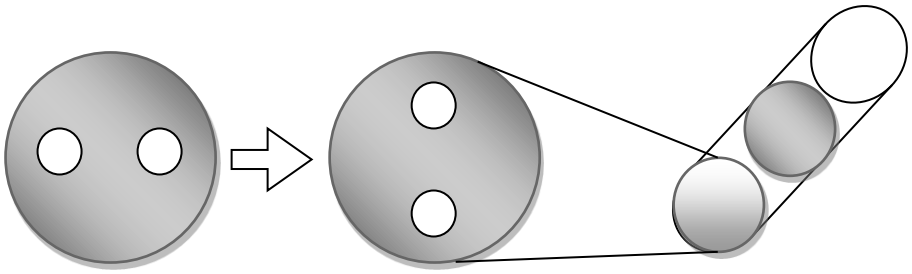

Proximal and Intermediate phalanges

- Wrap up the proximal phalanges (five bones with a single facet at the base) just like the metacarpals and insert them lengthways as before. Please insert the second upside down, the 3rd up, 4th upside down and the 5th up; the first is the smallest and can be squeezed in the top

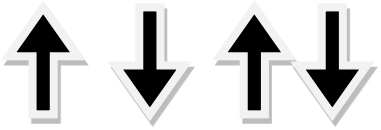

- Insert an open cell foam disc in the tube.
- Wrap up the remaining four bones (intermediate phalanges with a double facet on the base) and place in order as before(i.e. 2nd upside down, the 3rd up, 4th upside down and the 5th up).
- May have to add some foam to wedge the top stage so it is stable.

Samples analysed

Appendix A Table 1. Fossil sample composition. Where fossil metacarpals are not associated the fossils that comprise the composite metacarpi are given. LLR refers to side of the metacarpals used for composite, in this case a left Mc2 and 3 with a right Mc 4 or 5.*This sex designation only applies to AL438-1; AL333-141 is of unknown sex.

Fossil	Taxonomy	Side	Sex	Element	Unassociated metacarpals	Date	Reference
STW418	*A. africanus*	left	unknown	Mc1		1.95-2.95 mya	Pickering et al., 2011
SK84	*Homo/ Paranthropus*	left	unknown	Mc1		~1.6-1.8mya	Susman et al., 2001
Neanderthal 1, Feldhofer 1	*H. neanderthalensis*	left	unknown	Mc1		40 kya	Schmitz et al., 2002
Barma Grande 2	*H. sapiens*	left	male	Mc1		19 kya	Bisson et al., 1996
Malapa Hominin 2	*A. sediba*	right	female	Mc1-5		1.98 mya	Kivell et al., 2011
Kebara 2	*H. neanderthalensis*	left	male	Mc1-5		60 kya	Valladas et al., 1987
El Sidrón	*H. neanderthalensis*	left	unknown	Mc1-5	SD-661 SDR-73 SDR-74 SDR-70 SDR-77	49kya	Wood et al., 2013
Ohalo 2 H2	*H. sapiens*	left	male	Mc1-5		23 kya	Hershkovitz et al., 1995
Arene Candide 2	*H. sapiens*	left	male	Mc1-5		12kya	Formicola et al., 1990
Hadar, Afar localities 438 and 333	*A. afarenisis*	LLR	male*	Mc2, 3 and 5	AL438-1d AL438-1e AL333-141	~3-3.2mya	Kimbel et al., 2004
Sterkfontein Member 4	*A. africanus*	LLR	unknown	Mc2, 3 and 4	STW394 STW382 STW552	1.95-2.95 mya	Pickering et al., 2011
Tabun C1	*H. neanderthalensis*	left	female	Mc1, 3 and 5		~122 kya	Bar-Yosef and Callander, 1999

Appendix A Table 2. Extant sample composition. All metacarpals from each hand were analysed.

Taxonomy	Accession ID	Sex	Side	Institution
Gorilla gorilla gorilla	PC_MER_300	Female	Left	Powell-Cotton Museum, Birchington-on-sea
Gorilla gorilla gorilla	PC_MER_264	Male	Right	Powell-Cotton Museum, Birchington-on-sea
Gorilla gorilla gorilla	PC_MER_372	Male	Left	Powell-Cotton Museum, Birchington-on-sea
Gorilla gorilla gorilla	PC_MER_95	Female	Right	Powell-Cotton Museum, Birchington-on-sea
Gorilla gorilla gorilla	PC_MER_962	Male	Left	Powell-Cotton Museum, Birchington-on-sea
Gorilla gorilla gorilla	PC_CAMI_230	Male	Left	Powell-Cotton Museum, Birchington-on-sea
Gorilla gorilla gorilla	PC_MER_138	Female	Left	Powell-Cotton Museum, Birchington-on-sea
Gorilla gorilla gorilla	PC_MER_174	Male	Right	Powell-Cotton Museum, Birchington-on-sea
Gorilla gorilla gorilla	PC_MER_696	Female	Right	Powell-Cotton Museum, Birchington-on-sea
Gorilla gorilla gorilla	PC_MER_856	Female	Left	Powell-Cotton Museum, Birchington-on-sea
Gorilla gorilla gorilla	PC_MER_879	Male	Left	Powell-Cotton Museum, Birchington-on-sea
Gorilla gorilla gorilla	PC_ZVI_32	Male	Right	Powell-Cotton Museum, Birchington-on-sea
Pan troglodytes verus	MPITC_11789	Male	Right	Max Planck Institute for Evolutionary Anthropology, Leipzig
Pan troglodytes verus	MPITC_11778	Female	Right	Max Planck Institute for Evolutionary Anthropology, Leipzig
Pan troglodytes verus	MPITC_13439	Female	Right	Max Planck Institute for Evolutionary Anthropology, Leipzig
Pan troglodytes verus	MPITC_15002	Female	Left	Max Planck Institute for Evolutionary Anthropology, Leipzig
Pan troglodytes verus	MPITC_11800	Female	Right	Max Planck Institute for Evolutionary Anthropology, Leipzig
Pan troglodytes verus	MPITC_11903	Male	Left	Max Planck Institute for Evolutionary Anthropology, Leipzig
Pan troglodytes verus	MPITC_11781	Male	Left	Max Planck Institute for Evolutionary Anthropology, Leipzig
Pan troglodytes verus	MPITC_14996	Female	Left	Max Planck Institute for Evolutionary Anthropology, Leipzig
Pan troglodytes verus	MPITC_15012	Male	Right	Max Planck Institute for Evolutionary Anthropology, Leipzig
Pan troglodytes verus	MPITC_15013	Female	Right	Max Planck Institute for Evolutionary Anthropology, Leipzig
Pan troglodytes verus	MPITC_15014	Male	Right	Max Planck Institute for Evolutionary Anthropology, Leipzig
Pan troglodytes verus	MPITC_15032	Male	Left	Max Planck Institute for Evolutionary Anthropology, Leipzig
Pan troglodytes	ZSM_AP_122	Male	Right	Bavarian State Collection of Zoology, Munich
Pongo abelii	SMF_6785	Male	Right	Senckenberg Natural History Museum, Frankfurt
Pongo abelii	SMF_6779	Female	Left	Senckenberg Natural History Museum, Frankfurt
Pongo pygmaeus	ZSM_1907_0633b	Female	Right	Bavarian State Collection of Zoology, Munich
Pongo pygmaeus pygmaeus	ZSM_1907_0660	Female	Right	Bavarian State Collection of Zoology, Munich

Pongo sp. indet.	ZSM_AP-120	Male	Left	Bavarian State Collection of Zoology, Munich
Pongo pygmaeus pygmaeus	ZSM_1907_0483	Female	Right	Bavarian State Collection of Zoology, Munich
Pongo pygmaeus pygmaeus	ZSM_1909_0801	Male	Right	Bavarian State Collection of Zoology, Munich
Pongo abelii	NMNH_267325	Male	Left	Smithsonian Institution National Museum of Natural History, Washington D.C.
Pongo pygmaeus	ZMB_6948	Female	Left	Natural History Museum, Berlin
Pongo pygmaeus	ZMB_6947	Male	Left	Natural History Museum, Berlin
Pongo pygmaeus	ZMB_87092	Female	Right	Natural History Museum, Berlin
Pongo pygmaeus	ZMB_11647*	Unknown	Left	Natural History Museum, Berlin
Pan paniscus	MRAC_15293	Female	Left	Royal Museum for Central Africa, Tervuren
Pan paniscus	MRAC_15294	Male	Left	Royal Museum for Central Africa, Tervuren
Pan paniscus	MRAC_20881	Male	Left	Royal Museum for Central Africa, Tervuren
Pan paniscus	MRAC_27696	Male	Right	Royal Museum for Central Africa, Tervuren
Pan paniscus	MRAC_27698	Female	Left	Royal Museum for Central Africa, Tervuren
Pan paniscus	MRAC_29042	Female	Right	Royal Museum for Central Africa, Tervuren
Pan paniscus	MRAC_29044	Male	Right	Royal Museum for Central Africa, Tervuren
Pan paniscus	MRAC_29045	Female	Left	Royal Museum for Central Africa, Tervuren
Pan paniscus	MRAC_29052	Male	Right	Royal Museum for Central Africa, Tervuren
Pan paniscus	MRAC_29060	Female	Right	Royal Museum for Central Africa, Tervuren
Homo sapiens	GAUG-Inden_118	Male	Right	University of Göttingen, Göttingen
Homo sapiens	GAUG-Inden_119*	Male	Right	University of Göttingen, Göttingen
Homo sapiens	GAUG-Inden_311	Male	Right	University of Göttingen, Göttingen
Homo sapiens	GAUG-Inden_319	Unknown	Right	University of Göttingen, Göttingen
Homo sapiens	NHMW-Nubian_J2	Male	Right	Natural History Museum Vienna, Vienna
Homo sapiens	NHMW-Nubian_K13_3	Male	Right	Natural History Museum Vienna, Vienna
Homo sapiens	NHMW-Nubian_K18_2	female	Right	Natural History Museum Vienna, Vienna
Homo sapiens	NHMW-Nubian_K24_2	female	Right	Natural History Museum Vienna, Vienna
Homo sapiens	NHMW-Nubian_K5_2	Male	Right	Natural History Museum Vienna, Vienna
Homo sapiens	NHMW-Nubian_K78_2	female	Right	Natural History Museum Vienna, Vienna
Homo sapiens	UNIFL_3124	Unknown	Right	University of Florence, Florence
Homo sapiens	UNIFL_4865	Male	Right	University of Florence, Florence
Homo sapiens	UNIFL_4887	female	Right	University of Florence, Florence

* Only the Mc1 from this hand was used for analysis.

Fossil samples not analysed

Appendix A Table 3. Un-analysed fossils. The fossils were processed in medtool but were unsuitable for further analysis as the preservation of internal structure was not sufficient.

Fossil	Taxonomy	Element	Side
STW26	*Australopithecus africanus*	Mc4	Right
SK85	*Paranthropus robustus*	Mc4	Left
KB542	*Paranthropus robustus*	Unknown	Unknown
SKX5020	*Paranthropus robustus*	Mc1	Right
STW330	*Australopithecus africanus*	Mc4	Left
AL333-48	*Australopithecus afarensis*	Mc2	Left
AL333-18	*Australopithecus afarensis*	Mc4	Right
AL333-16	*Australopithecus afarensis*	Mc3	Left
AL333-56/AL333-81	*Australopithecus afarensis*	Mc4	Left
AL333-89	*Australopithecus afarensis*	Mc5	Left
AL333-14	*Australopithecus afarensis*	Mc5	Right
Barma Grande 2	*Homo sapiens*	Mc2-4	Left

Appendix B
Published work

MIA-Clustering: a novel method for segmentation of paleontological material

Christopher J. Dunmore[1], Gert Wollny[1] and Matthew M. Skinner[1,2]

[1] School of Anthropology and Conservation, University of Kent, Canterbury, Kent, UK
[2] Department of Human Evolution, Max Planck Institute for Evolutionary Anthropology, Leipzig, Germany

ABSTRACT

Paleontological research increasingly uses high-resolution micro-computed tomography (μCT) to study the inner architecture of modern and fossil bone material to answer important questions regarding vertebrate evolution. This non-destructive method allows for the measurement of otherwise inaccessible morphology. Digital measurement is predicated on the accurate segmentation of modern or fossilized bone from other structures imaged in μCT scans, as errors in segmentation can result in inaccurate calculations of structural parameters. Several approaches to image segmentation have been proposed with varying degrees of automation, ranging from completely manual segmentation, to the selection of input parameters required for computational algorithms. Many of these segmentation algorithms provide speed and reproducibility at the cost of flexibility that manual segmentation provides. In particular, the segmentation of modern and fossil bone in the presence of materials such as desiccated soft tissue, soil matrix or precipitated crystalline material can be difficult. Here we present a free open-source segmentation algorithm application capable of segmenting modern and fossil bone, which also reduces subjective user decisions to a minimum. We compare the effectiveness of this algorithm with another leading method by using both to measure the parameters of a known dimension reference object, as well as to segment an example problematic fossil scan. The results demonstrate that the medical image analysis-clustering method produces accurate segmentations and offers more flexibility than those of equivalent precision. Its free availability, flexibility to deal with non-bone inclusions and limited need for user input give it broad applicability in anthropological, anatomical, and paleontological contexts.

Subjects Anthropology, Bioinformatics
Keywords Digital image processing, Micro-CT, Machine-learning, Fossil, Trabecular bone

INTRODUCTION

Over the last decade there has been an abundance of high-resolution micro-computed tomography (μCT) studies within the paleontological and anthropological communities, likely due to the ability of this method to non-destructively image extant and fossil specimens. This has been used to investigate the inner osseous architecture of a diverse range of orders including: primates (*Ryan et al., 2010*), galliformes (*Pontzer et al., 2006*), xenarthrans (*Amson et al., 2017*) and diprotodontians (*Biewener et al., 1996*). The technique allows the visualization of internal structures, such as trabeculae

Submitted 1 November 2017
Accepted 25 January 2018
Published 23 February 2018

Corresponding author
Christopher J. Dunmore,
cjd37@kent.ac.uk

Academic editor
Philip Reno

Additional Information and Declarations can be found on page 16

DOI **10.7717/peerj.4374**

(*Fajardo et al., 2007*), the enamel–dentine junction of teeth (*Skinner et al., 2009*) or the inner ear (*Spoor et al., 2007*). This is of particular importance for fossils, whose inner architecture could only be destructively analyzed otherwise (*Witmer et al., 2008*; *Kivell, 2016*). To visualize very small biological structures, it is necessary to ensure adequate X-ray penetration of the bone or fossil material being CT-scanned, as well as to control for common artifacts such as beam hardening (*Herman, 1979*). To digitally measure these structures and their properties, it is necessary to define them in the scan image and so the image must be accurately segmented (*Hara et al., 2002*).

Various segmentation protocols have been developed for anthropological applications. Simple thresholding involves the visual selection of a grayscale value, any part of the image composed of voxels above this value is considered the phase of interest. Iterative adaptive thresholding (*Ridler & Calvard, 1978*; *Trussell, 1979*; *Ryan & Ketcham, 2002*) improves on this simple thresholding by optimizing the threshold value between the present phases. Conversely, half-maximum-height thresholding (*Spoor, Zonneveld & Macho, 1993*; *Coleman & Colbert, 2007*) recalculates the threshold over a row of pixels, which cross a phase boundary, periodically in the *z*-axis of a three-dimensional (3D) image. These three methods are all sensitive to intensity inhomogeneity and background noise in a scan (*Scherf & Tilgner, 2009*). In all cases, a grayscale value threshold calculated from a different or larger section of an image may not accurately segment all parts of the structure.

Instead of using grayscale values alone, region-based segmentation approaches incorporate the spatial information in a scan. Region growing methods use seed points, manually selected by the researcher, known to be in the phase of interest. A segmented region is then grown from the seed by connecting neighboring voxels that meet specific, pre-defined criteria (*Pham, Xu & Prince, 2000*). Region splitting, conversely, does not use seed points but divides the image into distinct regions and refuses the image based on selected criteria. Both region-based approaches, however, often require a priori knowledge of image features to select seed points or criteria, and can be sensitive to intensity inhomogeneity (*Pham, Xu & Prince, 2000*; *Dhanachandra & Chanu, 2017*).

Edge-detection-based segmentation offers an alternative method that discerns the transition between two phases and delineates these voxels as an edge. The Ray Casting Algorithm (RCA, *Scherf & Tilgner, 2009*) is an example of this method used in anthropology (*Tsegai et al., 2013*). This algorithm uses a 3D-Sobel filter to mark voxels at the peak of rapid changes in grayscale values and subsequently removes the rest of the image with a non-maximum suppression filter. To be considered part of the remaining edge of the phase of interest, the gradient of the grayscale transition must be above a user-defined "minimum edge strength" parameter. This one-voxel-thick edge may have infrequent gaps due to local, more gradual, transitions not quite satisfying the "minimum edge strength" threshold. In order to ameliorate this, a series of rays are subsequently cast at 11.25° steps around the normal of each edge voxel in an arc of ±45°. The rays are set to terminate on meeting a voxel with the specified "minimum edge strength," so edge voxels that neighbor these gaps terminate the rays at most angles, and

the gap is closed. The RCA segmentation produces a structure with the continuous edge described (*Tsegai et al., 2013*).

Edge-based segmentation techniques provide an advantage over other techniques in that they are resistant to the effects of both background noise and intensity inhomogeneity. Tests of segmentation methods have found RCA is more accurate than thresholding methods (*Scherf & Tilgner, 2009*). Similarly, algorithms such as RCA require less prior knowledge of the image, as they need no seed points or initial manual segmentation. Still, the RCA requires the selection of the "minimum edge strength" value and may also incorporate minimum or maximum threshold values. These input values are found during trial segmentation of a sub-set of the data (*Scherf & Tilgner, 2009*). The selection of these three parameters is partially subjective, as is the case with all segmentation algorithms. This input parameter selection represents another source of error, that an algorithm must be robust to, in addition to background noise and intensity inhomogeneity. An algorithm run with extreme parameters is unlikely to produce an accurate segmentation. With RCA, the same segmentation can be produced with different sets of input values. This equifinality is not a problem of the method per se, but allows for additional potential difficulty in reproducing the same segmentation. A researcher cannot be sure that a visually similar segmentation was produced using the same RCA parameters. Here we present a segmentation method, medical image analysis (MIA)-Clustering, implemented as free- and open-source software (*Wollny et al., 2013*), that reduces subjective user decisions to a minimum. Broadly, clustering approaches sort the voxels or pixels of an image into a number of clusters defined by the user. This sorting is accomplished by iteratively calculating the center of a cluster and its distance to the other voxels in that cluster. This iteration then converges on stable clusters by minimizing this distance and the voxels in each cluster are segmented as distinct phases. The MIA-Clustering algorithm performs this sorting both globally and locally to segment an image based on its properties.

We test the efficacy of the MIA-Clustering algorithm by segmenting a reference model of known thickness. Results of this segmentation and a RCA segmentation of the same material following *Scherf & Tilgner (2009)* are compared. To assess the robustcity of the MIA-Clustering algorithm to variation in parameter selection, segmentations of this synthetic material, produced by a range of inputs, are analyzed. Similarly, a fossil sample is segmented with different parameters to assess their effect on the segmentation of a highly variable, embedded, natural structure. This fossil also presents a challenging segmentation, due to multiple phases of invasive matrix as well as bright inclusions, and so permits an assessment of the MIA-Clustering algorithm's robusticity to background noise and intensity inhomogeneity. The fossil is also segmented using the RCA to compare the simplicity and accuracy of both methods.

MATERIALS

A coiled stainless steel wire, which is rectangular in cross-section, was used as a reference object of known thickness (40 μm). This materially homogeneous phantom was scanned in air, with the SkyScan 1173 μCT scanner at the Max Planck Institute, Leipzig at

80 kV and 62 μA. This shape of object has previously been shown to both approximate trabecular bone and be susceptible to beam hardening due to its structure (*Scherf & Tilgner, 2009*). The 4,224 × 4,224 × 2,240 voxel reconstructed image had an isometric voxel size of 7.86 μm. This was cropped to an image size of 3,240 × 3,240 × 150 voxels to reduce processing time. The example fossil was scanned at 90 kV and 200 μA using a Nikon Metrology XTH 225/320 at the University of the Witwatersrand. Permission to use this material was granted by Fossil Access Committee of the Evolutionary Studies Institute at this institution. The reconstructed image was 726 × 551 × 1,826 voxels and had an isometric voxel size of 22.6 μm.

METHODS

MIA-Clustering algorithm

The MIA-Clustering algorithm is a machine-learning approach, based on fuzzy *c*-means clustering (*Pham & Prince, 1999*) and initialized by the *K*-means algorithm (*Forgy, 1965*; *Lloyd, 1982*). First, the *K*-means algorithm clusters the input data, based on voxel intensity, into the number of classes specified by the user (Figs. 1A and 1B). A subsequent fuzzy *c*-means algorithm iteratively estimates all class membership probabilities for each voxel, expressed as a vector (Fig. 1C). Based on their highest membership probability, voxels are globally clustered into distinct classes representing structures in the whole image. However, this global segmentation does not always capture fine detail because the input images may suffer from intensity inhomogeneities, which result from scanning artifacts or different levels of fossil mineralization. Therefore, subsequent local fuzzy *c*-means segmentation is applied.

Based on a user-defined grid-size parameter, the volume is subdivided into overlapping cubes. For each cube, the class membership probability vector is initialized by using the globally obtained probabilities (Fig. 1D). If the sum of membership probabilities of all voxels in a sub-volume falls below a threshold, then this class is not taken into account for the local, refined *c*-means clustering. This threshold can be specified by the user if desired, but the default value of 2% appears to generate acceptable segmentations and was used in all cases here. Therefore in this case, if there was no more than 2% of a cube that was globally clustered as a certain class, this class was not considered for that cube's local *c*-means segmentation. Subsequently, class probabilities for each voxel in overlapping cubes are merged and voxels are assigned to the class for which they have the highest membership probability, producing the whole segmented image (Fig. 1E). This local segmentation allows the algorithm to adapt to local intensity variations. It follows that a grid-size value smaller than the structure of interest will cause the algorithm to attempt to find clusters within these structures, such as small inhomogeneities in cortical bone, that are generally not of interest. Therefore, to balance between adapting to inhomogeneities resulting from imaging artifacts and ignoring small inhomogeneities within the structures of interest, the grid-size parameter selected should be slightly larger than the largest dimension of the phase of interest for the segmentation. For a variable and continuous structure, such as trabecular bone, we recommend looking at two-dimensional (2D) cross-sections in each plane and measuring thicker trabeculae to

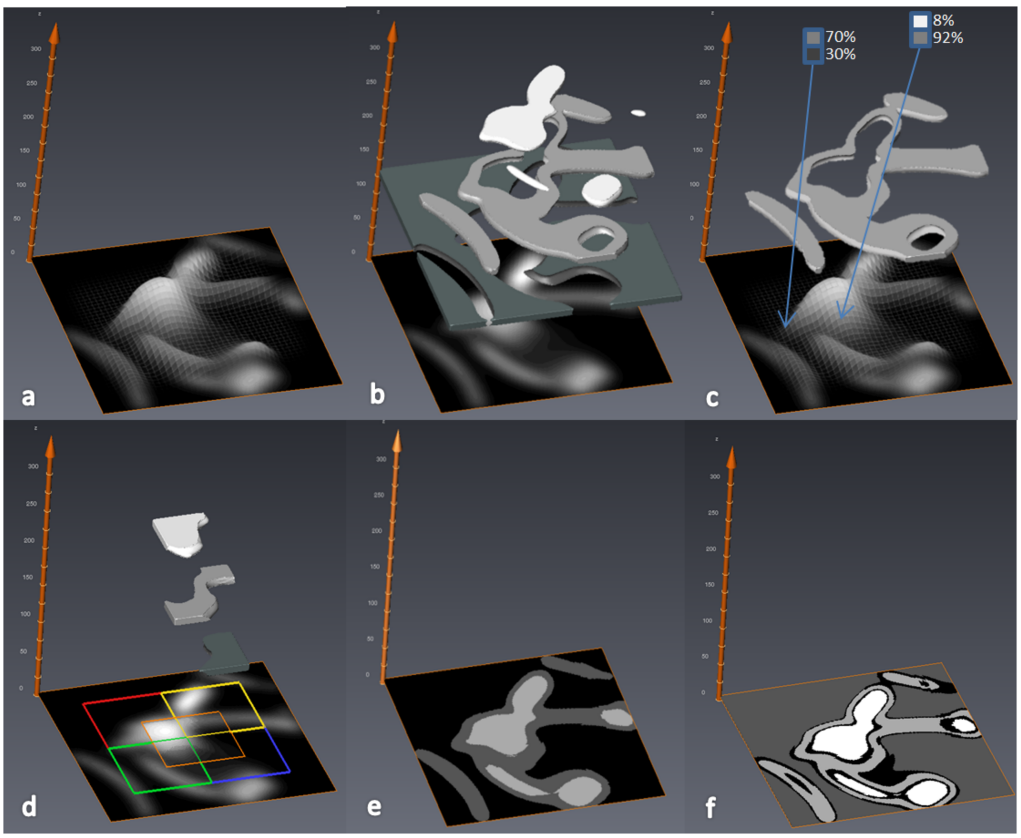

Figure 1 Diagram of MIA-Clustering algorithm in a 2D-image. (A) Gray values are mapped to the *z*-axis. (B) Gray values are initially clustered into three classes by the *K*-means algorithm; the black-class is represented as dark-gray in the 3D overlay for clarity. (C) The fuzzy *c*-means algorithm iteratively estimates a class membership probability vector for each voxel (two example voxels are shown in blue boxes) and globally clusters each voxel based on its highest class probability. (D) Local fuzzy *c*-means clustering is performed in overlapping sub-volumes, here represented by the colored squares. (E) Overlapping class probabilities are merged and voxels are clustered based on their highest membership probability. (F) An optional probability threshold is then applied at an arbitrary 75%, for illustrative purposes. All voxels with their highest membership probabilities below 75% are labeled as zero, or black, and voxels above this threshold are clustered into three classes labeled by gray values elevated by one; here one to three. Full-size DOI: 10.7717/peerj.4374/fig-1

ascertain their width in pixels. The grid-size value should then be set a few voxels larger than these measurements to ensure the local segmentation is not looking for features within the phase of interest. (e.g., Fig. 2). The global and local segmentations can be generated at the same time for comparison of each segmentation step.

Finally, an optional threshold can then also be applied to the calculated class membership probabilities of each voxel. A voxel is excluded from a class if its highest membership coefficient does not meet or exceed the threshold given. Voxels that do not meet the threshold for their highest class are assigned to a grayscale value of zero and all other classes are elevated by one gray value. Since the vector of membership probabilities sums to one, in practice, this allows the user 50 threshold values (51–100%) to fine tune the segmentation based on the initial, data-led, analysis. The black or zero-class voxels that did not meet the threshold can be considered a margin of error for the segmentation (Fig. 1F).

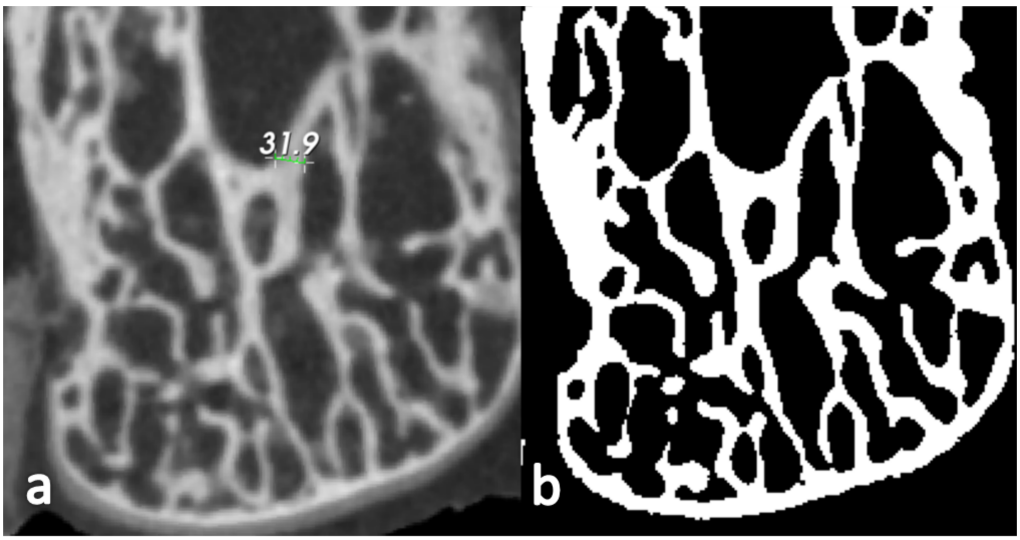

Figure 2 A 2D cross-section image of an example dry bone. (A) One of its thickest trabecular struts in the image measured at ~32 pixels. (B) A binarized image of the same cross-section after 3D segmentation of the bone, using the MIA-Clustering algorithm. The grid size input parameter selected for the segmentation was 35 voxels as this was just larger than the measurement in (A).
Full-size DOI: 10.7717/peerj.4374/fig-2

Wire segmentation

In order to test its efficacy, the MIA-Clustering algorithm was used to segment a scan of a machined wire phantom, previously measured at 40 μm thickness, following *Scherf & Tilgner (2009*; Fig. 3*)*. The RCA was also used to segment the same image for comparison. 3D-thickness was measured at every point, in each segmentation of the same 3,240 × 3,240 × 150 voxel volume in the center of the wire, using the BoneJ plugin for ImageJ (*Hildebrand & Rüegsegger, 1997*; *Doube et al., 2010*). Average 3D-thicknesses within one voxel, or ~8 μm, of the measured thickness were considered effective segmentations. In the case of RCA, 3,240 × 3,240 × 10 voxel trial segmentations were run to find the three input parameters that produced acceptable segmentations. In the case of the MIA-Clustering algorithm, the wire thickness of 40 μm divided by the resolution yielded a voxel size of approximately five, thus the grid size was set just above this at seven. The probability threshold used was found after two trial segmentations.

Parameter robusticity

In order to test the robusticity of MIA-Clustering algorithm, the full range of both input parameters was independently varied and average thickness of the wire in the resulting segmentations was measured. The probability threshold was varied in 5% increments from 50% to 95%. Grid size was varied from the smallest maximum dimension of the dataset, here 150 voxels, to the minimum value of three. The fossil specimen was segmented at grid sizes from 10 to100 voxels, since these more extreme values did not produce a visually satisfactory segmentation. This allowed comparison between segmentations produced by a range of possible values and the grid-size value attained

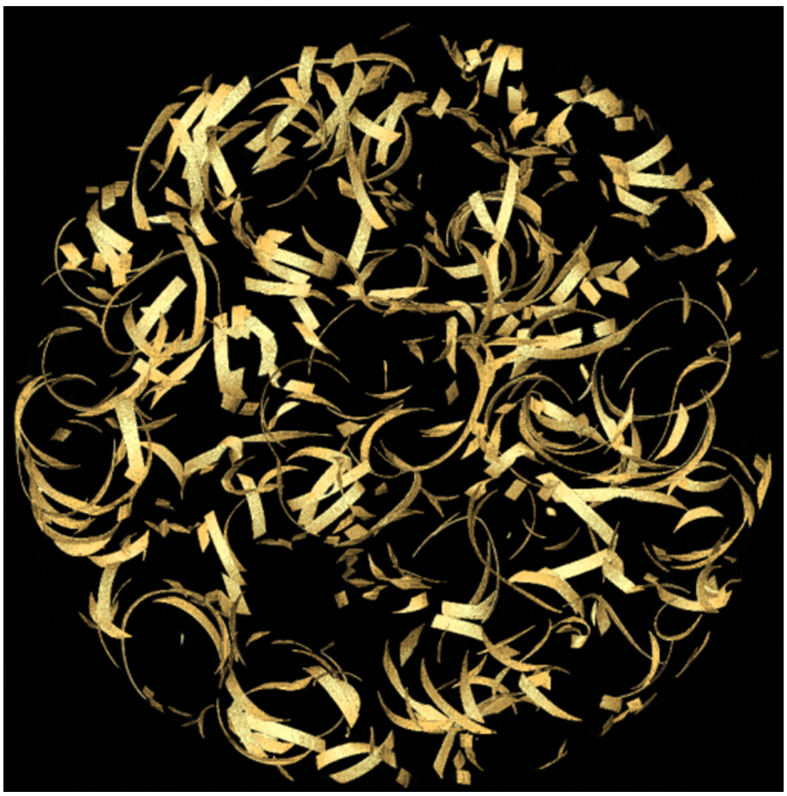

Figure 3 **A 3D-surface view of the machined wire phantom.**
Full-size DOI: 10.7717/peerj.4374/fig-3

from a cursory visual inspection (e.g., Fig. 2), in a variable structure of largely unknown thickness.

Fossil application

In order to assess the performance of the presented method on paleontological material, the fossil is segmented using the RCA as well as the MIA-Clustering algorithm; pre- and post-processing steps are described. Every fossil scan is likely to present different issues, owing to disparate diagenetic processes over varying timescales. In some fossils, invasive matrix may be relatively uniform, but overlap in attenuation intensity with the fossil bone phase preventing its removal by a global threshold. Similarly, small bright mineral inclusions may provide grayscale value outliers, thus decreasing contrast in the majority of the material, markedly affecting segmentation approaches based on thresholding of a grayscale value range such as the iterative, adaptive threshold method (*Ryan & Ketcham, 2002*; *Fajardo et al., 2007*). Also, cracks and multiple phases of invasive matrix may create edges within the fossil that are distinct from the fossil bone. The present fossil scan contains all of these issues to some extent, as well as a global gradient that becomes brighter towards the center of the fossil. This centrally higher attenuation artifact is the result of photons with less energy than is required to uniformly penetrate this dense fossil and is essentially the inverse of beam hardening.

Table 1 Mean and standard deviation of thickness calculated for each segmentation method.

Segmentation method	Thickness mean (pixels)	σ (pixels)	Thickness mean (μm)	σ (μm)
RCA.1	5.054	1.340	39.728	10.533
RCA.2	5.026	1.386	39.508	10.895
MIA-Clustering algorithm	5.111	0.952	40.176	7.484

Notes:
RCA.1 used parameters lower threshold: 7,000, upper threshold: 20,000 and minimum edge strength: 5,000; RCA.2 used lower threshold: 18,000, upper threshold: 26,000 and minimum edge strength: 20,000. Note the near identical measurements using two different sets of values. Parameters for the MIA-Clustering algorithm were grid size: 7 and probability threshold 85%.

Implementation

The RCA segmentations were run as a stand-alone executable on the Windows command line. The MIA-Clustering algorithm was run as command line tool using MIA (*Wollny et al., 2013*). MIA was run from a Docker image as a Docker container in order to run a lightweight virtual Linux machine in Windows (*Boettiger, 2015*). This approach allows MIA to be run on most widely available operating systems. Instructions for downloading and use of MIA are available at http://mia.sourceforge.net/.

RESULTS

Wire segmentation

Two acceptable sets of parameters were found for RCA segmentations, after at least 10 trial segmentations for each. The probability threshold value for the MIA-Clustering algorithm was found after two trial segmentations at 80% and 90%. MIA-Clustering algorithm segmentations of the 3 gigabyte wire phantom scan ran in ~10 min using four cores whereas RCA ran this object in ~8 min using 16 cores.

As can be seen in Table 1 and Fig. 4, both algorithms can produce accurate segmentations, segmenting the wire at thicknesses within 1 μm of the known width of the wire. Figure 5, however, demonstrates that at least for some local areas the MIA-Clustering algorithm segments the closely packed, fine structures more accurately than either of the equifinal RCA segmentations. The average thickness values are within 1% and 0.5% of the known thickness, respectively. This is considered acceptable given an isometric voxel size of 8 μm (Table 1). The standard deviation of the thickness measured in the RCA segmentation is slightly higher than the voxel size whereas the MIA-Clustering algorithm segmentation standard deviation is below this level of variability and therefore is the result of partial volume effects.

Parameter robusticisty

In order to evaluate the potential effect of input error in the MIA-Clustering algorithm, the wire was segmented over the full range of each input variable, and average 3D-thickness of each segmentation was measured. Figure 6A demonstrates the linear relationship between probability threshold and thickness for this image. The range of grid-size values result in a thickness range of 12 μm. Figure 6B demonstrates an exponential relationship from the maximum possible (150) to the minimum possible

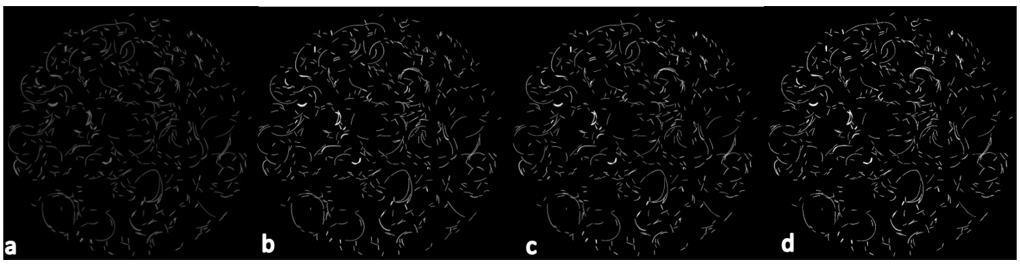

Figure 4 The mid-slice of the wire scan in superior view. (A) The reconstructed image. (B) The segmented image produced by the MIA-Clustering algorithm. (C) The segmented image produced by the RCA.1 and (D) the equifinal RCA.2 segmentation. Note the similarity of the segmentations of (A) in each method (B–D). Full-size DOI: 10.7717/peerj.4374/fig-4

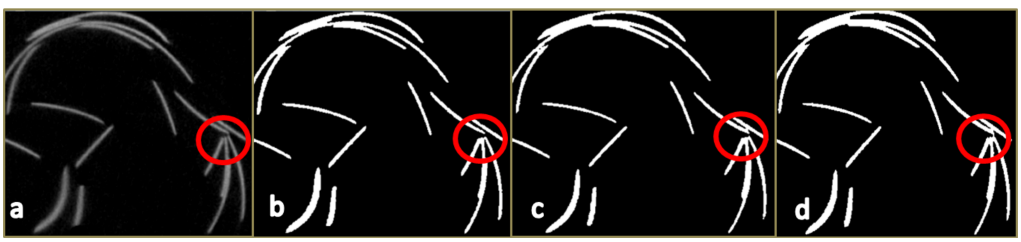

Figure 5 A magnified section of the mid-slice of the wire phantom scan (Fig. 4) in superior view. (A) The reconstructed image. (B) The segmented image produced by the MIA-Clustering algorithm. (C) The segmentation produced by the RCA.1 and (D) the equifinal RCA.2 segmentation. Note the separation of closely packed wire in the red circles in (A) and (B) but not in (C) and (D).
Full-size DOI: 10.7717/peerj.4374/fig-5

grid size (3) and a thickness range of 9 μm. This parameter quickly converges on values within 10% of the known thickness of the wire when grid size becomes small enough to segment the finer structures of the image at ~25 voxels. From this point lower grid sizes produce a larger variation in thickness values as fine structures are more consistently segmented, only underestimating thickness when a grid size smaller than the width of the fine structures is used. As expected, different grid sizes produced a wider range of mean thickness measures (~100 μm) for the structurally variable fossil, than the machined wire (Fig. 7). It should be noted that these values include cortical bone and reflect variation in segmentation of the whole image rather than a trabecular analysis. Despite this larger range, thickness values display an exponential relationship with grid size quickly converging on the value obtained from visual inspection. Much as in the grid size comparison for the machined wire (Fig. 6), when grid size becomes small enough to segment the finer structures of the image at ~35 voxels variation in thickness increases (Fig. 7). This trend continues until a grid size smaller than the width of the fine structures is used and the method begins to detect inhomogeneities within the osseous structure.

RCA fossil segmentation

Ray Casting Algorithm is only able to segment the highest attenuation phase in an image, because it will only exclude voxels on the other side of a gradient-defined edge if they have a lower gray value than the phase of interest. Since the structure of interest was not the

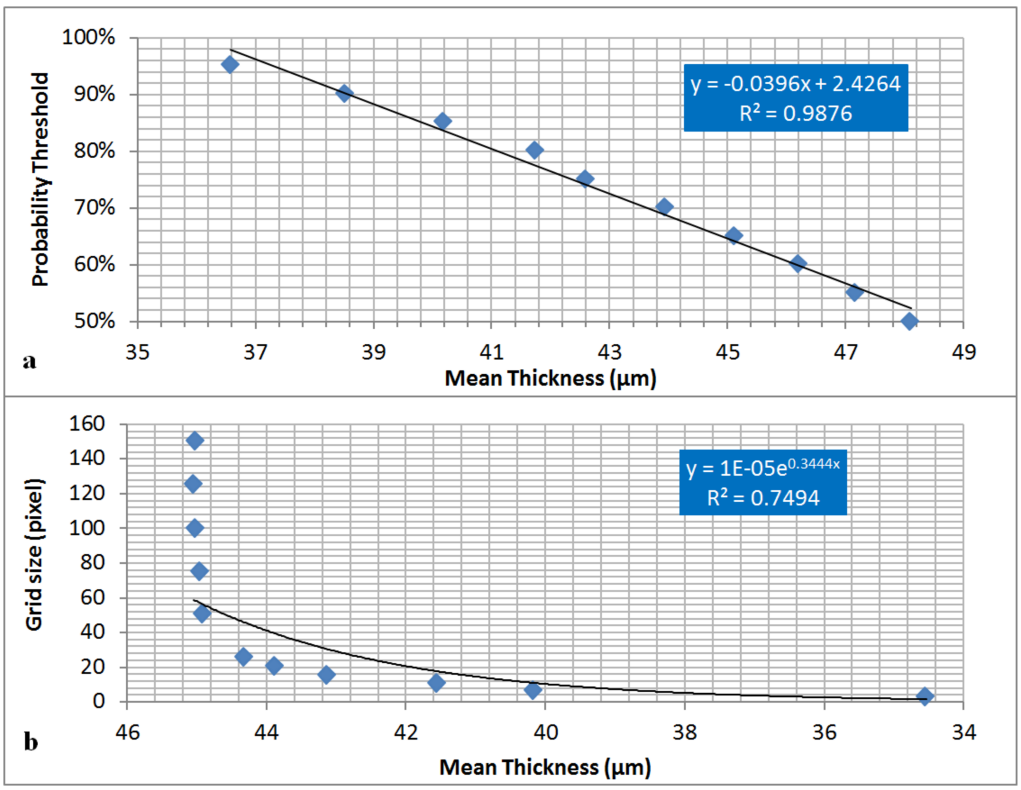

Figure 6 The effect of MIA-Clustering algorithm parameters on average thickness of the wire. (A) Full range of possible probability thresholds and with grid size of 7 held constant. (B) Full range of possible grid sizes with probability threshold held constant at 85%.

Full-size DOI: 10.7717/peerj.4374/fig-6

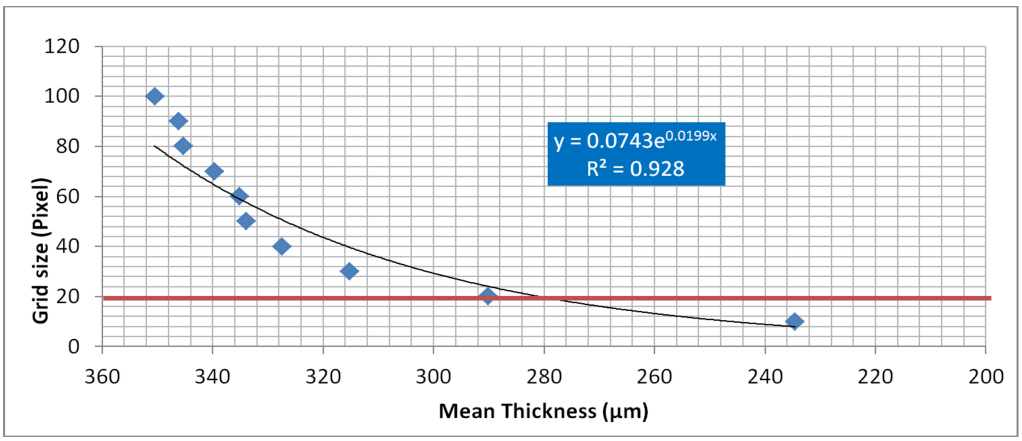

Figure 7 The effect of grid-size input on average thickness estimates of the fossil, after MIA-Clustering segmentation. Grid size ranged from 10 to 100 voxels. The red line represents the grid size of 20, ascertained from manual measurement of the fossil as per the technique in Fig. 2.

Full-size DOI: 10.7717/peerj.4374/fig-7

brightest part the image (Fig. 8A), it was necessary to invert the image in Avizo 6.3 (Visualization Sciences Group, Berlin, Germany, Fig. 8B). A median filter of kernel size three was run as part of the RCA program using a lower threshold of 19,000, an upper threshold of 29,000 and minimum edge strength of 2,500 (Fig. 8C). This was not a satisfactory segmentation of the image, as much of the trabeculae near the center of the bone were lost. Therefore in order to somewhat reduce the artifactual global gradient, the original image was subjected to a median filter of kernel size 25, largely obliterating structures but preserving the global gradient (Fig. 8D). The resultant image could then be added to the inverted image to "cancel-out" the global grayscale gradient without affecting the edge gradients of the trabeculae to a large extent (Fig. 8E). RCA segmentation could then produce an improved segmentation with same parameters as initially used (Fig. 8F).

MIA-Clustering algorithm fossil segmentation

As a pre-processing step, a noise reducing median filter of kernel size three was applied, and the image was thresholded at 10,000 to remove noise in the background of the image (Fig. 8A). The MIA-Clustering algorithm was run to look for three classes with a grid size of 20, since the thickest elements of the trabecular bone were ~15 voxels in dimension from a cursory inspection in Avizo 6.3 (Fig. 8G). No probability threshold was needed in this case for refinement, though running the command with a threshold of 50% achieves the same result. Subsequently the image was binarized on the second brightest class in the image, leaving only the fossil bone phase (Fig. 8H). This post-processing step allows for direct comparison with the RCA segmentation but is not necessary (Figs. 8F, 8C and 8I).

DISCUSSION

Wire segmentation

The current study presents a novel open-source method for segmenting bone or fossil bone phases from high-resolution μCT images. Tests using a wire phantom indicate that both this technique and RCA are capable of producing accurate segmentations that are within 1% of the wire phantom's thickness (Table 1; Figs. 4 and 5). Therefore in scans with high material contrast, including those of the present synthetic sample and many examples of dry bone, it appears both segmentation techniques would produce accurate results. However, in practice, the MIA-Clustering algorithm offers several advantages over other segmentation techniques by keeping subjective user decisions to a minimum to increase the reproducibility of results.

Parameter robusticity

Many segmentation approaches can require manual interaction with the image to provide appropriate input parameters, such as the placement of seed points for a region-based segmentation or the visual inspection of trial RCA segmentations. In this case the user must iteratively determine whether one set of trial RCA parameters produced a better segmentation of the wire phantom than the last and when these parameters could no longer be improved. It can often take many attempts to find acceptable parameters,

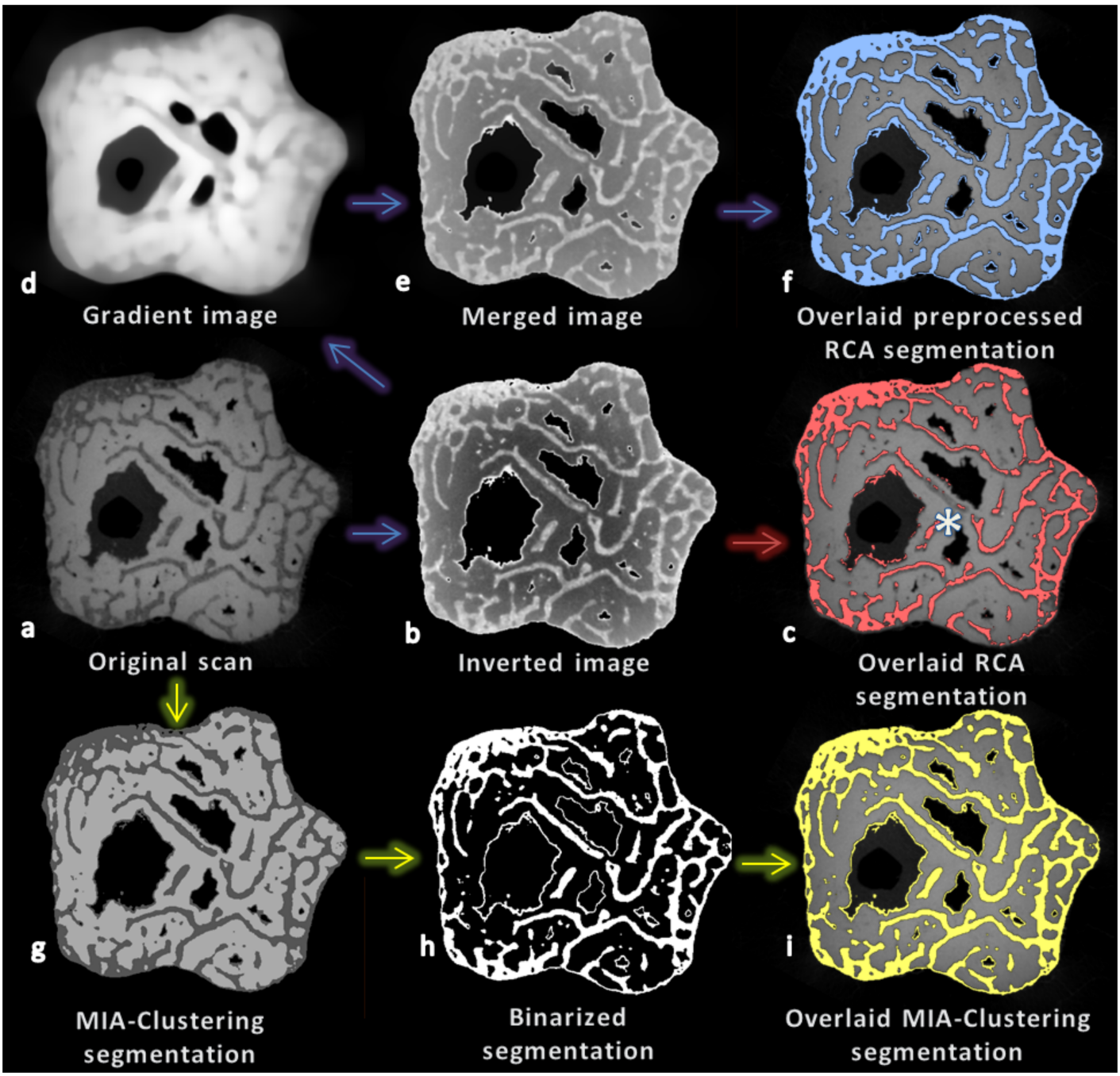

Figure 8 Cross-section (*XY* plane) through the fossil at various stages of segmentation using RCA and MIA-Clustering. (A) The fossil scan. (B) The image after foreground inversion. (C) The RCA segmentation of the inverted image overlaid on the original image (red), note the lack of segmentation of central trabeculae (e.g., above the white asterisk). (D) An image preserving the global gradient of the fossil scan but little of its spatial structure, after a strong median filter. (E) The result of merging the global gradient and the inverted image. (F) The RCA segmentation of the merged result overlaid on the original image (blue). (G) The MIA-Clustering segmentation of the three classes in the image. (H) The MIA-Clustering segmentation binarized on the second brightest class, the fossilized bone phase. (I) This binarized segmentation overlaid on the original image (yellow). See text for further details.

Full-size DOI: 10.7717/peerj.4374/fig-8

since there is no objective starting point other than the range of grayscale values in the image for the lower and upper thresholds. Since "minimum edge strength" is not easily visualized, it can be initially difficult to find an acceptable value for this parameter. Conversely, the MIA-Clustering algorithm input parameters are data-led, as grid size selection is based on the dimensions of the structure to be segmented, either through prior knowledge or an initial, manual, inspection of the material (Fig. 2). In the case of the wire, a grid size of seven is just larger than its, known, five voxel thickness and six voxels may be too small due to potential partial volume averaging effects. In the case of the fossil, cursory measurements in three orthogonal 2D-slices of the image were sufficient to determine an appropriate grid size of 20. Average thickness measures of segmentations produced by different grid sizes demonstrate that a grid size of 20 is within the range of values that greatly affect the segmentation result (Fig. 7) but is not so small that algorithm detects inhomogeneities within the phase of interest and begins to break-up and thin trabeculae (Figs. 8G–8I). In both cases, as the grid-size parameter selection was data-led, there was an objective justification for the value used. Though this value may not necessarily produce the optimal MIA-Clustering segmentation, especially in the fossil, it does provide a starting point within a narrow range of values that allow the segmentation of finer structures to varying degrees. Further, as the grid-size parameter defines a local reapplication of a machine-learning algorithm, it could be argued it is more objective than a user-defined threshold of either absolute grayscale values or their gradients. Therefore, this data-led parameter selection requires minimal manual interaction with an image and provides an objective justification for the value used, even when segmenting a structure of largely unknown and variable dimensions, such as osseous or fossil material.

The optional probability threshold parameter, however, is more subjective as it is only found by trialing values. Yet this final step of the algorithm may only fine tune the segmentation from the data-led clustering results. Indeed, over the full range of 50 possible values not only did the segmented wire phantom show just a 30% variation in measured average thickness, it did so in a predictable way with strong a linear relationship (Fig. 6A). This is due to the fact that voxels at the boundary of each segmented phase will have lower membership coefficients than those in the middle on the phase (Fig. 1C). As the threshold is raised, more of these boundary voxels are no longer considered part of this phase and the thickness of the structure will reduce in-kind (Fig. 1F). This relationship allows the user to potentially derive an acceptable value after just two trials. The probability threshold is particularly useful for the accurate segmentation of abrupt phase transitions, such as the edge of the machined wire. In structures with more gradual or complex edge transitions, such as fossilized or extant bone, this parameter is less useful as the effects of different values will be less predictable; the probability threshold was not used in the fossil segmentation. Therefore the MIA-Clustering algorithm keeps subjective user decisions to a minimum by basing input parameters on the properties of the image, rather than iterative manual interaction and more subjective refinement of the result is done in a predictable way, over a small range of input values.

Another way the MIA-Clustering algorithm reduces subjective user decisions is by limiting input parameters to a minimum. The algorithm only takes two input parameters, each with a smaller range of values than the three of RCA, since minimum edge strength ranges from 0 to 32,000 and the thresholding limits are based on the potential gray value range of 16 bit data, 0–65,535. Initially, the relatively small range of inputs for the MIA-Clustering algorithm could be seen as detrimental, affording the researcher less freedom to find values to segment the data accurately. However, this constraint allows for less error in parameter selection and is sufficient to quickly converge on a single pair of parameters that produce an acceptable segmentation (Fig. 6).

An additional benefit to having a small range of input values is that it does not allow for multiple combinations that yield similar results. Here, there are at least two sets of input parameters for the RCA that can produce near identical segmentations and thickness value measurements (Table 1; Figs. 4 and 5). The MIA-Clustering algorithm is not subject to the same equifinality and so results are more reproducible since they can only be achieved via the same input.

The MIA-Clustering algorithm appears to be as accurate as another leading segmentation technique, RCA, in segmenting the wire phantom. Yet the method presented here reduces subjective user decisions to a minimum by grounding input parameters in the properties of the image as well as limiting the range of these input parameters and in doing so, obviating the issue of equifinality. This increased objectivity allows for faster more reproducible segmentations. Indeed, since these parameters are not based on grayscale values but rather the structures at hand, they may be applied uniformly across a sample of different scans of similar synthetic, or dry osseous, material removing another potential source of error in segmentation and measurement across a sample. However, perhaps the most useful property of the MIA-Clustering algorithm is its ability to segment more complex, embedded structures, with less clear contrast, such as fossil material.

Fossil segmentation

One of the clearest challenges uniquely presented by segmentation of the fossil material is the high-attenuation invasive matrix. As the highest attenuation phase is selected by default in RCA, it was necessary to invert the foreground image, where matrix has a higher attenuation than the fossil bone (Fig. 8B), adding another pre-processing step and a potential source of error. Conversely, the MIA-Clustering method can segment multiple classes at once. Matrix, background and bone may each be a distinct initial cluster set, used to segment the image into separate gray value classes. Any of these classes can be extracted from the image via a simple threshold if subsequent analysis requires a binarized image (Fig. 8H). MIA (*Wollny et al., 2013*) offers a number of single-task command line tools, including a binarize filter that was used to produce the present result. The highest attenuation structure need not be the one of interest, and so the extra step of inverting the image is not required. Since matrix is also segmented it is also easier to compare the segmentation to the original image by eye, since the white of binarized image may appear larger than the original simply because it is brighter (e.g., Figs. 8A, 8G and 8H).

A further challenge of this particular fossil image is the global gradient which makes the center of the object appear brighter than the edges. The ray casting step of the RCA was invented to close gaps in Sobel filter defined edges that are caused by local grayscale transitions, not steep enough to meet the globally set "minimum edge strength" parameter. The first derivative of grayscale value transitions, rather than absolute values, is still based on a global, if locally applied, threshold. Therefore, although RCA mitigates the effects of a global gradient, it is not immune to them (*contra Scherf & Tilgner, 2009*). The global intensity gradient may affect one side of an edge more than the other if one edge is more central and in doing so, may change the grayscale gradient over the transition. Therefore, RCA may not find edges where they exist in the cases of these artifacts. The present fossil scan appears to be darker in the center of the inverted image (Fig. 8B). RCA accurately segments the trabeculae closer to the edge of the fossil but fails to segment the central trabeculae as their grayscale gradients relative to the matrix phase are not steeper than the "minimum edge strength" threshold applied (Fig. 8C). Ameliorating this global gradient as per the extra pre-processing steps allows the RCA with the same parameters to segment these central trabeculae (Fig. 8F). However, these extra un-prescribed steps make the segmentation process less efficient and potentially less reproducible. The MIA-Clustering algorithm, however, does not use grayscale-based thresholds but considers only the local sub-volumes at the edge or the center of the fossil when segmenting them and can therefore segment the trabeculae in both areas of the bone concurrently (Figs. 8G–8I).

Both fossil segmentations contain thin rings at the boundary of invasive matrix and air as these features are present in the initial image and have similar characteristics as trabecular bone (Figs. 8C, 8F and 8I). While both algorithms fully segment the image, researchers may wish to remove these features, before analysis, as they are not of biological origin. While this is beyond the scope of the current method, we would suggest applying a connected component algorithm, as available in software such as Avizo, to remove many of these features that are unconnected to the segmented bone. Unfortunately, to the authors' knowledge, remaining connected features must be removed manually at the researcher's discretion.

Unlike RCA and single threshold methods, the MIA-Clustering algorithm has the flexibility to concurrently segment multiple classes across a fossil specimen affected by a global gradient scanning artifact, segmenting a phase of interest that is not necessarily the brightest in the image. The preservation of multiple classes in the segmentation provides a higher fidelity comparison between the segmentation and the original image. Also, the lack of additional pre-processing steps required for this segmentation allows for fewer potential sources of error and greater reproducibility of results. Therefore, this method is particularly suitable for the segmentation of complex images containing several embedded structures. These images may include fossils with invasive matrix or possibly even images of several tissues produced by magnetic resonance imaging techniques. The presented algorithm can also be used on 8 bit data though the efficacy of the segmentation will depend on the clarity of the original image.

CONCLUSION

Here, we present a segmentation algorithm implemented in free open-source software, which can be run on most operating systems and is as effective as other leading algorithms. The move from a gray value-based approach to a data-led, machine-learning approach allows the MIA-Clustering algorithm to lessen the amount of subjective user choices required for segmentation. Therefore, MIA-Clustering segmentations of μCT data offer increased reproducibility. Further, the flexibility of this MIA-Clustering algorithm allows for segmentation of problematic modern or fossil material, which often contains more than two structures and may be affected by common scanning artifacts. The robusticity of the algorithm is demonstrated by the lack of need for additional image processing steps and by how quickly the range of possible input parameters converge on those acceptable for segmentation. The MIA-Clustering algorithm is a flexible, robust method that produces highly reproducible results, ideal for segmenting fossil bone.

ACKNOWLEDGEMENTS

The authors would like to thank Dr. Bernhard Zipfel for access to material curated by the Evolutionary Studies Institute, University of the Witwatersrand and Heiko Temming at the Max Planck Institute for Evolutionary Anthropology, for scanning assistance and expertise. We are also grateful for the reviewers' comments, which enhanced this manuscript.

ADDITIONAL INFORMATION AND DECLARATIONS

Funding

This research was supported by European Research Council Starting Grant #336301 and The Max Planck Society. The funders had no role in study design, data collection and analysis, decision to publish, or preparation of the manuscript.

Grant Disclosures

The following grant information was disclosed by the authors:
European Research Council Starting Grant: #336301.
The Max Planck Society.

Competing Interests

The authors declare that they have no competing interests.

Author Contributions

- Christopher J. Dunmore conceived and designed the experiments, performed the experiments, analyzed the data, prepared figures and/or tables.
- Gert Wollny contributed reagents/materials/analysis tools, authored or reviewed drafts of the paper.
- Matthew M. Skinner conceived and designed the experiments, authored or reviewed drafts of the paper.

Data Availability

The following information was supplied regarding data availability:

The software underpinning this method is freely available online and instructions of how to obtain it from http://mia.sourceforge.net/ are given in the article.

Supplemental Information

Supplemental information for this article can be found online at http://dx.doi.org/10.7717/peerj.4374#supplemental-information.

REFERENCES

Amson E, Arnold P, van Heteren AH, Canoville A, Nyakatura JA. 2017. Trabecular architecture in the forelimb epiphyses of extant xenarthrans (Mammalia). *Frontiers in Zoology* **14(1)**:52 DOI 10.1186/s12983-017-0241-x.

Biewener AA, Fazzalari NL, Konieczynski DD, Baudinette RV. 1996. Adaptive changes in trabecular architecture in relation to functional strain patterns and disuse. *Bone* **19(1)**:1–8 DOI 10.1016/8756-3282(96)00116-0.

Boettiger C. 2015. An introduction to Docker for reproducible research. *ACM SIGOPS Operating Systems Review* **49(1)**:71–79 DOI 10.1145/2723872.2723882.

Coleman MN, Colbert MW. 2007. CT thresholding protocols for taking measurements on three-dimensional models. *American Journal of Physical Anthropology* **133(1)**:723–725 DOI 10.1002/ajpa.20583.

Dhanachandra N, Chanu YJ. 2017. A survey on image segmentation methods using clustering techniques. *European Journal of Engineering Research and Science* **2(1)**:15–20 DOI 10.24018/ejers.2017.2.1.237.

Doube M, Kłosowski M, Arganda-Carreras I, Cordelières F, Dougherty RP, Jackson JS, Schmid B, Hutchinson JR, Shefelbine S. 2010. BoneJ: free and extensible bone image analysis in ImageJ. *Bone* **47(6)**:1076–1079 DOI 10.1016/j.bone.2010.08.023.

Fajardo RJ, Müller R, Ketcham RA, Colbert M. 2007. Nonhuman anthropoid primate femoral neck trabecular architecture and its relationship to locomotor mode. *Anatomical Record* **290(4)**:422–436 DOI 10.1002/ar.20493.

Forgy E. 1965. Cluster analysis of multivariate data: efficiency versus interpretability of classifications. *Biometrics* **21(3)**:768–769.

Hara T, Tanck E, Homminga J, Huiskes R. 2002. The influence of microcomputed tomography threshold variations on the assessment of structural and mechanical trabecular bone properties. *Bone* **31(1)**:107–109 DOI 10.1016/s8756-3282(02)00782-2.

Herman GT. 1979. Correction for beam hardening in computed tomography. *Physics in Medicine and Biology* **24(1)**:81–106 DOI 10.1088/0031-9155/24/1/008.

Hildebrand T, Rüegsegger P. 1997. A new method for the model-independent assessment of thickness in three-dimensional images. *Journal of Microscopy* **185(1)**:67–75 DOI 10.1046/j.1365-2818.1997.1340694.x.

Kivell TL. 2016. A review of trabecular bone functional adaptation: what have we learned from trabecular analyses in extant hominoids and what can we apply to fossils? *Journal of Anatomy* **228(4)**:569–594 DOI 10.1111/joa.12446.

Lloyd S. 1982. Least squares quantization in PCM. *IEEE Transactions on Information Theory* **28(2)**:129–137 DOI 10.1109/tit.1982.1056489.

Pham D, Prince JL. 1999. An adaptive fuzzy C-means algorithm for image segmentation in the presence of intensity in homogeneities. *Pattern Recognition Letters* **20(1)**:57–68 DOI 10.1016/s0167-8655(98)00121-4.

Pham DL, Xu C, Prince JL. 2000. Current methods in medical image segmentation. *Annual Review of Biomedical Engineering* **2(1)**:315–337 DOI 10.1146/annurev.bioeng.2.1.315.

Pontzer H, Lieberman DE, Momin E, Devlin MJ, Polk JD, Hallgrimsson B, Cooper D ML. 2006. Trabecular bone in the bird knee responds with high sensitivity to changes in load orientation. *Journal of Experimental Biology* **209(1)**:57–65 DOI 10.1242/jeb.01971.

Ridler TW, Calvard S. 1978. Picture thresholding using an iterative selection method. *IEEE Transactions on Systems, Man, and Cybernetics* **8(8)**:630–632 DOI 10.1109/tsmc.1978.4310039.

Ryan TM, Colbert M, Ketcham RA, Vinyard CJ. 2010. Trabecular bone structure in the mandibular condyles of gouging and nongouging platyrrhine primates. *American Journal of Physical Anthropology* **141(4)**:583–593 DOI 10.1002/ajpa.21178.

Ryan TM, Ketcham RA. 2002. The three-dimensional structure of trabecular bone in the femoral head of strepsirrhine primates. *Journal of Human Evolution* **43(1)**:1–26 DOI 10.1006/jhev.2002.0552.

Scherf H, Tilgner R. 2009. A new high-resolution computed tomography (CT) segmentation method for trabecular bone architectural analysis. *American Journal of Physical Anthropology* **140(1)**:39–51 DOI 10.1002/ajpa.21033.

Skinner MM, Gunz P, Wood BA, Boesch C, Hublin JJ. 2009. Discrimination of extant Panspecies and subspecies using the enamel-dentine junction morphology of lower molars. *American Journal of Physical Anthropology* **140(2)**:234–243 DOI 10.1002/ajpa.21057.

Spoor F, Garland T, Krovitz G, Ryan TM, Silcox MT, Walker A. 2007. The primate semicircular canal system and locomotion. *Proceedings of the National Academy of Sciences of the United States of America* **104(26)**:10808–10812 DOI 10.1073/pnas.0704250104.

Spoor CF, Zonneveld FW, Macho GA. 1993. Linear measurements of cortical bone and dental enamel by computed tomography: applications and problems. *American Journal of Physical Anthropology* **91(4)**:469–484 DOI 10.1002/ajpa.1330910405.

Trussell HJ. 1979. Comments on "Picture thresholding using an iterative selection method". *IEEE Transactions on Systems, Man, and Cybernetics* **9(5)**:311 DOI 10.1109/tsmc.1979.4310204.

Tsegai ZJ, Kivell TL, Gross T, Nguyen NH, Pahr DH, Smaers JB, Skinner MM. 2013. Trabecular bone structure correlates with hand posture and use in hominoids. *PLOS ONE* **8(11)**:e78781 DOI 10.1371/journal.pone.0078781.

Witmer LM, Ridgely RC, Dufeau DL, Semones MC. 2008. Using CT to peer into the past: 3D visualization of the brain and ear regions of birds, crocodiles, and nonavian dinosaurs. In: *Anatomical Imaging*. Tokyo: Springer, 67–87.

Wollny G, Kellman P, Ledesma-Carbayo MJ, Skinner MM, Hublin JJ, Hierl T. 2013. MIA—A free and open source software for gray scale medical image analysis. *Source Code for Biology and Medicine* **8(1)**:8–20 DOI 10.1186/1751-0473-8-20.

Journal of Anatomy

J. Anat. (2019) **235**, pp45–66 doi: 10.1111/joa.12966

Metacarpal trabecular bone varies with distinct hand-positions used in hominid locomotion

Christopher J. Dunmore,[1] Tracy L. Kivell,[1,2] Ameline Bardo[1] and Matthew M. Skinner[1,2]

[1]*Skeletal Biology Research Centre, School of Anthropology and Conservation, University of Kent, Canterbury, UK*
[2]*Department of Human Evolution, Max Planck Institute for Evolutionary Anthropology, Leipzig, Germany*

Abstract

Trabecular bone remodels during life in response to loading and thus should, at least in part, reflect potential variation in the magnitude, frequency and direction of joint loading across different hominid species. Here we analyse the trabecular structure across all non-pollical metacarpal distal heads (Mc2-5) in extant great apes, expanding on previous volume of interest and whole-epiphysis analyses that have largely focused on only the first or third metacarpal. Specifically, we employ both a univariate statistical mapping and a multivariate approach to test for both inter-ray and interspecific differences in relative trabecular bone volume fraction (RBV/TV) and degree of anisotropy (DA) in Mc2-5 subchondral trabecular bone. Results demonstrate that whereas DA values only separate *Pongo* from African apes (*Pan troglodytes, Pan paniscus, Gorilla gorilla*), RBV/TV distribution varies with the predicted loading of the metacarpophalangeal (McP) joints during locomotor behaviours in each species. *Gorilla* exhibits a relatively dorsal distribution of RBV/TV consistent with habitual hyper-extension of the McP joints during knuckle-walking, whereas *Pongo* has a palmar distribution consistent with flexed McP joints used to grasp arboreal substrates. Both *Pan* species possess a disto-dorsal distribution of RBV/TV, compatible with multiple hand postures associated with a more varied locomotor regime. Further inter-ray comparisons reveal RBV/TV patterns consistent with varied knuckle-walking postures in *Pan* species in contrast to higher RBV/TV values toward the midline of the hand in Mc2 and Mc5 of *Gorilla*, consistent with habitual palm-back knuckle-walking. These patterns of trabecular bone distribution and structure reflect different behavioural signals that could be useful for determining the behaviours of fossil hominins.

Key words: hominid; locomotion; metacarpal; trabeculae.

Introduction

Trabecular, or cancellous, bone has been experimentally shown to remodel (Cowin, 1986; Frost, 1987) in response to loading across a range of phylogenetically disparate taxa (Biewener et al. 1996; Pontzer et al. 2006; Barak et al. 2011). Therefore, trabecular architecture can provide additional information about how a bone was loaded during life, compared with external morphology alone (Ruff & Runestad, 1992; Tsegai et al. 2013). The term 'remodelling' is used here rather than 'modelling', as it occurs throughout life and is therefore key to a bone's 'ability to function in a changing mechanical environment' (Martin et al. 1998, p. 96; see Allen & Burr, 2014). Trabeculae preserved in fossil hominins have been used to infer habitual loading and reconstruct both locomotor (DeSilva & Devlin, 2012; Barak et al. 2013a; Su et al. 2013; Zeininger et al. 2016; Ryan et al. 2018) and manipulative (Skinner et al. 2015a; Stephens et al. 2018) behaviours during human evolution. These functional inferences rely on comparative analyses that associate known behaviours of extant primates with variation in trabecular architecture at particular joints (Orr, 2016).

The hand makes direct contact with the substrate during non-human primate locomotion, and therefore its trabecular structure may provide a clearer functional signal than skeletal elements that are further removed from substrate reaction forces, such as the humerus (Ryan & Walker, 2010; Scherf et al. 2016). Indeed, previous studies of the internal bone structure of hand bones have found substantial differences between primate species with distinct habitual locomotor modes (Lazenby et al. 2011; Zeininger et al. 2011; Tsegai et al. 2013; Matarazzo, 2015; Skinner et al. 2015a; Stephens et al. 2016; Barak et al. 2017; Chirchir et al. 2017). The majority of these studies have investigated trabecular bone structure in the third metacarpal (Mc3) head because

Correspondence
Christopher J. Dunmore, Skeletal Biology Research Centre, School of Anthropology and Conservation, University of Kent, Canterbury, UK.
E: cjd37@kent.ac.uk

Accepted for publication *22 January 2019*
Article published online *17 May 2019*

the central ray is buffered from medio-lateral forces, is consistently involved in weight-bearing during locomotion, and often experiences peak reaction forces in ape locomotion (Zeininger et al. 2011; Tsegai et al. 2013; Matarazzo, 2015; Barak et al. 2017; Chirchir et al. 2017).

Different methodological approaches to the analysis of trabecular structure in the primate Mc3 head have yielded varied results. Tsegai et al. (2013) applied a whole-epiphysis approach and found that African apes had higher trabecular bone volume fraction (BV/TV) and degree of anisotropy (DA) compared with suspensory hominoids, especially in the dorsal region of the Mc3 head, consistent with an extended metacarpophalangeal (McP) joint during knuckle-walking. Suspensory orangutans and hylobatids were found to have more isotropic trabeculae and lower overall BV/TV that was highest in the palmar aspect of the Mc3, consistent with flexed-finger arboreal grips. Using fewer volumes of interest (VOI) Chirchir et al. (2017) found that there were no significant differences in DA across a sample of chimpanzees, orangutans, baboons and humans, but that BV/TV was significantly higher in distal and palmar portions of the Mc3 head in orangutans and, to a lesser extent in humans, consistent with flexed-finger grips used during arboreal locomotion and manipulation, respectively. In contrast, Barak et al. (2017), using a similar method, found the dorsal VOI in both chimpanzees and humans had significantly lower BV/TV and DA than the distal or palmar VOIs. Despite these conflicting results, these studies uniformly found that humans possessed significantly less BV/TV throughout the Mc3 head relative to other primate species (Tsegai et al. 2013; Barak et al. 2017; Chirchir et al. 2017). This finding is consistent with other skeletal elements (Chirchir et al. 2015; Ryan & Shaw, 2015) and may reflect, at least in part, lower loading of the hand during manipulation compared with that of locomotion (Tsegai et al. 2013), or sedentism in recent human populations, or both (Ryan & Shaw, 2015).

Although the whole-epiphysis approach has found a relationship between variation in metacarpal trabecular structure and hand use (Tsegai et al. 2013), this approach has been limited to comparisons of average trabecular parameters (Tsegai et al. 2013; Skinner et al. 2015a; Stephens et al. 2016) or sections thereof (Georgiou et al. 2018). Recently some researchers have called for (Chirchir et al. 2017), or developed (Sylvester & Terhune, 2017), new methods that can better quantify and statistically compare trabecular structure across different individuals and species. Here, we build on this previous work by analysing trabecular structure across all of the non-pollical metacarpal heads (Mc2-Mc5) and applying a geometric morphometric, statistical mapping method to trabecular bone data produced by the whole-epiphysis approach. We compare relative trabecular bone volume fraction (RBV/TV) and degree of anisotropy (DA) between Mc2-5 both within and across the following species: bonobos (*Pan paniscus*), chimpanzees (*Pan troglodytes*), gorillas (*Gorilla gorilla gorilla*) and orangutans (*Pongo abelii* and *Pongo pygmaeus*). RBV/TV values are BV/TV values divided by the average BV/TV of each metacarpal head (see Materials and methods).This approach allows for the quantification of trabecular architecture in a heuristic sample, less affected by issues of sub-sampling of a continuous structure, to infer differences in habitual hand loading and posture associated with hominid locomotor modes.

Hand use and locomotion

Hand postures vary greatly during different types of arboreal and terrestrial locomotion in apes (Hunt et al. 1996; Schmitt et al. 2016). However, detailed studies of hominid hand postures in the wild (Hunt, 1991; Neufuss et al. 2017; Thompson et al. 2018) and captive settings (Wunderlich & Jungers, 2009; Matarazzo, 2013a,b; Samuel et al. 2018) can inform predictions of frequent McP joint positions and loading across the hand in different species. Although frequent McP joint postures may only reflect part of a large and varied locomotor repertoire, previous research suggests (Tsegai et al. 2013; Barak et al. 2017; Chirchir et al. 2017) that subchondral trabecular patterns of the metacarpal head can be statistically discerned among species with different locomotor modes.

Pongo

Pongo pygmeaus and *P. abelii* are primarily arboreal, engaging in suspensory locomotion to move through the canopy via tree branches and lianas (Cant, 1987; Sugardjito & Cant, 1994; Thorpe & Crompton, 2005). Specifically, researchers have emphasised the use of multiple supports and quadrumanous orthograde locomotion in *Pongo* (Thorpe & Crompton, 2006; Manduell et al. 2011), though specific hand grips have not been reported in detail (Thorpe & Crompton, 2005). However, during suspension, orangutans are thought to employ a hook grip, in which the proximal phalanges align with the proximo-distal axis of the metacarpal, such that the distal McP joint is thought to be loaded in tension (Sarmiento, 1988; Rose, 1988; Schmitt et al. 2016; Fig. 1A). Similarly a double-locked grip, in which all joints of the ray, including the McP, are greatly flexed around a small substrate, is also adopted in orangutan locomotion (Napier, 1960; Rose, 1988; Fig. 1B).

The McP joints in *Pongo* possess a limited degree of possible hyper-extension at 19 degrees (Susman, 1979; Rose, 1988). Mc2-4 are also dorso-palmarly thicker at the diaphysis, and all the non-pollical metacarpal heads possess palmarly wide articular heads suggestive of habitual McP flexion (Susman, 1979). As the fourth proximal phalanx may often equal or exceed the length of the third phalanx in orangutans (40%; Susman, 1979), Rose (1988) has argued that the fourth ray is more in line with the second and third rays, which would be advantageous for both hook and double-locked grips in which rays 2–5 are typically all engaged. Although body size in *Pongo* is sexually

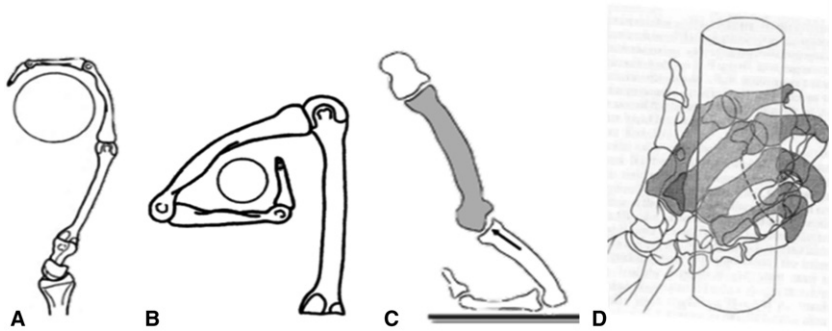

Fig. 1 Diagrammatic representations of the metacarpophalangeal postures during (A) a hook grip, (B) a 'double-locked' grip, (C) knuckle-walking and (D) a diagonal power grip. Images are adapted from Lewis (1977), Rose (1988) and Tsegai et al. (2013).

dimorphic (Rodman, 1984) and there is some evidence for differential locomotion between the sexes (Sugardjito & van Hooff, 1986), further work has found these differences to be relatively slight (Thorpe & Crompton, 2005). Therefore, we do not expect habitual prehensile postures to differ between male and female *Pongo*.

Gorilla

The most frequent locomotor mode of *Gorilla* is terrestrial knuckle-walking (Inouye, 1994; Doran, 1996; Remis, 1998); however, they can vary substantially in their degree of arboreality based on the species, sex and local ecology (Doran, 1996; Remis, 1998; Neufuss et al. 2017). The western lowland gorilla (*Gorilla gorilla gorilla*) is reported to spend probably at least 20% of its time in trees (Tuttle & Watts, 1985; Remis, 1998). During knuckle-walking, the McP joint is hyper-extended to place the arm above the weight-bearing intermediate phalanges (Tuttle, 1969; Matarazzo, 2013a,b; Fig. 1C). *Gorilla* usually uses a 'palm-back' hand posture during knuckle-walking, which places the McP orthogonal to the direction of travel while consistently loading rays 2–5, which differs from the more variable hand postures, as well as digit loading, found in *Pan* and probably reflects the relatively longer fifth digit of *Gorilla* (Tuttle, 1969; Susman, 1979; Inouye, 1992, 1994; Wunderlich & Jungers, 2009; Matarazzo, 2013a,b; but see Thompson et al. 2018). In a study of digit pressures during knuckle-walking in captive gorilla, Matarazzo (2013a,b) found that the fifth digit always touches down first, with the weight moving radially until the second (61%) or third (39%) digit lift-offs. Peak pressures were significantly lower on the fifth digit and highest on the third, but overall gorillas maintained a more even distribution of pressure across rays 2–5 than that of captive chimpanzees.

Compared with terrestrial knuckle-walking, far less is known about hand postures used by gorillas during arboreal locomotion. In captivity, *Gorilla* is described as using a power grip with little McP flexion when vertically climbing large-diameter substrates (Sarmiento, 1994). Neufuss et al. (2017) also described a similar type of power grip using all five digits and the palm-in of wild mountain gorillas (*Gorilla beringei*) when climbing larger substrates. However, when climbing medium-sized substrates (6–10 cm diameter), mountain gorillas used a diagonal power grip, in which the substrate lies diagonally across the fingers and palm, with an extremely ulnarly deviated wrist posture (Neufuss et al. 2017; Fig. 1D). In this diagonal power grip, weight appeared to be frequently borne by digits 2–4, while the fifth McP joint was unable to flex to the same extent due to the irregular shape of some substrates. Although similar data on arboreal hand postures are not available for *G. gorilla*, we assume that during arboreal locomotion, the *G. gorilla* McP joints are moderately flexed, and that this flexion increases as the substrate diameter decreases, with potentially less flexion at the fifth McP joint. However, this arboreal McP posture is likely less frequent than that associated with knuckle-walking in *Gorilla*. Indeed, although female individuals are more arboreal than larger males in *Gorilla* (Remis, 1995), the primary locomotor mode for both sexes is knuckle-walking (Tuttle & Watts, 1985; Remis, 1995; Crompton et al. 2010).

Pan troglodytes

Generally *P. troglodytes* is thought to be more arboreal than *Gorilla* (Remis, 1995; Doran, 1996; Thorpe & Crompton, 2006), though this may be the result of comparisons with mountain gorillas that are better habituated to humans compared with their more arboreal lowland counterparts (Doran, 1997; Hunt, 2004, Neufuss et al. 2017). There is a large degree of variation in the chimpanzee locomotor repertoire depending on the local ecology (Doran & Hunt, 1996; Carlson et al. 2006). *Pan troglodytes verus*, the subspecies that comprises the majority of the current sample, engages in knuckle-walking, both arboreal and terrestrial, in ~ 85% of their locomotion and spends more time in the trees than *P. troglodytes schweinfurthii* does (Doran & Hunt, 1996; Carlson et al. 2006). Compared with *Gorilla, P. troglodytes* uses more varied hand postures during knuckle-walking (Tuttle, 1969; Inouye, 1994; Matarazzo, 2013a,b). Chimpanzees have been thought to primarily load digits 3 and 4 during knuckle-walking (Tuttle, 1969; Tuttle & Basmajian, 1978). Inouye (1994) found that during captive terrestrial knuckle-walking, larger chimpanzees used their second digit significantly less often compared with gorillas of equivalent size, and both chimpanzees and bonobos generally used their fifth digit significantly less often than

gorillas did. Pressure studies also found that the fifth digit of chimpanzees did not touch-down in 20% of knuckle-walking steps and that this digit experienced significantly less load than the other digits when it was used (Wunderlich & Jungers, 2009; Matarazzo, 2013a,b). Further, *P. troglodytes* uses both 'palm-back' (~ 40%) and 'palm-in' (~ 60%) postures, compared with a more consistent use of mainly 'palm-back' (~ 86%) knuckle-walking postures in *Gorilla* (Wunderlich & Jungers, 2009; Matarazzo, 2013a,b). During 'palm-in' knuckle-walking, the intermediate phalanges roll radially in the direction of travel and the second or third digit usually experiences the highest pressures (Wunderlich & Jungers, 2009; Matarazzo, 2013a,b). In 'palm-back' knuckle-walking the third digit is typically placed in front the others and usually is the last to touch off, which may be related to the fact that the third ray may be relatively longer in chimpanzees than in gorillas (Matarazzo, 2013a,b). Compared with *Gorilla*, the peak pressures experienced by digits 2–4 are more variable in chimpanzees (Wunderlich & Jungers, 2009; Matarazzo, 2013a,b).

P. troglodytes verus most often uses climbing and scrambling locomotion in trees (60–77%; Doran, 1992, 1993). Chimpanzees are described as using power grips, diagonal power grips and hook grips during arboreal locomotion, all of which typically involve some degree of flexion at the McP joint (Napier, 1960; Hunt, 1991; Marzke et al. 1992; Alexander, 1994; Marzke & Wullstein, 1996). Climbing often encompasses vertical climbing and clambering in naturalistic studies. Hunt (1991) has emphasised the role of vertical climbing in wild *P. troglodytes* and although the grips employed tend to be ulnarly deviated at the wrist, they are dependent on substrate diameter. Neufuss et al. (2017) also found that chimpanzees used both power grips and diagonal power grips, but with a less ulnarly deviated wrist than in *Gorilla*. A diagonal power grip involves greater flexion of the more ulnar rays and in some cases, flexion at the fifth carpometacarpal joint, which may likely be associated with wrist adduction (Marzke & Wullstein, 1996; Fig. 1D). Therefore, the locomotor hand postures of *P. troglodytes* may be characterised as primarily those of knuckle-walking but with a more frequent arboreal grasping component than in *Gorilla*. Given the lower sexual dimorphism relative to *Gorilla* and *Pongo* (Doran, 1996), there may be less variation in grasping postures in this species.

Pan paniscus

While bonobos have a relatively similar locomotor repertoire to chimpanzees, they are thought to be more arboreal (Alison & Badrian, 1977; Susman et al. 1980; Susman, 1984) and have been shown to use significantly more palmigrady in the trees (Doran, 1993; Doran & Hunt, 1996; Crompton et al. 2010). Though the former claim may be an artefact of incomplete habituation of the individuals in these studies and more data are needed (Hunt, 2016), the relatively longer and heavier lower limbs of this species make for more generalised anatomy than that of chimpanzees (Zihlman, 1984; D'Août et al. 2004). During terrestrial knuckle-walking bonobos use the fifth digit even less than chimpanzees and Mc5 is shorter than the rest of the metacarpals in bonobos (Inouye, 1994). In a pressure study of arboreal locomotion, Samuel et al. (2018) found that captive bonobos used 'palm-back' (64%) or 'palm-in' (36%) knuckle-walking hand postures and that peak pressure was experienced by or around the third digit. However, unlike chimpanzees (Wunderlich & Jungers, 2009), they did not roll radially across their digits and the fifth digit always made contact with the substrate (Samuel et al. 2018). During vertical climbing and suspensory postures, bonobos used flexed-finger power grips similar to those described in other great apes and, again, peak pressure was experienced by or around the third digit (Samuel et al. 2018). In summary, the hand postures used during locomotion in *P. paniscus* can be characterised as similar to those of *P. troglodytes*, including a relatively low level of sexual dimorphism compared with other great apes (Doran, 1996), although more frequent palmigrady and arboreal grasping differentiate this species from *P. troglodytes*.

Predictions

Based on the summary above, we predict RBV/TV and DA in *Pongo* will be significantly higher in the disto-palmar region of the metacarpal heads compared with other hominids and no significant inter-ray differences in both measures due to the more consistent recruitment of rays 2–5 during hook and double-locked grasping. In *Gorilla* we predict a significantly higher dorsal distribution of RBV/TV and DA in each metacarpal head compared with all other hominids, reflecting McP joints frequently loaded in a hyperextended posture during knuckle-walking. As *P. troglodytes* may be more arboreal and uses more variable knuckle-walking postures, we predict this species will have significantly lower dorsal RBV/TV and DA, with more significant differences across rays, than that of *Gorilla*. We also predict this mixture of arboreality and terrestrially in *P. troglodytes* will elicit higher dorsal RBV/TV and DA than *Pongo* but with a more homogeneous distribution within each metacarpal head. We predict *P. paniscus* trabecular patterning will be similar to that of *P. troglodytes*, and thus possess significantly higher palmar distribution of RBV/TV and DA compared with *Gorilla* and a more dorsal distribution of these measures than seen in *Pongo.* However, we also expect *P. paniscus* to have lower DA and further homogenised distribution of RBV/TV compared with *P. troglodytes* due to more frequent use of palmigrady and arboreal grips.

Materials and methods

Subchondral trabecular bone was analysed in the metacarpus of *P. paniscus* (n = 10), *P. troglodytes* (n = 13), *G. gorilla gorilla* (n = 12), *Pongo* sp. indet. (n = 1), *P. pygmaeus* (n = 7) and *P. abelii* (n = 3).

Metacarpi were sampled from the Royal Museum for Central Africa, Tervuren, the Max Planck Institute for Evolutionary Anthropology, Leipzig, the Powell-Cotton Museum, Birchington, Bavarian State Collection of Zoology, Munich, the Natural History Museum, Berlin, the Senckenberg Natural History Museum, Frankfurt, and the Smithsonian National Museum of Natural History, Washington, DC (Table 1). All specimens were adult, wild shot and free from external signs of pathology. Within each taxon efforts were made to ensure the samples were sex balanced with even numbers of right and left metacarpi, neither ratio was more imbalanced than 5:7 for any sample. While great ape locomotion is sexually biased (Doran, 1996) and there has been some evidence for lateralised asymmetry

Table 1 Study sample.

Taxonomy	Accession ID	Sex	Side	Institution
Gorilla gorilla gorilla	PC_MER_300	Female	Left	Powell-Cotton Museum
Gorilla gorilla gorilla	PC_MER_264	Male	Right	Powell-Cotton Museum
Gorilla gorilla gorilla	PC_MER_372	Male	Left	Powell-Cotton Museum
Gorilla gorilla gorilla	PC_MER_95	Female	Right	Powell-Cotton Museum
Gorilla gorilla gorilla	PC_MER_962	Male	Left	Powell-Cotton Museum
Gorilla gorilla gorilla	PC_CAMI_230	Male	Left	Powell-Cotton Museum
Gorilla gorilla gorilla	PC_MER_138	Female	Left	Powell-Cotton Museum
Gorilla gorilla gorilla	PC_MER_174	Male	Right	Powell-Cotton Museum
Gorilla gorilla gorilla	PC_MER_696	Female	Right	Powell-Cotton Museum
Gorilla gorilla gorilla	PC_MER_856	Female	Left	Powell-Cotton Museum
Gorilla gorilla gorilla	PC_MER_879	Male	Left	Powell-Cotton Museum
Gorilla gorilla gorilla	PC_ZVI_32	Male	Right	Powell-Cotton Museum
Pan troglodytes verus	MPITC_11789	Male	Right	Max Planck Institute for Evolutionary Anthropology
Pan troglodytes verus	MPITC_11778	Female	Right	Max Planck Institute for Evolutionary Anthropology
Pan troglodytes verus	MPITC_13439	Female	Right	Max Planck Institute for Evolutionary Anthropology
Pan troglodytes verus	MPITC_15002	Female	Left	Max Planck Institute for Evolutionary Anthropology
Pan troglodytes verus	MPITC_11800	Female	Right	Max Planck Institute for Evolutionary Anthropology
Pan troglodytes verus	MPITC_11903	Male	Left	Max Planck Institute for Evolutionary Anthropology
Pan troglodytes verus	MPITC_11781	Male	Left	Max Planck Institute for Evolutionary Anthropology
Pan troglodytes verus	MPITC_14996	Female	Left	Max Planck Institute for Evolutionary Anthropology
Pan troglodytes verus	MPITC_15012	Male	Right	Max Planck Institute for Evolutionary Anthropology
Pan troglodytes verus	MPITC_15013	Female	Right	Max Planck Institute for Evolutionary Anthropology
Pan troglodytes verus	MPITC_15014	Male	Right	Max Planck Institute for Evolutionary Anthropology
Pan troglodytes verus	MPITC_15032	Male	Left	Max Planck Institute for Evolutionary Anthropology
*Pan troglodytes**	ZSM_AP_122	Male	Right	Bavarian State Collection of Zoology
Pongo abelii	SMF_6785	Male	Right	Senckenberg Natural History Museum, Frankfurt
Pongo abelii	SMF_6779	Female	Left	Senckenberg Natural History Museum, Frankfurt
Pongo pygmaeus	ZSM_1907_0633b	Female	Right	Bavarian State Collection of Zoology
Pongo pygmaeus pygmaeus	ZSM_1907_0660	Female	Right	Bavarian State Collection of Zoology
Pongo sp.	ZSM_AP-120	Male	Left	Bavarian State Collection of Zoology
Pongo pygmaeus pygmaeus	ZSM_1907_0483	Female	Right	Bavarian State Collection of Zoology
Pongo pygmaeus pygmaeus	ZSM_1909_0801	Male	Right	Bavarian State Collection of Zoology
Pongo abelii	NMNH_267325	Male	Left	Smithsonian Institution National Museum of Natural History
Pongo pygmaeus	ZMB_6948	Female	Left	Natural History Museum, Berlin
Pongo pygmaeus	ZMB_6947	Male	Left	Natural History Museum, Berlin
Pongo pygmaeus	ZMB_87092	Female	Right	Natural History Museum, Berlin
Pan paniscus	MRAC_15293	Female	Left	Royal Museum for Central Africa, Tervuren
Pan paniscus	MRAC_15294	Male	Left	Royal Museum for Central Africa, Tervuren
Pan paniscus	MRAC_20881	Male	Left	Royal Museum for Central Africa, Tervuren
Pan paniscus	MRAC_27696	Male	Right	Royal Museum for Central Africa, Tervuren
Pan paniscus	MRAC_27698	Female	Left	Royal Museum for Central Africa, Tervuren
Pan paniscus	MRAC_29042	Female	Right	Royal Museum for Central Africa, Tervuren
Pan paniscus	MRAC_29044	Male	Right	Royal Museum for Central Africa, Tervuren
Pan paniscus	MRAC_29045	Female	Left	Royal Museum for Central Africa, Tervuren
Pan paniscus	MRAC_29052	Male	Right	Royal Museum for Central Africa, Tervuren
Pan paniscus	MRAC_29060	Female	Right	Royal Museum for Central Africa, Tervuren

*Though this specimen was marked as *Pongo* in the collection, CT-scans demonstrate it has a fused scaphoid and os centrale, and so this specimen is treated as *Pan troglodytes*.

in both the trabecular (Stephens et al. 2016) and cortical bone of hominid metacarpals (Sarringhaus et al. 2005) we argue that neither of these signals is greater than the species locomotion differences under investigation here. Further, the use of evenly mixed samples should ameliorate these effects (see Discussion).

MicroCT scanning

Specimens were scanned with BIR ACTIS 225/300 and Diondo D3 high resolution microCT scanners at the Department of Human Evolution, Max Planck Institute for Evolutionary Anthropology, Germany, as well as with the Nikon 225/XTH scanner at the Cambridge Biotomography Centre, University of Cambridge, UK. Scan parameters were 100–160 kV and 100–140 μA, using a brass or copper filter of 0.2–0.5 mm, resulting in reconstructed images with an isometric voxel size of 24–45 μm.

Image processing

MicroCT scans of each metacarpal were isolated in Avizo 6.3 (Visualization Sciences Group; Fig. 2A) and segmented using the ray casting algorithm (Scherf & Tilgner, 2009). The segmented volume images were then processed as per the whole-epiphysis method, outlined in Gross et al. (2014). Briefly, a series of filtres run in MedTool 4.2 (Dr. Pahr Ingenieurs e.U.) isolated the inner trabecular structure (Fig. 2B) by casting rays at different angles from the outer cortical shell and terminating them on contact with background, non-bone voxels. A spherical kernel, with a diameter equal to the measured average trabecular thickness in that bone, was then used to close this inner structure (Pahr & Zysset, 2009). The 3D edge of this solid inner structure defined the boundary between subchondral trabecular and cortical bone. Subsequently, a regular 3D background grid, spaced at 2.5-mm intervals, was overlaid and a spherical VOI 5 mm in diameter was centred at each vertex of the grid in which BV/TV and DA was measured (Fig. 2c). Previous studies have shown that these two variables are correlated with the mechanical properties of trabecular bone, reflect bone functional adaptation (Odgaard et al. 1997; Uchiyama et al. 1999; Pontzer et al. 2006; Barak et al. 2011; Lambers et al. 2013a,b) and that they are not strongly allometric (Doube et al. 2011; Barak et al. 2013b; Ryan & Shaw, 2013). DA was measured via the mean intercept length (MIL) method and was bounded between 0 (total isotropy) and 1 (total anisotropy) using the calculation: 1 – (lowest eigenvalue of the fabric tensor/greatest eigenvalue fabric tensor). Both trabecular values were then separately interpolated on a regular 3D tetrahedral mesh of the trabecular model (Fig. 2D), created using CGAL (www.cgal.org). The surface of the trabecular mesh was extracted using Paraview (www.paraview.org) and smoothed, to permit landmark sliding (see below), in Meshlab (Cignoni et al. 2008) via a screened Poisson surface reconstruction filter (Kazhdan & Hoppe, 2013; Fig. 2E). For left-hand bones this surface mesh was mirrored in Meshlab so that it was oriented in the same was as those from right hands to permit homologous functional comparisons.

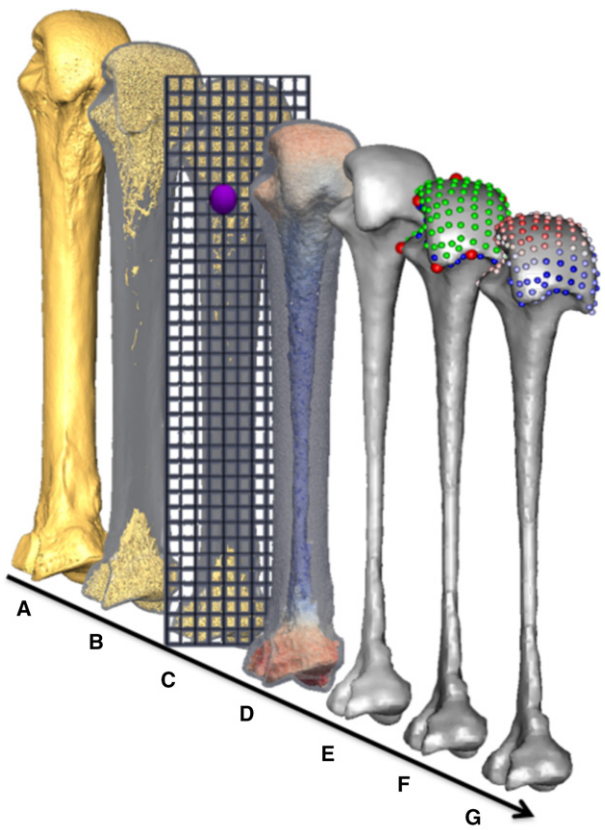

Fig. 2 Methodological stages of metacarpal trabecular analysis, shown in a third metacarpal as an example: (A) isosurface model, (B) segmented trabecular structure inside cortical shell, (C) diagram of the background grid and one of the VOIs at a vertex (purple), (D) volume mesh coloured by BV/TV (0–45%), (E) smoothed trabecular surface mesh, (F) surface landmarks (anatomical = red, semi-sliding landmarks on curves = blue and on surfaces = green), (G) RBV/TV interpolated to each surface landmark.

Geometric morphometric mapping

The whole-epiphysis method maps the entire volumetric trabecular model, but we focused our analysis on the trabecular bone beneath the articular surface of the metacarpal heads because external loads necessarily pass through these subchondral trabeculae before they can be transmitted to any other part of the trabecular structure (Zhou et al. 2014; Sylvester & Terhune, 2017). We employed a 3D geometric morphometric (GM) approach (Gunz & Mitteroecker, 2013) to trabecular analysis similar to that of Sylvester & Terhune (2017) and tested for significant differences between groups using homologous landmarks on the subchondral trabecular surface.

Anatomical landmark definitions

Many landmarks have been identified on the non-pollical metacarpals for morphometric studies (Susman, 1979; Inouye, 1992; Drapeau, 2015), but there have been relatively few studies that have applied GM methods to the primate metacarpus, and these have focused on the Mc1 base (Niewoehner, 2005; Marchi et al. 2017). Metatarsals are developmental serial homologues of metacarpals (Rolian et al. 2010) and a relatively recent study captured their shape variation using a patch of 3D landmarks (Fernández et al. 2015). A recent study of Mc3 head shape used most of the same landmarks that bordered on this metatarsal patch, at the homologous metacarpal locations (Rein, 2018). Based on these studies, the location and type (Bookstein, 1991) of anatomical landmarks used here are given in Table 2. Although the internal trabecular subchondral surface is landmarked, cortical bone is very thin at the

Table 2 Anatomical landmark definitions, types (Bookstein, 1991) and their provenance. Each article describes the landmark, using it as the terminus of a linear measure or directly for GM analysis.

Number	Type	Description	Provenance
1	Type II	Most proximal point under the ulnar palmar epicondyle (anterior eminence)	Yeh & Wolf (1977), Fernández et al. (2015), Rein (2018)
2	Type III	The point of maximum curvature on the inter-epicondylar ridge between points 1 and 3	Drapeau (2015), Fernández et al. (2015), Rein (2018)
3	Type II	Most proximal point under the radial palmar epicondyle (anterior eminence)	Yeh & Wolf (1977), Fernández et al. (2015), Rein (2018)
4	Type III	Point of maximum curvature on the radial ridge separating the articular surface from the radial lateral sulcus	Yeh & Wolf (1977), Fernández et al. (2015), Rein (2018)
5	Type II	Most radially projecting point under the ulnar dorsal tubercle	Yeh & Wolf (1977), Susman (1979), Inouye (1992), Fernández et al. (2015), Rein (2018)
6	Type III	Mid-point between the posterior tubercles on the intertubercular ridge, underlying the dorsal ridge if present.	Yeh & Wolf (1977), Fernández et al. (2015)
7	Type II	Most ulnarly projecting point under the ulnar dorsal tubercle	Yeh & Wolf (1977), Susman (1979), Inouye (1992), Fernández et al. (2015), Rein (2018)
8	Type III	Point of maximum curvature on the ulnar ridge separating the articular surface from the ulnar lateral sulcus	Yeh & Wolf (1977), Fernández et al. (2015), Rein (2018)
9	Type II	Most distally projecting point on the subchondral surface	Fernández et al. (2015); Susman (1979), Inouye (1992), Rein (2018)

metacarpal head in hominids (Tsegai et al. 2017) and so the correspondence between these surfaces is generally high. Though the articular surface may not cover the same area in all species studied, the same landmarks are used for comparison as they are present on all metacarpal heads studied.

Repeatability

Landmarks were manually placed in Checkpoint (Stratovan Corporation, Davis, CA, USA) and repeated 10 times on three randomly selected specimens from each species over several days. A different ray was used from each species to ensure landmarks were repeatable across elements following Fernández et al. (2015). The landmarks were then aligned using Procrustes superimposition in the Morpho package in R v3.3.0 (R Core Development Team, 2016; Schlager, 2017). Landmark configurations were then plotted in the first two principal components (PC) of shape space. Landmarks were considered stable if repeated measures were more clustered than those of different individuals. Significant pair-wise permutational manovas conducted on PC1 and PC2 scores demonstrated that group means of the three individuals and their repeats, are significantly different in each case and that variance in landmark placement is significantly less than that between specimens (Supporting Information Fig. S1).

Geometric morphometric procedure

To create the landmark template, a random specimen was selected and eight curves were defined at the margins of the sub-articular surface, in Checkpoint, each bordered by anatomical landmarks as recommended by Gunz et al. (2005). Three sliding semi-landmarks were placed on each of these curves and an additional 140 were equally distributed over the sub-articular surface in Avizo 6.3 (Visualization Sciences Group, Germany) to create a 173-landmark template. The anatomical landmarks were subsequently placed on every specimen and the landmark template (Fig. 2F) then projected onto each of the 183 other metacarpal heads and relaxed onto the surface of each metacarpal using the Morpho package in R (Schlager, 2017) by minimizing bending energy. This package was then used to slide the semi-landmarks along their respective curves and over the surface by minimizing Procrustes distances. This slid template is plotted on an individual Mc3 from each species to provide a sense of the shape variation present (Supporting Information Fig. S6).

Data mapping

Using a custom Python script plugin for Paraview (www.paraview.org) the non-smoothed surface mesh triangles inherited trabecular values from their originating tetrahedra. The Python module SciPy (Jones et al. 2001) was then used in medtool 4.2 (Dr. Pahr Ingenieurs e.U.) to interpolate the trabecular values to the nearest landmark; this was done separately for BV/TV and DA. Interpolating these trabecular values from the outer tetrahedra of the trabecular model is analogous to using spherical VOIs, 1 mm in diameter, centred 0.5 mm beneath an inner trabecular surface landmark. Finally, the geomorph package (Adams et al. 2017) in R was used to perform a generalised Procrustes procedure, resulting in 184 sets of 173 homologous landmarks each with two associated trabecular values (Fig. 2G).

Relative trabecular volume

We employ a relative measure of bone volume fraction (RBV/TV), in which the raw BV/TV value of each landmark is divided by the mean of all landmark BV/TV values on that metacarpal head. Thus RBV/TV values ~ 1 indicate landmarks close to the average BV/TV of that Mc head, while values above or below 1 indicate a deviation from this average at these landmarks. This relative measure was preferred because, while BV/TV can vary systemically across extant hominid species (Tsegai et al. 2018) and may show considerable intraspecific variation, the relative patterns of trabecular architecture appear to preserve a functional signal superimposed on this variation (Saers

et al. 2016). RBV/TV measures the position of the greatest subchondral trabecular bone of a given Mc head rather the absolute volume of bone and therefore is argued to reflect the habitually loaded joint positions of extant hominids while controlling, at least in part, for intra-species and systemic inter-species differences. Species average absolute BV/TV landmark values are depicted for comparison with RBV/TV values in Fig. 3 (see Supporting information).

Statistical analysis

We employ a 'mass-univariate' approach as advocated by Friston et al. (1995) similar to that used to statistically analyse cortical bone in ape metacarpals (Tsegai et al. 2017). Specifically, the trabecular values between species and rays at each landmark are independently analysed using univariate statistics. Inter-ray comparisons do not include comparisons between rays two and four or between rays three and five as they are not biologically contiguous and thus are less informative when prehensile hand postures are considered. However, comparisons of rays two and five are included to test for significant differences between the most ulnar and radial aspects of the metacarpus. Shapiro-Wilk tests found a non-normal distribution of data at one or more landmarks in one or both groups in every pair-wise, inter-ray and interspecific, comparison. To maintain consistent comparisons, a non-parametric Kruskal–Wallis test was applied at each landmark and a post-hoc test was used to test for pair-wise differences if the omnibus test was significant. Dunn's test was chosen as it uses the pooled variance of the Kruskal–Wallis tests and so is conservative. The level of significance was set at $P < 0.05$ subsequent to a Bonferroni correction in each case. This univariate approach means that homologous landmark values are compared across groups rather than with spatially correlated neighbouring landmarks. *Z*-scores were used to determine the polarity, as well as the effect size, of significant differences between groups. These *Z*-scores were transformed into absolute, rather than signed, values and summarised for significant landmark differences, in both interspecific and inter-ray pair-wise comparisons (Supporting Information Tables S1 and S2). Resulting plots of significant univariate differences map regional differences between species and rays but were only considered meaningful if they were found at nine contiguous landmarks, as this represents just over 5% of the sub-articular surface, in order to further ameliorate any Type I error. Despite the fact this univariate method can identify where regions of significant difference lie, it can be susceptible to Type I error and so to provide a multivariate corollary to this approach, a principle components analysis (PCA) of trabecular values, using landmarks as individual variables, was also run for all comparisons. Subsequent omnibus and pair-wise one-way permutational MANOVAs were run with a Bonferroni correction, using the VEGAN package (Oksanen et al. 2018) in R v3.3.0 (R Core Development Team 2016), on the principal component scores of these PCAs to test for significant overall, rather than regional, differences in trabecular patterns.

Results

Univariate landmark comparisons

Pongo

RBV/TV was highest in the palmar aspect of all metacarpal heads in *Pongo* (Fig. 3). The significant differences among the rays included those between Mc2 and Mc5, each of which had a small patch of significantly higher RBV/TV at the ulnar and radial aspects of the metacarpal head, respectively (Fig. 5). Mc3 also had a patch of significantly higher RBV/TV at radio-palmar landmarks relative to Mc2. Interspecifically, *Pongo* RBV/TV was significantly higher at landmarks in the palmar region of the metacarpal heads compared with *P. troglodytes* and especially *Gorilla* (Fig. 7). Compared with *P. paniscus, Pongo* was again significantly higher at more palmar landmarks in Mc4 and Mc5 but there were fewer significantly higher landmarks in Mc3 and almost none in the Mc2 comparison.

Pongo had high DA values throughout the sub-articular metacarpal heads with few significant differences between

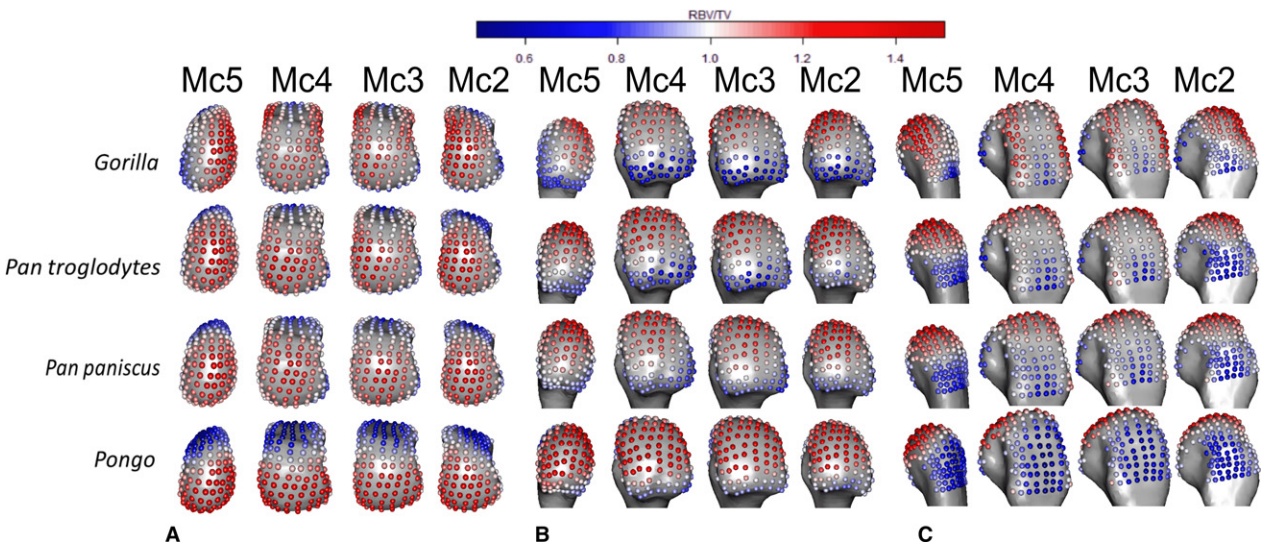

Fig. 3 Species average RBV/TV, mapped to average models of each Mc head in (A) distal, (B) palmar and (C) dorsal views. RBV/TV values around one (white) indicate landmarks close to the average BV/TV of that Mc head, while values above (red) or below one (blue) indicate a deviation from this average at these landmarks.

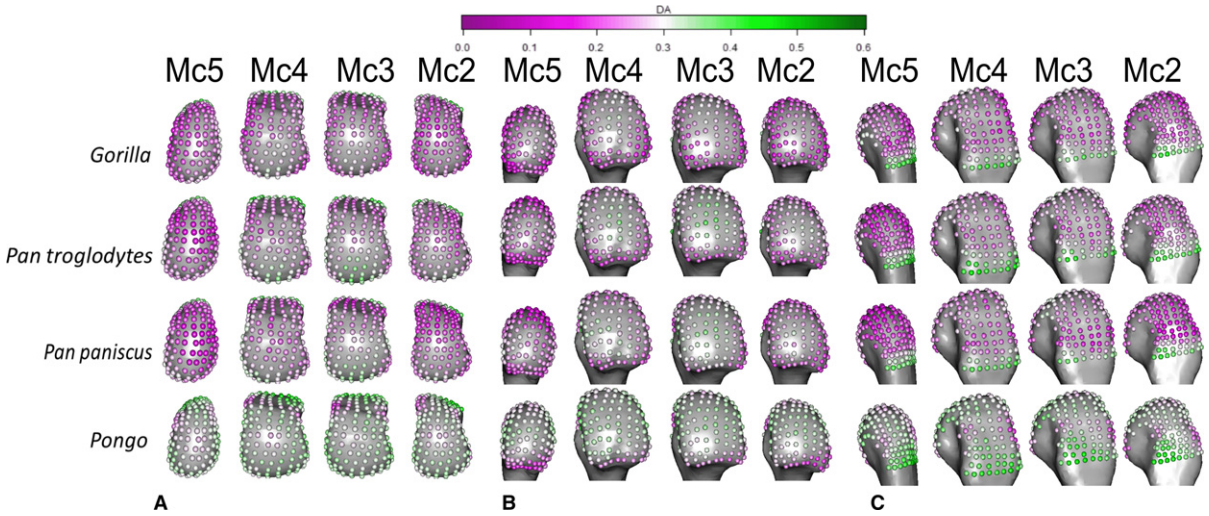

Fig. 4 Species average DA mapped to average models of each Mc head in (A) distal, (B) palmar and (C) dorsal views.

rays (Figs 4, 6 and S3). Interspecifically, *Pongo* DA was significantly greater than that of *Gorilla* in all metacarpal heads except for the central disto-palmar aspects of Mc3-4 and radio-palmar aspects of Mc5. *Pongo* had significantly higher DA on the disto-dorsal aspects of Mc2 and Mc5 relative to both *P. troglodytes* and *P. paniscus*. *Pongo* also had higher DA at landmarks situated on the dorsal aspects of Mc 3 and 4 relative to *P. paniscus* (Fig. 8).

Gorilla

The highest RBV/TV values in *Gorilla* were concentrated in the disto-dorsal portion of each metacarpal head extending dorsally on the medio-lateral edges of Mc3 and 4 but toward the midline of the hand in the Mc2 and Mc5 heads (Fig. 3). This latter pattern was clear in the inter-ray comparison, with significantly greater RBV/TV found at the radial aspect of Mc5 relative to Mc2 and Mc4 as well as on the ulnar aspect of these rays relative to Mc5 (Fig. 5). Interspecifically, *Gorilla* was significantly higher in RBV/TV dorsally compared with *Pongo*, though the radio-palmar aspect of Mc5 was not significantly different between these groups. Compared with *Pan*, *Gorilla* generally had significantly higher RBV/TV dorsally but this was restricted to the medio-lateral edges of each metacarpal head in the regional comparison (Fig. 7). Specifically, *Gorilla* had significantly higher RBV/TV than *Pan* species on the radio-dorsal aspect of Mc5 and both medio-lateral edges of Mc4, as well as the ulno-dorsal aspect of Mc2, though this is extended across the dorsal aspect in the *P. troglodytes* comparison. The Mc3 of *Gorilla* also had significantly higher RBV/TV than *P. paniscus* at landmarks on its dorso-ulnar aspect but was not significantly different from *P. troglodytes* in any region. *Gorilla* had less significant regional differences with *P. troglodytes* than with *P. paniscus* in RBV/TV.

Gorilla had low DA throughout the subchondral metacarpal head trabeculae with slightly higher values distally on Mc3 and Mc4, though only the ulnar-distal aspect of Mc3 had values that were significantly larger than Mc2 (Figs 4 and 6). Mc5 had significantly higher DA on its radial side relative to Mc2 (Fig. 6). *Gorilla* was not significantly higher in DA than were other taxa, apart from the radial border of the distal Mc5 head compared with *Pan paniscus* (Fig. 8).

Pan troglodytes

P. troglodytes had disto-dorsally higher RBV/TV values in the subchondral trabeculae of all the metacarpal heads, though this pattern was more dorsally positioned in Mc3 and Mc4 (Fig. 3). Mc2 and Mc5 showed significantly higher RBV/TV at their most palmar extent relative to Mc3 and Mc4, respectively (Fig. 5). Interspecifically, *P. troglodytes* showed almost no significant differentiation from *P. paniscus* in RBV/TV in any ray (Fig. 7). *P. troglodytes* had significantly higher RBV/TV across the palmar extent of Mc2, and disto-palmarly on the ulnar aspect of Mc5 compared with that of *Gorilla*, and significantly higher RBV/TV dorsally than *Pongo* in each ray.

P. troglodytes generally had low DA through all of the metacarpal heads, although DA values were slighter higher in the palmar regions of Mc3 and Mc4 (Fig. 4). DA values were significantly higher in Mc4 relative to Mc5 and higher in Mc3 relative to Mc2 (Fig. 6). *P. troglodytes* showed the fewest significant differences in DA with *P. paniscus*, significantly higher DA in the palmar aspects of Mc2 and Mc3 compared with *Gorilla*, and significantly lower DA than *Pongo* throughout all the rays (Fig. 8).

Pan paniscus

Like *P. troglodytes, P. paniscus* had the highest RBV/TV values at the disto-dorsal aspect of metacarpal heads but subchondral trabeculae structure was more homogenous within and between the rays (Figs 3 and 5). Interspecifically, *P. paniscus* showed the fewest significant differences with

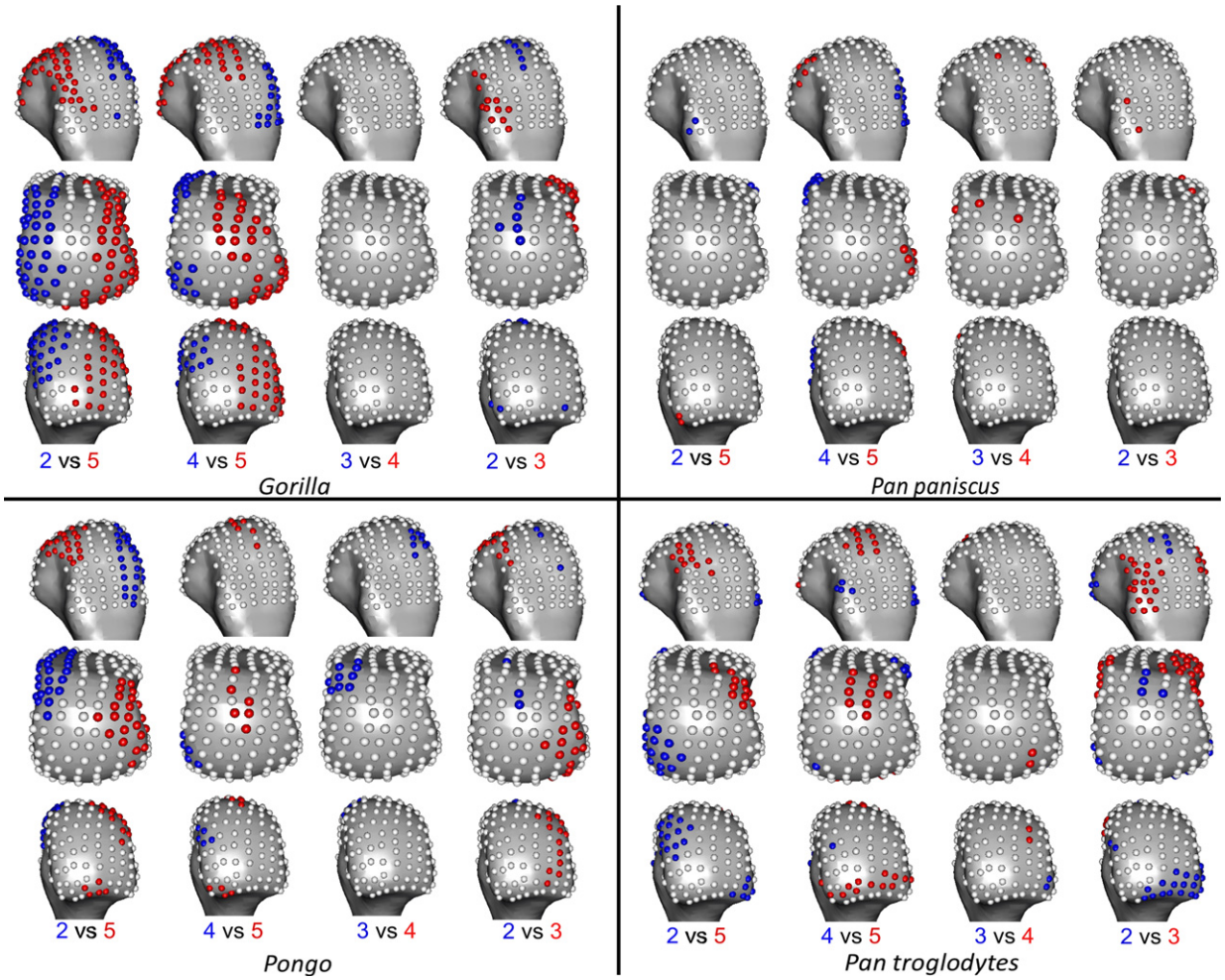

Fig. 5 Inter-ray significant differences in RBV/TV, mapped to an average right Mc3 head in each case in dorsal (top), distal (middle) and palmar (bottom) views. Where RBV/TV values at landmarks are significantly higher in one ray than the other, they are coloured as per the ray numbers in each comparison.

P. troglodytes apart from a small concentration of higher RBV/TV landmarks in the most palmar extent of Mc3 (Fig. 7). *P. paniscus* possessed significantly higher RBV/TV dorsally than *Pongo* across the rays and significantly higher palmar RBV/TV than *Gorilla* in all of the rays. This latter pattern extended distally on Mc2 and Mc5 (Figs 3 and 7).

P. paniscus had a similar DA pattern to *P. troglodytes*, with similar inter-ray significant differences and almost no significant differences between these species (Figs 4, 6 and 8). *P. paniscus* showed significantly higher DA than *Gorilla* did in landmarks across the Mc2 and Mc3 heads, in the palmar regions (Fig. 8). As with all other African apes, *P. paniscus* had significantly lower DA than *Pongo* did across the metacarpal heads, particularly in the dorsal regions.

Multivariate whole-surface comparisons

Interspecific results

Figure 9 depicts the results of the PCA on RBV/TV values, showing species differences within each metacarpal head. Within the Mc2-5 of all the taxa, the first principal component (PC1) explains 38–46% variation in RBV/TV and was driven by dorsal and palmar landmarks. PC2 in Mc2-Mc5 described 13–17% of the variation and reflected variation of values in landmarks that were distally and non-distally situated, respectively. In Mc5, PC3 described 14% of RBV/TV variation in values at radio-ulnar landmarks. Permutational MANOVA omnibus tests were run using PC1-3 in each case, as for some comparisons the PC2 and PC3 explained a similar amount of variance whereas further PCs each explained less than 10% of the variance. These omnibus tests were significant in every ray. As with the individual landmark comparisons described above, *Pongo* had significantly higher palmar RBV/TV compared with all other species, especially *Gorilla.* The overall configuration of *Gorilla* RBV/TV was significantly higher dorsally compared with all other species in Mc2-4 and radio-dorsally in Mc5 (Fig. 9, Table 3). *P. troglodytes* and *P. paniscus* were not significantly different from each other in any of the species comparisons (Table 3).

Following the limited interspecific differences in DA described above, a PCA of DA values yielded poor

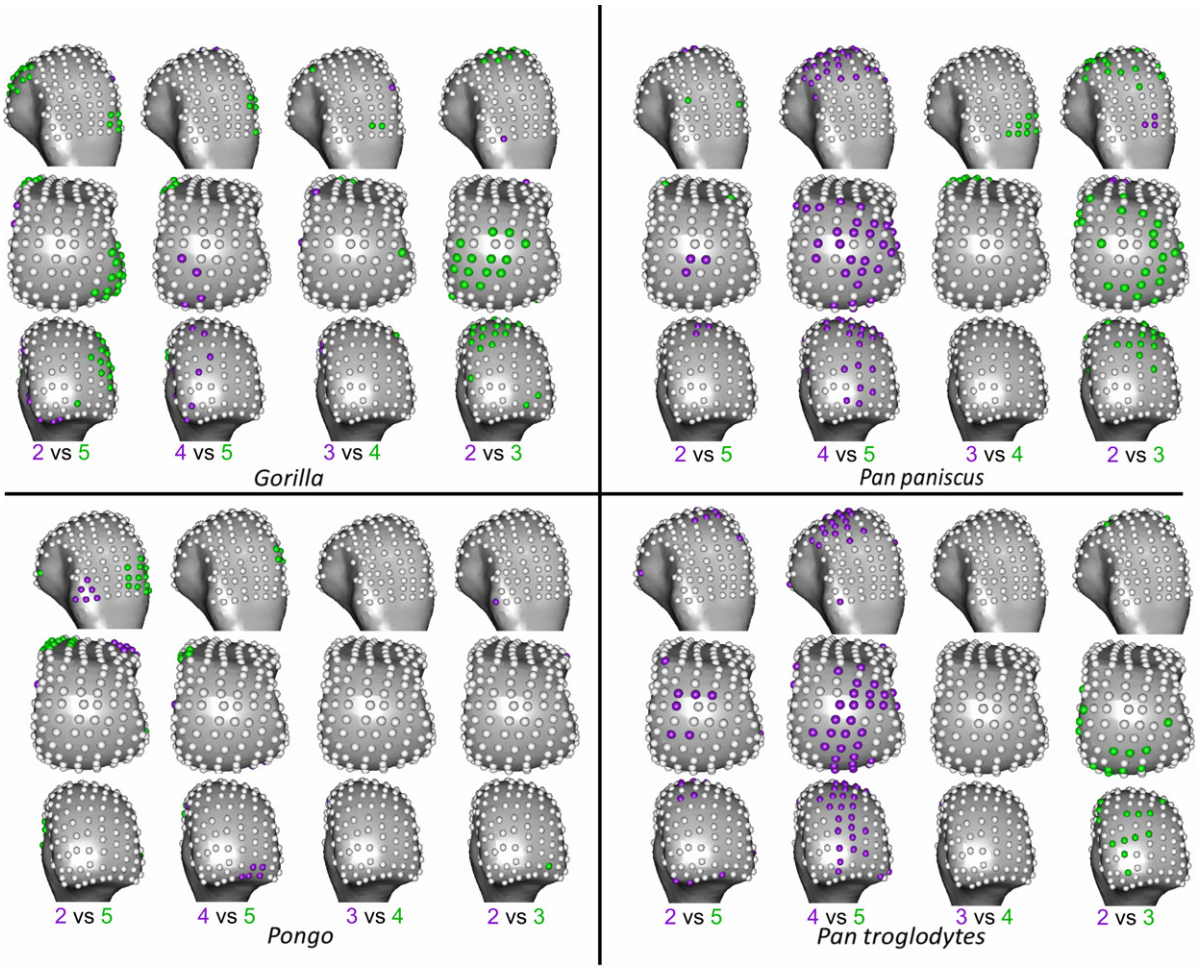

Fig. 6 Inter-ray significant differences in DA, mapped to an average right Mc3 head in each case in dorsal (top), distal (middle) and palmar (bottom) views. Where DA values at landmarks are significantly higher in one ray than the other, they are coloured as per the ray numbers in each comparison.

separation among the sampled taxa. As such, the results are depicted in the Supporting Information. PC1 in DA for each ray, across species, described 34–36% of the variation and was driven by higher values at most landmarks. PC2 described 10–14% of the variation and was driven by landmarks situated dorsally and disto-palmarly, respectively (Supporting Information Fig. S2). Although *Pongo* tended to occupy the positive end of PC1, reflecting higher DA, permutational MANOVAs on PC1-3 revealed that they were only significantly different in every ray from *Gorilla*. This result may be partially driven by the larger intra-species variation in *Pongo* DA relative to other species studied (Fig. S2, see Discussion). *Pongo* was significantly different from *P. paniscus* in Mc2, Mc3 and Mc5 as well as from *P. troglodytes* in Mc2 and Mc5, having generally higher DA (Table 3). Again, *P. paniscus* and *P. troglodytes* were not significantly different from each other at any ray, though both species were slightly, but significantly, higher in DA than *Gorilla* in most rays, *P. troglodytes* was not significantly different form *Gorilla* in DA across Mc4. Both *Pan* species had significantly lower DA than *Gorilla* in the radio-distal aspect of Mc5.

Inter-ray results

Figure 10 depicts the results of PCA of RBV/TV values, showing inter-ray differences within each species. Overall Mc head variation in RBV/TV across rays was different for each species but was generally consistent with individual landmark comparisons described above. In *Pongo,* PC1 explained 25% of the variation and was driven by dorso-palmar landmark values, whereas PC2 explained 18% of the variation and reflected radio-ulnar landmark RBV/TV. The significant omnibus result was driven solely by a Mc2 configuration that had significantly higher disto-ulnar RBV/TV than the other rays did. In *Gorilla,* PC1 reflected 27% of the variation as a result of radio-ulnar landmark values, whereas PC2 reflected 18% of the variation in RBV/TV due to distal and more dorso-palmarly located landmarks (Fig. 10). Permutational MANOVAs on PC1-3 demonstrated the *Gorilla* Mc5 had significantly higher

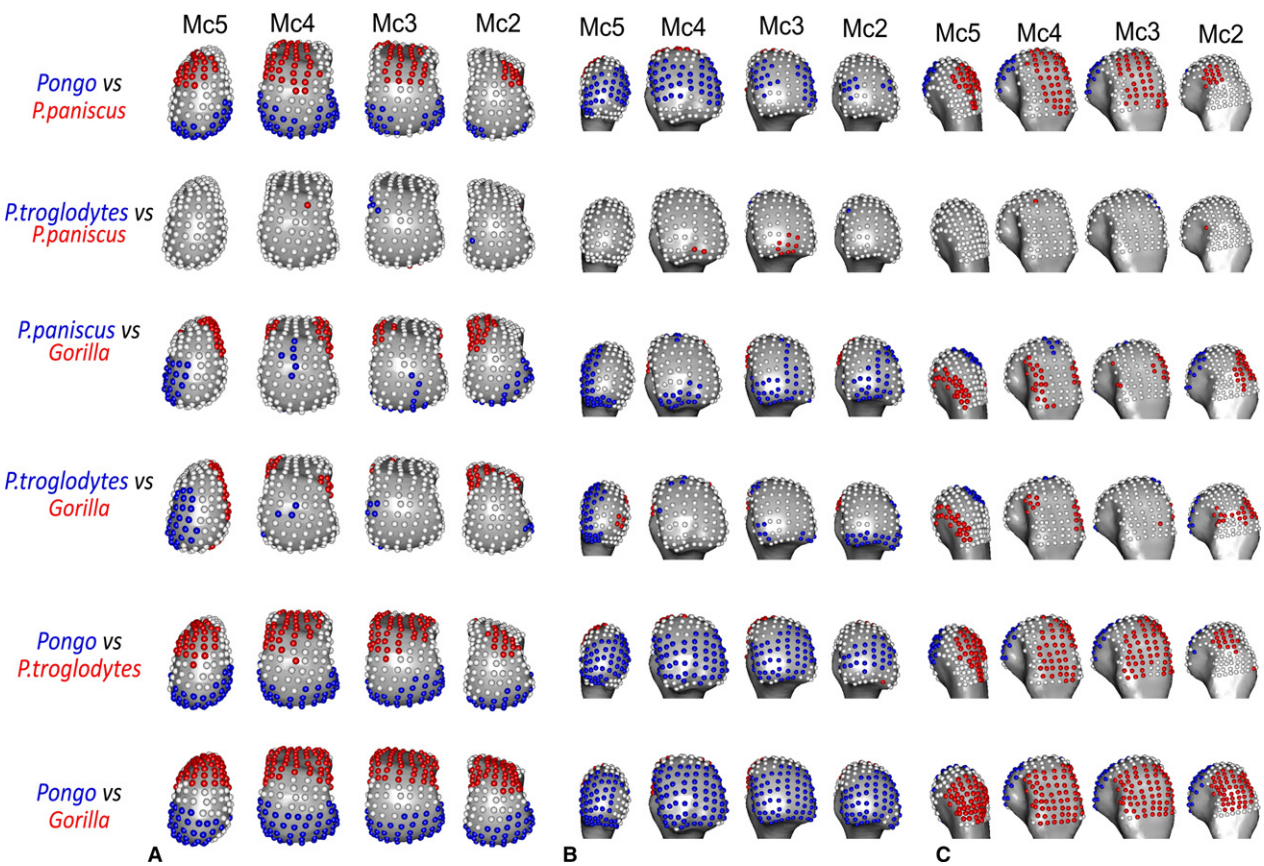

Fig. 7 Significant differences in RBV/TV between species, mapped to average models of each Mc head in (A) distal, (B) palmar and (C) dorsal views. Where RBV/TV values at landmarks are significantly higher in one species than the other, they are coloured as per the species in each comparison.

RBV/TV disto-radially relative to all other rays. *Gorilla* Mc2 had significantly higher disto-ulnar RBV/TV than the other rays, whereas Mc3 and Mc4 had significantly higher RBVTV dorsally than Mc2 and Mc5 and were not significantly different from each other (Table 3). For *P. troglodytes*, variation in overall RBV/TV was chiefly driven by dorso-palmar landmarks on PC1, which explained 32% of the variation, whereas PC2 explained 15% of the variation and reflected differences in the disto-ulnar landmarks. PC3 in *P. troglodytes* RBV/TV describes 12% of the variation and is driven by radio-ulnar landmarks (Fig. 10). *P. troglodytes* Mc2 had significantly higher RBTV/TV disto-palmarly on its ulnar aspect relative to all other rays, whereas Mc5 had significantly higher RBV/TV disto-palmarly on its ulnar aspect compared with Mc2 and Mc3. Mc3 and Mc4 were not significantly different from each other as both had higher dorsal RBV/TV, and Mc4 was not significantly different from Mc5. In *P. paniscus*, PC1 explained 36% of the variance in RBV/TV and was driven by dorso-palmar landmarks, whereas PC2 explained 24% of the variance and reflected distal and non-distal landmarks. However, no significant differences in RBV/TV were found between *P. paniscus* rays (Table 3).

Variation in DA values did not show many significant differences across the Mc heads but was broadly consistent with the individual landmark comparisons. For all species sampled, PC1 was driven by higher values at most landmarks in PC1 and explained 19–45% of the variation. PC2 described 10–16% of the variation in DA and reflected distal as opposed to non-distal landmarks in all species (Supporting Information Fig. S3). In *Pongo*, no ray was significantly different from any other in overall configuration of DA values (Table 3). In Gorilla, PC3 explained 9% of the variance and was driven by radio-ulnar landmarks. Mc5 in *Gorilla* had significantly higher DA at radial landmarks than Mc2 and Mc3 did. The *Gorilla* Mc4 had slightly, but significantly, higher DA over most landmarks relative to Mc2. Both *P. troglodytes* and *P. paniscus* had significantly lower DA at landmarks on the distal aspect of Mc5 compared with Mc3 and Mc4. *P. paniscus* alone also had significantly lower DA over most landmarks on Mc2 compared with Mc3.

Discussion

The aim of this study was to associate inferred loading during particular hand postures in great apes during locomotion with subchondral trabecular architecture across the non-pollical metacarpal heads. The results confirm and build upon previous studies of trabecular bone, most often

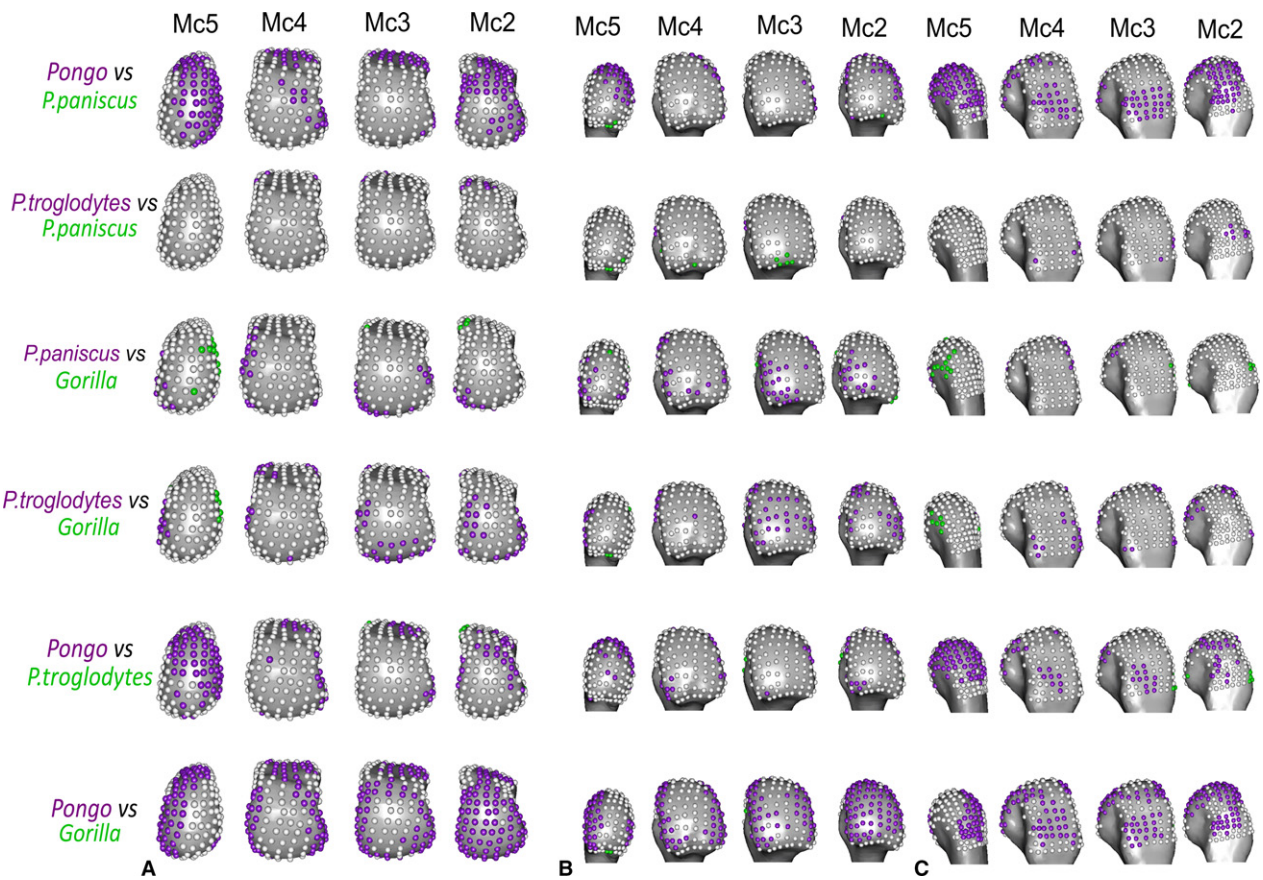

Fig. 8 Significant differences in DA between species, mapped to average models of each Mc head in (A) distal, (B) palmar and (C) dorsal views. Where DA values at landmarks are significantly higher in one species than the other, they are coloured as per the species in each comparison.

focused on only the Mc3 head (Tsegai et al. 2013; Barak et al. 2017; Chirchir et al. 2017), demonstrating not only that is this association possible but that regional trabecular patterns within metacarpal heads, both within and across species, can be statistically discerned. Further, locomotor signals within trabecular structure are not limited to the Mc3, and analysis of all non-pollical metacarpals can provide greater insight into inter-ray and interspecific differences in digit loading.

Relative trabecular bone volume fraction

Pongo

We predicted the orangutans would show significantly higher RBV/TV in the disto-palmar region of the metacarpal heads compared with other hominids and that there would be no significant differences between rays, reflecting the flexed or neutral McP joint posture of all the fingers that characterises flexed-finger power, hook and double-locked grips typically used during arboreal locomotion (Rose, 1988; Sarmiento, 1988). We found general support for these predictions. Orangutans demonstrated significantly higher RBV/TV in the disto-palmar aspect of the subchondral trabeculae in all non-pollical metacarpal heads than did all other taxa. We also found few inter-ray differences, with orangutans generally showing fewer significantly different landmarks in RBV/TV compared with gorillas and chimps (Fig. 5) and no significant difference in overall RBV/TV between adjacent rays (Table 3). The only exception to this was Mc2 of orangutans, which had significantly higher RBV/TV in the disto-dorsal region of its ulnar aspect, relative to the other rays (Figs 5 and 10). Overall, our results are consistent with previous studies using differing methodologies that also found a higher BV/TV in the disto-palmar region of the orangutan Mc3 head (Zeininger et al. 2011; Tsegai et al. 2013; Skinner et al. 2015a; Chirchir et al. 2017) and Mc5 head (Skinner et al. 2015a). It should be noted, however, that the present study sample includes five of the same Mc3 specimens and three of the Mc5 specimens used by Tsegai et al. (2013) and Skinner et al. (2015a), respectively. The generally similar pattern of RBV/TV distribution across the Mc2-5 heads is consistent with using all of the fingers during power, hook and double-lock grips to grasp arboreal substrates (Rose, 1988). The diverging pattern found in the orangutan Mc2 could reflect the relatively more extended second digit posture during a diagonal double-locked grip of very thin substrates, as pictured by Napier (1960) in captivity (Supporting Information Fig. S4).

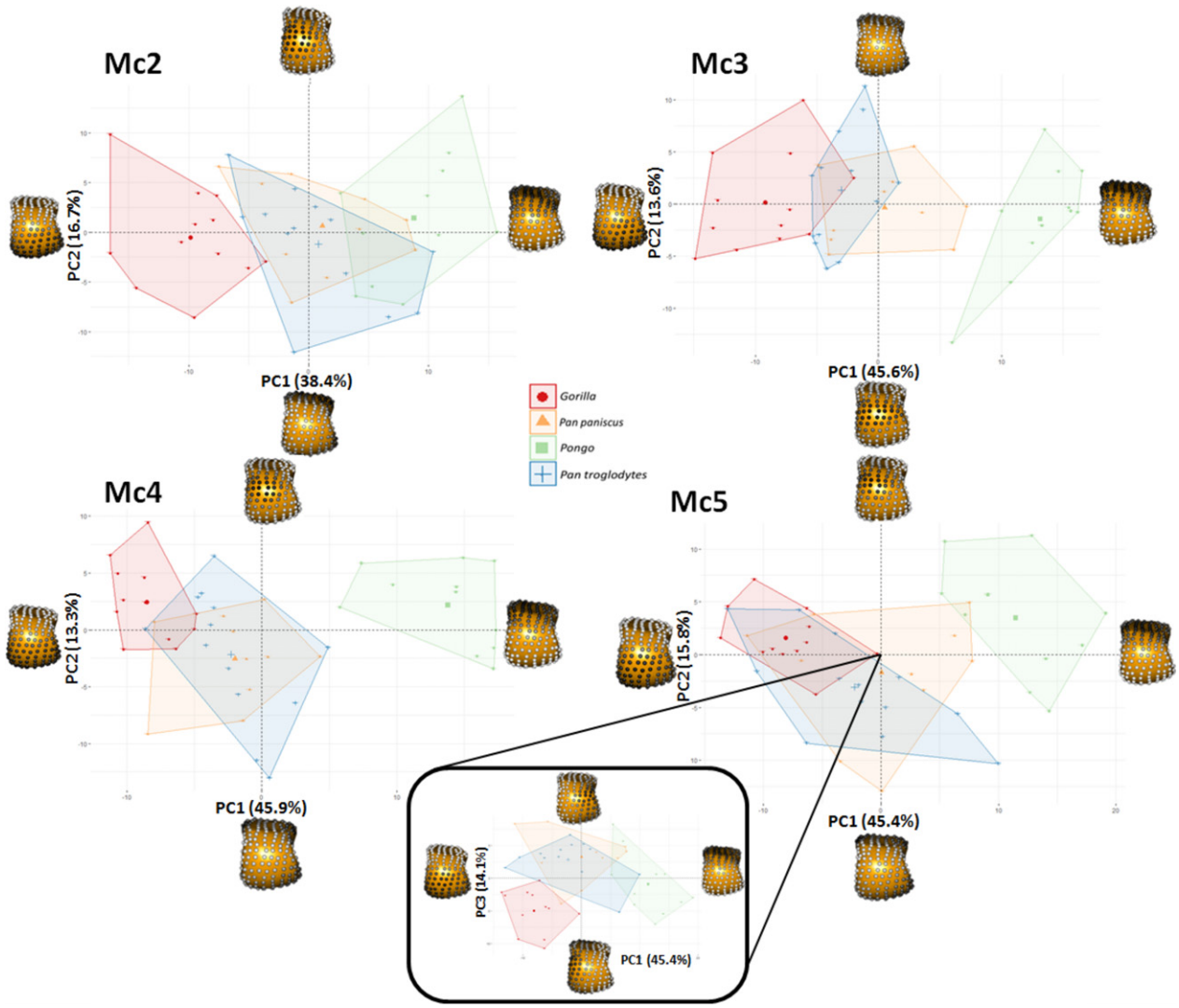

Fig. 9 RBV/TV PCA plots showing species differences within each metacarpal head. Each plot shows the first two principle components (PC) in each ray. For Mc5, PC3 is depicted with PC1 (inset), as PC2 and PC3 explain a similar amount of the variance (16 and 14%, respectively) in this case. Landmarks at each extreme of a PC are coloured in grayscale, according to their signed contribution to that PC and plotted on a Mc3 in distal view. White landmarks indicate the highest signed contribution to the PC and black the least.

However, although challenging data to collect, more behavioural studies of types and frequency of hand grips used by orangutans during arboreal locomotion are needed to substantiate this.

Gorilla

We predicted gorillas would show a significantly higher dorsal distribution of RBV/TV in each metacarpal head compared with all other hominids, reflecting McP joints loaded in a hyper-extended posture during frequent knuckle-walking; this prediction was supported. RBV/TV in the gorilla subchondral trabeculae was significantly higher dorsally than in all other species (Figs 7 and 9). This RBV/TV pattern was also found in previous studies of the Mc3 in gorillas (Tsegai et al. 2013; Skinner et al. 2015a). The present results, however, also revealed high RBV/TV along the disto-ulnar region of the Mc2 head and disto-radial region of the Mc5 head, which was not predicted, although a similar pattern was also found in the Mc5 by Skinner et al. (2015a). This pattern is present in the average male and female RBV/TV distribution (Supporting Information Fig. S5). The gorilla fifth digit is more frequently used in knuckle-walking (Inouye, 1994) and is more similar in length to the other rays compared with that of chimpanzees (Susman, 1979; Inouye, 1992), which may explain the more even distribution of knuckle-walking pressure across the digits in captive gorillas (Matarazzo, 2013a,b). As the fifth digit is often not involved in grips of thinner arboreal substrates (Neufuss et al. 2017) and this RBV/TV pattern is mirrored in the Mc2, it seems parsimonious to argue it reflects more frequent

Table 3 Permutational MANOVAS on the first three principle components between all groups.

	RBV/TV MC2	*RBV/TV MC3*	*RBV/TV MC4*	*RBV/TV MC5*		*RBV/TV Ggg*	*RBV/TV Pp*	*RBV/TV Ppy*	*RBV/TV Pt*
All	**0.0001**	**0.0001**	**0.0001**	**0.0001**	*All*	**0.0001**	0.1209	**0.0001**	**0.0001**
Ppy-Pp	**0.0066**	**0.0006**	**0.0006**	**0.0006**	*2–3*	**0.0258**	n/s	**0.0306**	**0.0012**
Pt-Pp	1.0000	0.6900	1.0000	1.0000	*3–4*	1.0000	n/s	0.9900	1.0000
Pp-Ggg	**0.0006**	**0.0006**	**0.0012**	**0.0006**	*4–5*	**0.0006**	n/s	0.0924	0.2340
Pt-Ggg	**0.0006**	**0.0120**	**0.0012**	**0.0006**	*2–5*	**0.0006**	n/s	**0.0012**	**0.0498**
Pt-Ppy	**0.0054**	**0.0006**	**0.0006**	**0.0006**	*3–5*	**0.0006**	n/s	0.1968	**0.0006**
Ppy-Ggg	**0.0006**	**0.0006**	**0.0006**	**0.0006**	*2–4*	**0.0012**	n/s	**0.0018**	**0.0084**
	DA MC2	*DA MC3*	*DA MC4*	*DA MC5*		*DA Ggg*	*DA Pp*	*DA Ppy*	*DA Pt*
All	**0.0001**	**0.0001**	**0.0001**	**0.0001**	*All*	**0.0003**	**0.0001**	0.2737	**0.0018**
Ppy-Pp	**0.0006**	**0.0222**	**0.0636**	**0.0024**	*2–3*	0.4032	**0.0264**	n/s	0.4710
Pt-Pp	0.6234	1.0000	1.0000	1.0000	*3–4*	1.0000	0.4302	n/s	1.0000
Pp-Ggg	**0.0402**	**0.0102**	**0.0378**	**0.0006**	*4–5*	0.0900	**0.0012**	n/s	**0.0162**
Pt-Ggg	**0.0180**	**0.0336**	**0.0828**	**0.0342**	*2–5*	**0.0096**	0.3318	n/s	0.3894
Pt-Ppy	**0.0054**	0.1626	0.0135	**0.0036**	*3–5*	**0.0108**	**0.0012**	n/s	**0.0036**
Ppy-Ggg	**0.0006**	**0.0006**	**0.0018**	**0.0036**	*2–4*	**0.0114**	0.0930	n/s	1.0000

Species abbreviations are: Ggg, *Gorilla;* Pt, *Pan troglodytes;* Pp, *Pan paniscus;* Ppy, *Pongo* spp. Subsequent pair-wise tests were carried out if the omnibus test was significant; otherwise pair-wise tests are marked as non-significant (N/S). All *P*-values reported are subsequent to a Bonferroni correction and are marked in bold where significant.

and less variable knuckle-walking hand postures in gorillas relative to chimpanzees and bonobos (Tuttle & Basmajian, 1978; Matarazzo, 2013a,b; Thompson et al. 2018). The Mc3 and Mc4 of gorillas also showed high RBV/TV dorsally, especially at the radio-ulnar margins (Figs 3 and 5), which is consistent with the idea that the fingers work in concert to buffer medio-lateral forces during locomotion (Chirchir et al. 2017). The medio-lateral forces generated during 'palm-back' knuckle-walking, which places the McP joints orthogonal to the direction of travel, may be considerable.

Pan troglodytes

We predicted that chimpanzees would have significantly higher dorsal RBV/TV than orangutans but lower than in gorillas, with a more homogeneous distribution of RBV/TV within each metacarpal head and more inter-ray differences, reflecting their more varied locomotor regimen. These predictions were generally supported. The disto-dorsal pattern of higher RBV/TV across the subchondral metacarpus of chimpanzees (Fig. 3) was more dorsally concentrated than in orangutans and more distally extended than in gorillas (Figs 7 and 9). This RBV/TV pattern is consistent with previous studies of chimpanzee subchondral trabecular bone (Zeininger et al. 2011) and whole-epiphyseal analyses that found a similar signal in the subchondral trabeculae of Mc3 and Mc5 (Tsegai et al. 2013; Skinner et al. 2015a). It should be noted, however, that the present study sample includes five of the same Mc3 specimens and four of the Mc5 specimens used by Tsegai et al. (2013) and Skinner et al. (2015a), respectively. In contrast to these analyses, studies using larger VOI methods have found higher BV/TV in centrally placed VOIs relative to palmar or dorsally placed VOI's in the chimpanzee Mc3 head (Barak et al. 2017; Chirchir et al. 2017). However, the use of fewer large VOIs in these studies, as opposed to the many smaller VOIs produced by the whole-epiphysis approach employed here, may exacerbate issues of VOI placement and size that have been shown to have a dramatic effect on trabecular measures in the primate Mc3 (Kivell et al. 2011).

In partial support of our prediction, we found that chimpanzees showed several significant differences in RBV/TV between the Mc heads, although there were not more differences than those found in gorillas. Specifically, RBV/TV in chimpanzees was significantly higher palmarly in Mc2 and Mc5 but higher distally in Mc3 and Mc4 (Figs 5 and 10). This pattern may reflect relatively more weight-bearing by digits 3 and 4 during knuckle-walking than in the second or fifth digit (Tuttle & Basmajian, 1978). Some captive chimpanzees with injuries to digits 2 and 5 appeared to be unimpaired when knuckle-walking and some healthy individuals were observed flexing these digits so that they did not bear weight during this mode of locomotion (Tuttle, 1967). Larger captive chimpanzees have been observed using their second digit significantly less often than gorillas of equivalent size during knuckle-walking and chimpanzees of all sizes used their fifth digit significantly less often, and loaded it less than gorillas did (Inouye, 1994; Wunderlich & Jungers, 2009; Matarazzo, 2013a,b). Matarazzo (2013a,b) found the third digit regularly lifted-off last during 'palm-back' knuckle-walking in captive chimpanzees and that peak pressure was often experienced by the third digit. Wunderlich & Jungers (2009) also found that peak pressures

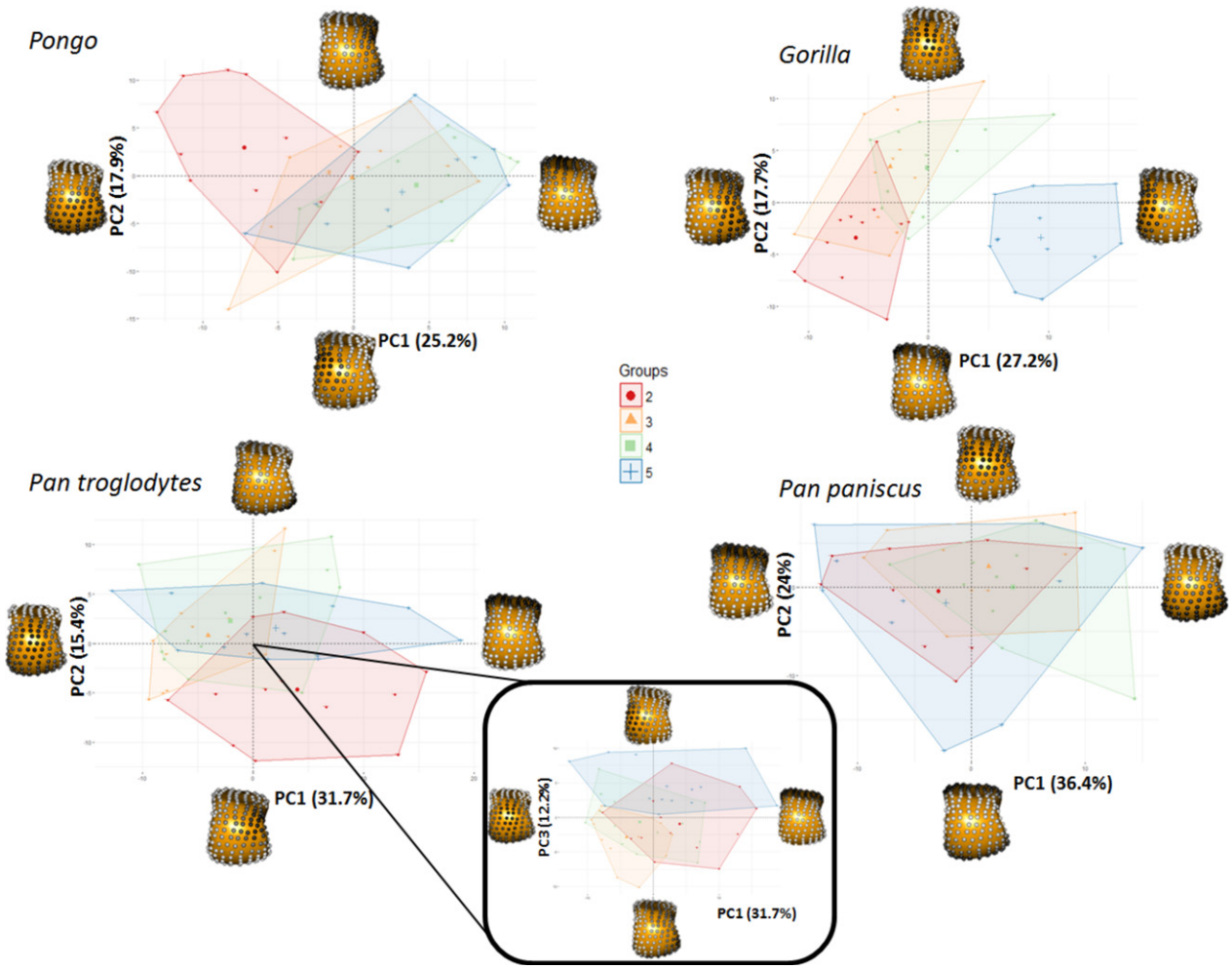

Fig. 10 RBV/TV PCA plots showing ray differences within each species. Each plot shows the first two principle components (PC) in each species, except for *Pan troglodytes*, where PC3 is depicted with PC1 (inset), as PC2 and PC3 explain a similar amount of the variance (15 and 12%, respectively) in this case. Landmarks at each extreme of a PC are coloured in greyscale, according to their signed contribution to that PC and plotted on a Mc3 in distal view. White landmarks indicate the highest signed contribution to the PC and black the least.

were higher on digits 3 and 4 than on digits 2 and 5 when young chimpanzees practised arboreal knuckle-walking and when they used a 'palm-back' posture during terrestrial knuckle-walking. Therefore, it could be argued that the more palmar RBV/TV distribution in Mc2 and Mc5, relative to Mc3 and Mc4, might reflect less loading in McP hyperextension during knuckle-walking and a need to flex digits 2 and 5 during arboreal grasping. Marzke & Wullstein (1996) have argued that the fifth digit should be the most flexed in diagonal power grips, known to be used by wild chimpanzees while vertically climbing (Hunt, 1991; Neufuss et al. 2017).

That being said, in previous hand pressure studies, all mature chimpanzees experienced peak pressures on digits 2–4 when terrestrially knuckle-walking, and the second digit usually lifts off during 'palm-in' knuckle-walking (Wunderlich & Jungers, 2009; Matarazzo, 2013a,b). Further, the second digit should be the most extended during diagonal power grips (Marzke & Wullstein, 1996), which is in contradiction to the relative flexion thought to be indicated here by the relatively palmar RBV/TV pattern found in the chimpanzee Mc2 head. Therefore, in the absence of kinematic and kinetic studies of locomotor hand postures in wild chimpanzees, we suggest that this pattern may reflect more varied hand postures and distribution of pressure across the digits during knuckle-walking (Wunderlich & Jungers, 2009; Matarazzo, 2013a,b) or more frequent arboreal grasping compared with gorillas, or a combination of both (Remis, 1995; Doran, 1996; Thorpe & Crompton, 2006).

Pan paniscus

Given the general similarities in locomotion and hand use between chimpanzees and bonobos, we predicted that bonobos would have a RBV/TV pattern that was very similar to that of chimpanzees, but with a more homogenised distribution of RBV/TV within each metacarpal head. Our

results supported these predictions; bonobos showed disto-dorsally higher RBV/TV that was more distally-extended than in gorillas and more dorsally concentrated than that of orangutans (Figs 3, 7 and 9). Bonobos differed from chimpanzees in that they possessed almost no significant inter-ray differences and they showed the most landmarks closest to the mean of BV/TV throughout the trabecular surface of each head (i.e. RBV/TV being ~ 1; Figs 3, 5 and 10). This RBV/TV distribution is consistent with the expectation raised by Tsegai et al. (2013) that bonobos would have an intermediate Mc3 trabecular structure between that of African apes and Asian apes (Fig. 9), and the intermediate thickness of Mc3 cortical bone in this species (Susman, 1979). If the relatively higher dorsal RBV/TV in chimpanzee Mc3 and Mc4 is a knuckle-walking signal, then the lack of it in bonobos, as well as the significantly higher palmar RBV/TV of Mc3, may reflect either more loading of a flexed McP joint consistent with the presumed greater arboreality in this species (Alison & Badrian, 1977; Susman et al. 1980; Susman, 1984; Crompton et al. 2010) or direct palmar loading of the metacarpal head as a result of a significant amount of arboreal palmigrady (Doran, 1993; Doran & Hunt, 1996).

Trabecular anisotropy

In contrast to the RBV/TV results, the degree of anisotropy (DA) in the subchondral trabecular bone was less variable, both in interspecies and inter-ray comparisons. Interestingly, every species studied possesses higher average DA values across the most dorsal aspect of each metacarpal (Fig. 4). As this pattern also appears in orangutans, it is likely not reflective of hyper-extension of the McP during knuckle-walking but may instead reflect fewer trabeculae at the limit of the sub-articular surface. Fewer subchondral trabecular struts would reduce the variability of alignment and thus increase DA. The main significant differences in DA were found in orangutans, which were generally more anisotropic than any other taxon, especially gorillas (Figs 4, 6, S2 and S3, Table 3). This did not support our prediction that orangutan DA would be significantly higher in the disto-palmar region, or that gorilla DA would be significantly higher in the dorsal region of the metacarpal heads compared with other hominids. Given this lack of specific regional differences it is difficult to attribute the general lack of inter-ray differences in orangutans and gorillas to functional grips as per our predictions (Figs 6 and S3). Conversely, chimpanzees and bonobos did partially support our predictions, as they showed the least significantly different landmarks in DA between them (Fig. 8) and the most inter-ray differences within each species (Fig. 6), though again it is difficult to link this to specific hand postures.

High DA in orangutans did not support our predictions and appears contradictory to previous results showing significantly lower DA in orangutans and other suspensory taxa (Tsegai et al. 2013). However, Tsegai et al. (2013) quantified and averaged trabecular DA throughout the entire Mc3 head, as opposed to just the subchondral trabeculae, which can mask the signal of higher DA in particular regions of the head. In particular, subchondral trabeculae are responsible for the initial dissipation of load from the articular, compact cortical bone through to the more internal trabecular structure in long bones such as metacarpals (Currey, 2002). Thus it may be possible that trabeculae in this region are more constrained in their orientation, as they must link the cortical shell of the metacarpal head and the deeper trabecular structure, explaining the lack of variability in DA in our sample. If this is true, the variation in DA we did find, significantly higher DA in orangutans than in other species, might be due to a general lower number of trabeculae in orangutans. However, Chirchir et al. (2017) also found that DA was consistently, if not significantly, higher in orangutans than chimpanzees in all three of their VOIs which were sampled in most of the Mc3 head. Further, higher DA has been found at the superior-central region than in other regions of the proximal *Pongo* humerus (Kivell et al. 2018). Therefore, it is unlikely that the significantly higher DA in orangutans is solely an artefact of sampling subchondral trabeculae.

High subchondral DA in orangutans may reflect a lower extension range of motion (19°) compared with that of African apes (50°) (Napier, 1960; Rose, 1988). Although orangutans have been assumed to load their hands in a greater range of postures to accommodate their diverse arboreal locomotor repertoire relative to the frequent and consistent knuckle-walking postures of African apes (Tsegai et al. 2013), the orangutan McP joint will, presumably, always been in a neutral-to-flexed posture when grasping arboreal substrates. Indeed, while variability in DA values for orangutans appears to be higher than in other taxa studied, higher average DA values are not solely driven by outlying individuals (Fig. S2) or, on further interrogation, by individuals of a particular species or sex. An analysis of trabeculae in the whole Mc3 head has reported similar intra-species variability in orangutans (Tsegai et al. 2013). Yet one constant across orangutan species and sexes is their high frequency of arboreal locomotion, requiring flexed McP grasping and perhaps a more stereotypically aligned trabecular structure, reflected in the high average DA found here. In contrast, African apes load their McP joints in both hyper-extension during knuckle-walking and a range of neutral-to-flexed postures during arboreal locomotion. The greater isotropy found within the subchondral trabeculae of African apes may reflect loading of the McP joint from multiple directions during arboreal, as well as terrestrial, behaviours.

Inferring bone functional adaptation

Many explorative comparative anatomy analyses, including the present study, can be thought of as adaptationist

(Gould & Lewontin, 1979), presenting functionally adaptive explanations for the observed data that are not easily falsified (Smith, 2016). Here, however, we submit that as the clearest differences in subchondral RBV/TV and DA patterns in the metacarpal heads are between the two species with the most disparate locomotor modes (orangutans and gorillas), and the least differences are between the two species with the most similar locomotor modes (chimpanzees and bonobos), this offers a kind of informal falsification. If the chimpanzees and bonobos were the most disparate in trabecular pattern, this would effectively falsify the broad underlying logic of our predictions. Conversely, with respect to our more specific predictions that were not confirmed, for example those regarding regional DA in *Pongo* and *Gorilla*, alternative data must be sought to explain these results (as detailed above). For example, future work that scales DA by trabecular number, analyses of the differences between subchondral and deeper trabecular structure, or detailed studies of locomotor hand postures in wild *Pongo*, could all potentially falsify some of these explanations. Nevertheless, it must be noted that the broader logic underlying more predictions holds for DA, as chimpanzees and bonobos did not display the most significant differences.

In the same vein, it could be argued that the lack of differences between chimpanzees and bonobos is due to their close phylogenetic distance rather than their similar locomotor regimes. Trabecular bone structure is controlled, at least to some extent, by genetic factors (Lovejoy et al. 2003; Havill et al. 2010; Judex et al. 2013; Almécija et al. 2015) and the role of trabecular remodelling is not solely functional (Skinner et al. 2015b); for example, trabecular bone is also important for mineral homeostasis (Clarke, 2008). There were clear differences in absolute BV/TV, however, such that bonobos demonstrated much greater subchondral BV/TV in all elements of the hand studied compared with chimpanzees (Supporting Information Fig. S7). This difference has been previously reported within the Mc3 of the same individuals in this study for which the phylogenetic influence was assessed (Tsegai et al. 2013). The relative measure used here appears to have effectively controlled for this difference in subchondral metacarpal head BV/TV. This suggests that the absolute difference in BV/TV is not functional in origin, as it is unlikely bonobos that practise a form of locomotion very similar to that of chimpanzees but with remarkably greater force. The only comparable kinematic data available demonstrate that both captive chimpanzees and captive bonobos experience similar peak pressures on their fingers during arboreal knuckle-walking (Wunderlich & Jungers, 2009; Samuel et al. 2018). If not functional in origin, the absolute difference in BV/TV between chimpanzees and bonobos may be systemic. Though a study of metatarsal trabeculae failed to find this difference in absolute BV/TV between chimpanzees and bonobos (Griffin et al. 2010), Tsegai et al. (2018) have noted that systemic differences in BV/TV between species may be variably pronounced at different anatomical sites. While the reasons for systemic differences in trabeculae might be varied, e.g. hormones, diet and disparate intestinal biomes (Tsegai et al. 2018), the difference is marked between these phylogenetically close species. As a corollary it would seem that there is little reason to suspect non-functional systematic forces are driving the similarities between RBV/TV in *Pan* species. Although the relative measure appears to have effectively controlled for possible systemic differences in subchondral trabeculae of the non-pollical metacarpal heads, there are still small differences between the species which, by process of elimination, appear to be functional in origin.

Work on intra-species variation in a large sample of a single species also supports this idea of both a systemic and functional signal in trabecular architecture. While current studies have focused on humans, likely due to the availability of specimens, data from several anatomical sites have demonstrated lower BV/TV in sedentary humans relative to mobile forager populations, primarily due to lower mechanical loading (Chirchir et al. 2015; Ryan & Shaw, 2015). Within the lower limb, this trabecular difference appears to be superimposed on a pattern of increasing trabecular gracility with increasingly distal elements of the limb (Saers et al. 2016). The transition to sedentism in human populations provides a natural experiment that allows the identification of a trabecular functional signal superimposed onto a structural limb-tapering signal, which is also found in cortical bone (Saers et al. 2016). We argue that the phylogenetic proximity and similar locomotion of *Pan* also provides a natural experiment that begins to separate functional and systemic differences between these species, as seen in the present RBV/TV results. Future work should consider the possibility of clarifying functional and systemic signals in trabecular bone.

It would be interesting to apply these methods to the pollicial metacarpal of hominids, and perhaps a larger sample of primates, in order to test for manipulative behaviour signals that may lie in the subchondral trabecular bone. Even this relatively small comparative sample may be used to contextualise fossil hominin trabeculae to shed light on their habitually loaded hand postures. Though relatively complete fossil hominin hands are rare in the archaeological record, this comparative sample demonstrates that isolated Mc2 or Mc5 elements are more important than previously thought for identifying habitual hand use in our ancestors.

Conclusion

Using a geometric morphometric approach, we demonstrated significant differences in the distribution of subchondral trabecular RBV/TV across great apes that were consistent with our predicted differences in McP joint loading during locomotion. Results of this study generally confirm previous analyses of metacarpal head trabecular

structure that have largely focused only on the Mc3, but provide for the first time a statistically robust comparison using the whole-epiphysis approach. By building upon previous work to look at trabecular structure across all of the non-pollical metacarpals, we revealed novel RBV/TV patterns in the inter-ray comparisons within *Gorilla* and *Pan* that are consistent with differences in hand posture during knuckle-walking and the frequency of arboreal locomotion. However, these inferences require testing with more detailed kinematic and kinetic analyses of the hand, ideally in wild African apes. Contrary to our predictions, we found few significant differences in DA across taxa, with *Pongo* demonstrating significantly higher DA than African ape taxa. We conclude that the interspecific variation in subchondral trabecular RBV/TV revealed here is consistent with what is currently known about great ape hand use and McP joint loading and, as such, provides a valuable comparative context in which to interpret the trabecular structure of fossil hominoid or hominin metacarpal heads.

Acknowledgements

We would like to thank Inbal Livne (Powell-Cotton Museum), Anneke van Heteren, Michael Hiermeier (Zoologische Staatssammlung München), Christophe Boesch, Uta Schwarz (MPI-EVA), and Ana Ragni (NMNH) for access to specimens. We would also like to thank David Plotzki (MPI-EVA) and Keturah Smithson (Cambridge Biotomography Centre) for assistance in scanning these specimens, as well as Matthew Tocheri for assistance with landmarking software and Leoni Georgiou for discussions that enhanced this manuscript. We are also grateful to two anonymous reviewers whose feedback greatly improved this manuscript. This research was supported by European Research Council Starting Grant #336301 (C.J.D., M.M.S., T.L.K.), the Max Planck Society and the Fyssen Foundation (A.B.).

References

Adams DC, Collyer ML, Kaliontzopoulou A, et al. (2017) Geomorph: Software for geometric morphometric analyses. R package version 3.0.5.

Alexander C (1994) Utilisation of joint movement range in arboreal primates compared with human subjects: an evolutionary frame for primary osteoarthritis. *Ann Rheum Dis* **53**, 720–725.

Alison F, Badrian N (1977) Pygmy chimpanzees. *Oryx* **13**, 463–468.

Allen MR, Burr DB (2014) Bone modeling and remodeling. In: *Basic and Applied Bone Biology* (eds Burr DB, Allen MR), pp. 75–90. London: Academic Press.

Almécija S, Wallace IJ, Judex S, et al. (2015) Comment on 'Human-like hand use in *Australopithecus africanus*'. *Science* **348**, 1101–1101.

Barak MM, Lieberman DE, Hublin JJ (2011) A Wolff in sheep's clothing: trabecular bone adaptation in response to changes in joint loading orientation. *Bone* **49**, 1141–1151.

Barak MM, Lieberman DE, Raichlen D, et al. (2013a) Trabecular evidence for a human-like gait in *Australopithecus africanus*. *PLoS ONE* **8**, e77687.

Barak MM, Lieberman DE, Hublin JJ (2013b) Of mice, rats and men: trabecular bone architecture in mammals scales to body mass with negative allometry. *J Struct Biol* **183**, 123–131.

Barak MM, Sherratt E, Lieberman DE (2017) Using principal trabecular orientation to differentiate joint loading orientation in the 3rd metacarpal heads of humans and chimpanzees. *J Hum Evol* **113**, 173–182.

Biewener AA, Fazzalari NL, Konieczynski DD, et al. (1996) Adaptive changes in trabecular architecture in relation to functional strain patterns and disuse. *Bone* **19**, 1–8.

Bookstein FL (1991) *Morphometric Tools for Landmark Data: Geometry and Biology*. Cambridge: Cambridge University Press.

Cant JG (1987) Positional behavior of female Bornean orangutans (*Pongo pygmaeus*). *Am J Primatol* **12**, 71–90.

Carlson KJ, Doran-Sheehy DM, Hunt KD, et al. (2006) Locomotor behavior and long bone morphology in individual free-ranging chimpanzees. *J Hum Evol* **50**, 394–404.

Chirchir H, Kivell TL, Ruff CB, et al. (2015) Recent origin of low trabecular bone density in modern humans. *Proc Natl Acad Sci U S A* **112**, 336–371.

Chirchir H, Zeininger A, Nakatsukasa M, et al. (2017) Does trabecular bone structure within the metacarpal heads of primates vary with hand posture? *CR Palevol* **16**, 533–544.

Cignoni P, Callieri M, Corsini M, et al. (2008) Meshlab: an open-source mesh processing tool. In: *Eurographics Italian Chapter Conference 2008*. (eds Scarano V, De Chiara R, Erra U), pp. 129–136. Salerno: Eurographics.

Clarke B (2008) Normal bone anatomy and physiology. *Clin J Am Soc Nephrol* **3**(Supplement 3), S131–S139.

Cowin SC (1986) Wolff's law of trabecular architecture at remodeling equilibrium. *J Biomech Eng* **108**, 83–88.

Crompton RH, Sellers WI, Thorpe SK (2010) Arboreality, terrestriality and bipedalism. *Philos Trans R Soc B* **365**, 3301–3314.

Currey JD (2002) *Bones: Structure and Mechanics*. Princeton: Princeton University Press.

D'Août K, Vereecke E, Schoonaert K, et al. (2004) Locomotion in bonobos (*Pan paniscus*): differences and similarities between bipedal and quadrupedal terrestrial walking, and a comparison with other locomotor modes. *J Anat* **204**, 353–361.

DeSilva JM, Devlin MJ (2012) A comparative study of the trabecular bony architecture of the talus in humans, non-human primates, and Australopithecus. *J Hum Evol* **63**, 536–551.

Doran DM (1992) The ontogeny of chimpanzee and pygmy chimpanzee locomotor behavior: a case study of paedomorphism and its behavioral correlates. *J Hum Evol* **23**, 139–157.

Doran DM (1993) Comparative locomotor behavior of chimpanzees and bonobos: the influence of morphology on locomotion. *Am J Phys Anthropol* **91**, 83–98.

Doran D (1996) Comparative positional behavior of the African apes. In: *Great Ape Societies* (eds McGrew WC, Marchant LF, Nishida T), pp. 213–224. Cambridge: Cambridge University Press.

Doran DM (1997) Ontogeny of locomotion in mountain gorillas and chimpanzees. *J Hum Evol* **32**, 323–344.

Doran DM, Hunt KD (1996) Comparative locomotor behavior of chimpanzees and bonobos. In: *Chimpanzee Cultures* (eds Wrangham RW, McGrew WC, de Waal FB, Heltne PG), pp. 93–108, Cambridge: Harvard University Press.

Doube M, Kłosowski MM, Wiktorowicz-Conroy AM, et al. (2011) Trabecular bone scales allometrically in mammals and birds. *Proc R Soc Lond B* **278**, 3067–3073.

Drapeau MS (2015) Metacarpal torsion in apes, humans, and early Australopithecus: implications for manipulatory abilities. *PeerJ* **3**, e1311.

Fernández PJ, Almécija S, Patel BA, et al. (2015) Functional aspects of metatarsal head shape in humans, apes, and Old World monkeys. *J Hum Evol* **86**, 136–146.

Friston KJ, Holmes AP, Worsley KJ, et al. (1995) Statistical parametric maps in functional imaging: a general linear approach. *Hum Brain Mapp* **2**, 189–210.

Frost HM (1987) Bone 'mass' and the 'mechanostat': a proposal. *Anat Rec (Hoboken)* **219**, 1–9.

Georgiou L, Kivell TP, Skinner M (2018) Trabecular bone patterning in the hominoid distal femur. *PeerJ* **6**, e5156.

Gould SJ, Lewontin RC (1979) The spandrels of San Marco and the Panglossian paradigm: a critique of the adaptationist programme. *Proc R Soc Lond Ser B* **205**, 581–598.

Griffin N, D'Août K, Ryan T, et al. (2010) Comparative forefoot trabecular bone architecture in extant hominids. *J Hum Evol* **59**, 202–213.

Gross T, Kivell TL, Skinner MM, et al. (2014) A CT-image-based framework for the holistic analysis of cortical and trabecular bone morphology. *Palaeontol Electronica* **17**, 1.

Gunz P, Mitteroecker P (2013) Semilandmarks: a method for quantifying curves and surfaces. *Hystrix* **24**, 103–109.

Gunz P, Mitteroecker P, Bookstein FL (2005) Semilandmarks in three dimensions. In: *Modern Morphometrics in Physical Anthropology* (ed. Slice DE), pp. 73–98. Boston: Springer.

Havill L, Allen M, Bredbenner T, et al. (2010) Heritability of lumbar trabecular bone mechanical properties in baboons. *Bone* **46**, 835–840.

Hunt K (1991) Mechanical implications of chimpanzee positional behavior. *Am J Phys Anthropol* **86**, 521–536.

Hunt K (2004) The special demands of great ape locomotion and posture. In: *The Evolution of Thought: Evolutionary Origins of Great Ape Intelligence* (eds Begun D, Russon A), pp. 172–189. Cambridge: Cambridge University Press.

Hunt KD (2016) Why are there apes? Evidence for the co-evolution of ape and monkey ecomorphology. *J Anat* **228**, 630–685.

Hunt KD, Cant JG, Gebo DL, et al. (1996) Standardized descriptions of primate locomotor and postural modes. *Primates* **37**, 363–387.

Inouye SE (1992) Ontogeny and allometry of African ape manual rays. *J Hum Evol* **23**, 107–138.

Inouye S (1994) Ontogeny of knuckle-walking hand postures in African apes. *J Hum Evol* **26**, 459–485.

Jones E, Oliphant T, Peterson P (2001) SciPy: open source scientific tools for Python. http://www.scipy.org/.

Judex S, Zhang W, Donahue LR, et al. (2013) Genetic loci that control the loss and regain of trabecular bone during unloading and reambulation. *J Bone Miner Res* **28**, 1537–1549.

Kazhdan M, Hoppe H (2013) Screened Poisson surface reconstruction. *ACM Trans Graph* **23**, 29–42.

Kivell TL, Skinner MM, Lazenby R, et al. (2011) Methodological considerations for analyzing trabecular architecture: an example from the primate hand. *J Anat* **218**, 209–225.

Kivell TL, Davenport R, Hublin JJ, et al. (2018) Trabecular architecture and joint loading of the proximal humerus in extant hominoids, Ateles, and *Australopithecus africanus*. *Am J Phys Anthropol* **167**, 348–365.

Lambers FM, Koch K, Kuhn G, et al. (2013a) Trabecular bone adapts to long-term cyclic loading by increasing stiffness and normalization of dynamic morphometric rates. *Bone* **55**, 325–334.

Lambers FM, Bouman AR, Rimnac CM, et al. (2013b) Microdamage caused by fatigue loading in human cancellous bone: relationship to reductions in bone biomechanical performance. *PLoS ONE* **8**, e83662.

Lazenby R, Skinner M, Hublin J, et al. (2011) Metacarpal trabecular architecture in the chimpanzee (*Pan troglodytes*): evidence for locomotion and tool use. *Am J Phys Anthropol* **144**, 215–225.

Lewis OJ (1977) Joint remodelling and the evolution of the human hand. *J Anat* **123**, 157–201.

Lovejoy CO, McCollum MA, Reno PL, et al. (2003) Developmental biology and human evolution. *Annu Rev Anthropol*, **32**, 85–109.

Manduell KL, Morrogh-Bernard HC, Thorpe SK (2011) Locomotor behavior of wild orangutans (*Pongo pygmaeus wurmbii*) in disturbed peat swamp forest, Sabangau, Central Kalimantan, Indonesia. *Am J Phys Anthropol* **145**, 348–359.

Marchi D, Proctor DJ, Huston E, et al. (2017) Morphological correlates of the first metacarpal proximal articular surface with manipulative capabilities in apes, humans and South African early hominins. *CR Palevol* **16**, 645–654.

Martin RB, Burr DB, Sharkey NA (1998) *Skeletal Tissue Mechanics*. New York: Springer.

Marzke MW, Wullstein KL (1996) Chimpanzee and human grips: a new classification with a focus on evolutionary morphology. *Int J Primatol* **17**, 117–139.

Marzke MW, Wullstein KL, Viegas SF (1992) Evolution of the power ('squeeze') grip and its morphological correlates in hominids. *Am J Phys Anthropol* **89**, 283–298.

Matarazzo SA (2013a) Manual pressure distribution patterns of knuckle-walking apes. *Am J Phys Anthropol* **152**, 44–50.

Matarazzo SA (2013b) Knuckle-Walking Signal in the Manual Phalanges and Metacarpals of the Great Apes (*Pan* and *Gorilla*) (Vol. Paper 755). UMass Amherst: PhD thesis.

Matarazzo SA (2015) Trabecular architecture of the manual elements reflects locomotor patterns in primates. *PLoS ONE* **10**, e0120436.

Napier JR (1960) Studies of the hands of living primates. *J Zool* **134**, 647–657.

Neufuss J, Robbins MM, Baeumer J, et al. (2017) Comparison of hand use and forelimb posture during vertical climbing in mountain gorillas (*Gorilla beringei beringei*) and chimpanzees (*Pan troglodytes*). *Am J Phys Anthropol* **164**, 651–664.

Niewoehner WA (2005) A geometric morphometric analysis of Late Pleistocene human metacarpal 1 base shape. In: *Modern Morphometrics in Physical Anthropology* (ed. Slice DE), pp. 285–298, Boston, MA: Springer.

Odgaard A, Kabel J, van Rietbergen B, et al. (1997) Fabric and elastic principal directions of cancellous bone are closely related. *J Biomech* **30**, 487–495.

Oksanen J, Blanchet F, Friendly M, et al. (2018) vegan: Community Ecology Package.

Orr CM (2016) Functional morphology of the primate hand: recent approaches using biomedical imaging, computer modeling, and engineering methods. In: *The Evolution of the Primate Hand* (eds Kivell T, Lemelin P, Richmond B, Schmitt D), pp. 227–257. New York: Springer.

Pahr DH, Zysset PK (2009) From high-resolution CT data to finite element models: development of an integrated modular

framework. *Comput Methods Biomech Biomed Engin* **12**, 45–57.

Pontzer H, Lieberman DE, Momin E, et al. (2006) Trabecular bone in the bird knee responds with high sensitivity to changes in load orientation. *J Exp Biol* **209**, 57–65.

R Core Development Team (2016) R: A language and environment for statistical computing. Vienna: R Foundation for Statistical Computing.

Rein TR (2018) A geometric morphometric examination of hominoid third metacarpal shape and its implications for inferring the precursor to terrestrial bipedalism. Anat Rec (Hoboken) https://doi.org/10.1002/ar.23985.

Remis M (1995) Effects of body size and social context on the arboreal activities of lowland gorillas in the Central African Republic. *Am J Phys Anthropol* **97**, 413–433.

Remis M (1998) The gorilla paradox: the effects of body size and habitat on the positional behavior of lowland and mountain gorillas. In: *Primate Locomotion* (eds Stasser E, Fleagle J, Rosenberge A, McHenry H), pp. 95–106. Boston: Springer.

Rodman P (1984) Foraging and social systems of orangutans and chimpanzees. In: *Adaptations for Foraging in Non-Human Primates* (eds Rodman P, Cant J), pp. 134–160. New York: Columbia University.

Rolian C, Lieberman DE, Hallgrímsson B (2010) The coevolution of human hands and feet. *Evolution* **64**, 1558–1568.

Rose MD (1988) Functional anatomy of the cheiridia. In: *Orangutan Biology* (ed. Schwartz J), pp. 299–310. Oxford: Oxford University Press.

Ruff CB, Runestad JA (1992) Primate limb bone structural adaptations. *Annu Rev Anthropol*, **21**, 407–433.

Ryan TM, Shaw CN (2013) Trabecular bone microstructure scales allometrically in the primate humerus and femur. *Proc R Soc Lond B* **280**, 20130172.

Ryan TM, Shaw CN (2015) Gracility of the modern *Homo sapiens* skeleton is the result of decreased biomechanical loading. *Proc Natl Acad Sci U S A* **112**, 372–377.

Ryan TM, Walker A (2010) Trabecular bone structure in the humeral and femoral heads of anthropoid primates. *Anat Rec (Hoboken)* **293**, 719–729.

Ryan TM, Carlson KJ, Gordon AD, et al. (2018) Human-like hip joint loading in *Australopithecus africanus* and *Paranthropus robustus*. *J Hum Evol* **121**, 12–24.

Saers JP, Cazorla-Bak Y, Shaw CN, et al. (2016) Trabecular bone structural variation throughout the human lower limb. *J Hum Evol* **97**, 97–108.

Samuel DS, Nauwelaerts S, Stevens JM, et al. (2018) Hand pressures during arboreal locomotion in captive bonobos (*Pan paniscus*). *J Exp Biol*, **221**, e170910.

Sarmiento EE (1988) Anatomy of the hominoid wrist joint: its evolutionary and functional implications. *Int J Primatol* **9**, 281–345.

Sarmiento EE (1994) Terrestrial traits in the hands and feet of gorillas. *Am Mus Novit* **3091**, 1–56.

Sarringhaus LA, Stock JT, Marchant LF, et al. (2005) Bilateral asymmetry in the limb bones of the chimpanzee (*Pan troglodytes*). *Am J Phys Anthropol* **128**, 840–845.

Scherf H, Tilgner R (2009) A new high-resolution computed tomography (CT) segmentation method for trabecular bone architectural analysis. *Am J Phys Anthropol* **140**, 39–51.

Scherf H, Wahl J, Hublin JJ, et al. (2016) Patterns of activity adaptation in humeral trabecular bone in Neolithic humans and present-day people. *Am J Phys Anthropol* **159**, 106–115.

Schlager S (2017) Morpho and Rvcg-shape analysis in R: R-packages for geometric morphometrics, shape analysis and surface manipulations. In: *Statistical Shape and Deformation Analysis: Methods, Implementation and Applications* (eds Zheng G, Li S, Székely G), pp. 217–256. Cambridge: Academic Press.

Schmitt D, Zeininger A, Granatosky MC (2016) Patterns, variability, and flexibility of hand posture during locomotion in primates. In: *The Evolution of the Primate Hand* (eds Kivell T, Lemelin P, Richmond B, Schmitt D), pp. 345–369. New York: Springer.

Skinner MM, Stephens NB, Tsegai ZJ, et al. (2015a) Human-like hand use in *Australopithecus africanus*. *Science* **347**, 395–399.

Skinner MM, Stephens NB, Tsegai ZJ, et al. (2015b) Response to comment on 'Human-like hand use in Australopithecus africanus'. *Science* **348**, 1101.

Smith RJ (2016) Explanations for adaptations, just-so stories, and limitations on evidence in evolutionary biology. *Evol Anthropol* **25**, 276–287.

Stephens NB, Kivell TL, Gross T, et al. (2016) Trabecular architecture in the thumb of *Pan* and *Homo*: implications for investigating hand use, loading, and hand preference in the fossil record. *Am J Phys Anthropol* **161**, 603–619.

Stephens NB, Kivell TL, Pahr DH, et al. (2018) Trabecular bone patterning across the human hand. *J Hum Evol*, **123**, 1–23.

Su A, Wallace IJ, Nakatsukasa M (2013) Trabecular bone anisotropy and orientation in an Early Pleistocene hominin talus from East Turkana, Kenya. *J Hum Evol* **64**, 667–677.

Sugardjito J, Cant JG (1994) Geographic and sex differences in positional behavior of orang-utans. *Treubia* **31**, 31–41.

Sugardjito J, van Hooff J (1986) Age-sex class differences in the positional behavior of the Sumatran orangutan (*Pongo pygmaeus abelii*) in the Gunung Leuser National Park, Indonesia. *Folia Primatol* **47**, 14–25.

Susman RL (1979) Comparative and functional morphology of hominoid fingers. *Am J Phys Anthropol* **50**, 215–236.

Susman RL (1984) The locomotor behavior of *Pan paniscus* in the Lomako Forest. In: *The Pygmy Chimpanze* (ed. Susman RL), pp. 369–393. Boston: Springer.

Susman RL, Badrian NL, Badrian AJ (1980) Locomotor behaviour of *Pan paniscusin* Zaire. *Am J Phys Anthropol* **53**, 69–80.

Sylvester AD, Terhune CE (2017) Trabecular mapping: leveraging geometric morphometrics for analyses of trabecular structure. *Am J Phys Anthropol* **163**, 553–569.

Thompson NE, Ostrofsky KR, McFarlin SC, et al. (2018) Unexpected terrestrial hand posture diversity in wild mountain gorillas. *Am J Phys Anthropol* **166**, 84–94.

Thorpe SK, Crompton RH (2005) Locomotor ecology of wild orangutans (*Pongo pygmaeus abelii*) in the Gunung Leuser Ecosystem, Sumatra, Indonesia: A multivariate analysis using log-linear modelling. *Am J Phys Anthropol* **127**, 58–78.

Thorpe SK, Crompton RH (2006) Orangutan positional behavior and the nature of arboreal locomotion in Hominoidea. *Am J Phys Anthropol* **131**, 384–401.

Tsegai ZJ, Kivell TL, Gross T, et al. (2013) Trabecular bone structure correlates with hand posture and use in hominoids. *PLoS ONE* **8**, e78781.

Tsegai ZJ, Stephens NB, Treece GM, et al. (2017) Cortical bone mapping: an application to hand and foot bones in hominoids. *CR Palevol* **16**, 690–701.

Tsegai ZJ, Skinner MM, Pahr DH, et al. (2018) Systemic patterns of trabecular bone across the human and chimpanzee skeleton. *J Anat*, **232**, 641–656.

Tuttle RH (1967) Knuckle-walking and the evolution of hominoid hands. *Am J Phys Anthropol* **26**, 171–206.

Tuttle RH, Basmajian JV (1978) Electromyography of pongid shoulder muscles. III. Quadrupedal positional behavior. *Am J Phys Anthropol*, **49**, 57–69.

Tuttle RH, Watts DP (1985) The positional behavior and adaptive complexes of Pan (Gorilla). In: *Primate Morphophysiology, Locomotor Analyses and Human Bipedalism* (ed. Kondo S), pp. 261–288. Tokyo: University of Tokyo Press.

Uchiyama T, Tanizawa T, Muramatsu H, et al. (1999) Three-dimensional microstructural analysis of human trabecular bone in relation to its mechanical properties. *Bone* **25**, 487–491.

Wunderlich RE, Jungers WL (2009) Manual digital pressures during knuckle-walking in chimpanzees (*Pan troglodytes*). *Am J Phys Anthropol* **139**, 394–403.

Yeh HC, Wolf BS (1977) Radiographic anatomical landmarks of the metacarpo-phalangeal joints. *Radiology* **122**, 353–355.

Zeininger A, Richmond BG, Hartman G (2011) Metacarpal head biomechanics: a comparative backscattered electron image analysis of trabecular bone mineral density in *Pan troglodytes*, *Pongo pygmaeus*, and *Homo sapiens*. *J Hum Evol* **60**, 703–710.

Zeininger A, Patel BA, Zipfel B, et al. (2016) Trabecular architecture in the StW 352 fossil hominin calcaneus. *J Hum Evol* **97**, 145–158.

Zhou G-Q, Pang Z-H, Chen Q-Q, et al. (2014) Reconstruction of the biomechanical transfer path of femoral head necrosis: a subject-specific finite element investigation. *Comput Biol Med* **52**, 96–101.

Zihlman AL (1984) Body build and tissue composition in *Pan paniscus* and *Pan troglodytes*, with comparisons to other hominoids. In: *The Pygmy Chimpanzee* (ed. Susman RL), pp. 179–200. Boston: Springer.

Supporting Information

Additional Supporting Information may be found in the online version of this article:

Fig. S1. Repeatability tests of landmarks.

Fig. S2. DA plots showing species differences within each metacarpal head.

Fig. S3. DA PCA plots showing ray differences within each species.

Fig. S4 A captive orangutan engaged in a diagonal 'double-locked' grip around a piece of string.

Fig. S5. *Gorilla* average RBV/TV by sex, mapped to average models of right Mc heads in distal view for (A) Male Mc5, (B) Male Mc2, (C) Female Mc5 and (D) Female Mc2, specimens. Note that the radio-ulnar bias is present in both sexes (see main text for details).

Fig. S6. Landmark template projected onto Mc3s of individual (A) *Gorilla gorilla*, (B) *Pan troglodytes,* (C) *Pan paniscus* and (d) *Pongo pygmaeus* specimens.

Fig. S7. Species average absolute BV/TV, mapped to average models of each Mc head in (A) distal, (B) palmar and (C) dorsal views.

Table S1. Descriptive statistics of absolute *Z*-scores from significant pair-wise inter-species landmark comparisons.

Table S2. Descriptive statistics of absolute *Z*-scores from significant pair-wise inter-ray landmark comparisons.